

MODELLING  
METHODOLOGY  
FOR PHYSIOLOGY AND  
MEDICINE

EWART CARSON  
CLAUDIO COBELLI



# Modelling Methodology for Physiology and Medicine

# Academic Press Series in Biomedical Engineering

The focus of this series will be twofold. First, the series will produce a series of core text/references for biomedical engineering undergraduate and graduate courses. With biomedical engineers from a variety of engineering and biomedical backgrounds, it will be necessary to create a new cross-disciplinary teaching and self-study books. Second, the series will also develop handbooks for each of the major subject areas of biomedical engineering.

The series editor, Joseph Bronzino, is one of the most renowned biomedical engineers in the world. Joseph Bronzino is the Vernon Roosa Professor of Applied Science at Trinity College in Hartford, Connecticut.

# Modelling Methodology for Physiology and Medicine

Ewart Carson, Editor

*Centre for Measurement and Information in Medicine  
City University  
London, England*

Claudio Cobelli, Editor

*Dipartimento di Elettronica  
Universita di Padova  
Padova, Italy*



**ACADEMIC PRESS**

---

*An Imprint of Elsevier*

San Diego San Francisco New York  
Boston London Sydney Tokyo

This book is printed on acid-free paper. ☺

Copyright © 2001 by Academic Press

All rights reserved.

No part of this publication may be reproduced or transmitted in any form or by any means, electronic or mechanical, including photocopy, recording, or any information storage and retrieval system, without permission in writing from the publisher.

Permissions may be sought directly from Elsevier's Science and Technology Rights Department in Oxford, UK. Phone: (44) 1865 843830, Fax: (44) 1865 853333, e-mail: [permissions@elsevier.co.uk](mailto:permissions@elsevier.co.uk). You may also complete your request on-line via the Elsevier homepage: <http://www.elsevier.com> by selecting "Customer Support" and then "Obtaining Permissions".

**ACADEMIC PRESS**

*An Imprint of Elsevier*

525 B Street, Suite 1900, San Diego, CA 92101-4495, USA

<http://www.academicpress.com>

Academic Press

Harcourt Place, 32 Jamestown Road, London NW1 7BY, UK

**Library of Congress Catalog Card Number: 00-104369**

**ISBN: 0-12-160245-1**

Printed in the United States of America

05 MB 9 8 7 6 5 4 3 2

# Contents

List of Contributors	xiii
Preface	xv

## Chapter 1

### An Introduction to Modelling Methodology

*Claudio Cobelli and Ewart Carson*

<b>1.1 Introduction</b>	<b>1</b>
<b>1.2 The Need for Models</b>	<b>2</b>
<b>1.3 Approaches to Modelling</b>	<b>4</b>
<b>1.4 Simulation</b>	<b>7</b>
<b>1.5 Model Identification</b>	<b>8</b>
<b>1.6 Model Validation</b>	<b>11</b>
<b>1.7 Reference</b>	<b>13</b>

## Chapter 2

### Control in Physiology And Medicine

*Ewart Carson, Tom Hennessy, and Abdul Roudsari*

<b>2.1 Introduction</b>	<b>15</b>
<b>2.2 A Systems and Control Approach</b>	<b>15</b>
<b>2.3 Control Mechanisms in Physiology</b>	<b>17</b>
<b>2.4 Control System Representations of the Clinical Process</b>	<b>24</b>
<b>2.5 Control System Approaches to Drug Therapy Planning and Administration</b>	<b>35</b>

<b>2.6 Conclusions</b>	<b>42</b>
<b>2.7 References</b>	<b>43</b>

## Chapter 3

### Deconvolution

*Giovanni Sparacino, Giuseppe De Nicolao, and Claudio Cobelli*

<b>3.1 Introduction</b>	<b>45</b>	
<b>3.2 Problem Statement</b>	<b>46</b>	
<b>3.3 Difficulty of the Deconvolution Problem</b>		<b>49</b>
<b>3.4 The Regularization Method</b>	<b>54</b>	
<b>3.5 Other Deconvolution Methods</b>	<b>68</b>	
<b>3.6 Conclusions</b>	<b>71</b>	
<b>3.7 Acknowledgements</b>	<b>72</b>	
<b>3.8 References</b>	<b>72</b>	

## Chapter 4

### *A priori* Identifiability of Physiological Parametric Models

*Maria Pia Saccomani, Leontina D'Angio', Stefania Audoly, and Claudio Cobelli*

<b>4.1 Introduction</b>	<b>77</b>	
<b>4.2 The System-Experiment Model</b>	<b>79</b>	
<b>4.3 <i>A Priori</i> Identifiability</b>	<b>80</b>	
<b>4.4 Available Methods</b>	<b>81</b>	
<b>4.5 An Identifiability Algorithm for Nonlinear Models</b>		<b>85</b>
<b>4.6 An Identifiability Algorithm for Linear Compartmental Models</b>	<b>93</b>	
<b>4.7 Conclusions</b>	<b>100</b>	
<b>4.8 References</b>	<b>101</b>	
<b>Appendix A: The Characteristic Set</b>		<b>103</b>
<b>Appendix B: THE Gröbner Basis</b>		<b>104</b>

## Chapter 5

### Parameter Estimation

*Roman Hovorka and Paolo Vicini*

<b>5.1 Introduction</b>	<b>107</b>
<b>5.2 Least Squares and Maximum Likelihood Estimators</b>	<b>108</b>

<b>5.3 Bayesian Estimator</b>	<b>126</b>
<b>5.4 Population Kinetic Analysis</b>	<b>136</b>
<b>5.5 Acknowledgement</b>	<b>148</b>
<b>5.6 References</b>	<b>148</b>

## Chapter 6

### Tracer Experiment Design for Metabolic Fluxes Estimation in Steady and Nonsteady State

*Andrea Caumo and Claudio Cobelli*

<b>6.1 Introduction</b>	<b>153</b>
<b>6.2 Fundamentals</b>	<b>153</b>
<b>6.3 Accessible-Pool and System Fluxes</b>	<b>156</b>
<b>6.4 The Tracer Probe</b>	<b>158</b>
<b>6.5 Estimation of Tracee Fluxes in Steady State</b>	<b>160</b>
<b>6.6 Estimation of Nonsteady-State Fluxes</b>	<b>165</b>
<b>6.7 Conclusions</b>	<b>176</b>
<b>6.8 References</b>	<b>177</b>

## Chapter 7

### Physiological Modelling of Positron Emission Tomography Images

*Alessandra Bertoldo and Claudio Cobelli*

<b>7.1 Introduction</b>	<b>179</b>
<b>7.2 Modeling Strategies</b>	<b>180</b>
<b>7.3 Positron Emission Tomography Measurement Error</b>	<b>182</b>
<b>7.4 Models of Regional Glucose Metabolism</b>	<b>185</b>
<b>7.5 Models of [<sup>15</sup>O]H<sub>2</sub>O Kinetics to Assess Blood Flow</b>	<b>195</b>
<b>7.6 Models of the Ligand-Receptor System</b>	<b>199</b>
<b>7.7 Conclusions</b>	<b>207</b>
<b>7.8 References</b>	<b>208</b>

## Chapter 8

### Identification and Physiological Interpretation of Aortic Impedance in Modelling

*Roberto Burattini*



<b>8.1 Introduction</b>	<b>213</b>
<b>8.2 The Modelling Process and Related Problems of Identifiability and Determinacy</b>	<b>216</b>
<b>8.3 Vascular Impedance</b>	<b>217</b>
<b>8.4 Data-Driven Models of Vascular Impedance (Frequency Response Technique)</b>	<b>221</b>
<b>8.5 Historical Development of Windkessel Models</b>	<b>222</b>
<b>8.6 Where Windkessel Models' Identification Meets Physiological Interpretation</b>	<b>228</b>
<b>8.7 Contradictions in Clinically Oriented Compliance Estimation Methods (How the Viscoelastic Windkessel Resolves them)</b>	<b>231</b>
<b>8.8 Distributed Description of Linear Arterial Systems to Infer Aortic Wave Reflection</b>	<b>235</b>
<b>8.9 Identifiability: A Key Issue in the Assessment of Physiological Relevance of T-Tube Model</b>	<b>242</b>
<b>8.10 Conclusions</b>	<b>247</b>
<b>8.11 References</b>	<b>248</b>

## Chapter 9

### Mathematical Modelling of Pulmonary Gas Exchange

*Stephen E. Rees, Søren Kjærgaard, and Steen Andreassen*

<b>9.1 Standard Equations Used to Describe Gas Transport in the Lungs</b>	<b>253</b>
<b>9.2 Models of Diffusion Limitation</b>	<b>258</b>
<b>9.3 Models of Ventilation Perfusion Mismatch</b>	<b>266</b>
<b>9.4 Application of Mathematical Models of Ventilation, Perfusion, and Diffusion</b>	<b>269</b>
<b>9.5 References</b>	<b>273</b>
<b>Appendix A: GLOSSARY</b>	<b>276</b>
<b>Appendix B: Calculations Necessary to Convert Inspired Gas at ATPD to BTPS</b>	<b>277</b>

## Chapter 10

### Mathematical Models of Respiratory Mechanics

*Gianluca Nucci and Claudio Cobelli*

<b>10.1 Introduction</b>	<b>279</b>
<b>10.2 Breathing Mechanics: Basic Concepts</b>	<b>280</b>

<b>10.3 First-Order Models</b>	<b>282</b>
<b>10.4 Second-Order Models</b>	<b>289</b>
<b>10.5 Respiratory Oscillation Mechanics</b>	<b>292</b>
<b>10.6 Simulation Models of Breathing Mechanics</b>	<b>295</b>
<b>10.7 Conclusions</b>	<b>300</b>
<b>10.8 References</b>	<b>301</b>

## Chapter 11

### Insulin Modelling

*Gianna Maria Toffolo*

<b>11.1 Introduction</b>	<b>305</b>
<b>11.2 Models of Whole-body Insulin Kinetics</b>	<b>306</b>
<b>11.3 An Organ Model of Insulin Secretion</b>	<b>310</b>
<b>11.4 Estimation of Insulin Secretion by Deconvolution</b>	<b>320</b>
<b>11.5 A Structural Model to Estimate Insulin Secretion and Secretory Indices</b>	<b>321</b>
<b>11.6 Estimation of Hepatic Insulin Extraction</b>	<b>329</b>
<b>11.7 Conclusions</b>	<b>331</b>
<b>11.8 References</b>	<b>333</b>

## Chapter 12

### Glucose Modeling

*Andrea Caumo, Monica Simeoni, Claudio Cobelli*

<b>12.1 Introduction</b>	<b>337</b>
<b>12.2 Models of Whole-body Kinetics in Steady State</b>	<b>337</b>
<b>12.3 Models of Regional Kinetics in Steady State</b>	<b>346</b>
<b>12.4 Models of Whole-body Kinetics in Nonsteady State</b>	<b>351</b>
<b>12.5 Models of Glucose and Insulin Control on Glucose Metabolism</b>	<b>359</b>
<b>12.6 Simulation Models</b>	<b>366</b>
<b>12.7 Conclusions</b>	<b>369</b>
<b>12.8 References</b>	<b>370</b>

## Chapter 13

### Blood-Tissue Exchange Modelling

*Paolo Vicini*

<b>13.1 Introduction</b>	<b>373</b>	
<b>13.2 Experimental Approaches</b>	<b>375</b>	
<b>13.3 Models of Blood-Tissue Exchange</b>		<b>377</b>
<b>13.4 Conclusions</b>	<b>397</b>	
<b>13.5 References</b>	<b>397</b>	

Index	403
-------	-----

# List of Contributors

Steen Andreassen	Department of Medical Informatics, Aalborg University, Aalborg, Denmark
Alessandra Bertoldo	Dipartimento di Elettronica e Informatica, Università di Padova, Padova, Italy
Roberto Burattini	Dipartimento di Elettronica e Automatica, Università di Ancona, Ancona, Italy Ancona, Italy
Ewart Carson	Centre for Measurement and Information in Medicine, City University, London, United Kingdom
Andrea Caumo	Scientific Institute San Raffaele, Milano, Italy
Claudio Cobelli	Dipartimento di Elettronica e Informatica, Università di Padova, Padova, Italy
Giuseppe De Nicolao	Dipartimento di Informatica e Sistemistica, Università di Pavia, Pavia, Italy
Tom Hennessy	Centre for Measurement and Information in Medicine, City University, London, United Kingdom
Roman Hovorka	Centre for Measurement and Information in Medicine, City University, London, United Kingdom
Søren Kjaergaard	Department of Medical Informatics, Aalborg University, Aalborg, Denmark
Gianluca Nucci	Dipartimento di Elettronica e Informatica, Università di Padova, Padova, Italy
Stephen Rees	Department Medical Informatics, Aalborg University, Aalborg, Denmark

- Abdul Roudsari      Centre for Measurement and Information in Medicine,  
City University, London, United Kingdom
- Maria Pia Saccomani      Dipartimento di Elettronica e Informatica, Universita'  
di Padova, Padova, Italy
- Monica Simeoni      Dipartimento di Elettronica e Informatica, Universita'  
di Padova, Padova, Italy
- Giovanni Sparacino      Dipartimento di Elettronica e Informatica, Universita'  
di Padova, Padova, Italy
- Gianna Toffolo      Dipartimento di Elettronica e Informatica, Universita'  
di Padova, Padova, Italy
- Paolo Vicini      Department of Bioengineering University of Washington,  
Seattle, USA

# Preface

Mathematical modelling is now widely adopted in physiology and medicine to support the life scientist and clinical worker. However, good modelling practice must be based upon sound methodology. This is the focus of this book. It builds upon the basic idea of an integrated methodology for the development and testing of mathematical models. It covers many specific areas of methodology where important advances have taken place over recent years and illustrates the application of good methodological practice in key areas of physiology and medicine.

Over the past few decades, several books have been written on mathematical modelling in physiology and medicine. Some have focused on methodology, while others have centred around a specific area of physiology and medicine. Over the past 20 years, we ourselves have contributed extensively to this field, including our volume from the early 1980s entitled *Mathematical Modelling of Metabolic and Endocrine Systems: Model Formulation, Identification and Validation*, which combined methodological detail with a demonstration of its applicability in relation to metabolics and endocrinology.

This present volume follows suit by combining advances in methodology with demonstrations of its applicability. It is one of two volumes on the theme of modelling included in this Biomedical Engineering series. The other one, which is currently in production, provides an introduction to modelling in physiology. The essence of our other volume is summarized in the first chapter of this book. This book serves as both a stand-alone volume and a complementary work. For the reader who has some experience in modelling, this volume will provide an accessible account of recent advances in the field. For the reader who has absorbed the messages of the introductory volume, the chapters herein build logically upon those insights.

This book has been designed to appeal to all those who wish to advance their knowledge of good modelling practice. It will be useful to postgraduate students and those in the final year of study who have chosen modelling

specialties as part of biomedical engineering or medical or health informatics courses. It is equally designed to meet the needs of advanced practitioners and researchers in the field of modelling as it applies to physiology and medicine.

Although formally an edited text, this volume is the collaborative work of two teams in London and Padova who together have extensive experience in communicating these ideas and concepts to a wide range of audiences, including undergraduate and postgraduate students, and researchers and professionals across a spectrum of disciplines from engineering and informatics to medicine and related clinical professions. Hence, this book has been produced as an integrated work, meant as tutorial in style and containing reference listing at the end of the volume.

In writing this volume, we thank those of our colleagues in our teams who have chosen to work with us in this project. Their support and encouragement has been greatly appreciated, and without their efforts, this volume would not exist. We also wish to thank our friends and colleagues who, over many years, have encouraged us to develop our modelling ideas, whether from their perspective as fellow engineers and computer scientists or from their invaluable viewpoint as physiologists and clinicians. There are many that we would wish to recognize including Riccardo Bonadonna, Derek Cramp, Ludwik Finkelstein, Antonio Lepschy, and Peter Sönksen.

Finally, we thank Joseph Bronzino, Editor-In-Chief of this Biomedical Engineering Series, and Joel Claypool, Jane Phelan, and colleagues at Academic Press for their encouragement, support, and tolerance in working with us to see our ideas come to fruition.

Ewart Carson  
Claudio Cobelli  
London, England and Padova, Italy  
July 2000

# An Introduction to Modelling Methodology

**Claudio Cobelli and Ewart Carson**

## 1.1. INTRODUCTION

The aim of this book is to describe more recent developments in modelling theory and practice in relation to physiology and medicine. The chapters that follow offer detailed accounts of several facets of modelling methodology (Chapters 2–6) as well as demonstration of how such methodological development can be applied in areas of physiology and medicine. This application material, contained in Chapters 7–13, is not intended to be comprehensive. Rather, topics have been chosen that span study in the circulatory and respiratory systems (Chapters 8–10) and key areas of metabolism and endocrinology (Chapters 7 and 11–13). The authors of the respective chapters have very considerable expertise in these areas of physiology and medicine.

Before moving into the more advanced areas of methodology, it is appropriate to review the fundamentals of the modelling process, which put simply can be viewed as a mapping or transforming of a physiological system into a model as shown in Figure 1.1. The process has now reached substantial maturity, and the basic ingredients are well established. This overall modelling framework is described in detail in the accompanying volume (Cobelli and Carson, 2001). In this chapter, we provide a distillation of that framework and revisit the fundamentals upon which the later, more detailed chapters are built.



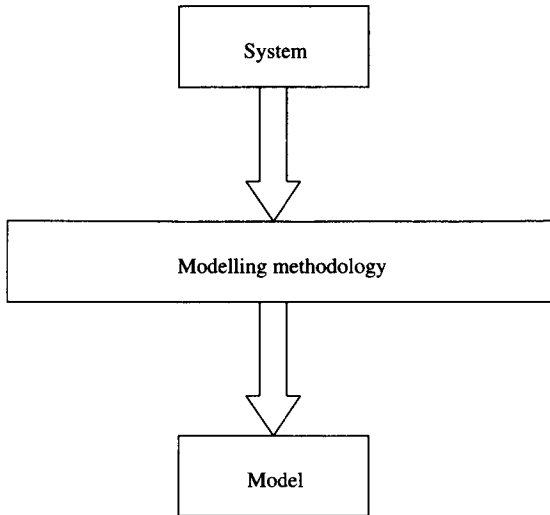


Figure 1.1. Modelling methodology: Transforming a system into a model.

## 1.2. THE NEED FOR MODELS

### 1.2.1. PHYSIOLOGICAL COMPLEXITY

Complexity is what characterises much of physiology, and we must have a method to address this. Complexity manifests itself through elements that comprise any physiological system through the nature of their connectivity, in terms of hierarchy, and through the existence of nonlinear, stochastic, and time-varying effects. Complexity is exhibited at each level of the hierarchy and across levels within the physiological system.

What do we mean by some of these concepts? First, the physiological hierarchy will include the levels of molecule, cell, organ, and organism. Complex processes of regulation and control are evident at each level. Feedback is another key feature that occurs in many forms. It is inherent in chemical reactions within the organism. There are explicit hormonal control mechanisms superimposed upon metabolic processes. The physiological organ systems exhibit explicit control mechanisms. In many instances, there is negative feedback, although examples of positive feedback also exist. Feedback offers examples of control action being taken not only in relation to changes in the value of a physiological variable *per se*, but also in response either to its rate of change or to the integral of its value over a period of time. Some of these concepts of feedback and control are examined in more detail in Chapter 2.

As a result of this physiological complexity, it is not often possible to measure directly (*in vivo*) the quantities of interest. Only indirect measures may be feasible, implying the need for some model to be able to infer the value of the quantity of real interest. Measurement constraints usually mean that it is only possible to obtain readings of blood values of a metabolite when the real interest lies in its value in body tissue. Equally, it is not generally possible to measure the secretions of the endocrine glands.

Overall, this complexity — coupled with the limitations that are imposed upon the measurement processes in physiology and medicine — means that models must be adopted to aid our understanding.

### 1.2.2. MODELS AND THEIR PURPOSES

What do we mean by the term *model*? In essence, it is a representation of reality involving some degree of approximation. Models can take many forms. They can be conceptual, mental, verbal, physical, statistical, mathematical, logical, or graphical in form. For the most part, this volume focuses on mathematical modelling.

Given that a model provides an approximate representation of reality, what is the purpose of modelling activity? As is shown in Figure 1.2, the purpose is a key driver of good modelling methodology. In classic scientific terms, modelling can be used to describe, interpret, predict, or explain. A mathematical expression, for example, a single exponential decay, can provide a compact description of data that approximate to a first-order process. A mathematical model can be used to interpret data collected as part of a lung function test. A model of renal function, which includes representations of the dynamics of urea and creatinine, can be used to predict the time at which a patient

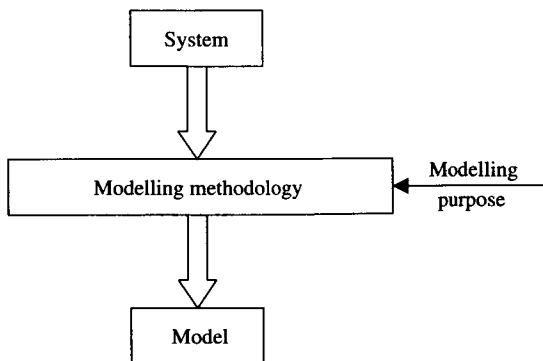


Figure 1.2. The purpose of modelling: A key driver of modelling methodology.

with end-stage renal disease should next undergo haemodialysis. A model of glucose and insulin can be used to gain additional insight into, and explanation of, the complex endocrine dynamics in the diabetic patient.

Rather, more specific purposes for modelling can be identified in the physiological context. These include aiding understanding, testing hypotheses, measuring inferences, teaching, simulating, and examining experimental design. For example, competing models, constituting alternative hypotheses, can be examined to determine which are compatible with physiological or clinical observation. Equally, a model of the relevant metabolic processes, when taken together with measurements of a metabolite made in the bloodstream, can be used to infer the value of that metabolite in the liver. Models also are increasingly used as a medium in teaching and learning processes, where, by means of simulation, the student can be exposed to a richer range of physiological and pathophysiological situations than would be possible in the conventional physiological laboratory setting. Models also can play a powerful role in experimental design. For instance, if the number of blood samples that can be withdrawn from a patient is limited in a given period of time, models can be used to determine the times at which blood samples should be withdrawn to obtain the maximum information from the experiment, for example, in relation to pharmacokinetic or pharmacodynamic effects.

Considering what is meant by a model and its purposes, we now focus on the nature of the process itself. As already indicated, this is the process of mapping from the physiological or pathophysiological system of interest to the completed model, as shown in Figure 1.1. The essential ingredients are model formulation, including determination of the degree to which the model is an approximation of reality; model identification, including parameter estimation; and model validation. These are discussed in the following sections.

### 1.3. APPROACHES TO MODELLING

In developing a mathematical model, two fundamental approaches are possible. The first is based on experimental data and is essentially a data-driven approach. The other is based on a fundamental understanding of the physical and chemical processes that give rise to the resultant experimental data. This can be referred to as *modelling the system*.

#### 1.3.1. MODELLING THE DATA

Models that are based on experimental data are generally known as *data-driven* or *black box models*. Fundamentally, this means seeking quantitative

descriptions of physiological systems based on input-output (I/O) descriptions derived from experimental data collected on the system. Simply put, these are mathematical descriptions of data, with only implicit correspondence to the underlying physiology.

Why should we use such data models? First, they are particularly appropriate where there is a lack of knowledge of the underlying physiology, whether *a priori* knowledge or knowledge acquired directly through measurement. Equally, they are appropriate when an overall I/O representation of the system's dynamics is needed, without knowing specifically how the physiological mechanisms gave rise to such I/O behaviour.

The methodological framework for modelling data is depicted in Figure 1.3. Several specific methods are available for formulating such data models, including time series methods, transfer function analysis, convolution-deconvolution techniques that are restricted to linear systems (discussed in Chapter 3), and impulse response methods.

### 1.3.2. MODELLING THE SYSTEM

In contrast to data modelling, when modelling the system there is an attempt to explicitly represent the underlying physiology, albeit at an appropriate level of approximation and resolution. The degree of approximation will be largely determined by the availability of *a priori* knowledge and the nature of the assumptions that can be made. The basic framework in this case is shown in Figure 1.4.

Models of the system, that is, models that are physiologically based, may be categorised in a number of ways according to the included attributes. This classification, corresponding to the approaches that can be adopted, includes static

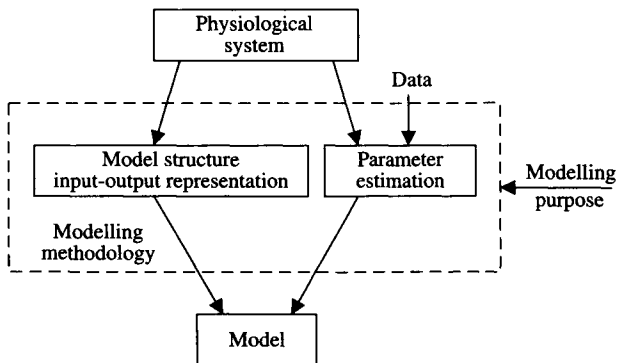
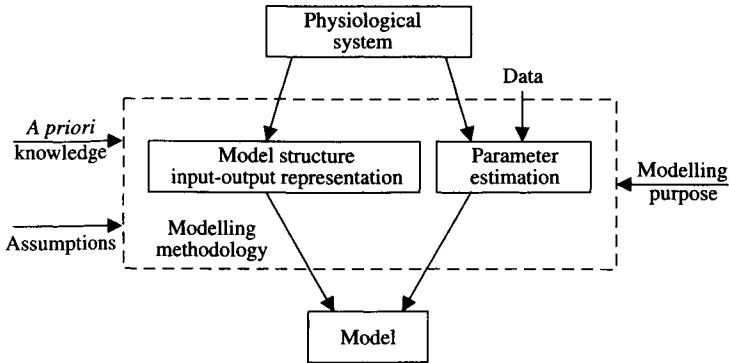


Figure 1.3. Modelling the data: A methodological framework.



**Figure 1.4.** Modelling the system: A methodological framework.

v. dynamic models, deterministic v. stochastic, time-invariant v. time-varying, lumped v. distributed, linear v. nonlinear and continuous v. discrete models. All combinations are possible so one could envisage a dynamic, deterministic, time-invariant, lumped, linear, continuous model in one case or a dynamic, stochastic, time-varying, distributed, nonlinear, discrete model at the other end of the spectrum.

A first classification is into static models and dynamic models. Clearly, static models are restricted to steady-state conditions and do not attempt to capture the richness of a system's dynamics. However, in the circulatory or respiratory context, for example, static models can provide useful relationships between mean pressure, flow, and impedance (or resistance in the linear case). Simple dynamic models have been employed in fields such as cellular dynamics and metabolic compartmental descriptions (e.g., one compartment elimination), and as simple descriptions of circulatory and respiratory dynamics.

In more complex formulations, distributed modelling enables spatial effects to be incorporated as well as the basic system dynamics. For example, a distributed model of the arterial system enables the blood pressure patterns along the length of any blood vessel to be analysed as well as variations of blood pressure over time.

Nonlinear modelling reflects the fact that almost all physiological phenomena are truly nonlinear. In some situations, however, it might be appropriate to assume that linearity applies, for example, if one is simply interested in the dynamics resultant from a small perturbation of the system from some steady-state operating condition. However, if it is the response to a large perturbation that is required (e.g., blood glucose dynamics following a large meal), a full nonlinear model of the relevant portions of the carbohydrate metabolism is needed.

Many physiological systems can be treated as if they were time-invariant; this means that system parameters are assumed not to vary with time. However, there are some circumstances in which this assumption would not hold. One example might be the change in the elastic properties of the blood vessels that occurs over a long period of time. A model that was intended for use over such an extended period would incorporate elastic parameters of the relevant blood vessels that did vary over time. At the other end of the time scale, a model designed to explore the rapid dynamics of the cardiovascular system that occur during the pumping cycle of the heart would incorporate time-varying representations of those parameters corresponding to the elastic properties of the heart chambers.

A further degree of approximation applies whenever it is assumed that a physiological system can be treated as deterministic. In reality there is usually some stochastic component present. If this component is small, it may be acceptable to treat the system as if it were deterministic. Where the stochastic effects are more dominant, as is the case when examining cellular dynamics, then stochasticity must be incorporated into the model, either as stochastic variation of key variables or as stochastic variation in the parameters.

A number of issues relating to model validation (validation is considered in more detail later in the chapter) must be considered at this stage. These include verification of the compatibility of the proposed model with the relevant physiology, regarding the validity of the assumptions, and the degree to which the complexity of the physiology has been reduced for the particular modelling purpose in question. The model also should be checked to ensure it is logically complete and consistent.

## 1.4. SIMULATION

Simulation is the process of solving the model (i.e., the equations that are the realisation of the model) to examine its output behaviour. Typically, this process involves examining the time course of one or more of the variables; in other words, performing computer experiments on the model.

When is simulation required? It can be used either during the process of model building or once the model is completed. During model building, simulation can be performed to clarify aspects of system behaviour to determine whether a proposed model representation is appropriate. This is done by comparison of the model response with experimental data from the same situation. When carried out on a complete, validated model, simulation yields output responses that provide information on system behaviour. Depending on the modelling purpose, this information assists in describing the system, predicting behaviour, or yielding additional insights (i.e., explanations).

Why use simulation? Simulation offers a way forward in situations in which it might not be appropriate, convenient, or desirable to perform particular experiments on the system. Such situations could include those in which experiments cannot be done at all, are too difficult, are too dangerous, are not ethical, or would take too long to obtain results. Therefore, we need an alternative way to experiment. Simulation offers an alternative that can overcome the preceding limitations. Such experimenting can provide information that, depending on the modelling purpose, aids description, prediction, or explanation.

How do we perform simulation? First, we need a mathematical model that is complete; that is, all its parameters are specified and initial conditions are defined for all the variables. If the model is not complete (i.e., has unspecified parameter values), parameter estimation techniques must be employed. Once a complete model is available, it is implemented on the computer. This assumes that the model equations cannot be, or are not being, solved analytically and that a numerical solution of the system is needed. The model is solved on the computer, this process of simulation yielding the time course of the system variables. In technical terms, the computer implementation is done using a standard programming language (e.g., FORTRAN, C) or a specialist simulation package (e.g., MATLAB).

## 1.5. MODEL IDENTIFICATION

### 1.5.1. A FRAMEWORK FOR IDENTIFICATION

To complete the transformation from system to model as depicted in Figure 1.1, we must have both a model structure and fully determined parameters corresponding to that structure. In other words, we need a complete model. However, we may not have such a model. We should by this stage have at least one candidate model, and we may have more than one to choose from. If a single model is incomplete, it will be due to some unknown parameter values. This is true whether the modelling approach adopted has been driven by the data or by the physiology of the system. We may be dealing with the whole model or just part of it. In either case, an integrated identification framework is needed. A schematic representation of this process is given in Figure 1.5.

The solution of this problem requires data. Data sometimes occur from the intrinsic dynamics of the system (e.g., spontaneous oscillations or noise). Electrophysiological signals would be instances of such output dynamics as they relate to brain, muscle, or cardiac function. Usually, however, we must design experiments. The question is then what experiments must be designed to yield appropriate data. Clearly, the I/O data from the experiment must contain

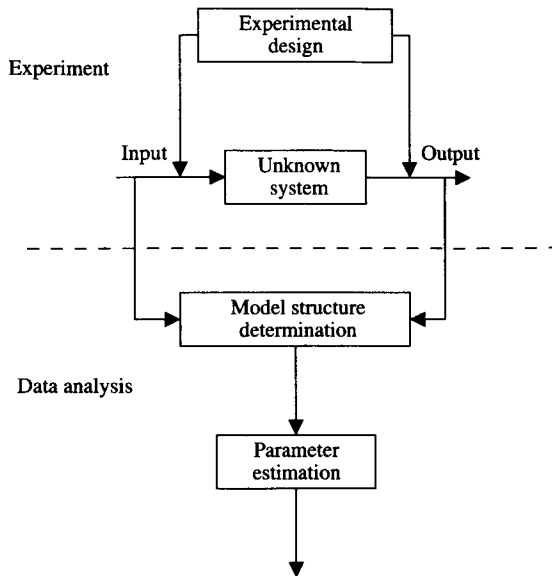


**Figure 1.5.** Model identification.

that part of the model with the unknown parameter values. Tracer methods, as discussed in Chapter 6, offer one approach to data generation convenient for the identification process.

In the identification process, data are mapped into parameter values by the model, where errors can occur in both the data and the model. The first arises as a consequence of measurement errors. The second involves errors in model structure, which arise as a consequence of more than one competing model. There are other types of errors, including noise on test signals and disturbances. However, one cannot address more than one type of noise at a time. In fact, rigorously we can only address measurement errors. Errors in model structure cannot be dealt with explicitly. They can only be solved by considering each competing model structure in turn. Therefore, it is customary to focus on a single model and concentrate on the impact of measurement errors that are assumed to be additive. The available approaches can be divided into two groups: situations with parametric models and those with nonparametric models.

### 1.5.2. IDENTIFICATION OF PARAMETRIC MODELS

The first issue to be addressed is that of identifiability. In essence, this is asking whether it would theoretically be possible to make unique estimates of



all the unknown parameters assuming that the experimental data were complete and noise-free. In other words, the experimental data must be rich enough to estimate all the unknown parameters. Problems of identifiability arise where there is a mismatch between the complexity of the model and the richness of the data. That is, the model is too complex (too many unknown parameters) for the available data, or the data are not sufficient for the model provided. In such cases, one must explore whether the model might, in a manner that retains validity, be reduced or whether the experimental design might be enriched: for example, by making measurements of an additional variable. Issues of identifiability are considered in Chapter 4.

If the model is uniquely identifiable, assuming perfect data, it is possible to proceed directly to estimating the parameters. In some situations, multiple solutions (finite, greater than one) may be theoretically possible for some parameters. In such cases, it might at the stage of validating the complete model be possible to select between these alternatives, such as on the basis of physiological plausibility. Where an infinite number of values is theoretically possible for one or more parameters, remedy must be sought to the mismatch between model and data outlined previously.

A range of techniques exists for parameter estimation once the model has passed the identifiability test. Those that are most widely adopted use an approach based on linear or nonlinear least squares. These are least demanding in terms of their requirements for *a priori* knowledge. In contrast, maximum likelihood and Bayesian estimation, which are discussed in detail in Chapter 5, require *a priori* knowledge (or assumptions) regarding the statistics of the situation being modelled.

Some effort has also been directed to the problem of “optimal experimental design.” This has largely focused on the interaction between the features of an experiment in which data are obtained as a set of discrete values over the experimental period following the application of an input test signal and the information content of the experiment in relation to the quality of the parameter values obtained by the estimating process.

### 1.5.3. IDENTIFICATION OF NONPARAMETRIC MODELS

Nonparametric models arise from some of the situations described earlier in which a data modelling approach has been adopted. In other words, an overall I/O model description has been obtained, such that it is specified as an integral equation. Such a description has essentially three ingredients: the input, the output, and the impulse response that provides the connection between them. Two of these are known, and the third is to be determined. The most usual situation is when the output is specified. Techniques available for solving this

problem can basically be classified as raw deconvolution and deterministic regularisation.

## 1.6. MODEL VALIDATION

Validating a model is essentially examining whether it is good enough in relation to its intended purpose. This assumes that, in a Popperian sense, it can be tested. Clearly, no model can have absolute unbounded validity given that, by definition, a model is an approximation of reality. If one is working with a set of competing candidate models, the validation process involves determining which of them is best in relation to its intended purpose. A valid model is one that has successfully passed through the validation process.

Validation is integral to the overall modelling process. It is an activity that should take place both during model building and upon model completion. The issue of validity testing during the process of model formulation was addressed in section 1.3.2. At this stage, we shall assume that the model is complete; that is, it has no unspecified parameters. The essence of the validation process at this stage is shown in Figure 1.6.

It cannot be stressed too strongly that in examining the validity of the complete model, the process is dependent upon model purpose; that is, it is problem-specific. The implication is that we are testing whether appropriate components are contained in the model. For example, we would be testing the appropriateness of model structure in relation to any intended use for hypothesis testing parameters that would be meaningful in the context of a specific disease (i.e., change in parameter values could correspond to the change from a healthy state to a diseased state). Dependent upon the purpose, usually some features of the model and system output (i.e., experimental output data) must correspond sufficiently for the same input (an acceptably small difference between them). In other words, within the necessary domain of validity, we are testing whether the model is credible. The model performance also may be tested out with its nominal specified domain of validity to define the effective boundary of the actual domain within which it may be considered valid.

The basic approach in validating a single model is to compare the model and system behaviour, based on appropriate output features of response. Any mismatch between system and model output should be analysed for plausibility of behaviour.

For cases in which formal parameter estimation procedures have been employed for the model, additional quantitative tools are available in the validation process. These include examining the residuals of the mismatch and the plausibility of the parameter estimates where the parameters have a clear physiological counterpart. In the case of competing models, choice can

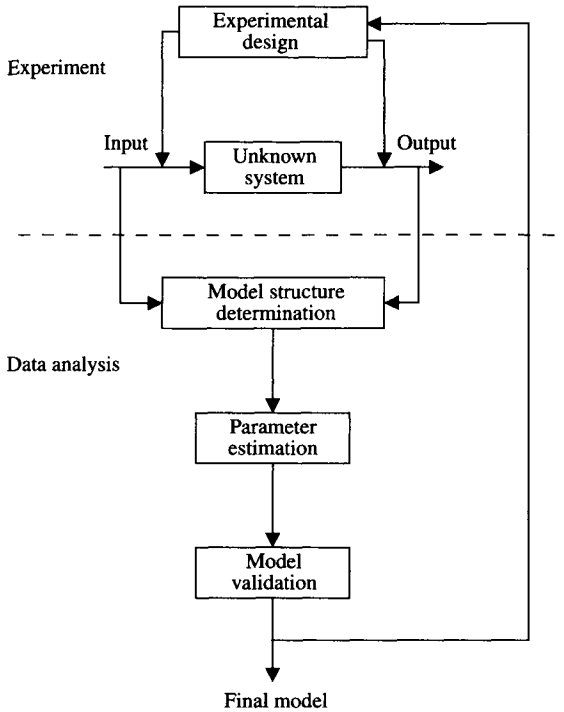


**Figure 1.6.** Validation of the complete model.

be aided by examining the parsimony of the models (by using the Akaike criterion in the case of linear models) and the features of response yielded by the model, again testing the plausibility.

In conclusion, one should always remain critical of a model and not love it too much! All models are approximations; hence, one should always be prepared to include new facts and observations. A good model (in a Popperian sense) is one that is clearly falsifiable and thus is readily capable of bringing about its own downfall. One also should remember that in situations of complexity, it may be appropriate to think of a set of models, where each would have its own (distinct) domain of validity. It then becomes a case of choosing the most appropriate in relation to, for instance, the level in the physiological hierarchy that is being represented and the time scale of interest in relation to dynamic response (e.g., short-term or long-term). A successful outcome to the modelling process is critically dependent on both the quality of the model and the quality of experimental data (see Figure 1.7).

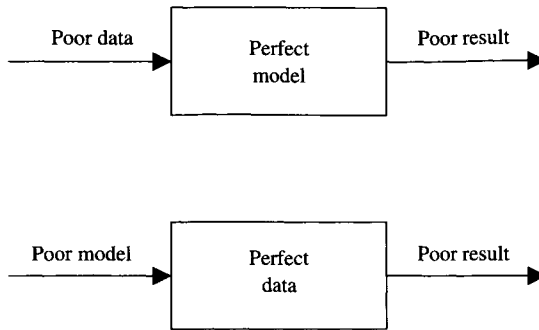


**Figure 1.7.** The garbage paradigm.

Following this brief tour through basic ingredients of good modelling methodology, subsequent chapters elaborate on methodological issues of current importance and demonstrate their applicability in selected domains of physiology and medicine.

## 1.7. REFERENCE

Cobelli, C. and E. R. Carson. 2001. *An Introduction to Physiological Modeling*. New York: Academic Press.

This Page Intentionally Left Blank

---

## Chapter 2

# Control in Physiology and Medicine

**Ewart Carson, Tom Hennessey, and Abdul Roudsari**

## 2.1. INTRODUCTION

This chapter examines ways in which concepts of control relate to the study of physiological and medical systems, both in the insight that can be gained and in therapy planning as part of the patient management processes.

The chapter introduces the conceptually simple, but powerful, framework of the four-element cybernetic model that provides a basis for examining the dynamics that occur in physiology and medicine. This basic model can be further developed at various levels of resolution. This is followed by an exploration of the basic control concepts, demonstrating, through examples, their relevance in describing and interpreting the processes and regulation of physiological dynamics.

The chapter focuses on the basic feedback model, developing this framework so as to encompass both the diagnostic and the therapeutic processes. It is then shown how this framework can be employed to specify the requirements for health care delivery systems, with an example from chronic disease management. Finally, the planning of drug therapy is viewed as a control problem, demonstrating the relevance of a feedback modelling framework, illustrating this view of drug administration with diabetes.

## 2.2. A SYSTEMS AND CONTROL APPROACH

The analysis of complex dynamic systems in physiology and medicine requires the use of modelling methods and techniques. A general methodology

for mathematical modelling of well-structured dynamic systems has already been presented in Chapter 1. Modelling provides a bridge between the real system and the resultant model.

The dynamic processes that take place in a system may represent the natural or involuntary operation or a series of changes in a situation. Such situational behaviour may appear to be goal-seeking, a special case of which is adaptive behaviour. Such adaptation is the result of environmental change. Changes in the environment (e.g., disturbances) may be acute. These will require short-term adaptive behaviour via regulation and control. If the changes are chronic, longer-term regulation and control mechanisms must maintain system integrity. Thus, a system requires a variety of control mechanisms designed to cope with environmental variables (Deutsch *et al.*, 1994). These mechanisms have evolved effectively across a range of physiological systems and are put in place in acute and chronic disease management.

One special interaction between the elements of a system is the feedback relationship. In general, feedback is a mutual causality in which variable  $x$  affects variable  $y$ , and in turn  $y$  affects  $x$ . If an increase in  $y$  effects a change in  $x$  that tends to decrease  $y$ , feedback is considered negative. Obvious physiological examples include body temperature regulation and the interaction of glucose and insulin in the case of a healthy subject. In contrast, positive feedback (e.g., the classic wage-price spiral) is a situation in which an increase in  $y$  causes a change in  $x$ , which then tends to increase  $y$ .

Feedback processes can be represented diagrammatically in the classic cybernetic loop with its four interlinked components, as shown in Figure 2.1. The control unit (controller) compares the measured state of the controlled process, via the information system, and acts upon any discrepancy, or error, between this and the desired state of the controlled process. This desired state may be regarded as a reference or set-point value. The output from the control unit is the control (or controlling) signal. The level of the regulated variable is measured by a sensor that forms part of the information system in the feedback loop. The function of the controller is to help maintain a given value of

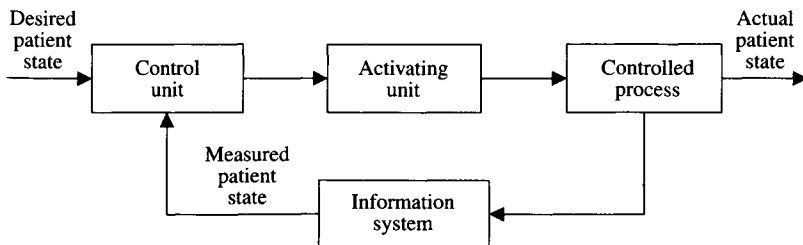


**Figure 2.1.** The classic four-element cybernetic feedback loop.

the controlled variable. The control signal (which can be considered the decision made by the decision-maker) is applied to the controlled process via the actuating or activating unit that effects the control action upon the controlled process.

If the controlling signal is fed directly to the controlled unit, the situation is termed *closed-loop feedback control*. In contrast, if a human agent is interposed, such that the control action is not automatic but is effected via that human agent, the situation is referred to as *open-loop feedback control*.

Any physiological system, which typically includes feedback control loops, functions within its environment. Environmental variables, or variables that have an effect on the system but are not affected by it, may control the regulating system or may simply disturb the level of the regulated variable. For example, the temperature of the human body is precisely regulated to within  $0.1^{\circ}\text{C}$ , with the centre for temperature regulation found within the brain. This centre receives information regarding temperature sensed in the skin. If the temperature is too low, messages are transmitted from that centre to the muscles to increase oxidation and the heat supply to the body. The reverse applies if the body temperature is too high. These are not the only heat-regulatory mechanisms. A high temperature produces dilatation of skin capillaries and increased heat loss by radiation. Other mechanisms include the excretion of sweat and loss of heat by evaporation (Deutsch *et al.*, 1994).

## 2.3. CONTROL MECHANISMS IN PHYSIOLOGY

The example of thermoregulation illustrates a rich variety of control mechanisms found in functioning physiological systems. There are mechanisms whose impairment gives rise to the majority of disease states.

Feedback regulatory mechanisms as means of effecting control are to be found in a variety of forms and locations within the human organism, both within chemical reactions occurring in the body and through the combination of individual effects. Some of this complexity can be seen in Figure 2.2, which shows the hierarchy of chemical reactions within the cell. It also shows how the totality of cellular effects, combined with the effects of explicit hormonal control, integrate to yield the physiological behaviour of the overall system.

### 2.3.1. INHERENT FEEDBACK REGULATION

At each level of the hierarchy of chemical reactions in the cell, feedback control mechanisms can be seen. However, in addition to a variety of explicit feedback control mechanisms, some of which are illustrated in the following



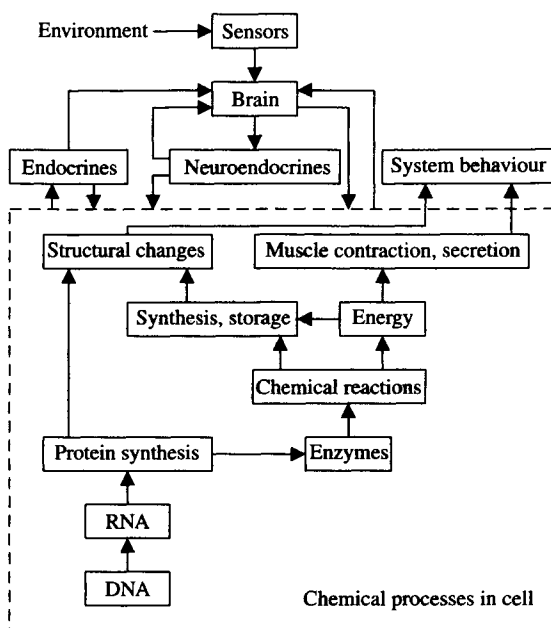


**Figure 2.2.** The hierarchy of control mechanisms in the human organism from a chemical perspective.

paragraph, regulation of a feedback nature can be found whenever chemical dynamics are in operation.

Consider the case of a simple chemical reaction taking place within the organism, in which it may be assumed that the rate of decrease (loss) of concentration of the metabolite  $M$  taking part in that reaction is directly proportional to its concentration. Mathematically, this can be expressed in the form:

$$dC_M/dt = -kC_M \quad (2.1)$$

where  $C_M$  is the concentration of metabolite  $M$ , and  $k$  is the rate constant for the reaction. Expressing (2.1) in the form of a signal flow diagram (Figure 2.3), it can be seen that there is effectively a negative feedback connection. That is, an increase in concentration results in an increase in the negative rate of change of concentration, leading, via the process of integrating that rate of concentration change, to a reduction in the concentration itself. In other words, there is a process that regulates the concentration of that metabolite. This is an example of an *inherent* regulatory effect exhibited in this chemical reaction, despite no *physical* feedback link.

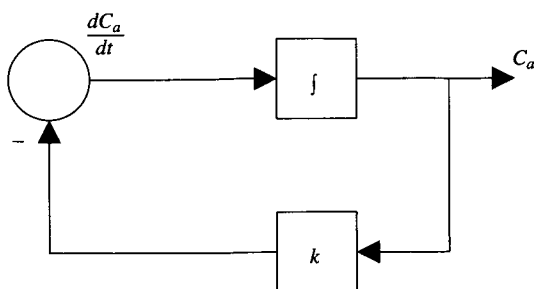


**Figure 2.3.** The signal flow diagram of a simple, first-order chemical reaction.

The phenomenon of inherent feedback that has been revealed is contained in any dynamic process that can be described mathematically in this way, represented in the next section in differential equation form.

### 2.3.2. ENZYME CONTROL

This concept of feedback control can next be seen at the level of enzymic activity. Consider the simplest enzyme reaction in which free-enzyme  $E$  and chemical substrate  $S$  react, reversibly, to yield an intermediate complex  $X$  that proceeds further to yield the product of the chemical reaction  $P$  and free-enzyme  $E$ . In essence the action of the enzyme as a chemical catalyst promotes the conversion of substrate  $S$  into product  $P$ .

Assuming that these chemical reactions can be approximated as first order, the following rate equations can be written:

$$d[S]/dt = -k_1[S][E] + k_2[X] \quad (2.2)$$

$$d[X]/dt = k_1[S][E] - (k_2 + k_3)[X] \quad (2.3)$$

$$d[E]/dt = (k_2 + k_3)[X] - k_1[S][E] \quad (2.4)$$

$$d[P]/dt = k_3[X] \quad (2.5)$$

where  $[S]$ ,  $[X]$ ,  $[E]$ , and  $[P]$  are the concentrations of  $S$ ,  $X$ ,  $E$ , and  $P$ , respectively. The rate constant of the respective reactions are denoted by  $k_1 - k_4$ . Figure 2.4 depicts the signal flow diagram for this simplest of enzymic reactions. The reversible reaction, whereby  $E$  and  $S$  combine to yield the intermediate complex  $X$ , gives rise to two negative feedback loops tending to regulate  $E$  and  $S$ . On the other hand, the regenerative cycle  $E \rightarrow X \rightarrow E$  leads to a positive feedback loop with a potentially destabilising effect.

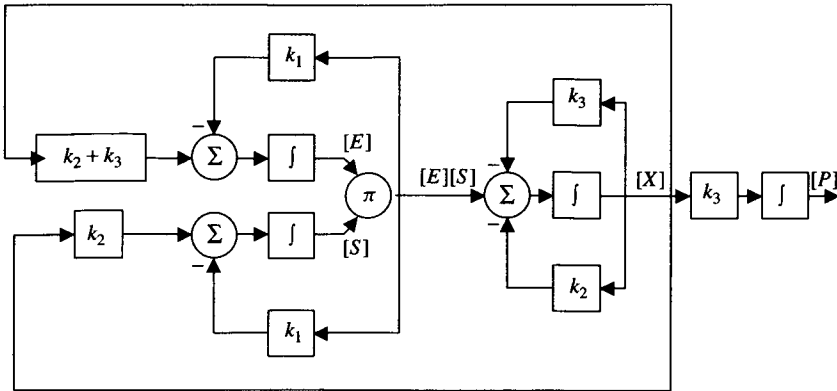


Figure 2.4. Signal flow diagram for a simple enzymic reaction.

What has been considered in this example is the simplest possible configuration of feedback control mechanisms to be found in an enzymic reaction. In practice, most enzyme-controlled reactions are much more complex in variety and number of feedback loops. For example, phosphofructokinase, which catalyses one of the reactions of glucose metabolism, exhibits regulatory mechanisms that are complicated by the presence of activators and inhibitors such that more than a dozen feedback pathways can be identified, resulting in highly complex patterns of control action.

### 2.3.3. NEGATIVE FEEDBACK

As already indicated, negative feedback is characterised by an increase in variable  $y$  that causes a change in variable  $x$  that, in turn, tends to decrease  $y$ . In other words, the signal output induces a response that feeds back to the signal generator to decrease its output. A classic example is the interaction of glucose and insulin, acting as its principal regulating hormone, as depicted in Figure 2.5. An increase in glucose concentration triggers the beta cells of the pancreas into producing more insulin, which, via a variety of enzyme-mediated chemical reactions, results in a lowering of the elevated blood glucose.

More complex patterns of feedback control action can be found among the hormonal control systems. Figure 2.6 shows the case of thyroid hormone regulation, demonstrating the existence of multiple feedback loops. Thyrotropin-releasing hormone (TRH), secreted by the hypothalamus, triggers the anterior pituitary into the production of thyrotropin (TSH). This, in turn, triggers the target gland, the thyroid, into producing the two hormones tri-iodothyronine ( $T_3$ ) and thyroxine ( $T_4$ ). The complexity of control within this system is such

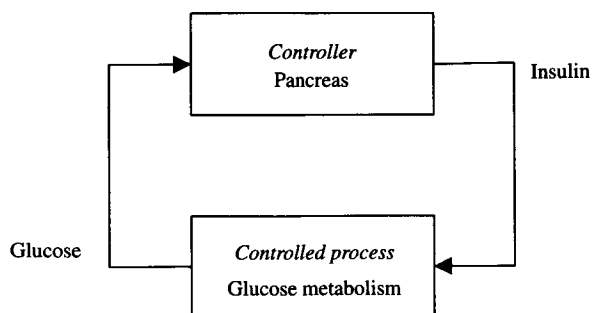


Figure 2.5. Glucose-insulin interaction depicted as a feedback control loop.

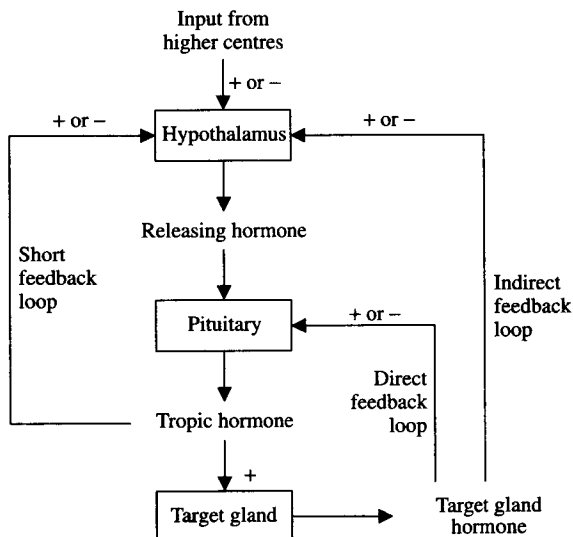


Figure 2.6. Feedback control structure associated with the regulation of the thyroid hormones (adapted from Cramp and Carson, 2000).

that it includes both direct and indirect feedback of  $T_3$  and  $T_4$ , as outlined in Figure 2.6, with TSH feedback on to the hypothalamus.

### 2.3.4. POSITIVE FEEDBACK

If an increase in variable  $y$  causes a change in  $x$  that tends to increase  $y$ , the feedback is positive. In other words, a further signal output is evoked by the

response that it induces or provokes. This is intrinsically an unstable system, but there are a number of physiological situations in which such control is found and performs a valuable function. In such a positive feedback situation, the signal output will continue until no further response is required. Suckling provides an example. Stimulation of nipple receptors by the suckling child provokes an increased release of the hormone oxytocin from the posterior pituitary gland, with a corresponding increase in the flow of milk. Removal of the stimulus causes cessation of oxytocin release (Cramp and Carson, 2000).

### 2.3.5. DERIVATIVE AND INTEGRAL CONTROL

Recalling the example of glucose regulation, evidence shows that insulin is produced in response not only to elevated glucose concentration, but also to a positive rate of change of glucose. This examples implies that this physiological system evidences not only proportional, but also derivative, control action (Cramp and Carson, 1981). A simplified diagrammatic representation showing the basis of these proportional and derivative effects is given in Figure 2.7, whereby excess glucose is laid down as glycogen in the liver as a result of the insulin action in the relevant enzyme-controlled chemical reactions. The presence of this derivative component improves the dynamic response of this physiological control system.

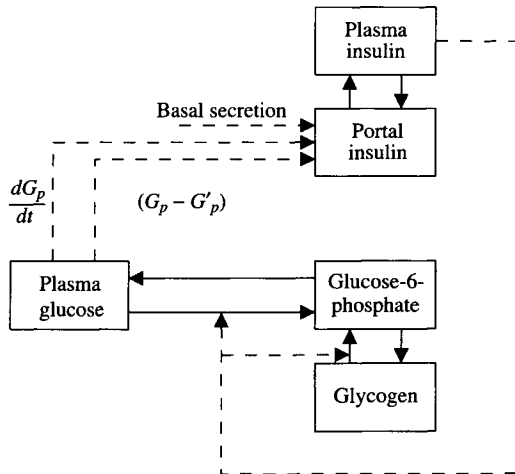


**Figure 2.7.** Diagrammatic representation of a portion of the glucose regulatory system indicating the action of insulin on enzyme-controlled reactions of the glucose metabolic pathway and the response of the pancreas to signals corresponding to glucose and its positive rate of change.

Classic control action typically involves some combination of proportional, derivative, and integral effects. In contrast to the previous example, which has been considered in terms of proportional and derivative action, this example incorporates integral feedback. From a control theoretic perspective, the addition of derivative control generally enhances dynamic response characteristics mentioned previously. However, such feedback systems can exhibit error in the steady-state condition between the desired value of a controlled variable and the value actually achieved by the control action. The incorporation of a term in the control action that is proportional to the integral of the difference between desired and actual state can help to eliminate such error.

An example of such integral action has been proposed by Saratchandran *et al.* (1976) to describe clinical data relating to the thyroid hormones. A simplified representation is shown in Figure 2.8. The two thyroid hormones,  $T_3$  and  $T_4$ , are assumed to bind reversibly to the plasma proteins albumin, thyroxine binding prealbumin and thyroid hormone globulin. One or both of the free thyroid hormones in the plasma ( $FT_3P$  and  $FT_4P$ ) exert an inhibitory effect on the secretion of TSH and, in turn, TSH exerts a stimulatory action on thyroid hormone secretion.

One of the experimental test situations used in the validation of this model was the inhibition of TSH secretion by the thyroid hormones; that is, small quantities of  $T_3$  and  $T_4$  given orally to normal subjects considerably blunt the TSH response to an intravenous injection of TRH. When feedback to the pituitary was assumed to involve only a  $T_3$  proportional signal, the blunting of the TSH response obtained was much less than that observed experimentally. It was then necessary to postulate the existence of both a delayed proportional feedback and an integral feedback effect, whereby the pituitary integrated the past excess plasma level of thyroid hormone  $T_3$  (compared with the steady-state level) over the previous 48 hours in adjusting its TSH output. The successful

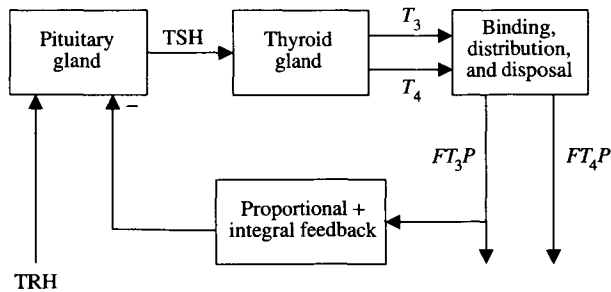


**Figure 2.8.** A portion of the thyroid hormone regulatory system, indicating a postulated component of integral feedback (adapted from Saratchandran *et al.*, 1976).

fitting of this modified model to the data indicated that this physiological system was behaving as if it incorporated an integral control component.

## **2.4. CONTROL SYSTEM REPRESENTATIONS OF THE CLINICAL PROCESS**

The basic ideas of systems and control modelling described earlier can form a framework for representing the diagnostic and therapeutic processes of clinical medicine. This framework is developed in this section. This section also shows how such a modelling framework can be used to specify the requirements for novel forms of clinical activity, such as are being developed and realised in telemedicine and telecare.

The functioning of the human organism, and its constituent physiological systems, in the normal healthy state is readily describable in systems concepts. For example, we can talk of a cardiovascular system made up of elements, including the chambers of the heart, combined with subsystems, such as the systemic and pulmonary arterial and venous trees, the behavioural patterns of which are influenced by an array of control mechanisms, both local and within the central nervous system.

In a similar manner, we discuss the glucose-insulin regulatory system in which the dynamics of blood glucose and related metabolites are controlled by the actions of insulin, and an array of other enzyme and hormonal effects, some of which have been considered in Section 2.3. This situation is depicted in simple form in Figure 2.5 as a controlled process, glucose metabolism, and a controller, the pancreas (the four-component feedback model condensed into two major components). In response to an elevation or positive rate of change of glucose, insulin is secreted by the pancreas. This insulin has its effect on a number of chemical reactions associated with the production and utilisation of glucose. The result is a lowered plasma glucose concentration, and a classic example of feedback control.

Many disease states can be analysed in terms of complete or partial failure of one or more feedback loops of the type depicted in Figure 2.9. For instance, diabetes results from a partial or complete failure of the pancreas to produce insulin in response to elevated blood glucose levels or to a reduction in the efficiency in producing the desired metabolic effect (in essence, a change in one or more parameters in the actuating or effectors component of the loop rather than the structural change—break in the loop—implied by a total failure to secrete insulin. Deviations from normality, or disease conditions, are frequently not deviations of controlled variables, but rather deviations in relations between variables. In other words, the deviations are observable only as a pattern of relations between variables.

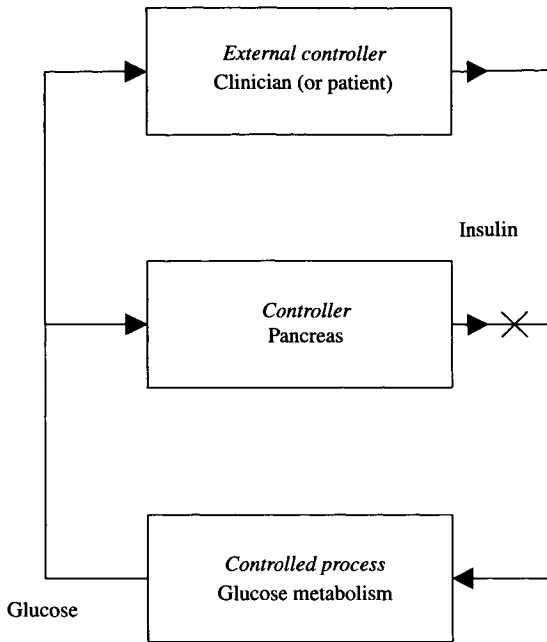


**Figure 2.9.** An external feedback control loop (clinical control) superimposed upon the impaired intrinsic glucose-insulin regulatory processes.

In the disease state, the impaired or broken internal control loop must be augmented by, or replaced with, an external loop corresponding to the clinical intervention. The situation in the case of diabetes is depicted in Figure 2.9. While the controller will usually be the physician or a member of another clinical profession, in the case of a chronic disease such as diabetes it is frequently the patient who makes the decision concerning the adjustment of insulin therapy, particularly on a day-to-day basis.

#### 2.4.1. THE FEEDBACK MODEL AS A FRAMEWORK FOR THE CLINICAL PROCESS

The classic feedback model thus constitutes a framework that can be adopted to gain insights into not only the dynamics of physiological regulation and control, but also the nature of the clinical domain with its diagnostic and therapeutic processes. In this context the feedback model can be represented as shown in Figure 2.10. In essence, the physician, nurse, or other clinician, acting as controller or decision-maker, makes decisions, based on



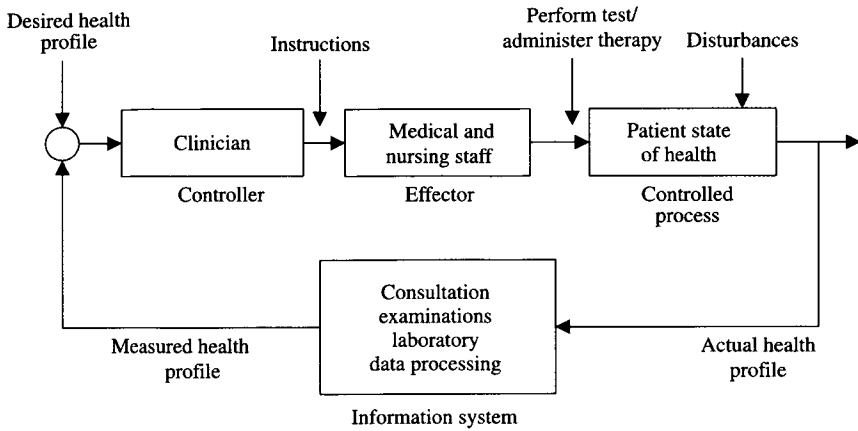


**Figure 2.10.** Information processing and control decision-making in health care delivery.

the best available information, that result in some particular clinical activity. The decision might relate to the diagnostic process, performing a laboratory test or carrying out an imaging examination, to increase the available information on the state of the patient. Equally, it might relate to the administration of drug or other therapy (or a decision to change the existing therapy) to improve the patient's state of health.

The information system in the feedback loop is then used either to provide increased knowledge concerning the state of the patient from a diagnostic perspective or to enable an assessment of the extent to which the chosen therapy has produced the desired change in the patient's condition. By increasing the availability of information to the clinical decision-maker, their uncertainty is lessened. Of course, this means that the data collected regarding patient state should have been processed and interpreted in the clinical context of that individual patient. In the early stages of clinical activity, decisions will be largely diagnostic in nature. They will focus on assessing patient state and, where appropriate, determining the need for investigations or tests to yield additional diagnostic information.

#### 2.4.2. DIAGNOSIS, DECISION-MAKING, AND TREATMENT

Although in some senses the processes of diagnosis and treatment are distinct, within this model-based control paradigm, diagnosis is essentially a component of the clinical management process, rather than being an end in itself. Diagnosis should be regarded operationally as the provisional assignment

of a patient to a treatment class rather than labelling of a disease state. Diagnosis can only be confirmed in this operational framework once the response to therapy is known. Moreover, diagnostic classification that does not distinguish between different management options does not generally improve health care.

The setting of diagnosis and treatment within a broader medical and social environment is depicted in Figure 2.11. In this representation, data from “medical sensors,” describing the patient and environment, are fed into the diagnostic subsystem. Here, adopting appropriate model-based processing and interpretation, the data can be mapped into a particular disease class or a set of statements that provide an assessment of the patient’s state. These diagnostic statements, with both raw and processed patient data, can then be used in the subsequent stages of decision-making to determine the best course of action.

One must decide whether treatment should be administered and, if so, which one. On the other hand, further investigations or tests may need to be performed to gain additional patient information (e.g., the current degree of uncertainty is too great to justify specific therapeutic action). Moreover, if therapy is administered, one should specify, in the light of the expected patient response, which variables should be observed and at what times the patient should be monitored. Again, clinical data are used as in diagnosis, but

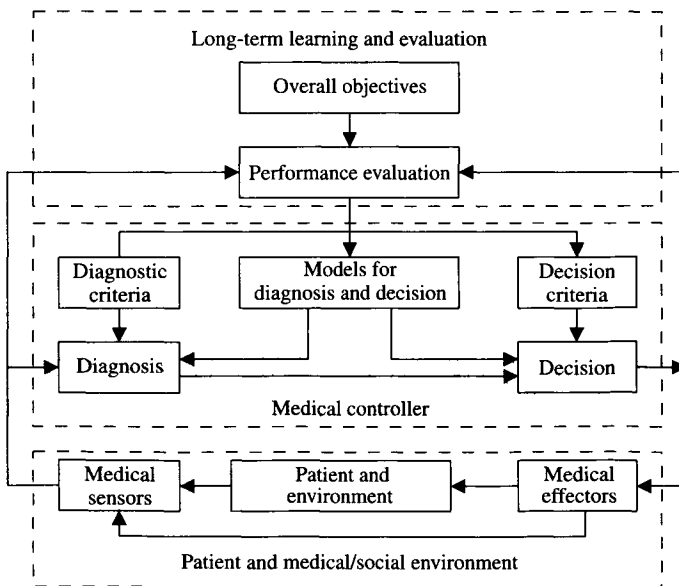


**Figure 2.11.** The processes of diagnosis and treatment viewed from a control perspective (adapted from Edwards *et al.*, 1978).

local treatment objectives are employed (Deutsch *et al.*, 1994; Edwards *et al.*, 1978).

As the decision-making process progresses, there is a change in the local objectives of the diagnostic and treatment processes. In diagnosis, the change is a refinement from the initial attempt at general diagnosis toward making efficient, therapy-related diagnostic statements from the relevant set of patient observations. For treatment, the transition moves from determining when therapy should be administered to monitoring the success of ongoing therapy. The selected treatment is then given to the patient or appropriate changes are made to his or her environment.

These processes are highly iterative, so there is a cycling around this control loop a number of times, rather than it being a one-off sequence of procedures. Ongoing data collection via the monitoring process enables the effectiveness of earlier decisions to be assessed and any necessary modifications or revisions to be made.

As seen from Figure 2.11, the performance evaluation carried out by the clinician is over and above the operational system. The clinician considers the sequence of observations, including all available clinical data and treatment information, to reflect his or her overall objectives. This may lead to modification of specific diagnostic or treatment objectives or to a reconsideration of the decision-making processes (Edwards *et al.*, 1978).

### 2.4.3. FEEDBACK AND FEEDFORWARD

The purely feedback schema as depicted in Figure 2.10 assumes that sufficient time is available for the operation of the information system in the feedback loop to take effect before a further clinical decision is required. Obviously, this assumption may not be valid in the initial stages of decision-making for a newly admitted patient, particularly when acute illness or trauma requires action before all relevant test results and clinical investigations are made available. This difficulty also may apply in the case of chronic disease management with its lengthy time scales for complete operation of the feedback loop. These are situations in which the dynamics of patient change are slow and clinic visits are comparatively infrequent.

In such cases, a model based solely on feedback cannot provide a completely adequate representation of the clinical control action. It must be complemented by a feedforward model. In fact, the actions of the clinician regarding patient management provide a good example of feedforward control. This involves taking quick action to produce a desired patient state or to prevent an undesired state that could be a possible consequence of a disease progression or future disturbance (Deutsch *et al.*, 1994).

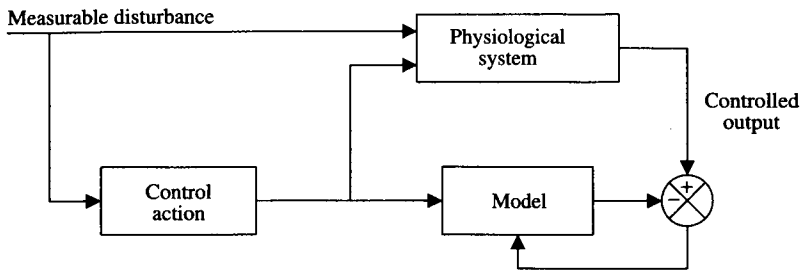


**Figure 2.12.** Feedforward action as an ingredient of clinical control.

The scheme of this anticipatory or feedforward control action is based on a model of the controlled process, or the patient. Such a model can be used in two ways. First, it can be used to infer the state of the patient. Second, it can be used as a basis for developing an adaptive control strategy for patient management. Figure 2.12 shows a model describing the effect of disturbances and control actions on the system output to be regulated. In response to a measurable disturbance, the clinician will try to eliminate the effects of that disturbance on the particular physiological process that has been deranged. In so doing, the clinician uses a conceptual model to choose an appropriate treatment. Looking to the future, such mental, conceptual models will increasingly be supported by a computer model. In this manner, the controlled output of the assumed model would tend to cancel out the effect of the measurable disturbance on the corresponding output of the real physiological system (Deutsch *et al.*, 1994).

This control action taken by the clinician is, in essence, anticipatory. It is carried out either when feedback is not available from the information system in the loop or when a rapid clinical decision is required before there is time to put the full cybernetic process into action. A general model of clinical control can be seen as one in which feedforward action is embedded within an overall feedback loop.

#### 2.4.4. THE OVERALL FEEDBACK MODEL OF HEALTH CARE DELIVERY

While the clinical feedback loop, based on its four elements, is at the centre of health care delivery, a wider perspective is necessary to encompass the overall processes of health care delivery. Figure 2.13 depicts a model comprising a set of interacting feedback loops. A number of points should be noted. First, the model is generic in its ability to be applied across a spectrum of diseases. Second, it is relevant whether in the clinical management of the

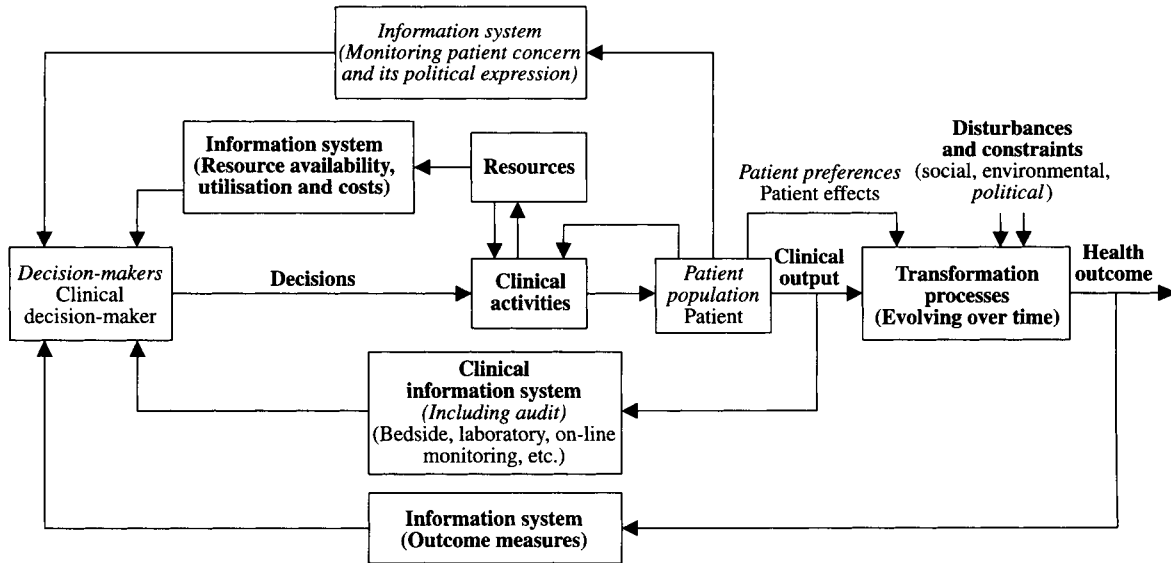


**Figure 2.13.** Overall model of the clinical decision-making and control processes depicted as a multiple feedback loop array (adapted from Cramp and Carson, 1995).

patient, or in the selection of a policy as to what forms of clinical management should be made available to a given patient population.

The model provides for health care delivery directed toward a wider view of health outcome, in addition to the direct output in readily measurable clinical variables. It accounts for patient preference, as well as resource availability, cost-effectiveness, and clinical effectiveness. In summary, it demonstrates that a control system model, in the form of interacting feedback loops to which a feedforward component can be added (as discussed previously), provides a useful aid both to the clinical decision-maker and to the health care planner.

#### **2.4.5. A MODELLING FRAMEWORK FOR SYSTEM REQUIREMENT SPECIFICATIONS**

The modelling framework presented as a representation of the processes of health care delivery can play an important role in systems specification and design. This applies not only in centralised modes of health care delivery, but also in distributed modes as exemplified by developments in telemedicine and telecare.

An illustration of this is given in relation to the development of a telematic home haemodialysis system that is being designed to support treatment of patients suffering from end-stage renal disease (ESRD). The approach of Cramp and Carson described previously can aid system specification, with the modelling activity carried out at successively fine levels of resolution. In this way, a conceptual model of the required telemedicine information and control architecture can be determined. In turn, the system hardware and software needed for realisation can be specified (Carson *et al.*, 1998a).

The management of ESRD represents a major clinical challenge. Home haemodialysis offers the patient with chronic kidney failure the convenience of home treatment, enhanced rehabilitation, and decreased treatment cost over time. Currently, its adoption across Europe is limited (not available in some countries) and is decreasing. Among the problems are a lack of support for the patient in the home setting and difficulty concerning the provision of treatment resources in the home. Telemedicine offers one way of overcoming such difficulties. This involves complementing conventional home dialysis with a telematic link (video, voice, data, and text) between the patient's home and the hospital control centre, typically a specialist renal unit with clinical expertise (Carson *et al.*, 1998a). The modelling approach described in the following paragraph has been carried out as part of the European-funded Health Telematics HOMER-D project (Carson *et al.*, 1997).

Figure 2.14 offers an overview of the control system modelling framework in the context of the specific example of developing and evaluating a telematic

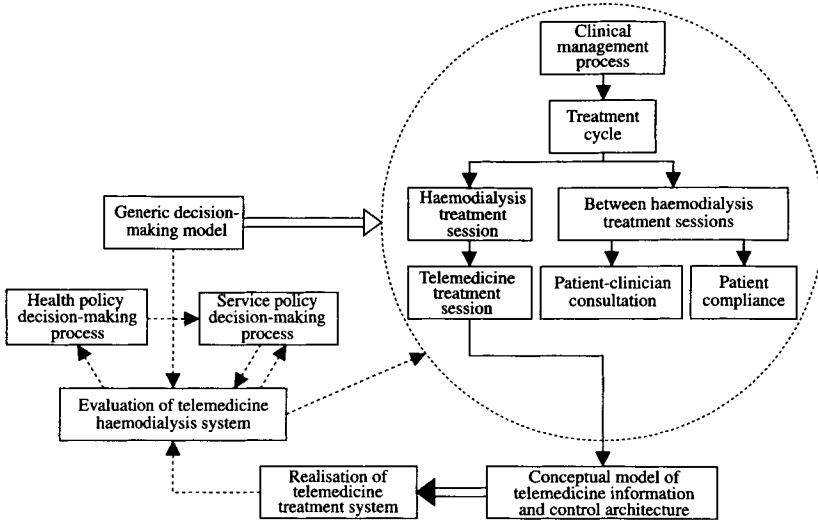


**Figure 2.14.** Control system model framework for the design, realisation, and evaluation of a telematic home haemodialysis system (adapted from Carson *et al.*, 1998a).

home haemodialysis system. This indicates that the generic decision-making, as depicted in Figure 2.1, is applied to each of the processes associated with managing ESRD. These are shown within the dotted circle at the right-hand side of the figure. In essence, the treatment cycle can be divided into those periods spent receiving haemodialysis therapy, typically 3 to 4 times per week, and the periods between those sessions. It is in relation to the haemodialysis sessions that the telemedicine is being designed. For simplicity, longer term concerns, such as those relating to rehabilitation of the patient, are omitted since they do not immediately impact upon the design of the telematic home haemodialysis system.

The essence of the telematic system features is that the state of the patient and his or her haemodialysis machine are monitored and these data are transmitted back to a central hospital station, typically located in a specialist renal unit. The patient receiving treatment would be either in his or her normal home setting or in a satellite dialysis centre, which could be located in a primary health care centre. From the specialist centre, where the data are monitored and interpreted, appropriate advice can be fed back to the patient via an appropriate telematic link. In this way, the patient benefits from receiving treatment in his or her home or local environment, while simultaneously benefiting from the expert care offered by the specialist renal unit.

The generic feedback decision-making model of Figure 2.1 is applied to each of these treatment cycle components of clinical management in turn representing these components in feedback terms. Figure 2.15 shows the result

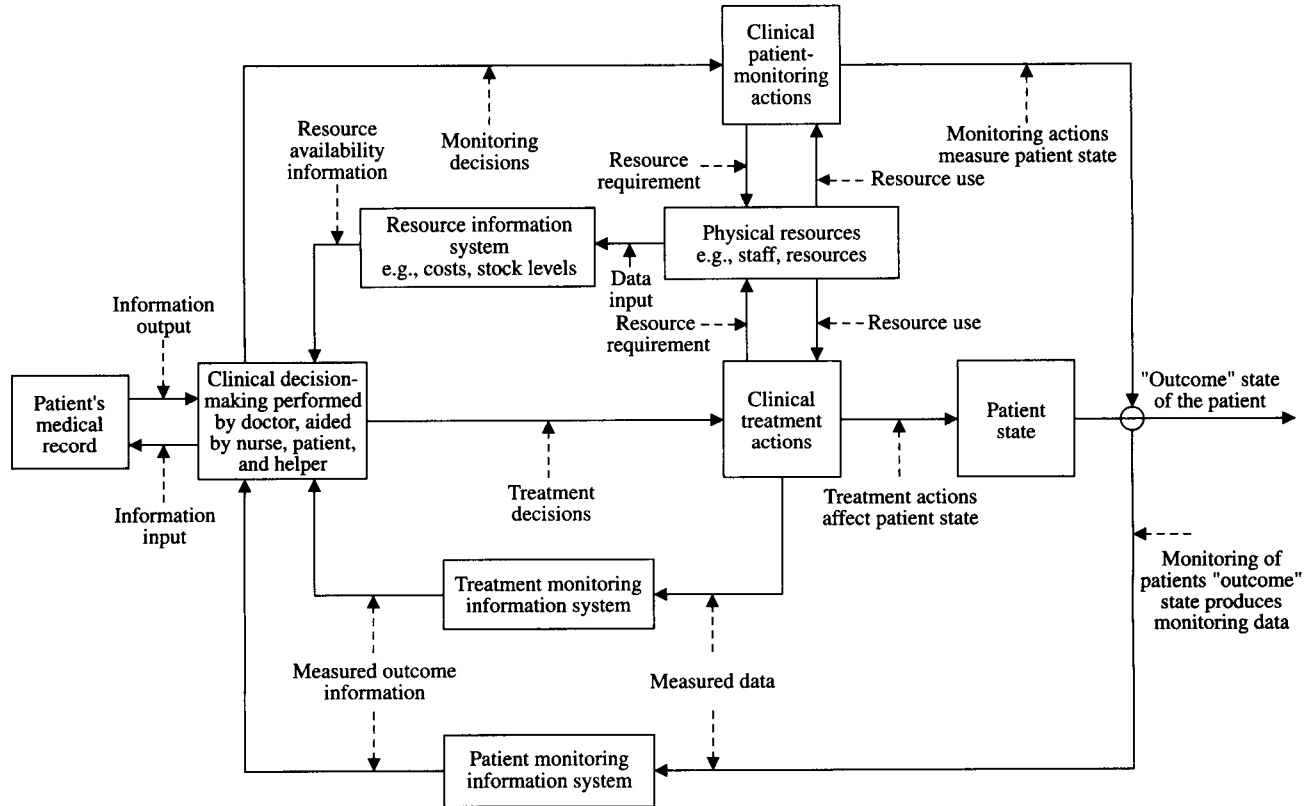


**Figure 2.15.** A conceptual model of the haemodialysis treatment session represented from a feedback perspective (adapted from Carson *et al.*, 1998a).



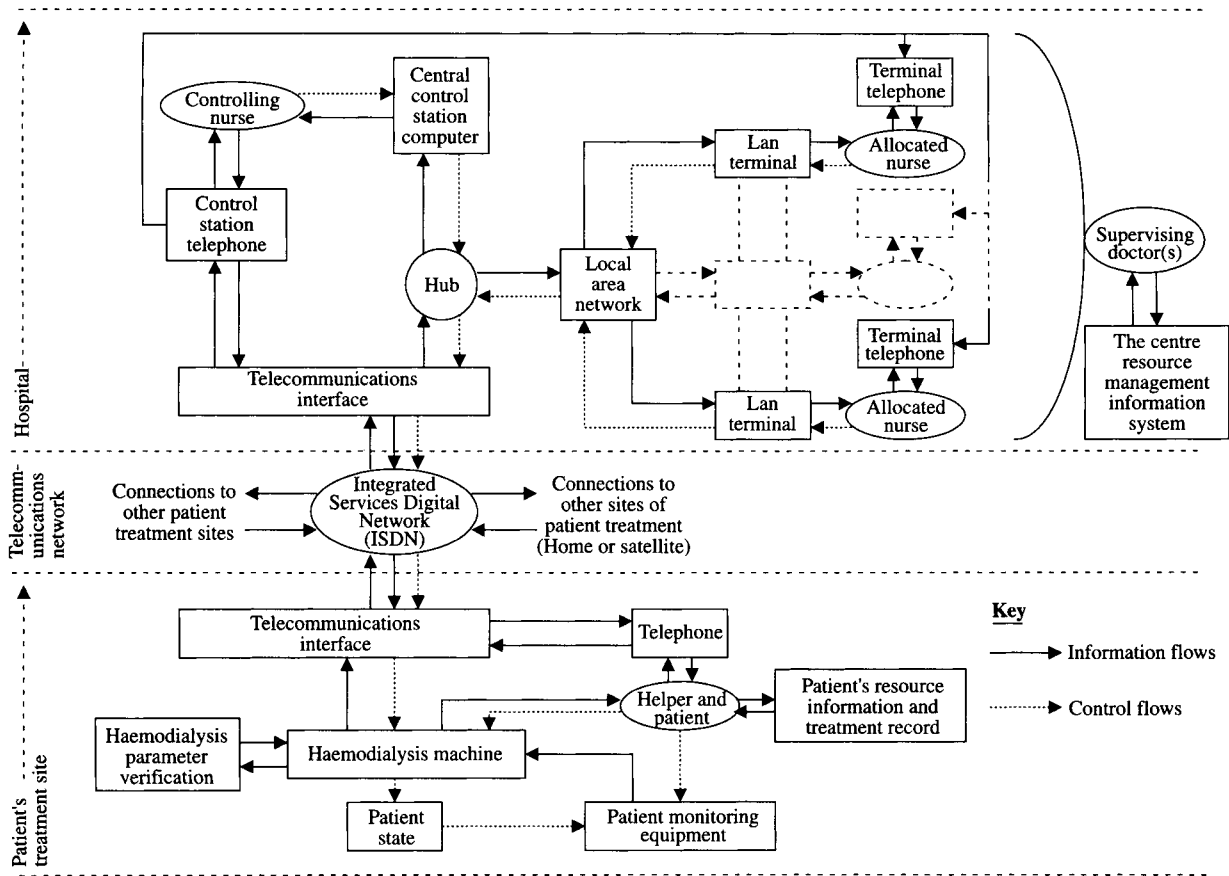


**Figure 2.16.** Conceptual model of the information and control architecture for hardware and software realisation of the telemedicine system (adapted from Carson *et al.*, 1997).

of carrying out this operation to the period of the haemodialysis treatment session. This model-based analysis can be applied with increasingly fine granularity until a representation of the telematic treatment session is produced, as depicted in Figure 2.16.

In progressing from these conceptual models, the information-gathering stage commences by taking a patient profile from the patient's medical record. Instructions are then given to the patient via the telematic link. Once done, a number of monitoring actions are carried out by the patient, such as measurement of blood pressure and body weight. These data are then fed back to the specialist hospital centre. Unless there is contraindication of the monitoring actions, the haemodialysis treatment is started. From this point, information generated by the haemodialysis machine (e.g., relating to the rate of blood flow through the machine) is monitored and fed back to the central control station. Normally, the information that has been monitored will only be acted upon when an alarm condition occurs. Where appropriate, any such alarm state detected during the monitoring process can be recorded in the patient's medical record. At the end of the treatment session, further monitoring actions are performed and the corresponding data are recorded in the patient's medical record (Carson *et al.*, 1998a).

By progressing through increasingly fine levels of resolution in the application of this modelling approach, a conceptual model of the required telemedicine information and control architecture is obtained, as shown in Figure 2.16. This conceptual representation of the architecture leads directly to the hardware and software required for adoption in the telemedicine system. The prototype system developed in the HOMER-D project has been tested as part of an overall programme of evaluation in three European countries. Again, this evaluation process, the methodology for which is described in Carson *et al.* (1998a), forms part of the overall feedback control system model depicted in Figure 2.14.

## 2.5. CONTROL SYSTEM APPROACHES TO DRUG THERAPY PLANNING AND ADMINISTRATION

Therapy as a component of the clinical management of the patient is essentially the implementation of control action. In the context of drug therapy, for example, observing the patient and administering drugs constitutes an operational feedback loop that consists of three main parts. These are the controlled process (the patient); a sensor of the patient's response to therapy (the measurement system that constitutes part of the feedback loop); and the controller, as depicted in Figure 2.17.

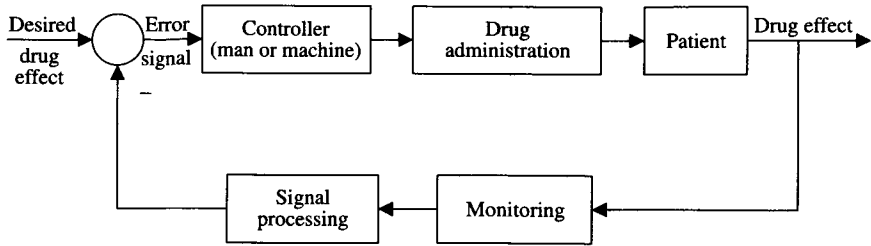


Figure 2.17. Schematic representation of feedback-controlled drug therapy.

### 2.5.1. THE PLANNING OF DRUG THERAPY

In taking such control action, the objective is to achieve a desired level of drug-elicited effect. The appropriate therapeutic action is attained without exceeding predetermined safety limits in relation to any possible adverse action. Problems arise as a consequence of drug response variability from one patient to the next, or over time in a single patient. Adjustment of the drug regimen attributes (route of administration, dosage, time schedule of delivery) can alter the effects of a drug. Completely different therapeutic and toxic responses may occur following the administration of the same drug quantity, depending on the manner and timing of the dose delivery. The individualisation of dosage adjustment is particularly critical for drugs with a rapid onset of action and a narrow therapeutic range. From a control perspective, additional complications arise when more than a single drug is administered. The possible impact of drug-drug interaction is such that only rarely will the total control action be simply the sum of the individual control effects.

The choice between alternative control actions (e.g., alternative drugs or dosage of a single drug) can be aided by the use of formal decision analysis using decision trees. In this way, the drug treatment of any illness can be modelled as having four potential outcomes. These are the four possible combinations of efficacy or no efficacy with toxicity or no toxicity. The form of the decision tree model is shown in Figure 2.18. Changes in the dosing with a single drug, for instance, will change the distribution of the probabilities for the four outcomes and the overall value of expected utility of the two branches of the tree. The information gained from such analysis can inform the planning process prior to the taking of the control action.

### 2.5.2. CONTROL APPROACHES IN DRUG THERAPY

When administering drug therapy as control action, the drug-elicited effect must be measured. In some cases, this can be readily carried out, such as

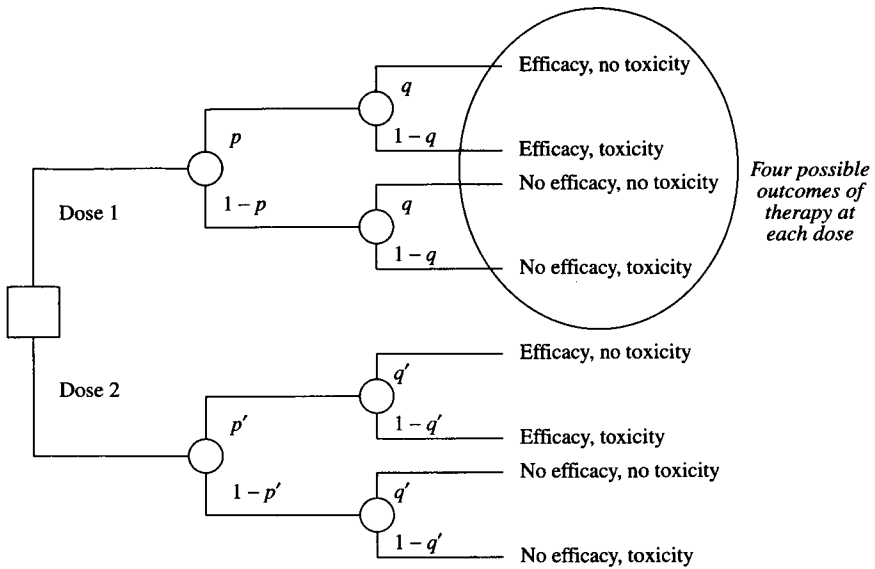


**Figure 2.18.** Decision tree representation of the outcomes of alternative drug therapy regimens. Changes in dosage alter  $p$ , the probability of efficacy, and  $q$ , the probability of toxicity (adapted from Lenert *et al.*, 1993).

where the effect is measured as a change in blood pressure. However, if the effect is depth of anaesthesia, the value of which is inferred from on-line measurement of the EEG, sophisticated signal processing will be needed for its assessment, as indicated in Figure 2.17.

In the operation of the feedback loop, the levels of drug effect actually observed in the patient are compared with the level of response being sought, and the difference (error signal) is fed into the controller that adjusts the drug dosage as required. The drug dosage as the control signal can be administered either as a continuous signal (e.g., intravenous infusion or inspiration of anaesthetic agent) or in discrete form (e.g., bolus injection or taking a tablet orally).

The controller can be the clinician (or patient) or machine. For relatively safe drugs, the control action can be taken by the human agent (e.g., clinician in the hospital). However, in the case of rapidly acting drugs, a computerised drug delivery system may be more appropriate.

Depending on whether the clinician (or patient acting in the role of controller) is included in the feedback loop, it is possible to distinguish between so-called “tight” and “loose” control methods. These are illustrated in Figure 2.19. In tight or fully closed-loop systems, drug administration does not require human intervention. For example, computerised devices can automatically

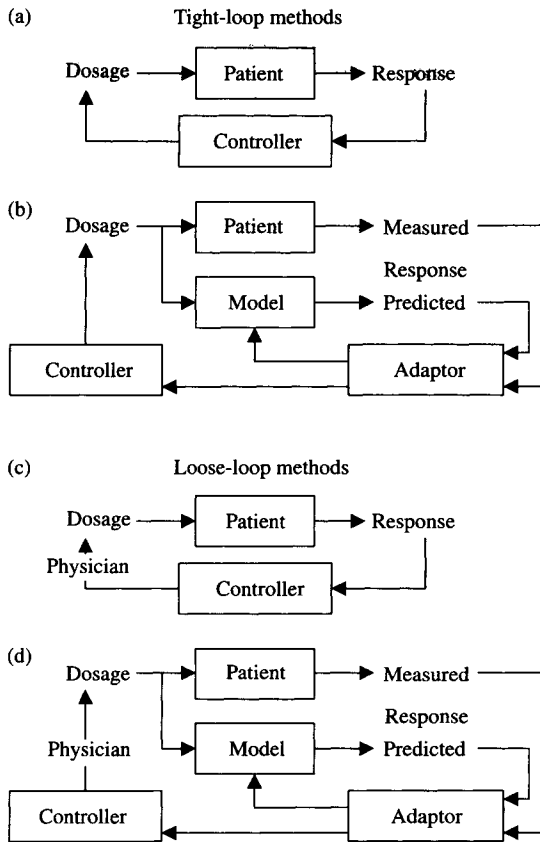


**Figure 2.19.** Types of feedback control that can be adopted in drug therapy. A and C, nonadaptive control; B and D, adaptive control (adapted from Vozeh and Steimer, 1985).

infuse antihypertensive agents on the basis of monitored blood pressure data (Deutsch *et al.*, 1994). In loose- or open-loop control, the clinician (or patient, in relation to day-by-day insulin dosage adjustment) is part of the loop, making final decisions about dosage and future monitoring patterns.

### 2.5.3. CONTROL SYSTEM APPROACHES IN THE MANAGEMENT OF DIABETES

In the context of diabetes, it is open-loop control that is the norm in regulating the glucose-insulin loop. Occasionally, an unstable diabetic subject

spending a short period of time as an inpatient may receive insulin therapy as a closed-loop feedback operation in order to stabilise the blood glucose level. Equally, looking to the future, once continuous monitoring of blood glucose becomes practicable on a safe, reliable, and robust basis, an imbedded control system operating mode could become a reality.

However, open-loop control is the norm. Hence, in the context of this chapter, one is considering the development of model-based schemes that can offer advice to the decision-maker. Focusing on advice relating to the adjustment of insulin dosage, three distinct decision-making problems can be identified. These can be classified in terms of the frequency of occurrence (Carson, 1998). The lowest frequency corresponds to strategic adjustment of the basic insulin regimen, such adjustment being made when the patient visits the clinic, typically at intervals of once every several weeks or months. Next, there is the fine-tuning of this strategic regimen, which the patient may make on a day-by-day basis. Finally, there is the one-off adjustment that might be required in anticipation of some sporting activity or celebratory meal. Each of these decisions has its own control characteristics that must be considered when devising the relevant decision support technology.

A wide range of model-based approaches has been proposed to provide decision support for these problems. Some make use of models that are explicitly based on the underlying dynamics of glucose-insulin interaction (process models). Others are based on interpreting clinical data, in essence data-driven models. Details of many of these approaches can be found in thematic issues of journals such as *Computer Methods and Programs in Biomedicine* and *Medical Informatics*, focusing on modelling and decision support in diabetes (e.g., Carson *et al.*, 1998b, 2000; Lehmann, 1996, 1997).

One approach that has been developed for the strategic, visit-by-visit problem of insulin adjustment is the UTOPIA system (**U**tilities for **O**ptimising **I**nsulin **A**ddjustment) (Deutsch *et al.*, 1996). This is a system that includes components of both data-driven and process modelling. This system seeks to provide advice based on the processing and interpretation of extended series of home-monitored blood glucose measurements. Such measurements are typically made by the patient up to four times a day, before each main meal and at bedtime.

Two principles are at the centre of this system. The first is that blood glucose data collected by the patient over time are assumed to be capable of yielding characteristic statistical patterns for that patient when following a particular regimen of insulin therapy. The extent of such a series of data might typically be a period of 2 to 3 months between successive visits to the clinic. The second principle is that successive clinic visits will produce a series of such patterns for the patient. Relationships between the particular insulin regimen and its response pattern may then be learned, providing a

patient-specific model that can be used as a basis for predicting the results, in terms of the change produced in the blood glucose profile, or a change to the regimen of insulin therapy.

The architecture of the UTOPIA system incorporates the four interrelated modules of Data Viewer, Data Interpreter, Patient-Specific Modeller, and Advisor, as depicted in Figure 2.20. Data Viewer permits the extended home-monitored data to be displayed with simple statistical analyses of the data and comparisons with clinical measures.

The Data Interpreter module extracts patterns from the blood glucose data, including the modal day, using methods of time series analysis or, in essence,

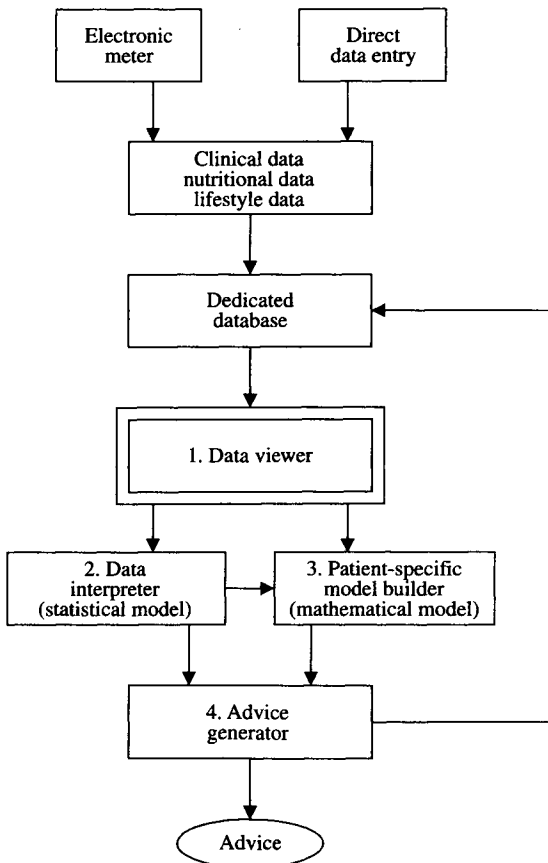


**Figure 2.20.** A schematic representation of the Utilities for Optimising Insulin Adjustment (UTOPIA) system, showing the four interrelated modules of this model-based decision support system (adapted from Deutsch *et al.*, 1996).

data-driven modelling (Harvey, 1989). The blood glucose data,  $BG_t$ , form a natural time series at time points  $t$ , comprising a level,  $L_t$ , a trend,  $T_t$ , a daily cycle,  $DC_t$ , and with a random disturbance,  $\epsilon_t$ , which leads to a simple model:

$$BG_t = L_t + T_t + DC_t + \epsilon_t \quad (2.6)$$

Level represents a mean evolving over time, while the trend allows for systematic growth or decline in the data. Inclusion of a daily cycle estimates deviations from the trend across the day (Deutsch *et al.*, 1996). An example of such data decomposition using this data-driven modelling approach is shown in Figure 2.21. The components have different clinical interpretations. Thus, for example, the daily cycle offers some detail of the control achieved at different stages of the day and shows whether the two or more daily insulin doses are properly distributed over a 24-hour period.

The Patient Specific Modeller enables a simple process-based model to be derived that characterises the patient's pharmacodynamic response to a change in insulin therapy. A linear model is used to express relationships between dose and response variables. This assumes that the dose adjustments are small on the occasion of each visit to the clinic, and they can be treated as local linearisations about the particular operating point.

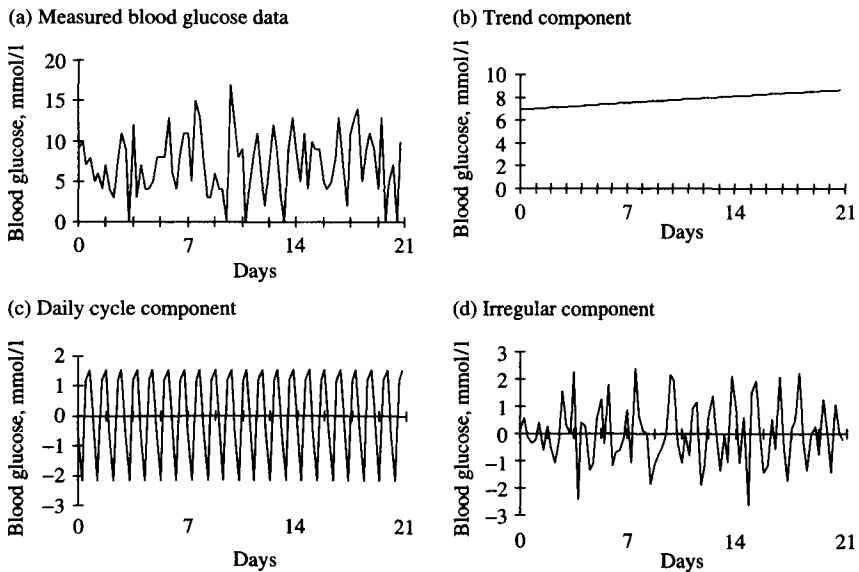


**Figure 2.21.** An example of an extended series of home-monitored blood glucose data, decomposed into clinically relevant components (adapted from Deutsch *et al.*, 1994).



The updating of the model parameters on the occasion of each visit to the clinic is carried out as a two-stage process. First, the old and the new insulin regimens are converted into circulating insulin levels using models of subcutaneous insulin absorption and disposition (Berger and Rodbard, 1991). The model relating glucose and insulin can then be written as (Deutsch *et al.*, 1996):

$$dGrel(t)/dt = -KGrel(t) - Sr(t)Iarel, \quad Grel(0) = 0 \quad (2.7)$$

where:

Grel = change in modal day blood glucose profiles

Iarel = change in active insulin profiles

$K$  = parameter that reflects the impact of glucose on its own metabolism

$r(t)$  = representation of the diurnal rhythm of insulin sensitivity on a scale {0–1} to cater for the elevated glucose resistance at some periods of the day

$S$  = parameter providing a measure of patient-specific insulin sensitivity.

Solving (2.7) at the four daily times of glucose measurement (before the three main meals and at bedtime),  $t_i$ , yields:

$$G(t_i, R2) = -S \int_{t_i-24}^{t_i} \{[1 - r(t)]Iarel(t)[\exp(-K(t_i - t))]\} dt + G(t_i, R1) \quad (2.8)$$

with  $R1$  and  $R2$  denoting two insulin regimens prescribed at two consecutive clinic visits. Using this model, the parameters  $K$  and  $S$  can be updated so as to fit the current change in modal day blood glucose response that has resulted from the most recent change in insulin therapy.

Given that the Patient Specific Modeller has enabled a current model to be provided for the particular patient, this model can then be used in the Advisor module to make predictions of changes in the patient's modal day blood glucose response in response to specific changes in the regimen of insulin therapy. The change that brings about the most desirable result can be adopted for that patient. The exploration of alternative candidate insulin regimens can be carried out either manually or automatically using a choice of exhaustive or linear programming algorithms. Full details of these procedures are given in Deutsch *et al.* (1996).

## 2.6. CONCLUSIONS

This chapter has demonstrated the ways in which control concepts, set within a clear modelling framework, are relevant in the study of physiological and medical systems. Benefits have been demonstrated both in insight and in

support of therapy planning as an ingredient of the overall patient management process.

A simple feedback model has provided a basis for examining the dynamics of physiological processes; a model capable of expansion and extension to yield insights into the complexities associated with the overall processes of health care delivery. Such models can play an important role in system design, as illustrated in the development of a telematic system for the provision of home hemodialysis. Finally, the role of model-based approaches in supporting the prescription of a therapeutic regimen (as a control problem) has been demonstrated in the context of managing diabetes.

## 2.7. REFERENCES

- Berger, M. P. and D. Rodbard. A pharmacodynamic approach to optimising insulin therapy. *Comput Methods Programs Biomed* 34(1991):241–53.
- Carson, E. R. Decision support systems in diabetes: a systems perspective. *Comput Methods Programs Biomed* 56(1998):77–91.
- Carson, E. R., G. D. Cramp, A. Darnige, D. Koutsikos and D. Murley. A systems methodology for the development and evaluation of a telemedicine home haemodialysis service. Proceedings of the 19th Annual International Conference of the IEEE Engineering in Medicine and Biology Society — Magnificent Milestones, Emerging Opportunities. Piscataway, N.J.: IEEE, 1997.
- Carson, E. R., S. Andreassen, D. Cavan and E. Gomez (eds.). Computers in diabetes '98. *Comput Methods Programs Biomed* 62(2000):153–264.
- Carson, E. R., D. G. Cramp, A. Morgan and A. V. Roudsari. Clinical decision support, systems methodology and telemedicine: their role in the management of chronic disease. *IEEE Trans IT Biomed* 2(1998a):80–88.
- Carson, E. R., S. Andreassen and R. Hovorka (eds.). Computers in diabetes. *Comput Methods Programs Biomed* 56(1998b):75–210.
- Cramp, D. G. and E. R. Carson. The dynamics of short-term blood glucose regulation. In: *Carbohydrate Metabolism: Quantitative Physiology and Mathematical Modelling*. Edited by C. Cobelli and R. N. Bergman. Chichester: Wiley, 1981:349–68.
- Cramp, D. G. and E. R. Carson. Health care planning and priority setting—a modelling approach. In: *Setting Priorities in Health Care*. Edited by M. Malek. Chichester: Wiley, 1994:95–102.
- Cramp, D. G. and E. R. Carson. 2000. Endocrine system. In: *The Biomedical Engineering Handbook*. 2nd ed. Edited by J. D. Bronzino. Boca Raton, FL: CRC Press, 2-1–2-8.
- Cramp, D. G. and E. R. Carson. Assessing health policy strategies: a model-based approach to decision support. Presented in Intelligent Systems for the 21st Century. Proceedings of the IEEE Conference on Systems, Man and Cybernetics. Piscataway, N.J.: IEEE, 1995:1969–73.
- Deutsch, T., E. R. Carson and E. Ludwig. 1994. *Dealing with Medical Knowledge: Computers in Clinical Decision Making*. New York: Plenum.
- Edwards, P. R., E. K. Britton, E. R. Carson, R. P. Ekins and L. Finkelstein. A control systems approach to the management of thyroid disease. In: *A Link Between Science and Automatic Control*. Edited by A. Niemi. Oxford: Pergamon Press, 1978:541–48.
- Harvey, A. C. 1989. *Forecasting, Structural Time Series Models and the Kalman Filter*. Cambridge: Cambridge University Press.

- Lehmann, E. D. (ed.). Application of information technology in clinical diabetes care. Part 1 Databases, algorithms and decision support. *Med Inf* 21(1996):255–374.
- Lehmann, E. D. (ed.). Application of information technology in clinical diabetes care. Part 2 Models and education. *Med Inf* 22(1997):1–118.
- Lenert, L. A., D. R. Markowitz and T. F. Blaschke. Primum non nocere? Valuing of the risk of drug toxicity in therapeutic decision making. *Clin Pharmacol Ther* 53(1993):285–91.
- Saratchandran, P., E. R. Carson and J. Reeve. An improved mathematical model of human thyroid hormone regulation. *Clin Endocrinol* 5(1976):473–83.
- Vozech, S. and J. L. Steimer. Feedback control methods for drug dosage optimisation. *Clin Pharmacokinet* 10(1985):457–76.

# Deconvolution

Giovanni Sparacino, Giuseppe De Nicolao, and Claudio Cobelli

## 3.1. INTRODUCTION

Many signals of interest for the quantitative understanding of physiological systems are not directly measurable *in vivo*. Some examples include the secretion rate of a gland, the production rate of a substrate, or the appearance rate of a drug in plasma after oral administration. Very often, it is only possible to measure the causally related effects of these signals in the circulation (e.g., the time course of plasma concentrations). Thus, there must be reconstruction of the unknown causes (e.g., hormone secretion rate) from the measured effects (e.g., hormone plasma concentration). In the mathematics/physics/engineering literature, this is referred to as an *inverse problem*; that is, instead of following the cause-effect chain (direct problem), one follows the reversal of this chain. If the unknown signal is the input of the system, the inverse problem is an *input estimation problem* (Figure 3.1), which, in the linear case, is called *deconvolution*.

Deconvolution is known to be *ill-conditioned*, which means a small percent error in the measured effect (e.g., the measured hormone concentration in plasma) can produce a much greater percent error in the estimated cause (e.g., the secretion rate reconstructed by deconvolution). Moreover, dealing with physiological signals adds to the complexity of the problem, since they are often nonnegative and sampled at a nonuniform and/or infrequent rate.

In this chapter, we introduce the deconvolution problem for physiological systems (Section 3.2) and its inherent difficulties (Section 3.3) in a formal manner. Then, we present a detailed description of the regularisation method (Section 3.4), a classic nonparametric approach that has some significant advantages over other techniques, especially if it is embedded in a stochastic setting. Finally, other deconvolution methods, both parametric

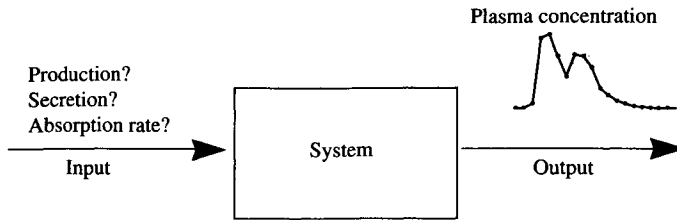


Figure 3.1. The input estimation problem.

and nonparametric, are briefly reviewed (Section 3.5). In discussing the deconvolution algorithms, computational as well as theoretical aspects are addressed. Real and simulated case studies are also provided to illustrate the challenges posed by the deconvolution of physiological signals.

### 3.2. PROBLEM STATEMENT

The deconvolution problem can be formalised as follows. Consider a linear time-invariant (LTI) single-input single-output dynamic system in which input is of interest but not directly measurable. Assuming that the system output is measurable, the input estimation problem illustrated in Figure 3.1 requires to solve the following integral equation:

$$c(t) = \int_0^t g(t - \tau)u(\tau)d\tau \quad (3.1)$$

where  $u(t)$  is the (unknown) input and  $c(t)$  is the (measurable) output of the system. The function  $g(t)$  describes the input-output behaviour of the system and is called the *impulse response* of the system. In fact,  $g(t)$  is the time course of the output when the system is forced by a unitary pulse input  $\delta(t)$ , the Dirac impulse, occurring at time zero. In (3.1)  $c(t)$  is the *convolution* of  $u(t)$  with  $g(t)$ : hence, the problem of obtaining  $u(t)$  from (3.1) given  $g(t)$  and  $c(t)$  is called *deconvolution* problem.

In real-world problems, only a finite number of output samples can be measured and the impulse response  $g(t)$  is a model (often a sum of exponentials), either identified through a specific input-output experiment or obtained from population studies.

A physiological example will help to better grasp the ingredients of the problem. Suppose we want to reconstruct insulin secretion rate from C-peptide concentration data (C-peptide, instead of insulin, is used because they are secreted equimolarly by the pancreas but C-peptide does not, at variance of insulin, undergo any liver extraction). In normal conditions, the pancreas

releases C-peptide (and insulin) in an oscillatory fashion with at least two detectable modes: rapid pulses, with period between 8 and 15 minutes, are superimposed to slower and larger oscillations, named ultradian oscillations (UO), whose period ranges between 90 and 150 minutes. If glucose concentration increases, for instance as an effect of a glucose stimulus, the spontaneous oscillations are obscured by the biphasic response of the pancreas. A sudden and large secretory peak (first phase) is followed by a smooth release (second phase). The pancreatic secretion is not directly measurable and the only available information is the plasma concentration of C-peptide. Panel A of Figure 3.2 shows the C-peptide plasma concentration measured every 20 minutes for 12 hours in a normal subject (Sturis *et al.*, 1991). The ultradian oscillatory pattern of the secretion (i.e., the cause) is evident from the measured

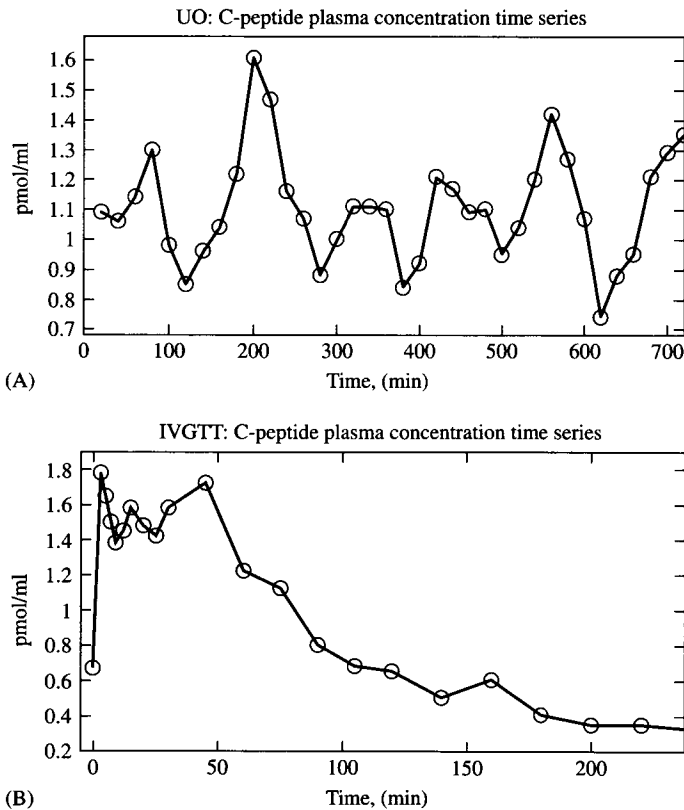


**Figure 3.2.** Estimation of insulin secretion rate (ISR) from C-peptide plasma concentration time series. *Panel A*, Spontaneous ultradian oscillations (UO) ( $n = 36$ ). *Panel B*, Intravenous glucose tolerance test (IVGTT) ( $n = 22$ ).

concentration (i.e., effect). The sampling rate is, however, insufficient to reveal the rapid pulses. Panel B of Figure 3.2 depicts the C-peptide plasma concentrations nonuniformly sampled for 4 hours in a normal subject during an intravenous glucose tolerance test (IVGTT) (Shapiro *et al.*, 1988). The time series clearly reflects the biphasic response of the pancreas to the glucose stimulus. For both cases, since C-peptide kinetics are linear, the problem of reconstructing the C-peptide secretion rate (i.e., the input of Figure 3.1) from the C-peptide plasma concentrations (i.e., the output of Figure 3.1) is a deconvolution problem. To solve it, the impulse response of the system is required. In the C-peptide case, an *ad hoc* experiment can be performed in the same individual of the “deconvolution experiment” on a separate occasion. After suppressing the spontaneous pancreatic secretion by means of a somatostatin infusion, an intravenous bolus of (biosynthetic) C-peptide is administered and plasma concentration samples are frequently collected. The impulse response  $g(t)$  is obtained by fitting a sum of two or three exponentials to the data by nonlinear least squares. A representative data set (Shapiro *et al.*, 1988) with the model fit is reported in Figure 3.3.

Biomedical applications of deconvolution include hormone secretion/substrate production (Pilo *et al.*, 1977; Polonsky *et al.*, 1986; Veldhuis *et al.*, 1987; Caumo and Cobelli, 1993; De Nicolao and Liberati, 1993; De Nicolao *et al.*, 1995; Sparacino and Cobelli, 1996; Sartorio *et al.*, 1997); pharmacokinetics (Cutler, 1978; Dix *et al.*, 1986; Gillespie and Veng-Pedersen, 1986; Iga *et al.*, 1986; Cobelli *et al.*, 1987; Charter and Gull, 1991; Tett *et al.*, 1992; Verotta, 1996; Hovorka *et al.*, 1998); radiography (Hunt, 1971); tracer data processing (Commenges and Brendel, 1982; Bates, 1991); and transport through organ studies (Bassingthwaighte *et al.*, 1966; Knopp *et al.*, 1976;

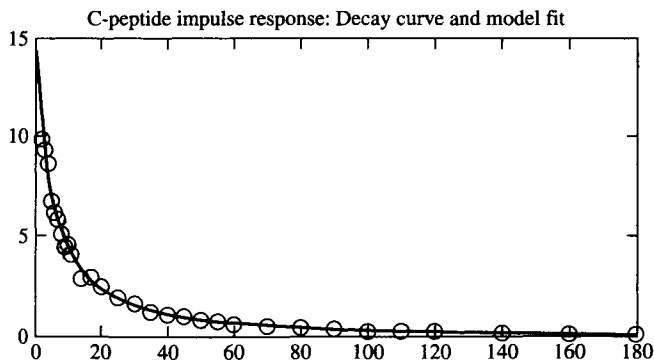


**Figure 3.3.** Determination of the C-peptide impulse response by fitting a sum of three exponentials against the C-peptide concentrations following a bolus.

Nakai, 1980; Bronikowsky *et al.*, 1983; Clough *et al.*, 1993; Sparacino *et al.*, 1998). However, the application of deconvolution is not restricted to the analysis of physiological systems. Other fields in which deconvolution problems arise include spectroscopy (Jansson, 1984); image restoration (Andrews and Hunt, 1977; Wernecke and D'Addario, 1977; Demoment, 1989; Donoho *et al.*, 1992); geophysics (Crump, 1974; Mendel, 1977); equalisation (Lawrence and Kaufman, 1971; Demoment *et al.*, 1979); and acoustics (Miyoshi and Kaneda, 1988).

If the system is linear time-varying (LTV), the input estimation problem becomes that of solving a Fredholm integral equation of the first kind:

$$c(t) = \int_0^t g(t, \tau)u(\tau)d\tau \quad (3.2)$$

The function  $g(t, \tau)$  is called the *kernel* of the system and depends on both  $t$  and  $\tau$  and not on their difference as in (3.1). The function  $g(t, \tau_0)$  describes the time course of the output when the system is forced by a unitary pulse input  $\delta(\tau_0)$  given at time  $\tau_0$ . For instance, the reconstruction of hepatic glucose production after a glucose perturbation can be stated as a Fredholm integral equation of the first kind, where the kernel  $g(t, \tau)$  is described by a linear two-compartment model of glucose kinetics with time-varying parameters (Caumo and Cobelli, 1993). In the literature, the solution of the Fredholm integral equation of the first kind is usually also called (albeit improperly) deconvolution.

*Remark 1.* In (3.1) and (3.2), it is implicitly assumed that  $u(t) = 0$  for  $t < 0$ . In several cases, this is not true, as when a basal spontaneous hormone secretion also occurs for  $t < 0$ . There are several ways to approach this problem. A possible solution is proposed in Remark 6 of Section 3.4.1.

*Remark 2.* Due to the symmetry of (3.1) regarding  $g(t)$  and  $u(t)$ , a deconvolution problem also arises whenever one wants to estimate the impulse response  $g(t)$  of the system given the input  $u(t)$  and the output  $c(t)$ . For instance, the transport function of a substance through an organ can be estimated by deconvolution of the inlet and outlet concentrations (Knopp *et al.*, 1976; Sparacino *et al.*, 1998). Hereafter, we address only input estimation problems.

### 3.3. DIFFICULTY OF THE DECONVOLUTION PROBLEM

In the mathematics/physics/engineering literature, deconvolution is known to be difficult because of its *ill-posedness* and *ill-conditioning*. Here, we discuss these “analytical” difficulties by using a classic example of the



literature (Hunt, 1971; Commenges, 1984; De Nicolao *et al.*, 1997), hereafter referred to as the *Hunt simulated problem*. Consider the input given by:

$$u(t) = e^{-[(t-400)/75]^2} + e^{-[(t-600)/75]^2}, \quad 0 \leq t \leq 1025 \quad (3.3)$$

and the impulse response of the system given by:

$$g(t) = \begin{cases} 1, & t \leq 250 \\ 0, & t > 250 \end{cases} \quad (3.4)$$

These functions must not necessarily have a physiological counterpart. Knowing  $u(t)$  and  $g(t)$ ,  $c(t)$  can be obtained from (3.1). Assume that  $n$  samples of  $c(t)$ ,  $\{c_k\}$  where  $c_k = c(t_k)$ , are measured without error on the uniform sampling grid  $\Omega_s = \{kT\}$ ,  $k = 1 \dots n$ , with  $T = 25$  and  $n = 41$ . The impulse response  $g(t)$ , the input  $u(t)$ , and the output  $c(t)$  together with the samples  $\{c_k\}$  are shown in Panels A, B, and C of Figure 3.4, respectively.

The problem of reconstructing the continuous-time function  $u(t)$  from the time series  $\{c_k\}$  does not admit a unique solution (Bertero, 1989). There is an infinite number of continuous-time functions that, once convoluted with the impulse response, perfectly describe the sampled data. Therefore, the deconvolution problem is an *ill-posed* problem.

To tackle ill-posedness, any deconvolution approach must in some way restrict the field of the functions among which the solution of the problem is sought. For instance, in the so-called *discrete deconvolution* the signal  $u(t)$  is assumed to be a piecewise constant within each interval of the sampling grid  $\Omega_s = \{t_1, t_2, \dots, t_n\}$ , i.e.,  $u(t) = u_i$  for  $t_{i-1} < t \leq t_i$ ,  $i = 1, 2, \dots, n$ , where  $t_0 = 0$ . From (3.2), which includes (3.1) as a particular case, it follows that:

$$c(t_k) = \int_0^{t_k} g(t_k, \tau) u(\tau) d\tau = \sum_{i=1}^k u_i \int_{t_{i-1}}^{t_i} g(t_k, \tau) d\tau \quad (3.5)$$

One may also think of  $u_i$  as the mean level of  $u(t)$  during the  $i$ -th sampling interval. By letting:

$$g_{k,i} = \int_{t_{i-1}}^{t_i} g(t_k, \tau) d\tau \quad (3.6)$$

it follows:

$$c_k = c(t_k) = \sum_{i=1}^k u_i g_{k,i} \quad (3.7)$$

Adopting a matrix notation:

$$c = Gu \quad (3.8)$$

where  $c = [c_1, c_2, \dots, c_n]^T$  is the  $n$ -dimensional vector of the sampled output,  $u = [u_1, u_2, \dots, u_n]^T$ , and  $G$  is a  $n \times n$  lower-triangular matrix, whose

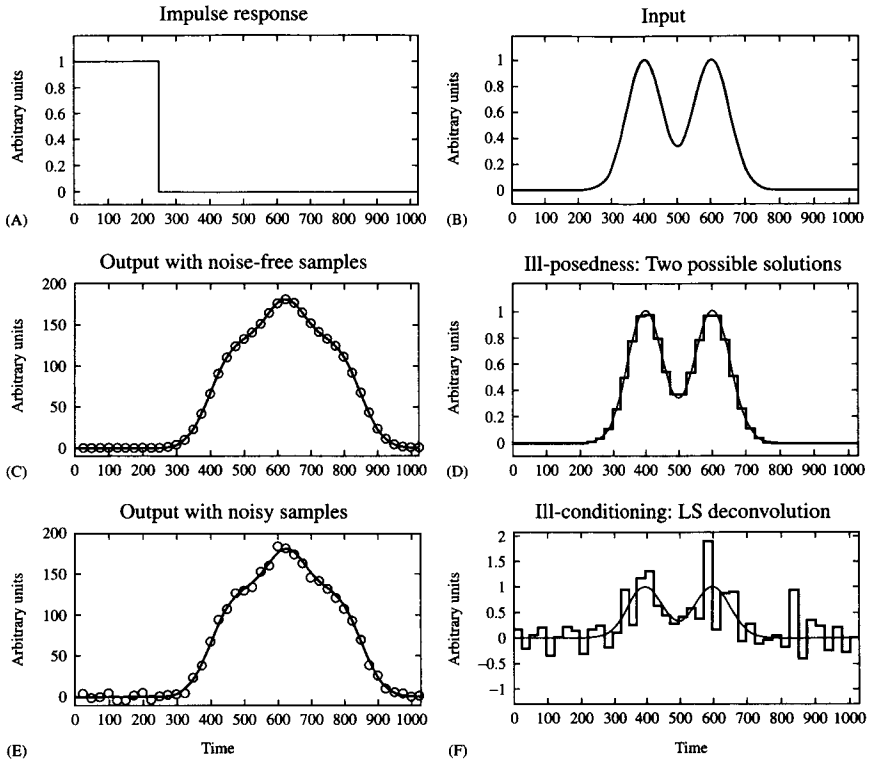


**Figure 3.4.** The Hunt simulated deconvolution problem. *Panel A*, Impulse response. *Panel B*, True input. *Panel C*, True continuous output with noise-free samples ( $n = 41$ ). *Panel D*, Ill-posedness of the deconvolution problem. The staircase function is a solution of the deconvolution problem with error-free data that perfectly describes the samples of Panel C just as the true input. *Panel E*, True continuous output and noisy samples ( $SD = 3$ ). *Panel F*, Ill-conditioning of the deconvolution problem. Solution provided by the least squares approach (staircase line) and true input (thin line) from the noisy output samples of Panel E.

entries are:

$$G(k, i) = \begin{cases} g_{k,i} & k \geq i \\ 0 & k < i \end{cases} \quad (3.9)$$

In the LTI case with uniform sampling  $G(k, i) = G(k - i)$ , so that  $G$  is a Toeplitz matrix and (3.7) represents a discrete-time convolution. If sampling is nonuniform or the system is time-varying, the Toeplitz structure of  $G$  is lost.

Provided that  $G$  is invertible, (3.8) admits a unique solution:  $\hat{u} = \hat{G}^{-1}c$ . For the Hunt simulated problem, this solution is displayed in Panel D of Figure 3.4. It should be noted that, given ill-posedness, this profile is only one

possible solution of the deconvolution problem with noise-free data. Once convoluted with  $g(t)$ , the staircase function perfectly describes the output samples just as the true input, providing an accurate approximation, apart from the staircase approximation.

The previous equation addresses the noise-free situation. However, output samples are usually affected by a measurement error, and this dramatically enhances the difficulty of the deconvolution problem. Let  $y_k$  denote the  $k$ -th measurement:

$$y_k = c_k + v_k \quad k = 1, 2, \dots, n \quad (3.10)$$

where  $v_k$  is the error. Thus, in vector notation:

$$y = Gu + v \quad (3.11)$$

where  $y = [y_1, y_2, \dots, y_n]^T$ , and  $v = [v_1, v_2, \dots, v_n]^T$ . Vector  $v$  is hereafter assumed a zero-mean random vector with covariance matrix  $\Sigma_v$  given by:

$$\Sigma_v = \sigma^2 B \quad (3.12)$$

where  $B$  is a  $n \times n$  positive definite matrix and  $\sigma^2$  is a scale factor, possibly an unknown. Usually, measurement errors are independent so that  $B$  is diagonal. For example, assuming a constant coefficient of variation (CV) for the measurement error,  $B = \text{diag}(y_1^2, y_2^2, \dots, y_n^2)$  and  $\sigma = CV$  (here CV is a real number), with  $\sigma$  possibly unknown. If the variance of the measurement error is constant and equal to  $\sigma^2$ , with  $\sigma^2$  possibly unknown,  $B = I_n$ .

The simplest estimate of  $u$  obtainable from (3.11) is:

$$\hat{u}_{LS} = G^{-1}y \quad (3.13)$$

The superscript LS stands for “least squares.” In fact, (3.13) is the solution of the LS problem:

$$\min_{\hat{u}} (y - G\hat{u})^T B^{-1} (y - G\hat{u}) \quad (3.14)$$

The presence of noise in the measurement vector  $y$  of (3.13) has a dramatic effect on the quality of the estimate. In Panel E of Figure 3.4, Gaussian noise (standard deviation SD = 3) was added to the data of the Hunt simulated problem and LS deconvolution was performed (Panel F). Note that wide, spurious, and unrealistic oscillations contaminate the estimated input, which also takes on negative values. The reason for this deterioration is that deconvolution is not only an ill-posed but also an *ill-conditioned* problem. Small errors in the observed data can be amplified, thus yielding much larger errors in the estimate (Wilkinson, 1967).

It could be hypothesised that increasing the number of samples is beneficial to the solution of the problem. On the contrary, both theory and practice show that increasing the sampling rate worsens ill-conditioning. In addition, the “smoother” the system kernel, the worse the ill-conditioning of the deconvolution problem. For example, the longer the hormone half-life and the higher the sampling rate, the more difficult the reconstructing of the hormone secretion rate by deconvolution (De Nicolao and Liberati, 1993). Analyses that explain the degree of ill-conditioning of a deconvolution problem as a function of sampling rate and kernel smoothness are available in the literature (Hunt, 1972; Ekstroem, 1973).

### 3.3.1. ADDRESSING PHYSIOLOGICAL SYSTEMS

The conceptual difficulties described previously made the deconvolution problem a classic of engineering/mathematics/physics literature. Unfortunately, addressing physiological signals adds to the complexity of the problem. For instance, parsimonious sampling schemes are needed to cope with technical and budget limitations as well as the patient’s comfort. Consequently, the data are often collected with *infrequent* and *nonuniform* sampling schedules (see Figure 3.2). Among other things, nonuniform sampling hinders the possible use of frequency domain techniques such as Wiener filtering. Furthermore, physiological inputs are often intrinsically *non-negative* (e.g., a hormone secretion or a substrate production rate. Thus, negative input estimates due to ill-conditioning (see Figure 3.4, Panel F) are physiologically unplausible. Finally, physiological systems are sometimes *time-varying* (e.g., the glucose-insulin system during a glucose perturbation).

### 3.3.2. A CLASSIFICATION OF THE DECONVOLUTION APPROACHES

Least squares deconvolution is appealingly simple but weak because it is too sensitive to ill-conditioning. In the literature many methods have been developed to circumvent ill-conditioning. Broadly speaking, these methods can be divided into two categories. The first, named *parametric deconvolution*, assumes the analytical expression of the input to be known except for a small number of parameters, so that the deconvolution problem becomes a parameter estimation problem. A second, often referred to as *nonparametric deconvolution*, does not require the postulation of an analytic form of the input. The most known nonparametric approach is the regularisation method that is described in detail in Section 3.4. Some other deconvolution approaches, both parametric and nonparametric, are briefly reviewed in Section 3.5.

### 3.4. THE REGULARISATION METHOD

#### 3.4.1. DETERMINISTIC VIEWPOINT

The regularisation method (sometimes also referred to as damped or penalised least squares) is a nonparametric approach that has been extensively exploited since the 1960s (Phillips, 1962; Tikhonov, 1963; Twomey, 1965; Morozov, 1966). The idea of the method is to identify a solution that provides a good data fit and simultaneously enjoys a certain degree of “smoothness.” This is done by solving the optimisation problem:

$$\min_{\hat{u}} (y - G\hat{u})^T B^{-1} (y - G\hat{u}) + \gamma \hat{u}^T F^T F \hat{u} \quad (3.15)$$

where  $B$  is an  $n \times n$  matrix as in (3.12),  $F$  is an  $n \times n$  penalty matrix (see below) and  $\gamma$  is a real non-negative parameter (see below). Problem (3.15) is quadratic and its solution:

$$\hat{u} = (G^T B^{-1} G + \gamma F^T F)^{-1} G^T B^{-1} y \quad (3.16)$$

linearly depends on the data vector  $y$ . Note that, if  $\gamma = 0$ , (3.16) coincides with (3.14) and the LS solution is obtained. When  $\gamma > 0$ , the cost function of (3.16) is made up of two terms. The first one penalises the distance, weighted by the inverse of  $B$ , between the model predictions  $G\hat{u}$  (the *reconstruction* vector) and the data. The second contribution,  $\hat{u}^T F^T F \hat{u}$ , is a term that penalises the “roughness” of the solution. The standard choice is to penalise the energy of the  $m$ -th order time derivatives, with  $m$  an integer parameter. For example, in Phillips (1962) the second derivative was considered, whereas in Commenges (1984) the energy of the first derivative was penalised. For uniform sampling, these choices correspond to selecting  $F$  as a square lower-triangular Toeplitz matrix (size  $n$ ) whose first column is  $F = [1, -2, 1, 0, \dots, 0]^T$  or  $F = [1, -1, 0, \dots, 0]^T$ , respectively. In general, one can penalise the energy of the  $m$ -th time derivatives by letting:

$$F = \Delta^m \quad (3.17)$$

$\Delta$  being a square lower-triangular Toeplitz matrix (size  $n$ ) whose first column is  $[1, -1, 0, \dots, 0]^T$ . The parameter  $m$  is usually adjusted by trials. Its choice is usually not considered a major issue, and  $m = 1$  or  $m = 2$  are normally used.

The relative weight given to data fit and solution regularity is governed by the so-called *regularisation parameter*  $\gamma$ . By raising  $\gamma$ , the cost of roughness increases and the data match becomes relatively less important. Conversely, by decreasing the value of  $\gamma$  the cost of roughness is lowered, and the fidelity

to the data becomes relatively more important. The choice of the regularisation parameter is a crucial problem: too large values of  $\gamma$  will lead to very smooth estimates of  $\hat{u}$  that may be not able to explain the data (oversmoothing), while too small values of  $\gamma$  will lead to ill-conditioned solutions of  $\hat{u}$  that accurately fit the data but exhibit spurious oscillations due to their sensitivity to noise (for  $\gamma \rightarrow 0$  the LS solution is approached). The importance of the choice of  $\gamma$  is demonstrated by the profiles reported in Panels A and C of Figure 3.5 for the Hunt simulated problem (Panels B and D display how well the estimated input, once convoluted with the impulse response, matches the data).

In the literature, several criteria have been proposed for the choice of the regularisation parameter, such as *discrepancy* (Twomey, 1965); *cross-validation* and *generalised cross-validation* (GCV) (Wahba, 1977; Golub *et al.*, 1979); *unbiased risk* (O'Sullivan, 1986); *minimum risk* (Hall and Titterton, 1989); and *L-curve* (Hansen and O'Leary, 1993). For an asymptotic/analytical comparison between some of these criteria, see O'Sullivan (1986), Rice (1986), Kay (1992), and Hansen (1992b). Two of the most popular criteria are described in the following section.

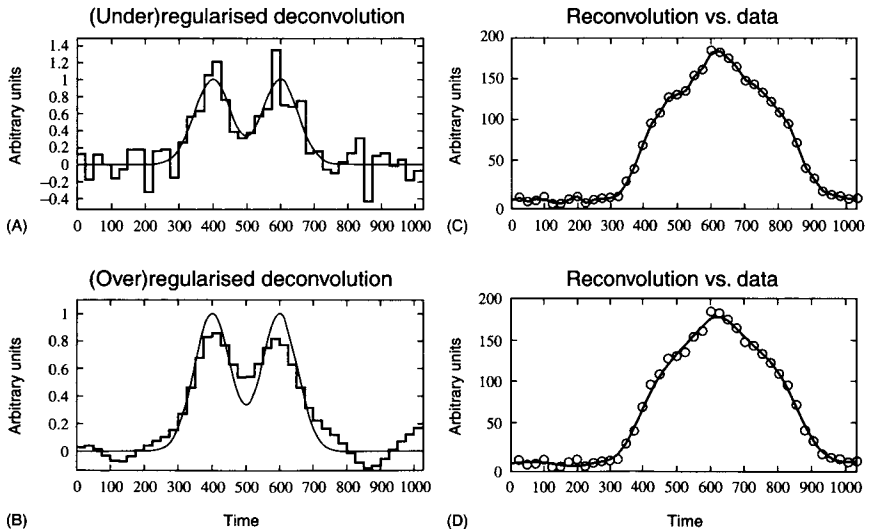


**Figure 3.5.** The Hunt simulated problem. *Panel A*, Regularised deconvolution obtained with a too small value of the regularisation parameter ( $\gamma = 0.5$ ). *Panel B*, Reconvolution obtained from the input of Panel A and data. *Panel C*, Regularised deconvolution obtained with a too large value of the regularisation parameter ( $\gamma = 400$ ). *Panel D*, Reconvolution obtained from the input of Panel C and data.

### 3.4.1.1 The Choice of the Regularisation Parameter

A popular criterion that goes under the name of the *discrepancy* (Twomey, 1965) suggests to compute the residuals vector:

$$r = y - G\hat{u} \quad (3.18)$$

and then adjust  $\gamma$  until the residual sum of squares equals the sum of the measurement error variances. In mathematical terms, the condition to be satisfied can be expressed as:

$$\text{WRSS} = (y - G\hat{u})^T B^{-1} (y - G\hat{u}) = n\sigma^2 \quad (3.19)$$

Since the residuals vector can be interpreted as an estimate of the measurement error vector  $v$ , the discrepancy criterion has a very intuitive motivation. For instance, in the case of  $B = I_n$  it is “logical” to expect that:

$$r^T r \cong E[v^T v] = \sum_{i=1}^n \text{var}(v_k) = n\sigma^2 \quad (3.20)$$

Unfortunately, this intuitive rationale has no solid theoretical foundation. In particular, as it will be discussed in the following, the discrepancy criterion is at risk of oversmoothing (Hall and Titterton, 1987; De Nicolao *et al.*, 1997).

Another popular regularisation criterion is GCV, a technique that has a wide application domain (Wahba, 1990). The regularisation parameter  $\gamma$  is selected as the minimiser of the cost function:

$$\text{GCV}(\gamma) = \frac{\text{WRSS}}{\text{trace}[I_n - \Psi]^2} \quad (3.22)$$

where  $\Psi$  is the so-called hat matrix:

$$\Psi = G(G^T B^{-1} G + \gamma F^T F)^{-1} G^T B^{-1} \quad (3.21)$$

and WRSS is the weighted residuals sum of squares defined as in (3.19).

*Remark 3.* While cross-validation (and thus GCV) aims at minimising the predictive mean square error (relative to the observations), a much more sensible objective to minimise in a deconvolution context is the error relative to the signal to be estimated. In fact, examples have been provided where GCV yields good predictive performances on the observations but fails to optimise the estimation error (Rice, 1986).

### 3.4.1.2 The Virtual Grid

Physiological signals are often sampled at a low and often nonuniform rate. The regularisation method is based on the discrete model (3.7), which

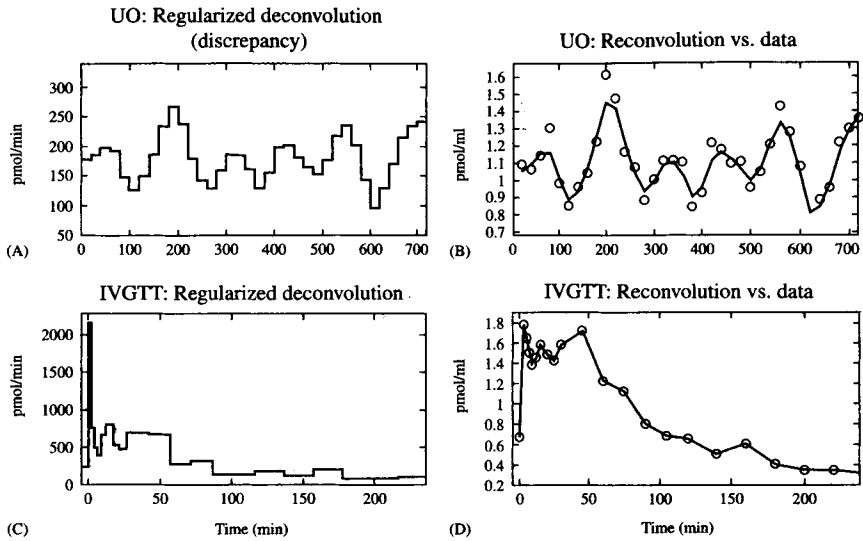


**Figure 3.6.** Estimation of ISR. *Panel A*, UO reconstructed by the regularisation method ( $\gamma = 0.0012$ ,  $q(\gamma) = 19.29$ , discrepancy criterion). *Panel B*, Reconvolution obtained from the input of *Panel A* and data. *Panel C*, ISR during IVGTT reconstructed by the regularisation method ( $\gamma = 0$ ,  $q(\gamma) = 22$ ). *Panel D*, Reconvolution obtained from the input of *Panel C* and data.

was derived assuming that the unknown input is constant during each sampling interval, no matter how long. In the infrequent sampling case, this results in a poor approximation of the signal. For instance, consider the problem of estimating insulin secretion rate. *Panel A* and *Panel C* of *Figure 3.6* show the C-peptide secretory profiles obtained by deconvoluting the data of *Panel A* and *Panel B* of *Figure 3.2*, respectively. Due to the infrequent sampling rate, the staircase approximation is hardly acceptable. *Panels B* and *D* show the data and how well the estimated input  $\hat{u}(t)$  predicts them once reconvoluted with the impulse response. The roughness of the staircase approximation can also be appreciated by examining the deconvoluted profiles obtained for the Hunt simulated problem, in both the ideal (*Figure 3.4*, *Panel D*) and noisy (*Figure 3.4*, *Panel F*; *Figure 3.5*, *Panels A* and *C*) case.

Such an unsatisfactory performance is due to the fact that the number of components of the unknown vector  $u$  is assumed to be equal to the number  $n$  of measurements. To remove this assumption, a different discretisation grid can be used for the input and the output (De Nicolao *et al.*, 1997). Let  $\Omega_s$  be the (experimental) sampling grid and  $\Omega_v = \{T_1, T_2, \dots, T_k, \dots, T_N\}$  a finer ( $N \geq n$ ) grid (possibly uniform) over which the unknown input  $u(t)$  is described as



a piecewise constant function.  $\Omega_v$  must contain  $\Omega_s$  but, apart from this, it is arbitrary and has no experimental counterpart. For this reason,  $\Omega_v$  is called the *virtual grid*. Let  $c_v(T_k)$  denote the (noise-free) output at the virtual sampling times  $T_k$ . Assuming that  $u(t)$  is piecewise constant within each time interval of the virtual grid, it follows that:

$$c_v(T_k) = \int_0^{T_k} g(T_k, \tau)u(\tau)d\tau = \sum_{i=1}^k u_i \int_{T_{i-1}}^{T_i} g(T_k, \tau)d\tau \quad (3.23)$$

where  $T_0 = 0$ . Adopting the usual matrix notation, one has  $c_v = G_v u$ , where  $c_v$  and  $u$  are  $N$ -dimensional vectors obtained by sampling  $c(t)$  and  $u(t)$  on the virtual grid, and  $G_v$  is a  $N \times N$  lower-triangular matrix. Times belonging to the virtual grid  $\Omega_v$  but not present in the sampling grid  $\Omega_s$  have no counterpart in the sampled output data. We can regard them as (virtually) missing data. Denote by  $G$  the  $n \times N$  matrix obtained by removing from  $G_v$  those rows that do not correspond to sampled output data. The measurement vector is thus:

$$y = Gu + v \quad (3.24)$$

where  $v$  is the  $n$ -dimensional vector of the measurement error,  $u$  is the  $N$ -dimensional vector of the input discretised over the virtual grid, and  $G$  is the  $n \times N$  matrix obtained by removing suitable rows of  $G_v$ . If the system is LTI and  $\Omega_v$  is uniform (note that a uniform  $\Omega_v$  can always be chosen),  $G$  has a near-to-Toeplitz structure, meaning that it misses some of the rows of the Toeplitz matrix  $G_v$ .

The estimate  $\hat{u}$  is obtained by solving (3.15), where  $G$  and  $u$  are those of (3.24) and  $F$  has size  $N \times N$ . Provided that  $\Omega_v$  has a fine time detail, this method yields a stepwise estimate that is virtually indistinguishable from a continuous profile.

Panel A of Figure 3.7 shows the results obtained with a 1-min virtual grid and employing the discrepancy criterion for the Hunt simulated problem of Panel E in Figure 3.4 (noisy data). The estimate is able to describe the true continuous-time input much better than the staircase functions of Figure 3.5. Panel B displays the reconvolution fit to the data. Other examples of the use of the virtual grid are reported in the following text.

*Remark 4.* Consider a virtual grid  $\Omega_v = \{k\tau\}$ ,  $k = 1, 2, \dots, N$ , with  $N\tau = t_n$ . By letting  $\tau \rightarrow 0$  and  $N \rightarrow \infty$ , one can obtain an input profile that tends to a continuous-time function. In De Nicolao *et al.* (1997), it was shown that this limit estimate is continuous up to the  $(2m - 2 + p)$ -th time derivative, where  $p$  is the relative degree of the system, or the difference between the degree of the denominator and that of the numerator of the Laplace transform of  $g(t)$ . This result offers a guideline for choosing the order of the time derivatives

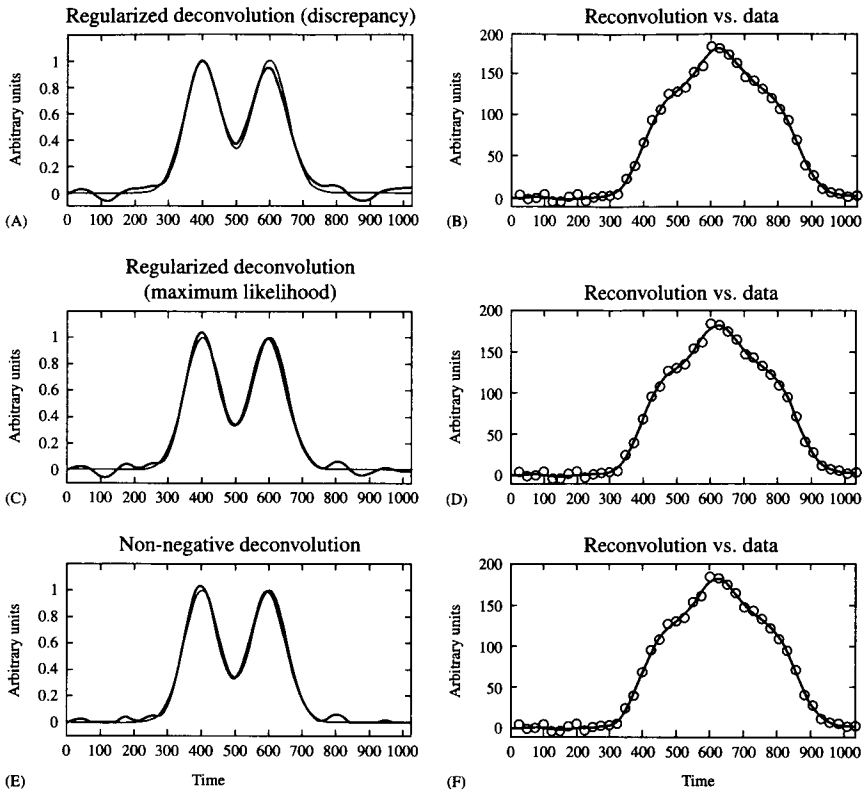


**Figure 3.7.** The Hunt simulated problem (virtual grid). *Panel A*, Regularised deconvolution using the discrepancy criterion ( $\gamma = 1.24e06$ ,  $q(\gamma) = 13.84$ ) and true input. *Panel B*, Reconvolution obtained from the input of *Panel A* and data. *Panel C*, Regularised deconvolution using the maximum likelihood criterion ML1 ( $\gamma = 6.18e05$ ,  $q(\gamma) = 15.55$ ) and true input. *Panel D*, Reconvolution obtained from the input of *Panel C* and data. *Panel E*, Non-negative deconvolution, obtained with the same  $\gamma$  of *Panel C*, and true input. *Panel F*, Reconvolution obtained from the input of *Panel E* and data.

to penalise. For instance, for a LTI system with  $p = 1$ , it will be sufficient to let  $m = 1$  to have an asymptotically continuous estimate together with its first time derivative. Of note is that if  $m = 0$ , (i.e., the energy of the signal itself is penalised), no continuity properties of the signal  $u(t)$  are ensured and the limit as  $\tau \rightarrow 0$  of the estimated input can degenerate in a sequence of pulses.

*Remark 5.* The problem of noncausal inputs (*Remark 1*, Section 3.2) can be easily addressed by estimating the input on a virtual grid starting at a negative time sufficiently far from 0, for example  $-100\tau$  (the input estimate

in the negative portion of the time axis is then discarded) (De Nicolao *et al.*, 1997).

### 3.4.1.3 Assessment of Confidence Limits

Since deconvolution provides an indirect way of measuring a nonaccessible variable, it is important to assess the reliability of such a measurement. In physiological systems analysis, confidence limits are particularly useful when one has to make inferences, such as choosing a threshold for detecting the number of pulses present in a hormone secretory pulsatile profile or deciding if a secretory profile is a pathological one.

For the estimation error  $\tilde{u} = u - \hat{u}$ , the following expression is easily derived:

$$\tilde{u} = -\Gamma v + [I_N - \Gamma G]u \quad (3.25)$$

where  $\Gamma = (G^T B^{-1} G + \gamma F^T F)^{-1} G^T B^{-1}$ . Given the variance of  $v$ , it is possible to obtain the variance of the first term in the right-hand side of (3.25). However, the second term, which is a bias term (its statistical expectation is nonzero if  $\gamma > 0$ ), cannot be computed since it depends on the true (unknown) vector  $u$ . Unless a probabilistic description of  $u$  is provided, confidence intervals accounting for the bias error cannot be obtained. This suggests to state the deconvolution problem within a stochastic embedding. As described in the following section, this also will allow the derivation of statistically based regularisation criteria.

## 3.4.2. STOCHASTIC VIEWPOINT

Consider the model (3.24), possibly derived by discretising (3.2) on a virtual grid, and assume that  $u$  and  $v$  are zero-mean random vectors whose covariance matrices  $\Sigma_u$  and  $\Sigma_v$  are known. It is assumed that  $\Sigma_v = \sigma^2 B$ , see (4.12), and  $\Sigma_u$  (size  $N \times N$ ) is factorised as:

$$\Sigma_u = \lambda^2 (F^T F)^{-1} \quad (3.26)$$

In this stochastic setting, the deconvolution problem — estimating  $u$  from  $y$  through model (3.24) — can be stated as a *linear minimum variance estimation problem*: find the estimate  $\hat{u}$ , linearly depending on the data vector  $y$ , such that  $E[\|u - \hat{u}\|^2]$  is minimised; that is, minimise the expectation of the squared Euclidean norm of the estimation error. Let  $\gamma^0 = \sigma^2/\lambda^2$ . If  $u$  and  $v$  in (3.24) are uncorrelated, the estimate  $\hat{u}$  coincides with the solution of the optimisation problem (3.15), provided that  $\gamma = \gamma^0$  (Beck and Arnold, 1977). When  $u$  and  $v$  are jointly Gaussian, the estimator (3.16) with  $\gamma = \gamma^0$  has minimum error variance among all estimators, either linear or nonlinear, of  $u$  given  $y$ .

To solve deconvolution as a linear minimum variance estimation problem, the *a priori* covariance matrix of the input vector  $u$ ,  $\Sigma_u = \lambda^2(F^T F)^{-1}$ , is required. However, we only know that the input  $u$  is a smooth function of time. A simple *a priori* probabilistic model of a smooth signal on a uniformly spaced grid is to describe it as the realisation of a stochastic process obtained by the cascade of  $m$  integrators driven by a zero-mean white noise process  $\{w_k\}$  with variance  $\lambda^2$  (De Nicolao *et al.*, 1997). For instance, for  $m = 1$  this corresponds to a random-walk model (Commenges, 1984):

$$u_k = u_{k-1} + w_k \quad k = 1, 2, \dots, N; \quad u_0 = 0 \quad (3.27)$$

In a Gaussian setting, (3.27) tells us that, given  $u_k$ ,  $u_{k+1}$  will be in the range  $u_k \pm 3\lambda$  with probability of 99.7%.

It is easily demonstrated that the covariance matrix of the random vector  $u$  whose components are obtained from  $m$  integrations of a white noise process of variance  $\lambda^2$  is given by (3.26) with  $F$  as in (3.17).

Both regularisation and minimum variance estimation determine the estimate by solving (3.16). This allows the establishment of an insightful analogy between the two approaches. In particular, penalising the  $m^{\text{th}}$  time derivatives energy in the regularisation method equals to model the unknown input by a  $(m - 1)$ -fold integrated random-walk process in the stochastic approach. In view of this analogy,  $\gamma^0 = \sigma^2/\lambda^2$  represents, in some sense, the “optimal” value of the regularisation parameter. Such a value is, however, unknown since  $\lambda^2$  and, possibly,  $\sigma^2$  are unknown. Obviously, the lower the  $\lambda^2$ , the smoother the  $\{u_k\}$ . Some statistical criteria for estimating  $\gamma^0$  are introduced in section 3.4.2.2.

### 3.4.2.1 Confidence Limits

In the stochastic embedding, one can cope with the problem of giving a statistical characterisation of the bias term affecting the solution (see Section 3.4.1). In view of (3.25), solving (3.15) for a *generic*  $\gamma$  in place of the unknown  $\gamma^0 = \sigma^2/\lambda^2$  yields:

$$\tilde{u} = u - \Gamma(Gu + v) = -\Gamma v + [I_N - \Gamma G]u \quad (3.28)$$

Equation (3.28) is apparently identical to (3.25) but now all the vectors involved are *stochastic*. Since  $v$  and  $u$  have zero expectation, one has  $E[\tilde{u}] = 0$ . For the variance, one has:

$$\text{var}[\tilde{u}] = \sigma^2 \Gamma B \Gamma^T + \lambda^2 [I_N - \Gamma G] (F^T F)^{-1} [I_N - \Gamma G]^T \quad (3.29)$$

By means of the matrix inversion lemma, it follows that:

$$\text{var}[\tilde{u}] = \sigma^2 \Gamma B \Gamma^T + \gamma \lambda^2 (G^T B^{-1} G + \gamma F^T F)^{-1} F^T F (G^T B^{-1} G + \gamma F^T F)^{-1} \quad (3.30)$$

It is easily verified that the contribution of noise to the error variance, or the first term in the right-hand side of (3.30), is a monotonically decreasing function (in the matrix sense) of  $\gamma$ , whereas the contribution of bias, or the second term of (3.30), is monotonically increasing. Not surprisingly, the *minimum* value of  $\text{var}[\tilde{u}]$  is obtained for the *optimal* value of  $\gamma$  that is  $\gamma = \gamma^0 = \sigma^2/\lambda^2$ :

$$\text{var}[\tilde{u}] = \sigma^2(G^T B^{-1} G + \gamma^0 F^T F)^{-1} \quad (3.31)$$

If reliable estimates of  $\gamma^0$  and  $\sigma^2$  are available, this covariance matrix can be used to compute the confidence intervals for the entries of  $\hat{u}$ .

### 3.4.2.2 Statistically Based Choice of the Regularisation Parameter

Let  $\text{WRSS} = (y - G\hat{u})^T B^{-1} (y - G\hat{u})$  and  $\text{WESS} = \hat{u}^T F^T F \hat{u}$  denote the weighted residuals sum of squares and the weighted estimates sum of squares, respectively. Both quantities depend on the regularised estimate  $\hat{u}$  and thus on the value of  $\gamma$ . In the stochastic setting, WRSS and WESS are random variables. For the linear minimum variance estimate, the following two properties hold (Sparacino and Cobelli, 1996):

$$E[\text{WESS}] = \lambda^2 q(\gamma^0) \quad (3.32)$$

$$E[\text{WRSS}] = \sigma^2 \{n - q(\gamma^0)\} \quad (3.33)$$

where:

$$q(\gamma^0) = \text{trace}(G(G^T B^{-1} G + \gamma^0 F^T F)^{-1} G^T B^{-1}) \quad (3.34)$$

Observe the analogy of (3.33) with a well-known property of linear regression models, where the averaged sum of squared residuals is a biased estimator of the error variance, with the bias depending on the (integer) number of degrees of freedom of the model. For this reason,  $q(\gamma)$  defined by (3.34) is named *equivalent degrees of freedom* associated with  $\gamma$ . The quantity  $q(\gamma)$  is a real number varying from 0 to  $n$ : if  $\gamma \rightarrow 0$  then  $q(\gamma) \rightarrow n$ , whereas if  $\gamma \rightarrow \infty$  then  $q(\gamma) \rightarrow 0$ . The fact that  $q(\gamma)$  is a real number is in agreement with the nature of the regularisation method, where the flexibility of the model (its degree of freedom) can be changed with continuity through the tuning of the regularisation parameter.

By dropping the expectations in (3.32) and (3.33) and recalling that  $\gamma^0 = \sigma^2/\lambda^2$ , two ‘‘consistency’’ criteria can be intuitively derived that allow the choice of  $\gamma$  when either  $\lambda^2$  or both  $\lambda^2$  and  $\sigma^2$  are unknown. The same criteria can be obtained on a firmer statistical ground under Gaussian assumptions by determining necessary conditions for  $\lambda^2$  and  $\sigma^2$  to maximise the likelihood of the data vector  $y$  (De Nicolao *et al.*, 1997). The two criteria are formulated as follows:

*Criterion ML1.* When  $\lambda^2$  is unknown ( $\sigma^2$  is assumed to be known), tune  $\gamma$  until

$$\text{WESS} = \lambda^2 q(\gamma) \quad (3.35)$$

with  $\lambda^2 \sigma^2 / \gamma$ .

*Criterion ML2.* When both  $\sigma^2$  and  $\lambda^2$  are unknown, tune  $\gamma$  until:

$$\frac{\text{WRSS}}{n - q(\gamma)} = \gamma \frac{\text{WESS}}{q(\gamma)} \quad (3.36)$$

and then estimate  $\sigma^2$  as:

$$\hat{\sigma}^2 = \frac{\text{WRSS}}{n - q(\gamma)} \quad (3.37)$$

according to (3.33).

Panel C of Figure 3.7 shows the input profile of the Hunt simulated problem estimated with the virtual grid and using the ML1 regularisation criterion. By comparing this profile with that of Panel A obtained using the discrepancy criterion, the latter is noticeably oversmoothed. In fact, by comparing (3.18) with (3.33), it is easily seen that the discrepancy criterion leads, on average, to oversmoothing.

Panel A of Figure 3.8 displays the reconstruction of ultradian oscillations from the time series of the Panel A of Figure 3.2 obtained by the stochastic approach employing criterion ML1. The 95% confidence intervals obtained from (3.31) also are reported. Panel C shows the reconstruction of insulin secretion rate during IVGTT obtained by the stochastic approach using criterion ML2. In this case,  $\Sigma_u$  was partitioned in two blocks to express the prior information concerning the biphasic response of the pancreatic beta cells to the glucose stimulus, (see Sparacino and Cobelli [1996] for details). In both cases, the use of the virtual grid renders these profiles more plausible than those of Figure 3.6.

*Remark 6.* Some regularisation criteria, such as discrepancy and minimum risk, are restricted to the case in which  $\sigma^2$  is known. In contrast, some others, such as L-curve and (generalised) cross-validation, do not require the knowledge of  $\sigma^2$  but do not use it when it is available. For instance, for a given data set, generalised cross-validation always selects the same  $\gamma$  (hence yielding to the same degree of regularisation) no matter whether the variance of the measurement error is known to be 1 or 100. The two ML criteria (ML1 and ML2) presented previously deal with cases of both known and unknown  $\sigma^2$ .

*Remark 7.* The examples show that the absolute value of  $\gamma$  is meaningless. In fact, this value depends on a number of ingredients of the problem,

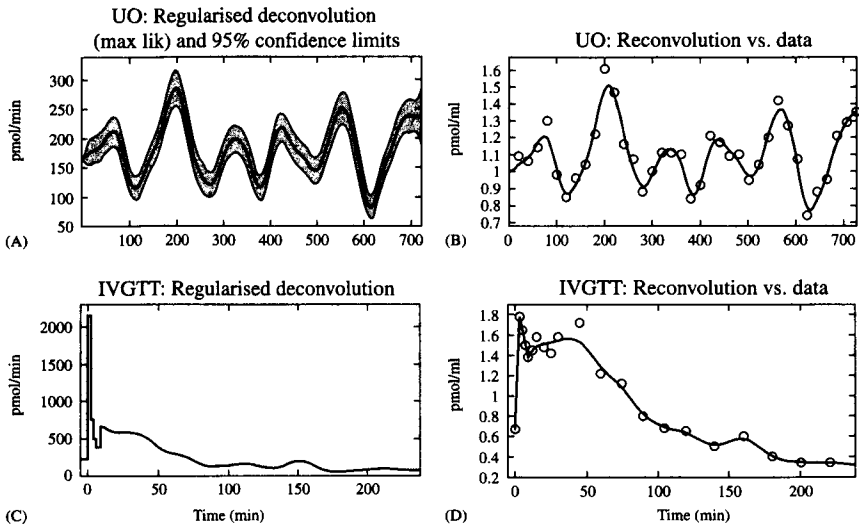


**Figure 3.8.** Estimation of ISR (virtual grid). *Panel A*, UO with 95% confidence limits ( $\gamma = 0.25$ ,  $q(\gamma) = 21.07$ , maximum likelihood criterion ML1). *Panel B*, Reconvolution obtained from the input of Panel A and data. *Panel C*, ISR during IVGTT ( $\gamma = 2.2e - 05$ ,  $q(\gamma) = 9.16$ , maximum likelihood criterion ML2). *Panel D*, Reconvolution obtained from the input of Panel C and data.

such as the sampling rate, the virtual grid, the noise variance, the impulse response, and even the units adopted for the signals under study. As a result, the comparison of the value  $\gamma$  used in different problems does not allow the comparison of the amount of regularisation employed. For instance, in the Hunt simulated problem without virtual grid,  $\gamma = 400$  leads to oversmoothing in Panel E of Figure 3.5, but  $\gamma = 6.18e05$  (fixed in agreement with criterion ML1 in presence of the virtual grid) leads to suitable regularisation in Panel C of Figure 3.7. A better indicator of the regularisation amount is the degrees of freedom  $q(\gamma)$ , since it is a real number varying from 0 to  $n$ . For instance, the degrees of freedom in the two cases were  $q(\gamma) = 11.31$  and  $q(\gamma) = 15.55$ , respectively, suggesting that less regularisation (in spite of a higher value of  $\gamma$ ) was used in the determination of the latter input estimate.

### 3.4.3. NUMERICAL ASPECTS

In the regularisation approach, the computation of the solution via (3.15) or (3.16) would require  $O(N^3)$  memory occupation and  $O(N^3)$  operations to accomplish matrix inversion (the notation  $O(f(N))$  means “of the same order of

magnitude as  $f(N)$ ). This computational burden can be reduced by applying the matrix inversion lemma to (3.16), thus obtaining:

$$\hat{u} = F^{-1}F^{-T}G^T(GF^{-1}F^{-T}G^T + \gamma B)^{-1}y \quad (3.38)$$

In this way an  $n \times n$  matrix must be inverted, at the price of  $O(n^3)$  operations. Note that if  $F$  is as in (3.17), its inverse admits an easy-to-derive analytic expression.

In the LTI system case with uniform sampling, matrices  $G$  and  $F$  in (3.15) exhibit a Toeplitz structure so that only their first columns must be stored. Then, an efficient numerical technique to compute the regularised estimate is available, first presented by Hunt (1971) and subsequently refined by Commenges (1984) and De Nicolao *et al.* (1997). In particular, (3.15) can be solved by the iterative conjugate gradient (CG) method, whose basic iteration can be performed in  $O(N \log N)$  operations through the Fast Fourier Transform (Commenges, 1984) or in  $O(N)$  operations by the use of recursive difference equations (De Nicolao *et al.*, 1997). The Toeplitz structure of the matrices also can be exploited to devise suitable “preconditioners” that improve the rate of convergence of the algorithm (Commenges, 1984). Since theory guarantees the convergence of the CG algorithm in  $N$  iterations at most, the overall complexity of the algorithm is  $O(N^2 \log N)$  or  $O(N^2)$ . Of note is that in the presence of time-varying systems, these numerically efficient methods do not apply equally well because matrix  $G$  does not have a Toeplitz structure.

However, the bottleneck of numerical algorithms for deconvolution is given by computing several trial solutions of (3.15). In fact, the tuning of the regularisation parameter  $\gamma$  (according to any criterion) requires a trial-and-error procedure. Here, we illustrate a possible way to reduce the computational burden (De Nicolao *et al.*, 1997). First, define:

$$H = B^{-1/2}GF^{-1} \quad (3.39)$$

where  $H$  is an  $n \times N$  matrix (if the virtual grid is not used, then  $N = n$ ) Consider the singular value decomposition (SVD) of  $H$ :

$$U^T H V = D \quad (3.40)$$

where  $U$  and  $V$  are unitary matrices of size  $n \times n$  and  $N \times N$ , respectively, and  $D$  is an  $n \times N$  “diagonal” matrix, whose diagonal elements  $D_{ii}$  are denoted by  $d_i$ ,  $i = 1, 2, \dots, n$ . Let us change the coordinates in the output space by letting  $\xi = U^T B^{-1/2}y$  and  $\varepsilon = U^T B^{-1/2}v$  and in the input space by letting  $\eta = V^T F u$ . In the new coordinates, (3.11) becomes:

$$\xi = D\eta + \varepsilon \quad (3.41)$$

It is easily demonstrated that  $\text{cov}(\varepsilon) = \sigma^2 I_n$  and  $\text{cov}(\eta) = \lambda^2 I_N$ .



Since  $D$  is diagonal, the set of  $n$  equations given by (3.41) is equivalent to the following set of  $n$  independent equations:

$$\xi_i = d_i \eta_i + \varepsilon_i, \quad i = 1, \dots, n \quad (3.42)$$

Note that  $\{\xi_i\}$ ,  $i = 1, 2, \dots, n$ , do not provide (*a posteriori*) information on  $\{\eta_i\}$  for  $i = n + 1, n + 2, \dots, N$ . In the new basis, the regularised input estimate obtained from (3.41) is:

$$\hat{\eta} = (D^T D + \gamma I_N)^{-1} D^T \xi \quad (3.43)$$

The diagonal structure of  $D$  allows the computation of each single component of the input estimate vector as:

$$\hat{\eta}_i = \frac{d_i}{d_i^2 + \gamma} \xi_i, \quad i = 1, \dots, n \quad (3.44)$$

$$\hat{\eta}_i = 0, \quad i = n + 1, \dots, N \quad (3.45)$$

In the new coordinates, the reconvolution vector is  $\hat{\xi} = D\hat{\eta}$ , the components of which are computable as:

$$\hat{\xi}_i = \frac{d_i^2}{d_i^2 + \gamma} \xi_i, \quad i = 1, \dots, n \quad (3.46)$$

Moreover, the residuals  $\rho = \xi - \hat{\xi}$  can be computed as:

$$\rho_i = \frac{\gamma}{d_i^2 + \gamma} \xi_i, \quad i = 1, 2, \dots, n \quad (3.47)$$

The quantities  $WRSS = (y - G\hat{u})^T B^{-1} (y - G\hat{u})$  and  $WESS = \hat{u}^T F^T F \hat{u}$  can now be easily computed:

$$WESS = \hat{u}^T F^T F \hat{u} = \hat{u}^T F^T V V^T F \hat{u} = \hat{\eta}^T \hat{\eta} = \sum_{i=1}^n \left( \frac{d_i \xi_i}{d_i^2 + \gamma} \right)^2 \quad (3.48)$$

$$\begin{aligned} WRSS &= r^T B^{-1} r = r^T B^{-1/2} B^{-1/2} r = r^T B^{-1/2} U U^T B^{-1/2} r \\ &= \rho^T \rho = \sum_{i=1}^n \left( \frac{\gamma \xi_i}{d_i^2 + \gamma} \right)^2 \end{aligned} \quad (3.49)$$

Finally, it is easily demonstrated that the degrees of freedom associated with  $\gamma$  are:

$$q(\gamma) = \sum_{i=1}^n \frac{d_i^2}{d_i^2 + \gamma} \quad (3.50)$$

In the transformed coordinates, input estimate, reconvolution, residuals, degrees of freedom, WESS, and WRSS can be computed via scalar operations and for a certain trial value of  $\gamma$  require only  $O(n)$  operations. The main computational burden of the overall deconvolution procedure lies in the SVD (3.40), which amounts to  $O(n^3)$  operations. However, since SVD is independent on  $\gamma$ , it is performed only once. Of particular note is that the complexity of the SVD is not affected by the dimension  $N$  of the virtual grid.

Once the “optimal” value of the regularisation parameter is achieved, the input estimate in the original coordinates is determined as:

$$\hat{u} = F^{-1}V\hat{\eta} \quad (3.51)$$

which is computable in  $O(nN^2)$  operations (note that multiplying an  $N$ -dimension vector by  $F^{-1}$  is equivalent to  $m$ -fold integration and requires only  $O(N)$  operations).

The above diagonalisation strategy also can be extended to the computation of the confidence intervals of the estimate which, in view of (3.31), depend on the diagonal elements of the  $N \times N$  matrix  $(G^T B^{-1} G + \gamma^0 F^T F)^{-1}$ . Using a standard matrix inversion procedure would require  $O(N^3)$  operations, a heavy computational burden. However, in the transformed coordinates, the confidence intervals can be derived in  $O(N^2)$  operations (De Nicolao *et al.*, 1997).

Since the complexity of the SVD-based algorithm is  $O(n^3)$ , irrespective of the size  $N$  of the virtual grid, this strategy is more convenient (at least when  $n$  is small compared to  $N$ ) than the methods based on the CG (De Nicolao *et al.*, 1997). In addition, since the efficiency of the diagonalisation procedure does not depend on the Toeplitz structure of  $G$ , the SVD-based algorithm can also be successfully employed in the time-varying case (Fredholm integral equation).

As an alternative to the use of SVD, another method that accounts for the solution of (3.15) for various trial values of the regularisation parameter is based on the use of the QR factorisation (Hanke and Hansen, 1993).

### 3.4.4. CONSTRAINED DECONVOLUTION

In a number of physiological cases, the input  $u(t)$  is known to be intrinsically nonnegative (e.g., hormone secretion rates, drug absorption rates). Nevertheless, due to measurement errors and impulse response model mismatch, the solution provided by (3.16) may take on negative values (see Figure 3.7, Panels A and C). To obtain nonnegative estimates, the regularisation method can be reformulated as a constrained optimisation

problem (Commenges, 1984; De Nicolao *et al.*, 1997):

$$\min_{\hat{u} \geq 0} (y - G\hat{u})^T B^{-1} (y - G\hat{u}) + \gamma \hat{u}^T F^T F \hat{u} \quad (3.52)$$

where  $\hat{u} \geq 0$  stands for  $\hat{u}_k \geq 0, \forall k$ . This problem does not admit a closed-form solution and must be solved by an iterative method such as the constrained CG algorithm (Hestenes, 1980).

Remarkably, the incorporation of nonnegativity constraints as in (3.52) makes the estimator nonlinear. This impairs the use of some regularisation criteria, such as GCV or ML. In addition, nonnegativity contradicts Gaussianity so that the computation of confidence intervals by exploiting analytic approaches is not possible. A possible empirical strategy is as follows:

1. Find the (linear) solution (3.16) with  $\gamma$  chosen according to some regularisation criterion.
2. Having zeroed the negative components of the solution, use it as an initial guess for the constrained CG algorithm that is launched to solve (3.52) with the same  $\gamma$  obtained in the unconstrained case.

As far as the confidence limits are concerned, a Monte Carlo approach can be adopted (De Nicolao *et al.*, 1997). Alternatively, since this approach is computationally demanding, an approximation of the confidence intervals can be obtained by attaching the intervals of the unconstrained estimate computed according to (3.31) to the solution of (3.52).

Panel E of Figure 3.7 shows, for the simulated problem, the input profile estimated with the nonnegativity constraint. The value of the regularisation parameter is the same adopted for the unconstrained estimate displayed in Panel C.

### 3.5. OTHER DECONVOLUTION METHODS

A number of deconvolution techniques, often referred to as *parametric deconvolution* methods, circumvent ill-posedness and ill-conditioning by making functional assumptions on the input. The analytic expression of the input is assumed to be known except for a small number of parameters, so that the deconvolution problem becomes a parameter estimation problem with more data than unknowns. This guarantees the uniqueness (at least locally) and regularity of the solution. In Cutler (1978), for example, the unknown input is described as an  $M$ -th order polynomial and one has only to estimate its  $M + 1$  coefficients. In Veng-Pedersen (1980a), a linear combination of  $M$  exponentials is used, so that deconvolution turns into the problem of determining the amplitudes and the rates ( $2M$  parameters). Similar methods

are discussed in other studies (Veng-Pedersen, 1980b; Gillespie and Veng Pedersen, 1986; Vajda *et al.*, 1988 and Verotta, 1990). Parametric approaches also were developed for more specific problems. For instance, in Veldhuis and Johnson (1992), episodic hormone release is described by assuming secretory spikes to be Gaussian shaped with each pulse characterised by three parameters: location, amplitude, and width. Lagged-normals models have been used in Knopp *et al.* (1976) and Pollastri *et al.* (1977) to approximate the transport function of an indicator into an organ and in Norwich (1977) to remove catheter distortion on indicator dilution curves.

The required heavy assumptions on the shape of the unknown input generally constitute a major drawback. Moreover, when a class of functional forms for the unknown input is considered, model order selection problems must be addressed, such as selecting the degree  $M$  of the polynomial in Cutler (1978), the number  $M$  of exponentials in Veng-Pedersen (1980), the number of addenda in the lagged-normals sum in Knopp *et al.* (1976), or the number of pulses that form the secretory profile in Veldhuis and Johnson (1992). In fact, increasing the model order leads to a better data fit but at the price of an increased noise sensitivity of the input estimate. Remarkably, model order selection resembles the problem of tuning the smoothing parameter in the regularisation method. When the regularisation parameter is too small, the estimate is overly sensitive to noise as if the model were overparameterised; conversely, for excessively large values of the regularisation parameter, the estimate does not explain the data as if the model were underparameterised. In parametric deconvolution, model order selection criteria must be used to avoid subjectivity in governing the fit versus smoothness trade-off, and some of the criteria defined for the regularisation method, such as cross-validation, discrepancy, and  $L$ -curve, can be extended to this purpose. In some parametric methods, it is difficult to impose nonnegativity constraints (Verotta, 1990) and to handle time-varying systems. Finally, the intrinsic nonlinearity of parametric deconvolution methods exposes them to the problem of correctly selecting the initial guess of the parameters to avoid local minima in parameter estimation (Verotta, 1990).

A parametric approach that allows a larger flexibility is based on *regression splines* (Verotta, 1993; 1996). In this approach, the input  $u(t)$  is a spline given by:

$$u(t) = \sum_{i=1}^M \mu_i B_{i,\tau}(t) \quad (3.53)$$

where  $\{\mu_i\}$  are scalars and  $B_{i,\tau}$  represents the  $i$ -th normalised component of the (cubic)  $B$ -spline basis,  $\tau$  being the knot position vector. Having fixed number and location of the spline knots, which means having chosen  $M$  and  $\tau$ , the reconvolution vector linearly depends on vector  $\mu = [\mu_1, \mu_2, \dots, \mu_M]^T$ ,

which can thus be estimated by least squares:

$$\min_{\mu} \|y - \Phi\mu\|^2 \quad (3.54)$$

where  $\Phi$  is a  $n \times M$  matrix. The major problems connected with the use of regression splines in deconvolution are related to the choice of the model order  $M$  and the knot location vector  $\tau$ . The problem of selecting  $M$  involves the usual fit versus smoothness trade-off. The problem of locating the spline knots is more complex. Intuitively, the density of knots should be higher where fast changes in the input are expected; see Verotta (1993) for empirical strategies. An appealing feature of the regression splines method is the possibility of incorporating monotonicity and nonnegativity constraints on the input by adding suitable inequality constraints on vector  $\mu$ . However, these constraints introduce nonlinearities, and empirical modifications of the Akaike and GCV criteria are needed to solve the model order selection problem (Verotta, 1993).

Turning back to nonparametric methods, it should be noted that, in addition to regularisation, there are other approaches to deconvolution. These include *truncated singular values decomposition* (TSVD), *conjugate gradient regularisation* (CGR), and *maximum entropy* (ME).

TSVD methods (Hanson, 1971; Varah, 1973; Hansen, 1987) first perform a singular value expansion of the algebraic system (3.11) and then determine an (unconstrained) estimate by truncating such an expansion before the small singular values start to dominate. The (integer) number  $k$  of the eigenvectors that are left in the expansion determines the regularity of the estimate, similarly to the regularisation parameter (Hansen, 1992a).

CGR is based on the fact that, when the CG algorithm is used to solve the system  $y = Gu$ , the low-frequency components of the solution tend to converge faster than the high-frequency components. Hence, the CG has some inherent regularisation effect where the number of CG iterations tunes the regularity of the solution (Van der Sluis and Van der Vorst, 1990).

Finally, ME methods (Wernecke and D'Addario, 1977; Charter and Gull, 1991; Donoho *et al.*, 1992) can be considered variants of the regularisation method where the term  $u^T \log u$  replaces the quadratic term  $u^T F^T F u$  in (3.15). In this way, for a fixed  $\gamma$ , the ME estimator provides (strictly) positive signals but it is no more linear in the parameters, so that a closed form solution does not exist and an iterative method is required to compute the estimate. The structure of the cost function makes ME methods particularly suitable to solve problems where the unknown input is essentially zero in the vast majority of its domain, for example with a nearly black image, (Donoho *et al.*, 1992).

In all the deconvolution approaches mentioned in this section, the computation of the confidence intervals is difficult either because the estimator is nonlinear or because of the deterministic setting in which they are stated. Finally, similarly to the regularisation method, all these approaches require

a trial-and-error procedure to adjust the fit versus smoothness trade-off. For instance, in parametric deconvolution, candidate solutions must be computed for several trial values of the model order  $M$ .

### 3.6. CONCLUSIONS

In this chapter, we have introduced the deconvolution problem critically reviewing the available methods against the real-world challenges arising in the analysis of physiological systems, including ill-conditioning, treatment of infrequently sampled data sets, computation of confidence intervals, nonnegativity constraints, and efficiency of the numerical algorithms. In this respect, the regularisation method makes only mild assumptions of the unknown input and has some important advantages over the other deconvolution approaches, especially in its stochastic formulation. In fact, the stochastic viewpoint offers a statistically sound solution to the problems of determining the smoothness versus data trade-off and estimating confidence intervals of the reconstructed input. By means of the virtual grid concept, the regularisation method also can handle effectively infrequent/nonuniform sampling schedules. Moreover, an SVD-based computational scheme allows the solution of the complete input estimation problem, including trial-and-error estimation of the regularisation parameter, in  $O(n^3)$  operations, where  $n$  denotes the number of observations, even when the number  $N$  of unknowns is much larger.

At the time of this writing, work on the regularisation approach focused on the development of enhanced numerical algorithms and the computation of confidence intervals of the input estimate also accounting for uncertainty of the parameters of the impulse response. A spectral factorisation approach can be exploited in the LTI case with uniform sampling to derive explicit formulae of the degrees of freedom  $q(\gamma)$  that speed up calculations (De Nicolao *et al.*, 2000). In the unconstrained case, using state-space methods, it has been shown that the regularised estimate is a weighted sum of  $N$  basis functions, with weights computable in  $O(n)$  operations by Kalman filtering (De Nicolao *et al.*, 1998). As far as confidence intervals are concerned, stochastic regularisation (Section 3.4.2) allows the estimation of confidence intervals that do not account for model uncertainty. However, in real-world problems, the impulse response is uncertain since its parameters are obtained from population studies or estimated from experimental data affected by error (see Figure 3.3). Reliable confidence limits of the input profile should therefore account for the impulse response model uncertainty. Analytical expressions similar to (3.31) are difficult to carry out. The simplest method to assess the joint effect of data and model uncertainty is based on a Monte Carlo strategy. First, the output

data and the nominal values of the impulse response parameters, with their precision, are used to artificially generate perturbed deconvolution problems, and then confidence intervals are worked out from the sample distribution of a sufficiently large number (some hundreds, typically) of perturbed solutions (Sparacino and Cobelli, 1996). A theoretically more sound approach is to determine the input estimate and its confidence intervals by employing Bayesian networks and Markov Chain Monte Carlo integration (Magni *et al.*, 1998).

### 3.7. ACKNOWLEDGEMENTS

We thank Dr. K. S. Polonsky (Department of Medicine, University of Chicago, IL) for allowing us access to the C-peptide data. This work was in part supported by NIH grants RR-11095 and RR-12609 and by a GlaxoWellcome Research and Development grant.

### 3.8. REFERENCES

- Andrews, H. C. and B. R. Hunt. 1977. *Digital Image Restoration*. Englewood Cliffs, NJ: Prentice Hall.
- Bassingthwaite, J. F., E. Ackerman and E. Wood. Applications of the lagged normal density curve as a model for arterial dilution curves. *Circ Res* 18(1966):398–415.
- Bates, J. T. H. Deconvolution of tracer and dilution data using the Wiener filter. *IEEE Trans Biomed Eng* 38(1991):1262–66.
- Beck, J. V. and K. J. Arnold. 1977. *Parameter Estimation in Engineering and Science*. New York: Wiley.
- Bertero, M. Linear inverse problems and ill-posed problems. *Adv Electronics Electron Phys* 75(1989):1–120.
- Bronikowsky, T., C. Dawson and J. Linehan. Model-free deconvolution techniques for estimation of vascular transport functions, *Int J Biomed Comput* 14(1983):411–29.
- Caumo, A. and C. Cobelli. Hepatic glucose production during the labelled IVGTT: estimation by deconvolution with a new minimal model. *Am J Physiol* 264(1993):E829–41.
- Charter, M. K. and S. F. Gull. Maximum entropy and drug absorption. *J Pharmacokinet Biopharm* 19(1991):497–520.
- Clough, A., D. Cui, J. H. Linehan, G. S. Krenz, C. A. Dawson and M. B. Maron. Model-free numerical deconvolution of recirculating indicator concentration curves, *J Appl Physiol* 75(1993):1444–53.
- Cobelli, C., A. Mari, S. Del Prato, S. De Kreutzenberg, R. Nosadini and I. Jensen. Reconstructing the rate of appearance of subcutaneous insulin by deconvolution. *Am J Physiol* 252(1987):E549–56.
- Commenges, D. and A. J. Brendel. A deconvolution program for processing radiotracer dilution curves, *Comput Methods Programs Biomed* 14(1982):271–76.
- Commenges, D. The deconvolution problem: fast algorithms including the preconditioned conjugate-gradient to compute a MAP estimator. *IEEE Trans Automat Contr* AC-29(1984):229–43.
- Crump, N. D. A Kalman filter approach to the deconvolution of seismic signals. *Geophysics* 39(1974):1–13.

- Cutler, D. J. Numerical deconvolution by least squares: use of polynomials to represent the input function. *J. Pharmacokinetic Biopharm* 6(1978):243–63.
- Demoment, G., C. L. Posca and D. Saint-Felix. Transducer smearing correction using a microprocessor based on discrete deconvolution. In: *Proceedings of 18th IEEE Conference on Decision and Control*, 1979:842–43.
- Demoment, G. Image reconstruction and restoration: overview of common estimation structures and problems. *IEEE Trans Acoust Speech Signal Process* 37(1989):2024–36.
- De Nicolao, G. and D. Liberati. Linear and nonlinear techniques for the deconvolution of hormone time-series. *IEEE Trans Biomed Eng* BME-40(1993):440–55.
- De Nicolao, G., D. Liberati and A. Sartorio. Deconvolution of infrequently sampled data for the estimation of growth hormone secretion. *IEEE Trans Biomed Eng* BME-42(1995):678–97.
- De Nicolao, G., G. Sparacino and C. Cobelli. Nonparametric input estimation in physiological systems: problems, methods, case studies. *Automatica* 33(1997):851–70.
- De Nicolao, G., G. Ferrari Trecate and G. Sparacino. Fast spline smoothing via spectral factorisation concepts. *Automatica* 36(2000) (in press).
- De Nicolao, G., G. Ferrari Trecate and M. Franzosi. Nonparametric deconvolution of hormone time-series: a state-space approach. In: *Proceedings of the 1998 IEEE International Conference on Control Applications, Trieste, Italy, 1–4 Sept. 1998*, 1998:346–50.
- Dix L. P., D. Frazier, M. Cooperstein and J. Riviere. Exponential intravenous infusion in toxicological studies: achieving identical serum drug concentration profiles in individuals with altered pharmacokinetic states. *J Pharm Sci* 75(1986):448–51.
- Donoho, D., I. M. Johnstone, J. Hoch and A. Stern. Maximum entropy and the nearly black object. *J Roy Statist Soc Ser B* 54(1992):41–81.
- Ekstroem, M. P. A spectral characterization of the ill-conditioning in numerical deconvolution. *IEEE Trans Audio Electroac* AU-(1973):344–48.
- Gillespie, W. and P. Veng-Pedersen. A polyexponential deconvolution method. Evaluation of the “gastrointestinal bioavailability” and mean in vivo dissolution time of some ibuprofen dosage forms. *J Pharmacokin Biopharm* 13(1985):289–307.
- Golub, G. H., M. Heath and G. Wahba. Generalized cross-validation as a method for choosing a good ridge parameter. *Technometrics* 21(1979):215–24.
- Hall, P. and D. M. Titterton. Common structure of techniques for choosing smoothing parameters in regression problems. *J Roy Statist Soc Ser B* 49(1987):184–98.
- Hansen, P. C. The truncated SVD as a method for regularization, *BIT* 27(1987):354–553.
- Hansen, P. C. Numerical tools for analysis and solution of Fredholm integral equation of the first kind. *Inverse Probl* 8(1992a):849–72.
- Hansen, P. C. Analysis of discrete ill-posed problems by means of the L-curve. *SIAM Rev* 34(1992b):561–80.
- Hansen, P. C. and O’Leary, D. P. The use of the L-curve in the regularization of discrete ill-posed problems. *SIAM J Sci Stat Comput* 14(1993):1487–1503.
- Hanson, R. J. A numerical method for solving Fredholm integral equations of the first kind using singular values. *SIAM J Numer Anal* 8(1971):616–22.
- Hanke, M. and P. C. Hansen. Regularization methods for large scale problems. *Surv Math Ind* 3(1993):253–315.
- Hestenes, M. R. 1980. *Conjugate Direction Methods in Optimization*. Berlin: Springer-Verlag.
- Hovorka, R., M. J. Chappell, K. R. Godfrey, F. N. Madden, M. K. Rouse and P. A. Soons. CODE: a deconvolution program implementing a regularization method of deconvolution constrained to non-negative values: description and pilot evaluation. *Biopharm Drug Dispos* 19(1998):39–53.
- Hunt, B. R. The inverse problem of radiography. *Math Biosci* 8(1970):161–79.
- Hunt, B. R. Biased estimation for nonparametric identification of linear systems. *Math Biosci* 10(1971):215–37.



- Hunt, B. R. A theorem on the difficulty of numerical deconvolution. *IEEE Trans Audio Electroac* AU-20(1972):94–5.
- Iga, K., Y. Ogawa, T. Yashiki and T. Shimamoto. Estimation of drug absorption rates using a deconvolution method with nonequal sampling times. *J Pharm Bio* 14(1986):213–25.
- Jansson, P. 1984. *Deconvolution with Applications in Spectroscopy*, New York: Academic Press.
- Kay, J. Asymptotic comparison factors for smoothing parameter choices in regression problems. *Statist Prob Lett* 15(1992):329–35.
- Knopp, T. J., W. A. Dobbs, J. F. Greenleaf and J. B. Bassingwaighe. Transcoronary intravascular transport functions obtained via a stable deconvolution technique. *Ann Biomed Eng* 4(1986):44–59.
- Lawrence, R. E. and H. Kaufman. The Kalman filter for equalization of a digital communication channel. *IEEE Trans Comm* COM-19(1971):1137–41.
- Magni, P., R. Bellazzi and G. De Nicolao. Bayesian function learning using MCMC methods. *IEEE Trans Patt Anal Mach Intell* 20(1998):1319–31.
- Mendel, J. M. White noise estimators for seismic data processing in oil exploration. *IEEE Trans Automat Contr* AC-22(1977):694–706.
- Morozov, V. A. On the solution of functional equations by the method of regularization, *Soviet Math Dokl* 7(1966):414–16.
- Miyoshi, M. and Y. Kaneda. Inverse filtering of room acoustics. *IEEE Trans Acoust Speech Signal Process* 36(1988):145–52.
- Nakai, M. Computation of transport function using multiple regression analysis. *Am J Physiol* 240(1981):H133–44.
- Norwich, K. 1977. *Molecular Dynamics in Biosystems*. Oxford: Pergamon Press.
- O'Sullivan, F. A statistical perspective on ill-posed inverse problems. *Stat Sci* 1(1986):502–27.
- Papoulis, A. 1984. *Probability, Random Variables and Stochastic Processes*. Singapore: McGraw-Hill.
- Phillips, D. L. A technique for the numerical solution of certain integral equations of the first kind. *J Assoc Comput Mach* 9(1962):97–101.
- Pilo, A., E. Ferrannini and R. Navalesi. Measurement of glucose-induced insulin delivery rate in man by deconvolution analysis. *Am J Physiol* 233(1977):E500–8.
- Pollastri, A., M. Pistolesi and C. Giuntini. A method for computing frequency functions from input-output vascular dilution curves. *J Nucl Med Allied Sci* 21(1977):165–77.
- Polonsky, K. S., J. Licinio-Paixao, B. D. Given, W. Pugh, P. Rue, J. Galloway, T. Karrison and B. Frank. Use of biosynthetic human C-peptide in the measurement of insulin secretion rates in normal volunteers and type I diabetic patients. *J Clin Invest* 51(1986):98–105.
- Rice, J. A. Choice of the smoothing parameter in deconvolution problems. *Contemp Math* 59(1986):137–51.
- Sartorio, A, G. De Nicolao, G. Pizzini and D. Liberati. Nonparametric deconvolution provides an objective assessment of GH responsiveness to GH releasing stimuli in normal subjects. *Clin Endocrinol* 46(1997):387–400.
- Shapiro, E. T., H. Tillil, A. H. Rubenstein and K. S. Polonsky. Peripheral insulin parallels changes in insulin secretion more closely than C-peptide after bolus intravenous glucose administration. *J Clin Endocrinol Metab* 67(1988):1094–99.
- Sparacino, G. and C. Cobelli. A stochastic deconvolution method to reconstruct insulin secretion rate after a glucose stimulus. *IEEE Trans Biomed Eng* 43(1996):512–29.
- Sparacino, G. and C. Cobelli. Impulse response model in reconstruction of insulin secretion by deconvolution. Role of input design in the identification experiment, *Ann Biomed Eng* 25(1997):398–416.
- Sparacino, G., R. Bonadonna, H. Steinberg, A. Baron and C. Cobelli. Estimation of organ transport function from recirculating indicator dilution curves, *Ann Biomed Eng* 26(1998):128–35.

- Sturis, J., E. Van Cauter, J. D. Blackman and K. S. Polonsky. Entrainment of pulsatile insulin secretion by oscillatory glucose infusion. *J Clin Invest* 87(1991):439–45.
- Tett, S. E., D. Cutler and R. Day. Bioavailability of hydroxychloroquine tablets assessed with deconvolution techniques. *J Pharm Sci* 81(1992):155–59.
- Tikhonov, A. N. Solution of incorrectly formulated problems and the regularization method. *Soviet Math Dokl* 4(1963):16–24.
- Tikhonov, A. N. and V. Y. Arsenin. 1977. *Solutions of Ill-Posed Problems*. Washington, DC: Winston/Wiley.
- Twomey, S. The application of numerical filtering to the solution of integral equations of the first kind encountered in indirect sensing measurements. *J Franklin Inst* 279(1965):95–109.
- Vajda, S., K. R. Godfrey and P. Valko. Numerical deconvolution using system identification methods. *J Pharmacokinet Biopharm* 16(1988):85–107.
- Van der Sluis, A. and H. A. Van der Vorst. SIRT and CG type methods for iterative solutions of sparse linear least-squares problems. *Lin Alg Appl* 130(1990):257–302.
- Varah, J. M. On the numerical solutions of ill-conditioned linear systems with applications to ill-posed problems. *SIAM J Numer Anal* 10(1973):257–69.
- Veldhuis, J. D., M. L. Carlson and M. L. Johnson. The pituitary gland secretes in bursts: appraising the nature of glandular secretory impulses by simultaneous multiple-parameter deconvolution of plasma hormone concentration. *Proc Natl Acad Sci USA* 4(1987a):7686–90.
- Veldhuis, J. D. and M. Johnson. Deconvolution analysis of hormone data. *Meth Enzymol* 210(1992):539–75.
- Veng-Pedersen, P. An algorithm and computer program for deconvolution in linear pharmacokinetics. *J Pharmacokinet Biopharm* 8(1980a):463–81.
- Veng-Pedersen, P. Novel deconvolution method for linear pharmacokinetic systems with poly-exponential impulse response. *J Pharm Sci* 3(1980b):312–18.
- Verotta, D. Comments on two recent deconvolution methods. *J Pharmacokinet Biopharm* 18(1990):483–89.
- Verotta, D. Estimation and model selection in constrained deconvolution. *Ann Biomed Eng* 21(1993):605–20.
- Verotta, D. Concepts, properties, and applications of linear systems to describe the distribution, identify input, and control endogenous substances and drugs in biological systems. *Crit Rev Bioeng* 24(1996):73–139.
- Wahba, G. Practical approximate solutions to linear operator equations when the data are noisy. *SIAM J Numer Anal* 14(1977):651–67.
- Wahba, G. 1990. *Splines Models for Observational Data*. CBMS–NFS Regional Conference Series. Philadelphia: SIAM.
- Wernecke, S. and L. D'Addario. Maximum entropy image reconstruction. *IEEE Trans Comput* 26(1977):351–64.
- Wilkinson, J. H. 1967. The solution of ill-conditioned linear equations. In: *Mathematical Methods for Digital Computers*. Edited by A. Ralston and H.S. Wilf. New York: Wiley.

This Page Intentionally Left Blank

# *A Priori* Identifiability of Physiological Parametric Models

Maria Pia Saccomani, Leontina D'Angio', Stefania Audoly, and Claudio Cobelli

## 4.1. INTRODUCTION

A fundamental question in parametric model identification is *a priori global identifiability*: whether or not, under ideal conditions of noise-free observations and error-free model structure, the unknown parameters of the postulated model can be estimated from the designed multi-input/multi-output experiment (Bellman and Aström, 1970; Cobelli and DiStefano, 1980; Walter, 1982; Carson *et al.*, 1983; Godfrey, 1983; Godfrey and DiStefano, 1987; Jacquez, 1996). The answer to this question is a necessary prerequisite for well-posedness of parameter estimation. Although necessary, *a priori* identifiability is obviously not sufficient to guarantee successful parameter estimation from real data (*a posteriori* or *numerical identifiability*) or, even more, model validity. In fact, an *a priori* identifiable model can be rejected for several reasons, such as it cannot explain the data or the precision with which its parameters can be estimated is poor due to a structure too complex for the data or the paucity of the data. However, these aspects should not detract from satisfying the *a priori* identifiability requirement for any model used to obtain parameter values of interest.

One also must emphasise the necessary testing of *a priori* identifiability *per se*; it cannot be tested when estimating the parameters from the data, such as by nonlinear least squares with software like SAAM II or ADAPT.

In fact, these software packages can only assess identifiability numerically and cannot distinguish nonidentifiability arising from *a priori* or *a posteriori* reasons (structure too complex or paucity of data), thus possibly interpreting as globally identifiable models that are only locally identifiable (Cobelli and Saccomani, 1990). This last issue is particularly critical when addressing physiological systems in which a different numerical estimate can characterise a pathological state from a normal state.

*A priori* global identifiability also is crucial in qualitative experiment design (Saccomani *et al.*, 1992; Saccomani *et al.*, 1993), which studies the input-output configuration necessary to ensure unique estimation of the unknown parameters. In fact, it allows distinction between those experiments that cannot succeed and those that might. Among these latter ones, it determines the minimal input-output configuration to ensure estimation of the unknown parameters. This is particularly relevant for physiological systems in which number and sites of inputs and outputs are severely constrained for ethical and technical reasons.

However, global identifiability of linear and nonlinear models is difficult to test. Whatever method used (e.g., transfer function, normal mode, exhaustive modelling, power series expansion, differential algebra) (Bellman and Aström, 1970; Cobelli and DiStefano, 1980; Walter and Lecourtier, 1981; Norton 1982; Walter and Lecourtier, 1982; Walter, 1982; Audoly and D'Angio', 1983; Carson *et al.*, 1983; Godfrey, 1983; Godfrey and DiStefano, 1987; Ljung and Glad, 1994; Jacquez, 1996), it requires the solution of a system of nonlinear algebraic equations that results in an increase in number of unknowns, number of terms, and nonlinearity degree with the model order. For nonlinear models, they also are infinite in number. Thus, the solution of the *a priori* identifiability problem is severely limited by computational bounds; this is why it is difficult to develop an algorithm to automate the identifiability testing, although it is most desirable for both linear and nonlinear models. In fact, the problem has been solved only for some specific linear and nonlinear structures and specific input-output experiments (Pohjanpalo, 1978; Cobelli *et al.*, 1979; Norton 1982; Carson *et al.*, 1983; Godfrey, 1983; Ollivier, 1990; Chappel and Godfrey, 1992; Ljung and Glad, 1994; D'Angio' *et al.*, 1994; Jacquez, 1996), but no solution exists in the general case. In addition, the available algorithms used with *a priori* identifiability either have only addressed some of its aspects (Walter and Lecourtier, 1982; Walter *et al.*, 1985; Jacquez and Perry, 1990) or are severely limited by computability bounds that make study of models difficult, even for order two or three (Ljung and Glad, 1994).

Recently, a new differential algebra method (Saccomani *et al.*, 1997) has been proposed that allows the testing of *a priori* identifiability of sufficiently general nonlinear model structures from multi-input/multi-output identification experiments. In addition, a computer algebra tool (GLOBI for GLOBAL

Identifiability) has become available that tests *a priori* global identifiability of linear compartmental models from a general output configuration (Audoly *et al.*, 1998). This is a very powerful tool to test linear models, because a general model structure of relatively large dimension (i.e., up to some 12 compartments) can be used.

In this chapter, after briefly reviewing some fundamentals, we discuss and present examples of the most recent theoretical and algorithmic developments in identifiability of linear and nonlinear models.

## 4.2. THE SYSTEM-EXPERIMENT MODEL

### 4.2.1. NONLINEAR MODELS

Nonlinear dynamic models of physiological systems, together with the input-output experiment designed for their identification, can be described in general form as (Cobelli and DiStefano, 1980; Carson *et al.*, 1983):

$$\dot{\mathbf{x}}(\mathbf{p}, t) = \mathbf{f}[\mathbf{x}(\mathbf{p}, t), \mathbf{u}(\mathbf{p}, t), \mathbf{p}] \quad \mathbf{x}(0) = \mathbf{i}(\mathbf{p}) \quad (4.1)$$

$$\mathbf{y}(\mathbf{p}, t) = \mathbf{g}[\mathbf{x}(\mathbf{p}, t), \mathbf{u}(\mathbf{p}, t), \mathbf{p}] \quad (4.2)$$

where  $\mathbf{x}$  is the  $n$ -dimension state variable vector, (e.g., masses), with initial conditions  $\mathbf{x}_0$ ;  $\mathbf{u}$  is the  $r$ -dimension input vector;  $\mathbf{y}$  is the  $m$ -dimension output vector;  $\mathbf{p}$  is the  $P$ -dimension parameter vector; and  $\mathbf{f}$ ,  $\mathbf{g}$ , and  $\mathbf{i}$  are vectors of polynomial functions.

Some equality constraints on parameters are usually available:

$$\mathbf{h}(\mathbf{p}) = \mathbf{0} \quad (4.3)$$

where  $\mathbf{h}$  is a vector of polynomial functions describing all the algebraic equality constraints (linear and nonlinear) among the components of  $\mathbf{p}$ .

### 4.2.2. LINEAR MODELS

A linear model with its input-output experiment can be written as (Cobelli and DiStefano, 1980; Carson *et al.*, 1983):

$$\dot{\mathbf{x}}(t) = \mathbf{K}(\mathbf{p})\mathbf{x}(t) + \mathbf{B}(\mathbf{p})\mathbf{u}(t) \quad \mathbf{x}(0) = \mathbf{x}_0 \quad (4.4)$$

$$\mathbf{y}(t, \mathbf{p}) = \mathbf{C}(\mathbf{p})\mathbf{x}(t, \mathbf{p}) \quad (4.5)$$

where  $\mathbf{K}$  is the  $n \times n$  state matrix;  $\mathbf{B}$  is the  $n \times r$  input matrix;  $\mathbf{C}$  is the  $m \times n$  output matrix; and  $\mathbf{p}$  is the  $P$ -dimension vector containing the  $\mathbf{K}$ ,  $\mathbf{B}$ , and  $\mathbf{C}$

parameters, or the  $k_{ij}$ ,  $b_{ij}$ , and  $c_{ij}$  belonging to the space  $\mathbf{P}$  (a subspace of the complex space  $\mathbf{C}$ ).

A class of linear dynamic models widely used for describing biological and physiological systems, such as the study of kinetics of endogenous and exogenous (drugs, tracers) substances (Carson *et al.*, 1983; Godfrey, 1983; Jacquez, 1996), is that of compartmental models. These models, based on mass conservation principles, are still described by (4.4) and (4.5), but the elements of  $\mathbf{K}$ , the transfer rate constants  $k_{ij}$ , satisfy the following conditions:

$$k_{ij} \geq 0 \quad i \neq j, \quad k_{ii} = - \sum_{j=0}^n k_{ji} \quad j \neq i \quad (4.6)$$

where  $k_{0i}$  is the transfer rate constant from compartment  $i$  to the external environment. In this case,  $\mathbf{p}$  belongs to the compartmental space, which is a real and positive subspace of  $\mathbf{C}$  characterised by constraints (4.6).

### 4.3. A PRIORI IDENTIFIABILITY

#### 4.3.1. THE PROBLEM

Given the model structure and the input-output configuration of equations (4.1) through (4.3) or (4.3) through (4.5), *a priori* identifiability deals with the uniqueness of the solution for the unknown parameters  $p_i$ ,  $i = 1, \dots, P$ , in the whole complex space under the ideal conditions of error-free model structure and noise-free data. To state the identifiability problem, it is convenient to consider the output  $\mathbf{y}$  in (4.2) or (4.5) as a function of time and of the *observational parameter* vector,  $\Phi = [\Phi_1 \Phi_2 \dots \Phi_R]$  (Jacquez and Greif, 1985):

$$\mathbf{y} = G(t, \Phi) \quad (4.7)$$

By definition, the components of  $\Phi$ ,  $\Phi_i$ ,  $i = 1, \dots, R$ , are identifiable since they can be evaluated from the designed experiment. Thus, each input-output experiment will provide a particular value  $\hat{\Phi}$  of  $\Phi$ . The observational parameters  $\Phi_i$ ,  $i = 1, \dots, R$ , are algebraic functions of the basic parameters  $p_i$ ,  $i = 1, \dots, P$ , which may or may not be identifiable:

$$\Phi = \Phi(\mathbf{p}) \quad (4.8)$$

In particular:

$$\hat{\Phi} = \Phi(\hat{\mathbf{p}}) \quad (4.9)$$

where  $\hat{\mathbf{p}}$  is that particular value of  $\mathbf{p}$  providing  $\hat{\Phi}$ .

Thus, to prove *a priori* identifiability of a parameter  $p_i$  it is equivalent to prove if, and only if, equal values of the output  $\mathbf{y}$ , now as a function of  $\Phi$ :

$$\mathbf{y}(\Phi(\mathbf{p}), t) = \mathbf{y}(\hat{\Phi}, t) \tag{4.10}$$

imply only one, a finite or an infinite number of solutions in  $\mathcal{C}$  for the corresponding parameter vector  $\mathbf{p}$  for any  $\mathbf{p} \in \mathbf{P}$  except for a set of zero measure, meaning for almost any  $\mathbf{p} \in \mathbf{P}$ .

### 4.3.2. DEFINITIONS

Identifiability analysis was put on a formal basis in the 1970s (Bellman and Aström, 1970). The definitions we adopt are general and holding for both linear and nonlinear dynamic models: (4.1) through (4.3) or (4.3) through (4.5).

Consider the system-experiment model described by (4.1) through (4.3) or (4.3) through (4.5). For the input class  $\mathbf{U}$  and  $\mathbf{p} \in \mathcal{C}$  (the complex space), the single parameter  $p_i$  is *a priori globally (uniquely) identifiable* if, and only if, for almost any  $\hat{\mathbf{p}} \in \mathbf{P}$ , the system of equations (4.10) has the one and only solution  $p_i = \hat{p}_i$ ; *locally (nonuniquely) identifiable* if, and only if, for almost any  $\hat{\mathbf{p}} \in \mathbf{P}$ , the system of equations (4.10) has for  $p_i$  more than one, but a finite number of solutions; *nonidentifiable* if, and only if, for almost any  $\hat{\mathbf{p}} \in \mathbf{P}$ , the system of equations (4.10) has for  $p_i$  an infinite number of solutions.

The model is *a priori: globally (uniquely) identifiable* if all its parameters are globally (uniquely) identifiable; *locally (nonuniquely) identifiable* if all its parameters are identifiable, either uniquely or nonuniquely, with at least one parameter nonuniquely identifiable; *nonidentifiable* if at least one of its parameters is nonidentifiable.

### 4.3.3. THE EXHAUSTIVE SUMMARY

In practice, to investigate *a priori* identifiability of the model parameters  $p_i$ , the system of nonlinear algebraic equations must be solved in the unknown  $p_i$  with known coefficients given by the observational parameters  $\hat{\Phi}_i$ :

$$\Phi(\mathbf{p}) = \hat{\Phi} \tag{4.11}$$

We will refer to (4.11) as the *exhaustive summary* of the model (Walter and Lecourtier, 1982). If some equality constraints (4.3) are present, these must be added to the algebraic equations of the exhaustive summary. The solution of (4.11) (and (4.3) if present) will give the number of parameter solutions



in the whole complex space  $\mathcal{C}$ . However, we are only interested in solutions belonging to the compartmental space  $\mathcal{P}$ . Thus, when dealing with compartmental models, one should verify that the results in  $\mathcal{C}$  can be extended to its real and positive subspace  $\mathcal{P}$ .

## 4.4. AVAILABLE METHODS

Since the definition of the identifiability problem in the 1970s, a growing body of literature has become available, showing both its importance and its difficulty.

### 4.4.1. NONLINEAR MODELS

To analyse *a priori* global identifiability of nonlinear models, very few results are available. A method that provides a necessary and sufficient condition for global identifiability of a large class of nonlinear models is proposed by Pohjanpalo (1978). It is based on the analysis of the power series expansion of the output function, (4.2) or (4.5), evaluated at time 0, denoted here  $t_0$ . More precisely, the exhaustive summary is given by:

$$\frac{d^k \mathbf{y}(\mathbf{x}(t_0, \mathbf{p}), \mathbf{p})}{dt^k} = \alpha_k(t_0) \quad k = 0, 1, 2, \dots \quad (4.12)$$

where  $\alpha_k$  are the observational parameters given by the coefficients of the power series of the output function. The exhaustive summary is thus constituted by an infinite number of equations. This makes the identifiability analysis difficult to solve in general, especially when the model is nonidentifiable.

The only way to solve the problem is to find a finite set of equations that contains all the information present in the infinite exhaustive summary. Chappel and Godfrey (1992) have proposed a method based on the state isomorphism theorem, which has been successfully applied to some specific nonlinear structures. However, this method does not seem suitable for constructing an automatic procedure, and it can easily fail when the dimension of the nonlinear algebraic system gets high. Ollivier (1990) and Ljung and Glad (1994) have resorted to differential algebra, or the *characteristic set* of a differential ideal (Ritt, 1950). Although differential algebra methods greatly enhance identifiability analysis of nonlinear models, the construction of an efficient algorithm is difficult. An algorithm that integrates both the Ollivier (1990) and Ljung and Glad (1994) strategies and employs computer algebra methods—in particular the Buchberger algorithm (Buchberger, 1988)—was proposed in D'Angio' *et al.* (1994), but its domain of applicability was

still significantly limited by computational complexity. More recently, a new differential algebra algorithm has been developed (Saccomani *et al.*, 1997), which improves the previous one by handling more general system-experiment model structures. This algorithm is described in Section 4.5.

#### 4.4.2. LINEAR MODELS

Various methods have been proposed to test *a priori* identifiability of linear models. Here, we present the salient features of the most used strategies.

The transfer function method (Bellman and Aström, 1970; Cobelli and DiStefano, 1980; Carson *et al.*, 1983; Godfrey and DiStefano, 1987) leads to an exhaustive summary characterised by high degree of nonlinearity (equal to the number of compartments) and high number of terms, which is usually solvable only for models with a maximum of five compartments (unpublished results).

The similarity transformation method (Walter and Lecourtier, 1981; Walter and Lecourtier, 1982; Godfrey and DiStefano, 1987) defines the exhaustive summary by generating, with a similarity transformation, all the output-indistinguishable models compatible with the given model structure. The transformation leads to a high number of bilinear equations, irrespective of the connectivity level of the model, with a high number of unknowns. Unfortunately, when dealing with multi-input/multi-output experiments, this method only works for specific configurations.

The modal matrix method (Norton, 1982; Godfrey and DiStefano, 1987) defines the exhaustive summary by the elements of the matrix having as columns the eigenvectors of the compartmental matrix and of its inverse: the unknowns are the components of these eigenvectors. These equations can have complex coefficients, generally making their solution difficult.

The transfer function topological method (Audoly and D'Angio', 1983) defines the exhaustive summary using as unknowns some topological functions of the transfer rate constants  $k_{ij}$  defined on the compartmental graph. This reduces the exhaustive summary complexity as compared with the classic transfer function method. The idea is to solve for these topological macroparameters and obtain the unknown  $k_{ij}$  from them. Two methods are available. In the first, the unknowns are the *cycles* and *paths* of the compartmental graph, which considerably reduce the number of terms and, even if the nonlinearity degree remains that of the transfer function method, also decrease the number of the high degree terms. In the second method, the unknowns are the *forms* and *reduced forms*, which are particular functions of cycles and paths. This last method allows a further reduction of the number of the equation's terms and of the nonlinearity degree since it combines the  $k_{ij}$  in more aggregated

parameters than cycles and paths. However, it is difficult to automate in the general case since it requires an "intelligent" decomposition of the model. In fact, only those forms and reduced forms necessary for the analysis of the given system-experiment model must be generated, and not of all the possible ones, which can often render the system of equations unsolvable (Saccomani *et al.*, 1992; Saccomani *et al.*, 1994). While this intelligent strategy can be employed by an experienced user, its explicit definition is not simple and hampers the automation of the method. However, the method works successfully for a certain class of compartmental models (Saccomani *et al.*, 1992).

All these methods work well for models of relatively low dimension, such as two or three compartments, and for special classes of compartmental models. However, the methods usually fail when applied to relatively large general structure models because the corresponding system of nonlinear algebraic equations becomes too difficult to solve. Symbolic computer languages (e.g., REDUCE, MAPLE) are helpful but have only been used to analyse specific structures, such as some four-compartment models (Walter, 1985).

The novel differential algebra approach originally proposed for nonlinear models (Ljung and Glad, 1994) could also be applied for studying *a priori* global identifiability of linear models. However, the computability bounds of the algorithm (implemented in MAPLE) only allow the handling of models characterised by "number of parameters plus number of states (compartments)  $\leq 10$ " (Ljung and Glad, 1994). This is a severe limitation when applied to linear compartmental models since only three-compartment models and some four-compartment models (but with not all the connections between compartments present) can be tested.

Very recently, a new algorithm has been proposed (Audoly *et al.*, 1998) to automatically test global identifiability of general structure linear compartmental models from multi-input/multi-output experiments. Given the importance of compartmental models in the study of physiological systems, the algorithm was originally proposed for linear compartmental models, but it also can be applied to general linear dynamic models. The algorithm is a two-stage one. First, the transfer function topological method (Audoly and D'Angio', 1983) is used to decrease the complexity of the problem by mapping the parameter space into that of the cycles and paths of the graph. Then, this new set of equations is solved by the Buchberger algorithm (Buchberger, 1988). The algorithm is described in Section 4.6.2, and it determines if there is one, more than one (and how many), or an infinite number of solutions for each model parameter. A software tool, the most recent version of which is GLOBI2, also has been developed and is described in Section 4.6.3.

*Remark.* It is worth emphasising that difficulties arise because we are interested in *a priori global* identifiability of dynamic models; that is, checking if there is a unique solution for the unknown parameters. A simpler, but less

informative, test is to check only *a priori* structural *local* identifiability of the models, that is, to distinguish between a nonidentifiable and an identifiable (globally or locally) model. In this case, there is no need to solve the system of nonlinear equations, and a software tool, IDENT (Jacquez and Perry, 1990), is available. However, IDENT cannot be used to study *a priori* unique identifiability of a model, which often is the crucial question. Also, in case of nonunique identifiability, IDENT does not provide the number of solutions.

## 4.5. AN IDENTIFIABILITY ALGORITHM FOR NONLINEAR MODELS

### 4.5.1. FUNDAMENTALS

Here, a brief description is given of the recently proposed differential algebra algorithm (Saccomani *et al.*, 1997) for studying *a priori* global identifiability of nonlinear models. The basic concept is the characteristic set of a differential ideal introduced by Ritt (1950), who also proposed an algorithm to construct it. The formal definition is given in Appendix A. Here, the characteristic set of a differential ideal is a finite set of differential polynomials that summarises all the information contained in the infinite differential ideal. Thus, a characteristic set of the differential ideal defined by the polynomials of the dynamic model, (4.1) and (4.2), is a finite set of nonlinear equations that contains the exhaustive summary of the nonlinear model itself. This overcomes the difficulties of handling an infinite number of equations.

Given the state-space description of the dynamic model, (4.1) and (4.2), the set of differential polynomials is:

$$\dot{\mathbf{x}}(\mathbf{p}, t) - \mathbf{f}[\mathbf{x}(\mathbf{p}, t), \mathbf{u}(\mathbf{p}, t), \mathbf{p}] \quad (4.13)$$

$$\mathbf{y}(\mathbf{p}, t) - \mathbf{g}[\mathbf{x}(\mathbf{p}, t), \mathbf{u}(\mathbf{p}, t), \mathbf{p}] \quad (4.14)$$

where  $\mathbf{f}$  and  $\mathbf{g}$  are Lipschitz functions in  $\mathbf{p}$  and  $t$ . Equations (4.13) and (4.14) are the generators of a differential ideal in a differential ring. The state-space description ensures the uniqueness of the characteristic set (Ljung and Glad, 1994).

The problems now are first to construct, in an algorithmic way, the characteristic set by starting from the model equations, and second to solve the algebraic nonlinear equations forming the exhaustive model summary.

Let us tackle the second problem first. It can be solved by the Buchberger algorithm. This algorithm calculates the Gröbner basis, which is a set of polynomials with specific properties that make it a powerful tool for solving systems of nonlinear equations, like those of the exhaustive summary (see Appendix B).

To solve the first problem, we have observed (see Appendix A) that the computability complexity is strongly influenced by the choice of the differential ring  $K[\mathbf{Z}]$  and ranking of the variables of the differential polynomials. This suggests developing the algorithm with focus on structure of the dynamic model equations and defining a suitable order relation; that is, not using an *a priori* one. Furthermore, since our interest is in physiological system models, general structures and input-output configurations must be considered, allowing for time-varying parameters, for constraints among parameters arising from physical realizability, for unknown parameters in the inputs, for multi-input/multi-output experiments, and for zero (i.e., nongeneric) initial conditions. Finally, it would be desirable to experience different input-output configurations on the same model without recalculating a new characteristic set. This is particularly useful when studying qualitative experiment design (Saccomani and Cobelli, 1992), specifically the minimal input-output configuration for *a priori* global identifiability. These issues are separately addressed in the following sections.

#### 4.5.2. CHOICE OF THE DIFFERENTIAL RING

The differential ideal can be considered in various rings depending on which elements are considered coefficients and which are variables of their differential polynomials. This is a crucial step for the construction of the characteristic set and has strong consequences on the number and complexity of the reductions required to calculate it. For example, Ljung and Glad (1994) choose a differential ring  $R[\mathbf{x}, \mathbf{y}, \mathbf{u}, \mathbf{p}]$  in which all the states, inputs, outputs, and unknown parameters are the variables. Thus, a characteristic set is achieved that is triangular in  $\mathbf{p}$  and immediately provides the identifiability results. In contrast, Ollivier (1990) chooses the characteristic set of polynomials (4.13 and 4.14) in the ring  $R(\mathbf{p})[\mathbf{x}, \mathbf{y}, \mathbf{u}]$ , in which the only variables are the states, inputs, and outputs. In this way, once the characteristic set is obtained, their coefficients are polynomials in  $\mathbf{p}$ . With this choice, there are as many polynomials as outputs only in the  $\mathbf{y}$  and  $\mathbf{u}$  variables (i.e., belonging to  $R(\mathbf{p})[\mathbf{y}, \mathbf{u}]$ ), and thus known. These polynomials allow the calculation of the exhaustive summary of the model. This strategy provides a very simplified reduction procedure, since the number of variables is significantly decreased. For this reason, the Ollivier ring was chosen.

#### 4.5.3. RANKING OF VARIABLES

Two criteria dictate the choice of the ranking, decrease the computability complexity, and extract the maximum information from the characteristic set.

It has been noted (Saccomani *et al.*, 1997) that computability complexity, and thus computer time, depends not only on state vector dimension and nonlinearity degree, but also on the ranking of the polynomial variables. In particular, the choice of the rank strongly affects the strategy of reductions and, thus, the efficiency of the algorithm. However, the rank chosen to decrease computability complexity may not immediately provide the information content of the characteristic set. The two principal ranks are:

$$\mathbf{u} < \mathbf{y} < \mathbf{x}, \quad i < j \Rightarrow u_i^{(k)} < u_j^{(h)}, \quad y_i^{(k)} < y_j^{(h)}, \quad x_i^{(k)} < x_j^{(h)} \quad \forall h, k \quad (4.15)$$

and

$$\mathbf{u} < \mathbf{y} < \mathbf{x}, \quad k < h \Rightarrow u_i^{(k)} < u_i^{(h)}, \quad y_j^{(k)} < y_j^{(h)}, \quad x_i^{(k)} < x_i^{(h)} \quad \forall i, j \quad (4.16)$$

Both ranking (4.15) and (4.16) define the inputs as the smallest components, followed by the outputs and the state variables, with (4.15) ranking the high class of variables first while (4.16) ranks the high order of derivatives first.

With the ranking of (4.15), the characteristic set is in triangular form. This form is particularly useful in physiological modelling. In fact, it reveals the identifiable parameterisation corresponding to different output equations without recalculation of the characteristic set, which helps the study of optimal experiment design. This form also allows easy information extraction on parameter identifiability from initial conditions.

If the system is of high dimension (i.e., high number of both states and parameters) and of high nonlinearity degree, the calculation of the characteristic set can become too complex. In this case, the ranking of (4.16) can be adopted to decrease the computational complexity.

#### 4.5.4. TIME-VARYING PARAMETERS

Handling time-varying parameters is often important in physiological modelling. Usually the functional form is assumed with one or more unknown parameters. If  $p_i$ ,  $1 \leq i \leq p$ , is a time-varying parameter, a rather general description is:

$$\dot{p}_i(t) = ag[p_i(t)] + b \quad (4.17)$$

were  $g$  is a rational function and  $a, b$  are known or unknown constant parameters. Equation (4.17) handles classic time-varying situations, such as:

$$g(t) = ae^{-bt}, \quad g(t) = at + b, \quad g(t) = a \operatorname{tg}(bt) \quad (4.18)$$

The strategy is to consider  $p_i(t)$  as a new minimum rank state variable and to introduce (4.17) as a new state equation in the model.

If the functional form of  $p_i(t)$  is known but (4.17) does not hold, a general method is not available. However, it is often possible to resort to some auxiliary variables satisfying the relation of (4.17) and express the derivatives of the time-varying parameter in state equation form. If this is possible, the derivatives are considered as new state variables to be ordered (see Example 2 in Section 4.5.7).

If the functional form of  $p_i(t)$  is unknown, the problem is more difficult. Strategies for this case are currently under study.

#### 4.5.5. KNOWN INITIAL CONDITIONS AND INPUT PARAMETERS

The characteristic set construction ignores the initial conditions, which are assumed to be generic. If they are known, this information can be used to complete the exhaustive summary by applying the following strategy. Once the characteristic set has been calculated, known coefficients are extracted by its polynomials, which do not include neither unknown states nor their derivatives. The remaining polynomials are calculated at the initial time, thus obtaining new polynomials in the unknown variables of the model. These polynomials are added to the previously extracted ones to form  $\Phi(\mathbf{p})$  of (4.11).

The above strategy is also helpful in handling the input parameter problem. If the inputs are known derivable functions with unknown parameters, the strategy outlined in Section 4.5.4 for the time-varying parameters can be adopted. If the inputs are nonderivable functions with known parameters, such as in the frequent case of an impulse (Dirac function) input of known dose, they can be considered known initial conditions of a zero-input system; hence, the initial conditions strategy outlined previously applies.

*Remark.* If initial conditions are zero, it is possible that information on some parameters is lost in the characteristic set. In fact, the calculation of the characteristic set assumes generic initial conditions, and one of its elements could have a differential polynomial as coefficient that, with zero initial conditions, vanishes in the solution. Hence useful information for the identifiability of that parameter is lost. The present version of the algorithm does not include a procedure to preserve the information provided by the experiment on a system with zero initial conditions. Possible strategies are currently under study.

#### 4.5.6. THE ALGORITHM

The principal steps of the algorithm are:

- 1). The starting point are the model equations that provide the differential polynomials. These are considered in the differential ring  $R(\mathbf{p})[\mathbf{x}]$ ;

- 2). The standard ranking of (4.15) is introduced first. Subsequently, it is possible to select the most suitable ranking by a careful analysis of the system characteristics (see Section 4.5.3);
- 3). The leaders of each polynomial are found;
- 4). The polynomials are ordered following the increasing leaders. Each polynomial is compared with the previous ones and, if it is of higher rank, is reduced with respect to them. This step is repeated until the chain of minimum rank is reached. This set of polynomials is the characteristic set in the differential polynomial ring  $R(\mathbf{p})[\mathbf{x}]$ . In particular, it contains as many polynomials free of  $\mathbf{x}$  with coefficients in  $R(\mathbf{p})$  as the model outputs are;
- 5). The common coefficients, if any, not containing variables are eliminated from each polynomial;
- 6). If some polynomials do not contain a monic monomial, this is generated by dividing all the polynomial terms for a suitable coefficient;
- 7). The coefficients belonging to the polynomial ring  $R(\mathbf{p})$  are extracted. These are the observational parameters of the model,  $\Phi(\mathbf{p})$  (see Section 4.3.3);
- 8). If unknown initial conditions are present, the remaining polynomials of the characteristic set are calculated for  $t = t_0$  and the obtained polynomials in  $R(\mathbf{p})$  are added to those calculated in Step 5;
- 9). A random numerical point  $\hat{\mathbf{p}}$  from the parameter space is calculated and equations  $\hat{\Phi} = \Phi(\hat{\mathbf{p}})$  are constructed, which form the exhaustive summary of the model;
- 10). The Buchberger algorithm is applied to solve the equations and the number of solutions for each parameter is provided.

If the algorithm does not successfully terminate because the characteristic set is too complex (i.e., the procedure of extraction of coefficients or the Buchberger algorithm fails), the algorithm can be reapplied by using a different ranking between the variables. The algorithm has been implemented in the Reduce 3.5 program and runs on any PC, from a 486 upwards.

#### 4.5.7. EXAMPLES

EXAMPLE 1. Consider the nonlinear model discussed in Walter *et al.* (1985) and shown in Figure 4.1. It is a two-compartment model that describes the kinetics of a drug in the human body. The drug is injected into the blood (compartment 1), where it exchanges linearly with the tissues (compartment 2); the drug can be irreversibly removed with a nonlinear saturative characteristic from compartment 1 and with a linear one from compartment 2. The input-output experiment takes place in compartment 1.



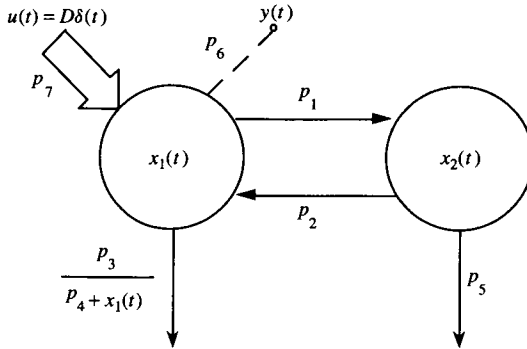


**Figure 4.1.** A nonlinear model of drug kinetics in the body. The input-output experiment configuration is also shown. The large arrow denotes the input into compartment 1 and the dashed line ending with a bullet denotes the output from compartment 1. The same notation is used in following figures.

The system-experiment model is:

$$\begin{cases} \dot{x}_1(t) = -\left(p_1 + \frac{p_3}{p_4 + x_1}\right)x_1(t) + p_2x_2(t) + p_7u(t) & x_1(0) = 0 \\ \dot{x}_2(t) = p_1x_1(t) - (p_2 + p_5)x_2(t) & x_2(0) = 0 \\ y(t) = p_6x_1(t) \end{cases} \quad (4.19)$$

where  $x_1$ ,  $x_2$  are drug mass in compartment 1 and 2, respectively,  $u$  is the drug input,  $y$  the measured drug output, and  $p_1, p_2, \dots, p_7$  are the unknown parameters.

The question is: are  $p_1, p_2, \dots, p_7$  globally identifiable from the designed input-output experiment? The algorithm starts from the polynomials:

$$\begin{cases} \dot{x}_1 + \left(p_1 + \frac{p_3}{p_4 + x_1}\right)x_1 - p_2x_2 - p_7u \\ \dot{x}_2 - p_1x_1 + (p_2 + p_5)x_2 \\ y - p_6x_1 \end{cases} \quad (4.20)$$

and its major steps are:

- 1). Choice of the ranking for ordering the polynomials:  $u < y < x_1 < x_2$ .
- 2). At this stage, the reduction procedure starts and the characteristic set is calculated. For sake of space, we report only the differential polynomial that contains the information on the model identifiability; the polynomial that does not contain  $x$  or its derivatives as variables:

$$\begin{aligned} & \dot{y}^2 + p_1p_5y^3 - (p_2p_6p_7 + p_5p_6p_7)y^2u + (p_1 + p_2 + p_5)\dot{y}y^2 - p_6p_7y^2\dot{u} \\ & + (2p_1p_4p_5p_6 + p_2p_3p_6)y^2 - 2(p_2p_4p_7p_6^2 + p_4p_5p_7p_6^2)uy \end{aligned}$$

$$\begin{aligned}
 &+ 2p_4p_6y\ddot{y} + 2(p_1p_4p_6 + p_2p_3p_6 + p_4p_5p_6)y\dot{y} - 2p_4p_7p_6^2\dot{u}y \\
 &+ p_4p_6^2(p_1p_5 + p_2p_3 + p_3p_5)y - (p_2p_4^2p_7p_6^3 + p_4^2p_6^3p_5p_7)u \\
 &+ p_4^2p_6^2\ddot{y} + (p_4^2p_6^2p_1 + p_4^2p_6^2p_2 + p_6^2p_4p_3 + p_4^2p_5p_6^2)\dot{y} - p_4p_6^3p_7\dot{u}
 \end{aligned} \tag{4.21}$$

3). The coefficients are extracted and evaluated at a numerical point  $\hat{\mathbf{p}}$  randomly chosen in the parameter space  $\mathbf{P}$ ,  $\hat{\mathbf{p}} = [1, 17, 11, 13, 3, 4, 7]$ . Each coefficient in its polynomial form is then set equal to its corresponding numerical value. The obtained equations are the exhaustive summary of the model.

4). The Buchberger algorithm is applied, and the Gröbner basis is:

$$\begin{aligned}
 &13p_3 - 11p_4 \\
 &p_1 - 1 \\
 &p_2 - 17 \\
 &- 13p_7 + 4p_4 + 39 \\
 &p_5 - 3 \\
 &p_4p_6 - 52
 \end{aligned} \tag{4.22}$$

It is easy to see that the system has an infinite number of solutions, thus the model is *a priori* nonidentifiable. If the input is assumed to be known (i.e.,  $p_7 = 1$ ), the model becomes *a priori* globally identifiable.

EXAMPLE 2. The model is shown in Figure 4.2 and has been proposed to assess glucose metabolism in the brain from positron emission tomography (PET) [ $^{18}\text{F}$ ]-fluorodeoxyglucose([ $^{18}\text{F}$ ]FDG) data (Schmidt *et al.*, 1991). It is a two-compartment model with two time-varying parameters that account for brain tissue heterogeneity.

The system-experiment model is:

$$\begin{cases} \dot{x}_1(t) = p_1u(t) - [p_2(t) + p_3(t)]x_1(t) & x_1(0) = 0 \\ \dot{x}_2(t) = p_3(t)x_1(t) & x_2(0) = 0 \\ y(t) = x_1(t) + x_2(t) \end{cases} \tag{4.23}$$

where  $x_1, x_2$  are [ $^{18}\text{F}$ ]FDG and [ $^{18}\text{F}$ ]-fluorodeoxyglucose-6-phosphate concentrations in the brain tissue,  $u$  is [ $^{18}\text{F}$ ]FDG plasma concentration, which acts as known input of the model,  $y$  is the measured output, and  $p_1, p_2, p_3, p_4$  are the unknown parameters with the time-varying ones described by:

$$\begin{aligned}
 p_2(t) &= p_2(1 + p_4e^{-p_5t}) \\
 p_3(t) &= p_3(1 + p_4e^{-p_5t})
 \end{aligned} \tag{4.24}$$

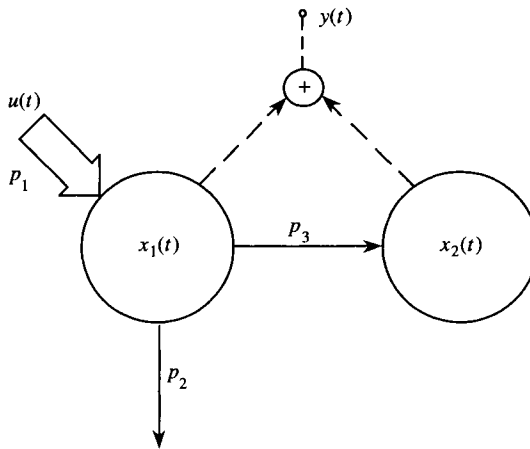


Figure 4.2. A time-varying parameter model of glucose metabolism in the brain.

The question is: are  $p_1$ ,  $p_2$ ,  $p_3$ ,  $p_4$ ,  $p_5$  globally identifiable from the designed experiment? By following the algorithmic steps outlined in Example 1, it is easy to prove that the model is *a priori* globally identifiable.

EXAMPLE 3. This example deals with a model describing the control of insulin on glucose utilisation (Caumo and Cobelli, 1993). The model is shown in Figure 4.3. The experiment consists of an impulse input of glucose labelled with a tracer and of the measurement in plasma of glucose, labelled glucose and insulin concentrations. The measured insulin concentration acts as model input  $u$ , while the model output  $y$  is the measured tracer glucose concentration. The control by insulin on the glucose system is exerted by insulin in a remote compartment ( $x_1$ ). The glucose system is described by two compartments that represent, respectively, glucose in rapidly ( $x_2$ ) and slowly equilibrating tissues ( $x_3$ ), which include muscles. Insulin control is exerted on glucose utilisation in compartment 2 (insulin-dependent tissues); only glucose utilisation of compartment 1 refers to insulin-independent tissues.

The system-experiment model is given by:

$$\begin{cases} \dot{x}_1(t) = -p_1x_1(t) + p_2u(t) & x_1(0) = 0 \\ \dot{x}_2(t) = -\left(p_3 + \frac{p_4p_5}{g(t)} + p_6\right)x_2(t) + p_7x_3(t) & x_2(0) = 0 \\ \dot{x}_3(t) = -(p_8 + x_1(t) + p_7)x_3(t) + p_6x_2(t) & x_3(0) = 0 \\ y(t) = p_5x_2(t) \end{cases} \quad (4.25)$$

where  $x_1$ ,  $x_2$ ,  $x_3$  are, respectively, concentration of insulin in a remote compartment and glucose mass in compartments 2 and 3,  $u$  is plasma insulin

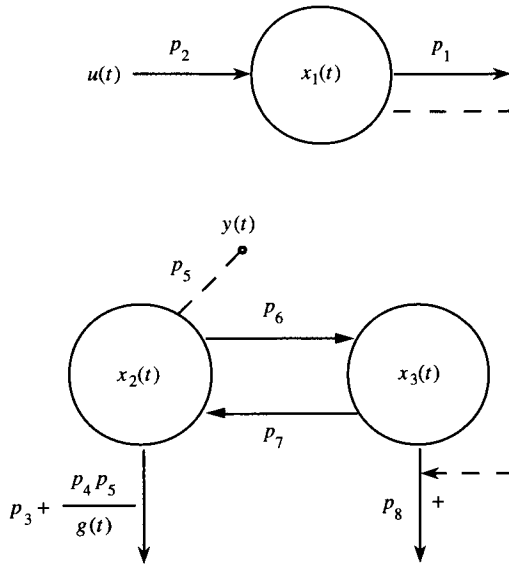


**Figure 4.3.** A nonlinear model of glucose utilisation in the body and its control by insulin.

concentration,  $g$  is plasma glucose concentration,  $y$  is the plasma tracer glucose concentration, and  $p_1, p_2, p_3, \dots, p_8$  are the unknown parameters.

The question is: are  $p_1, p_2, p_3, \dots, p_8$  *a priori* globally identifiable from the designed experiment? In Caumo and Cobelli (1993), the following physiological constraint was used to identify the model:

$$p_3 + \frac{p_4 p_5}{g_b} = \frac{3 p_6 p_8}{p_7 + p_8} \tag{4.26}$$

where  $g_b$  is the known pretest glucose concentration.

The algorithm shows that the model with the constraint of (4.26) is *a priori* globally identifiable. The same result was obtained in Caumo and Cobelli (1993), but the very laborious power series expansion method (Pohjanpalo, 1978) was employed.

#### 4.6. AN IDENTIFIABILITY ALGORITHM FOR LINEAR COMPARTMENTAL MODELS

Here, an algorithm for checking *a priori* global identifiability of linear compartmental models of general structure is described (Audoly *et al.*, 1998). This algorithm takes advantage of computer algebra, particularly the Gröbner

basis. In principle, all the available methods discussed in Section 4.4.2 can be used to generate the exhaustive summary. However, the transfer function topological method (Audoly and D'Angio', 1983) has been chosen, since it makes the algorithm to calculate the Gröbner basis most successful for the largest class of models. It allows a reduction of the complexity of the exhaustive summary in terms of number of unknowns, number of terms, and nonlinearity degree.

#### 4.6.1. THE TRANSFER FUNCTION TOPOLOGICAL METHOD

The transfer function topological method (Audoly and D'Angio', 1983) is based on the properties of the graph associated with the model. It defines the exhaustive summary using as unknowns some topological functions of the transfer rate constants  $k_{ij}$ . This considerably reduces the complexity of the exhaustive summary as compared with the classic transfer function method.

Briefly, it exploits the fact that the transfer function numerator and denominator coefficients are the sum of minors of suitable order of the compartmental matrix  $\mathbf{K}$  and, thus, can be written in terms of cycles and paths connecting the input to the output compartments in the compartmental graph. The idea is to write the transfer function coefficients, and thus the exhaustive summary, having cycles and paths as unknowns instead of the transfer rate constants.

Let us denote by  $G_n$  the graph associated to the  $n \times n$   $\mathbf{K}$  matrix by assigning the value  $k_{ij}$  to each arc  $(ji)$ . The cycles and paths of  $G_n$  are defined for  $ij = 1, \dots, n$  where  $j = 1, \dots, m$ , as:

$$c_{i_1 i_1} = k_{i_1 i_1} \quad (4.27)$$

$$c_{i_1 i_2 \dots i_m} = k_{i_2 i_1} k_{i_3 i_2} \dots k_{i_1 i_m} \quad m = 2, \dots, n \quad (4.28)$$

$$p_{i_1 i_2 \dots i_m} = k_{i_2 i_1} k_{i_3 i_2} \dots k_{i_m i_{m-1}} \quad m = 2, \dots, n \quad (4.29)$$

The algorithm generates all the cycles and paths present in the exhaustive summary coefficients by using concepts from graph theory—particularly the adjacency and reachability matrices—and calculates all the products of cycles and paths appearing in these coefficients. Thus, one moves from the transfer function exhaustive summary, where the known coefficients are the observational parameters and the unknowns are the  $k_{ij}$  parameters, to a set of simpler equations, regarding number of terms and nonlinearity degree, with cycles and paths as unknowns.

*Remark 1.* By definition, the transfer function deals only with systems with zero initial conditions. However, it is possible to study systems with nonzero initial conditions, known or unknown, simply by considering an

equivalent system with zero initial conditions and impulse inputs of the same value of the initial conditions.

*Remark 2.* Although the focus here is on compartmental models, the method also can be applied to linear models of general structure:

$$\dot{\mathbf{x}}(t) = \mathbf{A}\mathbf{x}(t) + \mathbf{B}\mathbf{u}(t) \quad \mathbf{x}(0) = \mathbf{x}_0 \tag{4.30}$$

$$\mathbf{y}(t) = \mathbf{C}\mathbf{x}(t) \tag{4.31}$$

where  $\mathbf{A}$  is now a generic state matrix. To analyse *a priori* identifiability of the (4.30) and (4.31) model, a corresponding compartmental matrix  $\mathbf{K}$  must be defined with the same structure of  $\mathbf{A}$  and with  $k_{0i} \neq 0 \forall i = 1, \dots, n$ .

### 4.6.2. THE ALGORITHM

The salient steps of the global identifiability algorithm are:

1). The algorithm calculates the observational parameters as functions of cycles and paths and writes the equations with these functions on the left side and the known observational parameters on the right side.

2). To solve these equations, a numerical right-hand side term, not a symbolic one, is needed. The algorithm assumes a numerical value for the components of the vector  $\mathbf{p}$ , which is a parameter solution  $\hat{\mathbf{p}}$  satisfying the compartmental (4.6) and the equality constraints (4.3), these last if present. From these, it calculates the numerical values of the observational parameters.

3). The Buchberger algorithm, as implemented in REDUCE (Mueller, 1991), is used to solve the equations where the variables are the cycles and paths. We use the default order relations of the algorithm: the inverse of the alphabetical order with the natural one for the indices among the variables and the lexicographical order among the monomials. This step can be unsuccessful for computational limits. In this case, the problem cannot be solved. If this step is successful, the algorithm returns a new basis expressed in terms of the same unknowns (cycles and paths), but now showing a significantly simplified form.

4). The algorithm substitutes to the cycles and paths of the basis their expressions in terms of the  $k_{ij}$  simply by applying their definition, (4.27) through (4.29). Also, this set of equations presents a reduction in the number of terms and nonlinearity degree in comparison with the corresponding one in the  $k_{ij}$  obtainable with the transfer function approach.

5). A second application of the Buchberger algorithm, if successful, provides a new basis of polynomials in the  $k_{ij}$ . This basis is characterised by specific properties that provide the answer to the global identifiability problem. In particular, when the model is identifiable, the basis is in triangular form and gives the number of solutions for each parameter.

The Buchberger algorithm can be unsuccessful since the choice of the order relation among the variables can affect the computational complexity of the Gröbner basis. In this case, the user should reapply the algorithm by choosing a different order relation among the variables. This can be done by using the switch GROEBOPT, present in the REDUCE implementation of the Buchberger algorithm, which allows the optimisation of the variable order in relation to the form of the equations to solve.

Two observations are in order:

1). The algorithm uses a numerical point since a symbolic point would dramatically affect the complexity of the Gröbner basis calculation. Thus, the answer of the algorithm is true with probability one. Note that the numerical point strategy is a sound alternative to the symbolic one (required to test a structural property, holding in the whole parameter space except for a zero measure set) since, while retaining mathematical rigour (Vajda, 1987), it allows to significantly enlarge the class of testable models.

2). The algorithm checks the uniqueness of parameter solutions in the whole complex space  $\mathcal{C}$ . When the result is global identifiability, meaning all the model parameters are uniquely identifiable, we are sure that this solution, belonging to  $\mathcal{C}$ , must coincide with the point  $\hat{\mathbf{p}}$  of the parameter space that has provided the particular value of the observational parameter vector  $\hat{\Phi}$  at the start of the algorithm. However, if some model parameters are locally identifiable or nonidentifiable, the user should know how many solutions belong to the real and positive subspace  $\mathbf{P}$  (4.6). This issue is of a fundamental nature and has nothing to do with algorithm implementation problems or with the chosen method. Briefly, to extend the global identifiability results obtained in  $\mathcal{C}$  to the compartmental subspace  $\mathbf{P}$ , we must distinguish between two situations: 1) If some model parameters are not uniquely identifiable, while the algorithm provides the exact number of solutions in  $\mathcal{C}$ , one cannot know how many of these solutions will be complex, how many will be real but negative, and how many will be real and positive when the one provided by the experiment will be available as an initial point. Thus, under these circumstances, the number of solutions provided by the algorithm is an upper bound of the number of solutions in  $\mathbf{P}$ . 2) If some model parameters are nonidentifiable in  $\mathcal{C}$ , this also holds in all the subspaces of  $\mathcal{C}$  (Ollivier, 1990); thus, the model also is nonidentifiable in  $\mathbf{P}$ .

### 4.6.3. THE SOFTWARE

The major features of the software GLOBI, which implements the algorithm described previously, are:

1). A graphical interface that permits the user to enter the model structure and the input-output experiment configuration in a very quick and easy way, also for very complex models.

2). An algorithm to test three necessary topological conditions for identifiability (Cobelli and Romanin Jacur, 1976; Cobelli *et al.*, 1979b; D'Angio', 1985) that allows the rejection of some nonidentifiable models before applying the global identifiability algorithm.

3). The global identifiability algorithm, which combines the cycle and path transfer function topological method and the Buchberger algorithm (described in Section 4.6.2).

4). An interface that permits the user to visualise and save the identifiability results together with the model structure and input-output configuration. This allows the construction of a library of case studies.

The original version of GLOBI was written in PASCAL 6.0, REDUCE 3.6; DELPHI 2 was used for the user graphical interface. Now, an upgrade of the program, GLOBI2, is available written in Visual C++ and REDUCE 3.6. In particular, the topological conditions algorithm and the graphical interface are in Visual C++, while the global identifiability algorithm is in REDUCE 3.6, which has a Gröbner basis package implementing the Buchberger algorithm. GLOBI2 runs on any IBM-compatible PC with at least 8 MB of RAM.

#### 4.6.4. EXAMPLES

GLOBI2 is used here to analyse *a priori* identifiability of some complex compartmental models of the biomedical literature. Other examples are included in the GLOBI2 library. The aim is to give an idea of the validity of GLOBI2, which is difficult to establish rigorously, in terms of model structure. In fact, this would require defining the limits of applicability of the Buchberger algorithm in solving the exhaustive summary of the model. However, the complexity of the exhaustive summary does depend not only on the model structure, but also on the input-output experimental configuration.

EXAMPLE 1. Consider the four-compartment model shown in Figure 4.4 together with a two-input/four-output experiment (Walter *et al.*, 1982).

The model has as unknowns the 12  $k_{ij}$ . GLOBI2 final result is:

$$59k_{43} + 97k_{01} - 784 = 0 \quad k_{41} + k_{01} - 4 = 0 \quad 531k_{34} - 154k_{01} - 754 = 0$$

$$59k_{32} - 22k_{01} - 310 = 0 \quad 531k_{24} - 539k_{01} - 2639 = 0 \quad k_{23} - 3 = 0$$

$$k_{21} - 5 = 0 \quad k_{13} - 9 = 0 \quad k_{12} - 4 = 0 \quad 59k_{03} - 97k_{01} - 396 = 0$$

$$59k_{02} + 99k_{01} - 257 = 0 \quad 77k_{01}^2 - 426k_{01} + 544 = 0$$

(4.32)



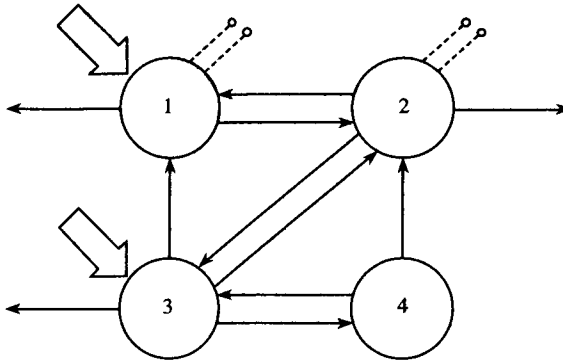


Figure 4.4. A four-compartment model.

This shows that all the parameters have two solutions, except for  $k_{21}$ ,  $k_{12}$ ,  $k_{23}$  and  $k_{13}$ , which have one. Thus, the model is locally identifiable.

EXAMPLE 2. A model of zinc metabolism in humans (Foster *et al.*, 1979; Godfrey, 1983) is shown in Figure 4.5. It has seven compartments, and the experiment is characterised by outputs taken from more than one compartment with all input-output parameters assumed to be known.

The model has thus as unknowns the 11  $k_{ij}$  (one of the  $k_{ij}$ ,  $k_{83}$ , is used to characterise the delay element, which is realised with a chain of compartments with equal rate constants). GLOBI2 shows that the model is globally identifiable.

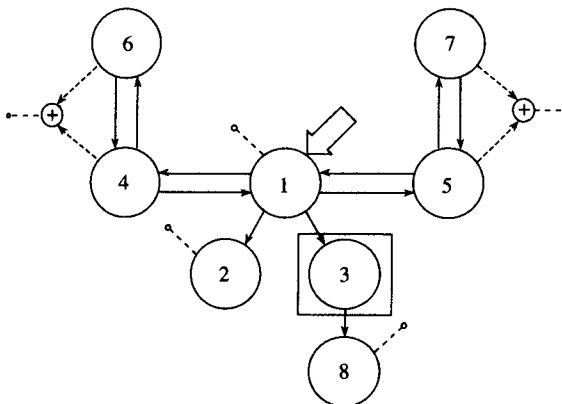


Figure 4.5. A model of zinc metabolism.

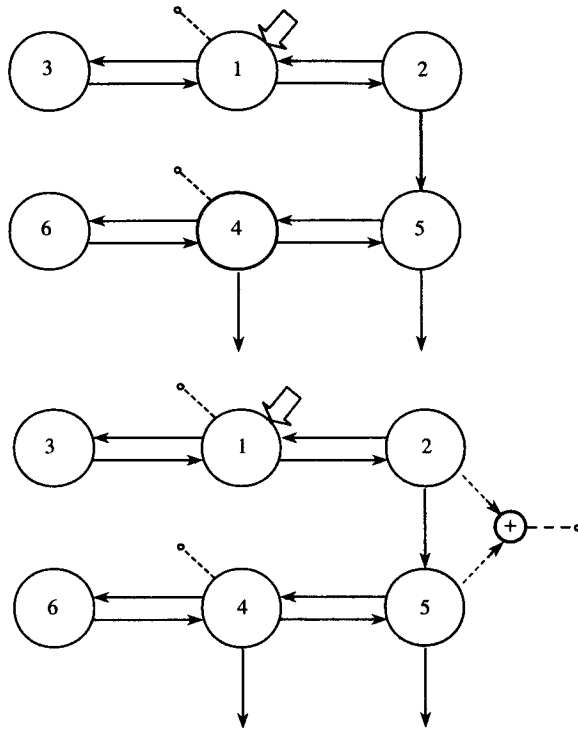


Figure 4.6. Models of bilirubin metabolism.

EXAMPLE 3. Two different models describing bilirubin metabolism (Cobelli and Romanin Jacur, 1976) are shown in Figure 4.6. Figure 4.6 (top) shows a six-compartment model with a single-input/two-output experiment.

The input parameters are assumed known, whereas both the output parameters are assumed to be equal to plasma volume,  $V$ . The model has 12 parameters as unknowns, the  $k_{ij}$  and  $V$ . The GLOBI2 result is  $k_{04}$ ,  $k_{05}$ ,  $k_{54}$ , and  $k_{64}$  are nonidentifiable, whereas the remaining parameters are globally identifiable. Thus, the model, with this experimental configuration, is nonidentifiable. A third output, from compartments 2 and 5, has then been added (Figure 4.6, bottom). With this richer experimental configuration, the model is globally identifiable.

EXAMPLE 4. A model of lipoprotein metabolism is shown in Figure 4.7. It is a seven-compartment model with, as unknowns, the 12  $k_{ij}$ . The input-output parameters are assumed to be known. Of note here is that GLOBI2 successfully tests *a priori* identifiability of the model with the alternative order relation (GROEBOPT), but not with the default one. A possible explanation

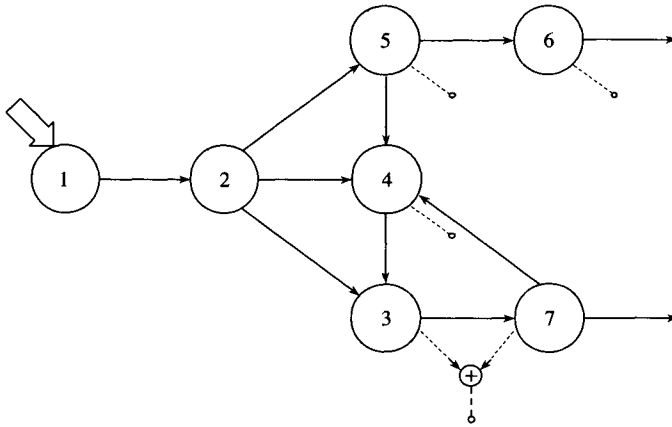


Figure 4.7. A model of lipoprotein metabolism.

lies in the difficulty of the default order relation to deal with unidirectional models, which are characterised by a high number of paths and a small number of cycles. GLOBI2 shows that the model is locally identifiable, in particular all the parameters have two solutions except for  $k_{06}$ ,  $k_{04}$ ,  $k_{65}$ ,  $k_{54}$ , and  $k_{43}$ , which have one.

EXAMPLE 5. Let us consider now a general linear dynamic model example, (4.30) and (4.31), not a compartmental one. It is described by:

$$\begin{bmatrix} \dot{x}_1(t) \\ \dot{x}_2(t) \\ \dot{x}_3(t) \\ \dot{x}_4(t) \end{bmatrix} = \begin{bmatrix} a_{11} & a_{12} & 0 & 0 \\ 0 & a_{22} & a_{23} & 0 \\ 0 & a_{32} & a_{33} & a_{34} \\ a_{41} & a_{42} & 0 & a_{44} \end{bmatrix} \begin{bmatrix} x_1(t) \\ x_2(t) \\ x_3(t) \\ x_4(t) \end{bmatrix} + \begin{bmatrix} 1 \\ 0 \\ 0 \\ 0 \end{bmatrix} u \quad \begin{bmatrix} x_1(0) \\ x_2(0) \\ x_3(0) \\ x_4(0) \end{bmatrix} = \begin{bmatrix} 0 \\ 0 \\ 0 \\ 0 \end{bmatrix} \tag{4.33}$$

where:

$$a_{12} = a_{33}, \quad a_{41} = a_{42} \quad a_{34}a_{23} = 2 \tag{4.34}$$

The output equations are given by:

$$\begin{bmatrix} y_1(t) \\ y_2(t) \\ y_3(t) \end{bmatrix} = \begin{bmatrix} c_1 & 0 & 0 & 0 \\ 0 & c_2 & 0 & 0 \\ 0 & 0 & c_3 & 0 \end{bmatrix} \begin{bmatrix} x_1(t) \\ x_2(t) \\ x_3(t) \\ x_4(t) \end{bmatrix} \tag{4.35}$$

where:

$$c_1 = c_2 = c_3 \tag{4.36}$$

GLOBI2 shows that all the unknown parameters have one solution, thus the model is *a priori* globally identifiable.

## 4.7. CONCLUSIONS

*A priori* identifiability is a necessary prerequisite for parameter estimation of physiological system models. In this chapter, the *a priori* global identifiability problem was first introduced, and the formal definition of identifiability was given. Checking global identifiability, or the uniqueness of the solution, is difficult in both nonlinear and linear models since it requires solving a system of nonlinear algebraic equations that increase in both number of terms and nonlinearity degree with increasing model order. After a brief overview of the available methods to test *a priori* global identifiability of both linear and nonlinear models, the two most recently proposed algorithms for attacking *a priori* identifiability of nonlinear and linear models were presented. The first algorithm tests automatically identifiability of general structure nonlinear models with a general multi-input/multi-output experimental configuration. It resorts to differential algebra concepts; in particular, it is based on the characteristic set of the ideal generated by the polynomials defining the model and on computer algebra methods, in particular the Buchberger algorithm. Examples of the use of this method have been reported. The second algorithm was developed for linear compartmental models. Its software implementation, GLOBI2, is the first computer algebra tool able to check global identifiability of general structure and high dimension linear compartmental models, up to some 12 compartment structures, with the most general multi-input/multi-output experimental configuration. This method is based on the transfer function topological method and uses the Buchberger algorithm. Examples of this method also have been presented.

## 4.8. REFERENCES

- Audoly, S. and L. D'Angio'. On the identifiability of linear compartmental systems: a revisited transfer function approach based on topological properties. *Math Biosci* 66(1983):201–28.
- Audoly, S., L. D'Angio', M. P. Saccomani and C. Cobelli. Global identifiability of linear compartmental models. A computer algebra algorithm. *IEEE Trans Biomed Eng* 45(1998):36–41.
- Becker, T. and W. Weispfenning. 1993. *Gröbner Bases: A Computational Approach to Commutative Algebra*, New York: Springer-Verlag.
- Bellman, R. and K. J. Aström. On structural identifiability. *Math Biosci* 7(1970):329–39.
- Buchberger, B. An algorithmical criterion for the solvability of algebraic system of equation. *Aequationes Mathematicae* 4(3)(1988):45–50.
- Carson, E. R., C. Cobelli and L. Finkelstein. 1983. *The Mathematical Modeling of Metabolic and Endocrine Systems*. New York: Wiley.
- Caumo, A. and C. Cobelli. Hepatic glucose production during the labeled IVGTT: estimation by deconvolution with a new minimal model. *Am Physiol* 264(1993):E829–41.
- Chappel, M. J. and K. R. Godfrey. Structural identifiability of the parameters of a nonlinear batch reactor model. *Math Biosci* 108(1992):245–51.
- Cobelli, C. and G. Romanin Jacur. On the structural identifiability of biological compartmental systems in a general input-output configuration. *Math Biosci* 30(1976):139–51.

- Cobelli, C., A. Lepschy and G. Romanin Jacur. Identifiability results on some constrained compartmental systems. *Math Biosci* 47(1979a):173–96.
- Cobelli, C., A. Lepschy and G. Romanin Jacur. Identifiability of compartment systems and related structural properties. *Math Biosci* 48(1979b):1–18.
- Cobelli, C. and J. J. DiStefano III. Parameter and structural identifiability concepts and ambiguities: a critical review and analysis. *Am J Physiol* 239(1980):R7–24.
- Cobelli, C. and M. P. Saccomani. Unappreciation of a priori identifiability in software packages causes ambiguities in numerical estimates. Letter to the Editor. *Am J Physiol* 21(1990):E1058–59.
- D'Angio', L. On some topological properties of a strongly connected compartmental system with application to the identifiability problem. *Math Biosci* 76(1985):207–20.
- D'Angio', L., S. Audoly, G. Bellu, M. P. Saccomani and C. Cobelli. 1994. Structural identifiability of nonlinear systems: algorithms based on differential ideals. In: *Proc. SYSID '94, 10th IFAC Symposium on System Identification*. Edited by M. Blanke and T. Söderström. Copenhagen: Danish Automation Society, 3:13–18.
- DiStefano, J. J. and C. Cobelli. Response to comments on: On parameter and structural identifiability: nonunique observability/reconstructibility for identifiable systems, other ambiguities and new definitions. *IEEE Trans Automat Contr* AC-26(1981):801–2.
- Foster, D. M., R. L. Aamodt, R. I. Henkin and M. Berman. Zinc metabolism in humans: a kinetic model. *Am J Physiol* 237(1979):R340–49.
- Godfrey, K. 1983. *Compartmental Models and Their Application*. London: Academic Press.
- Godfrey, K. R. and J. J. DiStefano III. 1987. Identifiability of model parameters. In: *Identifiability of Parametric Models*. Edited by E. Walter. Oxford: Pergamon Press, Ch. 1, 1–20.
- Jacquez, J. A. and P. Greif. Numerical parameter identifiability and estimability: integrating identifiability, estimability, and optimal sampling design. *Math Biosci* 77(1985):201–27.
- Jacquez, J. A. and T. Perry. Parameter estimation: local identifiability of parameters. *Am J Physiol* 258(1990):E727–36.
- Jacquez, J. A. 1996. *Compartmental Analysis in Biology and Medicine*. 3rd ed. Ann Arbor, MI: BioMedware.
- Ljung, L. and T. Glad. On global identifiability for arbitrary model parametrization. *Automatica* 30(2)(1994):265–76.
- Mueller, H. M. 1991. *Algebraic Computing with REDUCE*, M.A.H. Edited by Mac Callum and F.J. Wright. Oxford: Clarendon Press.
- Norton, J. P. On investigation of nonuniqueness in deterministic identifiability. *Math Biosci* 60(1982):89–108.
- Ollivier, F. 1990. Le problème de l'identifiabilité structurelle globale: étude théorique, méthodes effectives et bornes de complexité. Thèse de Doctorat en Science, École Polytechnique.
- Pohjanpalo, H. System identifiability based on the power series expansion of the solution. *Math Biosci* 41(1978):21–33.
- Ritt, J. 1950. *Differential Algebra*. Providence, RI: American Mathematical Society.
- Saccomani, M. P. and C. Cobelli. A minimal input-output configuration for a priori identifiability of a compartmental model of leucine metabolism. *IEEE Trans Biomed Eng* 40(1993):797–803.
- Saccomani, M. P. and C. Cobelli. Qualitative experiment design in physiological system identification. *IEEE Control Sys Mag* 12(6)(1992):18–23.
- Saccomani, M. P., R. Sattier, L. D'Angio', S. Audoly and C. Cobelli. 1992. An automatized topological method to test a priori global identifiability of a class of compartmental models. In: *Proceedings of IEEE EMBS 14th Annual International Conference*, Piscataway, NJ, 14(6): 2282–83.
- Saccomani, M. P., S. Audoly, L. D'Angio', R. Sattier and C. Cobelli 1994. PRIDE: a program to test a priori global identifiability of linear compartmental models. In: *Proceedings of SYSID*

'94 10th IFAC Symposium on System Identification, Edited by M. Blanke and T. Söderström. Copenhagen: Danish Automation Society, 3:25–30.

Saccomani, M. P., S. Audoly, G. Bellu, L. D'Angio' and C. Cobelli 1997. Global identifiability of nonlinear model parameters. In: *Proceedings of SYSID '97, 11th IFAC Symposium on Systems Identification*, Edited by Y. Sawaragi and S. Sagara. Nichigen Co., Kitakyushu, Japan, 1:214–19.

Schmidt, K., G. Mies and L. Sokoloff. Model of kinetic behavior of deoxyglucose in heterogeneous tissues in brain: a reinterpretation of the significance of parameters fitted to homogeneous tissue models. *J Cereb Blood Flow Metab* 11(1991):10–24.

Vajda, S. 1987. Identifiability of polynomial systems: structural and numerical aspects. In: *Identifiability of Parametric Models*. Edited by E. Walter. Oxford: Pergamon Press, Ch. 4, 42–49.

Walter, E. and Y. Lecourtier. Unidentifiable compartmental models: what to do? *Math Biosci* 56(1981):1–25.

Walter, E. 1982. *Identifiability of State Space Models*, Berlin: Springer-Verlag.

Walter, E. and Y. Lecourtier. Global approaches to identifiability testing for linear and nonlinear state space models. *Math Comput Simul* 24(1982):472–82.

Walter, E., Y. Lecourtier, A. Raksanyi and J. Happel. 1985. On the distinguishability of parametric models with different structures. In: *Mathematics and Computers in Biomedical Applications*. Edited by J. Eisenfeld and C. De Lisi. Amsterdam: Elsevier North-Holland, 145–60.

## Appendix A. THE CHARACTERISTIC SET

For a formal description of the fundamentals of differential algebra, see Ritt (1950). Definitions are briefly recalled here. Let  $\mathbf{Z}$  be a vector of variables and  $K$  the set of their coefficients. The totality of polynomials in the variables  $z$  and their derivatives with coefficients on  $K$  is a differential polynomial ring and will be denoted  $K[\mathbf{Z}]$ , where  $K$  can be a ring itself.

Consider a set  $I$  of differential polynomials belonging to  $K[\mathbf{Z}]$ . The totality of polynomials that can be formed by elements in  $I$  by addition, multiplication by elements in  $K[\mathbf{Z}]$  and differentiation, is a differential ideal having the elements of  $I$  as generators. To handle differentials ideals, the variables must be ranked; hence, the derivatives are ranked according to a system that satisfies the following relations:

$$z_i \leq dz_i; \quad z_i < z_j \Rightarrow dz_i < dz_j \tag{A.1}$$

where  $z_i$  and  $z_j$  are variables and  $d$  is an arbitrary derivation.

The “leader” of a polynomial  $A$  is the highest ranking derivative of that polynomial. In particular, it can be a derivative of order zero. The leader of a polynomial  $A$  will be denoted by  $uA$ . If  $uA \leq uB$  and  $\deg(uA) < \deg(uB)$ , then the polynomial  $A$  is said to be of lower rank than  $B$ . The “class” of a polynomial  $A$  is the greater  $p$  such that  $z_p$  is present in a term of  $A$ . If  $A_i$  is of class  $p > 0$ ,  $A_j$  will be “reduced” with respect to  $A_i$  if  $A_j$  is of lower rank than  $A_i$  in  $z_p$ . If a polynomial is not reduced, it can be reduced by a “pseudodivision,” meaning the polynomial of higher rank is substituted by the rest of the division between the two polynomials with respect to the leader of the first one.

The set of differential polynomials  $A_1, A_2, \dots, A_r$  will be called a “chain” if either  $r = 1$  and  $A_1$  is different from zero, or  $r > 1$  and for  $i > j$ ,  $A_j$  is of higher class than  $A_i$  and reduced with respect to  $A_i$ . The chain  $A_1, A_2, \dots, A_r$  will be said to be of higher rank than the chain  $B_1, B_2, \dots, B_s$  if either there is a  $j$  exceeding neither  $r$  nor  $s$ , such that  $A_i$  and  $B_i$  are of the same rank for  $i < j$  and  $A_j$  is higher than  $B_j$ , or if  $s > r$ ,  $A_i$  and  $B_i$  are of the same rank for  $i \leq r$ .

Let  $\Sigma$  be a finite or an infinite set of differential polynomials. Chains can be formed with different polynomials in  $\Sigma$ , and among all these chains, one or more have lower rank. Each chain will be called “characteristic set.” The peculiarity of the characteristic set is that it summarises all the information contained in the differential ideal into a finite number of polynomials.

With these definitions in hand, we return to the system-experiment model of (4.1) and (4.2). Let us assume that  $\mathbf{f}$  and  $\mathbf{g}$  are polynomial functions. Ljung and Glad (1994) have shown that the state-space description of the dynamic model ensures the uniqueness of the characteristic set of the differential ideal generated by the polynomials of (4.13) and (4.14). Thus, this characteristic set, which is a finite set of equations, contains the infinite exhaustive summary of the nonlinear model itself and, thus, can provide the identifiability properties of the model. The problem is now to construct, in an algorithmic way, the characteristic set by starting from the equations of the model. To do this, a sequence of chains is constructed of decreasing rank until the chain of minimum rank is reached.

## Appendix B. THE GRÖBNER BASIS

The exhaustive summary can be efficiently solved by resorting to the Gröbner basis, which is, in some sense, the analogue of gaussian elimination for systems of polynomial equations. To do so, we need a numerical value of the observational parameters. This can be derived from a parameter solution that satisfies the compartmental equation (4.6) and the equality constraints (4.3), these last if present. The consequences of this assumption have been examined in Audoly *et al.* (1998). Here, we briefly summarise the main properties of the Gröbner basis to explain why they are the instrument of choice for solving our problem. For more details, see Buchberger (1988) and Becker *et al.* (1993).

Consider the system of polynomial equations with real coefficients  $p_1 = 0, p_2 = 0, \dots, p_m = 0$ . Loosely speaking, the polynomial ideal generated by  $p_1 = 0, p_2 = 0, \dots, p_m = 0$  is the set of all the polynomials that can be formed by multiplying them with arbitrary polynomials having real coefficients. The ideal is denoted by  $I(p_1, p_2, \dots, p_m)$ , and  $p_1, p_2, \dots, p_m$  are called the generators of  $I$ . Set  $I$  can have more than one set of generators.

The Gröbner basis of an ideal is a set of generators of  $I$  with particular properties that make it an invaluable tool for solving systems of nonlinear algebraic equations. The monomials of each equation must be ordered, thus a total order relation must be introduced among the variables of the system. In particular, since our goal is to know the number of solutions of the system, it is convenient to adopt the lexicographic order relation for the monomials. In fact, this allows the results to be obtained in the following format, which is easy to interpret:

1). The system has a finite,  $n \geq 1$ , number of solutions if the Gröbner basis has a triangular form. The basis provides the number of solutions for each variable since: a) if the system has a unique solution, the basis contains only linear equations; b) if the system has a finite ( $>1$ ) number of solutions, the last polynomial of the basis provides the number of solutions for the lowest (according to order relation) variable, which is equal to the highest nonlinear degree of variable itself; by iteratively reordering the variables, one can have the number of solutions for each of them.

2). If the system has an infinite number of solutions, the Gröbner basis exhibits a nontriangular form. Our problem is now to move from the polynomial equations  $p_1 = 0, p_2 = 0, \dots, p_m = 0$  to the Gröbner basis. Buchberger (1988) proposed an algorithm for the computation of the basis, which is available in computer algebra software packages, such as REDUCE and MAPLE. However, the implementation of the Buchberger algorithm can fail because of the computational complexity that arises when high nonlinear degrees and/or high number of unknowns and terms are present. This particularly happens with nonrational coefficients. Also, the choice of the order relation of variables can significantly affect the computational complexity of the Gröbner basis.



This Page Intentionally Left Blank

# Parameter Estimation

Roman Hovorka and Paolo Vicini

## 5.1. INTRODUCTION

This chapter describes principles and methods applicable to the parameter estimation problem. In particular, it describes the least squares (LS) estimator, the maximum likelihood (ML) estimator, the Bayesian estimator, and methods related to population models.

Parameter estimation is a traditional modelling task. Generally, a model contains input variable(s), parameter(s), and output variable(s). It also describes, in a mathematical form for our purposes, how the output is related to the input and the parameters. A model can be viewed as a *template* of the modelled system. The parameter specification makes the template applicable to a particular experiment.

Experimental data have certain similar characteristics. First, measurement noise (error) is present. Second, the measurements are made at discrete time instances. These are the limitations of virtually all data sources and must be considered by all parameter estimation methods.

The task of the parameter estimation is to recover “true” parameter values from these imperfect measurements. Often, the true parameter values are not measurable by other (more direct) means or represent a theoretical concept without a physical counterpart. In any case, the presence of the measurement error always means that the exact parameter values cannot be determined with absolute confidence. These can be determined only within a certain confidence, and the parameter estimation problem includes the subproblem of assessing the accuracy and precision of parameter estimates. The accuracy and precision are crucial for the interpretation of results.

Throughout the chapter, we will assume that a model has already been developed and validated. That is, we will assume that *somebody* has already

decided that the model is correct for a given experimental scenario. Although the model development and the model validation greatly benefit from information obtained during parameter estimation, these aspects need special consideration and are outside the scope of this chapter.

A model is usually described by a set of differential equations in the application areas of physiological, metabolic, pharmacokinetic/pharmacodynamic, and organ modelling. The principles described in this chapter are applicable to other mathematical forms, such as difference equations or time series. The common aspect is the dependence on time. Invariably, models in these fields describe time evolution of a substrate/hormone/drug.

The next section describes the LS estimator, which is the traditional parameter estimation method. It has the widest application domain due to its simple principles and relatively easy computation. The ML estimator is also described because the two approaches share similar properties.

The principles of the Bayesian estimator are not new, but with the recent advances in the area of Markov chain Monte Carlo methods and Bayesian networks, the applications of stochastic parameter estimation are likely to benefit a wider range of problems.

Population modelling is a relatively novel application domain that demands special parameter estimation procedures. These problems are described in the final section of the chapter.

## 5.2. LEAST SQUARES AND MAXIMUM LIKELIHOOD ESTIMATORS

The LS method is the standard method for estimating parameters of compartment models. Its appeal is due to historical reasons and, to a significant extent, to its relation to the ML parameter estimator. The two methods are identical under reasonable assumptions and, as the latter is based on statistical considerations, the LS method has indirectly gained support for its simple but rather intuitive concept, the minimisation of square differences between measurements and model predictions.

We will examine the principles of the two methods, comment on aspects relevant to the modeller, such as the effect of the measurement error, and describe in greater detail the Marquardt algorithm, the most widely used approach to estimate parameters of nonlinear models.

We will also address the issue of parameter accuracy. Here, we are forced to incorporate the knowledge about the measurement error because the uncertainty in the measurements determines the uncertainty in the parameter estimates.

### 5.2.1. LEAST SQUARES ESTIMATOR

Suppose that each data point  $y_i$  measured at time  $t_i$  has its own standard deviation  $\sigma_i$ . The standard deviation quantifies the measurement error, and we assume that  $\sigma_i$  is known to the modeller. The model prediction is denoted  $y(t_i, p_1 \dots p_M)$ , where  $p_i$  represent model parameters. We omit the model input from  $y(t_i, p_1 \dots p_M)$  to simplify the notation.

The “chi-square” quantity measuring the quality of model fit is obtained as:

$$\chi^2 \equiv \sum_{i=1}^N \left[ \frac{y_i - y(t_i, p_1 \dots p_M)}{\sigma_i} \right]^2 \quad (5.1)$$

The quantities  $y_i - y(t_i, p_1 \dots p_M)$  and  $(y_i - y(t_i, p_1 \dots p_M))/\sigma_i$  are known as residuals and normalised residuals, respectively. The values  $1/\sigma_i^2$  are occasionally referred to as weights. Figure 5.1 shows an example of a model fit. The residuals can be both negative and positive, indicating model underestimation or overestimation. In some computer packages and literature, the signs can be reversed;  $\chi^2$  is often denoted as “sum of squares of residuals” (SSR), or more precisely as “sum of squares of weighted residuals” (SSWR).

Model predictions would normally differ from the measurements reflecting the presence of the measurement error. Intuitively, the predictions should differ by an amount similar to the “average” value of the measurement error. A too good fit characterised by a too low value of  $\chi^2$  normally suggests “overfitting”

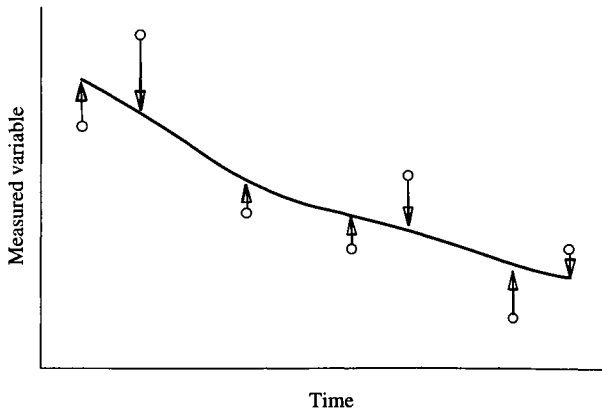


**Figure 5.1.** Differences between measured data (open circles) and model fit (solid line) are known as residuals (*arrows*). The residuals can be both positive and negative and are measured along a line parallel with the y-axis, not as the shortest distance between the measurements and the model fit.

caused by a large number of parameters. A too poor fit (a high value of  $\chi^2$ ) normally indicates the inability to fit data (model inadequacy).

So what is the expected value of  $\chi^2$ ? If the errors are normally distributed and the model is linear in parameters, it can be shown that at its minimum,  $\chi^2$  is distributed as the chi-square probability distribution with  $\nu = N - M$  degrees of freedom. The expected value of  $\chi^2$  is  $\nu$  and therefore a "good" model fit should have  $\chi^2$  close to  $\nu$ . Statistical testing on  $\chi^2$  can confirm model adequacy and the extent of the measurement error.

Nonlinear models do not have  $\chi^2$  distributed exactly as the chi-square distribution. However, as the models are often linearized around the  $\chi^2$  minimum during the parameter optimisation process and this approximation is adequate, it is often reasonable to assume the same properties for the nonlinear and linear models.

The parameter estimates obtained by the method of LS are those that minimise  $\chi^2$ . Linear models have a unique solution guaranteed, but nonlinear models can have a number of parameter combinations, which result in local and global minima. The process for solving the linear and nonlinear models is also very different.

The necessary condition for a parameter combination to achieve (local) minima is that the partial derivatives of  $\chi^2$  with respect to the parameters  $p_i$  are equal to zero:

$$0 = \frac{\partial \chi^2}{\partial p_k} = -2 \sum_{i=1}^N \left( \frac{y_i - y(t_i, p_1 \dots p_M)}{\sigma_i^2} \right) \times \left( \frac{\partial y(t_i, p_1 \dots p_M)}{\partial p_k} \right) \quad k = 1 \dots M \quad (5.2)$$

Equation (5.2) defines a set of  $M$ , in general, nonlinear equations with  $M$  unknown parameters. The principles and procedures used to solve the set of equations are described in the following section. Note that this is a classic problem of function minimisation in an  $M$ -dimensional space.

### 5.2.1.1 Models Linear in Parameters

Most biomedical models display nonlinearity in parameters. Therefore, linear models, i.e., those with model output dependent linearly on parameters, will be only briefly discussed. The benefit of linear models is a guaranteed unique solution of (5.2) under a reasonable condition, meaning that the number of measurements  $N$  is greater than the number of parameters  $M$ . We also can obtain exact confidence intervals of parameter estimates under the assumption of normal distribution of measurement errors.

The general form of a model linear in parameters is:

$$y(t) = \sum_{k=1}^M p_k z_k(t),$$

where  $z_k(t)$  are generally nonlinear functions of time and model input (omitted from the description to simplify the notation).

The condition of zero partial derivatives given by (5.2) is written for linear models as:

$$0 = \sum_{i=1}^N \left( \frac{y_i - \sum_{j=1}^M p_j z_j(t_i)}{\sigma_i^2} \right) z_k(t_i) \quad k = 1 \dots M \quad (5.3)$$

Equation (5.3) can be rearranged into the form:

$$\sum_{j=1}^M a_{kj} p_j = b_k, \quad (5.4)$$

where:

$$a_{kj} = \sum_{i=1}^N \frac{z_k(t_i) z_j(t_i)}{\sigma_i^2} \quad (5.5)$$

$$b_k = \sum_{i=1}^N \frac{y_i z_k(t_i)}{\sigma_i^2}$$

The set of equation given by (5.3) is known as normal equations of the LS problem and in the matrix form are written as  $\mathbf{A}\mathbf{p} = \mathbf{b}$ , where  $\mathbf{A}$  is a  $M \times M$  matrix and  $\mathbf{b}$  is a vector of length  $M$ . The solution is obtained by standard methods to solve a set of linear equations such as *LU* decomposition, Gauss-Jordan elimination, or Cholesky decomposition (Press *et al.*, 1992).

The inverse matrix  $\mathbf{A}^{-1}$  with elements  $a_{ij}^{-1}$  determines the accuracy of parameter estimates  $p_j$ . From (5.4), it follows that:

$$p_j = \sum_{k=1}^M a_{jk}^{-1} b_k = \sum_{k=1}^M a_{jk}^{-1} \left[ \sum_{i=1}^N \frac{y_i z_k(t_i)}{\sigma_i^2} \right] \quad (5.6)$$

from which we can derive that parameters  $p_j$  are obtained as a linear combination of measurements:

$$p_j = \sum_{i=1}^N c_i y_i \quad (5.7)$$

where:

$$c_i = \sum_{k=1}^M \frac{a_{jk}^{-1} z_k(t_i)}{\sigma_i^2} \quad (5.8)$$

Parameters  $p_j$ , therefore, follow the multivariate normal distribution as they result from a linear combination of normally distributed independent random variables  $y_i$  (Anderson, 1958) (assuming that measurement errors are normally distributed). Note that  $c_i$  is independent of  $y_i$  and that  $y_i$  is the only source of uncertainty. The variance  $\sigma^2(p_j)$  of a parameter  $p_j$  is obtained by definition due to the linear form of (5.6):

$$\sigma^2(p_j) = \sum_{i=1}^N c_i^2 \sigma_i^2 \quad (5.9)$$

Substituting for  $c_i$  from (5.8), we obtain:

$$\sigma^2(p_j) = \sum_{k=1}^M \sum_{l=1}^M a_{jk}^{-1} a_{jl}^{-1} \left[ \sum_{i=1}^N \frac{z_k(t_i) z_l(t_i)}{\sigma_i^2} \right] \quad (5.10)$$

The final term in the brackets is the element  $a_{lk}$  and (5.10) collapses to:

$$\sigma^2(p_j) = a_{jj}^{-1} \quad (5.11)$$

The diagonal elements of the matrix  $\mathbf{A}^{-1}$  represent the variances of parameter estimates. The matrix  $\mathbf{A}^{-1}$  is actually the covariance matrix associated with the multivariate normal distribution of parameters  $p_j$  and can be employed to calculate correlation coefficients between components of the parameter vector. Finally, if we do not make the assumption about normality of measurement errors, (5.11) will still hold. This is because (5.9) follows from (5.6) for any type of distribution of the measurement error.

### 5.2.1.2 Models Nonlinear in Parameters

Models nonlinear in parameters (nonlinear models further in the text) do not enjoy the same simple properties as linear models. We are not guaranteed a single solution of (5.2), the solution cannot be obtained from a closed formula, and the accuracy of parameter estimates cannot be calculated exactly. The problem is much harder.

As before, the LS method seeks a solution of a set of  $M$ , in this case nonlinear, equations with  $M$  unknowns (see [5.2]).  $\chi^2$  function represents a plane in an  $M + 1$  dimensional space, and the aim is to find a nadir on the plane surface.

Principles of most algorithms are very similar. One starts by selecting one point on the surface (i.e., a combination of parameter values) and calculates an associated value of  $\chi^2$ . The next step is to search, usually in the “neighbourhood” of the given parameter estimate, for another parameter combination with a smaller value of  $\chi^2$ . This iterative process of improving the  $\chi^2$  function is complete and a solution is found once  $\chi^2$  cannot be improved or the improvement is too small. It should be stressed that 1) the solution is always an approximation due to inherent numerical errors in finding the minimum; and 2) finding a global minimum is not guaranteed. The former point means that there will be models that will give gross differences in parameter estimates even if the initial estimate changes slightly. This is usually when the nadir is poorly defined, meaning the surface is “shallow” around the nadir and the iteration can finish in a wide area with a similar value of  $\chi^2$ . This also means that the parameters are estimated with reduced accuracy. As for the latter point, the  $\chi^2$  plane, which is determined by the model and the measurements, will be different for each data set, and can have, in general, an irregular shape with a number of nadirs (local minima). Figure 5.2 demonstrates this situation, employing an easily understandable plot with a single parameter.

The initial point can be identified by a grid search. A suitable grid is created over the range of feasible parameter values and  $\chi^2$  is calculated for all parameter combinations on the grid. This will usually require hundreds to thousands of  $\chi^2$  evaluations. The initial point is the one with the lowest value of  $\chi^2$ .

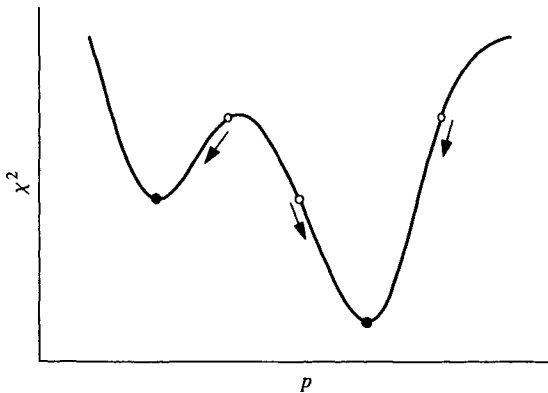


**Figure 5.2.** Plot of the objective function ( $\chi^2$ ) against a parameter value for a one-parameter optimisation problem. The objective function has one global minimum and one local minimum. Depending on the initial parameter estimate (open circles), gradient (descent) algorithms are able to find either the local or the global minimum (*solid circles*).



## 5.2.2. MAXIMUM LIKELIHOOD ESTIMATOR

The LS method minimises a sum of *squares* of residuals. The functional form to be minimised (squares) might seem somewhat arbitrary. Other functional forms, such as absolute values of residuals, could also be considered. In most cases, different functional forms will define different performance planes with different positions of local and global minima and thus will give different parameter estimates.

The benefit of the LS method is that it can be shown identical to the ML method. The latter method formulates the parameter estimation problem within a probabilistic framework. This greatly clarifies the interpretation of parameter estimates provided by both methods.

Suppose that we chose a parameter vector and employed it to make model predictions. As before, the residuals are defined as differences between predictions and measurements. We may now be interested in the probability of the occurrence of these residuals, which means we can evaluate the *conditional probability* of residuals given the parameter vector. This probability is called *likelihood*. It is natural to aim for a parameter vector maximising likelihood, and the ML estimator does exactly this.

The likelihood  $L$  is calculated:

$$L = \prod_{i=1}^N \frac{1}{\sigma_i \sqrt{2\pi}} \exp \left[ -\frac{1}{2} \left( \frac{y_i - y(t_i, p_1 \dots p_M)}{\sigma_i} \right)^2 \right] \quad (5.12)$$

Equation 5.12 assumes that the measurement errors (residuals) are uncorrelated and normally distributed with zero means and variances  $\sigma_i^2$ . Maximising  $L$  is identical to minimising a negative logarithm of  $L$ , namely, after removing some constant factors and multiplying by two:

$$\text{minimise : } \sum_{i=1}^N \left( \frac{y_i - y(t_i, p_1 \dots p_M)}{\sigma_i} \right)^2 + 2 \sum_{i=1}^N \ln(\sigma_i) \quad (5.13)$$

Equation 5.13 is identical to the definition of  $\chi^2$  (5.1) except for the addition of the sum on the right-hand side. Assuming  $\sigma_i$  to be independent from the predictions  $y(t_i, p_1 \dots p_M)$  (this is the usual case), the sum on the right is constant and can be removed. However, the sum is shown in (5.13), as it is important when considering model-based errors (see Section 5.2.3).

## 5.2.3. ERROR MODELS

The knowledge about the distribution of the measurement error is a prerequisite for parameter estimation. Often the modeller can obtain the qualitative

and quantitative properties of the measurement error from the knowledge of the measurement process. The error associated with a particular device/assay can be provided by the manufacturer or can be assessed independently by replicate measurements over a range of expected levels. It is also traditional (although somewhat arbitrary) to increase this estimate of the measurement error to reflect uncertainties associated with sampling times and other factors, such as pipetting errors.

Occasionally, the error is unknown or is known subject to a proportionality constant. In the former case, it became traditional to use “unit weighting,” i.e.,  $\sigma_i = 1$ . In the latter case, it is possible to use values proportional to  $\sigma_i$  to minimise (5.1). Note that the specification of  $\sigma_i$  subject to a proportionality constant does not affect minimisation of (5.1) and (5.13). However, it affects the calculation of parameter estimate accuracy. The proportionality constant can be calculated after the parameters are estimated from the expected value of  $\chi^2$  (the expected value equals the degrees of freedom  $\nu$  of  $\chi^2$ ).

Two types of a normally distributed measurement error are generally recognised, the multiplicative error and the additive error (a combination of the two is also feasible). The multiplicative error assumes that the coefficient of variation (CV) of the measurement error is constant:  $\sigma_i = CV y_i$ . The additive error assumes that  $\sigma_i$  is identical for all measurements:  $\sigma_i = \sigma$ .

From this, it is apparent that  $\sigma_i$  is calculated from the measurements  $y_i$  in case of the multiplicative error model. The question arises whether it would be more appropriate to use *model predictions*  $y(t_i, p_1 \dots p_M)$  to calculate  $\sigma_i$ . The model predictions, at “true” parameter values, are noise-free assuming that the model is correct, whereas the measurement errors are attached to the actual measurements. Some implementations are able to deal with this situation, meaning the error is calculated from the model rather than from the data. Note that this implies iterative reevaluation of  $\sigma_i$  as model predictions change during the iterative minimisation. This approach is called the extended LS method (Peck *et al.*, 1984). It also should be noted that (5.13) should be used instead of (5.1) if one aims for the ML estimation, as  $\sigma_i$  depends on model predictions.

There is one important class of measurement errors that does not follow the normal distribution. The error associated with the measurement of radioactivity (counts/disintegrations per minute) is known to follow the Poisson distribution. The variance of the Poisson distribution is equal to its expected value. In modelling terms, it means that  $\sigma_i$  should be made identical (or proportional) to  $\sqrt{y_i}$  (or  $\sqrt{y(t_i, p_1 \dots p_M)}$ ). It should be noted that the assumption of the Poisson distribution of the measurement error results in the LS estimator and the ML estimator providing, in general, different parameter estimates. For the sake of convenience, the LS estimator is often preferable to the ML estimator.

### 5.2.4. PARAMETER CONSTRAINTS

Physiological models usually adopt some simple parameter constraints; for example, parameters might be required to be non-negative to attain physiological interpretation. In addition, it is often appropriate to limit values of parameters during iterations to avoid divergence to nonfeasible (e.g., too low or too high) parameter values.

The simplest constraint is in the form of a finite range (a minimum and a maximum value). This constraint is usually easily implemented in iterative parameter estimation procedures. The simplest implementation is to reset a parameter value to its boundary whenever there is a tendency to surpass the limit.

More complicated linear and nonlinear constraints (Gill *et al.*, 1987) between parameters can be defined, although this is rarely required for physiological compartment models.

### 5.2.5. MULTI-OUTPUT EXPERIMENTS

Occasionally, one is confronted with a model and an experimental situation involving more than one output. For example, the experiment might involve measuring a number of substances and the model is expected to fit all these measurements given a single parameter vector. In general, the parameters affect all outputs and are estimated from a simultaneous analysis of all measurements.

In such situations, the knowledge of the measurement error is essential. The  $\chi^2$  definition remains virtually unchanged:

$$\chi^2 \equiv \sum_{j=1}^Q \sum_{i=1}^{N_j} \left( \frac{y_{ji} - y_j(t_{ji}, p_1 \dots p_M)}{\sigma_{ji}} \right)^2 \quad (5.14)$$

where  $j$  indicates the index of the model output, and the standard LS estimator or the ML estimator can be employed.

Without the exact knowledge of the measurement errors  $\sigma_{ji}$ , the minimization of (5.14) is meaningless. For example, changing the measurement unit of one output variable will affect undesirably the parameter estimates. The knowledge of the measurement error subject to a proportionality constant is sufficient, and a separate proportionality constant can be estimated from each measurement set during parameter estimation (Bell *et al.*, 1996).

### 5.2.6. CALCULATION PROCEDURES OF NONLINEAR MODELS

Parameter estimation of nonlinear models is more difficult than that of linear models. The search for optimal parameters can be formulated as a

minimisation problem, making a variety of function minimisation techniques available.

Many algorithms have been developed and differ in a number of features. First, the algorithm can search for a local minimum, as is the usual case, or for a global minimum. The search for a global minimum is much more difficult. The most widely used algorithms search for the local minimum.

The algorithms may or may not use the first derivatives of the objective function ( $\chi^2$ , 5.1) with respect to the parameters. The first derivatives provide information about the gradient at the position of parameters and about the direction with the greatest (and most likely) reduction in the objective function during the iterative parameter estimation process. The first derivatives can be calculated numerically using the finite difference method (model prediction is evaluated after an element in the parameter vector is incremented by a small amount) or from the sensitivity equations. The sensitivity equations are obtained by formal treatment of the differential equations specifying the model. However, the sensitivity equations are difficult to derive, even for modestly complicated models.

The most widely used algorithm in the biomedical sciences is the Marquardt method, which searches for a local minimum and requires the first derivatives to be evaluated.

### 5.2.6.1 Marquardt Algorithm

The Marquardt algorithm (Marquardt, 1963), also known as the Levenberg-Marquardt algorithm, exploits earlier insights by Levenberg (Levenberg, 1944). The algorithm minimises  $\chi^2$  (5.1) as a function of the parameter vector  $\mathbf{p} = (p_1 \dots p_M)$  and combines in an efficient way two other iterative methods, the quadratic approximation method and the steepest descent method.

The quadratic approximation method (the so-called inverse-Hessian method) approximates  $\chi^2$  in the neighbourhood  $\delta\mathbf{p}$  of a given parameter position  $\mathbf{p}$  by a quadratic form taking the first three elements of the Taylor series expansion:

$$\chi^2(\mathbf{p} + \delta\mathbf{p}) \approx c - 2 \cdot \mathbf{b} \cdot \delta\mathbf{p} + \delta\mathbf{p} \cdot \mathbf{A} \cdot \delta\mathbf{p} \quad (5.15)$$

where  $c$  represents  $\chi^2$  evaluated at the given parameter position  $\mathbf{p}$ ,  $\mathbf{b}$  is an  $M$ -vector, and  $\mathbf{A}$  is an  $M \times M$  matrix.

The  $\mathbf{b}$  vector is related to the gradient  $\partial\chi^2/\partial\mathbf{p}$ , the latter evaluated at the given parameter position:

$$b_k = -\frac{1}{2} \frac{\partial\chi^2}{\partial p_k} = \sum_{i=1}^N \frac{y_i - y(t_i, p_1 \dots p_M)}{\sigma_i^2} \frac{\partial y(t_i, p_1 \dots p_M)}{\partial p_k}$$

and the matrix  $\mathbf{A}$  with elements  $a_{kl}$  is related to the Hessian matrix (the matrix of second partial derivatives  $\partial^2\chi^2/\partial\mathbf{p}^2$ ) again evaluated at the given parameter

position:

$$\begin{aligned}
 a_{kl} &= \frac{1}{2} \frac{\partial^2 \chi^2}{\partial p_k \partial p_l} \\
 &= \sum_{i=1}^N \frac{1}{\sigma_i^2} \left[ \frac{\partial y(t_i, p_1 \dots p_M)}{\partial p_k} \frac{\partial y(t_i, p_1 \dots p_M)}{\partial p_l} \right. \\
 &\quad \left. - [y_i - y(t_i, p_1 \dots p_M)] \frac{\partial^2 y(t_i, p_1 \dots p_M)}{\partial p_k \partial p_l} \right]
 \end{aligned}$$

The second derivatives in the definition of  $a_{kl}$  are usually ignored by the minimisation algorithms. The main reason is that their inclusion might destabilise the minimisation process. This simplifies the calculation of  $a_{kl}$ :

$$a_{kl} = \sum_{i=1}^N \frac{1}{\sigma_i^2} \frac{\partial y(t_i, p_1 \dots p_M)}{\partial p_k} \frac{\partial y(t_i, p_1 \dots p_M)}{\partial p_l} \quad (5.16)$$

making it similar to the definition of elements  $a_{kl}$  for the linear models (5.5).

If the approximation by (5.15) is accurate, it is possible to go straight to the minimum  $\mathbf{p}^{\min}$  from a given parameter position  $\mathbf{p}^j$ :

$$\mathbf{p}^{\min} = \mathbf{p}^j + \mathbf{A}^{-1} \mathbf{b} \quad (5.17)$$

where  $\mathbf{b}$  and  $\mathbf{A}$  are evaluated at  $\mathbf{p}^j$ . This is, in principle, identical to the approach used in linear models (5.7). Even if the minimum is not reached, an iterative step can be made by replacing  $\mathbf{p}^{\min}$  by  $\mathbf{p}^{j+1}$  in (5.17).

The steepest descent method also employs the first derivatives when calculating a new parameter position. The vector  $\mathbf{b}$ , which is proportional to negative values of the gradient, indicates the direction in which  $\chi^2$  is being reduced by the greatest extent. A new parameter position  $\mathbf{p}^{j+1}$  is found as:

$$\mathbf{p}^{j+1} = \mathbf{p}^j + c\mathbf{b}$$

where  $c$  is a suitable constant.

The changes in the parameter position  $\delta\mathbf{p} = \mathbf{p}^{j+1} - \mathbf{p}^j$  defined by the two methods are written as:

$$\delta\mathbf{p} = \mathbf{A}^{-1} \mathbf{b} \quad (5.18)$$

$$\delta\mathbf{p} = c\mathbf{b} \quad (5.19)$$

The steepest descent method is usually efficient at parameter positions far from the minimum. The inverse-Hessian method is efficient close to the minimum. The Marquardt method smoothly mixes the two methods. When moving to a

new position, both (5.18) and (5.19) are utilised and the contribution of the two methods changes as the parameter position gets closer to the minimum.

The first important feature of the Marquardt algorithm is the derivation of the step of the steepest descent method. Marquardt suggested that the elements of the Hessian matrix can indicate the size of the step or, in other words, the constant  $c$  in (5.19). In fact, he suggested that a different value of the constant  $c$  be used for elements  $b_l$ , virtually modifying the gradient.

The diagonal elements of the Hessian matrix represent the curvature of  $\chi^2$  with respect to the parameter. The idea is that a dimension with a high curvature (large  $a_{kk}$ ) should be interpreted as unfavourable for a large move, whereas a move in a dimension with a small curvature is favourable. We still would like to retain scaling ability, and this is achieved by the introduction of a scaling factor  $\lambda$  in the equation:

$$\delta p_k = \frac{1}{\lambda a_{kk}} b_k \quad (5.20)$$

Notice that large values of  $\lambda$  reduce the step size.

The next important feature of the Marquardt algorithm is the mixing of the two methods: the inverse-Hessian method and that defined by (5.20). The inverse-Hessian method given by (5.18) can be rewritten as:

$$\sum_{l=1}^M a_{kl} \delta p_k = b_k \quad (5.21)$$

and (5.20) can be rewritten as:

$$\lambda a_{kk} \delta p_k = b_k \quad (5.22)$$

Combining (5.21) and (5.22) is achieved by creating a new matrix  $\mathbf{A}'$  with elements  $a'_{kl}$  such that:

$$\begin{aligned} a'_{kk} &= a_{kk}(1 + \lambda) \\ a'_{kl} &= a_{kl} \quad \text{if } k \neq l \end{aligned} \quad (5.23)$$

We then specify:

$$\sum_{l=1}^M a'_{kl} \delta p_k = b_k \quad (5.24)$$

It is interesting to consider the effect of  $\lambda$ . A very large value of  $\lambda$  will give matrix  $\mathbf{A}'$  a dominant diagonal, converting the Marquardt method virtually to the (steepest) descent method. However, the size of the step will be very small (5.20). A very small value of  $\lambda$  will make  $\mathbf{A}' \approx \mathbf{A}$  and the inverse-Hessian method will be used.

The Marquardt algorithm employs the following steps:

*Initialisation.* Select an initial estimate  $\mathbf{p}^0$ . Evaluate  $\chi^2(\mathbf{p}^0)$ . Select an initial value for  $\lambda$  (usually  $\lambda \approx 0.001$ ). Set  $j = 0$ .

*Solution.* Solve (5.24) for  $\delta\mathbf{p}$ . Evaluate  $\chi^2(\mathbf{p}^j + \delta\mathbf{p})$ .

*Incrementing  $\lambda$ .* If  $\chi^2(\mathbf{p}^j + \delta\mathbf{p}) \geq \chi^2(\mathbf{p}^j)$ , increase  $\lambda$  by a factor of 10. Go back to *Solution*.

*Decrementing  $\lambda$ .* If  $\chi^2(\mathbf{p}^j + \delta\mathbf{p}) < \chi^2(\mathbf{p}^j)$ , decrease  $\lambda$  by a factor of 10. Assign  $\mathbf{p}^{j+1} = \mathbf{p}^j + \delta\mathbf{p}$  and  $j = j + 1$ . Go to *Solution*.

The procedure terminates when  $\chi^2$  cannot be improved or the improvement is too small. The exact stopping criteria vary from implementation to implementation. In general, based on statistical criteria, it is not necessary to continue the iterations if the improvement in  $\chi^2$  is much smaller than unity. The stopping criteria sometimes also monitor the size of the parameter move  $|\delta\mathbf{p}|$ . The small value of the move is taken as an indicator of the algorithm converging to the minimum parameter value.

### 5.2.6.2 Other Algorithms

The Marquardt algorithm belongs to the family of gradient methods. These are approaches that use information about the local gradient (the first derivatives) to reduce the value of the objective function during the iterative minimisation process. Some methods store and employ information about previous iterative steps to minimise the number of iterations, such as the conjugate gradient (CG) method (Press *et al.*, 1992).

The gradient methods assume that the first derivative of the objective function with respect to the parameters can be calculated at any point. The derivatives can be obtained from the sensitivity equations or, when these are too difficult to be derived, can be calculated numerically. The numerical derivation can be affected by approximation errors, especially since the calculations often involve numerical solutions of differential equations. The effect of the approximation error is pronounced when the  $\chi^2$  plane is flat. The partial derivatives are small, which means that the increment (decrement) for the objective function for a fixed change in an element of the parameter vector is also small, and the errors due to numerical approximations of differential equations contribute significantly to the calculation of the first derivative.

For this reason, methods that avoid the use of the first derivatives have received considerable attention. The downhill simplex method (Nelder and Mead, 1965) has found application in the Adapt II package (D'Argenio and Schumitzky, 1997). In general, these methods are more robust, but the payoff has reduced efficiency, resulting in an increased number of iterations.

The simulated annealing method is one that seeks a global minimum, compared with the local minimum sought by methods mentioned earlier

(Kirkpatrick *et al.*, 1983). This method draws a parallel with the position of molecules during annealing (cooling of metals). During cooling, the molecules position themselves to minimise overall energy, although periodically the overall energy can be increased by random disturbances. The energy increase is more likely to occur at high temperatures.

The simulated annealing is an iterative algorithm and includes the following steps. The objective function (overall energy) is calculated for a parameter vector. Randomly, a new parameter vector is generated and the energy associated with it is evaluated. If the new energy is smaller, the new parameter vector is accepted. Otherwise, the new vector is accepted with probability depending on the “temperature.” The temperature controls the acceptance of unfavourable new parameter vectors; at high temperature levels, there is a high probability of new position acceptance. The temperature is reduced during the iterations, which means the algorithm is more likely to have the objective function increased in early stages than in late stages. The ability to “climb” the  $\chi^2$  plane enables local minima to be avoided or, more precisely, a local minimum close to the global minimum to be sought. The algorithm certainly has a poor performance in terms of efficiency, but it can be used to explore the  $\chi^2$  plane and to find a suitable initial estimate for a more efficient algorithm.

### 5.2.7. ACCURACY OF PARAMETERS

The determination of accuracy is an essential component of the parameter estimation process. The accuracy represents the quantitative assessment of the confidence the modeller has in the estimated parameters.

The uncertainty in parameter estimates has its origin in the presence of the measurement error. Suppose that the model is correct and that there exists a “true” parameter vector. Performing an experiment on the modelled system will enable measurements to be taken. The important factor is that the measurements include the measurement error. The parameter estimation employs these noisy measurements. However, the extent of the individual measurement errors is purely random. Repeating the experiment will most likely produce a different set of measurements and, in consequence, a different parameter estimate. Ideally, we want information on the relationship between the “true” parameters and the estimated parameters. However, this information is almost never accessible. The difference between parameter estimates and the “true” parameter vector cannot be computed because we do not know the “true” parameter vector. Thus, we must be satisfied with the accuracy of the estimates. The accuracy quantifies the variability in parameter estimates due to the presence of the measurement error. It relates the variability of the estimates to the expected variability of the measurements.



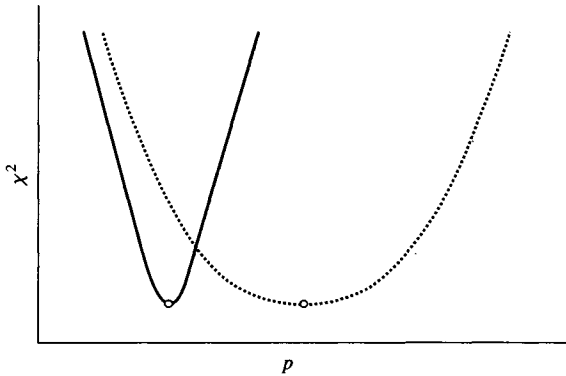


**Figure 5.3.** The shape of the objective function ( $\chi^2$ ) around the nadir (*open circles*) determines the accuracy of the parameter estimate. A well-defined nadir (*solid line*) signifies high accuracy, a shallow shape around the nadir (*dotted line*) signifies low accuracy. The curvature at the nadir is quantified by the second partial derivatives of the objective function with respect to the parameters.

Informally, the shape of the  $\chi^2$  plane determines the accuracy of the parameter estimates. A well-defined nadir means a better accuracy (a lower variance) of the parameter estimate (see Figure 5.3). This can be intuitively seen from the fact that one is more certain that a minimum was reached for a well-defined rather than a badly defined (“shallow”) nadir. It is also possible that a “valley” is present on the  $\chi^2$  surface. Suppose that as values of one parameter change, values of another parameter can be adjusted to give a very similar value of  $\chi^2$ . This results in the estimates of the two parameters to be correlated (positively or negatively depending on the adjustments). Highly correlated parameters, such as  $|r| > 0.95$ , usually signify high uncertainty in parameter estimates and should be carefully assessed by the modeller.

### 5.2.7.1 Analytical Approach

From the previous discussion, it can be intuitively seen that the accuracy of parameter estimates is related to the curvature around a nadir. The curvature is given by the second derivatives of  $\chi^2$  with respect to parameters, these evaluated at the parameter estimates.

The analytical estimation of the accuracy relies on a Rao-Cramer inequality (Rao, 1952) valid for the LS and the ML estimators:

$$\mathbf{S}(\mathbf{p}) \geq \mathbf{A}^{-1} \quad (5.25)$$

where  $\mathbf{S}(\mathbf{p})$  is the covariance matrix associated with the minimum parameter estimate  $\mathbf{p}$ , and  $\mathbf{A}$  is the Fisher information matrix derived as an expected

value of a function of the likelihood  $L$ :

$$\mathbf{A} = E \left[ \left( \frac{\partial \ln L}{\partial \mathbf{p}} \right)^2 \right]$$

with elements  $a_{kl}$ :

$$a_{kl} = E \left( \frac{\partial \ln L}{\partial p_k} \frac{\partial \ln L}{\partial p_l} \right)$$

It follows from the definition of likelihood (5.12) that:

$$\frac{\partial \ln L}{\partial p_k} = \sum_{i=1}^N \frac{y_i - y(t_i, p_1 \dots p_M)}{\sigma_i^2} \frac{\partial y(t_i, p_1 \dots p_M)}{\partial p_k}$$

The elements  $a_{kl}$  are thus calculated:

$$\begin{aligned} a_{kl} &= E \left\{ \left[ \sum_{i=1}^N \frac{y_i - y(t_i, p_1 \dots p_M)}{\sigma_i^2} \frac{\partial y(t_i, p_1 \dots p_M)}{\partial p_k} \right] \right. \\ &\quad \times \left. \left[ \sum_{i=1}^N \frac{y_i - y(t_i, p_1 \dots p_M)}{\sigma_i^2} \frac{\partial y(t_i, p_1 \dots p_M)}{\partial p_l} \right] \right\} \\ &= \sum_{i=1}^N \frac{1}{\sigma_i^4} \frac{\partial y(t_i, p_1 \dots p_M)}{\partial p_k} \frac{\partial y(t_i, p_1 \dots p_M)}{\partial p_l} E \left\{ [y_i - y(t_i, p_1 \dots p_M)]^2 \right\} \\ &= \sum_{i=1}^N \frac{1}{\sigma_i^2} \frac{\partial y(t_i, p_1 \dots p_M)}{\partial p_k} \frac{\partial y(t_i, p_1 \dots p_M)}{\partial p_l} \end{aligned} \tag{5.26}$$

The Fisher information matrix  $\mathbf{A}$  is therefore identical to the matrix employed by the Marquardt method, (5.16) and is calculated by the Marquardt method as the matrix  $\mathbf{A}'$  by setting  $\lambda = 0$ , (5.23) after the optimum parameter vector was found.

Equation 5.26 relies on the assumptions that the errors (residuals) are uncorrelated and normally distributed. For different types of the measurement error, the Fisher information matrix has a different form in principle, but this is ignored by most implementations.

The inequality given by (5.25) states that we are able to obtain a lower limit of the “true” covariances of the parameter estimates. Thus, the diagonal elements of  $\mathbf{A}^{-1}$  representing the variances associated with  $\mathbf{p}$  are only *lower* bounds of the true variances! The equality is achieved for linear models under the assumption of a normal distribution of the measurement error (5.11).

Sometimes confidence intervals for parameters are quoted. The calculations are based on the assumption of normal distribution of parameters. This is, however, incorrect, as parameters are not guaranteed to be normally distributed. The normal distribution is ensured for linear models (see Section 5.2.1.1).

It is often convenient to express the variance as a fractional standard deviation (or the coefficient of variation):

$$\text{FSD}(p_k) = \frac{p_k}{\sqrt{a_{kk}^{-1}}} \times 100\% \quad (5.27)$$

Values  $\text{FSD}(p_k) \gg 100\%$  indicate a poor accuracy of the  $k$ -component of the parameter vector; values  $< 10\%$  indicate an excellent accuracy. The poor accuracy implies that the model is not *a posteriori* identifiable (Carson *et al.*, 1983) for the given experimental data.

The analytical approach relies on statistical treatment of  $\chi^2$ . It exploits statistical properties, which apply to a large number of data points. However, little is known about the practical scenario with the limited size of the data set. The implementation details, such as the calculation of first derivatives, also greatly affect the quantification of accuracy and might result in considerable differences between implementations for some models (Heatherington *et al.*, 1998).

### 5.2.7.2 Monte Carlo Approaches

The enormous increase in computing power has enabled a wide use of methods based on Monte Carlo approaches. Whereas the analytical approach exploits statistical (asymptotic) properties with relatively undemanding calculations, the Monte Carlo approaches are usually simple in principle but computationally expensive.

There are two Monte Carlo approaches discussed here: one based on synthetic data sets and the other based on data resampling (i.e., the bootstrap method).

The method based on synthetic data sets is straightforward. The parameter estimator, or the LS method, estimates parameters  $\mathbf{p}^{\min}$  from the experimental data. Then, the model in connection *with* the parameters  $\mathbf{p}^{\min}$  is used to generate a large number (hundreds to thousands) of synthetic, noisy data sets. The parameter estimator calculates parameters  $\mathbf{p}^i$  from each synthetic data set. Finally, simple descriptive statistics, such as the variance of the differences  $p_k^i - p_k^{\min}$ , quantify parameter accuracy.

The generation of synthetic data sets is usually done in two steps. In the first, the parameter vector  $\mathbf{p}^{\min}$  is used by the model to calculate noise-free predictions. The number and timing of data points should be identical to those of the original data set.

The second step includes the “addition” of synthetic measurement errors to model predictions. Quantities representing measurement errors are generated and added to model predictions to create “noisy” synthetic measurements. There are algorithms able to generate errors from various probabilistic distributions (Press *et al.*, 1992). The critical decision steps are, however, which distribution and what parameters of the distribution should be used! We are again asked to provide statistically relevant information about the measurement error. This is a common feature of virtually all methods assessing parameter accuracy.

The bootstrap method (Efron, 1982) is the only method that does not explicitly require this information. It assumes that this information is included implicitly in the data.

The bootstrap method is identical to the method based on synthetic data sets, except for the data generation step. The data sets are not synthetically generated but obtained from the original data set by removing some data points in a random fashion (e.g., 20–30% of all data points) and randomly replacing each with a replicate from the remaining data points. The replacement is carried out to maintain the total number of samples identical to that of the original set.

It is apparent that the bootstrap method will analyse data sets with replicate data points. However, not all samples from the original data set will be present in the generated data sets. Clusters of replicates will occur according to their relative occurrence in the original data set. This, at least informally, indicates how the information about the measurement error is extracted from the original set.

Both Monte Carlo methods have gained credibility after years of neglect by a comprehensive statistical analysis of their properties.

### 5.2.8. INTERVAL IDENTIFIABILITY FOR NONIDENTIFIABLE MODELS

In the case where the model is *a priori* unidentifiable (Carson *et al.*, 1983), a possible strategy is to bound the feasible parameter space, if the particular model structure allows. Parameter bounding has been explored for linear and time-invariant multicompartmental models. The notions of *interval identifiability* (providing finite ranges for rate constants of unidentifiable compartmental models) and quasi-identifiability (the occurrence of very “narrow” such ranges) were first introduced by DiStefano (DiStefano III, 1983), who derived closed-form expressions for finite bounds on the rate constants of mammillary models of any order (with both input and output in the central compartment). Subsequent work allowed computation of the identifiable parameter combinations of mammillary models (Landaw *et al.*, 1984). Catenary models with

input and output in the same compartment were studied (Chen *et al.*, 1985; DiStefano III *et al.*, 1988), and such results were extended to the noisy data case for both mammillary and catenary models (Lindell *et al.*, 1988). Bounds for rate constants in certain mammillary models with input and output in the first compartment can be derived in terms of the parameters of the sum of the corresponding sum of exponentials (Godfrey, 1983). General methods are presented elsewhere for bounding the parameters of linear compartmental models (Vajda *et al.*, 1989). A computationally attractive approach, based on estimating the parameters of identifiable submodels of an unidentifiable model, has been described with application to a mathematical model of tracer glucose kinetics (Cobelli and Toffolo, 1987). Yet another alternative approach, based on Lyapunov functions, has been proposed (Eisenfeld, 1996).

### 5.2.9. IMPLEMENTATION PACKAGES AND HISTORICAL REMARKS

Apart from commercial software packages, such as the NAG library, the SAAM II program (Barrett *et al.*, 1998), and the PC/WinNonlin program, there are public domain packages, such as ADAPT II (D'Argenio and Schumitzky, 1997), which implement parameter estimation algorithms. The graphical user interface is part of the newer programs, WinNonlin or SAAM II, for example, and greatly simplifies model specification. Even spreadsheet programs, such as Microsoft Excel, include parameter optimisation tools that can be used for quick parameter estimation. A good source of information on modelling packages is the Internet; visit "[www.boomer.org/pkin/](http://www.boomer.org/pkin/)" or the PharmPK discussion list, for example. Considerable interest has been generated by the pharmacokinetic/pharmacodynamic research community and the pharmaceutical industry, and most (commercial) applications target these user groups.

On the historical note, the LS method was invented by A. M. Legendre at the end of the 18<sup>th</sup> century and used by K. F. Gauss in the beginning of the 19<sup>th</sup> century to trace the newly discovered asteroid Ceres, which was lost after initial sighting. The ML method was devised by the eminent statistician R. A. Fisher more than a century later in the early 1920s.

## 5.3. BAYESIAN ESTIMATOR

The ML estimator is justified on the grounds of a certain probabilistic concept. It considers the likelihood function, which is the conditional probability of data given parameters, and aims to maximise it.

The Bayesian estimator expands this concept. It considers not only the likelihood function, but also the *a priori* probability of the parameters. The

*a priori* probability represents our prior beliefs expressed in the form of a probability distribution and normally reflects our knowledge of, for instance, the population mean and variation of the parameters. It is also possible to specify a noninformative prior, for example, a uniform (“flat”) distribution for a mean value, expressing the lack of prior knowledge.

The Bayesian estimator updates the prior probability of parameters using measured data. The updated probability, the *a posteriori* probability  $\pi(\mathbf{p})$ , is obtained according to the Bayes’ theorem:

$$\pi(\mathbf{p}) = p(\mathbf{p}|y) = \frac{p(y|\mathbf{p})p(\mathbf{p})}{p(y)} \tag{5.28}$$

where  $\mathbf{y} = y_1 \dots y_N$  is the vector of measurements,  $p(\mathbf{p})$  is the (generally multivariate) prior probability of parameters,  $p(\mathbf{y})$  is the prior probability of measurements, and  $p(\mathbf{y}|\mathbf{p})$  is the conditional probability of measurements given data (similar to the likelihood given by [5.12]). The denominator in (5.28) is called the *normalisation* factor because it is independent of the parameters. It therefore follows that:

$$\pi(\mathbf{p}) \propto p(\mathbf{y}|\mathbf{p})p(\mathbf{p}) \tag{5.29}$$

There is one important difference between the Bayesian estimator on the one hand and the LS estimator on the other hand. The LS estimator returns a parameter vector, or a *point* estimate; the Bayesian estimator returns a *probability* distribution (Figure 5.4). Thus, the parameter estimation problem as defined by the Bayesian estimator is much more demanding. Instead of returning a parameter vector, the Bayesian estimator returns a value (probability) for all parameter vectors!

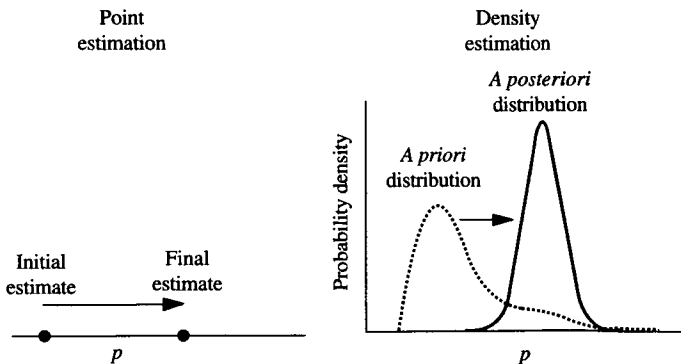


**Figure 5.4.** The nonlinear LS estimator seeks to find a parameter vector, or a point estimate, from an initial parameter vector. The Bayesian estimator calculates the posterior distribution by updating the prior distribution. The Bayesian estimator has a much more demanding task as posterior probability has to be returned for each feasible value of the parameter vector.

The benefits of the Bayesian estimator are that the parameter estimate can be summarised in a statistically coherent way. For instance, the confidence interval, the median, and the mode can be calculated for elements  $p_i$  from the marginal distributions of the posterior probability  $\pi(\mathbf{p})$ . The parameter estimation problem with multiple minima does not make any special demands on the Bayesian estimator. In such a case, the posterior probability  $\pi(\mathbf{p})$  will demonstrate multimodality. The lack of *a posteriori* identifiability of the LS method as demonstrated by high FSD (5.27) will result in the Bayesian estimator providing a wide confidence interval.

Parameters in the deterministic models represent *deterministic* quantities, but those in stochastic models represent *stochastic* quantities. This is also true for other model quantities, such as masses and fluxes. Even the uncertainties associated with the model input can be represented using the stochastic paradigm! These are additional benefits of stochastic models.

So why are stochastic models not used more widely in practice? The formula given (5.29) shows the simplicity of the formulation of the parameter estimation problem (i.e., the calculation of  $\pi[\mathbf{p}]$ ). This is, however, deceptive because the calculation of  $\pi(\mathbf{p})$  is in most cases a very difficult task.

Rarely, it is possible to find an analytical (closed-form) solution to (5.29). The specification of the model in the form of differential equations is hidden in the definition of the likelihood  $p(\mathbf{y}|\mathbf{p})$ . The analytical specification of the likelihood function is often not available and is obtained by a numerical solution of the differential equations.

These problems have hindered the practical use of the Bayesian estimator. However, recent advances in two techniques, the Markov chain Monte Carlo (MCMC) methods and Bayesian networks, facilitate a wider use of the Bayesian estimator. Thorough theoretical understanding of MCMC methods has facilitated wider use of the Bayesian models in research fields (Smith, 1991).

The MCMC methods are able to handle a variety of models. Bayesian networks are suitable for discrete-state and discrete-time models. Before going into further detail, it is beneficial to discuss differences between continuous-state and discrete-state stochastic models and their impact on the calculation procedures.

### 5.3.1. CONTINUOUS-STATE MODELS

Probabilistic continuous-state models are a natural extension of (deterministic) differential equations models. Model quantities, such as state variables, parameters, and input variables, can be represented as continuous stochastic variables with associated prior and posterior distributions.

For the majority of models, a closed form of the posterior distributions (and often prior distributions for model output) does not exist and the parameter estimation of continuous-state models is invariably obtained by numerical approximation: numerical integration of probability integrals, Monte Carlo integration, or sampling methods.

### 5.3.2. DISCRETE-STATE MODELS

The discrete-state models differ in many aspects. The finite number of states and the use of efficient algorithms allow exact calculations of prior and posterior distributions to be carried out. Thus, errors arise not from the calculation process but from another route. The discrete specification of random variables (parameters, masses, inputs) results in a reduced resolution of these quantities.

Despite the reduced resolution, discrete-state models found a place in the parameter estimation of, for instance, carbohydrate metabolism (Tudor *et al.*, 1998). The additional benefit of discrete-state models is that they can operate with low-quality measurement data (e.g., limited number of samples), although this is a general feature of all Bayesian parameter estimation procedures.

#### 5.3.2.1 Bayesian Networks

Bayesian networks (also called causal probabilistic networks) were originally developed to facilitate intelligent reasoning in probabilistic systems (Pearl, 1988).

From the perspective of a modeller, Bayesian networks can be seen as a parallel technology to the specification of a system by differential equations. The difference is that Bayesian networks can usually handle only discrete time instances and therefore the *differential* equation specification must be transformed to the *difference* equation specification.

A Bayesian network consists of a set of nodes and a set of directed links forming a directed acyclic graph. Each node represents a random variable and has a finite number of mutually exclusive states. The number of states is usually on the order of units to tens of units. The directed links represent the causal relationships and are quantified by (discrete) conditional probability tables.

A simple Bayesian network is shown in Figure 5.5. The example includes two parameters  $p_1$  and  $p_2$ , which represent the control of production and the control of removal of a substrate (e.g., plasma glucose). One time slice of a difference equation model is shown, but it is easy to imagine an extension of the model for additional time slices with parameters  $p_1$  and  $p_2$  entering each



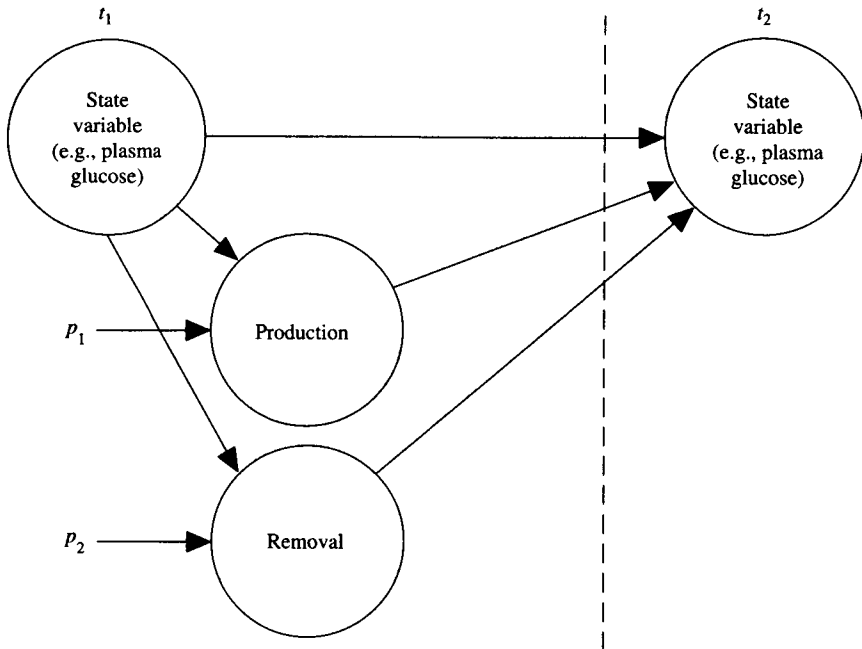


**Figure 5.5.** An example Bayesian network showing causal relationships between the amount of substrate at time  $t_1$ , the amount of substrate at time  $t_2$ , and the amount produced and removed during the time interval  $t_2-t_1$ . Parameters  $p_1$  and  $p_2$  influence production and removal rates.

time slice. These types of Bayesian networks are known as *dynamic* Bayesian networks.

The conditional probability tables specify the functional relationships between variables and implement the difference equations (Hejlesen *et al.*, 1997). Continuous variables also can be handled by Bayesian networks, but the relationships between such variables are restricted to a small family of conditional, usually multivariate normal distributions (Lauritzen, 1992).

### 5.3.3. CALCULATION PROCEDURES

We divide calculation techniques into two categories. One category estimates posterior distributions in continuous-state models. The other category calculates posteriors in discrete-state models (Bayesian networks).

The two categories are fundamentally different. Sampling-based methods are used for continuous-state models. Exact calculations are made to compute (discrete) posteriors associated with Bayesian networks.

Markov chain Monte Carlo (MCMC) denotes a category of sampling methods. These methods generate a Markov chain of (in our context) samples from the posterior distribution of parameters. Two prominent algorithms, the Metropolis-Hastings algorithm and Gibbs sampling, will be described, as they have achieved the widest application spectrum.

We will briefly comment on the method used to calculate posteriors in Bayesian networks. This method exploits insights into topographical structures of networks to limit the computational burden.

### 5.3.3.1 Metropolis-Hastings Algorithm

The Metropolis-Hastings algorithm (Metropolis *et al.*, 1953; Hastings, 1970) is an interesting algorithm to generate Markov chains representing samples from a probabilistic distribution. Despite its simplicity, however, it took about 20 years to establish its statistical properties, its convergence property in particular.

In the context of parameter estimation, the algorithm generates a chain  $\mathbf{p}^1, \mathbf{p}^2 \dots \mathbf{p}^j \dots \mathbf{p}^Q$ , which represents a sample from the posterior distribution  $\pi(\mathbf{p})$ . The  $(j + 1)$ -th element  $\mathbf{p}^{(j+1)}$  is obtained from the  $j$ -th element  $\mathbf{p}^j$  and is independent from other elements of the chain (the Markov property).

The generation of an element of the chain employs two steps. First, a candidate  $\mathbf{p}'$  is generated from  $\mathbf{p}^j$  using a random number generator. Second, a decision is made whether the candidate is “suitable.” Upon suitability, the candidate is accepted and  $\mathbf{p}^{(j+1)} = \mathbf{p}'$  otherwise the  $j$ -th element is retained  $\mathbf{p}^{(j+1)} = \mathbf{p}^j$ . It means that the chain may contain repeated elements.

The algorithm starts with an arbitrary parameter vector  $\mathbf{p}^0$ . It generates a candidate using the so-called transition kernel  $q(\mathbf{p}, \mathbf{p}')$ , which is (for the moment) an arbitrary probability function with two arguments:  $\mathbf{p}$  and  $\mathbf{p}'$ . The generation is done by fixing one argument of the kernel to  $\mathbf{p}^j$  and drawing a candidate using a probability density  $q(\mathbf{p}^j, \cdot)$ .

The candidate is accepted according to a probabilistic criterion. A random number is generated from a uniform distribution on the  $(0, 1)$  interval, and acceptance is declared if the random number is smaller than the acceptance probability  $\alpha(\mathbf{p}^j, \mathbf{p}')$ ,

$$\alpha(\mathbf{p}^j, \mathbf{p}') = \min \left\{ 1, \frac{\pi(\mathbf{p}')q(\mathbf{p}^j, \mathbf{p}')}{\pi(\mathbf{p}^j)q(\mathbf{p}', \mathbf{p}')} \right\} \quad (5.30)$$

Note that evaluation of (5.30) requires evaluations of both the kernel  $q(\cdot, \cdot)$  and the posterior probability  $\pi(\cdot)$ . Therefore, these should be relatively inexpensive to compute. Evaluation of the posterior probability  $\pi(\cdot)$  usually includes, in the context of compartment models, numerical solutions of differential equation for a particular parameter vector, and this is usually the most expensive step.

The other steps are the evaluation of the likelihood from residuals and the calculation of prior probability (see 5.29). It is worthwhile to stress that the posterior probability can be specified subject to a proportionality constant due to the ratio  $\pi(\mathbf{p}')/\pi(\mathbf{p}^j)$  in (5.30).

The Markov chain is guaranteed to converge eventually to the posterior distribution from any starting position. The initial portion of the chain representing the nonconvergent section is therefore disregarded. Furthermore, it is also possible to analyse only every  $k$ -th element of the chain to reduce correlation between successive elements. The size of the disregarded chain, the number of skipped elements, and indeed the size of the chain depends on how quickly the chain converges to the posterior distribution  $\pi(\mathbf{p})$ . In principle, it is not possible to make the decision on successful convergence on a purely theoretical basis, but indicative diagnostic criteria have been developed to demonstrate the opposite, such as the lack of convergence (Gilks *et al.*, 1996; Gamerman, 1997). It is also possible to run a number of chains with different starting parameter vectors and obtain information about convergence from multiple independent runs.

Different choices of the kernel  $q(\cdot, \cdot)$  clearly influence the acceptance rate and result in different algorithms. There is no “best” form of the kernel, and its selection is likely to be influenced by the parameter estimation problem. A convenient option is the random walk process,  $q(\mathbf{p}, \mathbf{p}') = q(\mathbf{p} - \mathbf{p}')$  with a multivariate normal distribution. If the kernel is symmetrical  $q(\mathbf{p}, \mathbf{p}') = q(\mathbf{p}', \mathbf{p})$ , it follows that  $\alpha(\mathbf{p}, \mathbf{p}') = \min[1, \pi(\mathbf{p}')/\pi(\mathbf{p})]$ .

The success rate, or the selection of the kernel in relation to the posterior distribution, greatly influences the success of the method, which is fast convergence to the posterior distribution. The key aspect is not to have the success rate appear too low or too high. Naively, one would be tempted to make small steps or penalise great deviations in the parameter vector during the generation step to make sure that the success rate is high (a very small step will result in the acceptance probability being close to unity). This leads, however, to the chain remaining in a small region and moving very slowly to other regions. On the other hand, changes too large in parameters are likely to result in a very low acceptance rate with many repetitions in the chain. Some authors suggest an acceptance rate between 20% and 50% (Bennett *et al.*, 1996).

The previous discussion assumed that during the generation step, all components of the parameter vector change simultaneously. This is not required, and the generation step can be simplified to generate from univariate rather than from multivariate distributions. This is carried out by generating and accepting or rejecting changes on a component-by-component basis. For example, the first component  $p'_1$  is generated using a special kernel  $q_1(\cdot, \cdot)$ , and its acceptance is evaluated using (5.30). A new proposal for the second component  $p'_2$

is generated using another kernel  $q_2(\cdot, \cdot)$  from the original parameter vector or a parameter vector with a modified first component depending on its acceptance. This systematically continues until all components have been exhausted and the newly formed vector represents a new element on the chain.

The components also can be blocked. This situation is suitable when parameters demonstrate high correlation, because generating on a component-by-component basis has a high rejection rate for highly correlated components.

An illustrative and more detailed description of the Metropolis-Hastings algorithm can be found elsewhere (Chib and Greenberg, 1995).

### 5.3.3.2 Gibbs Sampling

The Gibbs sampler (Hastings, 1970) is a special case from the Metropolis-Hastings family of algorithms and borrowed its name from its application to image reconstruction (Geman and Geman, 1984).

It has a wider application spectrum than other derivatives of the Metropolis-Hastings algorithm and has been used in the modelling domain, for example, in pharmacokinetics (Wakefield *et al.*, 1994).

The Gibbs sampler corresponds to the component-by-component updating structure of the Metropolis-Hastings algorithm. We denote  $\pi(p_i|\mathbf{p}_{-i})$  the conditional density of the  $i$ -th parameter component given all other components  $\mathbf{p}_{-i} = (p_j; j \neq i)$ . During the generation step, the algorithm successively draws random samples from the full conditional distributions  $\pi(p_i|\mathbf{p}_{-i})$ , namely:

$$\begin{aligned}
 p_1^{j+1} & \text{ from } \pi(p_1|\mathbf{p}_{-1}^j) \\
 p_2^{j+1} & \text{ from } \pi(p_2|p_1^{j+1}, p_3^j \dots p_M^j) \\
 p_3^{j+1} & \text{ from } \pi(p_3|p_1^{j+1}, p_2^{j+1} \dots p_M^j) \\
 & \vdots \\
 p_M^{j+1} & \text{ from } \pi(p_M|p_1^{j+1}, p_2^{j+1} \dots p_{M-1}^{j+1})
 \end{aligned}$$

All samples are accepted, meaning the acceptance probability as defined by (5.30) does not play a role in the Gibbs algorithm. The component kernels are  $q_i(\mathbf{p}, p_i') = \pi(p_i'|\mathbf{p}_{-i})$ , and for these types of kernels, the acceptance probability is guaranteed to be unity.

The essential feature of the Gibbs sampler is that one has to sample from the full conditional distribution  $\pi(p_i|\mathbf{p}_{-i})$ . This means that the full conditional should be known analytically or that some sort of numerical approach such as the acceptance-rejection sampling is adopted (Chib and Greenberg, 1995). In general, the full conditional densities change during each generation step and therefore must be reevaluated. For any modestly complicated compartment model, the full conditionals cannot be derived analytically; a numerical solution or a more general approach from the family of Metropolis-Hastings

algorithms should be adopted. Note that the Markov chain generated by the Gibbs sampler does not include repeated elements, but the price is paid by having to obtain the (potentially expensive) full conditionals  $\pi(p_i | \mathbf{p}_{-i})$ .

### 5.3.3.3 Updating Procedures for Bayesian Networks

The task of the Bayesian estimator in the context of parameter estimation is to update the probabilities in the network on the arrival of new evidence and, in particular, to calculate the posteriors (marginals) of the parameters (see Figure 5.6). The topological structure of the network has a pronounced effect on the complexity and approach to the calculations. Heavily connected networks are usually more computationally expensive to update.

Tree or multitree structures are the simplest forms of Bayesian networks. The (multi-)tree is defined in the normal way, which means there exists only one path between any nodes. Unlike trees, multitrees have more than one root node.

It turns out that updating of tree and multitree structures can be implemented by passing messages between nodes (Pearl, 1988). This is quite convenient and lent itself to an efficient object-oriented approach. A node has two functions: to collect and to distribute information. Updating is implementing by two synchronised passes through all nodes. Starting from root node(s), the

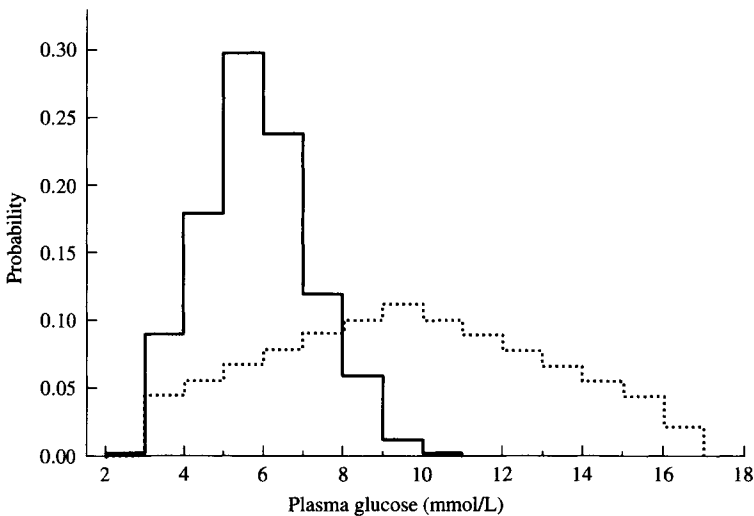


**Figure 5.6.** Bayesian networks normally deal with discrete random variables and therefore discrete prior and posterior distributions. Two sample distributions of plasma glucose are shown before (prior distribution, dotted line) and after (posterior distribution, solid line) arrival of measurement data. The resolution step of plasma glucose is 1 mmol/L.

information is distributed along all branches. Once the information has been distributed throughout the network, all leaf nodes begin sending messages back. The information is collected by “parent” nodes, which continue sending the information to their parent nodes, and the process terminates once root nodes are reached.

A much more complicated situation arises in structures with loops. A loop is present in a network when a nonunique path exists between two nodes. The network shown in Figure 5.5 has two loops.

The updating of networks with loops is a computationally hard task (Cooper, 1990). The problem is that using the same approach as for trees, a single piece of information could be “counted” more than once. The information can originate in one node but can get to another node via two or more different routes. If this is not recognised, the information can be given higher credibility than it actually carries.

The calculations in networks with loops can exploit a number of techniques including conditioning and clustering (Pearl, 1988) to avoid or limit the exponential growth in computational and space complexity for highly connected networks. However, the difficulties associated with an efficient updating of Bayesian networks still limit their use.

We will outline principles of one method (Lauritzen and Spiegelhalter, 1988). The basic idea is to alter the topological structure by aggregating and replicating nodes to create a super-tree structure.

A node in this super-tree represents a set of nodes (a clique) from the original network and holds a joint distribution of the clique. The main trick of the algorithm is the creation of the super-tree. This is done through several steps, which include identification of the loops, adding extra links between nodes (triangulation), identification of cliques, and creation of the super-tree.

The triangulation step can be carried out in a number of ways that greatly affect the complexity of the calculations. Clique sizes (the number of nodes in cliques) are determined by the triangulation step; as the joint probabilities of the cliques are maintained, large cliques will result in large joint probability tables. For example, a clique consisting of seven nodes, each node having 10 states, will require a joint probability table with  $10^7$  entries. The growth of these tables is exponential in both number of nodes and number of states!

Updating of super-trees is similar to updating trees as previously described. Again, information is passed between cliques in two coordinated passes: the distribute step and the collect step.

#### 5.3.4. IMPLEMENTATION PACKAGES AND HISTORICAL REMARKS

Unlike the traditional LS estimator, the Bayesian parameter estimator is implemented in a limited number of packages. The USC\*PACK programs

(which can be found at [www.usc.edu/hsc/lab\\_apk/software.html](http://www.usc.edu/hsc/lab_apk/software.html)) include modules for Bayesian forecasting and parameter estimation. The SAAM II package (Barrett *et al.*, 1998) implements a simple approach to include prior information about parameters within the context of the LS parameter estimation method.

Certain modelling packages designed for the pharmacokinetic/pharmacodynamic population studies implement fully some form of the MCMC approach such as the POPKAN program (Bennett and Wakefield, 1996). The BUGS program (Gilks *et al.*, 1994) is an example of an efficient and comprehensive public domain package.

The HUGIN commercial package (Andersen *et al.*, 1989) can be used to design and update Bayesian networks with loops and includes a graphical user interface. Several extensions of the program have been developed, such as the program dealing with dynamic Bayesian networks, dHugin (Kjaerulff, 1992).

Rev. T. Bayes' work on the inverse probability dates to 1763. Thanks to A. M. Legendre, the Bayes' theorem was rescued from oblivion about half a century later. The Gibbs sampler was proposed by W. K. Hastings in 1970, further elaborating work by N. Metropolis *et al.* in 1953. The graphical representation of knowledge by Bayesian networks is even more recent and benefits from contributions by J. Pearl, S. Lauritzen, and D. Spiegelhalter, to name but a few.

## 5.4. POPULATION KINETIC ANALYSIS

So far, we have been concerned with parameter estimation techniques in a single individual study. In modelling analysis at the individual level, the focus of interest is the mathematical form describing the relationship between a given experimental protocol and the resulting measurements. Such relationship usually differs markedly between individual subjects. This is the basic rationale for focusing on a *population* of individuals, where each individual can have a unique set of model parameter values (here "individual" encompasses any experimental subject). Such parameter differences are due to interindividual (intersubject) variability. An example is the clearance of a given drug or compound, or its rate of elimination, which can show considerable differences among different subjects, possibly due to variables such as diet, age, weight, or a combination of these factors. Given a specific population of individuals, an experiment repeated on each individual with similar modalities and an appropriate system model, population kinetic analysis can be defined as the study of the intersubject variability of the parameters of a kinetic model. In the statistics literature, population kinetic analysis is sometimes called "analysis

of repeated measurement data” or “analysis of longitudinal data” (Davidian and Giltinan, 1995).

To perform population analysis, each individual’s cause-effect relationship must be defined in terms of a model, which in turn depends on certain known quantities, such as the dosage regimen, sampling schedule design, and independently measured variates (e.g., body weight, height, age), which are often called *covariates*, and on certain unknown quantities, such as model parameters. These unknown parameters are assumed to be random variables with a common but unknown distribution (the population distribution). The problem tackled by population kinetic analysis is the estimation of this population distribution based on a *collection* of individual data (the population data).

Depending on the nature of prior knowledge available on the population distribution, two approaches can be used to facilitate its estimation. In the *parametric* approach, the population distribution is assumed to be known except for a certain number of unknown parameters. For example, the distribution can be assumed to be multivariate normal with unknown mean and covariance; the population analysis problem is the estimation of both the mean and the covariance. On the other hand, in the *nonparametric* approach, no functional form is assumed for the underlying population distribution, and the entire distribution is then estimated from the population data. The nonparametric method allows for non-normal and multimodal distributions such as would occur, for example, in a population of lean and obese, or young and ageing individuals. An approach that is “in-between” has also been proposed, the so-called *semiparametric* approach (Davidian and Gallant, 1993). This approach does not entail specific assumptions about the form of the underlying population distribution, but the class of allowable estimates is required to have certain smoothness properties. For this reason, this method is also termed the *smoothed nonparametric* approach.

All the methods that we will see for population modelling will fall in one of these classes. Lastly, there are two basic classes of methods for obtaining estimates and their variability, maximum likelihood and Bayesian methods. Maximum likelihood methods are based on the maximisation of the likelihood function (or approximations thereof) for the population problem, while Bayesian methods use Bayesian inference approaches to estimate the full conditional population distribution.

#### 5.4.1. DEFINITION OF THE POPULATION ANALYSIS PROBLEM

To improve readability, we will index vectors on integers. For example,  $\mathbf{y}_i$  denotes the vector of the observations for individual  $i$ . To denote a scalar element of a vector, we will use the following notation:  $y_{i(j)}$  denotes the



scalar element  $j$  of the measurement vector of subject  $i$ . In addition, for ease of notation, we will denote with  $\hat{\mathbf{p}}$  an estimate of the parameter vector  $\mathbf{p}$ .

Consider now a sequence of experiments, performed on a set of  $M$  different individuals. Each experiment can have its own experimental protocol and can comprise more than one measurement site (e.g., serum and urine concentrations). Mathematically, each experiment is then represented by a collection of finite dimensional vectors:

$$\mathbf{t}_i, \mathbf{y}_i, \quad i = 1, \dots, M \quad (5.31)$$

The vectors  $\mathbf{t}_i$  (size  $N_1, \dots, N_M$ ) are the vectors of sampling times and are assumed known. The random vectors  $\mathbf{y}_i$  (size  $N_1, \dots, N_M$ ) are the observable quantities. The components of  $\mathbf{y}_i$  contain all the measurements for individual  $i$  (e.g., plasma concentrations, urine amounts, etc.). Without loss of generality, we will assume from now on that there is only one site of measurement.

Let us now consider the general nonlinear regression model of the observations. The model has the form:

$$\mathbf{y}_i = \mathbf{f}_i(\mathbf{p}_i) + \mathbf{R}_i(\mathbf{p}_i)^{1/2} \mathbf{e}_i, \quad i = 1, \dots, M \quad (5.32)$$

where  $\mathbf{f}_i(\mathbf{p}_i)$  is a known, continuous vector-valued function and  $\mathbf{R}_i(\mathbf{p}_i)$  is a known, continuous matrix-valued function that is assumed to be positive definite (we have dropped the time dependence for ease of notation). The function  $\mathbf{f}_i(\mathbf{p}_i)$  is a *model for the mean of the data* since:

$$E[\mathbf{y}_i | \mathbf{p}_i] = \mathbf{f}_i(\mathbf{p}_i), \quad i = 1, \dots, M \quad (5.33)$$

The functions  $\mathbf{f}_i(\mathbf{p}_i)$  and  $\mathbf{R}_i(\mathbf{p}_i)$  depend (through indexing on  $i$ ) on all the conditions of experiment  $i$  (e.g., dose amounts, dose and sampling times, forcing functions, and other individual-specific covariates). The vectors  $\mathbf{e}_i$  are independent multivariate normal random (noise) vectors, each with zero mean and covariance given by  $\mathbf{R}_i(\mathbf{p}_i)$ . The  $\mathbf{e}_i$  and  $\mathbf{p}_i$  are mutually independent. The vectors  $\mathbf{p}_i$  are the parameters of the model for individual  $i$ , often called the *regression parameters for subject  $i$* . An example is clearance of a drug.

We have made the assumption of independent, identically distributed measurement errors since this is the most commonly assumption made and is verified in a number of experimental situations. There is no loss of generality since for our purposes the matrix  $\mathbf{R}_i(\mathbf{p}_i)$  might not be diagonal. Also, let us note that the covariance of the error  $\mathbf{R}_i(\mathbf{p}_i)$  (and therefore the weighting function for parameter estimation) is a function of the model parameters, and conversely of the model function  $\mathbf{f}_i(\mathbf{p}_i)$ . Often, the sample values  $\mathbf{y}_i$  are used to compute  $\mathbf{R}_i(\mathbf{p}_i)$ , instead of  $\mathbf{f}_i(\mathbf{p}_i)$ . However, this practice is avoided in the literature (although the approximation is often good for observations affected by low noise) since it is well known that this could influence the results by

introducing variation due to the sampling process into the estimate of the measurement error variance. The function  $R_i(\mathbf{p}_i)$  is therefore a *model for the variance of the data measurement error*:

$$\text{Cov}[\mathbf{e}_i | \mathbf{p}_i] = R_i(\mathbf{p}_i) \quad (5.34)$$

At this point, the additional hypothesis is made that  $\mathbf{p}_i$  are independent and identically distributed, with common, but unknown, probability distribution. Thus, the population analysis problem can be defined as determining the unknown distribution of the parameters  $\mathbf{p}$  in the population.

## 5.4.2. TWO-STAGE METHODS

The class of two-stage methods can be applied when the size of the data vector  $\mathbf{y}_i$  is such that the individual parameter estimation problem has a solution. The parameter vector must be estimated in each individual by, for example, weighted LS or ML methods, and this brings to a collection of estimates for each individual, namely  $\hat{\mathbf{p}}_1, \dots, \hat{\mathbf{p}}_M$ . Each estimate is also characterised by its estimated covariance, which we will call  $S_i$ . Note that  $S_i$  gives an estimate of intrasubject variability; that is, the parameter accuracy associated to the fact that the parameters for a given subject cannot be exactly determined.

### 5.4.2.1 Standard Two-Stage Analysis

The most common way of determining the distribution of the parameters  $\mathbf{p}$  within a population of subjects is to perform what is usually called a standard two-stage (STS) analysis. From the individual estimates described previously, it is possible to calculate the empirical sample mean as:

$$\mathbf{a} = \frac{1}{M} \sum_{i=1}^M \hat{\mathbf{p}}_i \quad (5.35)$$

and the empirical sample covariance as:

$$\mathbf{D} = \frac{1}{M-1} \sum_{i=1}^M (\hat{\mathbf{p}}_i - \mathbf{a})(\hat{\mathbf{p}}_i - \mathbf{a})^T \quad (5.36)$$

The matrix  $\mathbf{D}$  gives an estimate of interindividual variability, that is, how and how much the parameters vary among the different subjects within the population.

We will see further that the STS estimator can be envisioned as a nonparametric estimator with mass equal to  $1/M$  at each point estimate. This estimator is easy to calculate and can be very useful. However, its shortcomings are rather substantial. First, no information is gained in the analysis from the knowledge that the subjects belong to the same population. Second, the intraindividual variability given by the subject-specific covariance matrix  $\mathbf{S}_i$  is not taken into account, and this can bring to an overestimation of  $\mathbf{D}$ , as shown in Davidian and Giltinan (1995). Third, no measure of the precision of the estimates of  $\mathbf{a}$  and  $\mathbf{D}$  is available. Since the STS does not make any assumption on the distribution of the parameters among the population, it is usually treated as belonging to the class of nonparametric methods.

#### 5.4.2.2 Iterative Two-Stage Method

The iterative two-stage (ITS) method is a parametric iterative method, belonging to the family of expectation-maximisation (EM) algorithms (Schumitzky, 1995), based in particular on the maximum *a posteriori* probability (MAP) empirical Bayes estimator. It was proposed as a possible computationally attractive alternative to the nonlinear mixed-effects modelling approach (Steimer *et al.*, 1984). The steps of the ITS method are as follows ( $k$ ,  $k \geq 0$ , is the iteration index):

- Initialisation Step: assign  $\mathbf{a}^{(0)} = \mathbf{a}^{STS}$ ,  $\mathbf{D}^{(0)} = \mathbf{D}^{STS}$
- Expectation Step: obtain an estimate of the parameter vector in subject  $i$

$$\hat{\mathbf{p}}_i^{(k)} = \arg \min \{ [\mathbf{y}_i - \mathbf{f}_i(\mathbf{p}_i)] \mathbf{R}_i(\mathbf{p}_i) [\mathbf{y}_i - \mathbf{f}_i(\mathbf{p}_i)]^T + [\mathbf{p}_i - \mathbf{a}^{(k)}] \mathbf{D}^{(k)} [\mathbf{p}_i - \mathbf{a}^{(k)}]^T \} \quad (5.37)$$

where, with respect to standard LS, also the distance of the current parameter estimate from the population mean (the prior) is penalised. The estimates (individual estimates) obtained by minimising this objective function are called *empirical Bayes* estimates. It is worth noting that the values  $\hat{\mathbf{p}}_i^{(k)}$  calculated in the EM version of the global two-stage (GTS) method can also be interpreted as empirical Bayes estimates. It is again possible to calculate the precision of the estimate, or the matrix  $\mathbf{S}_i$ .

- Maximisation Step: calculate the new population mean:

$$\mathbf{a}^{(k+1)} = \frac{1}{M} \sum_{i=1}^M \mathbf{p}_i^{(k)} \quad (5.38)$$

and the new covariance:

$$\mathbf{D}^{(k+1)} = \frac{1}{M} \sum_{i=1}^M \{ \mathbf{S}_i^{(k)} + [\mathbf{p}_i^{(k)} - \mathbf{a}^{(k+1)}][\mathbf{p}_i - \mathbf{a}^{(k+1)}]^T \} \quad (5.39)$$

Check for convergence of the population mean  $\mathbf{a}^{(k+1)}$  and variance  $\mathbf{D}^{(k+1)}$  estimates, and of the individual parameter estimates  $\mathbf{p}_i^{(k)}$ , and repeat the EM steps as needed.

The iterative nature of the algorithm is apparent; it is also apparent that the objective function in (5.37) takes into account the information on the population mean explicitly and that the computation of the population covariance matrix in (5.39) includes the information on the precision of each estimate. This is at variance with the STS, which can be thought of as the initialisation step of the ITS. The ITS method has been extensively used in the pharmacokinetic literature to estimate population parameter mean and variances from reduced data sets (Drusano *et al.*, 1988). Another widely used two-stage method is the so-called GTS method (Steimer *et al.*, 1984). The GTS method can be “indirectly” recast as an iterative EM algorithm similar to the ITS (Davidian and Giltinan, 1995; Schumitzky, 1991; Schumitzky, 1995) or, alternatively, can be “directly” applied through ML methods.

### 5.4.3. MIXED-EFFECTS MODELS

The family of two-stage methods that we have considered are applicable only if each individual has enough data to enable both estimation of  $\hat{\mathbf{p}}_i$  and calculation of  $\mathbf{S}_i$ . However, this is often not the case, especially in clinical situations. It is not unusual to have only a handful of data points per subject. At the extreme, in the case of destructive sampling, such as in toxicokinetic studies in rats, only one data point per subject is available (corresponding to the time when the animal was sacrificed). The estimate  $\hat{\mathbf{p}}_i$  is therefore not available.

The simplest estimator that comes to mind entails pooling together all the available data as if they were coming from one animal (the *super-rat*) and performing an ordinary LS estimation to recover one set of parameter estimates  $\hat{\mathbf{p}}$ :

$$\hat{\mathbf{p}} = \arg \min \sum_{i=1}^M [\mathbf{y}_i - \mathbf{f}_i(\mathbf{p}_i)] \mathbf{R}_i(\mathbf{p}_i) [\mathbf{y}_i - \mathbf{f}_i(\mathbf{p}_i)]^T \quad (5.40)$$

This estimate (often called the *naive pooled* estimate) is unsatisfactory since it does not rest on any statistical grounds, does not take into account intra-individual noise, and does not permit quantification of parameter accuracy.

To escape from this apparent standstill, one might consider that the regression model parameters  $\mathbf{p}$  are not completely individual-specific but are characterised by some attributes that do not change across the population of subjects (i.e., are common to all individuals), and some others that do (i.e., are typical of a particular individual or, better, are different from individual to individual). In

other words, the variability intrinsic to the parameter vector can be dissected as a combination of parameters that change across the population (random population parameters, or *random effects*) and parameters that do not (fixed population parameters, or *fixed effects*). Simple but intuitive examples of fixed effects are the mean and the covariance of the population distribution of the random effects. Another example might be the parameter(s) describing the absorption phase of a drug or compound given orally, when this is thought not to change appreciably from subject to subject. The model for the observations thus stems from a combination of fixed and random parameters, or effects, hence, the jargon *mixed-effects modelling*. Mixed-effects modelling requires to postulate at least some characteristics of the population probability distribution for the random effects (e.g., Gaussian or log-normal). The methods we will now describe belong to the class of parametric methods, where the structure of the population distribution is assumed known and the population analysis problem becomes determining its parameters.

If we consider that the individual parameter vector can also be time-varying, and therefore we write the value of the vector  $\mathbf{p}_i$  at time  $j$  as  $\mathbf{p}_{ij}$ , in all generality we can write the following vector-valued function:

$$\mathbf{p}_{ij} = \mathbf{d}_{ij}(\mathbf{a}, \mathbf{b}_i) \quad (5.41)$$

that is,  $\mathbf{p}_i$  can be a linear or nonlinear function of the fixed effects ( $\mathbf{a}$ ) and the random effects ( $\mathbf{b}_i$ ). Other functional dependencies, such as time-varying covariates, are hidden in the function  $\mathbf{d}$ . While the fixed effects do not change across the population, random effects do. Their distribution must be specified as part of the modelling assumption. They are often assumed Gaussian, with zero mean and covariance defined by a positive definite matrix, a function of the fixed effects:

$$\text{Cov}[\mathbf{b}_i] = \mathbf{D}(\mathbf{a}) \quad (5.42)$$

The vector  $\mathbf{a}$ , on the other hand, groups the parameters common to the whole population of subjects. Note that  $\mathbf{a}$  is not a random vector. Possible parameterisations include the linear form:

$$\mathbf{p}_i = \mathbf{a}(1 + \mathbf{b}_i) \quad (5.43)$$

This entails that, under the normality assumption for  $\mathbf{b}_i$ , the vectors  $\mathbf{p}_i$  are also normal and the vectors  $\mathbf{b}_i$  have the interpretation of *coefficient of variation*, or percent variability. Another often-used parameterisation is the exponential form:

$$\mathbf{p}_i = \mathbf{a}e^{\mathbf{b}_i} \quad (5.44)$$

Under the assumption of normality of the random effects, the vectors  $\mathbf{p}_i$  defined in (5.44) belong to a log-normal distribution. The advantage of such

an assumption is that the vectors  $\mathbf{p}_i$  are always constrained to be positive. Not so for (5.43); if interindividual variability is large, it might happen that some  $\mathbf{p}_i$  become negative.

The choice of one or the other parameterisation should be dictated by independent physiological knowledge of the actual system and the experience of the investigator.

#### 5.4.4. MAXIMUM LIKELIHOOD METHODS

We will now define in a general way the ML estimate of the population distribution. Given the data  $\mathbf{y}_i$ ,  $i = 1, \dots, M$ , and a population distribution  $F$ , the density of  $\mathbf{y}_i$  given  $F$  is:

$$p_i(\mathbf{y}_i|F) = \int p_i(\mathbf{y}_i|\mathbf{p})dF(\mathbf{p}) \quad (5.45)$$

By the independence assumptions on  $\mathbf{e}_i$  and  $\mathbf{p}_i$ , the vectors  $\mathbf{y}_i$  are independent, and the log-likelihood of the data is:

$$L(F) = \sum_{i=1}^M \ln p_i(\mathbf{y}_i|F) \quad (5.46)$$

Now let  $\mathbf{F}$  be a set of probability distributions. A probability distribution  $F^{ML} \in \mathbf{F}$  is an ML estimate of the true distribution  $\bar{F}$ , if:

$$F^{ML} = \arg \max\{L(F) : F \in \mathbf{F}\} \quad (5.47)$$

In the parametric case,  $F$  is assumed to belong to a family of distributions defined by a finite number of parameters. In the most important example, this family  $\mathbf{F}$  is the class of all multivariate normal distributions with unknown mean vectors and unknown covariance matrices (which then become the unknowns of the problem). In the nonparametric case,  $F$  is assumed to belong to the family of all distributions defined on  $\mathbf{F}$ . There are two computational problems in determining the ML estimate  $F^{ML}$ : the integration in (5.45) and the optimisation in (5.47). Of these two problems, the integration is the more serious one since the dimensionality of typical kinetic problems grows very rapidly. For a four-parameter model, assuming a multivariate normal population distribution, there are four means and 10 covariances, which equals 14 parameters to be determined. The direct integration in (5.45) poses an overwhelming numerical problem. There have been only a few algorithms proposing to attack this problem directly. More commonly, to lessen the computational burden, most of the proposed methods focus on different analytical approximations to (5.45).

### 5.4.4.1 The First-Order Method

The first approach to population kinetic analysis method was the first-order (FO) linearisation of the model function. This approach was the original basis for the population analysis software NONMEM (acronym for NONlinear Mixed-Effects Model), which since then has accommodated several other different methods. The FO method (Beal and Sheiner, 1982) approximates the model function for individual  $i$  around zero random effects and thus results in the following approximate equation for subject  $i$ :

$$\mathbf{y}_i \approx \mathbf{f}_i(\mathbf{a}) + \frac{\partial \mathbf{f}_i}{\partial \mathbf{p}_i} \Big|_{\mathbf{b}_i=\mathbf{a}} \frac{\partial \mathbf{d}_i}{\partial \mathbf{b}_i} \Big|_{\mathbf{b}_i=0} (\mathbf{b}_i - \mathbf{a}) + \mathbf{R}_i(\mathbf{a})^{(1/2)} \mathbf{e}_i \quad (5.48)$$

It follows that  $p_i[\mathbf{y}_i|\mathbf{a}, \mathbf{D}(\mathbf{a})] \approx \mathcal{N}(\mathbf{r}_i, \mathbf{U}_i)$ , where:

$$\mathbf{r}_i = \mathbf{y}_i - \mathbf{f}_i(\mathbf{a}) \quad (5.49)$$

and:

$$\mathbf{U}_i = \left[ \frac{\partial \mathbf{f}_i}{\partial \mathbf{p}_i} \Big|_{\mathbf{p}_i=\mathbf{a}} \frac{\partial \mathbf{d}_i}{\partial \mathbf{b}_i} \Big|_{\mathbf{b}_i=0} \right]^T D \left[ \frac{\partial \mathbf{f}_i}{\partial \mathbf{p}_i} \Big|_{\mathbf{p}_i=\mathbf{a}} \frac{\partial \mathbf{d}_i}{\partial \mathbf{b}_i} \Big|_{\mathbf{b}_i=0} \right] + \mathbf{R}_i(\mathbf{a}) \quad (5.50)$$

In this case, maximising the corresponding approximate likelihood function is equivalent to minimising the function:

$$J_1(\mathbf{a}) = \sum_{i=1}^M [\ln \det \mathbf{U}_i + \mathbf{r}_i \mathbf{U}_i^{-1} \mathbf{r}_i^T] \quad (5.51)$$

The FO estimate of the fixed effects then minimises (5.51).

### 5.4.4.2 The First-Order Conditional Estimation Method

Especially for models that are nonlinear in the parameters, the approximation about the expectation of the random effects  $\mathbf{b}_i = 0$  to the likelihood given by the FO method might be rather poor, thus resulting in inconsistent estimates of the fixed effects (Spieler and Schumitzky, 1993). To overcome these problems, a more accurate algorithm, the first-order conditional estimation (FOCE), was developed by Beal and Sheiner (1992) and later discussed by Vonesh (1996). The Lindstrom-Bates algorithm (Lindstrom and Bates, 1990) is also related to the basic idea of FOCE. The FOCE method is based on considering linearization in the random effects about some value other than zero. In particular, the mode of the posterior distribution for  $\mathbf{b}_i$  (the MAP estimate) obtainable from individual  $i$ , given the fixed effects  $\mathbf{a}$  (the “conditional estimation” part arises because the estimates for  $\mathbf{b}_i$  are conditional on

the fixed effects). The approximation for the model function is then:

$$y_i \approx \mathbf{f}_i(\hat{\mathbf{p}}_i) + \left. \frac{\partial \mathbf{f}_i}{\partial \mathbf{p}_i} \frac{\partial \mathbf{d}_i}{\partial \mathbf{b}_i} \right|_{\mathbf{b}_i = \hat{\mathbf{b}}_i} (\mathbf{b}_i - \hat{\mathbf{b}}_i) + \mathbf{R}_i(\hat{\mathbf{p}}_i)^{(1/2)} \mathbf{e}_i \quad (5.52)$$

and the objective function can be formulated via the Laplace approximation to the integral (Bennett and Wakefield, 1996; Beal and Sheiner, 1992).

### 5.4.4.3 Other Parametric Methods

The FOCE method is in a similar spirit to the method of Lindstrom and Bates (1990) when the data are modelled with heterogeneous intraindividual error. The principal difference is that the FOCE method minimises an objective function, while the Lindstrom-Bates method is iterative. Another method belonging to the same family is the Laplace method (Beal and Sheiner, 1992), based on the Laplace approximation to the integral:

$$\int_{-\infty}^{+\infty} e^{-f(x)} dx \approx \det \left[ \frac{1}{2\pi} \frac{d^2 f(x)}{dx^2} \right]^{-1/2} e^{-f(x)} \Big|_{x=\hat{x}} \quad (5.53)$$

where  $\hat{x}$  is a minimise of  $f(x)$ . If this approximation is applied to the ML integral, where  $f(x)$  is the negative of the logarithm of the likelihood function, it results in a more accurate approximation when compared with FOCE, at the expense of an increased computational burden (second derivatives of the likelihood, or a good approximation, are now required). FO, FOCE, and the Laplace-based methods can be thought of as providing increasingly accurate approximations to the likelihood function.

### 5.4.5. NONPARAMETRIC AND SEMINONPARAMETRIC METHODS

Nonparametric methods are used when no assumptions can be safely made on the distribution of the random effects from which the individual parameters are drawn. The individual parameters are then drawn from a completely unknown distribution:

$$\mathbf{p}_i \in F \quad (5.54)$$

A fundamental result by Mallet (1986) states that the ML estimate of the unknown distribution is a discrete distribution, with support points on at most  $M$  points (as many as the individuals):

$$F = \sum_{i=1}^M w_i \delta(\mathbf{p}_i) \quad (5.55)$$



where  $\delta$  is the Dirac impulse. The problem of nonparametric estimation then reduces to the estimation of the parameters and the weights  $w_i$ ,  $i = 1, \dots, M$ . Despite this result, direct methods for the estimation of the distribution are quite challenging since the dimensionality of the problem grows very quickly with the number of individuals (Davidian and Giltinan, 1995). However, through duality theory, a connection can be made between nonparametric methods and D-optimality. Algorithms already developed for D-optimal designs can therefore be applied to nonparametric population analysis. Such methods have been proposed (Fedorov, 1972; Mallet, 1986; Schumitzky, 1991; Schumitzky, 1993), and a comprehensive review has been published (Davidian and Giltinan, 1995). A drawback of nonparametric methods is that they do not readily provide the accuracy of the estimated distribution. Features of the distribution, such as multimodality, cannot then be readily attributed to real features of the system or inaccuracies of the method.

The smooth nonparametric (SNP) approach (Davidian and Gallant, 1992) is based on the notion that the population distribution, although unknown, belongs to a class of distributions that is smooth:

$$\mathbf{p}_i \in F, F \in \mathcal{F} \quad (5.56)$$

The most important restriction on the class  $\mathcal{F}$  is differentiability up to a certain order ( $k/2$ , where  $k$  is the dimensionality of the problem). This implies that distributions in  $\mathcal{F}$  are “regular,” but still can exhibit multimodality and/or various degrees of skewness. This class of densities appeared first in econometrics. An important result is that these densities are well approximated by an appropriately truncated series expansion of multivariate normal densities. The number of elements in the series, which acts as a controller of the degree of smoothness of the distribution (Davidian and Giltinan, 1995), is accomplished via parsimony criteria (Davidian and Gallant, 1993). The problem then reduces to the estimation of the coefficients of the series expansion. This method has elements from both the parametric and the nonparametric approaches (for this reason, it has been termed the “seminonparametric” approach).

#### 5.4.6. BAYESIAN METHODS FOR POPULATION KINETIC ANALYSIS

Bayesian methods have enjoyed much interest recently, especially thanks to the progress made in computational speed. Comprehensive reviews have been published (Smith and Roberts, 1993; Davidian and Giltinan, 1995). The concept of Bayesian population analysis exploits the insight that nonlinear mixed-effects models are equivalent to the “nonlinear hierarchical models” of statistics. The hierarchy here has three levels, which we describe in the following list.

- A probabilistic model for the response of the individual subject, described as in (5.32), where the structure of intraindividual variability (e.g., due to measurement error) is given. Most often the model is that of Gaussian measurement error, with zero mean and unknown variance.
- A probabilistic model for the variability among different individuals in the population, described as in (5.41) and (5.42), where the structure of interindividual variability (e.g., due to heterogeneity of covariates) is given. The usual model is that of a normal or log-normal distribution for the individual parameters.
- A probabilistic model for the expected probability distribution of the fixed population parameters, such as the mean and the covariance of the parameter population. The presence of this third level differentiates the Bayesian approaches from all the other approaches that we have seen, in that the fixed population parameters are treated as random variables, and an informative or noninformative prior (depending on available knowledge) can be specified. Usually, the population means have a Gaussian prior distribution, the population covariances (or rather their inverses) belong to Wishart distributions, and the measurement error variances are thought of as belonging to a gamma distribution.

The most striking feature of Bayesian-based methods is that everything in the problem is treated as a random variable. Given all this information as input, the output of such methods is the full conditional distribution of the parameters. Even without entering in the details of such methods, one can easily realise that evaluating the conditional distribution integrals is a daunting task, and this explains why these methods have become popular with the advent of large-scale computing.

Different techniques can be used to generate the posterior distribution. The MCMC (Smith and Roberts, 1993) was first used in the context of the population pharmacokinetic analysis (Wakefield *et al.*, 1994), where Gibbs sampling was used. A Metropolis-Hastings step (Metropolis *et al.*, 1953; Hastings, 1970) has also been used. A nice, detailed introduction to the Bayesian approach is available from StatLib (Department of Statistics at Carnegie-Mellon University) on the World Wide Web (Wakefield *et al.*, 1999).

#### 5.4.7. COMPUTER PACKAGES

Several computer programs have been written to accomplish the task of population mixed-effects modelling. The emphasis has been mostly on population pharmacokinetics. The available software ranges from *in-house* programs to commercially distributed software.

Parametric methods are implemented in EMSA (Lyne *et al.*, 1992), IT2S (Forrest *et al.*, 1993), MIXLIN (Vonesh and Carter, 1992), NLME (Pinheiro *et al.*, 1993), P-PHARM (Gomeni *et al.*, 1994), WINNONMIX (Pharsight Corp. and Scientific Consulting Inc.), and finally the most frequently used, NONMEM (Beal and Sheiner, 1992), which implements a variety of parametric algorithms for population analysis.

Nonparametric programs are considerably less widespread. Available programs are NLMIX (Davidian and Gallant, 1993), which implements the smooth nonparametric method, NPEM (Schumitzky *et al.*, 1994), which accommodates both nonparametric and continuous EM algorithms, and NPML (Mallet, 1986), which includes a nonparametric and optimal design algorithm.

A new generation of programs uses full Bayesian inference; to this category belong BUGS and the newer WINBUGS (Spiegelhalter *et al.*, 1993), which use Bayesian estimation in a Gibbs sampling framework and are available as a public domain package from the web site [www.mrc-bsu.cam.ac.uk/bugs/](http://www.mrc-bsu.cam.ac.uk/bugs/). POPKAN (Bennett and Wakefield, 1996) uses Gibbs sampling for analysing simple compartmental models.

## 5.5. ACKNOWLEDGEMENT

This work has been partially performed under the aegis of NIH grants GM-53930 and RR-12609. P. V. would like to acknowledge fruitful discussions on the subject of population kinetic analysis with Drs. P. Hugh R. Barrett, Bradley M. Bell, David Foster, and Alan Schumitzky.

## 5.6. REFERENCES

- Andersen, S. K., K. G. Olessen, F. V. Jensen and F. Jensen 1989. Hugin — A shell for building Bayesian belief universes for expert systems. In: *Proceedings of IJCAI 1989*, pp. 1080–85.
- Anderson, T. W. 1958. *An Introduction to Multivariate Statistical Analysis*. New York: Wiley.
- Barrett, P. H. R., B. M. Bell, C. Cobelli, H. Golde, A. Schumitzky, P. Vicini and D. M. Foster. SAAM II: simulation, analysis, and modeling software for tracer and pharmacokinetic studies. *Metab Clin Exp* 47(1998):484–92.
- Beal, S. L. and L. B. Sheiner. Estimating population kinetics. *CRC Crit Rev Biomed Eng* 8(1982):195–222.
- Beal, S. L. and L. B. Sheiner. 1992. *NONMEM User's Guide*. NONMEM Project Group, San Francisco: University of California.
- Bell, B. M., J. Burke and A. Schumitzky. An algorithm for estimating parameters and variances in multiple data sets. *Comput Stat Data Anal* 22(1996):119–35.
- Bennett, J. E., A. Racine-Poon and J. C. Wakefield. 1996. MCMC for nonlinear hierarchical models. In: *Markov Chain Monte Carlo in Practice* Edited by W. Gilks, S. Richardson and D. Spiegelhalter. London: Chapman & Hall.

- Bennett, J. E. and J. C. Wakefield. A comparison of a Bayesian population method with two methods as implemented in commercially-available software. *J Pharmacokinetic Biopharm* 24(1996):403–32.
- Carson, E. R., C. Cobelli and L. Finkelstein. 1983. *The Mathematical Modelling of Metabolic and Endocrine Systems*. New York: Wiley.
- Chen, B. C., E. M. Landaw and J. J. DiStefano III. Algorithms for the identifiable parameter combinations and parameter bounds of unidentifiable catenary compartmental models. *Math Biosci* 76(1985):59–68.
- Chib, S. and E. Greenberg. Understanding the Metropolis-Hastings algorithm. *Am Stat* 49(1995):327–35.
- Cobelli, C. and G. Toffolo. 1987. Theoretical aspects and practical strategies for the identification of unidentifiable compartmental systems. In: *Identifiability of Parametric Models*. Edited by E. Walter. New York: Pergamon Press.
- Cooper, G. F. The computational complexity of probabilistic inference using Bayesian belief networks. *Artif Intell Med* 42(1990):393–405.
- D'Argenio, D. Z. and A. Schumitzky. 1997. *Adapt II User's Guide: Pharmacokinetic/Pharmacodynamic Systems Analysis Software*. Los Angeles: Biomedical Simulations Software.
- Davidian, M. and A. Gallant. Smooth nonparametric maximum likelihood estimation for population pharmacokinetics, with application to quinidine. *J Pharmacokinetic Biopharm* 20(1992):529–56.
- Davidian, M. and A. Gallant. The nonlinear mixed effects model with a smooth random effects. *Biometrika* 80(1993):475–88.
- Davidian, M. and D. Giltinan. 1995. *Nonlinear Models for Repeated Measurement Data*. New York: Chapman & Hall.
- DiStefano III, J. J. Complete parameter bounds and quasi-identifiability of some unidentifiable linear systems. *Math Biosci* 65(1983):51–68.
- DiStefano III, J. J., B. C. Chen and E. M. Landaw. Pool size and mass flux bounds and quasi-identifiability conditions for catenary models. *Math Biosci* 88(1988):1–14.
- Drusano, G. L., A. Forrest, M. J. Snyder and M. D. Reed. An evaluation of optimal sampling strategy and adaptive study design. *Clin Pharmacol Ther* 44(1988):232–38.
- Efron, B. 1982. *The Jackknife, the Bootstrap, and Other Resampling Plans*. Philadelphia: SIAM.
- Eisenfeld, J. Partial identifiability of underdetermined compartmental models: a method based on positive linear Lyapunov functions. *Math Biosci* 132(1996):111–40.
- Fedorov, V. V. 1972. *Theory of Optimal Experiments*. New York: Academic Press.
- Forrest, A., C. H. Ballow, D. E. Nix, M. C. Birmingham and J. J. Schentag. Development of a population pharmacokinetic model and optimal sampling strategies for intravenous ciprofloxacin. *Antimicrob Agents Chemother* 37(1993):1065–72.
- Gamerman, D. 1997. *Markov Chain Monte Carlo. Stochastic Simulation for Bayesian Inference*. London: Chapman & Hall.
- Geman, S. and D. Geman. Stochastic relaxation, Gibbs distributions and the Bayesian restoration of images. *IEEE Trans Pattern Anal Mach Intell* 6(1984):721–41.
- Gilks, W. R., S. Richardson and D. J. Spiegelhalter. 1996. *Markov Chain Monte Carlo in Practice*. London: Chapman & Hall.
- Gilks, W. R., A. Thomas and D. J. Spiegelhalter. A language and program for complex Bayesian modeling. *Statistician* 43(1994):169–77.
- Gill, P. E., W. Murray and M. Wright 1987. *Practical Optimization*. San Diego: Academic Press.
- Godfrey, K. R. 1983. *Compartmental Models and Their Application*. New York: Academic Press.
- Gomeni, R., G. Pineau and F. Mentre. Population kinetics and conditional assessment of the optimal dosage regimen using the P-PHARM software package. *Anticancer Res* 14(1994):2321–26.

- Hastings, W. K. Monte Carlo sampling methods using Markov chains and their applications. *Biometrika* 57(1970):97–109.
- Heatherington, A. C., P. Vicini and H. Golde. A pharmacokinetic/pharmacodynamic comparison of SAAM II and PC/WinNonlin modeling software. *J Pharm Sci* 87(1998):1255–63.
- Hejlesen, O. K., S. Andreassen, R. Hovorka and D. A. Cavan. DIAS — The diabetes advisory system: an outline of the system and the evaluation results obtained so far. *Comput Methods Programs Biomed* 54(1997):49–58.
- Kirkpatrick, S., C. D. Gelatt and M. P. Vecchi. Optimization by simulated annealing. *Science* 220(1983):671–80.
- Kjaerulf, U. 1992. A computational scheme for reasoning in dynamic probabilistic networks. In: *Proceedings of the Eighth Conference on Uncertainty in Artificial Intelligence*. San Francisco: Morgan Kaufmann, pp. 121–29.
- Landaw, E. M., B. C. Chen and J. J. DiStefano III. An algorithm for the identifiable parameter combinations of the general mamillary compartmental model. *Math Biosci* 72(1984):199–212.
- Lauritzen, S. L. Propagation of probabilities, means, and variances in mixed graphical association models. *J Am Stat Assoc* 87(1992):1098–108.
- Lauritzen, S. L. and D. J. Spiegelhalter. Local computations with probabilities on graphical structures and their application to expert systems. *J Roy Statist Soc B* 50(1988):157–224.
- Levenberg, K. A method for the solution of certain problems in least squares. *Q Appl Math* 2(1944):164–68.
- Lindell, R., J. J. DiStefano III and E. M. Landaw. Statistical variability of parameter bounds for n-pool unidentifiable mamillary and catenary compartmental models. *Math Biosci* 91(1988):175–99.
- Lindstrom, M. J. and D. M. Bates. Nonlinear mixed effects models for repeated measures data. *Biometrics* 46(1990):673–87.
- Lyne, A., R. Boston, K. Pettigrew and L. Zech. EMSA: a SAAM service for the estimation of population parameters based on model fits to identically replicated experiments. *Comput Methods Programs Biomed* 38(1992):117–51.
- Mallet, A. A maximum likelihood estimation method for random coefficient regression models. *Biometrika* 73(1986):645–56.
- Marquardt, D. W. An algorithm for least squares estimation of nonlinear parameters. *J Soc Ind Appl Math* 2(1963):431–41.
- Metropolis, N., A. W. Rosenbluth, M. N. Rosenbluth, A. H. Teller and E. Teller. Equation of state calculations by fast computing machine. *J Chem Phys* 21(1953):1087–91.
- Nelder, J. A. and R. Mead. A simplex method for function minimization. *Comput J* 7(1965):308–13.
- Pearl, J. 1988. *Probabilistic Reasoning in Intelligent Systems: Networks of Plausible Inference*. San Mateo: Morgan Kaufmann.
- Peck, C. C., S. L. Beal, L. B. Sheiner and A. I. Nichols. Extended least-squares nonlinear-regression — a possible solution to the choice of weights problem in analysis of individual pharmacokinetic data. *J Pharmacokinetic Biopharm* 12(1984):545–58.
- Pinheiro, J. C., D. M. Bates and M. J. Lindstrom. 1993. *Nonlinear Mixed Effects Classes and Methods for S*. TR-906, Department of Statistics, Wisconsin: University of Wisconsin.
- Press, W. H., S. A. Teukolsky, W. T. Vetterling and B. P. Flannery. 1992. *Numerical Recipes in C*. Cambridge: Cambridge University Press.
- Rao, C. R. 1952. *Advanced Statistical Methods in Biometric Research*. New York: Wiley.
- Schumitzky, A. Nonparametric EM algorithms for estimating prior distributions. *Appl Math Comput* 45(1991):141–57.
- Schumitzky, A. 1993. The non-parametric maximum likelihood approach to pharmacokinetic population analysis. In: *Proceedings of 1993 Western Simulation Multiconference — Simulation in Health Care*, San Diego: Society for Computer Simulation, pp. 95–100.

- Schumitzky, A. 1995. EM algorithms and two stage methods in pharmacokinetic population analysis. In: *Advanced Methods of Pharmacokinetic and Pharmacodynamic Systems Analysis*. Edited by D. Z. D'Argenio. New York: Plenum.
- Schumitzky, A., R. Jelliffe and M. Van Guilder. NPEM2: a program for pharmacokinetic population analysis. *Clin Pharmacol Therap* 55(1994):163.
- Smith, A. F. M. Bayesian computational methods. *Phil Trans R Soc Lond A* 337(1991):369–86.
- Smith, A. F. M. and G. O. Roberts. Bayesian computation via the Gibbs sampler and related Markov-chain Monte Carlo methods. *J Roy Statist Soc B* 55(1993):3–23.
- Spiegelhalter, D. J., A. Thomas and W. R. Gilks 1993. *BUGS Manual 0.20*. Cambridge: MRC Biostatistics Unit.
- Spieler, G. and A. Schumitzky. 1993. Asymptotic analysis of extended least squares estimators with application to population pharmacokinetics. In: *Proceedings of 1993 Biopharmaceutical Section*, pp. 177–82. American Statistical Society.
- Steimer, J. L., A. Mallet, J. L. Golmard and J. F. Boisvieux. Alternative approaches to estimation of population pharmacokinetic parameters: comparison with the nonlinear mixed-effect model. *Drug Metab Rev* 15(1984):265–92.
- Tudor, R. S., R. Hovorka, D. R. Meeking, D. A. Cavan, O. K. Hejlesen and S. Andreassen. DIAS-NIDDM: a model based decision support system for insulin dose adjustment in insulin-treated subjects with NIDDM. *Comput Methods Programs Biomed* 56(1998):175–92.
- Vajda, S., J. J. DiStefano III, K. R. Godfrey and J. Fagarasan. Parameter space boundaries for unidentifiable compartmental models. *Math Biosci* 97(1989):27–60.
- Vonesh, E. F. A note on the use of Laplace's approximation for nonlinear mixed-effects models. *Biometrika* 83(1996):447–52.
- Vonesh, E. F. and R. L. Carter. Mixed-effects nonlinear regressions for unbalanced repeated measures. *Biometrics* 48(1992):1–17.
- Wakefield, J., L. Aarons and A. Racine-Poon. 1999. *The Bayesian approach to population pharmacokinetic/pharmacodynamic modeling*. <http://www.stat.cmu.edu/meetings/Bayes97/wake.ps>.
- Wakefield, J. C., A. F. M. Smith, A. Racine-Poon and A. E. Gelfand. Bayesian-analysis of linear and nonlinear population-models by using the Gibbs sampler. *Appl Stat* 43(1994):201–21.

This Page Intentionally Left Blank

# Tracer Experiment Design for Metabolic Fluxes Estimation in Steady and Nonsteady State

Andrea Caumo and Claudio Cobelli

## 6.1. INTRODUCTION

Understanding the functioning of a metabolic system requires the quantitation of processes that are not directly measurable because they take place in the nonaccessible portion of the system. Among these processes, production and utilisation of substrates and secretion of hormones are of utmost importance for the investigator. The aim of this chapter is to describe tracer techniques for the quantitation of such fluxes under steady- and nonsteady-state conditions. Although the treatment is fairly general, we will use the glucose system as a prototype.

## 6.2. FUNDAMENTALS

The fundamental concepts underlying the use of tracers to measure production and utilisation fluxes of a substrate or a hormone can be better grasped by providing a formal description of the metabolic system under study.

We assume that the metabolic system can be described by a model having an accessible compartment (usually blood) where the concentration of the substance can be measured (the accessible compartment is denoted by the presence of the dashed line with the bullet) and other nonaccessible compartments variously interconnected. In the example shown in Figure 6.1, we can



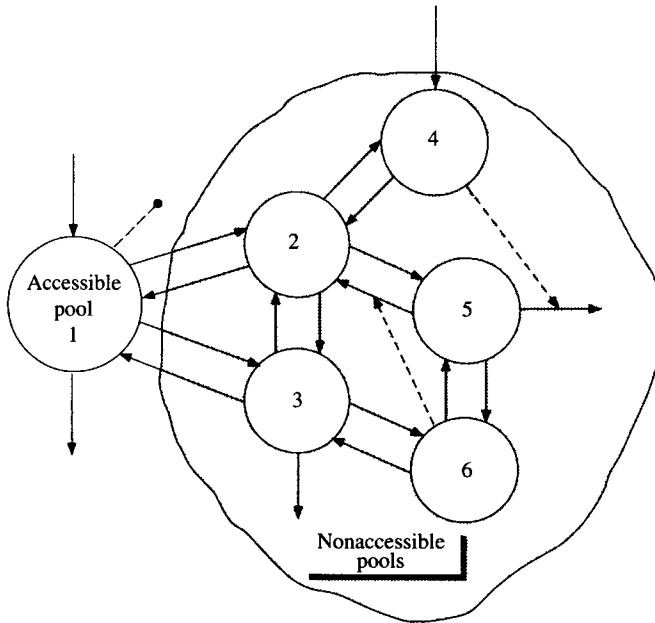


**Figure 6.1.** A multicompartmental model of a metabolic system. The accessible pool exchanges with the nonaccessible portion of the system. Continuous lines represent fluxes of material and dashed lines represent control actions.

see a compartmental model in which the nonaccessible portion is modelled by a five-pool structure. Continuous lines represent fluxes of material from one compartment to another, while dashed lines represent control signals.

Let Figure 6.2 represent the  $i^{\text{th}}$  compartment of the model, with  $Q_i(t)$  denoting the mass of the compartment. The arrows represent fluxes into and out of the compartment; the input flux into the compartment from outside the system, which is the *de novo* synthesis of material, is represented by  $\Phi_{i0}(t)$ ; the flux out of the system (excretion/degradation) by  $\Phi_{0i}(t)$ ; the flux from compartment  $i$  to compartment  $j$  by  $\Phi_{ji}(t)$ ; finally, exogenous input by  $E_i(t)$ . By applying the mass balance principle to each of the  $n$  compartments of the system and assuming that compartment #1 represents the accessible pool, we can write:

$$\dot{Q}_i(t) = - \sum_{\substack{j=0 \\ j \neq i}}^n \Phi_{ji}(t) + \sum_{\substack{j=0 \\ j \neq i}}^n \Phi_{ij}(t) + E_i(t) \quad (i, j = 1, \dots, n) \quad (6.1)$$

$$C(t) = Q_1(t)/V_1$$

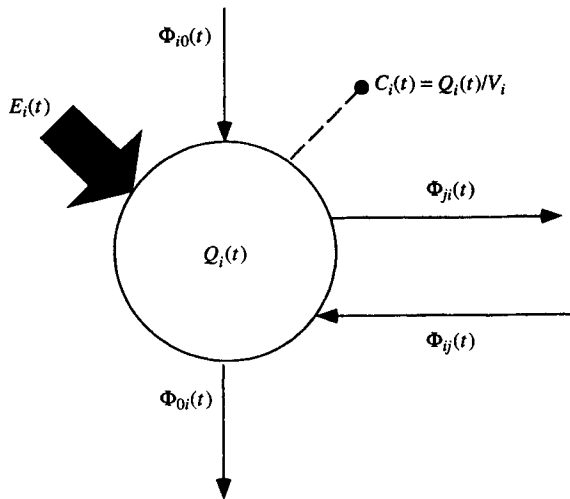


**Figure 6.2.** The  $i^{\text{th}}$  compartment of a  $n$ -compartment model showing fluxes into and out of the compartment, exogenous inputs, and measurement.

where  $C(t)$  is the concentration of compound measured in the accessible pool (subscript “1” indicating compartment 1 is omitted) and  $V_1$  is the volume of the accessible pool. Of note is that, usually, the only input to the system is the one applied to the accessible pool,  $E_1$ . In general, the flux of material  $\Phi_{ji}(t)$  from compartment  $i$  to compartment  $j$  is dependent on the mass of the compound not only in the source compartment  $i$  but also in other compartments of the system:

$$\Phi_{ji}(t) = \Phi_{ji}(Q_1(t), Q_2(t), \dots, Q_n(t)) \quad (j = 0, 1, \dots, n; i = 1, 2, \dots, n; j \neq i) \quad (6.2)$$

The nature of this functional dependence may be linear or nonlinear and may include threshold/saturation relationships (e.g., Michaelis-Menten kinetics) and control actions (e.g., the control exerted by a hormone on the fluxes of a substrate).

It is often more useful to express (6.1) in terms of the masses of the compound in the compartments. To do so, we render explicit the relationship between the generic flux  $\Phi_{ji}(t)$  and the mass in the source compartment,  $Q_i(t)$ :

$$\Phi_{ji}(t) = k_{ji}(Q_1(t), Q_2(t), \dots, Q_n(t)) \cdot Q_i(t) = k_{ji}(t) \cdot Q_i(t) \quad (6.3)$$

where  $k_{ji}(\geq 0)$  is the fractional transfer coefficient from compartment  $i$  to compartment  $j$ . If the system is linear and time-invariant,  $k_{ji}(t)$  is always constant, meaning  $k_{ji}(t) = k_{ji}$ . If the system is linear and time-varying (note

that a nonlinear system can be considered a linear system with time-varying parameters), we must distinguish between steady- and nonsteady-state conditions. If the system is in steady state, all the fluxes and masses are constant and thus  $k_{ji}$  is constant. If the system is in nonsteady state,  $k_{ji}$  may vary since saturation and control signals come into play. Using (6.3), (6.1) can be written as follows:

$$\begin{aligned} \dot{Q}_i(t) &= - \sum_{\substack{j=0 \\ j \neq i}}^n k_{ji}(t) Q_i(t) + \sum_{\substack{j=1 \\ j \neq i}}^n k_{ij}(t) Q_j(t) \\ &\quad + \Phi_{i0}(t) + E_i(t) \quad (i, j = 1, \dots, n) \\ C(t) &= Q_1(t)/V_1 \end{aligned} \quad (6.4)$$

### 6.3. ACCESSIBLE POOL AND SYSTEM FLUXES

To put the assessment of production and utilisation fluxes on a firm basis, it is useful to make a clear distinction between fluxes pertaining to the accessible pool and fluxes pertaining to the whole system. Let us begin with the fluxes that refer to the accessible pool.  $Ra(t)$  (rate of appearance) denotes the rate of entry of the compound into the accessible pool (*de novo* entry + exogenous input). Making reference to (6.1),  $Ra(t)$  can be expressed as follows:

$$Ra(t) = \Phi_{10}(t) + E_1(t) \quad (6.5)$$

$Rd(t)$  (rate of disappearance) is the net outflux of the compound from the accessible pool (resulting from the exchange of material between the pools).  $Rd(t)$  can be expressed in terms of compartmental fluxes as follows:

$$Rd(t) = \sum_{\substack{i=0 \\ i \neq 1}}^n \Phi_{i1}(t) - \sum_{i=2}^n \Phi_{1i}(t) \quad (6.6)$$

$Ra(t)$  and  $Rd(t)$  are related by the mass balance equation of the accessible pool:

$$\frac{dQ_1(t)}{dt} = Ra(t) - Rd(t) \quad (6.7)$$

As far as the whole system is concerned,  $P(t)$  will denote endogenous production and  $U(t)$  will denote whole-body uptake.  $P(t)$  equals the sum of all the *de novo* fluxes of the compound entering the system:

$$P(t) = \sum_{i=1}^n \Phi_{i0}(t) \quad (6.8)$$

$U(t)$  equals the sum of all the fluxes irreversibly leaving the system:

$$U(t) = \sum_{i=1}^n k_{0i}(t)Q_i(t) \quad (6.9)$$

$P(t)$  and  $U(t)$  are related by the mass-balance equation of the whole system:

$$\frac{dQ_T(t)}{dt} = P(t) - U(t) \quad (6.10)$$

where  $Q_T = \sum_{i=1}^n Q_i(t)$  is the total mass of the compound in the system. In general,  $P(t)$  and  $U(t)$  are different from  $Ra(t)$  and  $Rd(t)$ , respectively. If we assume, for the sake of simplicity, that the accessible pool is the only site of *de novo* entry of the compound,  $P(t)$  coincides with  $Ra(t)$  (minus any exogenous input of the compound, when present). In contrast, since the compound is usually utilised by tissues in both the accessible and the nonaccessible pools,  $U(t)$  is different from  $Rd(t)$  in general. In summary, while  $Ra(t)$  and  $Rd(t)$  refer only to the accessible pool,  $P(t)$  and  $U(t)$  refer to the whole system (accessible pool + nonaccessible pools).

When the focus of the investigation is the assessment of  $Ra(t)$ , the development of a compartmental model of the system may be simply not necessary. For instance, it may happen that one is interested in measuring endogenous glucose production or insulin secretion after a meal but is not interested in a detailed structural description of glucose or insulin kinetics. The assessment of  $Ra(t)$  can be posed as an input-estimation problem, in the sense that one must derive the unknown input to the system from its causally related effect on the concentration of the compound in the accessible pool (this issue is discussed in detail in Chapter 3). If the system is linear and time-varying (note, incidentally, that a nonlinear system can be thought of as a linear system with time-varying parameters), the input-estimation problem can be formalised by describing the input-output relationship between the unknown input,  $Ra(t)$ , and the measurable output,  $C(t)$ , with a Fredholm integral equation of the first kind:

$$C(t) = \int_{-\infty}^t h(t, \tau)Ra(\tau)d\tau \quad (6.11)$$

where  $h(t, \tau)$  describes the input-output behaviour of the system and is called the kernel of the system. The function  $h(t, \tau_0)$  represents the time course of the output when the system is forced by a unitary impulse given at time  $\tau_0$ . When the system is linear and time-invariant,  $h(t, \tau)$  depends only on the difference  $t - \tau$ , the right-hand side of (6.11) becomes a convolution integral, and the problem of determining  $Ra(t)$  given  $h(t)$  and  $C(t)$  is called *deconvolution*. In any case, the assessment of  $Ra(t)$  consists in solving backward (6.11), and

this requires the preliminary knowledge of the impulse response. How can the impulse response be described? We will distinguish two cases, depending on whether the system is linear and time-invariant or linear and time-varying. If the system is linear and time-invariant, its impulse response can be described by a model of data (no structural, i.e., compartmental, model) is needed. Usually, a good candidate of  $h(t)$  is:

$$h(t) = \sum_{i=1}^n A_i e^{-\alpha_i t} \quad (6.12)$$

where  $\alpha_i > 0$ . If the system is linear and time-varying (e.g., the glucose system), the kernel  $h(t, \tau)$  cannot be assessed unless a structural model is formulated that is capable of describing the time dependency of its parameters.

In summary, to quantitate fluxes of appearance/production and disappearance/utilisation, one may need to identify a structural model of the system or at least determine its impulse response (the two requirements coincide when the system is linear and time-varying). To accomplish these tasks, the ideal probe is a tracer experiment, as we will see in the following section.

## 6.4. THE TRACER PROBE

It is easy to realise that the availability of the compound concentration in the accessible pool is not sufficient to quantitate the production and removal processes. For instance, an increased compound plasma concentration might be the consequence of increased production, decreased removal from the circulation, or a combination of both processes. To quantitate these fluxes, we must perform an input-output (I/O) experiment in which an adequate database of dynamic data is generated. The tool of choice is the tracer probe, which is usually a radioactive or stable isotope. The two tracers differ in some aspects. Radiotracers can be given in negligible amounts (which do not perturb the system) and produce satisfactory signal-to-noise ratios but can be harmful. Stable-labelled tracers are safe but are naturally present in the body (natural abundance); in addition, the amount that is given to produce a satisfactory signal-to-noise ratio does not have negligible mass and may perturb the system. This makes the analysis of a stable isotope tracer experiment more complex than that of a radioactive tracer experiment. However, a kinetic formalism for the analysis of stable isotope tracer data has been recently developed, and its link with the radioactive kinetic formalism has been elucidated (Cobelli *et al.*, 1992).

An ideal tracer has the following characteristics:

- 1). It has the same metabolic behaviour as the substance being traced (denoted as tracee). This is known as tracer-tracee indistinguishability principle;
- 2). It is distinguishable from the tracee by the investigator;
- 3). It does not perturb the system.

Real tracers satisfy such conditions to different extents. Hereafter we will assume, for the sake of simplicity, that the tracer is ideal.

Why do tracers help in enhancing the information that can be gained from an I/O experiment? The reason is that the tracer travels in the system like the tracee, and thus tracer data measured in the accessible pool contain information about the tracee system. By applying the mass conservation law for the tracer to all the compartments of the model used to describe the behaviour of the tracee (6.1), one obtains a system of differential equations:

$$\begin{aligned} \dot{q}_i(t) &= - \sum_{\substack{j=0 \\ j \neq i}}^n k_{ji}(t)q_i(t) + \sum_{\substack{j=1 \\ j \neq i}}^n k_{ij}(t)q_j(t) \\ &\quad + e_i(t) \quad (i, j = 1, \dots, n) \\ c(t) &= q_1(t)/V_1 \end{aligned} \tag{6.13}$$

Note that we use lowercase letters to denote tracer-related variables:  $q_i(t)$  is the mass of the tracer in the  $i^{\text{th}}$  compartment;  $e_i(t)$  is the tracer input into the  $i^{\text{th}}$  compartment (usually the only tracer input to the system is the one applied to the accessible pool,  $e_1$ );  $c(t)$  is tracer concentration in the accessible pool (subscript "1" indicating compartment 1 is omitted). Of note is that, thanks to the tracer-tracee indistinguishability principle, the fractional transfer rates of the tracer model are the same as those of the tracee model.

By comparing (6.4) and (6.13), one can see that the tracer model has a definite advantage with respect to the tracee model: whereas the endogenous tracee input to the system is unknown (and is often what the investigator wants to determine), the tracer input is known. As a result, a suitably designed tracer experiment allows the investigator to identify the tracer model (using the appropriate parameter estimation techniques). Subsequently, the tracer model can be used, in conjunction with the tracee measurements, to quantitate the tracee model. Analogous considerations apply to the tracer impulse response. In fact, thanks to the tracer-tracee indistinguishability principle, the impulse response of the tracer is the same (apart from the units) as that of the tracee. The tracer impulse response can be determined from tracer I/O data and then used to estimate  $Ra(t)$  by solving backward (6.11).

It is useful to point out that, if the tracee is in a constant steady state, all the tracee fluxes ( $\Phi_{ji}$ ) and masses ( $Q_i$ ) are constant. As a result, all of the

fractional transfer coefficients  $k_{ji}$  are constant as well (see [6.3]). If the  $k_{ji}$  are constant, the tracer model described by (6.13) is linear, irrespective of whether the tracee system is linear or nonlinear. This greatly simplifies tracer data analysis. In particular, the tracer impulse response can be described by a model of the data, such as a multiexponential function. The price to be paid is that the tracer-derived parameters yield a picture of the steady-state operating point but cannot describe the dynamics of the system in its full nonlinear operation arising, for instance, from saturation kinetics and control signals.

Now that we have a good appreciation of the fundamentals of tracer methodology, we can turn our attention to the issue of tracer experiment design. In the following, we will discuss the most appropriate tracer administration strategies to measure production and utilisation fluxes under steady and nonsteady-state conditions.

## 6.5. ESTIMATION OF TRACEE FLUXES IN STEADY STATE

We begin by considering a system that is in steady state with respect to the tracee. In steady state, masses and fluxes in the system are constant. Assuming that there is no exogenous administration of tracee, the mass balance principle applied to the accessible pool and to the whole system states that:

$$Ra = Rd \quad (6.14)$$

$$P = U \quad (6.15)$$

Thus, in steady state the rate of entry into and exit from the accessible pool (as well as the whole system) is constant. These fluxes are collectively referred to as the turnover rate.

To estimate  $Ra$  (and thus the turnover rate), we can exploit the fact that, under steady-state conditions, (6.11) becomes an algebraic equation (time  $t$  in the integral sign goes to infinity) that can be easily solved for the unknown  $Ra$ :

$$Ra = \frac{C}{\int_0^{\infty} h(\tau) d\tau} \quad (6.16)$$

where  $C$  is the steady-state tracee concentration.

In principle, the integral of the impulse response can be estimated from the tracer data generated by any realisable tracer input. In the following, we will examine the three most common formats of tracer administration: the single injection, the constant infusion, and the primed constant infusion, which is a combination of the first two.

### 6.5.1. SINGLE INJECTION

The single-injection technique consists of a tracer bolus rapidly injected in vein followed by plasma sampling for measurement of tracer and tracee concentration. This input, at least ideally, is an impulse making reference to (6.13):  $e_1(t) = d\delta(t)$ , where  $d$  is the tracer dose, and thus the tracer disappearance curve following the tracer bolus can be interpreted as the impulse response of the system (Figure 6.3, upper panel).

Since the system is in steady state, the impulse response of the tracer is that of a linear and time-invariant system and can be described by a sum of decaying exponentials. Thus, the time course of tracer concentration following the tracer injection is given by:

$$c(t) = d \cdot h(t) = d \sum_{i=1}^n A_i e^{-\alpha_i t} \quad (6.17)$$

where  $c$  is tracer concentration in plasma and  $(A_i)$  and  $(\alpha_i)$  are the coefficients and eigenvalues, respectively, of the multiexponential impulse response. One uses a parameter estimation technique to identify the sum of exponentials model and employs parsimony criteria, such as the Akaike information (Carson *et al.*, 1983), to select the appropriate number,  $n$ , of exponential terms. Once  $h(t)$  is known,  $Ra$  can be calculated by deconvolution:

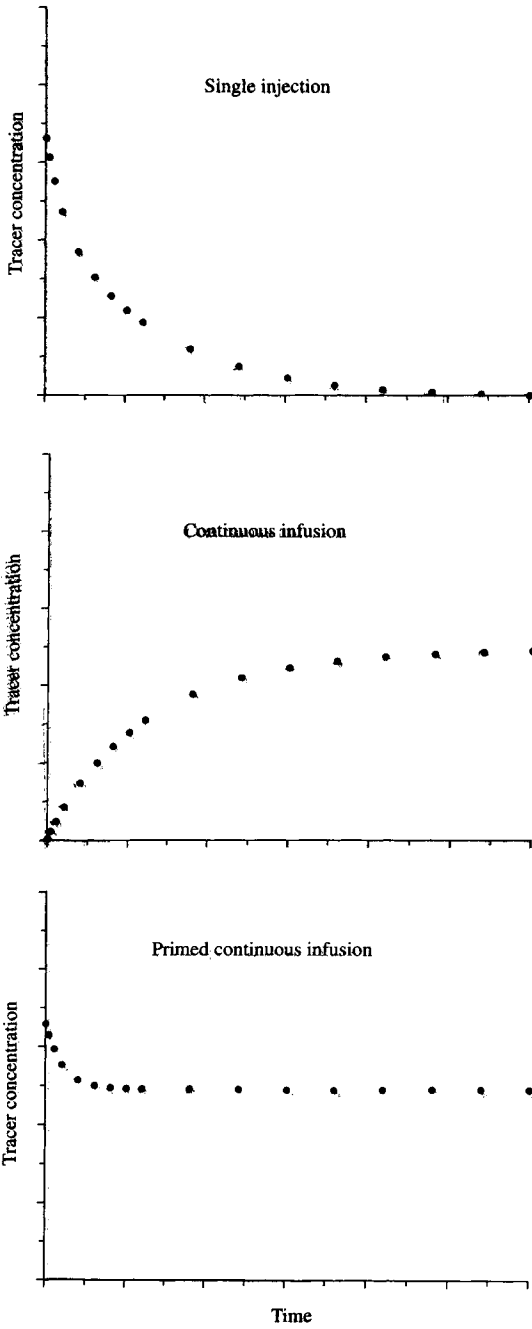
$$Ra = \frac{d \cdot C}{\int_0^{\infty} c(\tau) d\tau} = \frac{C}{\sum_{i=1}^n \frac{A_i}{\alpha_i}} \quad (6.18)$$

The single injection is the most simple and economical format of tracer administration because it does not require an infusion pump. However, the estimation of turnover from the tracer disappearance curve is not straightforward because it requires frequent sampling, especially in the initial portion of the study, and a data analysis entailing the use of parameter estimation techniques. In addition, the experiment duration may be rather long since sampling must be continued for at least two to three times the slowest time constant in the system.

### 6.5.2. CONSTANT INFUSION

With the constant-infusion technique, the tracer is administered intravenously at a constant rate until the tracer achieves a steady-state level (Figure 6.3, middle panel). This input, at least ideally, is a step centred at





time 0, making reference to (6.13):  $e_1(t) = ra\delta_{-1}(t)$ , where  $ra$  is the constant tracer infusion rate. Since the step is the integral of the impulse, the response to a unit constant infusion will coincide with the integral of the response to a unit dose injection. Thus, by integrating (6.17), one obtains that the time course of tracer concentration during the constant tracer infusion is given by:

$$c(t) = ra \sum_{i=1}^n \frac{A_i}{\alpha_i} (1 - e^{-\alpha_i t}) \quad (6.19)$$

Under such conditions of steady state for both the tracer and the tracee, the tracer and tracee concentrations in plasma will be proportional to their respective rates of entry. Calculation of turnover is straightforward since it only requires the measurement of plasma tracer and tracee concentrations at tracer steady state:

$$Ra = ra \frac{C}{c} = \frac{ra}{z} \quad (6.20)$$

where  $z$  is the constant tracer-to-tracee ratio (Cobelli *et al.*, 1992) (this ratio coincides with the specific activity when a radiotracer is used).

Evaluation of tracee turnover is thus simpler with the constant-infusion technique than with the single-injection technique. Another advantage of the constant infusion with respect to the single-injection protocol is that one circumvents the need of determining the system order and of using a parameter estimation technique.

Achievement of a true tracer steady state is important for a correct calculation of turnover when the constant-infusion technique is adopted. The time needed to achieve the steady state depends on the size of the slowest time constant of the system: the smaller its value, the longer the time required to reach the steady state. Thus, it may take a very long time to reach tracer steady state with the constant infusion alone, especially for substances and in subjects having a low turnover. To cope with this problem, the primed continuous-infusion strategy has been devised.

### 6.5.3. PRIMED CONTINUOUS INFUSION

When a rapid achievement of the tracer steady state is of primary importance (this happens, for instance, when the experimental protocol is long

---

**Figure 6.3.** Assessment of turnover in steady state: tracer concentration profiles during a bolus injection (upper panel), a constant infusion (middle panel), and a primed continuous infusion (lower panel).

because the steady state is followed by a nonsteady-state period), the tracer administration format of choice is the so-called primed continuous infusion, which is an impulse followed by a step input. The reason why this format is preferable to the constant infusion is because the priming dose, when appropriately chosen, considerably speeds up the attainment of the tracer steady state (see Figure 6.3, lower panel). To appreciate intuitively why this occurs, we must think that the tracer curve following the primed continuous infusion is, thanks to the linearity of the tracer system in steady state, the superposition of the individual responses to a single injection and to a constant infusion. The final decaying portion of the tracer disappearance curve due to the single injection and the final raising portion of tracer appearance curve are both governed by the slow time constant of the system. Therefore, the time needed to achieve the tracer steady state can be reduced if the amplitudes associated to the slow component in the impulse and in the step responses are identical and, being of opposite sign, cancel each other. This can be accomplished by selecting the appropriate size of the priming dose with respect to the constant infusion rate. To understand how one can optimally select the priming dose, it is useful to resort to the analytical expression of the system response to a primed continuous infusion, which coincides with the sum of individual responses to an impulse (6.17) and to a step (6.19):

$$c(t) = ra \sum_{i=1}^n \frac{A_i}{\alpha_i} \left[ 1 + e^{-\alpha_i t} \left( \frac{d}{ra} \alpha_i - 1 \right) \right] \quad (6.21)$$

From (6.21), one can see that if the ratio  $d/ra$  equals the inverse of the slowest exponential time constant ( $1/\alpha_n$ ), the contribution of the slowest exponential component,  $e^{-\alpha_n t}$ , is cancelled out and the tracer steady state is achieved more quickly. In particular, if the impulse response contains only a single exponential term, the selection of a priming ratio equal to  $1/\alpha_1$  will result in an instantaneous tracer steady state. If the system has a multiexponential impulse response, the achievement of the tracer steady state will require a transient period whose duration will be dictated by the less rapid among the remaining exponential components. For instance, if the system is second order, then the transient period (above the final steady state) will be monoexponential. Thus, the investigator can design the priming ratio provided he or she knows in advance the impulse response of the system. However, in practice, this does not happen, and assumptions about the slowest time constant must be made on the basis of available physiological knowledge.

When tracer steady state has been obtained, turnover can be calculated as with the constant-infusion technique (6.20). It must be emphasised that the calculation is accurate only if a true steady state for the tracer is achieved at the end of the test. However, it may happen (especially with compounds and subjects having a low turnover) that the final portion of the tracer equilibration

curve varies so slowly that a false impression of the tracer steady state is given at times when the true plateau level has not been reached (this situation has been extensively investigated for the glucose system (Hother-Nielsen and Beck-Nielsen, 1990; Hovorka *et al.*, 1997). In this case, the use of (6.20) would lead to a biased estimate of tracee turnover. If we suspect that the tracer steady state has not been achieved yet at the end of the test, we can still estimate accurately turnover provided we have sampled the tracer curve throughout the experiment, particularly when tracer concentration rapidly decays after the prime. In this case, we will fit all the available tracer data (i.e., the final quasi-steady state, as well as the initial dynamic data) to (6.21) and we will estimate the impulse response parameters ( $A_i$ ) and ( $\alpha_i$ ). These parameters will then be used to calculate the area of the impulse response, which, substituted in (6.16), will yield turnover. What warrants emphasis is that one can resort to this approach to circumvent the lack of a reliable tracer steady only if an adequately frequent sampling schedule has been adopted in the initial part of the test when the fastest components of the system play an important role.

In the study of the glucose system in normal subjects, a priming ratio equal to 100 (corresponding to a slowest exponential component of  $0.01 \text{ min}^{-1}$ ) is commonly used. However, in groups in which the slowest component is altered, the ratio must be changed to match the slowest time constant. For instance, the priming modality plays a crucial role in the assessment of basal glucose turnover in non-insulin-dependent diabetes mellitus (NIDDM) because, if appropriate adjustment of the priming ratio is not accomplished, the observation period can be insufficient to achieve the tracer steady state and, as a consequence, glucose turnover is overestimated. Fortunately, in recent years, guidelines have been developed to individualise the priming ratio in NIDDM patients as a function of their fasting glucose concentration (Hother-Nielsen and Beck-Nielsen, 1990).

## 6.6. ESTIMATION OF NONSTEADY-STATE FLUXES

Let us suppose that the experimental protocol comprises two phases: a first phase with tracee in steady state and tracer brought to a steady state via a tracer administration — typically a primed continuous infusion — and a second phase in which the investigator imposes a perturbation that pushes the system out of steady state. Such a nonsteady-state transition ends up with a steady state that may be either the initial or a new. In nonsteady state,  $Ra$ ,  $Rd$ ,  $P$ , and  $U$  are all functions of time, and their estimation is much more complex than in steady state. At variance with steady state (see [6.14] and [6.15]), in nonsteady state  $Ra(t)$  (which equals the sum of the endogenous and exogenous tracee appearance rates) is different from  $Rd(t)$ , which is, in turn, different from  $U(t)$ . We will devote the next sections of this chapter to

outline tracer infusion strategies to obtain an accurate estimation of  $Ra(t)$  and then an accurate estimation of  $Rd(t)$  and  $U(t)$ .

In nonsteady state, the estimation of  $Ra(t)$  on the basis of the convolution integral (6.11) is more complex than in steady state. In principle,  $Ra(t)$  estimation is performed in two steps. First, the impulse response  $h(t, \tau)$  is identified from tracer data, and then  $Ra(t)$  is reconstructed from the impulse response and tracee data by deconvolution. How can  $h(t, \tau)$  be assessed? If the system under investigation is linear and time-invariant, the impulse response does not change when the system is pushed out of steady state and can be described by a multiexponential function. The parameters of the multiexponential function can be estimated from the tracer I/O experiment performed in steady state provided that the tracer time course has been adequately sampled (e.g., the rapid decay of tracer concentration immediately following a tracer bolus). In this case, no further tracer administration is required during the nonsteady state. On the other hand, if the system is linear but time-varying (e.g., the glucose system), the impulse cannot be assessed unless hypotheses are made on the structure of the system. In other words, to determine  $h(t, \tau)$  it is necessary to formulate and identify from nonsteady-state tracer data a structural model, such as the one depicted by (6.13), capable of describing the system functioning during the nonsteady state. In particular, one must specify which are the time-varying parameters of the model and how they change during the nonsteady state. Different models will yield different estimates of  $Ra(t)$ . Due to the complexity of metabolic systems, it is difficult to work out a general-purpose model and, usually, models aimed to describe the behaviour of the system in each specific experimental situation are developed. In any case, striving for model accuracy must be balanced against the need of practical identification. It is possible to render the estimation of  $Ra(t)$  less dependent on the chosen model if one carefully designs the tracer infusion during the nonsteady state in the most appropriate way. In the next section, we will examine how to do it.

### 6.6.1. ASSESSMENT OF $Ra$ : THE TRACER-TO-TRACEE CLAMP

Nonsteady-state theory (Norwich, 1973; Cobelli *et al.*, 1987) suggests that the accuracy of the estimation of  $Ra(t)$  can be enhanced if the tracer is infused during the nonsteady state in such a way as to reduce the changes in the tracer-to-tracee ratio,  $z(t)$ , during the experiment (since this procedure has been originally devised for radiotracers, it is known as specific activity clamp). Ideally, if  $z(t)$  is maintained perfectly constant during the experiment, an accurate estimate of  $Ra(t)$  can be obtained irrespective of the model used to interpret the nonsteady state. To understand how this happens, let us

suppose that the tracee system is in steady state and a tracer experiment is carried out—typically a primed continuous infusion—until the tracer reaches a steady state throughout the system. In the basal steady state, the tracer-to-tracee ratio,  $z_b$ , (subscript “b” denotes “basal”) coincides with the ratio between basal tracer infusion and basal production. Let us now suppose that a perturbation, for instance, an exogenous administration of tracee, pushes the system out of the steady state. If  $Ra(t)$  changes in time with respect to basal  $P$  and the tracer is still infused at a constant rate during the nonsteady state, the tracer-to-tracee ratio will change as well. Theory suggests that this change in the tracer-to-tracee ratio should be prevented by infusing the tracer in such a way as to follow the changes of  $Ra(t)$ . If the tracer infusion rate,  $ra(t)$ , is adjusted so that  $ra(t) = Ra(t) \cdot z_b$ ,  $z(t)$  remains equal to  $z_b$  throughout the experiment and  $Ra(t)$  is given by:

$$Ra(t) = \frac{ra(t)}{z_b} \quad (6.22)$$

In other words,  $ra(t)$  must have the same shape of  $Ra(t)$ , with the proportionality factor between the two being the desired target value  $z_b$ . Of note is that (6.22) is similar to (6.20), which is the one used to calculate steady-state  $Ra$ , but here both  $ra(t)$  and  $Ra(t)$  change in time. A theoretical proof that the rate of appearance is predicted correctly in nonsteady state by (6.22) if  $z(t)$  remains constant has been given by Norwich (1973, 1977) for a distributed system characterised by the assumption of convective diffusion. For a generic compartmental model describing tracee and tracer dynamics by (6.4) and (6.13), respectively, it can be shown (Cobelli *et al.*, 1987) that:

$$Ra(t) = \frac{ra(t)}{z_1(t)} - \frac{Q_1(t)}{z_1(t)} \dot{z}_1(t) - \sum_{i=2}^n \left( 1 - \frac{z_i(t)}{z_1(t)} \right) k_{1i} Q_i(t) \quad (6.23)$$

where  $z_i$  is the tracer-to-tracee ratio in the  $i^{\text{th}}$  compartment ( $z_1$  is the tracer-to-tracee ratio measured in the accessible pool and thus coincides with  $z$ ). The relevance of this equation lies in the fact that, if the tracer administration is adjusted so as to induce no changes in  $z(t)$  over time, the time derivative of  $z(t)$  in the accessible pool is zero and the contributions of the second and third term in (6.23) become null. As a result,  $Ra(t)$  coincides with the expression given in (6.22) and becomes model-independent because it only hinges on what can be measured in the accessible pool.

In practice, it is impossible to maintain plasma  $z(t)$  at an absolutely constant level. Nevertheless, it is useful for the investigator to try to clamp  $z(t)$  at a constant level by changing the tracer infusion rate in a suitable way because a reduction in the rate of change of  $z(t)$  will provide an estimate of  $Ra(t)$  much less dependent on the validity of the model used with respect to a “blind” constant tracer infusion.

What are the possible approaches to clamp  $z(t)$ ? The development of a closed-loop tracer administration scheme requires the availability of measurement methods of tracer and tracee plasma concentration that are rapid enough. Usually, however, the tracer concentration cannot be measured rapidly enough and an open-loop approach to clamp  $z(t)$  has to be adopted. Therefore, guidelines are needed to design the most appropriate open-loop scheme of tracer infusion. We have seen previously that, to keep  $z(t)$  constant,  $ra(t)$  should have the same shape of the unknown  $Ra(t)$ . In general, there are two sources of tracee contributing to  $Ra(t)$  (see Figure 6.4, left panels): one is the endogenous production, while the other, when present, is the rate of appearance of the tracee that the investigator administers exogenously in relation with the purpose of the study. For instance, during a euglycaemic hyperinsulinaemic clamp (DeFronzo *et al.*, 1979), glucose is infused intravenously at a known rate in such a way to maintain glucose concentration constant throughout the study. Thus, we can write:

$$Ra(t) = P(t) + Ra_{\text{exg}}(t) \quad (6.24)$$

where  $Ra_{\text{exg}}(t)$  is the rate of appearance of the exogenous tracee. Also, the measured tracee concentration can be thought of as the sum of two components (see Figure 6.4, right panels): endogenous,  $C_{\text{end}}(t)$ , and exogenous concentration,  $C_{\text{exg}}(t)$ :

$$C(t) = C_{\text{end}}(t) + C_{\text{exg}}(t) \quad (6.25)$$

The distinction between the endogenous and exogenous tracee sources and concentrations leads naturally to a tracer infusion strategy that has general applicability. In fact, one viable approach to minimise the changes in  $z(t)$  consists in using two distinct tracer infusions, one proportional to the exogenous tracee infusion (Figure 6.5, upper panel) and the other proportional to the endogenous tracee production (Figure 6.5, lower panel). Implementing the first tracer infusion scheme is simple: one has to add some tracer to the exogenous tracee so that the tracer-to-tracee ratio of the labelled infusate,  $z_{\text{inf}}$ , is equal to  $z_b$ . The realisation of the second tracer infusion scheme is more difficult because it is necessary to change the basal rate of tracer infusion in such a way as to mimic the expected time course of  $P(t)$  during the experiment. This may sound like circular reasoning because adjusting the tracer infusion rate requires the knowledge of  $P(t)$ , which is exactly what one is trying to determine. However, usually some information about the behaviour of  $P(t)$  during the nonsteady state is available. This *a priori* knowledge can be used to design a tentative format of tracer administration for the first trial (educated guess). This guess can be later verified by measuring  $z(t)$  and, if  $z(t)$  is not constant, one learns from the error and refines the format of tracer administration in the subsequent experiment. This procedure can be repeated a few times

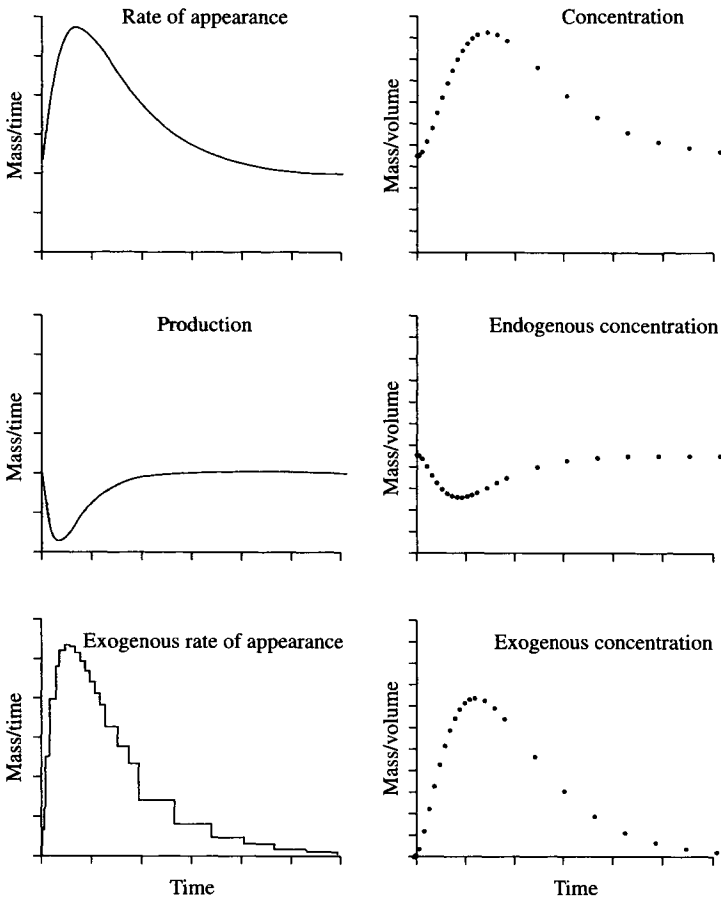


**Figure 6.4.** Tracee appearance fluxes (*left panels*) and concentrations (*right panels*) during the nonsteady state. The rate of appearance of a compound (*left, upper panel*) can be thought of as the sum of two components: endogenous production (*right, middle panel*) and exogenous appearance rate. Dually, the measured plasma concentration of the compound (*left, upper panel*) can be thought of as the sum of an endogenous (*left, middle panel*) and an exogenous (*left, lower panel*) component.

until a satisfactory format is obtained. In our experience, a few iterations are sufficient to achieve acceptable results.

Usually, the task of changing the tracer infusion in such a way as to mimic the expected time course of  $P(t)$  can be automatized using a preprogrammable pump. This allows the investigator to change the infusion rate as frequently as he or she wishes without adding complexity to the experiment. On the other hand, it is of no value to frequently change the tracer infusion rate if



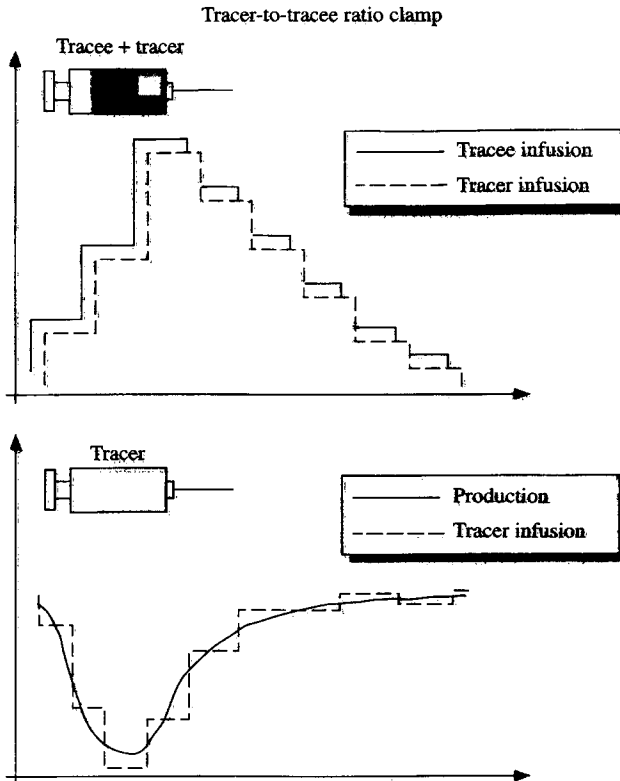


**Figure 6.5.** A tracer administration strategy to clamp the tracer-to-tracee ratio during the non-steady state. Two distinct tracer infusions are employed during the experiment: one is proportional to the exogenous tracee infusion (*upper panel*) and the other to the endogenous tracee production (*lower panel*). The former tracer infusion can be implemented by adding a proper amount of tracer (see page 168) to the exogenous tracee infusion, whereas the latter tracer infusion is realised by administering the tracer in such a way as to mimic the expected time course of endogenous production during the experiment.

blood samples are not collected frequently enough. It is sufficient to change the staircase tracer infusion rate immediately after each sample and keep the tracer infusion constant between two consecutive samples (the tracer infusion will be proportional to the average of  $P(t)$  in that interval). An important *caveat* is that the frequency of blood sampling (and thus the number of steps in the tracer infusion rate) should be increased whenever  $P(t)$  is expected to change most rapidly and variability among subjects is elevated.

Using the glucose system as a prototype, we will provide examples of the use of this technique to clamp  $z(t)$  under experimental conditions that

commonly arise in clinical investigation. Specifically, we shall deal with three distinct situations: first, when the exogenous source of the tracee is absent; second, when the exogenous source of the tracee is present and known; and third, when the exogenous source of the tracee is present but unknown.

#### 6.6.1.1 No Exogenous Source of Tracee

There are studies in which the only tracee source is endogenous. As a result, the measured tracee concentration coincides with  $C_{\text{end}}$ . An example of this situation is the study of glucose turnover during physical exercise. During physical exercise, glucose production increases to compensate for the increased glucose utilisation by muscles. To clamp  $z(t)$  in this situation, one has simply to administer the tracer in such a way as to mimic the expected pattern of increase of  $P(t)$ . In Coggan *et al.* (1995), the authors approximated the increase of  $P(t)$  during exercise by an increasing mono-exponential function and achieved an excellent tracer-to-tracee clamp.

#### 6.6.1.2 Known Exogenous Source of Tracee

In many circumstances, the tracee is administered exogenously and its rate of delivery into the systemic circulation is known. Two examples of this situation are the meal-like study and the euglycaemic hyperinsulinaemic clamp.

The meal-like study consists in an experimental protocol in which glucose and insulin are infused so as to reproduce the plasma glucose and insulin concentration profiles that are typically observed after carbohydrate ingestion in healthy subjects (Alzaid *et al.*, 1994). To clamp  $z(t)$ , a single tracer can be used to clamp the exogenous and endogenous tracee sources: some tracer is added to the glucose infusate, while the basal tracer infusion is changed with a pattern mimicking the expected time course of  $P(t)$ .

The euglycaemic hyperinsulinaemic clamp is the most widely used approach to investigate the effects of insulin on glucose metabolism (DeFronzo *et al.*, 1979). Insulin is infused at a constant rate throughout the study, while glucose is infused at a variable rate so as to maintain constant its level in plasma. Thus, at any time the exogenous glucose infusion rate,  $Ra_{\text{exg}}(t)$ , equals the difference  $Rd(t) - P(t)$ , and when a new steady state is attained one can measure the dose-response effect of insulin on both glucose uptake and production. To clamp  $z(t)$  during the euglycaemic hyperinsulinaemic clamp, one can use the approach described previously for the meal-like study, which is to add some tracer to the glucose infusate in such a way that  $z_{\text{inf}} = z_b$ , and to change the basal tracer infusion mimicking the expected time course of  $P(t)$ .

This strategy is the ideal one because it allows, at least in theory, to achieve a perfect tracer-to-tracee ratio clamp. However, it may turn out to be too

complex and labour-intensive, especially if the glucose clamp is to be used in population studies. Finegood *et al.* (1987) devised a simpler approach, in which one adds some label to the exogenous glucose infusate and maintains the basal tracer infusion unchanged throughout the study. If one interprets Finegood *et al.*'s approach in the light of the general approach outlined beforehand, it is evident that keeping constant the rate of tracer infusion — instead of mimicking the time course of  $P(t)$  — will produce an excess of tracer in the system. The idea devised by the authors to compensate for this tracer excess consists in underlabelling the exogenous infusate, that is, preparing an exogenous infusate having  $z_{\text{inf}} < z_b$ . To correctly choose  $z_{\text{inf}}$ , some *a priori* information about the likely behaviour of the glucose system at the end of the clamp is needed. Specifically, assuming that at the end of the clamp both  $P$  and  $Rd$  have reached a new steady state, the expression for  $z_{\text{inf}}$  is given by:

$$z_{\text{inf}} = z_b \left[ 1 - \frac{P_b - P_{ss}}{Rd_{ss} - P_{ss}} \right] \quad (6.26)$$

where  $P_b$ ,  $P_{ss}$ ,  $Rd_{ss}$  are, respectively, basal and final steady-state values of  $P$  and  $Rd$ .

The advantage of Finegood *et al.*'s approach with respect to the general approach is that it keeps the experimental effort to a minimum and does not require to guess the whole time course of  $P(t)$  but only the steady-state values of  $P$  and  $Rd$  at the end of the study. The disadvantage is that such a technique cannot be refined as more information about the nonsteady-state behaviour of  $P(t)$  becomes available. In addition, it only ensures that the value of  $z(t)$  measured at the end of the clamp is equal to  $z_b$ , but does not guarantee that it remains constant throughout the study. We have previously shown (Butler *et al.*, 1993) that  $z(t)$  will remain constant only if the inhibition of production is proportional to the stimulation of glucose disappearance. Since  $P(t)$  and  $Rd(t)$  may exhibit different time courses or differences between disease states, systematic deviations may arise. Despite these limitations, this approach works reasonably well and, because of its simplicity, is widely used to clamp the tracer-to-tracee ratio during the euglycaemic hyperinsulinaemic clamp.

In principle, Finegood *et al.*'s approach is applicable to the hyperglycaemic and hypoglycaemic clamp. The ingredients that allow one to choose  $z_{\text{inf}}$  under such experimental conditions are always the same of (6.26), which means  $P_b$  and the expected values of  $P$  and  $Rd$  at the end of the experiment. Since during a hyperglycaemic and a hypoglycaemic clamp, glucose does not remain to the baseline but is purposely brought to a new level, systematic deviations of  $z(t)$  from constancy are likely to occur in the initial part of the test. For instance, in the initial part of the hyperglycaemic clamp, the need of rapidly elevating glucose concentration by means of an exogenous glucose infusion will increase glucose concentration more than tracer concentration, so that  $z(t)$

may exhibit a transient undershoot. To prevent this undershoot, one has to add some more tracer in the initial part of the test. This can be done by using, only in the initial part of the test, a labelled infusion having a  $z_{\text{inf}}$  value higher than the one dictated by (6.26). Alternatively, one can increase temporarily and then restore the basal tracer infusion. During the hypoglycaemic clamp, the exogenous glucose infusion rate initiates when glucose reaches the desired hypoglycaemic level. If basal tracer infusion rate remains unchanged in the initial part of the test when exogenous glucose is not administered,  $z(t)$  may exhibit a transient overshoot. To prevent this overshoot, one can temporarily reduce the basal tracer infusion and restore it in concomitance with the initiation of the exogenous glucose infusion.

### 6.6.1.3 Unknown Exogenous Source of Tracee

In some experimental situations, the rate of appearance of the exogenously administered tracee is not known. For instance, when glucose is given orally (e.g., during a meal or an oral glucose tolerance test), exogenous glucose is absorbed through the gastrointestinal tract and is delivered into the systemic circulation with a pattern that is unknown and highly variable among subjects. It is intuitive that adding to the orally administered glucose the same tracer that is infused intravenously would prevent the estimation of  $P(t)$  because the contribution of ingested glucose to total  $Ra(t)$  could not be determined. Thus, to single out the contribution of glucose production, it is necessary to label the ingested glucose with a tracer that is *different* from the one infused intravenously (Taylor *et al.*, 1997). Whereas the tracer given orally is aimed to trace the exogenous glucose source, the tracer infused intravenously at a variable rate mimics the time course of  $P(t)$ . Since we measure two different tracer concentrations in plasma,  $c'(t)$  and  $c''(t)$ , we will also have to deal with two different  $z$  profiles, one referred to the tracer infused intravenously and the other to the tracer given orally. How does one recognise if the tracer-to-tracee clamp is successful? One convenient strategy is to calculate  $z(t)$  not with respect to the measured glucose concentration, but with respect to endogenous glucose concentration, that is the component of total glucose concentration that is due exclusively to  $P(t)$ . Endogenous glucose concentration cannot be measured directly but can be derived in a model-independent way (Cobelli and Toffolo, 1990) by subtracting from the measured total glucose concentration the exogenous component, where the latter is proportional—thanks to the tracer-tracee indistinguishability principle—to the concentration profile of the tracer mixed to orally administered glucose:

$$C_{\text{end}}(t) = C(t) - C_{\text{exg}}(t) = C(t) - c''(t)/z_{\text{oral}} \quad (6.27)$$

where  $c''(t)$  is plasma concentration of the tracer mixed to oral glucose and  $z_{\text{oral}}$  is the tracer-to-tracee ratio of the oral glucose administration. The endogenous glucose profile, which looks roughly like a delayed version of  $P(t)$ , can then be compared with the concentration of the tracer infused intravenously,  $c'(t)$ . If the tracer has been infused in a successful way, so as to match satisfactorily the profile of  $P(t)$ , the plasma profiles of  $c'(t)$  and  $C_{\text{end}}(t)$  will change in parallel and their tracer-to-tracee ratio,  $z_{\text{end}}(t)$ , will be constant. In other words, instead of calculating  $P(t)$  as the difference between the estimates of  $Ra(t)$  and of the appearance rate of orally administered glucose, one first calculates  $C_{\text{end}}(t)$  and uses it, in conjunction with  $z_{\text{end}}(t)$ , to estimate  $P(t)$ . Figure 6.6 shows the results of a study (Taylor *et al.*, 1997) in which glucose production during a meal was estimated with the approach just described.

Two tracers were employed: a stable tracer,  $[2\text{-}^2\text{H}]\text{glucose}$ , and a radioactive tracer,  $[3\text{-}^3\text{H}]\text{glucose}$ . The former was added to the meal, while the latter was infused in such a way as to mimic the expected time course of  $P(t)$ . The format of  $[3\text{-}^3\text{H}]\text{glucose}$  administration was refined on the basis of the results obtained in the first three subjects who underwent the study and was then kept fixed in the other subjects participating in the study.  $[3\text{-}^3\text{H}]\text{glucose}$  plasma concentration well matched endogenous glucose concentration derived from the  $[2\text{-}^2\text{H}]\text{glucose}$  data (Figure 6.6, upper panel). This provided a relatively stable endogenous tracer-to-tracee ratio, or  $[3\text{-}^3\text{H}]\text{glucose}$  over endogenous glucose concentration (Figure 6.6, middle panel), thus allowing a presumably accurate estimate of  $P(t)$  (Figure 6.6, lower panel). It is interesting to observe that in the period when  $P(t)$  was inhibited (0–200 min), the clamp of endogenous glucose concentration was reasonably good. Clamping  $z_{\text{end}}(t)$  between 200 and 320 min was more difficult because the time when  $P(t)$  began its resumption to the basal level varied markedly among subjects. In that period, both tracer and endogenous glucose concentration were very low so that their ratio was extremely sensitive to changes in either tracer or endogenous glucose concentration. Thus, even a small increase in tracer concentration not accompanied by a concomitant increase in endogenous glucose concentration induced a noticeable increase in  $z_{\text{end}}(t)$ .

It is worth noting that such a dual-tracer protocol allows minimisation of the nonsteady-state error associated with the estimate of  $P(t)$ , but not of the error associated with the estimate of  $Ra(t)$ . In fact, whereas the estimate of  $P(t)$  relies on the tracer-to-tracee ratio of the plasma concentrations of the intravenous tracer and endogenous glucose, the estimate of  $Ra(t)$  relies on the tracer-to-tracee ratio of the plasma concentrations of the same tracer and total glucose. If the former  $z(t)$  is almost constant, the latter will change considerably, thus making it difficult to accurately estimate  $Ra(t)$ . In particular, one can expect an underestimation of  $Ra(t)$  in the initial part of the test (when  $z(t)$  increases) and a subsequent overestimation (when  $z(t)$  decreases). Of

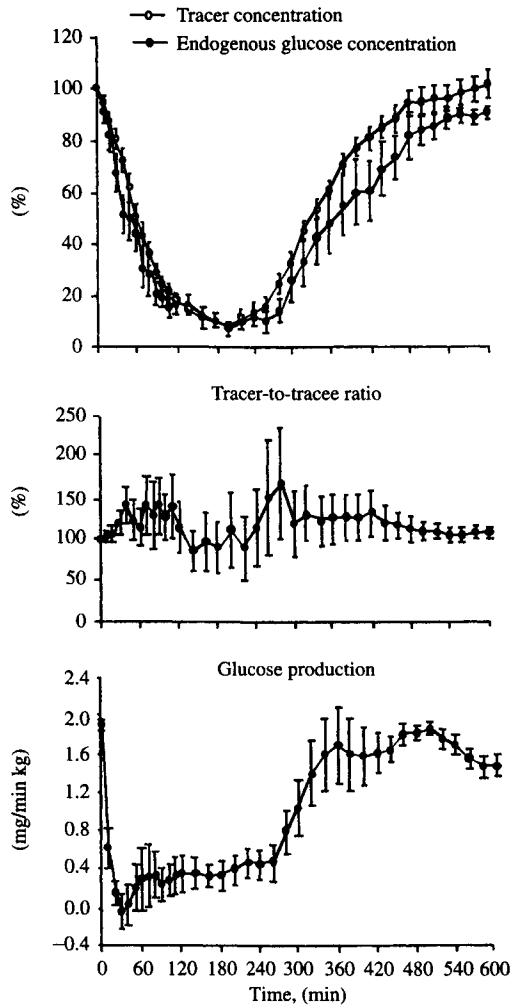


**Figure 6.6.** The tracer-to-tracee-ratio clamp technique for estimating glucose production during a meal (Taylor *et al.*, 1997). *Upper panel:* endogenous glucose concentration and concentration of the tracer infused so as to mimic the expected glucose production profile (percent with respect to basal). *Middle panel:* endogenous tracer-to-tracee ratio (percent with respect to basal). *Lower panel:* estimated profile of glucose production.

course, the same trend can be expected for the estimate of the appearance rate of the glucose administered orally, which can be derived by subtracting  $P(t)$  from  $Ra(t)$ . To accurately estimate  $Ra(t)$ , one must resort to a third tracer that will be administered intravenously as a primed continuous infusion in the

premeal steady state and as a variable infusion during the meal in such a way as to mimic the expected time course of  $Ra(t)$ .

### 6.6.2. ASSESSMENT OF $Rd$ AND $U$

In nonsteady state,  $Rd(t)$  and  $U(t)$  are no longer equal, and, in general, both of them require a model of system to be estimated (Mari *et al.*, 1994; Caumo *et al.*, 1995). Nevertheless, it is easy to recognise that the assessment of  $Rd(t)$  is less problematic than that of  $U(t)$  because of the different relationship that these two fluxes have with  $Ra(t)$ :

$$Rd(t) = Ra(t) - \frac{dQ_1(t)}{dt} \quad (6.28)$$

$$U(t) = Ra(t) - \frac{dQ_T(t)}{dt} \quad (6.29)$$

Both  $Rd(t)$  and  $U(t)$  can be derived from  $Ra(t)$ , which, as shown previously, can be accurately calculated, even with an approximate model, by resorting to the tracer-to-tracee ratio clamp. However, whereas the estimation of  $Rd(t)$  requires only measurement of the rate of change of the substance mass in the accessible pool, estimation of  $U(t)$  requires the knowledge of the rate of change of the substance mass in the nonaccessible compartments as well. Estimation of  $Rd(t)$  is thus relatively easier than that of  $U(t)$ . In fact, if the volume of the accessible pool is available,  $Rd(t)$  can be accurately measured — without the need of postulating a model of the system — by keeping  $z(t)$  constant. In contrast, the estimation of  $U(t)$  always requires a model of the system (accessible and nonaccessible pools). Despite the fact that  $Rd(t)$  pertains only to the accessible pool, its estimation is important because its knowledge allows inferences concerning  $U(t)$ . In fact, for a system that starts in steady state, goes into a nonsteady-state period, and then returns to the former steady state, the following relationship between  $Rd(t)$  and  $U(t)$  holds (Caumo *et al.*, 1995):

$$AUC[Rd(t)] = AUC[U(t)] \quad (6.30)$$

where  $AUC$  denotes the area under the curve. A more specific relationship between the time courses of  $Rd(t)$  and  $U(t)$  during the nonsteady state can be derived if one assumes that the only time-varying parameter is the irreversible loss of the accessible pool (Caumo *et al.*, 1995). Particularly, for a system that goes into a nonsteady-state period in which substance concentration increases, one has:

$$Rd(t) > U(t) \quad (6.31)$$

Conversely, for a system that goes into a period in which substance concentration decreases, one has:

$$Rd(t) < U(t) \quad (6.32)$$

## 6.7. CONCLUSIONS

In this chapter, focus has been placed on tracer experiment design strategies needed to quantitate production and utilisation fluxes of a substance under both steady- and nonsteady-state conditions. The steady-state problem is easy to tackle, and it has been emphasised that, under steady-state conditions, approaches to a rapid attainment of the tracer steady state require attention in selecting the ratio between the priming dose and the constant infusion. The nonsteady-state situation is far more complex, and the adoption of “intelligent” infusion strategies becomes a must. In particular, it has been shown that, under nonsteady-state conditions, the tracer infusion should be varied in such a way that the tracer-to-tracee ratio remains as constant as possible to reduce the impact of model error. In this context, the partitioning of the tracee source and concentration into two components, endogenous and exogenous, provides a general framework that helps the investigator to achieve this goal under various experimental conditions.

## 6.8. REFERENCES

- Alzaid, A. A., S. F. Dinneen, D. J. Turk, *et al.* Assessment of insulin action and glucose effectiveness in diabetic and nondiabetic humans. *J Clin Invest* 94(1994):2341–48.
- Butler, P. C., A. Caumo, A. Zerman, *et al.* Methods for assessment of the rate of onset and offset of insulin action during nonsteady state in humans [see comments]. *Am J Physiol* 264(1993):E548–60.
- Carson, E. R., C. Cobelli and L. Finkelstein. 1983. *The Mathematical Modelling of Metabolic and Endocrine Systems*. New York: Wiley.
- Caumo, A., M. Homan, H. Katz, *et al.* Glucose turnover in presence of changing glucose concentrations: error analysis for glucose disappearance. *Am J Physiol* 269(1995):E557–67.
- Cobelli, C., A. Mari and E. Ferrannini. Non-steady state: error analysis of Steele’s model and development for glucose kinetics. *Am J Physiol* 252(1987):E679–89.
- Cobelli, C., and G. Toffolo. Constant specific activity input allows reconstruction of endogenous glucose concentration in non-steady state. *Am J Physiol* 258 (*Endocrinol. Metab.*, vol. 21) (1990):E1037–40.
- Cobelli, C., G. Toffolo and D. M. Foster. Tracer-to-tracee ratio for analysis of stable isotope tracer data. *Am J Physiol* 262(1992):E968–75.
- Coggan, A. R., C. A. Raguso, B. D. Williams, *et al.* Glucose kinetics during high-intensity exercise in endurance-trained and untrained humans [see comments]. *J Appl Physiol* 78(3)(1995): 1203–7.
- DeFronzo, R. A., J. D. Tobin and R. Andres. Glucose clamp technique: a method for quantifying insulin secretion and resistance. *Am J Physiol* 237(3)(1979):E214–23.



- Finegood, D. T., R. N. Bergman and M. Vranic. Estimation of endogenous glucose production during hyperinsulinemic-euglycemic glucose clamps: comparison of unlabeled and labeled exogenous glucose infusates. *Diabetes* 36(1987):914–24.
- Hother-Nielsen, O. and H. Beck Nielsen. On the determination of basal glucose production rate in patients with type 2 (non-insulin-dependent) diabetes mellitus using primed-continuous 3-3H-glucose infusion. *Diabetologia* 33(10)(1990):603–10.
- Hovorka, R., D. J. Eckland, D. Halliday, *et al.* Constant infusion and bolus injection of stable-label tracer give reproducible and comparable fasting HGO. *Am J Physiol* 273(1 Pt 1)(1997): E192–201.
- Mari, A., P. Butler, A. Caumo, *et al.* On the calculation of glucose rate of disappearance in nonsteady state. Letter to the Editor. *Am J Physiol* 265(1994):E825–28.
- Norwich, K. N., Measuring rates of appearance in systems which are not in steady state. *Can J Physiol Pharmacol* 51(1973): 91–101.
- Norwich K. N. 1977. *The Kinetics of Tracers in the Intact Organism*. Oxford, UK: Pergamon.
- Taylor, R., I. Magnusson, D. L. Rothman, *et al.* Direct assessment of liver glycogen storage by <sup>13</sup>C nuclear magnetic resonance spectroscopy and regulation of glucose homeostasis after a mixed meal in normal subjects. *J Clin Invest* 97(1973):126–32.

# Physiological Modelling of Positron Emission Tomography Images

Alessandra Bertoldo and Claudio Cobelli

## 7.1. INTRODUCTION

Positron emission tomography (PET) has made it possible to detect accurately and noninvasively at the regional level (i.e., organ and tissue), the *in vivo* concentration of radiopharmaceuticals tagged with positron emitters. Image analysis can be made both qualitatively and quantitatively. For some clinical PET studies, a qualitative analysis is appropriate to answer biological questions, such as when the localisation of metabolic defects is the principal purpose of the study. However, quantitative information often is necessary, and this requires interpretation of the PET tracer measurement with a mathematical model of the underlying physiological process. PET kinetic modelling allows, for example, the estimation of the glucose metabolic rate and blood flow in the brain (Phelps *et al.*, 1979; Iida *et al.*, 1986), in skeletal muscle (Kelley *et al.*, 1999a; Kelley *et al.*, 1996; Ruotsalainen *et al.*, 1997), and in myocardium (Gambhir *et al.*, 1989; Bergman *et al.*, 1984), as well as estimation of receptor affinity in specific cerebral structures (Wong *et al.*, 1986). After presenting fundamentals on modelling strategies and on measurement error, this chapter gives the quantitation of three physiological processes, namely, glucose metabolism, blood flow, and ligand-receptor interaction.

## 7.2. MODELLING STRATEGIES

Various models have been proposed in the past 20 years to convert the radioactive tracer concentrations detected by a PET tomograph in an organ or tissue (more precisely, in a region of interest [ROI] or in a unit of image [pixel or voxel]) into measures of physiological parameters. The most frequently used belong to three model classes: compartmental models, input-output (I/O) models, and graphical methods. While I/O models and graphical methods are essentially linear modelling techniques used for quantitation of physiological systems in steady state, compartmental models can be linear or nonlinear and also can describe their nonsteady-state behaviour. In addition, the quantitative physiological portrait provided by compartmental models is richer than the one of I/O models and graphical methods. Clearly, all this is at the expense of an increased modelling effort.

*Compartmental models* are widely employed for describing regional tracer kinetics since the landmark contribution of Sokoloff *et al.* (1977). One must postulate a linear or nonlinear structure in number of compartments and interconnections and resolve it from the data (Carson *et al.*, 1983; Jacquez, 1996; Cobelli *et al.*, 2000). The structure must have firm and sound grounds in biochemistry and physiology since one usually describes the intimate function of the system in terms of diffusion, transport, metabolism, or receptor-ligand binding. In the following paragraph, we will see several examples of linear and nonlinear compartmental models discussing glucose metabolism, blood flow, and receptor-ligand interaction. More details are given on the theory of compartmental models and their identification from the data in several other studies (Carson *et al.*, 1983; Jacquez, 1996; Cobelli *et al.*, 2000).

*Input-output models* give, at variance with compartmental models, only a black-box representation of the physiological system. The most widely employed I/O model is the so-called *spectral analysis (SA) method* introduced by Cunningham *et al.* (1993) and generalised by Bertoldo *et al.* (1999). If the system is linear, the impulse response can be written as:

$$h(t) = \sum_{j=1}^M \alpha_j e^{-\beta_j t} \quad (7.1)$$

with  $\beta_j \geq 0$ , for every  $j$ , and the tissue tracer concentration  $C_i(t)$  is simply the convolution of  $h(t)$  with the plasma tracer concentration  $C_p(t)$ :

$$C_i(t) = \sum_{j=1}^M \alpha_j \int_0^t C_p(\tau) e^{-\beta_j(t-\tau)} d\tau \quad (7.2)$$

The estimation of  $\alpha_j$  and  $\beta_j$  from the data provides useful insight into the system behaviour. For the sake of reasoning, let's make a distinction between low, intermediate, and high eigenvalues  $\beta_j$  (also referred to as frequency components, thus the term *spectral analysis*).

The amplitude  $\alpha$  corresponding to the highest eigenvalue ( $\beta \rightarrow \infty$ ) gives a measure of the vasculature within the ROI since  $\int_0^t C_p(\tau)e^{-\beta(t-\tau)}d\tau \rightarrow (1/\beta)C_p(t)$ . The number of amplitudes  $\alpha_i$  corresponding to the intermediate  $\beta_i$  gives the number of reversible compartments that can be discriminated in the tissue. However, nothing can be said in terms of compartment connectivity; for example, two amplitudes at the intermediate frequencies do not establish whether the corresponding reversible tissue compartments are parallel (heterogeneous tissue) or in cascade (homogeneous tissue) since these two structures are kinetically indistinguishable. Finally, the amplitude  $\alpha$  corresponding to the lowest eigenvalue ( $\beta \rightarrow 0$ ) reveals the presence of an irreversible process within the region since  $\int_0^t C_p(\tau)e^{-\beta(t-\tau)}d\tau \rightarrow \int_0^t C_p(\tau)d\tau$ .

Thus, the intermediate- and low-frequency components of the spectrum reflect the extravascular behaviour of the tracer or the activity of the tracer within the tissue.

These models, by definition, cannot provide a physiological interpretation of the system but are of tremendous help in the model selection process. In fact, if used in conjunction with sound parameter-estimation techniques and parsimony criteria (Bertoldo *et al.*, 1999), they provide a statistically sound, model-independent guide to characterise the reversible and irreversible system components and estimate the minimum number of system compartments. Sometimes SA also is used to obtain kinetic parameters of the system (Meikle *et al.*, 1998a; Meikle *et al.*, 1998b; Richardson *et al.*, 1996; Turkheimer *et al.*, 1994). However, in this case it is associated with a specific compartmental or noncompartmental system structure and thus gives the same answer of the underlying model.

**Graphical methods** are appealingly easy to use and for this reason are very popular in the quantitation of PET images. Generally, they estimate the physiological parameters by performing simple calculations on the plasma and tissue time activity curves. Even if these methods are easily implemented, one has to keep in mind the hypotheses on which they are based. Graphical methods emerge from simplifying a more complex system model, often compartmental, so violation of these simplifying assumptions can lead to an unreliable or an under- or overestimate of the physiological parameter. Finally, these models allow only the estimation of some macroscopic parameters and do not portray the microscopic nature of the physiological process. For example, in a study with a PET glucose analogue, a graphical method can provide the metabolic rate of glucose but not the rate constants of transport into and

out of the tissue. In sections 7.4 and 7.6, we shall discuss two widely used graphical methods for quantifying glucose metabolism and ligand-receptor interaction.

### 7.3. POSITRON EMISSION TOMOGRAPHY MEASUREMENT ERROR

A reliable description of PET measurement error is crucial for sound model identification and for estimation of the physiological parameter of interest. An important practical limitation of radionuclide imaging and of PET in particular is the small number of counts and the resulting large statistical uncertainty (noise). In digital scintigraphic images, each picture element (pixel or voxel in three-dimensional [3-D] reconstruction method) is characterised by a number of counts. From radioactive tracer theory, the random error of the number of counts in a given pixel is characterised by Poisson statistics, which are variance equal to the counts, if the pixel count is independent of that in the other image pixels. This is not true in PET. Specifically, in tomographic image reconstruction by filtered back-projection, the counts in a given bin of the projection image data are distributed among the pixels along the sampling line and subsequently removed from the inappropriate pixels by mathematical filtering. Thus, the arithmetic operations composing back-projection propagate the random error in the projection image data among all the pixels along the sampling line.

Although it is difficult to generally characterise the statistical uncertainty in tomographic images, there has been significant work in describing the noise in two-dimensional (2-D) PET images (Alpert *et al.*, 1982; Budinger *et al.*, 1978; Budinger *et al.*, 1977; Carson *et al.*, 1993; Huesman *et al.*, 1984; Huesman *et al.*, 1977), while less is available for the 3-D images (Defrise *et al.*, 1990; Pajevic *et al.*, 1998). One of the first contributions was that of Budinger *et al.* (1977), where the percent standard deviation (%SD) in a single uniform object in a tomographic image reconstructed by using a ramp filter was derived as:

$$\%SD = 1.2 \frac{(\text{number of resolution cells in the object})^{3/4}}{(\text{total number of events})^{1/2}} \times 100 \quad (7.3)$$

where the factor 1.2 is related to the particular form of the filter function (a ramp here) and a resolution cell is a square area within the object whose sides are equal to the linear sampling distance. The formula also shows the relationship between the total number of counts required to achieve a specified %SD and the number of resolution cells in an object in a reconstructed tomographic image. For example, to achieve a 20% uncertainty in an image of

$3 \cdot 10^3$  resolution cells, the formula predicts that  $6 \cdot 10^6$  total events are necessary; however, if one increases to  $10^4$  the resolution cell number,  $36 \cdot 10^6$  total events are required.

This simple equation has been widely used to describe ROI noise, but it does not explicitly account for the many factors that contribute to noise in both 2-D and 3-D PET images, such as attenuation, correction for random coincidences, correction for scattered radiation, and change in statistical quality due to radioactive decay during measurement with short-lived radionuclides. Alpert *et al.* (1982), observed that in 2-D PET the measured coincidence can be considered the sum of three factors: the true coincidence, the random coincidence, and the scatter measured values. Thus, the recovery of the true coincidence rate can be obtained at the expense of an increase in the statistical noise due to the subtraction of two "not true" values. However, prompt scatter is not easily measurable and usually is minimised by appropriate shielding of the tomograph, whereas random coincidence rates can be routinely estimated during each experiment. Neglecting the prompt scatter contribution, the true coincidence values can be estimated by subtracting the random coincidences from the measured ones. Moreover, photon attenuation decreases the signal, thereby increasing the relative noise level. A variance formula has been derived that explicitly includes all these effects. In particular, if the filtered back-projection algorithm is employed, the reconstructed concentration of radioactivity,  $\hat{C}$ , and its variance,  $\hat{\sigma}^2$ , are given by:

$$\hat{C}(x, y) = \left(\frac{\pi}{m}\right)^2 \sum_{j=1}^m \int [\hat{p}_p(\phi_j, u) - \hat{p}_r(\phi_j, u)] A_M(\phi_j, u) S(u) h(x' - u) du \quad (7.4)$$

$$\hat{\sigma}^2(x, y) = \left(\frac{\pi}{m}\right)^2 \sum_{j=1}^m \int [\hat{p}_p(\phi_j, u) - \hat{p}_r(\phi_j, u)] A_M^2(\phi_j, u) S^2(u) h^2(x' - u) du \quad (7.5)$$

where  $\phi$  is the projection angle,  $p$  the projection measurement,  $h$  the reconstruction filter,  $m$  the number of projections,  $A$  the attenuation correction,  $S$  the correction factor for detector nonuniformity (assumed to be noiseless), with subscripts  $p$  and  $r$  denoting measured and random coincidences, respectively.

Huesman *et al.* (1977, 1984) derived a formula to calculate 2-D ROI variance directly from the projection data without image reconstruction, but usually ROIs are drawn on images long after data acquisition. To permit a more practical approach, Carson *et al.* (1993) developed an approximation formula that determines the variance of ROI values without using the raw data projection data like in the formula of Huesman *et al.* This formula was derived by applying a series of approximations to the filtered back-projection reconstruction algorithm and gives an approximation of the variance of an

arbitrary ROI and not an exact value like the one derived in Alpert *et al.* (1982). In particular, it requires the filtered back-projection algorithm and accounts for radioactivity distribution, attenuation, randoms, scatter, deadtime, detector normalisation, scan length, decay, and reconstruction filter. If  $F$  is the mean value of the  $n$  pixels in the ROI:

$$F = \frac{1}{n} \sum_{i=1}^n f_i \quad (7.6)$$

where  $f_i$  is the individual pixel value, the variance of the ROI value is given by:

$$\sigma^2(F) = \frac{1}{n^2} \sum_{i=1}^n \sum_{j=1}^n \text{Cov}(f_i, f_j) \cong \frac{\hat{V}}{n^2} \sum_{i=1}^n \sum_{j=1}^n \rho(d_{i,j}) \quad (7.7)$$

where  $\sigma^2$  is the variance of the ROI,  $\hat{V}$  the average pixel variance within the ROI,  $n$  number of pixels in the ROI, Cov the covariance matrix, and  $\rho(d)$  is the predicted correlation as a function of interpixel distance. It is possible to show that:

$$\sigma^2(F) = \frac{\hat{V}}{n^2} \sum_{i=1}^n \sum_{j=1}^n \frac{\sum_{\theta=1}^{n_\theta} \sum_{r=1}^{n_r} h_{r,\theta}^{(i)} h_{r,\theta}^{(j)} A_{r,\theta}^2 N_{r,\theta}^2 W_{r,\theta}^2 p_{r,\theta}}{\sqrt{\left[ \sum_{\theta=1}^{n_\theta} \sum_{r=1}^{n_r} (h_{r,\theta}^{(i)})^2 A_{r,\theta}^2 N_{r,\theta}^2 W_{r,\theta}^2 p_{r,\theta} \right] \left[ \sum_{\theta=1}^{n_\theta} \sum_{r=1}^{n_r} (h_{r,\theta}^{(j)})^2 A_{r,\theta}^2 N_{r,\theta}^2 W_{r,\theta}^2 p_{r,\theta} \right]}} \quad (7.8)$$

where  $h_{r,\theta}^{(i)}$  is the reconstruction matrix value for the pixel  $i$ ,  $A_{r,\theta}$  the attenuation correction factor,  $N_{r,\theta}$  the normalisation correction factor,  $W_{r,\theta}$  the wobble correction factor, and  $p_{r,\theta}$  the total counts for angle  $\theta$  and ray  $r$ .

All these formulae require some knowledge of the tomographic device and reconstruction method. To overcome potential difficulties in using (7.5) or (7.8) to estimate the variance, Mazoyer *et al.* (1986) presented a simple formula for the variance of measurement error:

$$\sigma_{C(t_k)}^2 = \frac{C(t_k)}{t_k - t_{k-1}} = \frac{C(t_k)}{\Delta t_k} \quad (7.9)$$

where  $C(t_k)$  represents the mean value of the activity,  $a(t)$ , over the time interval  $\Delta t_k = t_k - t_{k-1}$ , meaning  $a(t_k) = C(t_k) \cdot \Delta t_k$ . Note that if  $a(t_k)$  has a

Poisson distribution, this means  $\sigma_{a(t_k)}^2 = a(t_k)$ ,  $C(t_k)$  has a variance:

$$\sigma_{C(t_k)}^2 = \frac{\sigma_{a(t_k)}^2}{\Delta t_k^2} = \frac{a(t_k)}{\Delta t_k^2} = \frac{C(t_k)}{\Delta t_k} \quad (7.10)$$

This approach was used by Delforge *et al.* (1990, 1995, 1999) in studies on receptor-ligand system and recently by ourselves in brain and myocardium glucose metabolism human studies (Bertoldo *et al.*, 1998). This formula is appealing because it is independent from the particular PET scanner and reconstruction algorithm. The formula assumes that the noise of  $C(t_k)$  is independent of the activities in the neighbouring ROI or pixel area.

Three-dimensional PET offers higher sensitivity than 2-D PET because of the increased number of lines of response (LOR) detected in 3-D PET when the septa are removed. However, this increase in sensitivity is not uniform throughout the whole image volume. In the region near both ends of the scanner, the sensitivity is lower than in the central regions because fewer oblique LORs are detected. Therefore, the noise also becomes a function of the spatial location of the concerned region. Pajevic *et al.* (1998) have analysed the noise characteristic of 2-D and 3-D images obtained from the General Electric Advance PET scanner. The results of this study show that 3-D noise decreases by 9, 15, and 18% with respect to 2-D for ROIs that cover 2, 4, and 10 slices, respectively, in the central regions of the scanner, and the ROI noise ratio between 3-D and 2-D is independent of the transaxial dimension of the ROI.

## 7.4. MODELS OF REGIONAL GLUCOSE METABOLISM

The ideal tracer to quantitate regional glucose metabolism is [ $^{11}\text{C}$ ]-glucose. However, the interpretative model of its tissue activity must describe the complexity of [ $^{11}\text{C}$ ]-glucose kinetics, which means it has to explicitly account for its metabolic products along the glycolysis and glycogenosynthesis pathways. A rich compartmental model is probably the model of choice, but there is a necessarily limited information content of PET data. A parsimonious model has been proposed by Blomqvist *et al.* (1985, 1990) and used by Powers *et al.* (1995) and Fanelli *et al.* (1998).

The difficulties in handling the complexity of  $^{11}\text{C}$ -glucose kinetics has favoured an alternative strategy inspired by the landmark model of 2- $^{14}\text{C}$ Deoxyglucose kinetics developed by Sokoloff *et al.* (1977) in the brain. The elected tracer was [ $^{18}\text{F}$ ]fluorodeoxyglucose ([ $^{18}\text{F}$ ]FDG). [ $^{18}\text{F}$ ]FDG is a glucose analogue, which competes with glucose for facilitated transport sites and with hexokinase for



phosphorylation to [ $^{18}\text{F}$ ]FDG-6-phosphate ([ $^{18}\text{F}$ ]FDG-6-P). The advantage of this analogue is that [ $^{18}\text{F}$ ]FDG-6-P is trapped in the tissue and released very slowly. In other words, [ $^{18}\text{F}$ ]FDG-6-P cannot be metabolised further, while glucose-6-P does so along the glycolysis and glycogenosynthesis pathways. The major disadvantage of [ $^{18}\text{F}$ ]FDG is the necessity to correct for the differences in transport and phosphorylation between the analogue [ $^{18}\text{F}$ ]FDG and glucose. A correction factor called lumped constant (LC) can be employed to convert [ $^{18}\text{F}$ ]FDG fractional uptake (but not the microscopic [ $^{18}\text{F}$ ]FDG transport rate parameters) to that of glucose. The value of LC is dependent upon the type of tissue (brain, skeletal muscle, myocardium) and may also be dependent upon specific study conditions, such as insulin and competing substrate concentrations or oxygen availability. Several studies are available on LC in the human brain (Hasselbalch *et al.*, 1996; Spence *et al.*, 1998) and myocardium (Botker *et al.*, 1999; Krivokapich *et al.*, 1987) tissue, but few in human skeletal muscle (Utriainen *et al.*, 1998; Kelley *et al.*, 1999b).

In Section 7.4.1, we discuss first the [ $^{11}\text{C}$ ]glucose model and then the various [ $^{18}\text{F}$ ]FDG models that have been proposed for regional studies of glucose metabolism. Glucose metabolism is assumed in steady state, and tracer theory predicts that [ $^{11}\text{C}$ ]glucose and [ $^{18}\text{F}$ ]FDG kinetics are described by linear time-invariant differential equations.

### 7.4.1. [ $^{11}\text{C}$ ]GLUCOSE MODELS

[ $^{11}\text{C}$ ]glucose is the ideal tracer to study regional glucose metabolism with PET since a rich parametric portrait can be obtained that includes the glucose transport and phosphorylation fluxes. However, [ $^{11}\text{C}$ ]glucose modelling must account for the regional loss of all [ $^{11}\text{C}$ ]metabolites, mainly [ $^{11}\text{C}$ ]CO<sub>2</sub>. In 1985, Blomqvist *et al.* proposed a three-compartment model (Figure 7.1) to describe [ $^{11}\text{C}$ ]glucose kinetics in which the loss of tracer was explicitly considered. The model is described by the following equations:

$$\begin{aligned} \dot{C}_e(t) &= k_1 C_p(t) - (k_2 + k_3) C_e & C_e(0) &= 0 \\ \dot{C}_m(t) &= k_3 C_e(t) - \dot{C}_c & C_m(0) &= 0 \end{aligned} \quad (7.11)$$

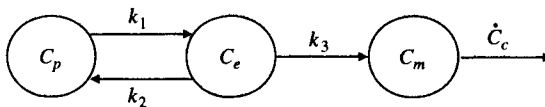


Figure 7.1. The [ $^{11}\text{C}$ ]glucose model of Blomqvist *et al.* (1985).

where  $C_p(t)$  is the arterial concentration of nonmetabolised [ $^{11}\text{C}$ ]glucose in plasma,  $C_e(t)$  the concentration of [ $^{11}\text{C}$ ]glucose in tissue,  $C_m(t)$  the concentration of the various [ $^{11}\text{C}$ ]-labelled metabolic products,  $\dot{C}_c(t)$  denotes the loss of [ $^{11}\text{C}$ ]glucose metabolites,  $k_1$  and  $k_2$  the rate constants of [ $^{11}\text{C}$ ]glucose forward and reverse transcappillary membrane transport, and  $k_3$  the rate constant of [ $^{11}\text{C}$ ]glucose metabolism. The dephosphorylation process was neglected in the model (this parameter is usually denoted  $k_4$  in the literature, thus  $k_4 = 0$ ), and it also is assumed that there are no recirculating labelled metabolites in arterial blood.

By considering that loss of labelled metabolites besides [ $^{11}\text{C}$ ]CO<sub>2</sub> can, to a good approximation, be neglected, the average cumulated loss of [ $^{11}\text{C}$ ]glucose at different times can be described as:

$$C_c(t) = f \int_0^t \Delta_{AV} C_c(\tau) d\tau \quad (7.12)$$

where  $\Delta_{AV} C_c(t)$  is the arteriovenous difference of [ $^{11}\text{C}$ ]CO<sub>2</sub> and  $f$  is the tissue perfusion (blood flow per unit mass of tissue). For model identification,  $C_p(t)$  is used as the known noise-free input. The PET measurement is:

$$C_i(t) = (1 - V_b)(C_e(t) + C_m(t)) + V_b C_b(t) \quad (7.13)$$

where  $C_i$  is the total [ $^{11}\text{C}$ ] activity in the tissue,  $C_b$ , is the [ $^{11}\text{C}$ ] activity in blood, and  $V_b$  (unitless) accounts for the vascular volume present in the tissue. All the four-model parameters  $k_1, k_2, k_3, V_b$  are *a priori* uniquely identifiable (Carson *et al.*, 1983; Cobelli *et al.*, 2000). The model parameters can be estimated, as described in Bertoldo *et al.* (1998), by weighted nonlinear least squares minimising the cost function:

$$\text{WRSS}(\mathbf{p}) = \sum_{j=1}^N w_j [C_i^{\text{obs}}(t_j) - C_i(\mathbf{p}, t_j)]^2 \quad (7.14)$$

where  $C_i^{\text{obs}}$  is the measured PET datum,  $\mathbf{p}$  the vector of unknown model parameters of dimension  $P$ ,  $C_i(\mathbf{p}, t)$  the model prediction, and  $w_j$  the weight of the  $j$ -th datum chosen optimally (Carson *et al.*, 1983) as:

$$w_j = \frac{\Delta t_j}{C_i^{\text{obs}}(t_j)} \quad (7.15)$$

where  $\Delta t_j$  is the length of the scanning interval relative to  $C_i^{\text{obs}}(t_j)$ . Precision of the parameter estimates can be evaluated from the inverse of the Fisher information matrix  $\mathbf{M}$  by:

$$\text{COV}(\hat{\mathbf{p}}) = \gamma \mathbf{M}^{-1} \quad (7.16)$$

where  $\gamma$  is an unknown proportionality constant estimated *a posteriori* (Carson *et al.*, 1983; Cobelli *et al.*, 2000) as:

$$\gamma = \frac{\text{WRSS}(\hat{\mathbf{p}})}{N - P} \quad (7.17)$$

where  $\text{WRSS}(\hat{\mathbf{p}})$  is the value of the cost function evaluated at the minimum.

The model allows the calculation of the fractional uptake of [ $^{11}\text{C}$ ]glucose:

$$K = \frac{k_1 k_3}{k_2 + k_3} \quad (7.18)$$

and the regional metabolic rate of glucose as:

$$rGl = \frac{k_1 k_3}{k_2 + k_3} C_{p-g} \quad (7.19)$$

where  $C_{p-g}$  is the arterial plasma concentration of glucose.

Starting from Blomqvist *et al.* (1990) demonstration that the rate of loss of [ $^{11}\text{C}$ ]CO<sub>2</sub> is a constant fraction of the available amount of labelled metabolites, Powers *et al.* (1995) introduced into the model of Figure 7.1 a fourth rate constant to describe the loss of all labelled metabolites. This model is shown in Figure 7.2.

The model equations are:

$$\begin{aligned} \dot{C}_e(t) &= k_1 C_p(t) - (k_2 + k_3) C_e(t) & C_e(0) &= 0 \\ \dot{C}_m(t) &= k_3 C_e(t) - k_5 C_m(t) & C_m(0) &= 0 \\ \dot{C}_{vb}(t) &= k_5 C_m(t) - k_6 C_{vb}(t) & C_{vb}(0) &= 0 \end{aligned} \quad (7.20)$$

where  $C_p$ ,  $C_e$ ,  $C_m$ ,  $k_1$ ,  $k_2$ , and  $k_3$  have the same meanings as before,  $C_{vb}(t)$  represents the vascular concentration of the metabolites normalised to tissue volume,  $k_5$  the rate constant describing [ $^{11}\text{C}$ ]glucose metabolites leaving the tissue, and  $k_6$  the rate constant of [ $^{11}\text{C}$ ]glucose metabolites washout. In particular,  $k_6$  is defined as  $f/V_b$ , or the reciprocal of the vascular mean transit time.

The PET measurement is described by:

$$C_i(t) = (1 - V_b)(C_e(t) + C_m(t) + C_{vb}(t)) + V_b C_b(t) \quad (7.21)$$

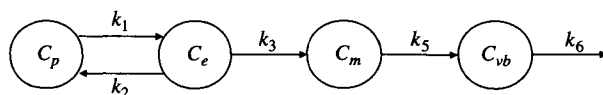


Figure 7.2. The  $^{11}\text{C}$ -glucose model of Powers *et al.* (1995).

where  $C_i$  is total [ $^{11}\text{C}$ ] activity in the tissue and  $C_b$  is [ $^{11}\text{C}$ ]glucose activity in blood. The model is *a priori* nonuniquely identifiable (Carson *et al.*, 1983; Cobelli *et al.*, 2000). It becomes *a priori* uniquely identifiable if  $k_6$  is assumed to be known. Since  $k_6 = f/V_b$ , one can use values for  $V_b$  and  $f$  previously obtained by quantitative analysis of PET images employing, respectively, the [ $^{15}\text{O}$ ]CO and [ $^{15}\text{O}$ ]H $_2$ O tracers. The fractional uptake of [ $^{11}\text{C}$ ]glucose,  $K$ , and the regional metabolic rate of glucose,  $rGl$ , can be estimated by using (7.18) and (7.19). This model does not require venous sampling for [ $^{11}\text{C}$ ]glucose metabolites and does not assume that the loss of labelled metabolites is proportional to regional blood flow. This model has been used by Fanelli *et al.* (1998) to measure brain glucose metabolic rate in poorly controlled insulin-dependent diabetes.

### 7.4.2. [ $^{18}\text{F}$ ]FDG MODELS

#### The 3K Model

The two-tissue three-compartment rate constants model, 3K, proposed by Sokoloff *et al.* (1977) was originally developed for autoradiographic studies in the brain with 2- [ $^{14}\text{C}$ ]deoxyglucose as tracer and subsequently used for PET [ $^{18}\text{F}$ ]FDG studies in the brain and other tissues organs. The 3K model of [ $^{18}\text{F}$ ]FDG kinetics of Sokoloff *et al.* is shown in Figure 7.3, where  $C_p^*$  is [ $^{18}\text{F}$ ]FDG plasma arterial concentration,  $C_e^*$  the [ $^{18}\text{F}$ ]FDG tissue concentration,  $C_m^*$  [ $^{18}\text{F}$ ]FDG-6-P concentration in tissue,  $k_1^*$  and  $k_2^*$ , respectively, the rate constants of [ $^{18}\text{F}$ ]FDG forward and reverse transcapillary membrane transport, and  $k_3^*$  the rate constant of [ $^{18}\text{F}$ ]FDG phosphorylation. The asterisk indicates a tracer analogue and not an ideal tracer; for example, the  $k_i^*$  of Figure 7.3. are different from the  $k_i$  of Figure 7.2.

The kinetics of [ $^{18}\text{F}$ ]FDG in the tissue is described by:

$$\begin{aligned} \dot{C}_e^*(t) &= k_1^* C_p^*(t) - (k_2^* + k_3^*) C_e^*(t) & C_e^*(0) &= 0 \\ \dot{C}_m^*(t) &= k_3^* C_e^*(t) & C_m^*(0) &= 0 \end{aligned} \tag{7.22}$$

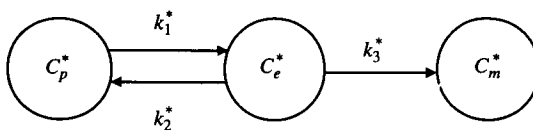


Figure 7.3. The 3K model.

At any time following the introduction of [ $^{18}\text{F}$ ]FDG into the blood, the total concentration of radioactivity in the tissue,  $C_i^*$ , is equal to the sum of the concentrations of [ $^{18}\text{F}$ ]FDG and [ $^{18}\text{F}$ ]FDG-6-P:

$$C_i^*(t) = C_e^*(t) + C_m^*(t) \quad (7.23)$$

With the limited spatial resolution of the PET scanner, however, measurement of radioactivity in a ROI includes the radioactivity in the blood volume present within the tissue, so the measured tracer activity is the sum of the tissue activities and a certain fraction,  $V_b^*$ , of the blood  $^{18}\text{F}$  concentration,  $C_b^*$ :

$$C_i^*(t) = (1 - V_b^*)(C_e^*(t) + C_m^*(t)) + V_b^*C_b^*(t) \quad (7.24)$$

In particular, in brain and skeletal muscle,  $V_b^*$  accounts for the vascular volume present in the tissue ROI, while, for example, in the heart it mainly accounts for the spillover effects from blood to tissue (negligible in brain and skeletal muscle). All the four-model parameters  $k_1^*$ ,  $k_2^*$ ,  $k_3^*$ ,  $V_b^*$  are *a priori* uniquely identifiable (Carson *et al.*, 1983; Cobelli *et al.*, 2000).

The model allows calculation of the fractional uptake of [ $^{18}\text{F}$ ]FDG:

$$K^* = \frac{k_1^*k_3^*}{k_2^* + k_3^*} \quad (7.25)$$

Once  $K^*$  is known, the regional metabolic rate of glucose can be calculated as (Phelps *et al.*, 1979):

$$rGl = \frac{k_1^*k_3^*}{k_2^* + k_3^*} \frac{C_{p-g}}{LC} \quad (7.26)$$

where  $C_{p-g}$  is the arterial plasma glucose concentration and LC is the lumped constant, or the factor that describes the relation between the glucose analogue [ $^{18}\text{F}$ ]FDG and glucose itself. LC is given by:

$$LC = \frac{E^{\text{FDG}}}{E^{\text{GLU}}} \quad (7.27)$$

where  $E^{\text{FDG}}$  and  $E^{\text{GLU}}$  are, respectively, the extraction of [ $^{18}\text{F}$ ]FDG and glucose. For the 3K model, LC becomes:

$$LC = \frac{k_1^*k_3^*}{k_2^* + k_3^*} / \frac{k_1k_3}{k_2 + k_3} \quad (7.28)$$

### The 4K Model

In 1979, Phelps *et al.* proposed a modification of the 3K model by observing that after 120 minutes, following a pulse of [ $^{18}\text{F}$ ]FDG, total tissue activity was

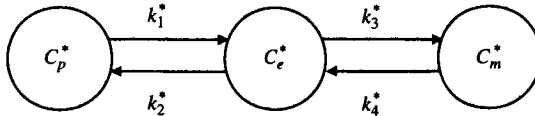


Figure 7.4. The 4K model.

declining, thus indicating a loss of product. The authors allowed dephosphorylation of [ $^{18}\text{F}$ ]FDG-6-P, thus an additional rate constant was incorporated into the 3K model, which becomes a four-rate constants model (4K). The 4K model is shown in Figure 7.4. The meaning of  $C_p^*$ ,  $C_e^*$ ,  $C_m^*$  and of the rate constants is the same as for the 3K model, while  $k_4^*$  is the dephosphorylation rate constant.

The model equations of tissue activity are:

$$\begin{aligned} \dot{C}_e^*(t) &= k_1^* C_p^*(t) - (k_2^* + k_3^*) C_e^*(t) + k_4^* C_m^*(t) & C_e^*(0) &= 0 \\ \dot{C}_m^*(t) &= k_3^* C_e^*(t) - k_4^* C_m^*(t) & C_m^*(0) &= 0 \end{aligned} \quad (7.29)$$

The PET measurement equation is the same as that of the 3K model (7.24). All model parameters ( $k_1^*$ ,  $k_2^*$ ,  $k_3^*$ ,  $k_4^*$ ,  $V_b^*$ ) are *a priori* uniquely identifiable (Carson *et al.*, 1983; Cobelli *et al.*, 2000). Also, for the 4K model, a measure can be obtained of the fractional uptake of [ $^{18}\text{F}$ ]FDG and of regional metabolic rate of glucose: they are given by (7.25) and (7.26), respectively (Phelps *et al.*, 1979).

### The Heterogeneous Model

Schmidt *et al.* (1991, 1992) proposed a model that accounts for the heterogeneous composition of a tissue. In fact, the regions represented in the PET images often are kinetically heterogeneous with respect to structure, blood flow, tracer transport, and metabolism, above all for the brain tissue where white matter and gray matter are difficult to separate in a single ROI. In addition, the limited spatial resolution of the current generation of PET scanners sometimes does not permit an accurate delimitation of a homogeneous region. The model is an extension of the 3K model to a heterogeneous tissue and is shown in Figure 7.5. The heterogeneous tissue is assumed to consist of smaller homogeneous subregions.  $C_{e1}^*$ ,  $C_{e2}^*$ , ...,  $C_{en}^*$  represent [ $^{18}\text{F}$ ]FDG concentration in each homogeneous region,  $C_{m1}^*$ ,  $C_{m2}^*$ , ...,  $C_{mn}^*$  [ $^{18}\text{F}$ ]FDG-6-P concentration in these same subregions,  $k_{1i}^*$ ,  $k_{2i}^*$ ,  $k_{3i}^*$  the corresponding rate constants for transport and phosphorylation of [ $^{18}\text{F}$ ]FDG, and  $C_p^*(t)$  arterial plasma concentration.

The model assumptions are the same as those of the 3K model, only the tissue is now considered heterogeneous. The differential equations describing

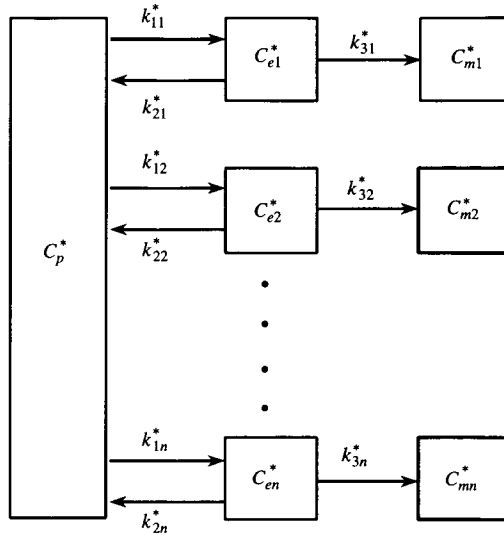


Figure 7.5. The TH model.

the rate of change of [ $^{18}\text{F}$ ]FDG in each subregion are:

$$\begin{aligned} \frac{dC_{e1}^*(t)}{dt} &= k_{11}^* C_p^*(t) - (k_{21}^* + k_{31}^*) C_{e1}^*(t) \quad C_{e1}^*(0) = 0 \\ \frac{dC_{e2}^*(t)}{dt} &= k_{12}^* C_p^*(t) - (k_{22}^* + k_{32}^*) C_{e2}^*(t) \quad C_{e2}^*(0) = 0 \\ &\vdots \\ \frac{dC_{en}^*(t)}{dt} &= k_{1n}^* C_p^*(t) - (k_{2n}^* + k_{3n}^*) C_{en}^*(t) \quad C_{en}^*(0) = 0 \end{aligned} \tag{7.30}$$

Consequently, the rate of change of [ $^{18}\text{F}$ ]FDG in the heterogeneous tissue can be found by summing up the concentration in each subregion weighted by its relative tissue mass,  $w_1, w_2, \dots, w_n$  with  $\sum_{i=1}^n w_i = 1$ :

$$\frac{d\bar{C}_e^*(t)}{dt} = \sum_{i=1}^n w_i \frac{dC_{ei}^*(t)}{dt} = \left( \sum_{i=1}^n w_i k_{1i}^* \right) C_p^*(t) - \left[ \sum_{i=1}^n w_i (k_{2i}^* + k_{3i}^*) C_{ei}^*(t) \right] \tag{7.31}$$

where  $\bar{C}_e^*(t)$  gives the [ $^{18}\text{F}$ ]FDG concentration in the heterogeneous tissue. By defining:

$$\bar{k}_1^* = \sum_{i=1}^n w_i k_{1i}^* \tag{7.32}$$

after a simple manipulation one has:

$$\frac{d\bar{C}_e^*(t)}{dt} = \bar{k}_1^* C_p^*(t) - \frac{\left[ \sum_{i=1}^n w_i (k_{2i}^* + k_{3i}^*) C_{ei}^*(t) \right]}{\left[ \sum_{i=1}^n w_i C_{ei}^*(t) \right]} \bar{C}_e^*(t) \quad (7.33)$$

Defining:

$$k_2^*(t) = \frac{\sum_{i=1}^n w_i k_{2i}^* C_{ei}^*(t)}{\sum_{i=1}^n w_i C_{ei}^*(t)} \quad (7.34)$$

as the parameter describing the efflux of [<sup>18</sup>F]FDG from the heterogeneous tissue to plasma, and

$$k_3^*(t) = \frac{\sum_{i=1}^n w_i k_{3i}^* C_{ei}^*(t)}{\sum_{i=1}^n w_i C_{ei}^*(t)} \quad (7.35)$$

as the parameter describing phosphorylation of [<sup>18</sup>F]FDG to [<sup>18</sup>F]FDG-6-P, then [<sup>18</sup>F]FDG concentration in the tissue becomes:

$$\frac{d\bar{C}_e^*(t)}{dt} = \bar{k}_1^* C_p^*(t) - (k_2^*(t) + k_3^*(t)) \bar{C}_e^*(t) \quad (7.36)$$

The rate of change of [<sup>18</sup>F]FDG-6-P in each subregion is given by:

$$\begin{aligned} \frac{dC_{m1}^*(t)}{dt} &= k_{31}^* C_{e1}^*(t) \quad C_{m1}^*(0) = 0 \\ \frac{dC_{m2}^*(t)}{dt} &= k_{32}^* C_{e2}^*(t) \quad C_{m2}^*(0) = 0 \\ &\vdots \\ \frac{dC_{mn}^*(t)}{dt} &= k_{3n}^* C_{en}^*(t) \quad C_{mn}^*(0) = 0 \end{aligned} \quad (7.37)$$

and thus the rate of change of [<sup>18</sup>F]FDG-6-P in the heterogeneous tissue,  $\bar{C}_m^*$ , becomes:

$$\frac{d\bar{C}_m^*(t)}{dt} = k_3^*(t) \bar{C}_e^*(t) \quad (7.38)$$



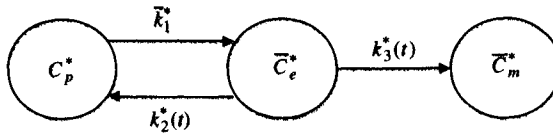


Figure 7.6. The time-variant TH model.

Thus, the resulting model becomes time-variant (Figure 7.6):

$$\begin{aligned} \dot{\bar{C}}_e^* &= \bar{k}_1^* C_p^*(t) - [k_2^*(t) + k_3^*(t)] \bar{C}_e^*(t) & \bar{C}_e^*(0) &= 0 \\ \dot{\bar{C}}_m^* &= k_3^*(t) \bar{C}_e^*(t) & \bar{C}_m^*(0) &= 0 \end{aligned} \tag{7.39}$$

The time-varying parameters for efflux and phosphorylation have been described by an exponential function as:

$$\begin{aligned} k_2^*(t) &= \bar{k}_2^* (1 + A e^{-Bt}) \\ k_3^*(t) &= \bar{k}_3^* (1 + A e^{-Bt}) \end{aligned} \tag{7.40}$$

The PET measurement is described by:

$$C_i^*(t) = (1 - V_b^*) (\bar{C}_e^*(t) + \bar{C}_m^*(t)) + V_b^* C_b^*(t) \tag{7.41}$$

All model parameters,  $\bar{k}_1^*, \bar{k}_2^*, \bar{k}_3^*, A, B, V_b^*$ , are *a priori* uniquely identifiable (Carson *et al.*, 1983; Cobelli *et al.*, 2000).  $[^{18}\text{F}]\text{FDG}$  fractional uptake  $K^*$  can be calculated as (Bertoldo *et al.*, 1998):

$$K^* = \sum_{j=1}^N w_j K_j^* = \sum_{j=1}^N w_j \frac{k_{1j}^* k_{3j}^*}{k_{2j}^* + k_{3j}^*} = \frac{\bar{k}_1^* \bar{k}_3^*}{\bar{k}_2^* + \bar{k}_3^*} \tag{7.42}$$

Finally, the regional metabolic rate of glucose is given by:

$$rGl = \frac{\bar{k}_1^* \bar{k}_3^*}{\bar{k}_2^* + \bar{k}_3^*} \frac{C_{p-g}}{LC} \tag{7.43}$$

### The Patlak Graphical Method

Patlak *et al.* (1983) have developed a graphical method to estimate the regional metabolic glucose rate starting from a general compartmental model of blood-tissue exchange, which means no particular arrangement or number of compartments is assumed. We have to refer the reader to the original reference for the mathematical details and will focus here on the essential ingredients

of the method. By using the tracer tissue and plasma measurements, one plots the points on a Cartesian plane:

$$x = \frac{\int_0^t C_p^*(\tau) d\tau}{C_p^*(t)}, y = \frac{C_i^*(t)}{C_p^*(t)} \quad (7.44)$$

If there is a time  $t^*$  such that for all  $t > t^*$  the amount in the exchangeable compartments is in equilibrium with the plasma tracer concentration, then, if the resultant curve for  $t > t^*$  is a straight line, there is a completely irreversible region where a tracer can enter but cannot move back into blood or into the exchangeable tissue compartments. If, on the contrary, the resultant curve for  $t > t^*$  is a straight line parallel to the abscissa (with slope equal to 0), there is no irreversible region, only reversible regions. Finally, if the resultant curve for  $t > t^*$  is concave, there is a noncompletely irreversible compartment so that there is a slow loss of the tracer from this compartment to blood.

This graphical method applies equally well to heterogeneous and homogeneous tissues (Patlak *et al.*, 1985). In particular, when the Patlak plot is used with [ $^{18}\text{F}$ ]FDG data, if one has a straight line with slope equal to  $m$ , then  $k_4^* = 0$ , thus 3K and TH models are correct and  $rGl$  can be calculated as:

$$rGl = m \frac{C_p}{LC} \quad (7.45)$$

If, on the contrary, the curve is concave,  $k_4^* \neq 0$  and the quantitation of the glucose metabolic rate is more complex.

However, the apparent simplicity of this method is limited by the difficulty to objectively determine the time  $t^*$  after which all the tissue pools can be considered in equilibrium with the blood pool. An incorrect  $t^*$  value can, for example, lead to the conclusion of a product loss from the irreversible compartment, meaning a concave curve for  $t > t^*$ , while this is only due to the lack of equilibration between tissue and plasma compartments. The  $t^*$  value changes with different tracers and different tissue regions. In some cases,  $t^*$  may exceed the time over which a particular experiment can be run, and this makes the method unusable. Finally, the Patlak method permits neither to understand if the tissue is homogeneous nor to estimate other physiological parameters of interest such as the blood-tissue exchange parameters.

## 7.5. MODELS OF [ $^{15}\text{O}$ ]H $_2$ O KINETICS TO ASSESS BLOOD FLOW

In the past, various techniques and models for *in vivo* measurement of blood flow in humans have been developed using as PET tracers [ $^{15}\text{O}$ ]H $_2$ O

and  $[^{13}\text{N}]\text{NH}_3$ . The basis is the Kety and Schmidt method (Kety and Schmidt, 1948), which utilises low concentrations of a freely diffusible, chemically inert gas ( $\text{N}_2\text{O}$ ) and is based on the Fick principle. If a chemically inert substance, which is one that is neither consumed nor produced by the organ or tissue, is introduced into the blood, the amount of the tracer in the organ depends on the difference in rates at which the tracer is brought to the organ by the arterial blood and removed from it by the venous blood:

$$dQ(t)/dt = F_A C_A(t) - F_V C_V(t) \quad (7.46)$$

where  $Q(t)$  is the tracer amount in the organ or tissue;  $F_A$  and  $F_V$  are the steady-state rates of arterial inflow and venous outflow, respectively;  $C_A(t)$  and  $C_V(t)$  are the concentrations of the tracer in the arterial and venous blood.

In steady state,  $F_A = F_V = F$  and the equation becomes:

$$dQ(t)/dt = F[C_A(t) - C_V(t)] \quad (7.47)$$

For tissues that are homogeneous with respect to the rate of perfusion and solubility of tracer, the following equation holds:

$$dQ_i(t)/dt = F_i[C_A(t) - C_{V_i}(t)] \quad (7.48)$$

where  $Q_i(t)$  is the quantity of tracer in the homogeneous tissue  $i$ ;  $F_i$  [ml/min] is the steady-state rate of blood flow through tissue  $i$ ;  $C_{V_i}$  is the venous tracer concentration in the homogenous tissue  $i$ . The difference between homogeneous and heterogeneous tissue is important if one considers, for example, brain studies. The brain is a heterogeneous organ with many component structures functioning more or less autonomously (Sokoloff, 1996). Consequently, blood flow differs in these different structures accordingly with the variety of regulated local functions and the metabolic needs of the structural units.

For a chemically inert tracer, the difference between arterial and venous concentrations can be expressed as (Kety *et al.*, 1951):

$$[C_A(t) - C_{V_i}(t)] = m[C_A(t) - C_i(t)/\lambda_i] \quad (7.49)$$

where  $C_i$  is the tracer concentration in tissue  $i$ ,  $\lambda_i$  [ml/ml] is the tissue/blood partition coefficient for the tracer in tissue  $i$  defined as:

$$\lambda_i = \lim_{t \rightarrow \infty} \frac{C_{\text{tissue}}(t)}{C_{\text{blood}}(t)} \quad (7.50)$$

and  $m$  is a constant between 0 and 1 that represents the effect of factors such as arteriovenous shunts presence and capillary impermeability that limit the equilibration of the tissue with the blood. In the absence of arteriovenous shunts and diffusion limitations of the tracer,  $m = 1$ . Dividing (7.48) by the mass of

tissue  $i$ ,  $W_i$  [gr], and using (7.49), one has:

$$\frac{dC_i(t)}{dt} = \frac{mF_i}{\lambda_i W_i} [\lambda_i C_A(t) - C_i(t)] = \frac{mF_i}{W_i} C_A(t) - \frac{mF_i}{\lambda_i W_i} C_i(t) \quad (7.51)$$

where  $F_i/W_i$  [ml/g/min] is the rate of blood flow per unit mass of tissue, and it is more properly denoted as perfusion,  $f_i$ :

$$\frac{dC_i(t)}{dt} = m f_i C_A(t) - \frac{m}{\lambda_i} f_i C_i(t) \quad (7.52)$$

Even if Kety and Schmidt have developed their method by using  $N_2O$ , the equations also can be applied when the tracer is not a gas. However, it is essential that the tracer be physiologically inert in the concentrations employed and capable of diffusing rapidly.

$[^{15}O]H_2O$  is the most frequently used positron-emitting tracer for the measurement of blood perfusion by PET. By using  $[^{15}O]H_2O$ , it was possible to develop a simple, reliable, and noninvasive method to quantitate cerebral blood flow (Iida *et al.*, 1986) and skeletal muscle blood flow (Ruotsalainen *et al.*, 1997) in humans. The method does not require the use of local anaesthesia, and, consequently, it minimises the possibility of functional alterations in the tissue or organ. However,  $[^{15}O]H_2O$  tracer is not the only one used to measure blood flow with PET. Often, for myocardial blood flow,  $[^{13}N]$ -labelled ammonia is preferred even if the compartmental model needed to describe the  $[^{13}N]$ -ammonia ( $[^{13}N]NH_3$ ) is more complex than the  $[^{15}O]H_2O$  one. The advantage is that  $[^{13}N]NH_3$  gives high-contrast, cross-sectional images of the myocardium since the tracer moves from the vascular space to tissue by both active transport (sodium-potassium pump) and passive diffusion. Once inside cells, this tracer is metabolised on the contrary of labelled water. These properties together with the high tissue retention fraction permit to obtain high-contrast, cross-sectional images of the myocardium.

$[^{15}O]H_2O$  tracer has the important property that once introduced into the tissue or organ, it is not involved in any biochemical reaction (i.e., inert tracer). Moreover,  $[^{15}O]H_2O$  is nearly completely diffusible (even if Eichling *et al.*, 1974, showed that there is some limitation in the  $[^{15}O]H_2O$  diffusion) so that the  $m \approx 1$  approximation is reasonable.

The transport of  $[^{15}O]H_2O$  across the capillary wall is quite fast. Furthermore, the cell membrane usually is not a large barrier for water transport. Therefore, the vascular, interstitial, and cellular spaces can be merged into a single compartment. At this point, it is simple to develop the compartmental model (Figure 7.7) to describe the  $[^{15}O]H_2O$  tracer kinetics under the hypotheses that the tissue is homogeneous and that the tracer is physiologically inert at the concentrations employed and is capable of diffusing rapidly across the capillary wall.

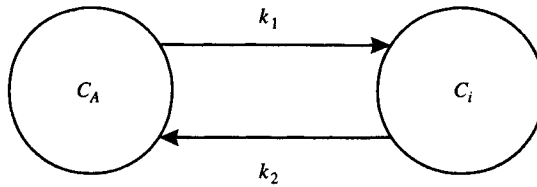


Figure 7.7. The compartmental model for the blood flow estimation with  $[^{15}\text{O}]\text{H}_2\text{O}$ .

By defining  $k_1 = f_i$  [ml/gr/min],  $k_2 = f_i/\lambda_i$  [1/min] one has:

$$\frac{dC_i(t)}{dt} = k_1 C_A(t) - k_2 C_i(t) \quad C_i(0) = 0 \quad (7.53)$$

where  $C_i(t)$  is the tissue concentration of  $[^{15}\text{O}]\text{H}_2\text{O}$  and  $C_A(t)$  is its arterial plasma concentration. The knowledge of the two tracer concentration curves allows the estimation of the two-model parameters and thus of  $k_1/k_2 = \lambda_i$ .

The two parameters of physiological interest are  $f_i$  (reported as rBF or regional blood flow) representing the blood flow value per unit of mass of tissue  $i$  (perfusion) and the value of the tissue or blood partition coefficient  $\lambda_i$ .

The use of  $^{15}\text{O}$  labelled water has the advantage that it allows a series of repeated studies to be carried out in a short experimental time and to follow rapid changes in tissue activity after experimental manoeuvres like, in the case of cerebral tissue, visual or sound stimuli. In dynamic studies with  $[^{15}\text{O}]\text{H}_2\text{O}$  the PET procedure requires the injection at zero time of a tracer bolus and to simultaneously start with the PET scans and arterial blood sampling (usually from a radial artery). Since  $^{15}\text{O}$  has a half-life of 122.1 s, the total scan time is usually less than 3 min; as a result, PET scans and plasma samples must be frequent enough to allow, respectively, the correct detection of tracer kinetics and an accurate description of the input function. It is, however, difficult to obtain exactly the true input function in a human study because the measured plasma arterial curve is affected both by external dispersion due to the sampling system (blood withdrawal speed and catheter length) and by internal dispersion in the arm artery. Another practical problem that might degrade the quality of the measured input function is the time shift between the measured and the true plasma curve, such as the blood tracer concentration in the tissue ROI (Iida *et al.*, 1986). Summarising, the peripherally sampled arterial curve,  $C_c(t)$ , is related to the true input function,  $C_A(t)$ , as:

$$C_c(t + \Delta t) = C_A(t) \otimes d(t) \quad (7.54)$$

where  $\Delta t$  is the time delay of the peripheral arterial curve relative to the true input function and  $d(t)$  is the effective dispersion function usually described

by using a single exponential function:

$$d(t) = \frac{1}{\tau} \exp\left(-\frac{t}{\tau}\right) \quad (7.55)$$

Consequently, the true input function that will be the forcing function of the model can be obtained from the peripheral arterial curve by using deconvolution technique. Even if this technique is widely used to correct the input function for delay and dispersion, it is affected by some approximations. First, the external dispersion in the sampling system (catheter) depends not only on the withdrawal speed and catheter length but also on other factors such as the haematocrit value. In addition, both internal and external dispersions are described by a simple single exponential, which is probably a rough approximation of reality. Starting from these observations and avoiding the invasive arterial blood sampling, Watabe *et al.* (1993) have proposed a new method for the calculation of the rBF that involves the elimination of the arterial input function term during cerebral studies. The model is based on the assumption of two distinct cerebral regions, ROI1 and ROI2, both described by using the compartmental model showed in Figure 7.7:

$$\frac{dC_{i1}(t)}{dt} = k_{11}C_A(t) - k_{21}C_{i1}(t) \quad C_{i1}(0) = 0 \quad (7.56)$$

$$\frac{dC_{i2}(t)}{dt} = k_{12}C_A(t) - k_{22}C_{i2}(t) \quad C_{i2}(0) = 0 \quad (7.57)$$

where it is assumed that the input function,  $C_A(t)$ , is the same for the two regions. By integrating (7.56) and (7.57) twice from time 0 to  $T$ , one has:

$$\int_0^T C_{i1}(t)dt = k_{11} \int_0^T dt \int_0^t C_A(s)ds - k_{21} \int_0^T dt \int_0^t C_{i1}(s)ds \quad (7.58)$$

$$\int_0^T C_{i2}(t)dt = k_{12} \int_0^T dt \int_0^t C_A(s)ds - k_{22} \int_0^T dt \int_0^t C_{i2}(s)ds \quad (7.59)$$

From (7.58) and (7.59), the arterial input function can be eliminated to give:

$$\begin{aligned} \int_0^T C_{i1}(t)dt &= \frac{k_{11}}{k_{12}} \int_0^T C_{i2}(t)dt + k_{22} \int_0^T dt \int_0^t C_{i2}(s)ds \\ &\quad - k_{21} \int_0^T dt \int_0^t C_{i1}(s)ds \end{aligned} \quad (7.60)$$

The method provides regional cerebral blood flow values from the knowledge of the two tissue curves of ROI1 and ROI2 and does not require arterial blood sampling.

## 7.6. MODELS OF THE LIGAND-RECEPTOR SYSTEM

Positron emission tomography allows the study of receptor density and radioligand affinity in the brain and myocardium. Quantification of the ligand-receptor system is of fundamental importance not only in understanding how the brain works (e.g., how it performs the various commands and reacts to stimuli) but also in investigating the pathogenesis of important diseases like Alzheimer's and Parkinson's. In recent years, PET has become an increasingly used tool to quantitate important parameters, such as the receptor density and the binding affinity of radioligands, and several models have been proposed of specific ligand-receptor interactions including dopaminergic (Ito *et al.*, 1999; Backman *et al.*, 1997; Farde *et al.*, 1989) and benzodiazepimergic (Malizia *et al.*, 1998; Sihver *et al.*, 1997; Delforge *et al.*, 1997; Delforge *et al.*, 1995) receptors in the brain, and muscarinic binding sites in the myocardium (Le Guludec *et al.*, 1997; Delforge *et al.*, 1993). In Sections 7.6.1–7.6.4, we discuss some of the most representative models.

### 7.6.1. THE THREE- AND TWO-TISSUE COMPARTMENT MODELS

The ligand-receptor interactions can be schematised as in Figure 7.8. A compartmental model reflecting the major kinetic events is shown in Figure 7.9, where  $C_p$  is the arterial plasma concentration corrected for metabolites,  $C_f$  the concentration of free ligand,  $C_{ns}$  the concentration of nonspecifically bound ligand, and  $C_s$  the concentration of specifically bound ligand.

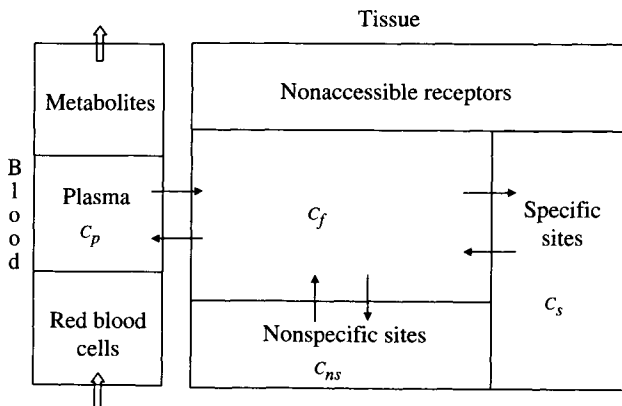


Figure 7.8. The ligand-receptor system.

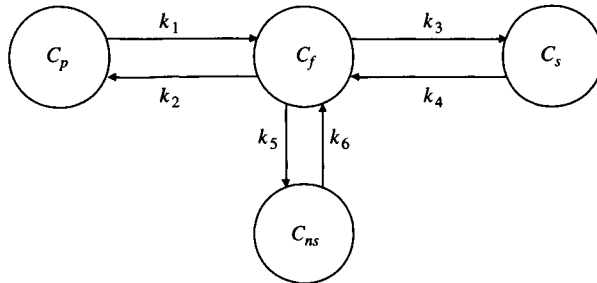


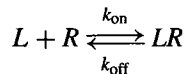
Figure 7.9. The three-tissue compartment model of the ligand-receptor system.

The model equations are:

$$\begin{aligned}
 \dot{C}_f(t) &= k_1 C_p(t) - (k_2 + k_3 + k_5) C_f(t) + k_4 C_s(t) + k_6 C_{ns}(t) C_f(0) = 0 \\
 \dot{C}_s(t) &= k_3 C_f(t) - k_4 C_s(t) \quad C_s(0) = 0 \\
 \dot{C}_{ns}(t) &= k_5 C_f(t) - k_6 C_{ns}(t) \quad C_{ns}(0) = 0
 \end{aligned}
 \tag{7.61}$$

where  $k_1$  [ml/ml/min] is the rate constant of transfer from plasma to free ligand tissue compartment and  $k_2, k_3, k_4, k_5, k_6$  are the rate constants of ligand transfer from tissue to plasma and inside the tissue.

To better understand the physiological meaning of parameters  $k_3$  and  $k_4$ , let's assume that the binding of the ligand to the receptor site is describable as a bimolecular reaction:



where  $L$  represents the ligand,  $R$  the receptor site,  $LR$  the binding product,  $k_{\text{on}}$  is the association rate of the ligand with the receptor sites, and  $k_{\text{off}}$  the dissociation rate of the specifically bound reaction product. In Figure 7.9, one has that  $C_f$  and  $C_s$  represent,  $L$  and  $LR$ , respectively, thus:

$$\frac{dC_s(t)}{dt} = k_{\text{on}} C_f(t) C_r(t) - k_{\text{off}} C_s(t)
 \tag{7.62}$$

where  $C_r$  denotes the concentration of receptors. If  $B_{\text{max}}$  is the total number of available reactions sites, then:

$$B_{\text{max}} = C_s + C_r
 \tag{7.63}$$

and, if the ligand is present in tracer concentration, the concentration  $C_s$  is negligible, and thus:

$$B_{\text{max}} \approx C_r
 \tag{7.64}$$



Equation (7.62) becomes:

$$\frac{dC_s(t)}{dt} = k_{\text{on}}B_{\text{max}}C_f(t) - k_{\text{off}}C_s(t) = k_3C_f(t) - k_4C_s(t) \quad (7.65)$$

with  $k_3 = k_{\text{on}}B_{\text{max}}$  and  $k_4 = k_{\text{off}}$ .

An important parameter is also the equilibrium-binding constant  $K_d$ , which is defined with the ligand-receptor reaction in steady state as:

$$K_d = \frac{C_s}{C_r C_f} = \frac{k_{\text{on}}}{k_{\text{off}}} \quad (7.66)$$

The PET measurement is the result of the tracer present in the tissue and of that present in the blood of the ROI. Consequently, the measurement equation is:

$$C_i(t) = (1 - V_b)(C_f(t) + C_{ns}(t) + C_s(t)) + V_b C_b(t) \quad (7.67)$$

where  $C_b$  is whole blood tracer concentration and  $V_b$  is the vascular volume.

The model is *a priori* only locally (nonuniquely) identifiable; in particular, it admits two solutions for each parameter. To ensure unique identifiability, it is usually assumed that the exchange rates between the free tissue and nonspecific binding pools are sufficiently rapid (compared with the other rates of the model) so that the three-tissue compartment model of Figure 7.10 reduces to the two-tissue model of Figure 7.7, where  $C_{f+ns}(t) = C_f(t) + C_{ns}(t)$  is the free and nonspecific binding tracer concentration.

The model equations are:

$$\begin{aligned} \dot{C}_{f+ns}(t) &= k_1 C_p(t) - (k_2 + k_3)C_{f+ns}(t) + k_4 C_s(t) & C_{f+ns}(0) &= 0 \\ \dot{C}_s(t) &= k_3 C_{f+ns}(t) - k_4 C_s(t) & C_s(0) &= 0 \end{aligned} \quad (7.68)$$

with:

$$k_3 = k_{\text{on}}B_{\text{max}}f \quad (7.69)$$

where  $f$  is given by:

$$f \equiv \frac{C_f}{C_{f+ns}} = \frac{C_f}{C_f + C_{ns}} = \frac{C_f}{C_f \left(1 + \frac{C_{ns}}{C_f}\right)} = \frac{1}{1 + \frac{k_5}{k_6}} \quad (7.70)$$

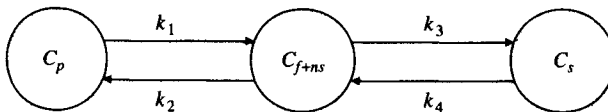


Figure 7.10. The two-tissue compartment model of the ligand-receptor system.

The measurement equation becomes:

$$C_i(t) = (1 - V_b)(C_{f+ns}(t) + C_s(t)) + V_b C_b(t) \tag{7.71}$$

where  $C_b$  is whole blood tracer concentration.

The model of Figure 7.10 is *a priori* uniquely identifiable and, in addition to  $k_1, k_2, k_3, k_4, V_b$ , it is also possible to estimate the binding potential (BP):

$$BP = \frac{B_{max}}{K_d} = \frac{k_3}{k_4} \tag{7.72}$$

### 7.6.2. THE REFERENCE TISSUE MODELS

The ligand-receptor models described previously require the knowledge of the plasma-labelled ligand concentration, which is the forcing function of the models for their identification. A method has been described by Lammertsma *et al.* (1996a, 1996b) that allows the quantification of receptor kinetics without measuring the arterial input function. This method relies on the presence of a region without specific binding of the ligand that can be considered as reference for all the other regions.

The model is shown in Figure 7.11, where  $C_r$  is the concentration in the reference tissue and  $C_p$ , the plasma concentration corrected for metabolites and assumed to be the same for both regions.

The model equations are:

$$\begin{aligned} \dot{C}_r(t) &= k'_1 C_p(t) - k'_2 C_r(t) & C_r(0) &= 0 \\ \dot{C}_{f+ns}(t) &= k_1 C_p(t) - (k_2 + k_3) C_{f+ns}(t) + k_4 C_s(t) & C_{f+ns}(0) &= 0 \\ \dot{C}_s(t) &= k_3 C_{f+ns}(t) - k_4 C_s(t) & C_s(0) &= 0 \end{aligned} \tag{7.73}$$

with

$$k_3 = k_{on} B_{max} f \tag{7.74}$$

$$k_4 = k_{off} \tag{7.75}$$

where  $f$  has the expression of (7.70).

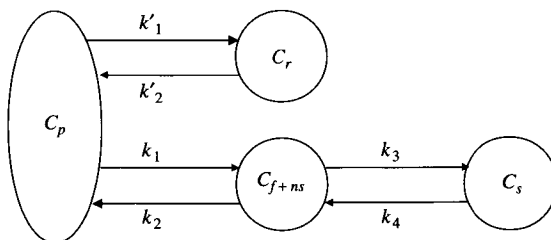


Figure 7.11. The reference ligand-receptor model.

The model is *a priori* uniquely identifiable if one defines  $R_1$  as:

$$R_1 = \frac{k_1}{k'_1} \quad (7.76)$$

and assumes that volume of distribution of the not specifically bound tracer in both tissues is the same, meaning:

$$V_d = \frac{C_{f+ns}}{C_p} = \frac{C_r}{C_p} \quad (7.77)$$

and thus:

$$\frac{k_1}{k_2} = \frac{k'_1}{k'_2} \quad (7.78)$$

with these assumptions, the model output can be written as:

$$C_{f+ns}(t) + C_s(t) = R_1 C_r(t) + a \int_0^t C_r(\tau) e^{-c(t-\tau)} d\tau + b \int_0^t C_r(\tau) e^{-d(t-\tau)} d\tau \quad (7.79)$$

where  $C_r$  is the model input and  $a$ ,  $b$ ,  $c$ ,  $d$  are combinations of parameters  $R_1$ ,  $k_2$ ,  $k_3$ ,  $k_4$ .

The measurement equation is:

$$C_i(t) = C_{f+ns}(t) + C_s(t) \quad (7.80)$$

The four-model parameters  $R_1$ ,  $k_2$ ,  $k_3$ ,  $k_4$  can be estimated together with their precision by using nonlinear least squares as previously described. The model also provides the BP as:

$$BP = \frac{k_3}{k_4} \quad (7.81)$$

If the tracer kinetics in the target region are such that it is difficult to distinguish between free and specifically bound compartments, the reference tissue model can be simplified as in Figure 7.12.

The equations are:

$$\begin{aligned} \dot{C}_r(t) &= k'_1 C_p(t) - k'_2 C_r(t) & C_r(0) &= 0 \\ \dot{C}_t(t) &= k_1 C_p(t) - k_{2a} C_t(t) & C_t(0) &= 0 \end{aligned} \quad (7.82)$$

where  $C_t(t) = C_{f+ns}(t) + C_r(t)$  is the total tracer concentration in the tissue and  $k_{2a}$  the apparent rate constant of transfer from the specifically bound compartment to plasma related to the parameters  $k_2$ ,  $k_3$ ,  $k_4$  of the model of Figure 7.11 as:

$$k_{2a} = \frac{k_2}{1 + BP} = \frac{k_2}{1 + k_3/k_4} \quad (7.83)$$

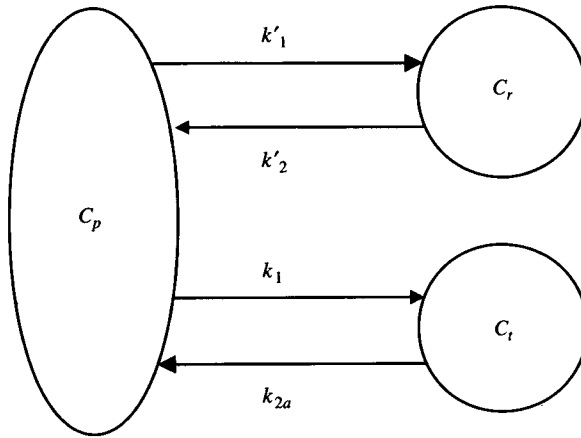


Figure 7.12. The simplified reference ligand-receptor model.

Assuming that (7.76) and (7.78) still hold, the equation corresponding to (7.79) becomes:

$$C_r(t) = R_1 C_r(t) + \left[ k_2 - \frac{R_1 k_2}{1 + BP} \right] \int_0^t C_r(\tau) e^{-(k_2/1+BP)(t-\tau)} d\tau \quad (7.84)$$

The measurement equation is:

$$C_i(t) = C_t(t) \quad (7.85)$$

By using nonlinear least squares, the three-model parameters  $R_1, k_2, BP$  can be estimated together with their precision.

### 7.6.3. A NONLINEAR MODEL OF THE LIGAND-RECEPTOR SYSTEM

All the linear compartmental models discussed earlier do not permit an estimation of the individual values of  $B_{max}, k_{on},$  and  $K_d$ . To do so, it is necessary to move from a single-labelled ligand experiment to a protocol including an injection of unlabelled ligand. Under these circumstances, most receptor sites become occupied,  $C_s$  in (7.62) is not negligible, and thus  $k_3$  is no longer a constant. Equation (7.62) becomes:

$$\frac{dC_s(t)}{dt} = k_{on}(B_{max} - C_s(t))C_f(t) - k_{off}C_s(t) = k_3(t)C_f(t) - k_{off}C_s(t) \quad (7.86)$$

with:

$$\begin{aligned}
 k_3(t) &= k_{\text{on}}(B_{\text{max}} - C_s(t)) \\
 k_4 &= k_{\text{off}}
 \end{aligned}
 \tag{7.87}$$

There is thus the need to describe the unlabelled ligand kinetics. The model is shown in Figure 7.13.

It is nonlinear and its equations are:

$$\begin{aligned}
 \dot{C}_{f+ns}(t) &= k_1 C_p(t) - (k_2 + k_3(t))C_{f+ns}(t) + k_4 C_s(t) & C_{f+ns}(0) &= 0 \\
 \dot{C}_s(t) &= k_3(t)C_{f+ns}(t) - k_{\text{off}}C_s(t) & C_s(0) &= 0 \\
 \dot{C}'_{f+ns}(t) &= k_1 C'_p(t) - (k_2 + k_3(t))C'_{f+ns}(t) + k_4 C'_s(t) & C'_{f+ns}(0) &= 0 \\
 \dot{C}'_s(t) &= k_3(t)C'_{f+ns}(t) - k_{\text{off}}C'_s(t) & C'_s(0) &= 0
 \end{aligned}
 \tag{7.88}$$

where  $C_p$ ,  $C_{f+ns}$ , and  $C_s$  have the same meaning as before and  $C'_p$ ,  $C'_{f+ns}$ , and  $C'_s$  are, respectively, the unlabelled ligand plasma concentration (corrected for metabolites), free plus nonspecifically bound unlabelled ligand concentration, and specifically bound unlabelled ligand concentration. The measurement equation is still given by (7.71).

The model is *a priori* uniquely identifiable from the measurements  $C_i$ ,  $C_p$ , and  $C'_p$  of a labelled plus unlabelled ligand injection experiment ( $C_b$  can be calculated from  $C_p$  by using well-known formulae involving haematocrit). In particular, one can estimate  $k_1, k_2, k_{\text{on}}, B_{\text{max}}, k_{\text{off}}, V_b$  parameters and thus the ligand affinity  $K_d$ . Often, to improve *a posteriori* (numerical) identifiability of the model, the experimental protocol involves several injections of labelled or unlabelled ligand, such as (Delforge *et al.*, 1993) a tracer dose of [ $^{11}\text{C}$ ]flumazenil, a specific ligand of benzodiazepine receptors, followed by two cold injections of flumazenil and a subsequent coinjection of labelled and unlabelled flumazenil.

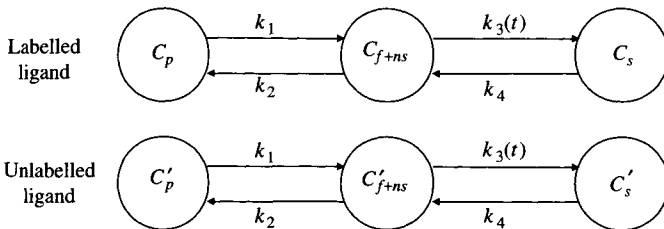


**Figure 7.13.** The labelled and unlabelled ligand two-tissue compartment model of the ligand-receptor system.

### 7.6.4. THE LOGAN GRAPHICAL METHOD

All the ligand-receptor models presented previously require numerical identification such as by nonlinear least squares, from the data to quantitate the receptor system. Simpler approaches based on graphical methods have been developed, and because of their simplicity they are frequently employed for system quantification. A popular graphical method for BP quantification has been proposed by Logan *et al.* (1990). Assuming that the two-tissue compartment model of Figure 7.10. accurately describes tracer kinetics in the tissue, the method uses the plasma and tissue tracer concentration curves and proposes (see Logan *et al.*, 1990) to plot the points of coordinates on the Cartesian plane:

$$x = \frac{\int_0^t C_p(\tau) d\tau}{C_i(t)}, \quad y = \frac{\int_0^t C_i(\tau) d\tau}{C_i(t)} \quad (7.89)$$

If there exists a time  $t^*$  such that the tissue regions are in equilibrium with plasma, the plot yields, after time  $t^*$ , a straight line with slope  $m$  equal to:

$$m = \frac{k_1}{k_2} + \frac{k_1 k_3}{k_2 k_4} + V_b = V_d \left( 1 + \frac{B_{\max}}{K_d} \right) + V_b = V_d(1 + BP) + V_b \quad (7.90)$$

Assuming  $V_d$  known and  $V_b$  known or negligible (i.e., for the brain tissue  $V_b \cong 3 - 4\%$ ), it is possible to estimate BP from the  $m$  value.

In 1996, Logan *et al.* also proposed another graphical method for determining the distribution volume ratio (DVR) (a linear function of receptor availability) that does not require blood sampling. Like in the model of Lammertsma *et al.* (1996a, 1996b), one uses data from a region not containing specific receptors. An additional assumption is needed on the tissue to plasma efflux constant, which is fixed to a population value.

## 7.7. CONCLUSIONS

Positron emission tomography images interpreted with physiological models allow the noninvasive quantification of important physiological processes at the organ level, such as glucose metabolism, blood flow and receptor density and affinity. To arrive at a reliable quantification of these processes and parameters, several ingredients must concur, including the quality of PET scanner, radiotracer, image-processing method, and physiological model. In this chapter, we have concentrated on available modelling and identification strategies for interpreting PET images. We have focused on linear and nonlinear compartmental models to quantitate glucose metabolism, blood flow,

and ligand-receptor interaction. The importance of I/O modelling as an aid and guide in model structure selection also has been stressed. Finally, popular graphical methods have been reviewed in light of their underlying assumptions.

## 7.8. REFERENCES

- Alpert, N. M., D. A. Chesler, J. A. Correia, R. H. Ackerman, J. Y. Chang, S. Finklestein, S. M. Davis, G. L. Brownell and J. M. Taveras. Estimation of the local statistical noise in emission computed tomography. *IEEE Trans Med Imag* MI-1 (1982):142–46.
- Backman, L., T. B. Robins-Wahlin, A. Lundin, N. Ginovart and L. Farde. Cognitive deficits in Huntington's disease are predicted by dopaminergic PET markers and brain volumes. *Brain* 120(1997):2207–17.
- Bergmann, S. R., K. A. Fox, A. L. Rand, K. D. McElvany, M. J. Welch, J. Markham and B. E. Sobel. Quantification of regional myocardial blood flow *in vivo* with  $H_2^{15}O$ . *Circulation* 70(1984):724–33.
- Bertoldo, A., P. Vicini, G. Sambuceti, A. A. Lammertsma, O. Parodi and C. Cobelli. Evaluation of compartmental and spectral analysis models of [ $^{18}F$ ]FDG kinetics for heart and brain studies with PET. *IEEE Trans Biomed Eng* 45(1998):1429–48.
- Bertoldo, A and C. Cobelli. A more general and statistically robust spectral analysis method. *J Cereb Blood Flow Metab* 19(1999):S762.
- Blomqvist, G., K. Bergström, M. Bergström, E. Ehrin, L. Eriksson, B. Garmelius, B. Lindberg, A. Lilja, J. E. Litton, L. Lundmark, H. Lundqvist, P. Malmberg, U. Moström, L. Nilsson, S. Stone-Elander and L. Widen 1985. Models for  $^{11}C$ -glucose. In: *The Metabolism of the Human Brain Studied with Positron Emission Tomography*. Edited by T. Greitz, D. H. Ingvar and L. Widen. New York: Raven Press.
- Blomqvist, G., S. Stone-Elander, C. Halldin, P. E. Roland, L. Widen, M. Lindqvist, C. G. Swahn, B. Langstrom and F. A. Wiesel. Positron emission tomographic measurements of cerebral glucose utilization using [ $^{1-11}C$ ]D-glucose. *J Cereb Blood Flow Metab* 10(1990):467–83.
- Botker, H. E., G. W. Goodwin, J. E. Holden, T. Doenst, A. Gjedde and H. Taegtmeier. Myocardial glucose uptake measured with fluorodeoxyglucose: a proposed method to account for variable lumped constants. *J Nucl Med* 40(1999):1186–96.
- Budinger, T. F., S. E. Derenzo, W. L. Greenberg, G. T. Gullberg and R. H. Huesman. Quantitative potentials of dynamic emission computed tomography. *J Nucl Med* 19(1978):309–15.
- Budinger, T. F., S. E. Derenzo, G. T. Gullberg, W. L. Greenberg and R. H. Huesman. Emission computed assisted tomography with single-photon and positron annihilation emitters. *J Comput Assist Tomogr* 1(1977):131–45.
- Carson, E., C. Cobelli and L. Finkelstein. 1983. *The Mathematical Modelling of Metabolic and Endocrine Systems*. New York: Wiley.
- Carson, R. E., Y. Yan, M. E. Daube-Witherspoon, N. Freedman, S. L. Bacharach and P. Herscovitch. An approximation formula for the variance of PET region-of-interest values. *IEEE Trans Med Imag* 12(1993):240–50.
- Cobelli, C., D. M. Foster and G. Toffolo. 2000. *Tracer Kinetics in Biomedical Research: From Data to Model*. New York: Kluwer.
- Cunningham, V. and T. Jones. Spectral analysis of dynamic PET studies. *J Cereb Blood Flow Metab* 13(1993):15–23.
- Defrise, M., D. W. Townsend and F. Deconinck. Statistical noise in three-dimensional positron emission tomography. *Phys Med Biol* 35(1990):131–38.

- Delforge, J., D. Le Guludec, A. Syrota, B. Bendriem, C. Crouzel, M. Slama and P. Merlet. Quantification of myocardial muscarinic receptors with PET in humans. *J Nucl Med* 34(1993):981–91.
- Delforge, J., S. Pappata, P. Millet, Y. Samson, B. Bendriem, A. Jobert, C. Crouzel and A. Syrota. Quantification of benzodiazepine receptors in human brain using PET, [<sup>11</sup>C]flumazenil, and a single-experiment protocol. *J Cereb Blood Flow Metab* 15(1995):284–300.
- Delforge, J., L. Spelle, B. Bendriem, Y. Samson and A. Syrota. Parametric images of benzodiazepine receptor concentration using a partial-saturation injection. *J Cereb Blood Flow Metab* 17(1997):343–55.
- Delforge, J., A. Syrota and B. M. Mazoyer. Identifiability analysis and parameter identification of an *in vivo* ligand-receptor model from PET data. *IEEE Trans Biomed Eng* 37(1990):653–61.
- Delforge, J., M. Bottlaender, C. Loc'h, I. Guenther, C. Fuseau, B. Bendriem, A. Syrota and B. Maziere. Quantitation of extrastriatal D2 receptors using a very high-affinity ligand (FLB 457) and the multi-injection approach. *J Cereb Blood Flow Metab* 19(1999):533–46.
- Eichling, J. O., M. A. Raichle, R. L. Grubb and M. M. Ter-Pergossian. Evidence of the limitations of water as a freely diffusible tracer in brain of the rhesus monkey. *Circ Res* 35(1974):358–64.
- Fanelli, C. G., C. S. Dence, J. Markham, T. O. Videen, D. S. Paramore, P. E. Cryer and W. J. Powers. Blood-to-brain glucose transport and cerebral glucose metabolism are not reduced in poorly controlled type 1 diabetes. *Diabetes* 47(1998):1444–50.
- Farde, L., L. Eriksson, G. Blomquist and C. Halldin. Kinetic analysis of central [<sup>11</sup>C]raclopride binding to D2-dopamine receptors studied by PET — a comparison to the equilibrium analysis. *J Cereb Blood Flow Metab* 9(1989):696–708.
- Gambhir, S., M. Schwaiger, S. C. Huang, J. Krivokapich, H. R. Schelbert, C. A. Nienaber and M. E. Phelps. Simple noninvasive quantification method for measuring myocardial glucose utilization in humans employing positron emission tomography and fluorine-18 deoxyglucose. *J Nucl Med* 30(1989):359–66.
- Hasselbalch, S. G., G. M. Knudsen, S. Holm, L. P. Hageman, B. Capaldo, O. B. Paulson. Transport of D-glucose and 2-fluorodeoxyglucose across the blood-brain barrier in humans. *J Cereb Blood Flow Metab* 16(1996):659–66.
- Huesman, R. H. A new fast algorithm for the evaluation of regions of interest and statistical uncertainty in computed tomography. *Phys Med Biol* 29(1984):543–52.
- Huesman, R. H. The effects of a finite number of projection angles and finite laterale sampling of projections on the propagation of statistical errors in transverse section reconstruction. *Phys Med Biol* 22(1977):511–21.
- Iida, H., I. Kanno, S. Miura, M. Murakami, K. Takahashi and K. Uemura. Error analysis of a quantitative cerebral blood flow measurement using H<sub>2</sub><sup>15</sup>O autoradiography and positron emission tomography, with respect to the dispersion of the input function. *J Cereb Blood Flow Metab* 6(1986):536–45.
- Ito, H., Y. Okubo, C. Halldin and L. Farde. Mapping of central D2 dopamine receptors in man using [<sup>11</sup>C]raclopride: PET with anatomic standardization technique. *Neuroimage* 9(1999):235–42.
- Jacquez, J. A. 1996. *Compartmental Analysis in Biology and Medicine*. 3rd ed. Ann Arbor, MI: BioMedware.
- Kelley, D. E., M. A. Mintun, S. C. Watkins, J.-A. Simoneau, F. Jadali, A. Fredrickson, J. Beattie and R. Thériault. The effect of non-insulin-dependent diabetes mellitus and obesity on glucose transport and phosphorylation in skeletal muscle. *J Clin Invest* 97(1996):2705–13.
- Kelley, D. E., K. V. Williams and J. C. Price. Insulin regulation of glucose transport and phosphorylation in skeletal muscle assessed by PET. *Am J Physiol* 277(1999a):E361–69.
- Kelley, D. E., K. V. Williams, J. C. Price and B. Goodpaster. Determination of the lumped constant for [<sup>18</sup>F]FDG in human skeletal muscle. *J Nucl Med* 40(1999b):1798–1804.



- Kety, S. S. The theory and application of the exchange of inert gas at the lungs and tissues. *Pharmacol Rev* 3(1951):1–41.
- Kety, S. S. and C. F. Schmidt. The nitrous oxide method for the quantitative determination of cerebral blood flow in man: theory, procedure, and normal values. *J Clin Invest* 27(1948):476–83.
- Krivokapich, J., S. C. Huang, C. E. Selin and M. E. Phelps. Fluorodeoxyglucose rate constants, lumped constant, and glucose metabolic rate in rabbit heart. *Am J Physiol* 252(1987):H777–87.
- Lammertsma, A. A., C. J. Bench, S. P. Hume, S. Osman, K. Gunn, D. J. Brooks and R. S. Frackowiak. Comparison of methods for analysis of clinical [<sup>11</sup>C]raclopride studies. *J Cereb Blood Flow Metab* 16(1996a):42–52.
- Lammertsma, A. A. and S. P. Hume. Simplified reference tissue model for PET receptor studies. *Neuroimage* 4(1996b):153–58.
- Le Guludec, D., A. Cohen Solal, J. Delforge, N. Delahaye, A. Syrota and P. Merlet. Increased myocardial muscarinic receptor density in idiopathic dilated cardiomyopathy: an *in vivo* PET study. *Circulation* 96(1997):3416–22.
- Logan, J., J. S. Fowler, N. D. Volkow, A. P. Wolf, S. L. Dewey, D. J. Schlyer, R. R. MacGregor, R. Hitzemann, B. Bendriem, S. J. Gatley and D. R. Christman. Graphical analysis of reversible radioligand binding from time-activity measurements applied to [<sup>11</sup>C-methyl]-(-)-cocaine PET studies in human subjects. *J Cereb Blood Flow Metab* 10(1990):740–47.
- Logan, J., J. S. Fowler, N. D. Volkow, G. J. Wang, Y. S. Ding and D. L. Alexoff. Distribution volume ratios without blood sampling from graphical analysis of PET data. *J Cereb Blood Flow Metab* 16(1996):834–40.
- Malizia, A. L., V. J. Cunningham, C. J. Bell, P. F. Liddle, T. Jones and D. J. Nutt. Decreased brain GABA(A)-benzodiazepine receptor binding in panic disorder: preliminary results from a quantitative PET study. *Arch Gen Psychiatry* 55(1998):715–20.
- Mazoyer, B. M., R. H. Huesman, T. F. Budinger and B. L. Knittel. Dynamic PET data analysis. *J Comput Assist Tomogr* 10(1986):645–53.
- Meikle, S. R., J. C. Matthews, C. S. Brock, P. Wells, R. J. Harte, V. J. Cunningham, T. Jones and P. Price. Pharmacokinetic assessment of novel anti-cancer drugs using spectral analysis and positron emission tomography: a feasibility study. *Cancer Chemother Pharmacol* 42(1998a):183–93.
- Meikle, S. R., J. C. Matthews, V. J. Cunningham, D. L. Bailey, L. Livieratos, T. Jones and P. Price. Parametric image reconstruction using spectral analysis of PET projection data. *Phys Med Biol* 43(1998b):651–66.
- Pajevic, S., M. E. Daube-Witherspoon, S. L. Bacharach and R. E. Carson. Noise characteristics of 3-D and 2-D PET images. *IEEE Trans Med Imag* 17(1998):9–23.
- Patlak, C. S. and R. G. Blasberg. Graphical evaluation of blood-to-brain transfer constants from multiple-time uptake data. Generalizations. *J Cereb Blood Flow Metab* 5(1985):584–90.
- Patlak, C. S., R. G. Blasberg and J. D. Fenstermacher. Graphical evaluation of blood-to-brain transfer constants from multiple-time uptake data. *J Cereb Blood Flow Metab* 3(1983):1–7.
- Phelps, M. E., S. C. Huang, E. J. Hoffman, C. Selin, L. Sokoloff and D. E. Kuhl. Tomographic measurement of local cerebral glucose metabolic rate in humans with (F-18)2-fluoro-2-deoxy-D-glucose: validation of method. *Ann Neurol* 6(1979):371–88.
- Powers, W. J., J. S. Dagogo, J. Markham, K. B. Larson and C. S. Dence. Cerebral transport and metabolism of 1-<sup>11</sup>C-D-glucose during stepped hypoglycemia. *Ann Neurol* 38(1995):599–609.
- Richardson, M. P., M. J. Koeppe, D. J. Brooks, D. R. Fish and J. S. Duncan. Benzodiazepine receptors in focal epilepsy with cortical dysgenesis: an <sup>11</sup>C-flumazenil PET study. *Ann Neurol* 40(1996):188–98.
- Ruotsalainen, U., M. Raitakari, P. Nuutila, V. Oikonen, H. Sipila, M. Teras, M. J. Knuuti, P. M. Bloomfield and H. Iida. Quantitative blood flow measurement of skeletal muscle using oxygen-15-water and PET. *J Nucl Med* 38(1997):314–19.

- Schmidt, K., G. Lucignani, R. M. Moresco, G. Rizzo, M. C. Gilardi, C. Messa, F. Colombo, F. Fazio and L. Sokoloff. Errors introduced by tissue heterogeneity in estimation of local cerebral glucose utilization with current kinetic models of the [18F]fluorodeoxyglucose method. *J Cereb Blood Flow Metab* 12(1992):823–34.
- Schmidt, K., G. Mies and L. Sokoloff. Model of kinetic behavior of deoxyglucose in heterogeneous tissues in brain: a reinterpretation of the significance of parameters fitted to homogeneous tissue models. *J Cereb Blood Flow Metab* 11(1991):10–24.
- Sihver, W., S. Sihver, M. Bergstrom, T. Murata, K. Matsumura, H. Onoe, Y. Andersson, P. Bjurling, K. J. Fasth, G. Westerberg, M. Ogren, G. Jacobsson, H. Lundqvist, L. Oreland, Y. Watanabe and B. Langstrom. Methodological aspects for *in vitro* characterization of receptor binding using 11C-labeled receptor ligands: a detailed study with the benzodiazepine receptor antagonist [11C]Ro 15-1788. *Nucl Med Biol* 24(1997):723–31.
- Sokoloff, L., M. Reivich, C. Kennedy, M. H. Des-Rosiers, C. S. Patlak, K. D. Pettigrew, O. Sakurada and M. Shinohara. The [14C]deoxyglucose method for the measurement of local cerebral glucose utilization: theory, procedure, and normal values in the conscious and anesthetized albino rat. *J Neurochem* 28(1977):897–916.
- Sokoloff, L. 1996. Cerebral metabolism and visualization of cerebral activity. In: *Comprehensive Human Physiology*. Edited by R. Greger and U. Windhorst. New York: Springer-Verlag.
- A. M. Spence, M. Muzi, M. M. Graham, F. O'Sullivan, K. A. Krohn, J. M. Link, T. K. Lewellen, B. Lewellen, S. D. Freeman, M. S. Berger and G. A. Ojemann. Glucose metabolism in human malignant gliomas measured quantitatively with PET, 1-[C-11]glucose and FDG: analysis of the FDG lumped constant. *J Nucl Med* 39(1998):440–48.
- Turkheimer, F., R. M. Moresco, G. Lucignani, L. Sokoloff, F. Fazio and K. Schmidt. The use of spectral analysis to determine regional cerebral glucose utilization with positron emission tomography and [18F]fluorodeoxyglucose: theory, implementation, and optimization procedures. *J Cereb Blood Flow Metab* 14(1994):406–22.
- Utriainen, T., S. Mäkimattilla, S. Lovisatti, A. Bertoldo, R. Bonadonna, S. Weintraub, R. De-Fronzo, C. Cobelli and H. Yki-Järvinen. Lumped constant for [14C]deoxy-D-glucose in human skeletal muscle. *Diabetologia* 41(1998):A187.
- Watabe, H., M. Itoh, V. J. Cunningham, A. A. Lammertsma, P. M. Bloomfield, M. Mejia, T. Fujiwara, A. K. P. Jones, T. Jones and T. Nakamura. 1993. Noninvasive quantification of rCBF using positron emission tomography. In: *Quantification of Brain Function Using PET*. Edited by R. Myers, V. Cunningham, D. Bailey and T. Jones. London: Academic Press.
- Wong, D. F., A. Gjedde and H. N. Wagner Jr. Quantification of neuroreceptors in the living human brain. I. Irreversible binding of ligands. *J Cereb Blood Flow Metab* 6(1986):137–46.

This Page Intentionally Left Blank

# Identification and Physiological Interpretation of Aortic Impedance in Modelling

Roberto Burattini

## 8.1. INTRODUCTION

The systemic arterial system is a branching network of tubes that accepts flow from the left ventricle of the heart and passes it on to bodily organs and tissues. Because the action of the heart is intermittent, aortic pressure and flow are oscillatory. Due to cushioning function of large compliant arteries, however, flow pulsations are smoothed so that blood is directed through the organs and tissues in an almost steady stream. Wave shapes of pulsatile pressure and flow are determined by the complex interaction of the heart and the arterial system. Optimal ventriculovascular coupling should minimise left ventricular load and energy requirements while achieving perfusion to the tissues and organs of the body according to need. Disease states that primarily affect overall left ventricular performance, such as dilated cardiomyopathy and ischaemic heart disease, may result in secondary alterations of the peripheral vasculature that help maintain adequate tissue perfusion. Conversely, primary alterations in arterial properties such as those that occur with aging, atherosclerosis, arteriosclerosis, diabetes, and systemic hypertension lead to changes in hydraulic load that must be accommodated by the ventricle for the maintenance of adequate cardiac output (Milnor, 1982; Nichols and O'Rourke, 1990; Noordergraaf, 1978; O'Rourke, 1982).

Quantitative evaluation of the physical properties of the arterial system is important to understand the dynamics of pressure-flow relationships and implications of alterations in these properties with respect to vascular-ventricular interaction, pressure monitoring, and logical approach to therapy (O'Rourke, 1990, 1995). Because the overall arterial system's properties are presently impossible or impractical to measure directly, they must be estimated indirectly from continuous pressure and flow measurements using various models of the circulation. The concept of vascular input impedance has been generally recognised as an important haemodynamic approach to formulate and verify models of physical aspects of the dynamics of pressure-flow relationships in the ascending aorta and, in general, in a site of an artery feeding a particular vascular bed. Since its earliest applications, the concept of vascular input impedance has been immensely valuable for the understanding of arterial properties and arterial function and has made it possible to model the arterial tree in a variety of forms of very different complexity (Burattini, 1989; Kenner, 1979; Milnor, 1982; Nichols and O'Rourke, 1990; Noordergraaf, 1978; Westerhof *et al.*, 1979; Wetterer and Kenner, 1968).

Traditionally, clinicians have modelled the arterial system according to Poiseuille's equation as a simple hydraulic circuit in which pressure is a function of flow and resistance only. Although this simple resistance model may fulfill the goal of describing the relations between mean aortic pressure and cardiac output, it does not explain how the pulsatile flow wave generated by left ventricular contraction is converted into the sustained aortic pressure wave that is essential for normal organ perfusion. To describe these pressure-flow relationships in the pulsatile (dynamic) regimen, models are needed that take into account not only peripheral resistance but also arterial compliance, inertial properties of blood motion, and effect of both pressure and flow wave reflections within the arterial tree (Marcus *et al.*, 1994; Milnor, 1982; Nichols and O'Rourke, 1990; Noordergraaf, 1978; Poiseuille, 1840; Westerhof, 1993).

Arterial compliance, defined as the change in the arterial blood volume due to a given change in distending pressure, participates in arterial function by damping the fluctuations in pressure and flow arising from intermittent ventricular ejection, by uncoupling the left ventricle from high-resistance terminal arterioles and by playing a major role in arterial wave transmission phenomena. These functions are affected by acute changes in compliance in response to changes in arterial pressure and sympathetic nervous activity and by long-term changes in compliance due to processes associated with disease and aging (Elzinga and Westerhof, 1973; Gross, 1989; Milnor, 1982; Nichols and O'Rourke, 1990; Noordergraaf, 1978; O'Rourke, 1982; Sunagawa *et al.*, 1984; Yin and Liu, 1989). It is logical that the estimation *in vivo* of arterial compliance and the assessment of its role in arterial function with

acute and chronic changes has long interested clinicians and researchers of cardiovascular physiology.

Most attempts to quantify arterial compliance have been based on the Windkessel theory (Stergiopoulos *et al.*, 1995; Yin and Liu, 1989). This approach assumes that the Windkessel compliance represents the sum of all compliances throughout the arterial system, so that evaluation of the distributed and heterogeneous changes that may occur in compliance are not possible. Also, Windkessel-type models can make no claims whatsoever to handle wave propagation. To retain simplicity, while still representing major distributed characteristics of the arterial system proximal to the heart and involving certain features of wave travel and reflection, several partially distributed arterial models have been proposed (Burattini, 1989; Burattini and Campbell 1993; Liu *et al.*, 1989; Wetterer and Kenner, 1968; Nichols and O'Rourke, 1990, Sipkema and Westerhof, 1975).

None of these models, however, yielded methods to quantify overall arterial elastic properties and to account for wave propagation phenomena that are universally accepted. Indeed, vascular impedance properties, such as viscoelasticity and wave travel and reflection, are not incorporated in the current conceptual framework for evaluation of cardiovascular pathophysiology. Presumable causes of failure of models to gain clinical eminence has been seen in paucity of invasive data in humans and difficulty in the assessment of noninvasive methodology for the acquisition of continuous pressure and flow measurements and also in a generic communication gap between those who develop arterial models and those who must apply them in clinical setting. Especially, it has been observed that model makers have focused their attention on model accuracy (associated to mathematical complexity) rather than on providing clinically accessible, functional models that can be easily applied at the bedside (Marcus *et al.*, 1994). To the experience of this author, however, communication gap in respect to those who should apply these models in clinical setting is not in model complexity but in that physiologists and clinicians hardly accept the concept that the modelling process is essentially iterative. Model formulation (even the simplest) is closely interrelated with experimental design and identifiability problems in computer-based estimation of model parameters and their physiological interpretation. Especially, the selection of the form of a model most appropriate for a given application cannot be separated from the choice of an identification method. Theoretical understanding of the problems associated with the interrelationships between the structural form of a model, the parameters to be estimated, and the design of experiments to be used in the identification process cannot be distinct from physiological interpretation.

Based on these considerations, vascular impedance modelling is discussed here within a general framework of systems identification (Cobelli and Di Stefano III, 1980). The aim is to show how identification and identifiability

issues fit in the process of validating lumped and distributed parameter models through appropriate experimental design, data fit, and settlement of physiological interpretation. With this aim in mind, a brief summary is given of essential concepts in modelling and identification issues (an exhaustive discussion of these issues is given in Chapters 4 and 5). Principles of vascular impedance identification are revisited in light of the general frequency response technique (Graupe, 1976). This is followed by a discussion of ascending aortic impedance patterns in respect to their approximation by simple frequency response functions and to their physiological interpretation by different Windkessel models. Contradictions in Windkessel-based methods for estimation of total arterial compliance are addressed. Eventually, interpretation of aspects of wave propagation in the arterial system based on use of tube models is discussed. Special emphasis is placed on the resolution of a long-standing problem of identifiability for this class of models.

## **8.2. THE MODELLING PROCESS AND RELATED PROBLEMS OF IDENTIFIABILITY AND DETERMINACY**

Whatever we perceive and are able to express in words, equations, or any other form of information transmission is a model of the observed system or event. Thus, models are simplified abstractions of reality that we can comprehend and communicate to others in easy-to-understand forms. Fundamentally, a model serves to put a hypothesis into concise quantitative form that should make the ideas free of ambiguities, such that comparison about physiological system behaviour is brought to a less vague comparison. In biology and physiology, the terms *model* and *modelling* are often used in a somewhat extended meaning for the description of certain experimental procedures. On this basis, the circulation of any animal may be seen as a model of the human circulation. This explains why, in the need of invasive procedures for detection of data, most of the experimental studies have been originally conducted in animals and some of the results have been extrapolated to humans (Kenner, 1979; Gross, 1979).

In the present dissertation, the term *modelling* will refer to the process of assessing simplified abstractions of reality, notably the arterial system, that are simultaneously data models and system models. Namely, these models are required to give an overall input-output (I/O) description derived from pressure and flow data (or, equivalently, impedance data) collected from the system (data models) and, at the same time, represent the underlying physiology at an appropriate level of approximation and resolution (system models). The degree of approximation will be largely determined by the model's purpose,

the availability of *a priori* knowledge, and the nature of the assumptions to be made.

Models of the arterial system can serve several purposes. They can assist in the understanding of the system's function as it relates to measurable physical properties. They may help to identify and define specific future experiments that are required to more realistically describe a system's function. Making use of accessible measurements, they may serve as a means to estimate parameters that are presently impossible or impractical to measure directly. This purpose is of particular interest for clinical applications. It requires the formalisation of suitable models that are simple and are characterised by a limited number of parameters that are representative of physiological attributes characteristic of the studied function.

The selection of the model form that is most appropriate for a given application cannot be separated from the choice of an identification method, such as parameter selection and criterion formulation, as well as algorithm minimisation and computer programming. Once a model is formulated, the notion of identifiability addresses the question as to whether it is possible to obtain a set of solutions for the unknown parameters of the model from fitting to experimental data. Typically, a fitting procedure consists of the minimisation of a cost function defined as the square of the differences between the model output and the real system's output (that is, the least squares output error). Usual questions to be answered in identifiability problems are mathematical and physical. The mathematical issue is which parameters, or combination of parameters, of the model are uniquely identifiable and which are not. The physical issue is to what extent the parameters estimated from I/O measurements give insight into the physical properties of the modelled physiological system. The question of parameter uniqueness for a general class of both linear and nonlinear models of dynamic systems evolved in the late 1960s and early 1970s into the identifiability concept in the systems theory and applications. These concepts have found extensive applications in compartmental modelling of metabolic and endocrine systems (Bellman and Åström, 1970; Carson *et al.*, 1983; Cobelli and Di Stefano III, 1980). The advantages of these applications clearly emerge in later chapters. Rather, identifiability has received much less attention in cardiovascular system modelling.

A special problem in identifiability is encountered when a fitting procedure yields more than one set of solutions for the unknown parameters. In this circumstance, the questions arise as to whether there exists one solution with clear physiological meaning. If this solution exists, the problem is to find a way to select it. This and broader questions associated with poor experimental design, noise measurements, and practical difficulties that influence the uniqueness and reliability of parameter estimates have been grouped together in terms of what has been called *determinacy problem* (Brown and Godfrey,



1978). A typical problem of determinacy affecting tube models of the arterial system is discussed in Section 8.9.

### 8.3. VASCULAR IMPEDANCE

The impedance concept was borrowed from electrical engineering concepts, where it is used to describe the relationship between alternating electric currents and voltages. By analogy with electrical systems, vascular impedance expresses the relationship between sinusoidal components of blood pressure and flow. Several types of impedance have been defined, such as longitudinal impedance, transverse impedance, input impedance, and characteristic impedance. When the general term *impedance* is applied to the vascular system, it is usually in reference to input impedance, this being the relationship between pulsatile pressure and pulsatile flow in a site of an artery feeding a particular vascular bed (for a review see Nichols and O'Rourke, 1990; Westerhof *et al.* 1979; Wetterer and Kenner, 1968).

The experimental procedure generally used to determine input impedance at a selected point in the circulation is to measure the instantaneous pressure,  $p(t)$ , and flow,  $q(t)$ , simultaneously. The resulting data are subjected to Fourier analysis, which translates the observed pressure and flow data into the sum of their mean value and a series of sinusoidal waves at specified frequencies (Milnor, 1982; Nichols and O'Rourke, 1990):

$$p(t) = P_0 + \sum_{n=1}^N P_n \cos(n\omega t + \Phi_n) \quad (8.1)$$

$$q(t) = Q_0 + \sum_{m=1}^N Q_m \cos(m\omega t + \Theta_m) \quad (8.2)$$

In these equations,  $P_0$  and  $Q_0$  are mean pressure and mean flow, respectively; the subscripts  $n$  and  $m$  indicate the  $n$ th pressure term and  $m$ th flow term, respectively, in the Fourier series;  $N$  is the total number of terms included in the series;  $P_n$  and  $Q_m$  are the amplitudes of the  $n$ th term of pressure and the  $m$ th term of flow, respectively, and  $\Phi_n$  and  $\Theta_m$  are the related phase angles;  $\omega$  is the fundamental frequency of heart pulsation in rad/s. This is related to the heart period,  $T$ , by the equation  $\omega = 2\pi/T$ .

To obtain a Fourier series of signals, they must be repetitive and must not contain an infinite number of discontinuities (Dirichlet conditions). Within an acceptable degree of approximation, haemodynamic signals like pressure and flow, in steady state, are repetitive at a constant heart rate and held respiration and do not contain discontinuities. Therefore, the Dirichlet conditions are

satisfied. Theoretically, an infinite number of harmonics should be considered in the Fourier series ( $N = \infty$ ). In practice, it has been observed that a limited number of harmonics gives information about the actual pressure and flow waves. Depending on the site of interest, this number is usually less than 20 (see Figure 4 in Westerhof *et al.*, 1979). This choice implies that the range of frequencies of physiological interest is from the mean term at 0 Hz to the term at 20 times the heart rate expressed in Hz.

Each harmonic,  $P(jn\omega)$  and  $Q(jm\omega)$ , obtained from Fourier analysis is complex in the mathematical sense and is expressed by its modulus,  $P_n$  and  $Q_m$ , phase angle,  $\Phi_n$  and  $\Theta_m$ , that is, timing with respect to other harmonics, and angular frequency,  $\omega$ :

$$P(jn\omega) = P_n[\exp j(n\omega t + \Phi_n)] \tag{8.3}$$

$$Q(jm\omega) = Q_m[\exp j(m\omega t + \Theta_m)] \tag{8.4}$$

The ratio of pressure harmonic to flow harmonic at the same frequency is called the impedance,  $Z(jn\omega)$ , at that frequency:

$$Z(jn\omega) = \frac{P_n \exp[j(n\omega t + \Phi_n)]}{Q_n \exp[j(n\omega t + \Theta_n)]} = \frac{P_n}{Q_n} \exp[j(\Phi_n - \Theta_n)] \tag{8.5}$$

Equation (8.5) refers to the generic  $n$ th frequency. If  $Z_n$  is the ratio of  $P_n$  to  $Q_n$ , and  $\Psi_n$  is the difference between  $\Phi_n$  and  $\Theta_n$ , the impedance,  $Z(jn\omega)$ , is expressed, frequency by frequency, by its modulus,  $Z_n$ , and its phase angle  $\Psi_n$ :

$$Z(jn\omega) = Z_n \exp(j\Psi_n) \tag{8.6}$$

Implicit in the derivation of impedance is that the system analysed is linear and time-invariant. Over the range of frequencies of physiological interest, impedance is expressed graphically as a spectrum of moduli and a spectrum of phase angles versus frequency (Figure 8.1). The resolution of the Fourier method is limited since only information at multiples of heart rate are obtained. To improve resolution, one can pace the heart at several fixed rates and perform Fourier analysis for every heart rate in the steady state (O'Rourke and Taylor, 1966).

The vascular input impedance in the ascending aorta is of particular significance. Not only does this characterise the properties of the whole systemic circulation, but also it can be taken to represent the hydraulic load presented by the systemic circulation to the left ventricle of the heart. The original experimental study of the input impedance of systemic and pulmonary arterial circulation has been performed on dogs (Patel *et al.*, 1963a). Data from other experimental animals and humans were reported soon afterward (Nichols and O'Rourke, 1990; Westerhof *et al.*, 1979). These impedance patterns are

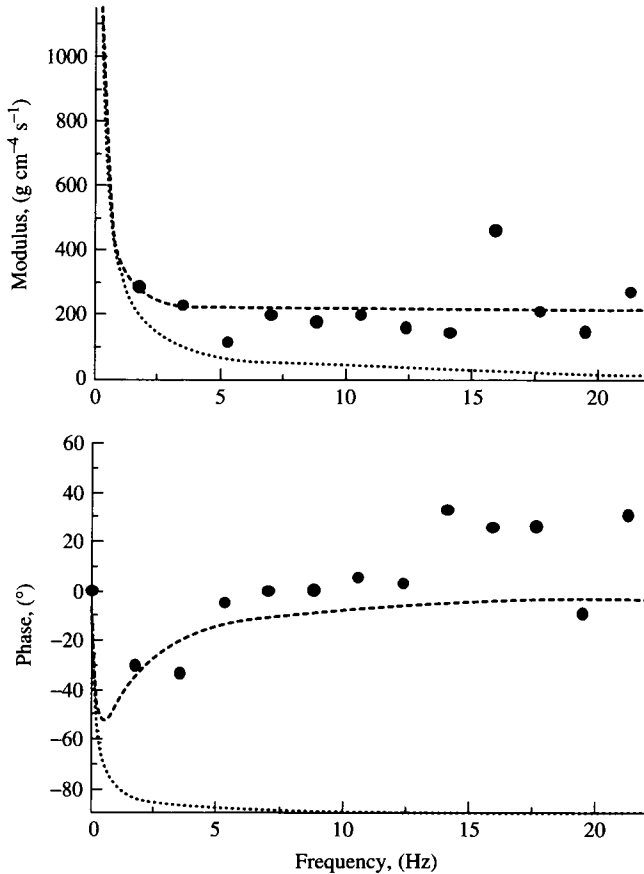


**Figure 8.1.** Full circles are experimental impedance modulus (*above*) and phase angle (*below*) in the ascending aorta of a dog in basal state. Dotted lines and dashed lines pertain to the best approximating impedance patterns obtained from a one-pole frequency response (8.7) and a one-zero over one-pole frequency response (8.8), respectively.

qualitatively similar to the data from a dog displayed in Figure 8.1. At zero frequency, the impedance modulus is equal to peripheral resistance (ratio of mean pressure to mean flow), whereas the phase angle is zero. Phase is negative (i.e., flow leads pressure) at low frequencies, crosses zero in the neighbourhood of the minimum impedance modulus, and becomes positive (i.e., flow lags pressure) at higher frequencies. In some circumstances, impedance modulus falls steeply from the value at zero frequency (total peripheral resistance) to a minimal value (which usually occurs between 2 and 4 Hz in the dog); this minimum is followed by a maximum and a second minimum

(between 5 and 10 Hz in the dog). In other circumstances (e.g., Figure 8.1), the impedance modulus shows a single minimum in the range from 0 to 10 Hz. High-frequency fluctuation of impedance moduli settle about a value that is 5 to 15% of total peripheral resistance. The minima of the input impedance moduli and the zero crossing of the phase angle are attributed to the presence of reflection phenomena in the arterial system. Extensive discussions of this issue are found in Burattini *et al.* (1991), Nichols and O'Rourke (1990), O'Rourke (1982), and O'Rourke and Taylor (1967).

#### **8.4. DATA-DRIVEN MODELS OF VASCULAR IMPEDANCE (FREQUENCY RESPONSE TECHNIQUE)**

It is commonly understood that measurements of ascending aortic input impedance provide information about the physical state of left ventricular load as it relates to peripheral resistance, overall arterial compliance and inertial properties of blood motion, and effects of both pressure and flow wave travel and reflections. However, quantitative evaluations of changes in these properties from changes in impedance patterns require making reference to a formal model. This model must be able to closely approximate experimental impedance and be characterised by parameters that have physiological relevance.

The frequency response technique (Graupe, 1976) is here discussed as a proper general framework for identifying models of vascular impedance. In accordance with the guidelines in modelling methodology discussed in Chapter 1, these models may be developed in two steps. The first step is to look for data-driven, or black box, models where all that is required is an overall representation of pressure-flow dynamics in a site of a vascular system, without needing to know specifically how the physiological system gives rise to such an I/O behaviour. This goal is achieved after finding a model the frequency response of which gives a satisfactory approximation of the considered vascular impedance data. This frequency response can be given the generalised form of a gain multiplied by the ratio between zeros and poles where the characteristic parameters (time constants, damping factors, natural pulsations) are purely phenomenological. The subsequent step in the modelling process is to find structures that are compatible with the identified frequency responses and to address how these model structures help in interpreting the physical processes that give rise to experimental observations (Burattini *et al.*, 1994a).

### 8.4.1. SIMPLE DATA-DRIVEN MODELS OF ASCENDING AORTIC IMPEDANCE

Our analysis is limited here to a one-pole function:

$$Z_p(jn\omega) = \frac{P(jn\omega)}{Q(jn\omega)} = \frac{G}{1 + jn\omega\tau} \quad (8.7)$$

and a one-zero over one-pole function:

$$Z_{zp}(jn\omega) = \frac{P(jn\omega)}{Q(jn\omega)} = G \frac{1 + jn\omega\tau_n}{1 + jn\omega\tau_d} \quad (8.8)$$

since these are of particular interest for subsequent discussion of Windkessel-type models of the ascending aortic impedance and related physiological interpretation. No hypothesis on a model structure associated with the generalised frequency responses of (8.7) and (8.8) is requested. The time constants,  $\tau$ ,  $\tau_n$  and  $\tau_d$ , are purely phenomenological parameters and do not imply that a specific physical property may be associated with them. They allow any number of physical processes to be responsible for the apparent low-pass filter behaviour of the considered vascular beds. The gain  $G$  is the value of the frequency response at zero frequency, that is, the ratio of mean pressure to mean flow. If venous pressure is so small with respect to arterial pressure that it may be disregarded (as it is currently done),  $G$  represents total peripheral resistance as seen from the impedance measurement site. The two parameters,  $\tau$  and  $G$ , of (8.7) and the three parameters,  $G$ ,  $\tau_n$  and  $\tau_d$ , of (8.8) can be estimated by fitting these equations (models) to the data collected during a steady state. Optimised model parameters can be obtained in the frequency domain by minimising the difference between experimental and model predicted impedance spectra (Canty *et al.*, 1985; Yoshigi and Keller, 1997). A time domain approach also can be used. This consists of minimising the difference between experimental pressure (flow) and pressure (flow) predicted by the model using flow (pressure) as input (Burattini and Gnudi, 1982, 1983; Burattini *et al.*, 1987; Toorop *et al.*, 1987). Because transformation between the time and frequency domains is easily applied for linear models, these alternative parameter estimation procedures must be regarded as complementary. Figure 8.1 shows the approximation of ascending aortic impedance data (solid circles) in a dog by the frequency responses of (8.7) and (8.8). Figure 8.2 shows the corresponding fits to pressure data. This example is representative of what is found, in general, in humans and different species of animals. It clearly shows that the one-pole frequency response of (8.7) is inadequate to describe the dynamics of ascending aortic pressure-flow relationships.

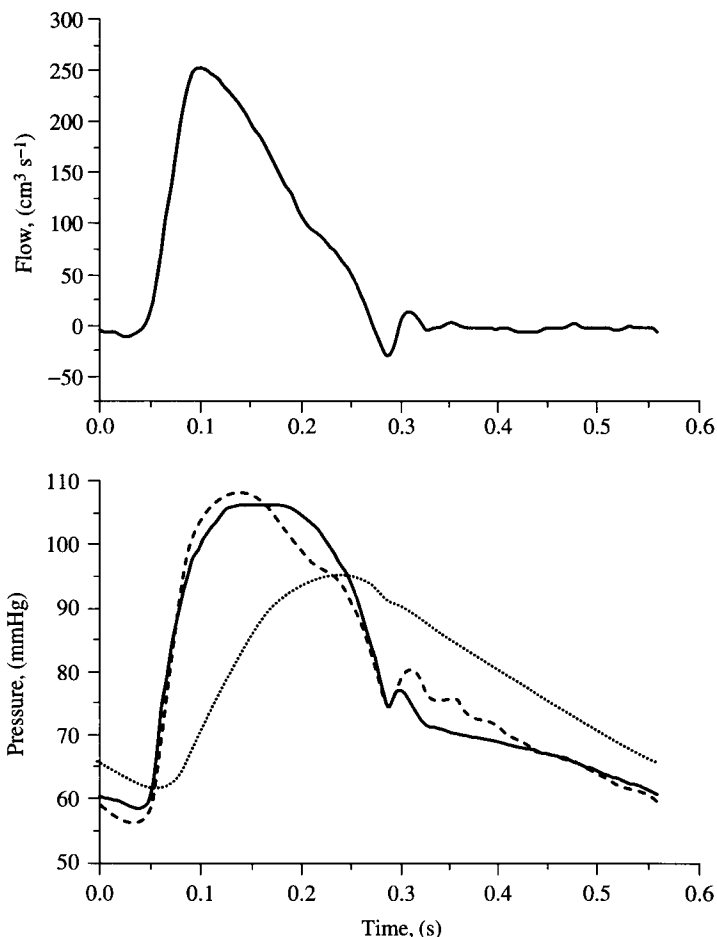


**Figure 8.2.** Upper panel, Flow measured in the ascending aorta of a dog under basal state. Lower panel, Fits between experimental ascending aortic pressure wave (solid line) and pressure waves obtained from a model described by the (8.7) (dotted line) and a model described by the (8.8) (dashed line).

The assumption of a model structure becomes essential if we want a specific interpretation of the physical and physiological properties that give rise to observed input impedance spectra and the limitations in model-based approximation of impedance data.

Physiological interpretation is the issue where the modern system’s identification approach meets the understanding of physiological functions as it has been historically assessed from experimental observations.

## 8.5. HISTORICAL DEVELOPMENT OF WINDKESSEL MODELS

### 8.5.1. ELASTIC WINDKESSEL MODELS

Quantitative studies of the circulation may have commenced with the work of Hales (1733). He discussed arterial and venous elasticity, measured blood pressure and pressure flow relations of vascular beds, estimated cardiac output, and emphasised the importance of arterial elasticity aiding in acceptance of pulsatile flow from the ventricle of the heart, and converting this into steady flow through the smallest high-resistance vessels. Frank (1899) and his school pioneered in putting Hales' idea into mathematical form, giving rise to what became known as the *Windkessel* model. In this lumped model, all pressure changes within the arterial tree are considered simultaneous (i.e., infinite wave velocity).

With reference to Figure 8.3, the mathematical formulation of Frank's Windkessel is obtained as follows. Input flow to the arterial system,  $Q_{in}(t)$ , is equal to the sum of the outflow,  $Q_{out}(t)$ , of blood from the arterial system into

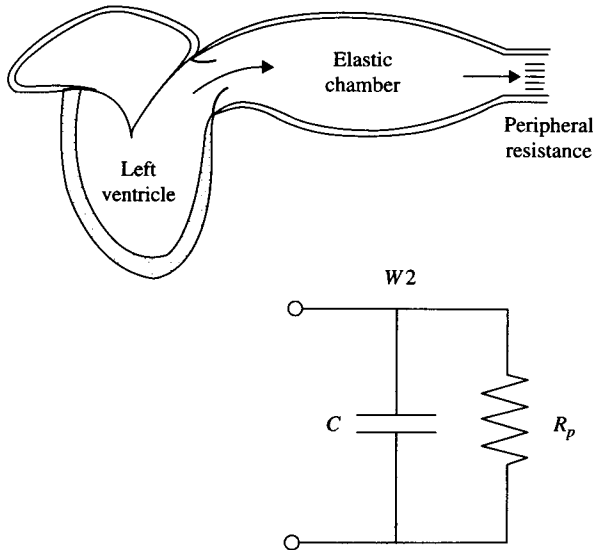


**Figure 8.3.** Schematic representation of the classic Windkessel concept. The arterial tree operates as an elastic reservoir that accepts pulsatile flow from the left ventricle of the heart and converts this into an almost steady flow through the smallest high-resistance vessels. The electrical analogue of the classic Windkessel (W2) consists of a capacitor,  $C$ , representing total systemic arterial compliance, connected in parallel to a resistor,  $R_p$ , representing total peripheral resistance.

the venous system, and the rate ( $dV/dt$ ) of storage (continuity equation):

$$Q_{\text{in}}(t) = \frac{dV(t)}{dt} + Q_{\text{out}}(t) \quad (8.9)$$

Under the hypothesis of linear pressure-volume relationship, the total arterial compliance,  $C$ , is constant throughout a heartbeat. Its value is:

$$C = \frac{dV(t)}{dP(t)} \quad (8.10)$$

The outflow,  $Q_{\text{out}}(t)$ , is assumed proportional to the aortic pressure  $P(t)$ , that is:

$$Q_{\text{out}}(t) = \frac{P(t)}{R_p} \quad (8.11)$$

where  $R_p$  is total peripheral resistance. Substitution of (8.10) and (8.11) into (8.9) yields:

$$Q_{\text{in}}(t) = C \frac{dP(t)}{dt} + \frac{P(t)}{R_p} \quad (8.12)$$

Since there is flow into the arterial system only during ventricular systole,  $Q_{\text{in}}$  is zero in diastole. If  $t^*$  is the time of end of ventricular ejection (in principle it can be the time at an arbitrarily chosen reference point in the diastolic phase) and  $T$  is total duration of the cardiac cycle, the governing equation for the system in diastole is:

$$C \frac{dP(t)}{dt} + \frac{P(t)}{R_p} = 0; \quad t^* < t < T \quad (8.13)$$

The solution of this equation is:

$$P(t) = P^* \exp \left[ -\frac{t - t^*}{\tau} \right]; \quad t^* < t < T \quad (8.14)$$

where  $P^*$  is pressure at the time  $t^*$  and the time constant  $\tau$  equals the product  $R_p C$ . Thus, under the assumption that ascending aortic flow is zero during diastole, the Windkessel model describes the diastolic aortic pressure decay as a monoexponential function with a time constant,  $\tau$ , equal to arterial compliance times peripheral resistance.

If we state a correspondence between voltage and pressure and between current and volume flow, the equations that describe the Windkessel model are formally identical to the equations that describe the dynamics of voltage-current relationships in a circuit that consists of an electrical capacitor,  $C$ , and a resistor,  $R_p$ , connected in parallel. Thus, the two-element circuit depicted in Figure 8.3 is the electrical analogue of the classic Windkessel (W2).



Lauded by pragmatists desiring a quick noninvasive technique for the determination of cardiac output, and despised by theoreticians without such requirements, the Windkessel concept continues to provide a fertile breeding ground for new variations on a classic theme (Noordergraaf, 1978).

Historical applications and improvements of the W2 have been elegantly reviewed elsewhere (Kenner, 1979; Nichols and O'Rourke, 1990; Noordergraaf, 1978; Wetterer and Kenner, 1968). Especially, it has been reported by Kenner (1979) that, in an early experimental setup (Broemser and Ranke, 1930) of an air chamber model supplied by a pressure pump with negligibly small internal resistance, aortic flow pulses were observed that were unlike natural aortic flow pulses. Thus, an additional resistance was introduced at the inlet to improve the Windkessel. This model was called an *improved Windkessel* (Wetterer and Kenner, 1968). The main issue with this improvement was the physiological interpretation of the additional series resistance. In subsequent works, this resistance was given the meaning of internal resistance of the left ventricle, aortic valvular resistance, and, eventually, characteristic impedance of the central aorta (Kenner, 1979). These three different interpretations of the series resistance formalise three different conceptual models. In the first and second model, the series resistance pertains to the source and should be located before or outside the classic Windkessel. Only the third model can be called an improved Windkessel in the sense of a model with the purpose of representing the gross behaviour of the arterial system (Westerhof *et al.*, 1971). The Windkessel with the series resistance representing aortic characteristic impedance (Figure 8.4) is currently referred to as the *three-element Windkessel*

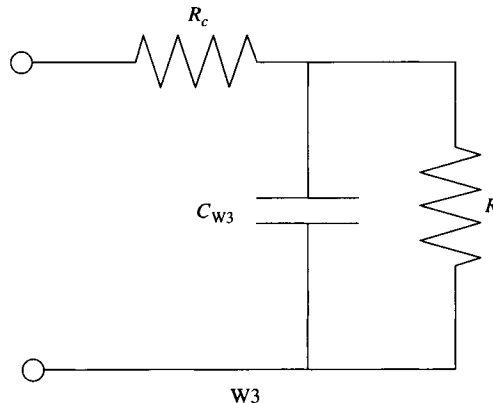


**Figure 8.4.** Electrical analogue of the three-element Windkessel model (W3). The capacitor,  $C_{W3}$ , represents total arterial compliance. The resistor,  $R_c$ , represents aortic characteristic impedance, and the resistor  $R$  is taken equal to the difference between total peripheral resistance,  $R_p$ , and  $R_c$  to keep the total resistance value equal to  $R_p$ .

(W3) and has been widely used to describe and interpret the hydraulic load faced by the left ventricle of the heart (Burkhoff *et al.*, 1988; Burattini and Campbell, 1999, Burattini *et al.*, 1987; Fogliardi *et al.*, 1996; Gnudi, 1998a, b; Hettrick *et al.*, 1995; Sunagawa *et al.*, 1982; Stergiopulos *et al.*, 1995; Toorop *et al.*, 1987).

### 8.5.2. VISCOELASTIC WINDKESSEL MODEL

It is generally accepted that the deformation suffered by the arterial wall depends on both the magnitude of the stress and the rate at which it is applied (Apter *et al.*, 1966; Bergel, 1972; Dobrin, 1983; Learoyd and Taylor, 1966; Milnor, 1982; Nichols and O'Rourke, 1990; Westerhof and Noordergraaf, 1970). As a consequence, the arteries are more likely to be conceived as a viscoelastic reservoir where fluid storage capacity is associated with viscous losses of wall motion. The hypothesis that arterial viscoelasticity, rather than pure elasticity, might affect aortic pressure-flow relationships yielded a modified Windkessel configuration, called *viscoelastic Windkessel* (VW) (Figure 8.5). This model configuration was first interpreted in terms of viscoelasticity by Canty *et al.* (1985) for the coronary circulation. It was later discussed by Burattini and Campbell (1993) and Burattini *et al.* (1992, 1994a, 1997) in experimental applications to distal circulatory districts, involving even more sophisticated descriptions of viscoelasticity than the Voigt cell. Marcus *et al.* (1994) attempted an application of the VW to the ascending aortic pressure-flow relationships. This study, however, was limited to the evaluation of static compliance since the

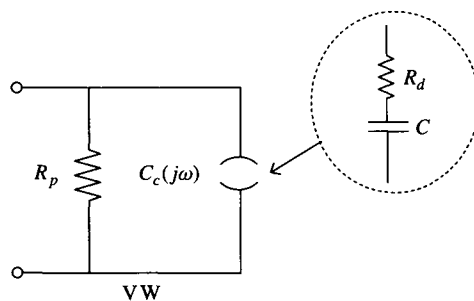


**Figure 8.5.** Electrical analogue of the viscoelastic Windkessel model (VW). This model consists of total peripheral resistance,  $R_p$ , parallel with a complex and frequency-dependent compliance,  $C_c(j\omega)$ , expressed by (8.24). This complex compliance is described by a Voigt cell. The electrical analogue of this cell consists of a resistor,  $R_d$ , accounting for viscous losses of wall motion, in series with a capacitor,  $C_{VW}$ , representing static compliance. Adapted from Burattini and Natalucci (1998, Figure 2, p. 504 with permission from Elsevier Science).

noninvasive experimental setup did not allow a satisfactory characterisation of the viscous parameter. Eventually, a more complete identification and validation of the VW model was carried out by Burattini and Natalucci (1998), making use of invasive pressure and flow measurements in dogs. An intriguing finding in the process of VW model validation was that the complex and frequency-dependent compliance of this model resolves contradictions in the estimates of total arterial compliance based on the elastic Windkessel theory. To understand these contradictions and how to address them, physiological interpretation of aortic impedance by the Windkessel models is reviewed in the following sections in light of the more general identification approach discussed in Section 8.4.

## 8.6. WHERE WINDKESSEL MODELS' IDENTIFICATION MEETS PHYSIOLOGICAL INTERPRETATION

The aortic input impedance as described by the  $W2$  model is:

$$Z_{W2}(jn\omega) = \frac{R_p}{1 + jn\omega R_p C_{W2}} \quad (8.15)$$

This is equivalent to the one-pole frequency response of (8.7) under the following conditions:

$$\tau = R_p C_{W2} \quad (8.16)$$

$$G = R_p \quad (8.17)$$

Equations (8.16) and (8.17) yield a unique solution for the physical parameters  $R_p$  and  $C_{W2}$ . Thus, in accordance with concepts of identifiability of parametric models (Bellman and Åström, 1970; Cobelli and Di Stefano III, 1980) the  $W2$  model is uniquely identifiable from an I/O experiment; that is, from pressure and flow measurements.

$W3$  and the VW are two candidate model structures that are compatible with the frequency response of (8.8). The equivalence between the aortic input impedance as described by the  $W3$  model and (8.8) requires that the following conditions be satisfied:

$$\tau_n = \frac{R \cdot R_c}{R + R_c} C_{W3} \quad (8.18)$$

$$\tau_d = R \cdot C_{W3} \quad (8.19)$$

$$G = R + R_c \quad (8.20)$$

If the VW model is assumed to describe the aortic input impedance, the following relationships hold:

$$\tau_n = R_d C_{VW} \tag{8.21}$$

$$\tau_d = (R_p + R_d) \cdot C_{VW} \tag{8.22}$$

$$G = R_p \tag{8.23}$$

The W3 model is uniquely identifiable from pressure and flow measurements because the parameters  $C_{W3}$ ,  $R$ , and  $R_c$  can be evaluated uniquely from (8.18) to (8.20). Likewise, the VW model is uniquely identifiable because the parameters  $C_{VW}$ ,  $R_p$ , and  $R_d$  can be evaluated uniquely from (8.21) to (8.23).

Of course, if the W3 or the VW model structures are assumed to be *a priori*, as done in most of the reported experimental studies, the resistive and capacitive parameters of these models can be directly estimated from fitting to data. Then, phenomenological parameters  $G$ ,  $\tau_n$  and  $\tau_d$ , of model's frequency response can be determined from (8.18) to (8.20) in case the W3 model is assumed and from (8.21) to (8.23) in case the VW model is assumed. It has been verified on experimental basis that both the W3 and the VW model, when applied to the same pressure-flow data, yield the same  $G$ ,  $\tau_n$ , and  $\tau_d$  values as expected on theoretical basis (Burattini and Natalucci, 1998).

In conclusion, there is no question that the competing W3 and VW models constitute alternative hypotheses for a gross description of the dynamics of the left ventricular load that are equivalent in terms of data fit (Burattini, 1989; Burattini and Natalucci, 1998; Westerhof and Krams, 1986). These models, however, are different in terms of physiological interpretation of the mechanisms that give rise to the observed data. There is a need to examine the hypotheses underlying the W3 and VW structures to determine which are compatible with physiological and clinical observations and, on this basis, to make a choice between these competing structures.

In the W3 model, the gain  $G$  of the generalised frequency response of (8.8) has the meaning of total peripheral resistance. However, this resistance is dissected into two components:  $R$  and  $R_c$  (8.20). This assumption implies that the arterial system stores blood during systole with the left ventricle facing total peripheral resistance, whereas, during diastole, the stored blood flows through a lower resistor,  $R$ , and the decay of pressure is exponential with a time constant,  $\tau_d$ , equal to the product of  $R$  and  $C_{W3}$  (8.19). The series resistor,  $R_c$ , is assumed to represent the characteristic impedance of the proximal aorta (Westerhof *et al.*, 1971). This implies the further assumption that the characteristic impedance is approximately a real number and, therefore, dimensionally comparable to a resistor. These assumptions find

contradictions in that the characteristic impedance does not exist for mean pressure and flow and does not dissipate energy. Recently, a test of the W3 model behaviour versus a complex simulator of the arterial system showed that, over the frequency range of physiological interest, the  $R_c$  parameter is inconsistent with the meaning of aortic characteristic impedance originally assigned to it (Stergiopoulos *et al.*, 1995). A further limitation of placing  $R_c$  in series to the W2 model is that the behaviour of compliance is affected. During diastole, the resistor  $R_c$  causes the pressure applied to capacitor  $C_{W3}$  (that is, to the wall of the elastic reservoir) to drop lower than the pressure generated by the heart. It has been observed in dogs that this pressure drop was as low as  $(2.3 \pm 0.4)\%$  of mean pressure, in the pressure range over 110 mmHg, and increased up to  $(14.3 \pm 1.7)\%$  in the pressure range below 70 mmHg (Burattini and Natalucci, 1998).

In conclusion, the resistance  $R_c$  introduces a zero factor in the frequency response of the Windkessel that improves the approximation of pressure-flow data observed in the frequency domain and, equivalently, in the time domain. The interpretation of  $R_c$  in terms of wave propagation phenomena, however, shows significant drawbacks, as discussed previously. These drawbacks fit in the conceptual framework that interpretation in terms of wave propagation reads too much into the nature of the lumped Windkessel theory.

In the VW model, the gain  $G$  in (8.8) correctly represents total peripheral resistance  $R_p$  (8.23) and the model configuration does not change from systole to diastole. Physiological meaning of  $C_{VW}$  and  $R_d$  is inferred from the assumption that the whole arterial system behaves as a viscoelastic, rather than purely elastic, reservoir. In accordance with the Voigt model for viscoelasticity (Westerhof and Noordergraaf, 1970), the resistor,  $R_d$ , accounts for viscous losses of wall motion, and the capacitor,  $C_{VW}$ , represents static compliance. These two elements give rise to a complex compliance,  $C_c(jn\omega)$ , that changes in frequency according to the following equation (Burattini and Natalucci, 1998):

$$C_c(jn\omega) = C_{VW} \frac{1}{1 + jn\omega R_d C_{VW}} = C_{VW} \frac{1}{1 + jn\omega \tau_n} \quad (8.24)$$

The time constant,  $\tau_n = R_d C_{VW}$ , is related to *creep* (Westerhof and Noordergraaf, 1970) and characterises the zero factor of the VW model's frequency response (8.8) and (8.21). The presence of this zero factor yields the improvement in the approximation of pressure-flow data by the VW model with respect to the purely elastic W2 model (Figure 8.2). This improvement can be read as follows. The viscous element  $R_d$  introduces a phase lag between pressure and

flow that tends to compensate the phase lead of flow with respect to pressure that is caused by the purely elastic element.

The W2 is a special case of the VW model that results from neglecting the viscous losses. Indeed, when  $R_d$  is zero, the frequency response of (8.8), associated with (8.21) to (8.23), reduces to (8.15) associated with (8.16) to (8.17). These equalities imply that  $C_{VW}$  equals  $C_{W2}$ . This was demonstrated by Burattini and Natalucci (1998). These authors compared the W2 and VW models using measurements of ascending aortic pressure and flow taken from four dogs under a variety of haemodynamic states that produced a broad mean-pressure range of 40 to 165 mmHg. Total peripheral resistance was computed as the ratio of mean pressure to mean flow. The other model parameters (i.e.,  $C_{W2}$  in the W2 model and  $R_d$  and  $C_{VW}$  in the VW model) were estimated by fitting to the entire cycle of experimental pressure (full pressure method, FPM). An almost perfect correlation ( $\rho = 0.999$ ) between  $C_{W2}$  and  $C_{VW}$  estimates (Figure 8.6) indicated that the static (zero-frequency) compliance of the VW model is consistent with the compliance of the W2 model.

In the study by Burattini and Natalucci (1998), the FPM was also applied to the W3 model and the parameters  $R$ ,  $R_c$ , and  $C_{W3}$  were estimated. The

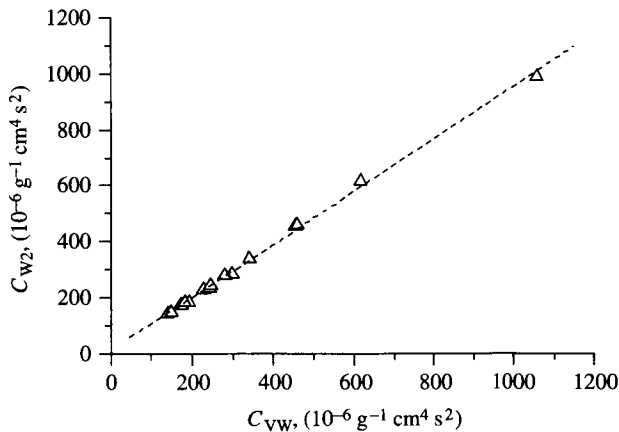


**Figure 8.6.** Scattergram of estimates of compliance,  $C_{W2}$ , obtained from application of the full pressure fit method (FPM) to the classic Windkessel model, versus the corresponding estimates of static compliance,  $C_{VW}$ , provided by the viscoelastic Windkessel model. Linear regression yielded the dashed line:  $C_{W2} = 0.94C_{VW} + 11.9$ ;  $\rho = 0.999$ . From Burattini and Natalucci (1998, Figure 9, p. 511 with permission from Elsevier Science).

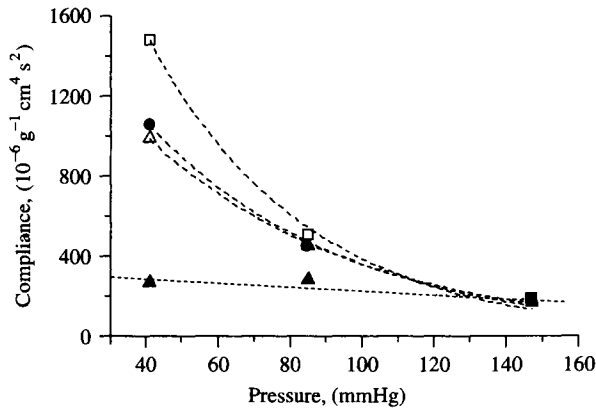


**Figure 8.7.** Estimates of total arterial compliance as a function of mean aortic pressure in one dog obtained from applying the full pressure fit method (FPM) to the classic Windkessel (W2) (open triangles), viscoelastic Windkessel (VW) (full circles), and three-element Windkessel (W3) (open squares) models. Dashed lines are first-order exponential fitting curves. Full triangles are estimates of total arterial compliance obtained from the W2-based pulse pressure method (PPM). Dotted line is linear.

estimates of  $C_{W3}$  were practically coincident with those of  $C_{VW}$  and  $C_{W2}$  in the higher pressure range but diverged toward higher values with decreasing pressure (Figure 8.7) owing to an increasing effect of the resistance  $R_c$ .

## 8.7. CONTRADICTIONS IN CLINICALLY ORIENTED COMPLIANCE ESTIMATION METHODS (HOW THE VISCOELASTIC WINDKESSEL RESOLVES THEM)

The comparative analysis of the most common structures of Windkessel models as discussed previously is based on frequency-response identification method. This means that the information contained in the full pressure and flow wave is used for model identification. For linear systems, it does not matter whether model identification is performed by fitting to impedance data or to the full-time course of pressure (or flow) over a cardiac cycle in steady state because frequency-domain and time-domain analyses are complementary (Graupe, 1976).

Paucity of invasive data in humans and the absence (or difficulty in the assessment) of noninvasive methodology for continuous data acquisition, notably the flow pulse, have limited the application of the frequency-response

technique, thus leading pragmatists to the development of simplified experimental protocols easy to apply in clinical settings. The tendency has been to measure pressure pulse and cardiac output and to use the W2 model to estimate total arterial compliance. Among these W2-based methods, the decay time method (DTM), the area method (AM), and the pulse pressure method (PPM) are reviewed in the following paragraphs. The aim is to discuss the limitations of these methods and address the contradictions arising from the finding that the PPM yields significantly different estimates of total arterial compliance with respect to the DTM, the AM, and even the FPM applied to the W2.

### 8.7.1. DECAY TIME METHOD AND AREA METHOD

In accordance with (8.14), the DTM estimates total arterial compliance by fitting an exponential function to the diastolic decay of aortic pressure (Liu *et al.*, 1986; Stergiopoulos *et al.*, 1995; Yin and Liu, 1989). For practical applications, (8.14) assumes the form:

$$P(t) = P_0 \exp \left[ -\frac{t - t_0}{\tau} \right]; \quad t_0 \leq t \leq t_1 \quad (8.25)$$

Where the starting time  $t_0$  and final time  $t_1$ , arbitrarily chosen, mark the part of diastole from which compliance is estimated. This method has the advantage that a measurement of cardiac output (relatively easy to do) is needed to estimate peripheral resistance,  $R_p$ , from mean pressure. The time constant  $\tau$  is estimated from diastolic pressure fit, such that an estimate,  $C_{dt}$ , of compliance is obtained from the ratio between  $\tau$  and  $R_p$ . Drawbacks of this method are that there is no golden rule as to the best choice of  $t_0$  and  $t_1$  and that the pressure decay may not be an exact exponential or is distorted from a true exponential by reflections or other causes (Yin and Liu, 1989).

The AM essentially represents an integral variation of the exponential decay method. According to the originators of this method (Randall *et al.*, 1976) and the researchers who used it (Liu *et al.*, 1986), the advantage is that it does not require a strictly exponential aortic pressure decay. Compliance,  $C_{am}$ , is estimated from knowledge of the area,  $A$ , under the diastolic portion of the pressure curve marked by the values  $P_0$  and  $P_1$  at times  $t_0 < t_1$ , respectively:

$$C_{am} = \frac{A}{R_p(P_0 - P_1)} \quad (8.26)$$



where:

$$A = \int_{t_0}^{t_1} P(t) dt \quad (8.27)$$

Comparative analyses based on experimental and simulated data have shown that the DTM and the AM, when applicable, yield essentially similar estimates of total arterial compliance (Burattini and Natalucci, 1998; Stergiopoulos *et al.*, 1995). This similarity is consistent with the concept that the underlying model (i.e., the W2 model) is the same for the two competing estimation methods. Some scatter of parameter estimates is caused by noise on test signals and distortions. Indeed, it has been reported that both the DTM and the AM are very sensitive to diastolic pressure wave distortion due to wave reflection and other causes, and to the starting and final instants that mark the part of diastole from which compliance is estimated (Burattini and Natalucci, 1998; Stergiopoulos *et al.*, 1995; Yin and Liu, 1989).

### 8.7.2. PULSE PRESSURE METHOD

The PPM is a further simplified method for estimating arterial compliance that is based on the W2 model (Stergiopoulos *et al.*, 1994, 1995). Pulsatile flow measured in the ascending aorta is used as model input, and the pulse pressure,  $\Delta\hat{P}$ , defined as systolic minus diastolic aortic pressure, is predicted by the W2 model filled with total peripheral resistance (determined as the ratio of mean pressure to mean flow) and an assumed compliance value,  $C_{pp}$ . An iterative procedure looks for the value of the best estimate of  $C_{pp}$  by fitting  $\Delta\hat{P}$  to the experimental pulse pressure,  $\Delta P$ .

Compared with the DTM and the AM, the PPM makes use of the information contained in the systolic, rather than diastolic, portion of pressure. A measurement of the flow pulse, however, is needed to predict pulse pressure. Because all these methods are based on the W2 model, where compliance is assumed to be constant throughout the heart cycle, the compliance estimates obtained from information contained in the PPM, as part of the systolic portion of pressure, and those obtained from information contained in the diastolic portions of pressure (either AM or DTM) should be similar. In contrast to this logical deduction from systems identification theory, reported experimental studies showed significant differences between estimates of total arterial compliance provided by the PPM with respect to those provided by both the AM and the DTM (Burattini and Natalucci, 1998; Carlier *et al.*, 1998). Another contradiction is in the reported assumption (not demonstrated experimentally, however) that an estimation procedure that fits the pressure predicted by the W2 model to the full-pressure wave (W2-FPM) would not yield estimates of total arterial

compliance as satisfactory as those obtained from the PPM (Stergiopoulos *et al.*, 1994). Common sense of modellers and logical deduction from systems identification theory would suggest that the W2-FPM should work better because the full-pressure wave should contain more information than the pulse pressure alone. Experimental tests performed by Burattini and Natalucci (1998) showed that the PPM and the W2-FPM yielded significantly different estimates of total arterial compliance. Over a broad mean pressure range, the W2-FPM-based estimates of  $C_{W2}$  as a function of mean pressure showed an exponential decrease with increasing pressure. By contrast, the PPM-based estimates showed a relatively non-pressure-dependent trend (Figure 8.7). The difference in the estimates of  $C_{W2}$  and  $C_{PP}$  was low at higher mean pressure values and increased exponentially with decreasing pressure. Although in experimental studies there is no *gold standard* to test model-based estimates of compliance, it is generally agreed that no significant pressure dependence of compliance estimates is in disagreement with well-documented experimental observations (Bergel, 1972; Cox, 1975; Dobrin, 1983; Hallock and Benson, 1937; Langewouters *et al.*, 1984; Liu and Yin, 1986; Milnor, 1982; Nichols and O'Rourke, 1990; Weizsäcker, 2000; Weizsäcker *et al.*, 1983).

### 8.7.3. RECONCILIATION WITH THE VISCOELASTIC WINDKESSEL

Models are psychologically most appealing when they succeed but logically strongest when they fail (Yates, 1978). Indeed, the apparent failure of the PPM can stimulate a modeller (and it did) to answer the question as to why the information contained in the systolic portion of pressure yields an underestimation of W2 model compliance. The VW model concept helps to address this question in light of the underlying assumption that, under dynamic conditions, total arterial compliance is expressed by a complex number (8.24) whose modulus decreases with increasing frequency. Because the PPM, by definition, uses the information contained in the moduli of the first harmonics of pressure and flow, it might yield a value of dynamic, rather than static, compliance related to the heart pulsation,  $\omega_h = 2\pi/T$ . Following this line of thought, Burattini and Natalucci (1998) found that the modulus of dynamic compliance,  $|C_c(\omega_h)|$ , provided by the VW model (8.24) showed a correlation with compliance estimates,  $C_{PP}$ , provided by the PPM, as good as it is displayed in Figure 8.8, the correlation coefficient equalling 0.975. In light of the VW model, the estimates of compliance obtained from the DTM and the AM, which take advantage of the information contained in the diastolic decay of pressure, are logically close to the estimates of the static Windkessel compliance (either  $C_{W2}$  or  $C_{VW}$ ) because of the slow dynamics of pressure decay (Burattini and Natalucci, 1998).

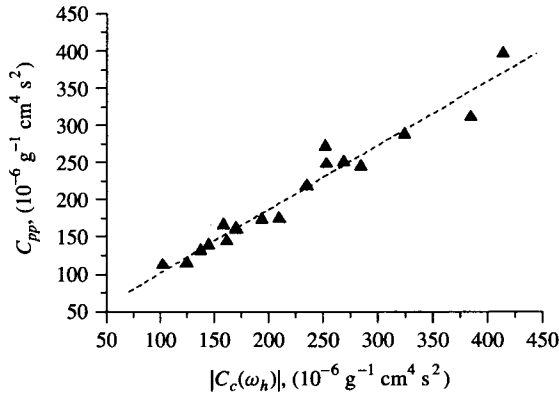


**Figure 8.8.** Scattergram of estimates of compliance,  $C_{pp}$ , obtained from application of the pulse pressure method (PPM) to the W2 model, versus the corresponding moduli of dynamic compliance,  $|C_c(\omega_h)|$ , provided by the VW model (8.24), at the heart rate pulsation,  $\omega_h$ . Linear regression yielded the dashed line:  $C_{pp} = 0.85|C_c(\omega_h)| + 16.6$ ;  $\rho = 0.975$ . From Burattini and Natalucci (1998, Figure 10, p. 511 with permission from Elsevier Science).

## 8.8. DISTRIBUTED DESCRIPTION OF LINEAR ARTERIAL SYSTEMS TO INFER AORTIC WAVE REFLECTION

There is overwhelming evidence for the existence of reflected waves in the systemic arterial circulation and their importance in influencing the pressure and flow pulse contour from the ejecting ventricle (Latham, 1989; Nichols and O'Rourke, 1990; O'Rourke, 1982; Sipkema *et al.*, 1980; Westerhof *et al.*, 1972). However, there is still dispute as to the quantitative description of reflected waves and location of reflecting sites as seen from the heart (Burattini and Di Carlo, 1988; Burattini, 1989; Burattini and Campbell, 1999b; Burattini *et al.*, 1991, 1994b; Campbell *et al.*, 1989; Papageorgiou and Jones, 1988; Sipkema *et al.*, 1975). Models with distributed, rather than lumped, parameters are needed for quantitative analysis of wave propagation and reflection. Taylor conducted the first quantitative studies on the impact of wave reflection on arterial pulse waves and impedance patterns making use of simple, uniform and nonuniform elastic tubes (transmission lines, in the electrical analogy) terminating in a real impedance (Taylor, 1957a, b, 1965). This terminal impedance may be regarded, in the steady-state solution, as the resultant of all impedances lying beyond the tube termination. In other words, it lumps together all the more distal ramifications and terminations of the arterial systems, such that a functionally discrete reflection site is seen (Taylor, 1957a,

1966). Subsequent refinements of Taylor's approach yielded tube models that assumed the form of a single uniform elastic tube terminating in a complex and frequency-dependent load (Burattini and Di Carlo, 1988; Burattini and Gnudi, 1982, 1983; Sipkema and Westerhof, 1975), two tubes in series (Wetterer and Kenner, 1968), and two tubes in parallel (Burattini and Campbell, 1989, 1993; Campbell *et al.*, 1990; Chang *et al.*, 1995; Liu *et al.*, 1989; Nichols and O'Rourke, 1990; O'Rourke, 1982). Models consisting of two elastic tubes connected in parallel have been referred to as *T-tube models*. These models, better than others, have aided the interpretation of aortic pressure-flow relationships in terms of wave travel and reflection.

### 8.8.1. THE ORIGINAL *T*-TUBE MODEL

The *T*-tube model was suggested as a conceptual framework to interpret the morphology of ascending aortic pressure waves and impedance patterns in terms of two uniform elastic wave-transmission tubes of different lengths, connected in parallel and terminating in a purely resistive load (McDonald, 1968; Nichols and O'Rourke, 1990; O'Rourke, 1982). These two transmission paths represent the two separate vascular beds perfused by the ascending aorta. These are the upper part of the body, with the summation of arterial terminations relatively close, and the lower part of the body, with the summed arterial terminations much farther away. This model was extensively used by O'Rourke and coworkers (O'Rourke and Taylor, 1967; Nichols and O'Rourke, 1990; Nichols *et al.*, 1986; O'Rourke, 1982), although it never lent itself to a clear mathematical and physiological assessment.

The first zero crossing of the input impedance phase angle observed in the head-end and the body-end circulations was assumed to occur at a quarter wavelength in analogy with what happens in a loss-free elastic tube loaded with a purely resistive load. The quarter wavelength formula:

$$d = \frac{v}{4f_0} \quad (8.28)$$

where  $f_0$  is the frequency at the first zero crossing of the impedance phase angle and  $v$  is the pulse wave velocity along the considered transmission tube, was used to estimate the tube length (Nichols and O'Rourke, 1990). This length has become a parameter of great physiological interest since it represents the distance to an effective reflection site from which it appears to the heart that the pulse wave is reflected back. It is generally referred to as the effective length of the considered portion of the circulation represented by a tube model (Burattini and Di Carlo, 1988; Burattini and Campbell, 1993;

Burattini *et al.*, 1994b; Campbell *et al.*, 1989; Nichols and O'Rourke, 1990; Sipkema and Westerhof, 1975).

Two effective lengths,  $d_h$  and  $d_b$ , characterise the  $T$ -tube model. These lengths quantify the distances to two effective reflecting sites as seen in the head-end and body-end portions of the circulation, respectively. Average estimates for  $d_h$  and  $d_b$ , pursued from the literature and reported by Nichols and O'Rourke (1990, their Figure 11.27) are, respectively, 3.2 and 9.5 cm, in the guinea pig; 8.4 and 25 cm in the rabbit, 20 and 38 cm in the dog; 23 and 65 cm in the sheep; 29 and 41 cm in the human. Nichols *et al.* (1986) assumed 12 and 48 cm for  $d_h$  and  $d_b$ , respectively, in the kangaroo.

If the reliability of all these estimates of effective lengths is evaluated in light of the hypotheses underlying the original  $T$ -tube model, several contradictions emerge. In this model, the assumption of a purely resistive terminal load, equal to total peripheral resistance, formalises the hypothesis that wave reflection, as seen from the heart, originates at level of arterioles and capillaries. The estimated values for  $d_h$  and  $d_b$ , however, are inconsistent with this assumption. For instance, the 38-cm length of the body-end arm of the  $T$ -tube estimated for the dog locates the effective reflection site in the terminal aortic circulation (compare with the dimensions of the dog's average aortic tree constructed by Patel *et al.*, 1963b). The tube-loading system as seen downstream of this location, however, cannot be represented by a pure resistance (Burattini *et al.*, 1994a). A further criticism is that the terminal resistance of both the head-end and body-end transmission tubes is much higher than the related tube's characteristic impedance, such that the input impedance of each transmission path oscillates very strongly and shows little resemblance to input impedance data (Sipkema and Westerhof, 1975; Westerhof *et al.*, 1979). To reduce these impedance oscillations and improve the approximation to reality, longitudinal losses were introduced in the transmission tubes (Nichols *et al.*, 1986). This assumption is, however, contradictory with the experimental evidence of negligible losses in the vessels proximal to the heart that these transmission paths supposedly represent. In a recent study on three dogs, Burattini and Campbell (2000) found that fitting a frictional tube model with resistive terminal load to pressure-flow data measured in the high descending aorta yielded an average ( $\pm$ SE) distance to the body-end effective reflecting site of  $53.4 \pm 3.7$  cm. Relatively high frictional losses enabled this tube model to fit the data, such that a mean pressure drop of  $7.1 \pm 2.3$  mmHg was predicted across the descending aorta. This mean pressure drop is contradictory with the common knowledge in physiology that, in experimental animals and healthy young humans, the conduit and cushioning functions are discharged with great efficiency by the large arteries, such that the mean pressure drop between the ascending aorta and a large peripheral

artery in the forearm or leg is minute, perhaps only 2 to 3 mmHg when the body is supine (O'Rourke, 1995).

### 8.8.2. THE MODIFIED T-TUBE MODEL

To resolve limitations in the original *T*-tube model, the systemic arterial circulation was characterised in terms of a modified *T*-tube model (Figure 8.9) consisting of two loss-free transmission tubes connected in parallel and terminating in first-order low-pass filter loads, rather than simply resistive loads (Burattini and Campbell, 1989, 1993; Burattini *et al.*, 1991; Campbell *et al.*, 1990). The complex terminal loads are described, in a generalised form, by a frequency response function formally identical to (8.8) (see (8.32) in Section 8.9), (Burattini and Campbell, 1993).

This *T*-tube model formulation is characterised by five body-end parameters (subscript *b*) plus five head-end parameters (subscript *h*). These are  $Z_{cb}$  and  $Z_{ch}$ , body-end and head-end tube characteristic impedances, respectively;  $\tau_b$  and  $\tau_h$ , body-end and head-end one-way wave transit times;  $R_{pb}$  and  $R_{ph}$ , body-end and head-end peripheral resistances;  $\tau_{nb}$ ,  $\tau_{db}$ ,  $\tau_{nh}$ ,  $\tau_{dh}$  time constants of body-end and head-end terminal load impedances.

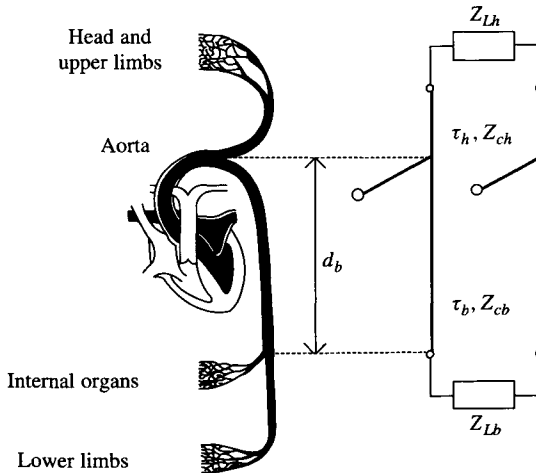


**Figure 8.9.** Modified asymmetric *T*-tube model of the systemic arterial circulation consisting of body-end and head-end circulations that represent, respectively, the upper part of the body, with the summation of arterial terminations relatively close, and the descending aortic circulation, with the summed arterial terminations much further away. See text for details.

The minimum set of measurements required to estimate these model parameters was assessed after analysis of data fit and accuracy of model parameter estimates. It consists of simultaneous measurements of ascending aortic pressure and ascending and upper descending aortic flows (Campbell *et al.*, 1990). Six parameters ( $Z_{cb}$ ,  $Z_{ch}$ ,  $\tau_b$ ,  $\tau_h$ ,  $\tau_{nb}$ , and  $\tau_{nh}$ ) are estimated from fitting to ascending aortic and descending aortic flows. The peripheral resistances  $R_{pb}$  and  $R_{ph}$  are calculated directly from the measured data. The remaining time constants,  $\tau_{db}$  and  $\tau_{dh}$ , of terminal loads are derived from the assumption that, with increasing frequency, the load impedance approximates the tube characteristic impedance (see (8.33) in Section 8.9).

To quantify the overall resistive and capacitive properties of the terminal load impedances from the estimates of body-end parameters,  $R_{pb}$ ,  $\tau_{nb}$ , and  $\tau_{db}$ , and head-end parameters  $R_{ph}$ ,  $\tau_{nh}$  and  $\tau_{dh}$ , the model structure of either the W3 (8.18) to (8.20) or the VW (8.21) to (8.23) can be assumed. The VW model has been the preferred structural representation of these terminal loads (Burattini and Campbell, 1993; Shroff *et al.*, 1995).

The modified *T*-tube model of Figure 8.9 has proven successful in explaining changes in features of ascending aortic pressure and flow waves under several physiological conditions in relation to wave-reflection events as they appear to arise from two effective reflecting sites (Burattini and Campbell, 1989, 1993; Burattini *et al.*, 1991; Campbell *et al.*, 1990; Shroff *et al.*, 1995). This model also explained how, in some circumstances, the two reflecting sites may appear as one to the heart (Burattini *et al.*, 1991).

Due to the assumption of complex terminal loads, the effective reflecting sites are complex, such that the load reflection coefficient is complex and frequency-dependent. In this circumstance, the effective length can be estimated according to the following equation:

$$d_i = \frac{v_i}{4f_{0i}} \left( 1 + \frac{\vartheta_i(f_{0i})}{\pi} \right); \quad i = h \text{ or } b \quad (8.29)$$

where  $v_i$  is the pulse wave velocity along the head-end ( $i = h$ ) or body-end ( $i = b$ ) transmission tube,  $f_{0i}$  is the frequency at the first zero crossing of the (head-end or body-end) impedance phase angle, and  $\vartheta_i(f_{0i})$  is the related phase of the load reflection coefficient at  $f_{0i}$ . This phase affects the timing of reflected aortic waves. Equation (8.29) reduces to the quarter wavelength formula when  $\vartheta_i(f_{0i})$  is zero. This happens when an elastic and frictionless tube is loaded with a resistor (Burattini and Di Carlo, 1988; Burattini and Campbell, 1993).

Physiological interpretation inferred from the head-end arm of the modified *T*-tube model is limited because the head-end transmission path supposedly represents the net effects of several equivalent sized head-end vessels directed to the forelimbs and the head, not just one vessel. Thus, it is not possible to

identify a correlation between model structure and anatomy. This observation also holds for the original *T*-tube model. On the other hand, the descending aorta is the dominant vessel in the body-end section. Here, discrete landmarks can be identified, such as location of abdominal branching and terminal aortic bifurcation (or trifurcation). Based on this consideration, Burattini and Campbell (1993) investigated the correlation between structure of the body-end transmission model and anatomy by comparing estimates of tube length and tube compliance with independent assessments of these properties from the descending aorta. The study was made in five anaesthetised dogs under normal conditions. Pressure and flow in the ascending aorta and flow in the upper descending aorta were measured and used to estimate the parameters of modified *T*-tube model. An extra measurement of pressure in the abdominal aorta near the origin of renal arteries was made and used to estimate aortic pulse wave velocity. Together with estimated model parameters, pulse wave velocity allowed calculation of length and compliance of the body-end transmission tube. Calculated length averaged  $30.3 \pm 2.8$  cm and approximated the measured length ( $30.6 \pm 3.0$  cm) of the aorta from the arch to the region of the origin of renal arteries. Additionally, the comparison between model-predicted pressure waveform at the termination of the body-end tube and the experimentally measured pressure waveform near the site of renal artery origin showed a remarkably good agreement. Thus, the junction between the body-end tube and its terminal load (body-end effective reflecting site) was apparently located in this region. Compliance of the body-end transmission tube averaged  $(123 \pm 20) 10^{-6} \text{ g}^{-1} \text{ cm}^4 \text{ s}^2$  and was interpreted as the aortic compliance from the arch to the renal arteries (descending thoracic aortic compliance). The ratio of this compliance to the tube length estimated the effective distributed compliance, meaning the descending aortic compliance per unit length that would be observed in the absence of tapering. This ratio averaged  $(4.10 \pm 0.86) 10^{-6} \text{ g}^{-1} \text{ cm}^3 \text{ s}^2$  and fell between the values of local aortic compliance, from the arch to the abdominal aorta, independently estimated from measurements of pressure and diameter. Thus, the compliance of the body-end transmission path of modified *T*-tube model resulted in a physically identifiable property (Burattini and Campbell, 1993).

In a subsequent work, Shroff *et al.* (1995) tested the ability of the body-end arm of modified *T*-tube model to correctly discriminate between proximal and distal physical properties of descending aortic circulation. They placed a balloon in the external iliac artery to induce changes in the arterial system that would be limited to the portion of body-end arm of the *T*-tube distal to the abdominal aortic region where the effective reflecting site should be located. They found that the balloon inflation solely affected the body-end terminal-load parameters, whereas tube parameters remained practically unchanged with respect to control condition. They concluded that the



terminal-load parameters correspond to the distal arterial system properties as seen from the left ventricle. Proximal arterial mechanical properties, corresponding to tube characteristic impedance and transit time (or tube compliance and inertance), are independent of distal properties, such as load compliances and resistances. Shroff *et al.* (1995) also tested the ability of the model to track the expected changes in proximal and distal mechanical arterial properties after administration of vasoactive drugs. Model behaviour under various vasoactive conditions conformed to the expected patterns and further validated the capability of the model to discriminate between proximal and distal changes in the arterial system properties.

In the original and modified *T*-tube model formulations, arterial tapering is disregarded. Because the descending aorta is the portion of the arterial system where tapering is more evident, Fogliardi *et al.* (1997) evaluated the effects of incorporating an exponential tapering in the body-end arm of modified *T*-tube model. The conclusion of their study was that the complexity added to the uniform tube model by introducing an exponential aortic tapering gives rise only to a better curve fitting but does not show identifiable benefits regarding physiological interpretation of descending aortic impedance. Again, the uniform body-end transmission path yielded estimates of parameters well correlated with the mechanical properties of the descending thoracic aorta. The average of estimated tube lengths of three dogs under normal conditions approximated 29 cm and was close to the measured distance of approximately 28 cm to the abdominal aorta, at level of renal artery origin. Further, a satisfactory resemblance was found between measured terminal aortic pressure and pressure predicted by the model at the junction between transmission tube and its complex terminal load.

## **8.9. IDENTIFIABILITY: A KEY ISSUE IN THE ASSESSMENT OF PHYSIOLOGICAL RELEVANCE OF *T*-TUBE MODEL**

The reported ability of the body-end arm of the modified *T*-tube model of Figure 8.9 to provide a suitable description of wave travel and reflection along the aorta and to discriminate between proximal and distal mechanical properties of the descending aortic circulation seems to conflict with the reported finding by Campbell *et al.* (1989) that the interpretation of arterial impedance by uniform tube models leaves room for an infinite number of exact solutions for tube-length and terminal-load impedance.

There is no question that this problem in uniqueness of tube model parameter solutions must be resolved in the process of model validation. The

aim of the following discussion is to demonstrate that this problem can be resolved for the body-end portion of the systemic arterial bed by means of theoretical identifiability analysis and the concept of determinacy that relates to the selection of suitable parameter values, from a multiplicity of solutions (see Section 8.2).

Let us consider the following expression to describe the input impedance,  $Z_b(jn\omega)$ , of the body-end arm of modified  $T$ -tube model displayed in Figure 8.9:

$$Z_b(jn\omega) = Z_{cb} \frac{1 + \Gamma_{Lb}(jn\omega) \cdot \exp(-j2n\omega\tau_b)}{1 - \Gamma_{Lb}(jn\omega) \cdot \exp(-j2n\omega\tau_b)} \quad (8.30)$$

In accordance with Fourier analysis of pressure and flow waves,  $n$  is an integer that varies in practice from 0 to 15–20,  $\omega = 2\pi/T$  is the fundamental frequency of heart pulsation in rad/s,  $j$  is  $\sqrt{-1}$ ,  $\tau_b$  is the wave transit time from the entrance to the end of the transmission tube, and  $Z_{cb}$  is the tube characteristic impedance.  $\Gamma_{Lb}(jn\omega)$  is the reflection coefficient at the junction between tube and terminal load. This reflection coefficient is a function of  $Z_{cb}$  and of the load impedance,  $Z_{Lb}(jn\omega)$ :

$$\Gamma_{Lb}(jn\omega) = \frac{Z_{Lb}(jn\omega) - Z_{cb}}{Z_{Lb}(jn\omega) + Z_{cb}} \quad (8.31)$$

The load impedance is given the following first-order low-pass filter form:

$$Z_{Lb}(jn\omega) = R_{pb} \frac{1 + jn\omega\tau_{nb}}{1 + jn\omega\tau_{db}} \quad (8.32)$$

The assumption that, with increasing frequency, the load impedance approximates the tube characteristic impedance yields the following additional constraint:

$$\tau_{db} = R_{pb} \frac{\tau_{nb}}{Z_{cb}} \quad (8.33)$$

In (8.30), the wave transit time,  $\tau_b$ , appears in the exponential,  $\exp(-j2n\omega\tau_b)$ . Because this is a periodic function, all values  $\tau_{bi}$  of  $\tau_b$  that are contained in the series:

$$\tau_{bi} = \tau_{b0} + i \frac{T}{2}; \quad i = 0, 1, 2, \dots, N \quad (8.34)$$

with  $N$  large at will yield the same value for the exponential. This theoretical consideration suggests that it is not possible to determine a suitable estimate of  $\tau_b$  uniquely, from measurements of I/O data. When multiplied by an estimate of pulse wave velocity,  $v_b$ , each  $\tau_{bi}$  value yields a value for tube length,  $d_{bi}$ , which is, for the effective length of descending aortic circulation. The presence of multiple solutions for the wave transit time and, as a consequence, for the effective length enhances a problem of determinacy (Brown and Godfrey, 1978) that is related to the selection of the only one solution among  $\tau_{bi}$  and

$d_{bi}$ , values that has clear physiological meaning. If this solution exists, the problem of its selection can be resolved on heuristic basis by fitting the model and data to obtain numerical values for all sets of solutions and, eventually, by contrasting these solutions to the information available on the physical properties of descending aortic circulation, select the solution compatible with the real system.

### 8.9.1. EXPERIMENTAL RESOLUTION OF THE DETERMINACY PROBLEM

There are three free parameters of the body-end arm of modified  $T$ -tube model to be estimated from pressure and flow measurements at the inlet of descending aortic circulation: 1) the tube characteristic impedance,  $Z_{cb}$ ; 2) the wave transit time,  $\tau_b$ , from the input to the termination of the transmission tube; and 3) the time constant,  $\tau_{nb}$ , of the terminal load.  $R_{pb}$  is calculated from the ratio of mean pressure to mean flow, whereas  $\tau_{db}$  is calculated from  $\tau_{nb}$ ,  $Z_{cb}$ , and  $R_{pb}$  making use of (8.33).

Model parameter estimation was accomplished in five anaesthetised, open-chest dogs. Pulsatile pressures were measured from the termination of the ascending aorta near the arch and from the abdominal aorta, close to the origin of the renal arteries. Flow was measured from the ascending aorta and the upper descending thoracic aorta. The distance between the two pressure transducers and the distance between the upper transducer and the origins of the two renal arteries also were measured. These distances were determined at the end of the experiment after the animal had been sacrificed but while the aorta remained longitudinally tethered to the position it held during life. More details are given elsewhere (Burattini and Campbell, 1993).

The parameters  $\tau_b$ ,  $Z_{cb}$ , and  $\tau_{nb}$  were estimated by minimising (with a modified Levenberg-Marquardt algorithm, *Minpack*, Argonne National Laboratory, Argonne, IL) a cost function,  $F_\eta$ , defined as the sum of squared differences between the sampled values of measured and model predicted descending aortic flow. To test the convergence of this procedure to equivalent minima of the cost function associated with different estimates of  $\tau_{bi}$ , repeated runs of the parameter estimation procedure were performed. The first run ( $i = 0$ ) was performed assuming 50 ms as starting value for the wave transit time. This value is commensurate with the physical dimensions, in the dog, of the descending thoracic aorta and expected wave transmission velocity. In accordance with (8.34), the starting values for subsequent runs were assumed equal to  $50 + iT/2$  ms,  $i = 1, 2, \dots, N$ . The starting values for  $\tau_{nb}$  and  $Z_{cb}$  were kept equal to 100 ms and  $500 \text{ g cm}^{-4} \text{ s}^{-1}$ , respectively. Analysis of three runs ( $N = 2$ ) gave sufficient evidence of the existence and the magnitude of multiple solutions for  $\tau_{bi}$ .

In all five experimental cases, the first run ( $i = 0$ ) of the parameter estimation procedure converged to the minimal value,  $\tau_{b0}$ , among all possible solutions of  $\tau_{bi}$ . The average of  $\tau_{b0}$  over these five cases was  $66 \pm 10$  ms. Estimates of the other free parameters,  $Z_{cb}$  and  $\tau_{nb}$ , averaged  $572 \pm 102 \text{ g cm}^{-4}\text{s}^{-1}$  and  $110 \pm 46$  ms, respectively. Average parameter estimation errors, as a percentage of the related parameter estimates, were  $(3.8 \pm 1.3)\%$  for  $\tau_{b0}$ ,  $(4.6 \pm 3.0)\%$  for  $Z_{cb}$ , and  $(12 \pm 11)\%$  for  $\tau_{nb}$  (Burattini *et al.*, 1994b).

The second ( $i = 1$ ) and the third ( $i = 2$ ) runs of the fitting procedure yielded  $\tau_{bi}$  estimates that were in good agreement with predictions of (8.34), whereas the parameters  $Z_{cb}$  and  $\tau_{nb}$  were practically the same as those provided by the first run.

A graphical view of some of the minima of the cost function,  $F_\eta$ , observed in one experimental case is displayed in Figures 8.10 and 8.11. Figure 8.10 displays the three-dimensional (3-D) plot (upper panel) and contour plot (lower panel)

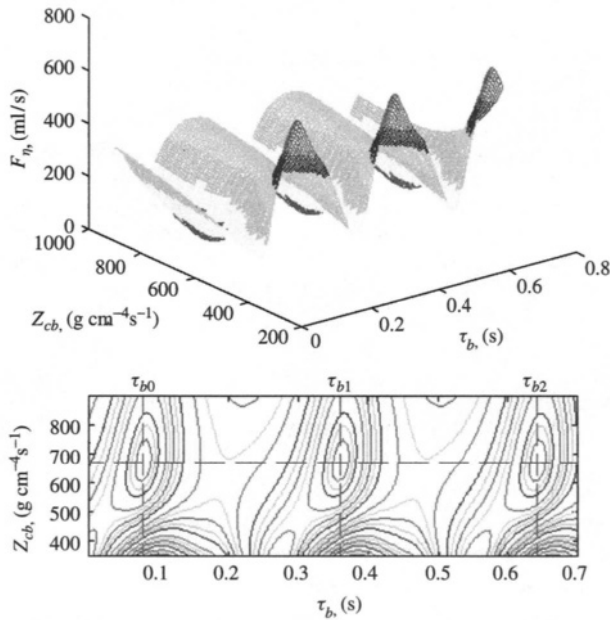


**Figure 8.10.** Three-dimensional plot (*upper panel*) and contour plot (*lower panel*) of the cost function,  $F_\eta$ , (defined as the sum of squared differences between experimental and model predicted descending aortic flow) in one dog, as a function of the body-end wave transit time,  $\tau_b$ , and tube characteristic impedance,  $Z_{cb}$ . The other free model parameter,  $\tau_{nb}$  (i.e., one of the two time constants of the terminal load impedance), is fixed at the optimal value obtained from the fitting procedure described in the text. Broken line crossings that are visible in the contour plot locate the minima of  $F_\eta$ .

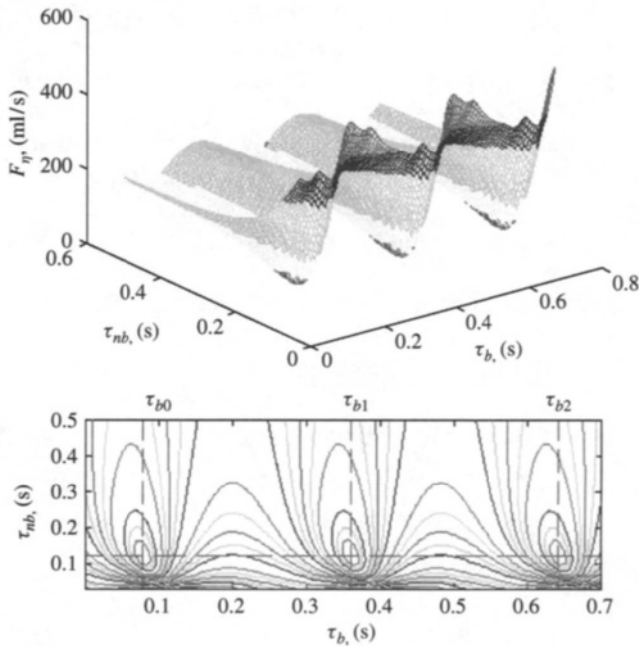


**Figure 8.11.** Three-dimensional plot (*upper panel*) and contour plot (*lower panel*) of the cost function,  $F_\eta$ , (defined as the sum of squared differences between experimental and model predicted descending aortic flow) as a function of the body-end wave transit time,  $\tau_b$ , and terminal load time constant,  $\tau_{nb}$ . The other free model parameter,  $Z_{cb}$  (i.e., the tube characteristic impedance), is fixed at the optimal value obtained from the fitting procedure. Broken line crossings that are visible in the contour plot locate the minima of  $F_\eta$ .

panel) of  $F_\eta$  as a function of  $\tau_b$  and  $Z_{cb}$ , with  $\tau_{nb}$  fixed at the optimal value obtained from the best fitting procedure described earlier. The presence of multiple equivalent minima associated with different  $\tau_{bi}$  values and a unique (optimal) value of  $Z_{cb}$  is evident. Likewise, the 3-D and contour plots of Figure 8.11 show that, after giving  $Z_{cb}$  its optimal value, the cost function  $F_\eta$ , as a function of  $\tau_b$  and  $\tau_{nb}$ , is characterised by multiple equivalent minima associated with different  $\tau_{bi}$  values and a unique (optimal) value of  $\tau_{nb}$ . These figures are representative of all considered experimental cases.

To calculate pulse wave velocity,  $v_b$ , the distance between ascending aortic and abdominal aortic pressure transducers was divided by the foot-to-foot time delay between the measured pressure waves. Average  $v_b$  over all five dogs was  $452 \pm 81$  cm/s.

The product between  $v_b$  and  $\tau_{bi}$ , with  $i = 0, 1$ , and 2 yielded the following average values for the effective length of the descending aortic circulation. The

minimum value, associated with  $\tau_{b_0}$ , was  $d_{b_0} = 29.2 \pm 2.8$  cm. The subsequent lengths,  $d_{b_1}$  and  $d_{b_2}$ , respectively, associated with  $\tau_{b_1}$  and  $\tau_{b_2}$ , averaged  $147 \pm 23$  cm and  $265 \pm 44$  cm. The estimated value of  $d_{b_0}$  approximated the measured distance,  $30.6 \pm 3.0$  cm, from the aortic site where the input pressure transducer was located to the abdominal aortic region nearby the origin of renal arteries. The lengths  $d_{b_1}$  and  $d_{b_2}$  (and the higher values of  $d_{b_3}$ ,  $d_{b_4}$ , and so forth) would locate the effective reflection site out of the body.

Based on these results, the problem in uniqueness of estimates for the wave transit time,  $\tau_b$ , finds a solution in that only the selection of  $\tau_{b_0}$ , among the infinite  $\tau_{b_i}$  solutions, is compatible with the physical and topological properties of descending aortic circulation. In other words, the selection of  $\tau_{b_0}$  yields a distance,  $d_{b_0}$ , to the effective reflecting site that meets the requirement that this length be no longer than the dimensions of the body. This result supports the reported findings (Burattini and Campbell, 1993; Fogliardi *et al.*, 1997; Shroff *et al.*, 1995) that the body-end arm of modified T-tube model provides a suitable description of wave travel and reflection along the aorta and is able to discriminate between proximal and distal mechanical properties of the descending aortic circulation.

## 8.10. CONCLUSIONS

Complexity is what characterises the vascular system as well as much of physiology. As a result of this physiological complexity, it is not often possible to measure directly (*in vivo*) the quantities of interest such as, for instance, total arterial compliance and peripheral resistance. Only indirect measures of such quantities may be feasible, implying the need for some model in order to be able to draw inference as to the value of the quantity of real interest. Vascular impedance data derived from measurements of pulsatile pressure and flow and vascular impedance models of various complexity have been extensively used in the process of raising our understanding of arterial haemodynamics in health and disease. Models of reduced complexity are appealing in that they can be easily communicable and understandable and are characterised by a low number of parameters that may be assumed as markers of some physical properties of the actual system. The need of simplification in the process of model formulation conflicts with the complexity of the biological system on the one hand and the risk of oversimplification on the other. Hopefully, the issues of aortic impedance modelling discussed in this chapter can contribute to bring the reader around the point that the purpose of modelling is a key driver of good modelling methodology in the search of a compromise between complexity and oversimplification. The concept of goodness or badness of modelling, however, cannot be based on taste. Once the

purpose of a model is defined, the process of modelling cannot merely be one that takes arbitrary assumptions, shakes them up, and comes out with arbitrary conclusions that have the ring of science. Rather, an integrated identification framework (as discussed in Chapter 1) is needed for dealing with models that are physiologically based. This implies that the hypotheses taken in the process of transformation from system to model are put into a mathematical form and a model structure and the corresponding parameters are determined. Problems of identifiability, as, for instance, those discussed in Section 8.9, need to be resolved for reliable physiological interpretation. Data fit, parameter estimation errors, and physiological relevance of parameter estimates need to be tested in the process of model validation, which is essentially that of examining whether the model is good enough in relation to its intended purpose. Eventually, it should not be forgotten that the formulas deduced from a model are the result of mathematical formalisation of the hypotheses underlying the model itself. Thus, their use should always be sound with these hypotheses. For instance, the assumption of an arterial model that consists of a loss-free elastic tube terminating in a resistor yields the quarter wavelength formula (8.28) for calculation of the effective length of the considered arterial system. As soon as it is recognised that the introduction of longitudinal frictional losses or the assumption of a complex and frequency-dependent terminal load improves the behaviour of the model, it should also be recognised that the quarter wavelength formula falls short because it is not sound with the new hypothesis.

## 8.11. REFERENCES

- Apter, J. T., M. Rabinowitz and D. H. Cummings. Correlation of visco-elastic properties of large arteries with microscopic structure. I, II, and III. *Circ Res* 19(1966):104–21.
- Bellman, R. and K. J. Åström. On structural identifiability. *Math Biosci* 7(1970):329–39.
- Bergel, D. H. 1972. The properties of blood vessels. In: *Biomechanic: Its Foundations and Objectives*. Edited by Y. C. Fung, N. Perrone and M. Anliker, Englewood Cliffs, NJ: Prentice Hall.
- Broemser, Ph. and O. F. Ranke. Über Die Messung des Schlagvolumens des Herzens auf unblutigem Weg. *Z Biol* 90(1930):467–507.
- Brown, R. F. and K. R. Godfrey. Problems of determinacy in compartmental modeling with application to bilirubin kinetics. *Math Biosci* 40(1978):205–24.
- Burattini, R. 1989. Reduced models of the systemic arterial circulation. In: *Vascular Dynamics: Physiological Perspectives*. Edited by N. Westerhof and D. R. Gross, New York: Plenum.
- Burattini, R. and K. B. Campbell. Modified asymmetric *T*-tube model to infer arterial wave reflection at the aortic root. *IEEE Trans Biomed Eng* 36(1989):805–14.
- Burattini, R. and K. B. Campbell. Effective distributed compliance of the canine descending aorta estimated by modified *T*-tube model. *Am J Physiol* 264 (*Heart Circ Physiol* 33)(1993):H1977–87.
- Burattini, R. and K. B. Campbell. Assessment of aortic pressure power components and their link to overall elastic and resistive arterial properties. *Med Biol Eng Comput* 37(1999):366–76.

- Burattini, R. and K. B. Campbell. Physiological relevance of uniform elastic tube models to infer descending aortic valve reflection: a problem of identifiability. *Ann Biomed Eng* 28(2000): in press.
- Burattini, R. and S. Di Carlo. Effective length of the arterial circulation determined in the dog by aid of a model of the systemic input impedance. *IEEE Trans Biomed Eng* 35(1988):53–61.
- Burattini, R. and G. Gnudi. Computer identification of models for the arterial tree input impedance: comparison between two new simple models and first experimental results. *Med Biol Eng Comput* 20(1982):134–44.
- Burattini, R. and G. Gnudi. Assessment of a parametric identification procedure of simple models for left ventricular afterload. *Med Biol Eng Comput* 21(1983):39–46.
- Burattini, R. and S. Natalucci. Complex and frequency-dependent compliance of viscoelastic Windkessel resolves contradictions in elastic Windkessels. *Med Eng Phys* 20(1998):502–14.
- Burattini, R., G. Gnudi, N. Westerhof and S. Fioretti. Total systemic arterial compliance and aortic characteristic impedance in the dog as a function of pressure: a model based study. *Comput Biomed Res* 20(1987):154–65.
- Burattini, R., G. G. Knowlen and K. B. Campbell. Two arterial effective reflecting sites may appear as one to the heart. *Circ Res* 68(1991):85–99.
- Burattini, R., L. Montanari, L. J. Mulligan, M. S. Cannon and D. R. Gross. Evaluation of hypercholesterol diet-induced changes in viscoelastic properties of carotid circulation in pigs. *Am J Physiol* 263 (*Heart Circ Physiol* 32)(1992):H1919–26.
- Burattini, R., R. Fogliardi and K. B. Campbell. Lumped model of terminal aortic impedance in the dog. *Ann Biomed Eng* 22(1994a):381–91.
- Burattini, R., R. Fogliardi and K. B. Campbell. 1994b. Effective reflecting sites and effective lengths in the arterial system. In: *Biomedical Engineering: Recent Developments*. Edited by J. Vossoughi. University of the District of Columbia, Washington, D.C.
- Burattini, R., V. Carrozzo, S. Natalucci and D. R. Gross. Evaluation of the effects of high cholesterol diet on mechanical properties of carotid circulation using an inertance-viscoelastic Windkessel model. *Intern Med* 5(1997):45–55.
- Burkhoff, D., J. Alexander Jr. and J. Schipke. Assessment of Windkessel as a model of aortic input impedance. *Am J Physiol* 255 (*Heart Circ Physiol* 24)(1988):H742–53.
- Campbell, K. B., L. C. Lee, H. F. Frasch and A. Noordergraaf. Pulse reflection sites and effective length of the arterial system. *Am J Physiol* 256 (*Heart Circ Physiol* 25)(1989):H1684–89.
- Campbell, K. B., R. Burattini, D. L. Bell, R. D. Kirkpatrick and G. G. Knowlen. Time-domain formulation of asymmetric T-tube model of arterial system. *Am J Physiol* 258 (*Heart Circ Physiol* 27)(1990):H1761–74.
- Canty, J. M. Jr., F. J. Klocke and R. E. Mates. Pressure and tone dependence of coronary diastolic input impedance and capacitance. *Am J Physiol* 248 (*Heart Circ Physiol* 17)(1985):H700–11.
- Carlier, S., P. Segers, G. Armstrong, N. Stergiopoulos, P. Verdonck and J. D. Thomas. The pulse pressure method versus the area method: non-invasive in vivo validation. (Abst). *J Cardiovasc Diagn Proc* 15(1998):149.
- Carson, E. R., C. Cobelli and L. Finkelstein. 1983. *The Mathematical Modelling of Metabolic and Endocrine Systems*. New York: Wiley.
- Chang, K. C., Y. Z. Tseng, T. S. Kuo and H. I. Chen. Impedance and wave reflection in arterial system: simulation with geometrically tapered T-tubes. *Med Biol Eng Comput* 33(1995):652–60.
- Cobelli, C. and J. J. Di Stefano III. Parameter and structural identifiability concepts and ambiguities: a critical review and analysis. *Am J Physiol* 239 (*Reg Integrative Comp Physiol* 8)(1980):R7–24.
- Cox, R. H. Pressure dependence of the mechanical properties of arteries in vivo. *Am J Physiol* 229(5)(1975):1371–75.



- Dobrin, P. B. 1983. Vascular mechanics. In: *Handbook of Physiology, the Cardiovascular System*. Edited by J. T. Shepherd, F. C. Abboud and S. R. Geiger. Bethesda, MD: American Physiological Society.
- Elzinga, G. and N. Westerhof. Pressure and flow generated by the left ventricle against different impedances. *Circ Res* 32(1973):178–86.
- Fogliardi, R., M. Di Donfrancesco and R. Burattini. Comparison of linear and nonlinear formulations of the three-element Windkessel model. *Am J Physiol* 271 (*Heart Circ Physiol* 40)(1996): H2661–68.
- Fogliardi, R., R. Burattini and K. B. Campbell. Identification and physiological relevance of an exponentially tapered tube model of canine descending aortic circulation. *Med Eng Phys* 19(1997):201–11.
- Frank, O. Die grundform des arteriellen pulses erste abhandlung: mathematische analyse. *Z Biol* 37(1899):483–526.
- Gentile, B. J., D. R. Gross, C. J. C. Chuong and N. H. C. Hwang. Segmental volume distensibility of the canine thoracic aorta in vivo. *Cardiovasc Res* 22(1988):385–89.
- Gnudi, G. Analytical relationship between arterial input impedance and the three-element Windkessel series resistance. *Med Biol Eng Comput* 36(1998a):480–84.
- Gnudi, G. New closed-form expressions for the estimation of arterial Windkessel compliance. *Comput Biol Med* 28(1998b):207–23.
- Graupe, D. 1976. *Identification of Systems*. Huntington, NY: Krieger.
- Gross, D. R. 1979. Animal models in cardiovascular research. In: *Quantitative Cardiovascular Studies: Clinical and Research Applications of Engineering Principles*. Edited by N. H. C. Hwang, D. R. Gross and D. J. Patel. Baltimore, MD: University Park Press.
- Gross, D. R. 1989. Compliance and aging. In: *Vascular Dynamics: Physiological Perspectives*. Edited by N. Westerhof and D. R. Gross. New York: Plenum.
- Hales, S. 1733. *Statical Essays: Containing Haemastatics*, vol 2. London: Innys and Manby. Reprint, *History of Medicine Series, Library of New York Academy of Medicine*. New York: Hafner Publishing, 1964.
- Hallock, P. and I. C. Benson. Studies on the elastic properties of human isolated aorta. *J Clin Invest* 16(1937):595–602.
- Hettrick, D. A., P. S. Pagel and D. C. Warltier. Differential effects of isoflurane and halotane on aortic input impedance quantified using a three-element Windkessel model. *Anesthesiology* 83(1995):361–73.
- Kenner, T. 1979. Physical and mathematical modelling in cardiovascular systems. In: *Quantitative Cardiovascular Studies: Clinical and Research Applications of Engineering Principles*. Edited by N. H. C. Hwang, D. R. Gross and D. J. Patel. Baltimore, MD: University Park Press.
- Langewouters, G. J., K. H. Wesseling and W. J. A. Goedhard. The static elastic properties of 45 human thoracic and 20 abdominal aortas *in vitro* and the parameters of a new model. *J Biomech* 17(1984):425–35.
- Latham, R. D., N. Westerhof, P. Sipkema, B. J. Rubal, P. Reuderink and J. P. Murgu. Regional wave travel and reflections along the human aorta: a study with six simultaneous micromanometric pressures. *Circulation* 72:1257–69.
- Latham, R. D. 1989. Pulse propagation in the systemic arterial tree. In: *Vascular Dynamics: Physiological Perspectives*. Edited by N. Westerhof and D. R. Gross. New York: Plenum.
- Learoyd, B. and M. G. Taylor. Alterations with age in the viscoelastic properties of human arterial walls. *Circ Res* 18(1966):278–92.
- Liu, Z., K. P. Brin and F. C. P. Yin. Estimation of total arterial compliance: an improved method and evaluation of current methods. *Am J Physiol* 251 (*Heart Circ Physiol* 20)(1986):H588–600.
- Liu, Z., F. Shen and F. C. P. Yin. Impedance of arterial system simulated by viscoelastic *T* tubes terminated in Windkessels. *Am J Physiol* 256 (*Heart Circ Physiol* 25)(1989):H1087–99.

- Marcus, R. H., C. Korcarz, G. McCray, A. Neumann, M. Murphy, K. Borow, L. Weinert, J. Bednarz, D. D. Gretler, K. T. Spencer, P. Sareli and R. M. Lang. Noninvasive method for determination of arterial compliance using doppler echocardiography and subclavian pulse tracings. *Circulation* 89(1994):2688–99.
- McDonald, D. A. Hemodynamics. *Annu Rev Physiol* 30(1968):525–56.
- Milnor, W. R. 1982. *Hemodynamics*. Baltimore, MD: Williams & Wilkins.
- Nichols, W. W., A. P. Avolio and M. F. O'Rourke. Ascending aortic impedance patterns in the kangaroo: their explanation and relation to pressure waveforms. *Circ Res* 59(1986):247–55.
- Nichols, W. W. and M. F. O'Rourke. 1990. *McDonald's Blood Flow in Arteries*. 3rd ed. London: Edward Arnold.
- Noordergraaf, A. 1978. *Circulatory System Dynamics*. New York: Academic.
- O'Rourke, M. F. 1982. *Arterial Function in Health and Disease*. Edinburgh: Churchill Livingstone.
- O'Rourke, M. F. Arterial stiffness, systolic blood pressure and logical treatment of arterial hypertension. *Hypertension* 15(1990):339–47.
- O'Rourke, M. F. Mechanical principles in arterial disease. *Hypertension* 26(1995):2–9.
- O'Rourke, M. F. and M. G. Taylor. Vascular impedance of the femoral bed. *Circ Res* 18(1966):126–39.
- O'Rourke, M. F. and M. G. Taylor. Input impedance of the systemic circulation. *Circ Res* 20(1967):365–80.
- Papageorgiou, G. L. and N. B. Jones. Wave reflection and hydraulic impedance in the healthy arterial system: a controversial subject. *Med Biol Eng Comput* 26(1988):237–42.
- Patel, D. J., F. M. De Freitas and D. L. Fry. Hydraulic input impedance to aorta and pulmonary artery in dogs. *J Appl Physiol* 18(1963a):134–40.
- Patel, D. J., F. M. De Freitas, J. C. Greenfield, Jr. and D. L. Fry. Relationship of radius to pressure along the aorta in living dogs. *J Appl Physiol* 18(1963b):1111–17.
- Poiseuille, J. M. Recherches experimentales sur le mouvement des liquides dans les tubes de tres petits diametres. *Comptes Rendus Acad Sci* 11(1840):1041–48.
- Randall, O. S., M. D. Esler, R. V. Calfee, G. F. Bulloch, A. S. Maisel and B. Culp. Arterial compliance in hypertension. *Aust N Z J Med* 6 (suppl. 2)(1976):49–59.
- Shroff, S. G., D. S. Berger, C. Korcarz, R. M. Lang, R. H. Marcus and D. E. Miller. Physiological relevance of T-tube model parameters with emphasis on arterial compliances. *Am J Physiol* 269 (*Heart Circ Physiol* 38)(1995):H365–74.
- Sipkema, P. and N. Westerhof. Effective length of the arterial system. *Ann Biomed Eng* 3(1975):296–307.
- Sipkema, P., N. Westerhof and O. S. Randall. The arterial system characterised in the time domain. *Cardiovasc Res* 14(1980):270–79.
- Stergiopoulos, N., J.-J. Meister and N. Westerhof. Simple and accurate way for estimating total and segmental arterial compliance: the pulse pressure method. *Ann Biomed Eng* 22(1994):392–97.
- Stergiopoulos, N., J.-J. Meister and N. Westerhof. Evaluation of methods for estimation of total arterial compliance. *Am J Physiol* 268 (*Heart Circ Physiol* 37)(1995):H1540–48.
- Sunagawa, K., D. Burkhoff, K. D. Lim and K. Sagawa. Impedance loading servo pump system for exercised canine ventricle. *Am J Physiol* 243 (*Heart Circ Physiol* 12)(1982):H346–50.
- Sunagawa, K., K. Sagawa and W. L. Maughan. Ventricular interaction with the loading system. *Ann Biomed Eng* 12(1984):163–89.
- Taylor, M. G. An approach to an analysis of the arterial pulse wave. I. Oscillations in an attenuating line. *Phys Med Biol* 1(1957a):258–69.
- Taylor, M. G. An approach to an analysis of the arterial pulse wave. II. Fluid oscillations in an elastic pipe. *Phys Med Biol* 1(1957b):321–29.
- Taylor, M. G. Wave travel in a non-uniform transmission line, in relation to pulses in arteries. *Phys Med Biol* 10(1965):539–50.

- Taylor, M. G. The input impedance of an assembly of randomly branching elastic tubes. *Biophys J* 6(1966):29–51.
- Toorop, G. P., N. Westerhof and G. Elzinga. Beat-to-beat estimation of peripheral resistance and arterial compliance during pressure transients. *Am J Physiol* 252 (*Heart Circ Physiol* 21)(1987): H1275–83.
- Weizsäcker, H. W. Beschreibung und Messung der Arterienelastizität. In: *Physiologie an der Schwelle zum 21. Jahrhundert*. Edited by H. Hinghofer-Szalkay. Berlin: Blackwell Wissenschafts-Verlag GmbH, 2000.
- Weizsäcker, H. W., H. Lambert and K. Pascale. Analysis of the passive mechanical properties of rat carotid arteries. *J Biomech* 16(1983):703–15.
- Westerhof, N. 1993. Arterial haemodynamics. In: *The Physics of Heart and Circulation*. Edited by J. Strackee and N. Westerhof. Bristol, UK: Institute of Physics Publishing.
- Westerhof, N. and R. Krams. Comments on “Pressure and tone dependence of coronary diastolic input impedance and capacitance.” Letter to the Editor. *Am J Physiol* 250 (*Heart Circ Physiol* 19)(1986):H330–31.
- Westerhof, N. and A. Noordergraaf. Arterial viscoelasticity: a generalized model. *J Biomech* 3(1970):357–79.
- Westerhof, N., G. Elzinga and P. Sipkema. An artificial arterial system for pumping hearts. *J Appl Physiol* 31(1971):776–81.
- Westerhof, N., P. Sipkema, G. C. Van Den Bos and K. Elzinga. Forward and backward waves in the arterial system. *Cardiovasc Res* 6(1972):648–56.
- Westerhof, N., P. Sipkema, G. Elzinga, J. P. Murgu and J. P. Giolma 1979. Arterial impedance. In: *Quantitative Cardiovascular Studies: Clinical and Research Applications of Engineering Principles*. Edited by N. H. C. Hwang, D. R. Gross and D. J. Patel. Baltimore, MD: University Park Press.
- Wetterer, E. and T. Kenner 1968. *Grundlagen der Dynamik des Arterienpulses*. Berlin: Springer-Verlag.
- Yates, F. E. Good manners in good modeling: mathematical models and computer simulations of physiological systems. *Am J Physiol (Reg Integrative Comp Physiol)* 3(1978):R159–60.
- Yin, F. C. P. and Z. Liu 1989. Arterial compliance—physiological viewpoint. In: *Vascular Dynamics: Physiological Perspectives*. Edited by N. Westerhof and D. R. Gross. New York: Plenum.
- Yoshigi, M. and B. B. Keller. Characterization of embryonic aortic impedance with lumped parameter models. *Am J Physiol* 273 (*Heart Circ Physiol* 42)(1997):H19–27.

# Mathematical Modelling of Pulmonary Gas Exchange

Stephen E. Rees, Søren Kjærgaard, and Steen Andreassen

This chapter describes mathematical models used to quantify abnormalities of pulmonary gas exchange (i.e., abnormalities of diffusion, ventilation, and perfusion). It begins by deriving the standard equations of pulmonary gas exchange, showing how these equations can be used to obtain more complex models of ventilation/diffusion/perfusion mismatch in the lung. The application of these models is then reviewed in both experimental and clinical environments.

## 9.1. STANDARD EQUATIONS USED TO DESCRIBE GAS TRANSPORT IN THE LUNGS

Figure 9.1 illustrates a conceptual model of the lung including three compartments representing alveolar dead space, which are alveoli ventilated but not perfused; pulmonary shunt, which are alveoli perfused but not ventilated; and effective alveoli, which are those involved in gas exchange and are both ventilated and perfused. For alveoli involved in gas exchange, Figure 9.1 includes a resistance to gas diffusion across the alveoli/lung capillary membrane.

The conceptual model illustrated in Figure 9.1 is simple and does not include a large number of compartments describing heterogeneity of ventilation, diffusion, or perfusion within the lung. As such, the mathematical formulation of this model includes equations that are well recognised within the field of respiratory physiology, equations that can be seen as the building blocks of more complex models of gas exchange. These equations are the alveolar air equation, the venous admixture equation, Fick's law of diffusion,

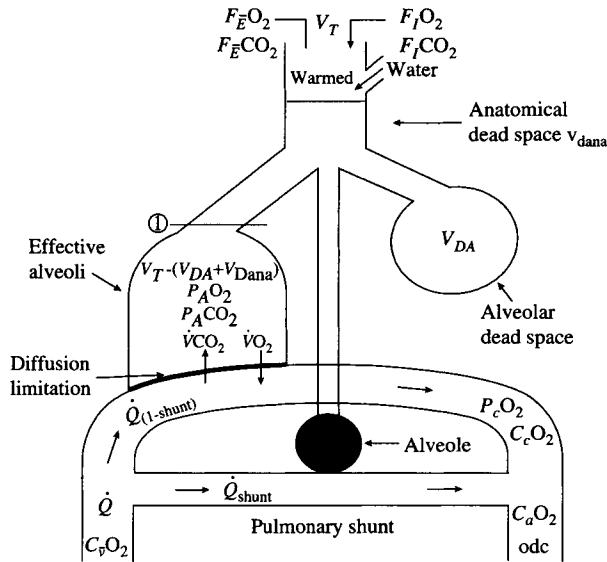


**Figure 9.1.** A three-compartment model of the lung including alveolar dead space, pulmonary shunt, and resistance to gas diffusion across the alveoli/lung capillary membrane.

the Fick principle of blood flow, and the Bohr equation for the estimation of dead space. The derivation and description of these equations now follows; all relevant nomenclature is included in the glossary (Appendix A)

### 9.1.1. THE ALVEOLAR AIR EQUATION

The alveolar air equation can be derived by considering the volume of gas flowing in and out of the effective alveoli. The volume of gas flowing into the effective alveoli (i.e., across line 1, Figure 9.1) is the product of the fraction of gas in the inspired air ( $F_I$ ) warmed and humidified ( $F_{I,BTPS}$ ) and the ventilation of the effective alveoli ( $\dot{V}_{A,BTPS}$ ). Similarly the volume of gas flowing out of the effective alveoli is the fraction of gas in the effective alveoli on expiration ( $F_{A,BPTS}$ ) multiplied by  $\dot{V}_{A,BTPS}$ , plus the gas diffusing into blood during gas exchange ( $\dot{V}$ ). Assuming all gases are expressed at body temperature and pressure and saturated with water, this gives:

$$F_A \dot{V}_A + \dot{V} = F_I \dot{V}_A \tag{9.1}$$

Converting alveolar fraction to pressure ( $P_A = F_A P_B$ ), (9.1) can be written as:

$$\frac{P_A}{P_B} \dot{V}_A + \dot{V} = F_I \dot{V}_A \tag{9.2}$$

Rearranging (9.2) gives the most general form of the alveolar air equation:

$$P_A = F_I P_B - \frac{\dot{V} P_B}{\dot{V}_A} \quad (9.3)$$

For oxygen and carbon dioxide, this equation may be written as:

$$P_{A\text{O}_2} = F_{I\text{O}_2} P_B - \frac{\dot{V}\text{O}_2 P_B}{\dot{V}_A} \quad (9.4)$$

$$P_{A\text{CO}_2} = F_{I\text{CO}_2} P_B + \frac{\dot{V}\text{CO}_2 P_B}{\dot{V}_A} \quad (9.5)$$

where  $\dot{V}\text{O}_2$  is the oxygen consumption and  $\dot{V}\text{CO}_2$  is the carbon dioxide production.  $\dot{V}_A$  is calculated as the respiratory frequency ( $f$ ) multiplied by the effective tidal volume ( $V_{T,\text{BTPS}} - [V_{\text{Dana}} + V_{\text{Dalv}}]$ ), which is:

$$\dot{V}_A = f(V_{T,\text{BTPS}} - (V_{\text{Dana}} + V_{\text{Dalv}})) \quad (9.6)$$

In (9.1) to (9.6), ventilation of effective alveoli ( $\dot{V}_A$ ), the fraction of gas flowing into the alveoli ( $F_I$ ), and the tidal volume ( $V_T$ ) are described at body temperature and pressure and fully saturated with water, or BTPS. Inspired gas is usually dry and at ambient temperature and pressure (ATPD), being warmed and humidified during inspiration. Inspired volumes and fractions are usually measured at ATPD but may be converted into the equivalent values at BTPS, as described in Appendix B.

Equations (9.4) to (9.6), and the corrections for humidification and warming of the inspiration ([B.1] to [B.10], Appendix B), are often used to estimate alveolar oxygen partial pressure ( $P_{A\text{O}_2}$ ) which cannot be directly measured. Where measurements of mixed venous blood ( $C_{\bar{v}\text{O}_2}$ ) and cardiac output ( $\dot{Q}$ ) are possible,  $\dot{V}\text{O}_2$  can be calculated from the Fick principle of blood flow (see Section 9.1.4) and used with measurements of ventilation ( $F_{I\text{O}_2}$ ,  $f$ ,  $V_T$ ) and estimates of dead space ( $V_{\text{Dana}}$ ,  $V_{\text{Dalv}}$ ) to calculate  $\dot{V}_A$  from (9.6), and hence  $P_{A\text{O}_2}$  from (9.4). In the absence of pulmonary artery catheter measurements of  $C_{\bar{v}\text{O}_2}$  or  $\dot{Q}$ , an indirect estimate of  $P_{A\text{O}_2}$  is possible using information from the carbon dioxide ( $\text{CO}_2$ ) system. First, (9.5) is solved to obtain an estimate for  $\dot{V}\text{CO}_2$ . This is done by making two assumptions: that the alveolar and arterial  $P\text{CO}_2$  are equivalent ( $P_{A\text{CO}_2} \simeq P_a\text{CO}_2$ ), where  $P_a\text{CO}_2$  is measured from an arterial blood sample; and that the inspired  $\text{CO}_2$  concentration is negligible ( $F_{I\text{CO}_2} = 0$ ). Calculated  $\dot{V}\text{CO}_2$  can then be used to estimate  $\dot{V}\text{O}_2$ , assuming a value of the respiratory quotient ( $R$ , normal value 0.8) and using the equation:

$$\dot{V}\text{CO}_2 = R \dot{V}\text{O}_2 \quad (9.7)$$

which links oxygen consumption ( $\dot{V}O_2$ ) and carbon dioxide production ( $\dot{V}CO_2$ ) under steady-state conditions of both  $O_2$  and  $CO_2$ . The estimated value of  $\dot{V}O_2$  can then be inserted into (9.4) and  $P_AO_2$  calculated. The alveolar air equation can be written in many forms, with the appropriate form chosen based on the available measurements. A common form of this equation, used when mixed expired gases can be measured, is given below:

$$P_AO_2 = P_I O_2 - P_a CO_2 \frac{F_I O_2 - F_E O_2}{F_E CO_2} \quad (9.8)$$

### 9.1.2. VENOUS ADMIXTURE

The venous admixture or “shunt fraction (shunt)” is the fraction of total cardiac output ( $\dot{Q}$ ) that is not involved in gas exchange. As illustrated in Figure 9.1, total blood flow ( $\dot{Q}$ ) is the sum of that flowing through lung capillaries ( $\dot{Q}(1\text{-shunt})$ ) and that which is not involved in gas exchange ( $\dot{Q}$  shunt):

$$\dot{Q} = \dot{Q} \text{ shunt} + \dot{Q}(1\text{-shunt}) \quad (9.9)$$

In the same way, the flow of oxygen into the arteries ( $\dot{Q} C_a O_2$ ) can be described as the sum of that coming from blood leaving the lung capillaries ( $\dot{Q}(1\text{-shunt}) C_c O_2$ ) and that coming from shunted mixed venous blood ( $\dot{Q}$  shunt  $C_{\bar{v}} O_2$ ):

$$\dot{Q} C_a O_2 = \dot{Q} \text{ shunt} C_{\bar{v}} O_2 + \dot{Q}(1\text{-shunt}) C_c O_2 \quad (9.10)$$

By rearranging (9.10), we obtain the shunt equation:

$$\text{shunt} = \frac{C_c O_2 - C_a O_2}{C_c O_2 - C_{\bar{v}} O_2} \quad (9.11)$$

The oxygen content of blood leaving the lung capillaries ( $C_c O_2$ ) cannot be measured. To calculate shunt, it is usually assumed that alveoli and blood leaving the lung capillaries are at equilibrium for  $PO_2$ , or  $P_c O_2 = P_A O_2$ .  $P_A O_2$ , estimated from the alveolar air equation, can then be used to calculate  $C_c O_2$ .

### 9.1.3. FICK'S FIRST LAW OF DIFFUSION

This law states that the rate of diffusion ( $\dot{V}$ ) of gas across a tissue barrier is proportional to the partial pressure difference across that barrier:

$$\dot{V} = D_L (P_A - P_c) \quad (9.12)$$

where  $P_c$  is the partial pressure of gas in the lung capillary gas, and  $D_L$  is the diffusion capacity of the gas.

### 9.1.4. THE FICK PRINCIPLE OF BLOOD FLOW

The Fick principle describes the oxygen consumption ( $\dot{V}O_2$ ) as a function of the arteriovenous oxygen concentration difference and the cardiac output ( $\dot{Q}$ ), and can be used to calculate either  $\dot{Q}$  or  $\dot{V}O_2$ . The equation is written as:

$$\dot{V}O_2 = \dot{Q}(C_aO_2 - C_vO_2) \quad (9.13)$$

### 9.1.5. ESTIMATION OF RESPIRATORY DEAD SPACE

Respiratory dead space is that part of the tidal volume ( $V_T$ ) which does not take part in gas exchange. This includes all nonalveolar ventilation (anatomical dead space  $V_{Dana}$ ), and ventilation of alveoli that are not perfused (alveolar dead space  $V_{DA}$ ). The sum of  $V_{Dana}$  and  $V_{DA}$  is known as physiological dead space ( $V_{Dp}$ ).

The Bohr equation, which is used to describe dead space, can be derived by describing  $CO_2$  expiration in three ways. At the mouth, the total  $CO_2$  expired can be described either as the product of mixed expired  $CO_2$  fraction ( $F_{\bar{E}}CO_{2,BTPS}$ ) and tidal volume ( $V_{T,BTPS}$ ) or as the product of end tidal  $CO_2$  fraction ( $F_{E'}CO_2$ ) and the volume of end tidal gases ( $V_{T,BTPS} - V_{Dana}$ ), where end tidal gases are those expired after anatomical dead space has been washed out. Equating these and converting fractions to pressure (i.e.,  $P_{\bar{E}}CO_2 = F_{\bar{E}}CO_2 P_B$ ,  $P_{E'}CO_2 = F_{E'}CO_2 P_B$ ) gives:

$$P_{E'}CO_2(V_{T,BTPS} - V_{Dana}) = P_{\bar{E}}CO_2 V_{T,BTPS} \quad (9.14)$$

Equation (9.14) can be rearranged to give the Bohr equation for the estimation of anatomical dead space:

$$V_{Dana} = V_T \frac{(P_{E'}CO_2 - P_{\bar{E}}CO_2)}{P_{E'}CO_2} \quad (9.15)$$

where all gases are represented at BTPS.

Total  $CO_2$  expiration also can be described at the effective alveoli as the product of alveolar  $CO_2$  fraction ( $F_ACO_{2,BTPS}$ ) and the volume of effective alveolar ventilation ( $V_{T,BTPS} - [V_{Dana} + V_{DA}]$ ). Converting fraction to pressure ( $P_ACO_2 = F_ACO_2 P_B$ ) and equating  $CO_2$  expiration at the effective alveoli and the mouth gives:

$$P_ACO_{2,BTPS}(V_{T,BTPS} - (V_{Dana} + V_{DA})) = P_{\bar{E}}CO_2 V_{T,BTPS} \quad (9.16)$$



which can be rearranged to give the Bohr equation for the estimation of physiological dead space:

$$V_{D_p} = V_{D_{ana}} + V_{D_A} = V_T \frac{(P_A\text{CO}_2 - P_{\bar{E}}\text{CO}_2)}{P_A\text{CO}_2} \tag{9.17}$$

where all gases are expressed in BTPS.

## 9.2. MODELS OF DIFFUSION LIMITATION

Figure 9.2 illustrates the diffusion of oxygen from alveoli to lung capillary blood. During the transport of blood through the lung capillaries, the partial pressure of oxygen in the blood equilibrates with the partial pressure of oxygen in the alveoli, with equilibrium usually reached during the blood transport through the capillaries (Nunn, 1993). When diffusion is impaired, equilibrium may not be reached and an alveolar-arterial oxygen pressure difference may occur. Figure 9.2 illustrates some of the possible causes of this difference due to “diffusion” limitation. These are a short transit time of the blood through the lung capillary, and a reduced diffusion capacity from alveoli to lung capillaries ( $D_L\text{O}_2$ ), which can be due to either reduced diffusion capacity across the lung capillary membrane ( $D_M\text{O}_2$ ) or slow binding of oxygen to Hb in the erythrocyte.

Much of the theory of mathematical models constructed to explain diffusion abnormalities within the lung can be understood by the application of Fick’s

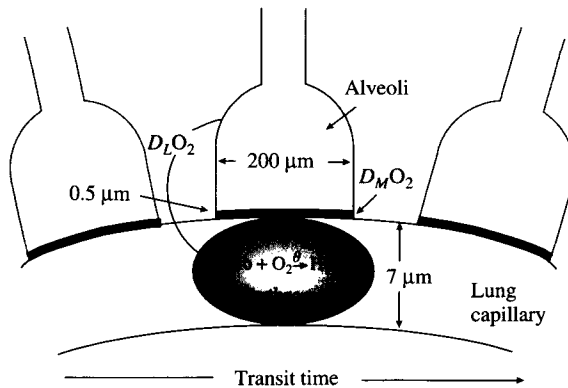


**Figure 9.2.** Diffusion of oxygen from alveoli to lung capillary blood.  $D_L\text{O}_2$  is the total diffusion capacity of O<sub>2</sub> from alveoli to the blood,  $D_M\text{O}_2$  is the diffusion capacity of the lung capillary membrane, and  $\theta$  is rate of oxygen binding in the blood.

First Law of Diffusion. This law was first applied to study the diffusion properties of oxygen by Bohr (1909) and states that for blood transverseing the lung capillary, the total oxygen transport ( $\dot{V}O_2$ ) is proportional to the alveolar-lung capillary  $PO_2$  difference:

$$\dot{V}O_2 = D_L O_2 (P_A O_2 - P_c O_2) \tag{9.18}$$

An expression for the change in  $P_c O_2$  as blood flows through the lung capillaries can be derived by considering the flow of oxygen into a single ‘‘slice’’ of blood flowing through the capillary. Assuming that blood flow through the lungs can be represented as a single capillary length  $X$  and cross-sectional area  $A$ , then for a single slice of blood, width  $dx$ , total  $\dot{V}O_2$  is the sum of  $\dot{V}O_2$  values as the slice flows through the capillary:

$$\dot{V}O_2 = \int_0^X \dot{V}O_2(x) dx \tag{9.19}$$

If the slice of blood flows through the capillary from time  $t$  to time  $t + dt$ , oxygen transport into the slice ( $\dot{V}O_2(x) dx dt$ ) is equal to the change in  $O_2$  mass in the slice ( $[C_c O_2(t + dt) - C_c O_2(t)] V_s$ ) during this time:

$$\dot{V}O_2(x) dx dt = [C_c O_2(t + dt) - C_c O_2(t)] V_s \tag{9.20}$$

where  $V_s$  is the volume of the slice of blood and  $[C_c O_2(t + dt) - C_c O_2(t)]$  is the change in oxygen concentration ( $dC_c O_2(t)$ ).  $V_s$  is the product of the cross-sectional area of the capillary ( $A$ ) and  $dx$ . Substituting for  $V_s$  and  $dC_c O_2(t)$  in (9.20) gives:

$$\dot{V}O_2(x) = A \frac{dC_c O_2(t)}{dt} \tag{9.21}$$

The flow of oxygen from the alveoli into the slice of blood ( $\dot{V}O_2(x) dx$ ) also can be described using Fick’s First Law of Diffusion, which means as the product of the diffusion capacity over the slice ( $D_L O_2 dx/X$ ) and the partial pressure difference at time  $t$  ( $P_A O_2 - P_c O_2(t)$ ):

$$\dot{V}O_2(x) dx = D_L O_2 dx/X (P_A O_2 - P_c O_2(t)) \tag{9.22}$$

Eliminating  $\dot{V}O_2(x)$  from (9.21) and (9.22) gives:

$$A \frac{dC_c O_2(t)}{dt} = D_L O_2/X (P_A O_2 - P_c O_2(t)) \tag{9.23}$$

The volume of lung capillary blood  $V_c$  equals the product of the cross-sectional area ( $A$ ) and the capillary length ( $X$ ), replacing for  $A$  and  $X$  in (9.23) gives:

$$\frac{dC_c O_2(t)}{dt} = D_L O_2/V_c (P_A O_2 - P_c O_2(t)) \tag{9.24}$$

which can be rearranged to give:

$$\int 1/(P_A O_2 - P_c O_2(t)) dC_c O_2 = \int D_L O_2 / V_c dt \quad (9.25)$$

This equation cannot be solved algebraically to obtain an expression describing the change in  $P_c O_2$  as blood passes through the lung capillary because of the complicated relationship between oxygen partial pressure ( $P_c O_2$ ) and concentration ( $C_c O_2$ ). Binding of  $O_2$  to haemoglobin is described by the oxygen dissociation curve (ODC), a nonlinear function relating  $PO_2$  to the oxygen saturation of haemoglobin in the blood ( $S_c O_2$ ), which means  $S_c O_2 = ODC(P_c O_2)$ . Total  $O_2$  concentration is therefore:

$$C_c O_2 = P_c O_2 \alpha_{O_2} + Hb \text{ ODC}(P_c O_2) \quad (9.26)$$

where  $\alpha_{O_2}$  is the solubility of oxygen in the blood, normal value 0.01 (mmol/(1 kPa), 0.0014 mmol/(1 mmHg) (Siggaard-Andersen, 1974).

With knowledge of the concentration and pressure of oxygen in the venous blood and in blood coming from the lung capillaries, assuming a constant alveolar oxygen partial pressure ( $P_A O_2$ ) and pulmonary capillary blood volume ( $V_c$ ), and using the oxygen dissociation curve, Bohr was able to use graphical/numerical methods, known as *Bohr integration*, to solve (9.25) and estimate the diffusing capacity for oxygen ( $D_L O_2$ ).

For an inert gas, Henry's law applies such that the partial pressure is proportional to concentration:

$$C = \beta P \quad (9.27)$$

where  $\beta$  is the solubility of the gas in blood. As shown by Wagner (1977), for inert gases it is possible to obtain an expression for the partial pressure of gas in blood as it passes through the lung capillary that is algebraically solvable, as follows. Equation (9.25) can be written for an inert gas as:

$$\dot{P}_c(t) = \frac{D_L}{V_c \beta} (P_A - P_c(t)) \quad (9.28)$$

by integrating (9.28) an algebraic expression can be obtained for the partial of the gas in blood as it passes through the lung capillary:

$$P_c(t) = P_A - (P_A - P_{\bar{v}}) e^{-(D_L/(V_c \beta))t} \quad (9.29)$$

The change in partial pressure of the gas in the lung capillary can therefore be described by a single exponential. For oxygen, (9.29) can be written as:

$$P_c O_2(t) = P_A O_2 - (P_A O_2 - P_{\bar{v}} O_2) e^{-(D_L O_2/(V_c \beta))t} \quad (9.30)$$

and can be used to simulate the change in  $PO_2$  in the lung capillary blood, accounting for the fact that Henry's law is not obeyed, meaning that the

relationship between concentration and pressure is the nonlinear ODC, such that  $\beta$  varies with  $PO_2$ , Figure 9.3(A) illustrates the change in  $PO_2$  in the lung capillary blood ( $P_cO_2$ ) as it equilibrates with  $P_AO_2$ , for both: varying values of  $\beta$  (solid curve) according to the relationship between oxygen content and pressure illustrated in Figure 9.3(B); and for a constant value of  $\beta = 0.8 \text{ mmol/l/kPa}$  (dotted curve), a value of  $\beta$  that occurs at the lower end of the pressure content curve seen in Figure 9.3(B). It can be clearly seen that  $\beta$  decreases with increasing  $PO_2$ , causing more rapid equilibration between  $P_cO_2$  and  $P_AO_2$ . Under normal circumstances, equilibrium is reached within 0.25 s, one third of the normal capillary transit time (0.75 s) (Wagner, 1977).

A modification of the original Bohr method was made by Riley *et al.* (1951a, 1951b). Their approach eliminated Bohr's assumption that arterial blood and blood leaving the lung capillaries were at the same  $PO_2$ , making it possible to investigate the situation where both a diffusion abnormality and a pulmonary shunt are present. Riley *et al.* (1951a, 1951b) performed

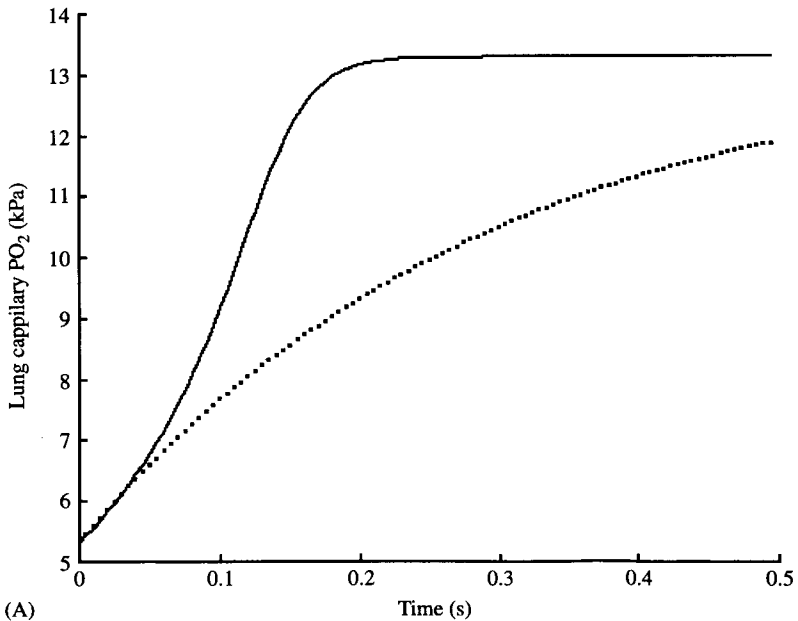


**Figure 9.3.** A, Model predicted simulations (iterative solution of equation 9.30) illustrating the change in  $PO_2$  in lung capillary blood ( $P_cO_2$ ) when equilibrated with alveolar  $P_AO_2$ , using values of  $D_LO_2 = 12.5 \text{ mmol}/(\text{min kPa})$  ( $40 \text{ ml}/(\text{min mmHg})$ ),  $V_c = 0.075 \text{ l}$ ,  $P_AO_2 = 13.3 \text{ kPa}$  ( $100 \text{ mmHg}$ ) and  $P_{\bar{v}}O_2 = 5.3 \text{ kPa}$  ( $40 \text{ mmHg}$ ). *Solid line*, solution of (9.30) varying values of  $\beta$  according to Figure 9.3(B); *dotted line*, solution of (9.30) with constant  $\beta = 0.8 \text{ mmol}/\text{l/kPa}$ .

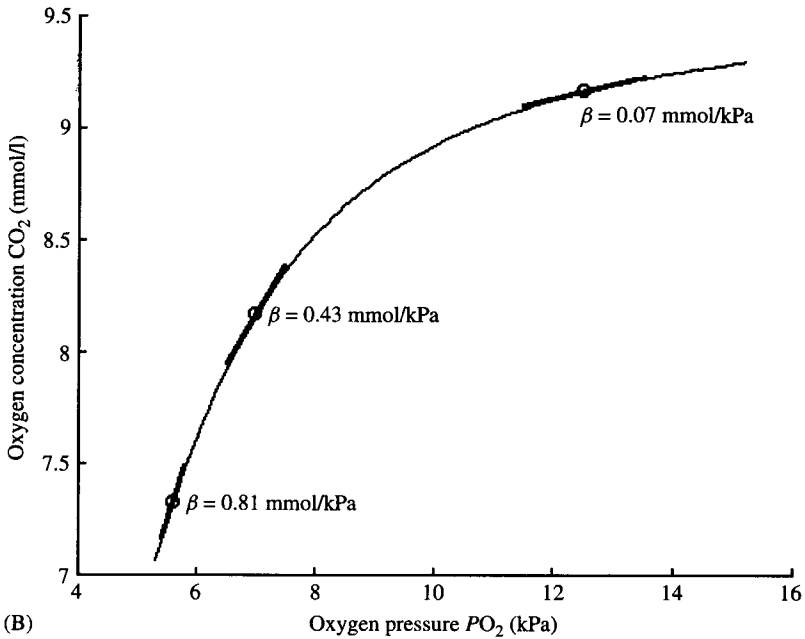


**Figure 9.3.** (Continued) B, Oxygen pressure ( $PO_2$ ), concentration ( $CO_2$ ) curve for blood. Plotted using (9.26) with  $Hb = 9.3$  mmol/l,  $\alpha_{O_2} = 0.01$  mmol/(l kPa). In (9.26), the ODC is the oxygen dissociation curve for blood implemented as described by Siggaard-Andersen *et al.*, 1984 (i.e., that included in the oxygen status algorithm [Version 3, Siggaard-Andersen, 1995]).  $\beta$ , the slope of the  $CO_2$ ,  $PO_2$  curve decreases with increasing values of  $PO_2$ .

an experiment where patients were studied at two inspired oxygen fractions to achieve arterial oxygen saturations of 82 and 95%. At each  $F_I O_2$ , estimates of  $P_A O_2$  were obtained from the alveolar air equation (9.8). The resultant  $P_A O_2 - P_a O_2$  differences were then partitioned into  $P_A O_2 - P_c O_2$  and  $P_c O_2 - P_a O_2$  differences using Bohr integration. In effect, the overall  $P_A O_2 - P_a O_2$  disorder was partitioned into that due to a diffusion abnormality and that due to pulmonary shunt.

As illustrated in Figure 9.2, the oxygen diffusion capacity  $D_L O_2$  is a composite measure of the ability of oxygen to travel from the alveoli to the lung capillary plasma and then to bind with haemoglobin in the erythrocyte. Estimation of a constant  $D_L O_2$  is therefore a mean across the whole capillary, which assumes that the speed of oxygen binding to haemoglobin is constant. This assumption is invalidated by two physiological mechanisms that work in opposite directions. First, as the haemoglobin is saturated with oxygen, its ability to bind further oxygen is reduced.

Second, each molecule of haemoglobin binds four molecules of oxygen with the rate constants of these reactions varying such that binding of the fourth molecule is significantly quicker than the other three (Staub *et al.*, 1961). Staub *et al.* (1962) proposed a model, previously derived for carbon monoxide (Roughton *et al.*, 1957), that accounted for these two effects. In doing so, the total oxygen diffusion capacity  $D_L O_2$  was divided into terms describing the diffusion capacity across the blood gas barrier ( $D_M O_2$ ) and the diffusion capacity associated with oxygen binding to haemoglobin ( $V_c \theta$ ).  $\theta$  is the rate of oxygen binding in the blood per unit time, for a given pressure of oxygen in the blood and for the number of litres of blood. The equation proposed by Staub *et al.* (1962) was:

$$\frac{1}{D_L O_2} = \frac{1}{D_M O_2} + \frac{1}{V_c \theta} \tag{9.31}$$

Staub *et al.* (1962) described the relationship between  $\theta$  and the oxygen saturation ( $SO_2$ ).  $\theta$  was found to decrease with increasing oxygenation when the blood was more than 75% saturated with oxygen, decreasing from 810 (mmol  $O_2$ /[min kPa l]), (2.6/[ml  $O_2$ /(min mmHg ml)]) at 75% oxygen saturation to 160 (mmol  $O_2$ /[min kPa l]), (0.5 [ml  $O_2$ /(min mmHg ml)]) at 98% oxygen saturation.

An overall measure of  $D_L O_2$  is therefore more appropriately explained as a higher value of  $D_L O_2$  (increased oxygen diffusion capacity) during the early stages of gas exchange and smaller value of  $D_L O_2$  during the latter stages. This effect is illustrated in Figure 9.4, which shows the change in  $P_c O_2$  for a constant  $D_L O_2$  (dashed line) and for varying values of  $D_L O_2$  (solid line) given by the relationship between  $\theta$  and  $SO_2$  described by Staub (1962). By substituting for  $D_L O_2$  in (9.30) using (9.31), an expression can be obtained describing oxygenation of the lung capillary blood:

$$P_c O_2(t) = P_A O_2 - (P_A O_2 - P_v O_2) e^{-\frac{1}{D_M O_2 + 1/(V_c \theta)}(1/(V_c \beta x))t} \tag{9.32}$$

Where oxygen diffusion abnormalities exist, high values of  $\theta$  imply that these abnormalities are present in the alveolar capillary membrane, while low values imply that the abnormality occurs in the blood, most likely due to oxygen binding to haemoglobin. The original study of Staub (1962) reported rather low initial values of  $\theta$  of 2.6 ml  $O_2$ /(min mmHg ml blood), but more recent studies (Yamaguchi, 1985) have reported values of  $\theta$  as high as 3.9 ml  $O_2$ /(min mmHg ml blood), implying a greater diffusion abnormality in the lung capillary membrane than previously believed.

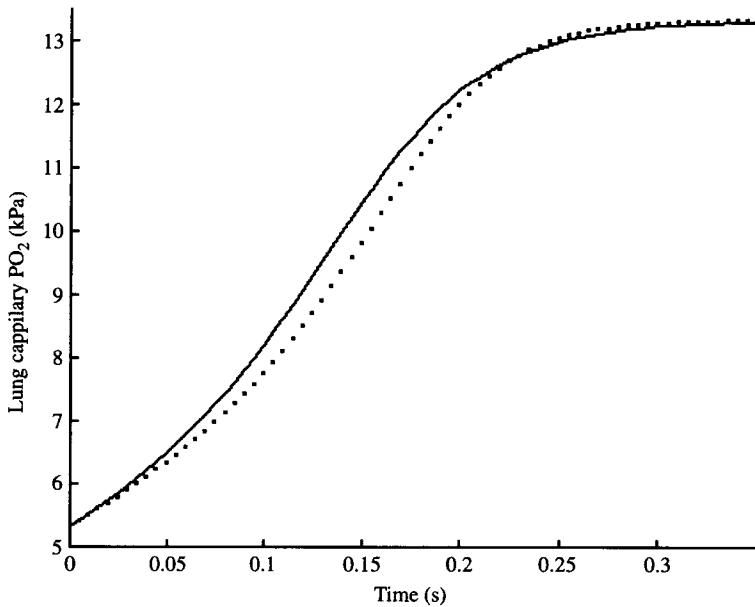


**Figure 9.4.** Model predicted simulations illustrating the change in  $P_cO_2$  when equilibrated with  $P_AO_2 = 13.3$  kPa (100 mmHg). *Dashed line*, solution of (9.30) using a constant value of  $D_L O_2 = 9.0$  mmol/(min kPa) (29 ml/[min mmHg]), varying  $\beta$  according to Figure 9.3(B); *solid line*, solution of (9.32) varying values of  $\theta$  according to Staub *et al.* (1962) while assuming a constant value of  $D_M O_2 = 12.5$  mmol/(min kPa) (40 ml/[min mmHg]), and varying  $\beta$  according to Figure 9.3b. For both lines,  $V_c = 0.075$  l and  $P_{\bar{v}}O_2 = 5.3$  kPa (40 mmHg).

### 9.2.1. GAS EXCHANGE ABNORMALITIES DESCRIBED BY HETEROGENEITY OF DIFFUSION/PERFUSION $D/\dot{Q}$ .

Figure 9.1 illustrates a lung with a single compartment involved in gas exchange. This model is that applied by Riley *et al.* (1951a, 1951b) and assumes that all nonshunted blood passes through this single lung compartment. Piiper *et al.* (1960), when using a similar approach to Riley in estimating the shunt and diffusion abnormalities in anaesthetised dogs, found that the model with a single gas exchange compartment was inadequate to describe alveolar-arterial oxygen differences. To account for these differences, Piiper *et al.* (1960) proposed the concept of a diffusion/perfusion ( $D/\dot{Q}$ ) mismatch in a heterogeneous lung, which is a lung with a number of compartments involved in gas exchange, each with varying diffusion properties ( $D_{L1}O_2, D_{L2}O_2$ ) and with varying fractions of the total nonshunted blood ( $\dot{Q}_1, \dot{Q}_2$ ) flowing through these compartments. This picture is illustrated for two compartments in Figure 9.5.

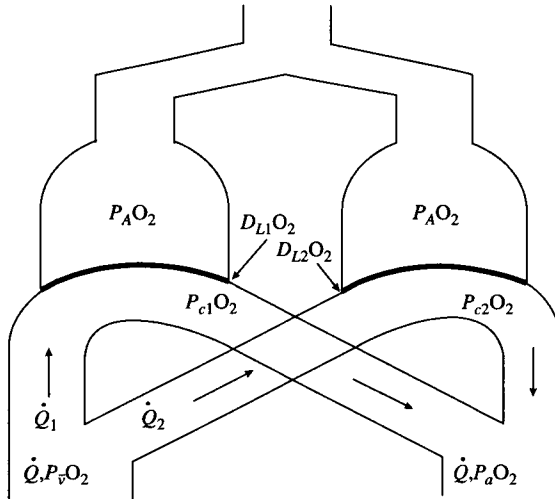


**Figure 9.5.** A conceptual model of the lung, including two compartments involved in gas exchange. These compartments have different diffusion capacities ( $D_{L1}O_2, D_{L2}O_2$ ) and perfusion properties ( $\dot{Q}_1, \dot{Q}_2$ ), resulting in varying partial pressures of oxygen flowing from the lung capillaries ( $P_{c1}O_2, P_{c2}O_2$ ) for each compartment.

For oxygen transport, the diffusion/perfusion mismatch ( $D_L O_2 / \dot{Q}$ ) can be represented mathematically by modifying (9.30), substituting for transit time ( $t$ ). For blood leaving the lung capillaries,  $t$  can be expressed as:

$$t = \frac{\text{Volume of pulmonary capillary blood}}{\text{Rate of blood flow through the capillary}} = \frac{V_c}{\dot{Q}}$$

substituting for  $t$  in (9.30) gives:

$$P_{c2} O_2 = P_A O_2 - (P_A O_2 - P_{\bar{v}} O_2) e^{-(1/\beta)(D_L O_2 / \dot{Q})} \tag{9.33}$$

which describes  $P_{c2} O_2$  as an exponential function of the solubility ( $\beta$ ) and the  $D/\dot{Q}$  ratio. For a model with two compartments involved in gas exchange (Figure 9.5), (9.33) can be written to describe the partial pressure of oxygen in blood from each of the compartments ( $P_{c1} O_2, P_{c2} O_2$ ).

Piiper *et al.* (1981, 1992) have used the term *equilibration index* to describe the ratio  $D/(\dot{Q}\beta)$ , using this index to quantify the extent to which gas exchange abnormalities can be partitioned into a diffusion or perfusion problem. This index is particularly applicable where  $\beta$  is constant, meaning for inert gases or for oxygen during hypoxia where the slope of the oxygen dissociation curve is almost constant.



This section has given a mathematical description of oxygen diffusion. In the pulmonary physiology laboratory, the diffusion properties of the lung are more frequently estimated using carbon monoxide ( $D_L\text{CO}$ ). Unlike oxygen, the partial pressure of CO in lung capillary plasma can be assumed to be negligible so that diffusion into the blood depends solely on the driving pressure in the alveoli.

Numerous methods exist for estimating  $D_L\text{CO}$ . These include methods where a steady-state PCO is obtained in the alveoli, a single breath is taken, or experiments involving rebreathing. Whilst the details of these techniques are beyond the scope of this chapter, they are all based on applying Fick's First Law of Diffusion, which for carbon monoxide can be written as:

$$D_L\text{CO} = \frac{\dot{V}\text{CO}}{P_A\text{CO} - P_c\text{CO}}$$

where the lung capillary partial pressure of carbon monoxide ( $P_c\text{CO}$ ) is assumed to be zero. Estimates of  $D_L\text{O}_2$  are then made by multiplying  $D_L\text{CO}$  by 1.23 to account for the different density and solubility of the two gases.

### 9.3. MODELS OF VENTILATION PERFUSION MISMATCH

Figure 9.1 illustrates a lung with a single compartment involved in gas exchange. This model is a simplification of the true situation in which different regions of the lung have varying ventilation ( $\dot{V}$ ) and perfusion ( $\dot{Q}$ ). Figure 9.6 illustrates a conceptual model of the lung with two compartments involved in gas exchange, each with a different ventilation/perfusion  $\dot{V}/\dot{Q}$  ratio.

The two-compartment model illustrated in Figure 9.6 has four parameters ( $\dot{V}_{A1}$ ,  $\dot{V}_{A2}$ ,  $\dot{Q}_1$ ,  $\dot{Q}_2$ ), the unique identification of which is not possible from routine clinical measurements of  $\text{O}_2$  and  $\text{CO}_2$  in expired air and blood. Estimation of parameters describing multicompartment  $\dot{V}/\dot{Q}$  heterogeneity has been made possible by development of the multiple inert gas elimination technique (MIGET) (Wagner *et al.*, 1974). The MIGET has been widely applied in clinical and experimental research and includes both a mathematical model of  $\dot{V}/\dot{Q}$  heterogeneity and an experimental technique using multiple inert gases as tracers.

A detailed description of the experimental technique is beyond the scope of this chapter. The mathematical model included in the MIGET illustrates how the effects of  $\dot{V}/\dot{Q}$  heterogeneity can be mathematically formulated and is described in the following section.

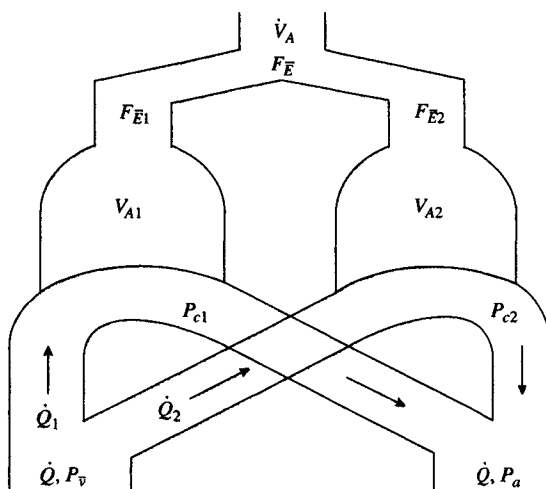


**Figure 9.6.** A conceptual model of the lung, including two compartments involved in gas exchange. These compartments have different ventilation ( $\dot{V}_{A1}$ ,  $\dot{V}_{A2}$ ) and perfusion ( $\dot{Q}_1$ ,  $\dot{Q}_2$ ) properties resulting in varying end capillary partial pressures ( $P_{c1}$ ,  $P_{c2}$ ).

### 9.3.1. THE MULTIPLE INERT GAS ELIMINATION TECHNIQUE (MIGET)

In the MIGET, multiple inert gases are simultaneously infused into a vein. Inert gases are used as tracers and, as such, eliminate the need for perturbing the underlying oxygen system, which may change the nature of the gas exchange abnormality. The MIGET assumes no diffusion limitation exist for inert gases, such that end lung capillary blood is at equilibrium with the alveoli. The key to the MIGET is that gases with a higher solubility are retained more readily in blood during its transport through lung capillaries. By choosing tracer gases with a wide range of solubilities and by measuring their concentration in both expired air and venous/arterial blood, a more complete description of the  $\dot{V}/\dot{Q}$  characteristics of the lung can be obtained.

The mathematical formulation used in the MIGET analysis can be derived from a mass balance equation similar to the Fick principle of blood flow (9.13) and the alveolar air equation, which is for a single tracer gas in a single alveolar gas exchange compartment:

$$\dot{V} = \dot{Q}(C_c - C_v) \tag{9.34}$$

$$P_A = F_I P_B - \frac{\dot{V} P_B}{\dot{V}_A} \tag{9.35}$$

For inert gases, inspired fraction ( $F_I$ ) is zero. Eliminating  $\dot{V}$  in (9.34) and (9.35) and replacing concentrations with pressures using Henry's law (9.27) gives:

$$\dot{V}_A P_A/P_B = \beta \dot{Q}(P\bar{v} - P_c) \quad (9.36)$$

Assuming no diffusion limitation  $P_A = P_c$  so that:

$$\dot{V}_A P_c/P_B = \beta \dot{Q}(P\bar{v} - P_c) \quad (9.37)$$

This equation can be rearranged to describe the retention ( $R$ ) of the gas as blood passes through the lung capillary, which means the  $P_c/P\bar{v}$  ratio:

$$R = \frac{P_c}{P\bar{v}} = \frac{\beta P_B}{\dot{V}_A/\dot{Q} + (\beta P_B)} \quad (9.38)$$

which is the equation originally described by Wagner *et al.* (1974), modified to include barometric pressure ( $P_B$ ).

High-solubility gases are retained more readily in the blood such that as  $\beta \rightarrow \infty$  the retention ( $R$ )  $\rightarrow \beta/\beta = 1$ . For low-solubility gases, the retention depends more on the  $\dot{V}/\dot{Q}$  ratio of the lung unit. Excretion ( $E$ ) is defined in a similar way to retention as the ratio of alveolar to venous gas pressures,  $P_A/P\bar{v}$ .

The retention of inert gas in a multicompartmental lung can be described by considering the mass of gas in blood leaving each of the perfusion compartments. For the two-compartment model illustrated in Figure 9.6, this can be described as:

$$\dot{Q} \beta P_a = \dot{Q}_1 \beta P_{c1} + \dot{Q}_2 \beta P_{c2} \quad (9.38)$$

Dividing through by  $P\bar{v}$  and cancelling  $\beta$  in each of the terms gives:

$$\dot{Q} \frac{P_a}{P\bar{v}} = \dot{Q}_1 \frac{P_{c1}}{P\bar{v}} + \dot{Q}_2 \frac{P_{c2}}{P\bar{v}} \quad (9.39)$$

giving:

$$\dot{Q}R = \dot{Q}_1 R_1 + \dot{Q}_2 R_2 \quad (9.40)$$

For multiple compartments ( $i = 1 : n$ ), the overall retention ( $R$ ), which is the ratio of pressure in arterial to venous blood, can be described as:

$$R = \frac{1}{\dot{Q}} \sum_{i=1}^n \dot{Q}_i R_i = \frac{1}{\dot{Q}} \sum_{i=1}^n \dot{Q}_i \frac{\beta}{\dot{V}_{Ai}/\dot{Q}_i + \beta} \quad (9.41)$$

Excretion is described in a similar way:

$$E = \frac{1}{\dot{V}} \sum_{i=1}^n \dot{V}_i R_i = \frac{1}{\dot{V}} \sum_{i=1}^n \dot{V}_{Ai} \frac{\beta}{\dot{V}_{Ai}/\dot{Q}_i + \beta} \quad (9.42)$$

Measurements of retention ( $P_a/P_{\bar{v}}$ ) and excretion ( $P_A/P_{\bar{v}}$ ) are obtained for each inert gas (usually 6) by sampling blood and expired gas. By dividing the lung into a number of compartments, usually 50, each with a fixed  $\dot{V}/\dot{Q}$  ratio, (9.41) and (9.42) are fitted to measured values of  $R$  and  $E$  by varying the perfusion ( $\dot{Q}_i$ ) and ventilation ( $\dot{V}_{A_i}$ ) of each of the compartments. Results of these analyses are then reported as distributions of blood flow and ventilation across the range of possible  $\dot{V}/\dot{Q}$  regions in the lung.

## 9.4. APPLICATION OF MATHEMATICAL MODELS OF VENTILATION, PERFUSION, AND DIFFUSION

### 9.4.1. APPLICATION OF MODELS IN PHYSIOLOGICAL AND CLINICAL EXPERIMENTATION

Despite the research into diffusion abnormalities, the standard method of describing pulmonary gas exchange in experimental studies is the MIGET, which is considered to be a reliable technique for quantifying shunt, physiological dead space, and the distribution of  $\dot{V}/\dot{Q}$  ratios in the lung. Indeed, in studies using the MIGET, the concept of diffusion impairment is seldom required to describe abnormalities in gas exchange, except in cases of pulmonary fibrosis (Agusti *et al.*, 1991), exercise, or mild exercise during hypoxia (Torre-Bueno *et al.*, 1985; Wagner *et al.*, 1986). A brief summary of the application of the a MIGET in anaesthesia, intensive care medicine, and pulmonary medicine now follows, with emphasis on major improvements in understanding enabled by the application of this technique.

In anaesthesiological research, the MIGET has been used to describe gas exchange abnormalities following different types of anaesthesia: inhalation (Tokics *et al.*, 1996; Bindslev *et al.*, 1981; Lundh *et al.*, 1984; Gunnarsson *et al.*, 1989), intravenous (Anjou Lindskog *et al.*, 1985), and epidural (Lundh *et al.*, 1983; Hachenberg *et al.*, 1997), and after numerous interventions during anaesthesia such as surgery (Hedenstierna *et al.*, 1983; Lundh *et al.*, 1983b; Hachenberg *et al.*, 1994), variation in positive end-expiratory pressure (PEEP) (Bindslev *et al.*, 1981; Tokics *et al.*, 1987), or infusion of inotropic agents (Hachenberg *et al.*, 1998). The findings of these studies consistently show an increased shunt and  $\dot{V}/\dot{Q}$  mismatch following anaesthesia, with increases in PEEP reducing the shunt fraction.

Investigations using the MIGET in intensive care have provided understanding of the pathophysiology of disorders such as acute respiratory distress syndrome (ARDS) and pneumonia, and the effects of therapeutic interventions in patients with these severe disorders. The application of the MIGET in studying ARDS and pneumonia has been reviewed by Melot (1994), the

main finding being an increased shunt and increased perfusion of low  $\dot{V}/\dot{Q}$  areas to explain severe hypoxaemia seen in these patients. The use of MIGET to study therapeutic intervention in these patients has shown that PEEP improves oxygenation via a reduction in shunt fraction (Dantzker *et al.*, 1979; Matamis *et al.*, 1984); turning patients from supine to prone position reduces shunt (Pappert *et al.*, 1994; Bein *et al.*, 1998); and inhalation of prostacyclin or nitric oxide causes a redistribution of blood flow to regions with normal  $\dot{V}/\dot{Q}$  (Rossaint *et al.*, 1993; Walmrath *et al.*, 1993; Bender *et al.*, 1997).

The MIGET has been used extensively in pulmonary laboratories to describe gas exchange in patients with chronic pulmonary disease. The major finding of these studies has been an increased number of low  $\dot{V}/\dot{Q}$  regions of the lung (Agusti *et al.*, 1994; Sandek *et al.*, 1995; Rossi *et al.*, 1994), although the results are less consistent than those obtained from research in anaesthesiology and intensive care medicine. In studies of patients with pulmonary fibrosis,  $\dot{V}/\dot{Q}$  mismatch accounts for 80% of the hypoxaemia at rest and only 60% during exercise (Agusti *et al.*, 1991), indicating severe diffusion abnormalities in these patients.

While the MIGET has found widespread application as an experimental tool, its use as a routine clinical tool has been somewhat limited (Wagner *et al.*, 1987). This is largely the result of the cost and complexity of the technique. The MIGET requires a very systematic and detailed technical procedure that involves preparation of an infusate containing six inert gases, sampling blood and gas after 30 minutes of infusion, and analysing these using gas chromatography. The complexity and invasive nature of the original technique has led to development of less invasive experimental techniques intended to introduce the MIGET into clinical practice (Roca *et al.*, 1993).

#### 9.4.2. APPLICATION OF MODELS IN ROUTINE CLINICAL PRACTICE

Estimation of the parameters of multicompartmental models, including  $\dot{D}/\dot{Q}$  or  $\dot{V}/\dot{Q}$  heterogeneity, is seldom routinely performed outside the pulmonary laboratory. In the surgical theatre, intensive care unit, recovery room, or more general wards, the clinician usually relies upon other measurements to assess the patients oxygenation problems and prevent hypoxaemia. These measurements include single measurements of arterial oxygen tensions, calculations of alveolar-arterial oxygen difference (A-aO<sub>2</sub>), or, as the clinical state of the art, estimation of the shunt fraction using information obtained from mixed venous blood sampling through a pulmonary artery catheter (Wandrup, 1992). These measurements are an attempt to describe the clinical oxygenation problem and have insufficient detail to interpret problems in physiological

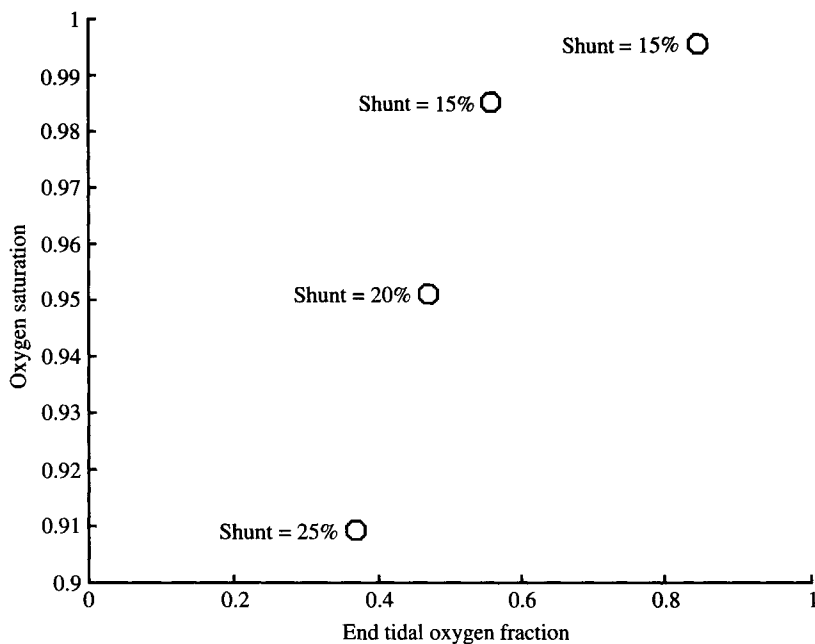


**Figure 9.7.** The shunt fraction estimated for one patient at varying values of  $F_E' O_2$ .

terms. However, even the estimation of shunt cannot adequately describe the clinical picture seen in patients when the inspired oxygen fraction is varied. This situation is illustrated in Figure 9.7, where the variation in oxygen saturation of arterial blood is plotted against expired oxygen fraction for one postoperative patient, and the shunt equation, (9.11), is solved for each data point. No single value of shunt adequately describes this patient, the estimated shunt increasing at lower values of end tidal oxygen fraction ( $F_E' O_2$ ).

The realisation that a shunt only model cannot fit data where  $F_I O_2$  is varied was recognised by Riley *et al.* (1951a, 1951b) and later by King *et al.* (1974). To solve this problem, these authors divided the oxygenation problem into that due to an alveolar-lung capillary drop in the partial pressure of oxygen and that due to pulmonary shunt. To estimate two parameters describing the oxygenation problem then required no more than obtaining routine measurements of blood gases and ventilation at varying inspired oxygen fractions. These two-parameter models, although a relatively poor description of the physiology, are a substantial improvement over a shunt only model. They describe the effects of varying  $F_I O_2$ , which is a routine therapeutic intervention in mechanically ventilated patients.

Recently, Andreassen *et al.* (1993, 1996), Sapsford *et al.* (1995), Gray *et al.* (1997), and Roe *et al.* (1997) have presented the use of two-parameter mathematical models of oxygen transport, the oxygenation problem described as shunt combined with either a resistance to oxygen diffusion (labelled Rdiff) (Andreassen *et al.* 1993, 1996) or a  $P_I O_2 - P_c O_2$  difference due to  $\dot{V}/\dot{Q}$  mismatch (Sapsford *et al.*, 1995; de Gray *et al.*, 1997; Roe *et al.*, 1997). These model representations have been shown to provide identical fits to routine blood gas and ventilatory data obtained by varying  $F_I O_2$  (Rees *et al.*, 1997). The clinical relevance of these two parameter models has been illustrated by both these groups of authors and is illustrated in Figure 9.8 for the model of Andreassen *et al.* (1993, 1996).

As illustrated in Figure 9.8, increases in the pulmonary shunt parameter results in a vertical depression of the plateau of the  $F_E O_2 / S_a O_2$  curve, while abnormalities in the second parameter (ventilation perfusion  $\dot{V}/\dot{Q}$  mismatch, or oxygen diffusion resistance [Rdiff]) cause a lateral displacement of the  $F_E O_2 / S_a O_2$  curve. The lateral displacement of the  $F_E O_2 / S_a O_2$  curve can be seen as a more clinically significant problem, as it describes a situation where large changes in oxygen saturation can occur for only small changes in  $F_I O_2$ .

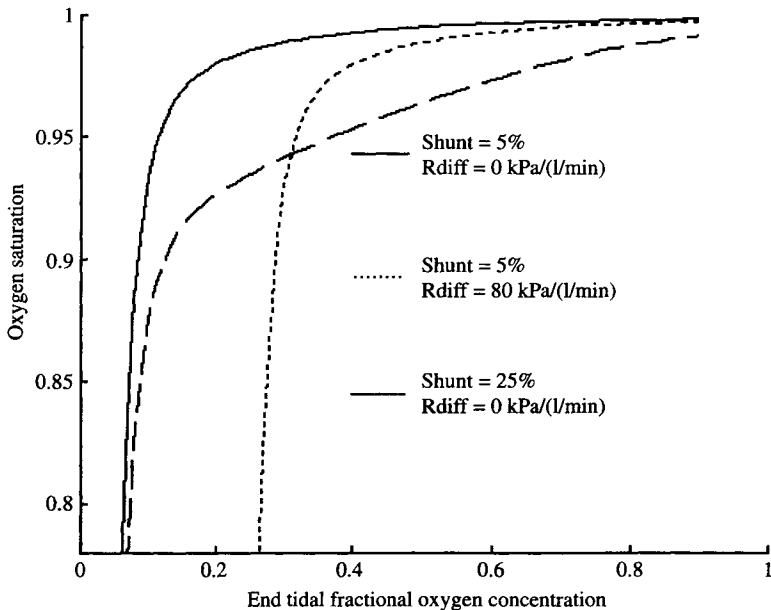


**Figure 9.8.** Model predicted arterial oxygen saturations for 1) a normal subject with shunt = 5% and no diffusion abnormality Rdiff = 0 kPa/(l/min); 2) a hypothetical patient with a diffusion abnormality; and 3) a hypothetical patient with a shunt disorder.

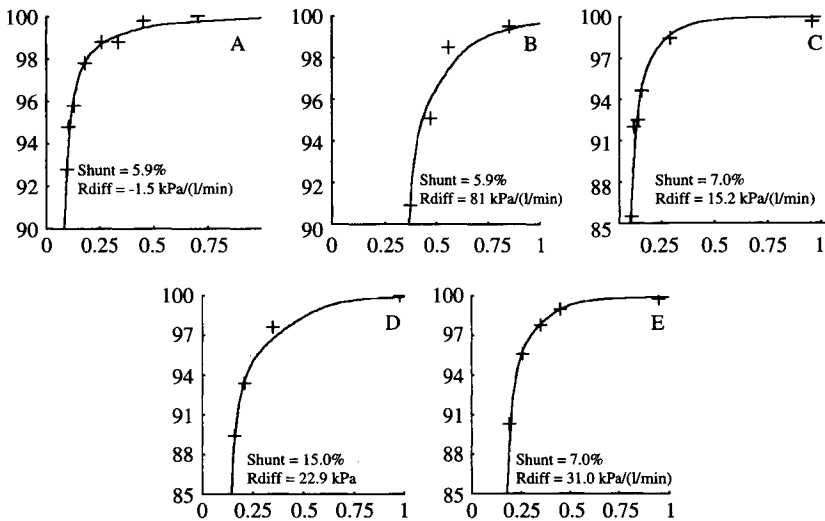


**Figure 9.9.**  $F_{E}O_2/S_aO_2$  data (crosses) and model fits, to data from A, a normal subject; B, a postoperative cardiac patient; C; a postoperative hysterectomy patient; D, a poorly compensated cardiac patient; and E, a patient residing in the intensive care unit.

The two-parameter model of Sapsford *et al.* (1995) has been shown to fit data from normal subjects; patients before and after thoracotomy (Sapsford *et al.*, 1995; de Gray *et al.*, 1997) and patients during (Sapsford *et al.*, 1995; Roe *et al.*, 1997) and after (Roe *et al.*, 1997) abdominal surgery. Similarly, the two-parameter model described by Andreassen *et al.* (1993, 1996) has been shown to fit data from normal subject and postoperative cardiac patients (Andreassen *et al.*, 1998) and a wide range of as yet unpublished results. Some of the results of this latter group are illustrated in Figure 9.9, including one patient from each of the study populations.

These two-parameter models have yet to be used in clinical practice, but with pulse oximetry technology enabling noninvasive estimation of the  $F_{E}O_2/S_aO_2$  curve, the estimation of the parameters of such models is a relatively simple task that might be performed as a routine part of clinical practice.

## 9.5. REFERENCES

- Agusti, A. G. N., J. Roca, J. Gea, P. D. Wagner, A. Xaubet and R. Rodriguez-Roisin. Mechanisms of gas exchange impairment in idiopathic pulmonary fibrosis. *Am Rev Respir Dis* 143(1991):219–25.



- Agusti, A. G. N. and J. A. Barbera. Contribution of multiple inert gas elimination technique to pulmonary medicine. 2. Chronic pulmonary diseases: chronic obstructive pulmonary disease and idiopathic pulmonary fibrosis. *Thorax* 49(1994):924–32.
- Andreassen, S., J. Egeberg, M. P. Schrøter and P. T. Andersen. Estimation of pulmonary diffusion resistance and shunt in an oxygen status model. *Comput Methods Programs Biomed* 51(1996):95–105.
- Andreassen, S., S. E. Rees, S. Kjærgaard, P. Thorgaard, S. M. Winter and C. J. Morgan, P. Alstrup and E. Toft. 1999. Hypoxemia after coronary bypass surgery modeled by resistance to oxygen diffusion. *Crit Care Med* 27(1999):2445–53.
- Anjou Lindskog, E., L. Broman, M. Broman, A. Holmgren, G. Settergren and G. Ohqvist. Effects of intravenous anesthesia on VA/Q distribution: a study performed during ventilation with air and with 50% oxygen, supine and in the lateral position. *Anesthesiology* 62(1985):485–92.
- Bein, T., A. Reber, C. Metz, K. W. Jauch and G. Hedenstierna. Acute effects of continuous rotational therapy on ventilation-perfusion inequality in lung injury. *Intensive Care Med* 24(1998):132–37.
- Bender, K. A., J. A. Alexander, J. M. Enos and J. W. Skimming. Effects of inhaled nitric oxide in patients with hypoxemia and pulmonary hypertension after cardiac surgery. *Am J Crit Care* 6(1997):127–31.
- Bindslev, L., G. Hedenstierna, J. Santesson, I. Gottlieb and A. Carvallhas. Ventilation-perfusion distribution during inhalation anaesthesia. Effects of spontaneous breathing, mechanical ventilation and positive end-expiratory pressure. *Acta Anaesthesiol Scand* 25(1981):360–71.
- Bohr, C. Über die spezifisch Tätigkeit der Lungen bei der respiratorischen Gasaufnahme und ihr Verhalten zu der durch die Alveolarwand stattfindenden Gasdiffusion. *Skand Arch Physiol* 22(1909):221–80.
- Dantzer, D. R., C. J. Brook, P. DeHart, J. P. Lynch and J. G. Weg. Ventilation-perfusion distributions in the adult respiratory distress syndrome. *Am J Respir Dis* 120(1979):1039–52.
- de Gray, L., E. M. Rush and J. G. Jones. A non-invasive method for evaluating the effect of thoracotomy on shunt and ventilation perfusion inequality. *Anaesthesia* 52(1997):630–35.
- Gunnarsson L., A. Strandberg, B. Brismar, L. Tokics, H. Lundquis and G. Hedenstierna. Atelectasis and gas exchange impairment during enflurane/nitrous oxide anaesthesia. *Acta Anaesthesiol Scand* 33(1989):629–37.
- Hachenberg T., A. Tenling, S. O. Nystrom, H. Tyden and G. Hedenstierna. Ventilation-perfusion inequality in patients undergoing cardiac surgery. *Anesthesiology* 80(1994):509–19.
- Hachenberg T., D. Holst, C. Ebel, B. Pfeiffer, H. Thomas, M. Wendt and G. Hedenstierna. Effect of thoracic epidural anaesthesia on ventilation-perfusion distribution and intrathoracic blood volume before and after induction of general anaesthesia. *Acta Anaesthesiol Scand* 41(1997):1142–48.
- Hachenberg T., S. Karmann, B. Pfeiffer, H. Thomas, M. Gründling and M. Wendt. The effect of dexopamine on ventilation perfusion distribution and pulmonary gas exchange in anesthetized, paralyzed patients. *Anesth Analg* 86(1998):314–19.
- Hedenstierna, G., C. Mebius and S. Bygdeman. Ventilation-perfusion relationship during hip arthroplasty. *Acta Anaesthesiol Scand* 27(1983):56–61.
- King, T. K.C, B. Weber, A. Okinaka, S. A. Friedman, J. P. Smith and W. A. Briscoe. Oxygen transfer in catastrophic respiratory failure. *Chest* 65(1974):40S–44S.
- Kobayashi, H., J. Piiper and P. Scheid. Effect of curvature of the O<sub>2</sub> equilibrium curve on alveolar O<sub>2</sub> uptake. *Respir Physiol* 83(1991):255–60.
- Lundh, R., G. Hedenstierna and H. Johansson. Ventilation-perfusion relationships during epidural analgesia. *Acta Anaesthesiol Scand* 27(1983):410–16.
- Lundh, R. and G. Hedenstierna. Ventilation-perfusion relationships during anaesthesia and abdominal surgery. *Acta Anaesthesiol Scand* 27(1983b):167–73.

- Lundh R. and G. Hedenstierna. Ventilation-perfusion relationships during halothane anaesthesia and mechanical ventilation. Effects of varying inspired oxygen concentration. *Acta Anaesthesiol Scand* 28(1984):191–98.
- Matamis D., F. Lemaire, F. Harf, B. Teisseire and C. Brun-Buisson. Redistribution of pulmonary blood flow induced by positive end-expiratory pressure and dopamine infusion in acute respiratory failure. *Am J Respir Dis* 129(1984):39–44.
- Melot C. Contribution of multiple inert gas elimination technique to pulmonary medicine. 5. Ventilation-perfusion relationships in acute respiratory failure. *Thorax* 49(1994):1251–58.
- Nunn J. F. 1993. *Nunn's Applied Respiratory Physiology*. London: Butterworth-Heinemann.
- Pappert D., R. Rossaint, K. Slama, T. Gruning and K. J. Falke. Influence of positioning on ventilation-perfusion relationships in severe adult respiratory distress syndrome. *Chest* 106(1994):1511–16.
- Piiper, J., P. Haab and H. Rahn. Unequal distribution of pulmonary diffusing capacity in the anesthetized dog. *J Appl Physiol* 16(3)(1960):499–506.
- Piiper, J. and P. Scheid. Model for capillary-alveolar equilibration with special reference to O<sub>2</sub> uptake in hypoxia. *Respir Physiol* 46(1981):193–208.
- Piiper, J. Diffusion-perfusion inhomogeneity and alveolar-arterial O<sub>2</sub> diffusion limitation: theory. *Respir Physiol* 87(1992):349–56.
- Rees S. E., G. W. Rutledge, P. T. Andersen and S. Andreassen. Are alveolar block and ventilation-perfusion mismatch distinguishable in routine clinical data. in: *Selected Abstracts of the Annual Meeting of the European Society for Computing and Technology in Anaesthesia and Intensive Care*. Edited by N. Lutter. *Intl J Clin Monit Comput* 14(1998):541–53.
- Riley, R. L. and A. Counard. Analysis of factors affecting partial pressure of oxygen and carbon dioxide in gas and blood of the lungs: theory. *J Appl Physiol* 4(1951a):77–101.
- Riley, R. L., A. Counard and K. W. Donald. Analysis of factors affecting partial pressure of oxygen and carbon dioxide in gas and blood of the lungs: method. *J Appl Physiol* 4(1951b):102–20.
- Roca, J., P. D. Wagner. Contribution of multiple inert gas elimination technique to pulmonary medicine. 1. Principles and information content of the multiple inert gas elimination technique. *Thorax* 49(1993):815–24.
- Roe P. G., R. Gadelrab, D. Sapsford and J. G. Jones. Intra-operative gas exchange and post-operative hypoxaemia. *Eur J Anaesthesiol* 14(1997):203–10.
- Rossaint R., K. J. Falke, F. Lopez, K. Slama, U. Pison and W. M. Zapol. Inhaled nitric oxide for the adult respiratory distress syndrome. *N Engl J Med* 328(1993):399–405.
- Rossi, C. Santos, J. Roca, A. Torres, M. A. Félez and R. Rodriguez-Roisin. Effects of PEEP on  $\dot{V}_A/\dot{Q}$  mismatching in ventilated patients with chronic airflow obstruction. *Am J Respir Care Med* 149(1994):1077–84.
- Roughton, F. J. W. and Forster, R. E. Relative importance of diffusion and chemical reaction rates in determining rate of exchange of gases in the human lung, with special reference to true diffusing capacity of pulmonary membrane and volume of blood in the lung capillaries. *J Appl Physiol* 11(2)(1957):290–302.
- Sandek, K., T. Andersson, T. Bratel, L. Lagerstrand. Ventilation-perfusion inequality in nocturnal hypoxemia due to chronic obstructive lung disease (COLD). *Clin Physiol* 15(1995):499–513.
- Sapsford, D. J. and J. G. Jones. The P<sub>i</sub>O<sub>2</sub> vs. SpO<sub>2</sub> diagram: a non-invasive measure of pulmonary oxygen exchange. *Eur J Anaesthesiol* 12(1995)369–74.
- Siggaard-Andersen, O. 1974. *The Acid-Base Status of the Blood*. Copenhagen: Munksgaard.
- Siggaard-Andersen, O., P. D. Wimberley, I. Gothgen and M. Siggaard-Andersen. A mathematical model of the hemoglobin-oxygen dissociation curve of human blood and of the oxygen partial pressure as a function of temperature. *Clin Chem* 30(1984):1646–51.

- Siggaard-Andersen, M., O. Siggaard-Andersen. Oxygen status algorithm, version 3, with some applications. *Acta Anaesthesiol Scand* 39, Supp. 107, (1985):13–20.
- Staub, N. C., J. M. Bishop and R. E. Forster. Velocity of O<sub>2</sub> uptake by human red blood cells. *J Appl Physiol* 16(2)(1961):511–16.
- Staub, N. C., J. M. Bishop and R. E. Forster. Importance of diffusion and chemical reaction rates in O<sub>2</sub> uptake in the lung. *J Appl Physiol* 17(1)(1962):21–27.
- Staub, N. C. Alveolar-arterial oxygen tension gradient due to diffusion. *J Appl Physiol* 18(4)(1963):673–680.
- Tokics, L., G. Hedenstierna, Å. Strandberg, B. Brismar and H. Lundquist. Lung collapse and gas exchange during general anesthesia: effects of spontaneous breathing, muscle paralysis and positive end-expiratory pressure. *Anesthesiology* 66(1987):157–67.
- Tokics, L., G. Hedenstierna, L. Svensson, B. Brismar, T. Cederlund, H. Lundquist and A. Strandberg. V/Q distribution and correlation to atelectasis in anesthetized paralyzed humans. *J Appl Physiol* 81(1996):1822–33.
- Torre-Bueno, J. R., P. D. Wagner, H. A. Saltzman, G. E. Gale and R. E. Moon. Diffusion limitation in normal humans during exercise at sea level and simulated altitude. *J Appl Physiol* 58(1985):989–95.
- Wagner, P. D., H. A. Saltzman and J. B. West. Measurement of continuous distributions of ventilation-perfusion ratios: theory. *J Appl Physiol* 36(5)(1974):588–99.
- Wagner, P. D. Diffusion and chemical reaction in pulmonary gas exchange. *Physiol Rev* 57(2):257–312.
- Wagner, P. D., G. E. Gale, R. E. Moon, J. R. Torre-Bueno, B. W. Stolp and H. A. Saltzman. Pulmonary gas exchange in humans exercising at sea level and simulated altitude. *J Appl Physiol* 61(1986):260–70.
- Wagner, P. D., G. Hedenstierna and G. Bylin. Ventilation-perfusion inequality in chronic asthma. *Am Rev Respir Dis* 136(1987):605–12.
- Walrmath, D., T. Schneider, J. Pilch, F. Grimminger and W. Seeger. Aerosolized prostacyclin in adult respiratory distress syndrome. *Lancet* 342(1993):961–62.
- Wandrup, J. Oxygen uptake in the lungs. Shortcuts in clinical assessment of pulmonary oxygenation. *Blood Gas News* 1(1)(1992):3–5.
- Yamaguchi, K., D. Nguyen-Phu, P. Scheid and J. Piiper. Kinetics of O<sub>2</sub> uptake and release by human erythrocytes studied by a stopped flow technique. *J Appl Physiol* 58(4)(1985):1215–24.

## APPENDIX A. GLOSSARY

Each symbol is constructed from three parts: the quantity, the location, and the substance. These three parts can take the following values:

**Quantity** pressure ( $P$ ), concentration ( $C$ ), saturation ( $S$ ), volume ( $V$ ), fraction ( $F$ ), and diffusion capacity ( $D$ ). Flows are denoted by a point over the quantity term.

**Location** arterial blood ( $a$ ), venous blood ( $v$ ), lung capillary blood ( $c$ ), alveoli ( $A$ ), inspired gas ( $I$ ), expired gas ( $E$ ), alveolar-lung capillary membrane ( $M$ ). An overbar is used to represent a mixed pool, a “” is used to represent an end tidal expired gas.

**Substance** oxygen (O<sub>2</sub>), carbon dioxide (CO<sub>2</sub>), water (H<sub>2</sub>O), haemoglobin (Hb).

Examples of this nomenclature are arterial oxygen pressure  $P_{aO_2}$ , inspired carbon dioxide fraction  $F_I CO_2$ , flow of oxygen (oxygen consumption)  $\dot{V}O_2$ , flow of blood (cardiac output)  $\dot{Q}$ , mixed venous oxygen concentration  $C_{\bar{v}}O_2$ , end tidal oxygen fraction  $F'_{E}O_2$ .

Gases are expressed at three temperatures and pressures: standard (STP—0°C, 101 kPa), ambient (ATP), and body (BTP). Gases are also expressed as either dry (*D*) or saturated with water (*S*). Wet and dry gases at ambient or body temperature and pressure are represented using the subscripts ATPS, ATPD, BTPS, and BTPD, respectively.

Exceptions to these rules are listed here:

Tidal volume	$V_T$
Dead space	$V_D$
Anatomical dead space	$V_{Dana}$
Alveolar dead space	$V_{DA}$
Physiological dead space	$V_{DP}$
Barometric pressure	$P_B$
Respiratory frequency	$f$
Alveolar oxygen diffusion resistance	$R_{diff}$
Arteriovenous shunt	shunt
Respiratory quotient	$R$
Diffusion capacity alveoli to blood	$D_L$
Rate of oxygen binding to blood	$\theta$
Solubility coefficient of gas in blood	$\beta$
Oxygen dissociation curve	ODC

## APPENDIX B. CALCULATIONS NECESSARY TO CONVERT INSPIRED GAS AT ATPD TO BTPS

### *Addition of water*

On addition of water to dry inspired gas volume is increased such that:

$$V_{T, ATPS} = V_{T, ATPD} + V_{H_2O, added} \tag{B.1}$$

Where  $V_{H_2O, added}$  is the volume of water added during inspiration. The fraction of  $H_2O$  in fully saturated inspired gasses ( $F_{H_2O, ATPS}$ ) is approximately 6%, so that  $V_{H_2O, added}$  can be calculated as follows:

$$V_{H_2O, added} = F_{H_2O, ATPS} V_{T, ATPS} \tag{B.2}$$

substituting for  $V_{H_2O, added}$  in equation B.1 gives:

$$V_{T, ATPS} = V_{T, ATPD} + F_{H_2O, ATPS} V_{T, ATPS} \tag{B.3}$$

which can be rearranged to give an expression describing the tidal volume of wet gases in terms of the dry inspired gases:

$$V_{T,ATPS} = \frac{V_{T,ATPD}}{1 - F_{H_2O,ATPS}} \quad (\text{B.4})$$

Addition of water to the inspired gas lowers the fraction of all other gases in the inspiration. An equation describing the relationship between the fraction of oxygen ( $O_2$ ) in inspired gases before and after addition of water can be derived by considering the volume of  $O_2$  in the dry ( $F_I O_{2,ATPD} V_{T,ATPD}$ ) and humidified ( $F_I O_{2,ATPS} V_{T,ATPS}$ ) gas. This volume remains constant such that:

$$F_I O_{2,ATPD} V_{T,ATPD} = F_I O_{2,ATPS} V_{T,ATPS} \quad (\text{B.5})$$

substituting for  $V_{T,ATPS}$  in (B.4) gives:

$$F_I O_{2,ATPD} V_{T,ATPD} = F_I O_{2,ATPS} \frac{V_{T,ATPD}}{1 - F_{H_2O,ATPS}}$$

which rearranged gives an expression describing the fraction of oxygen in wet gas in terms of the dry inspired gases:

$$F_I O_{2,ATPS} = F_I O_{2,ATPD} (1 - F_{H_2O,ATPS}) \quad (\text{B.6})$$

### *Warming of inspired gases*

Warming of the inspiration causes the gases to expand but does not change the fraction of each gas in the inspiration, which means  $F_{I,BTPS} = F_{I,ATPS}$  for all gases. The increase in volume can be described by considering the gas laws, such as Charles' law and Boyle's law, which together state that for a fixed mass of gas the pressure multiplied by the volume is proportional to the temperature:

$$PV = RT \quad (\text{B.7})$$

where  $R$  is the universal gas constant. Equation (B.7) can be written for humidified inspired gas at both ambient ( $AT$ ) and body ( $BT$ ) temperature:

$$P_B V_{T,ATPS} = R AT \quad (\text{B.8})$$

$$P_B V_{T,BTPS} = R BT \quad (\text{B.9})$$

Dividing (B.8) and (B.9) gives an expression for the tidal volume of the inspired gases at body temperature in terms of the tidal volume at ambient temperature:

$$V_{T,BTPS} = V_{T,ATPS} \frac{BT}{AT} \quad (\text{B.10})$$

# Mathematical Models of Respiratory Mechanics

**Gianluca Nucci and Claudio Cobelli**

## 10.1. INTRODUCTION

This chapter is dedicated to the description and interpretation of techniques for the simulation and quantification of breathing mechanics, with particular attention to those methods that are suitable for adoption in intensive care units. As a matter of fact, estimation of parameters of respiratory mechanics, revealing the overall lung function, is crucially important in mechanically ventilated patients since it enables monitoring of patient status and disease as well as the effectiveness of therapy and treatment. The assessment of respiratory mechanics is a process invariably involving modelling and estimation issues. The proposal of simple models based on physiological and anatomical considerations, suitable to be represented in terms of electrical or mechanical analogues, eased their interpretation and helped their adoption. This led to a number of distinct approaches that have useful clinical applications. However, our understanding of pulmonary mechanics is inseparable from the mathematical (and theoretical) representation of the system we are interested in. Moreover, the model selection and the kind of physiopathological insight that can be obtained strictly depends on the type of applied input (frequency content, amplitude) and output (sampling site and frequency) that can be designed for the specific application. After a brief introduction of the basic definitions of breathing mechanics and some signal measurement issues, the rest of this chapter is dedicated to a review of the different methods (and hence models) to quantify the breathing mechanics. The last section is dedicated to simulation models of breathing mechanics. Emphasis is posed

on an anatomically consistent model that has found extensive application for the investigation of various facets of constrictive diseases. In this chapter, the schematic representation of models of lung mechanics will take advantage, when possible, of an electrical analogue.

## 10.2. BREATHING MECHANICS: BASIC CONCEPTS

The mechanical properties of the respiratory system can be schematised in term of resistance, compliance, and inertance. The latter is generally considered less important in determining the overall mechanical behaviour at the breathing frequencies. Before entering the details of modelling and simulation of breathing mechanics, the basic definition of each property is given.

Resistance is defined as the pressure difference required to cause a unit of gas flow:

$$\text{resistance} = \frac{\Delta \text{pressure}}{\text{flow rate}}$$

In the study of respiratory mechanics, it is frequently expressed in  $\text{cmH}_2\text{O s/l}$ . When pressure is measured in mmHg, Pa, Bar and/or the flow in  $\text{ml/s}$ , the units for resistance are accordingly modified. As air passes through the different airway generations, the cross-sectional area of airways increases. Air flow can be considered essentially laminar in the small airways, while it is both laminar and turbulent in the upper airways. Energy dissipated in resistive elements is irreversibly lost to heat. The total flow resistance is determined by the friction of gas flowing into the airways and the friction due to movement of tissues of the lung and of the chest wall. Since pressure applied to the airways is first transmitted to the lung and then to the chest wall, these elements are considered in series and thus additive, even if the chest wall contribution to total respiratory system resistance is considered relatively modest. An abnormal airway resistance, due to a decreased airway calibre, is always found in patients with obstructive disease, oedema, or inflammation of the bronchial mucosa. Tissue resistance is more volume-dependent and has its greatest contribution at low frequencies (Loring, 1998).

Compliance is defined as the volume variation per unit pressure change:

$$\text{compliance} = \frac{\Delta \text{volume}}{\Delta \text{pressure}}$$

and is usually expressed in  $\text{l/cmH}_2\text{O}$  or in  $\text{ml/cmH}_2\text{O}$ . Compliance is a measure of respiratory system distensibility. In this chapter, we will frequently use the reciprocal of compliance, elastance, as measure of respiratory system rigidity. Being the lung and the chest in series, the elastance of respiratory system is the sum of lung and chest wall elastance. Several diseases can alter respiratory

system elastance. An increase in chest wall stiffness invariably results in an augmented respiratory system elastance. Overall lung elastance is indirectly increased by inhomogeneous constriction of airways that limits the number of alveoli participating in ventilation. In acute respiratory distress syndrome (ARDS), elastance is increased because of the inflammatory fluids that fill the alveolar spaces subtracting space to gas volume.

Inertance is a measure of the tendency of the respiratory system to resist changes in flow and can be defined as:

$$\text{inertance} = \frac{\Delta \text{pressure}}{\Delta \text{flow rate}}$$

and is expressed in  $\text{cmH}_2\text{O s}^2/\text{l}$  or  $\text{cmH}_2\text{O s}^2/\text{ml}$ . From the definition, it appears that during steady (or slowly changing) flow the inertial pressure change is zero (or negligible). The inertial pressure is in counterphase with respect to elastic recoil pressure. Thus, it compensates the stiffness of respiratory system and becomes dominant over elastance at frequencies greater than 5 to 10 Hz in normal human adults (Peslin *et al.*, 1986).

The principal measurement sites in a mechanically ventilated patient are shown in Figure 10.1 together with the relations between pressures and equipment/anatomical counterparts. By convention, all the pressure measured are taken with respect to body surface pressure, which is considered equal to atmospheric pressure. In a nonintubated subject, special care must be posed in avoiding the confounding influence of upper airways and cheeks compliance.

The most important measurement site is the entrance of the endotracheal tube (ETT) where the airway opening pressure ( $P_{ao}$ ) and mouth flow ( $\dot{V}$ ) are accessible through appropriate transducers. Although easily accessible,

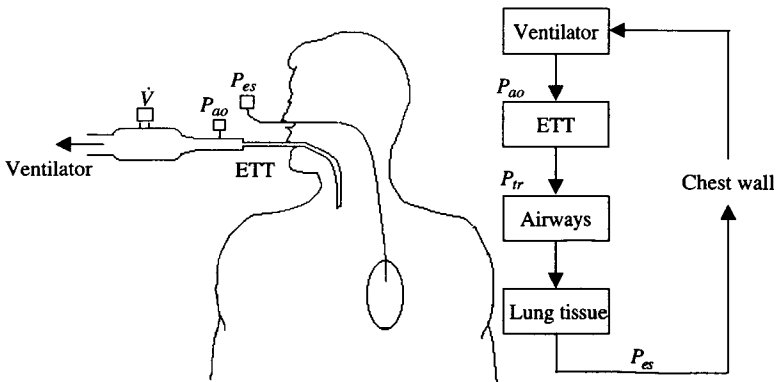


**Figure 10.1.** Schematic depiction of signal measurement sites and the corresponding pressure block diagram in an artificially ventilated patient.



the pressure measured in this way is influenced by the high resistive pressure drop along the ETT and therefore is an overestimation of the true airway pressure (tracheal pressure  $P_{tr}$ ). Different approaches are used to account for this pressure difference: *in vitro* calculations of ETT impedance and subsequent compensation (Peslin *et al.*, 1993) or insertion of a thin catheter equipped with a pressure transducer in the ETT.

$P_{ao}$  (or  $P_{tr}$ ) and  $\dot{V}$  characterise the respiratory system mechanics (including the chest wall) in the passive patient (without respiratory muscles activity). During spontaneous breathing, an estimate of pleural pressure ( $P_{pl}$ ) is needed. In fact, with  $P_{pl}$  equal to the total pressure drop given by the chest wall plus the respiratory muscles, the difference between  $P_{tr}$  and  $P_{pl}$  yields the transpulmonary pressure ( $P_{tp}$ ), which is the driving pressure for lung mechanics alone. Fortunately, oesophageal pressure ( $P_{es}$ ) displays a good agreement with  $P_{pl}$  and can be acquired using the oesophageal balloon with a minimally invasive technique. Even if not necessary for the assessment of respiratory system mechanics in a passive patient,  $P_{es}$  is needed to partition between lung and chest wall characteristics.

### 10.3. FIRST-ORDER MODELS

The simplest and probably the most commonly used model of the respiratory system mechanics is the first-order linear model depicted in Figure 10.2, which is governed by the equation:

$$P_A(t) = P_R(t) + P_E(t) + P_I(t) = R_{rs}\dot{V}(t) + E_{rs}V(t) + L_{rs}\ddot{V}(t) \quad (10.1)$$

where, at any time  $t$ ,  $P_A$  is the total pressure applied, either by the subject or by the ventilator, to inflate the respiratory system. This model is based on

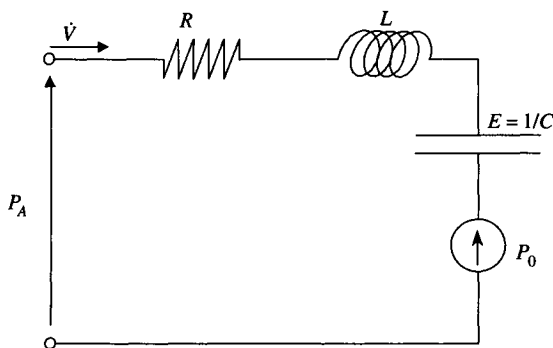


**Figure 10.2.** Electrical analogue of the first-order viscoelastic model of breathing mechanics.

the consideration that the pressure drop across the whole system is the sum of a resistive pressure difference ( $P_R$ ), an elastic pressure difference ( $P_E$ ), and, possibly, an accelerative (inertial) pressure term ( $P_I$ ). Thus, in Figure 10.2, each of these pressure components is linked to a single, lumped parameter of the total respiratory system: respiratory system resistance ( $R_{rs}$ ), elastance ( $E_{rs}$ , or its equivalent inverse, compliance  $C_{rs}$ ), and inertance ( $L_{rs}$ ).

These characteristics can be estimated using Neergard and Wirz technique (von Neergard and Wirz, 1927), elastic subtraction method (Mead and Whittemberger, 1953), or multiple linear regression (Wald *et al.*, 1969) both in time (Uhl *et al.*, 1974) or in the frequency domain (Jackson *et al.*, 1987). Most of the methods commonly used for the assessment of breathing mechanics in mechanically ventilated patients have adopted this model even if it offers an unspecific picture of respiratory system, by lumping together airway and tissue properties, and lacks explanation for the volume and frequency dependence of breathing mechanics.

Inertive forces are considered to have negligible effects in (10.1) within the physiological breathing frequencies (<2.5 Hz). This leads to simplify the first-order model of breathing mechanics:

$$P_A(t) = R_{rs}\dot{V}(t) + E_{rs}V(t) + P_0 \quad (10.2)$$

where  $P_0$  is the pressure value at end expiration, when both flow and volume are zero.

Historically, the first methods for the assessment of respiratory mechanics are based on the assumption of (10.2), which enable to calculate the so-called dynamic-elastance of respiratory system as the ratio between the change in pressure at the instants of zero flow and the corresponding change in volume in the same breath. Using the same hypothesis, the average pulmonary flow resistance can be calculated as the ratio of the change in pressure between two points at identical lung volume and the corresponding change in flow. Depending on the site of  $P_A$  measurement, the estimated parameters represent airway, pulmonary, or chest wall characteristics. For example, by estimating the mean alveolar pressure using the body plethysmography (Dubois *et al.*, 1956a), airway resistance can be calculated as the difference between airway opening pressure and alveolar pressure divided by the air flow.

Although important and still utilised in the clinical practice, these methods have been gradually replaced by the multiple linear regression method, meaning the linear least square fit of (10.2) to pressure and flow data acquired from the subject (volume changes are generally obtained by numerical integration of the flow signal). The fit provided by the model (Figure 10.3) is generally good, especially if the flow signal is quasi-sinusoidal (hence with a poor spectral content) and the subject has normal respiratory mechanics (see Bates, 1998).

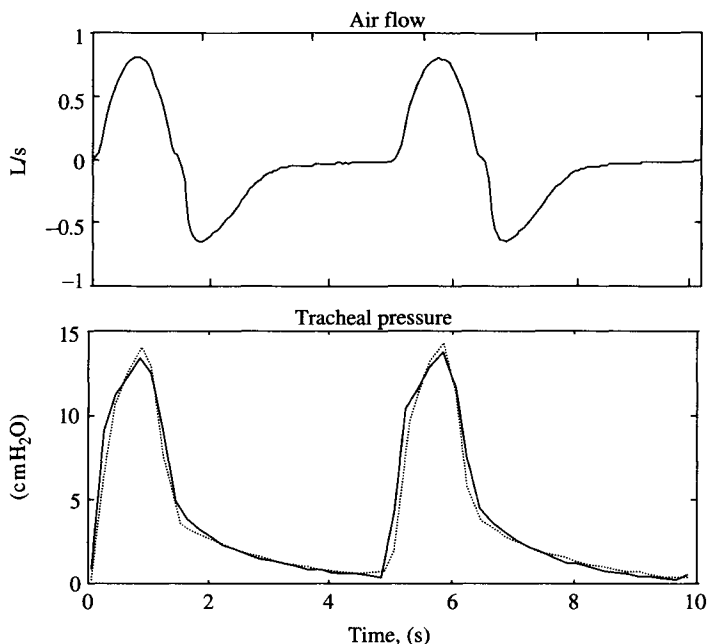


**Figure 10.3.** Fit of the linear first-order model of breathing mechanics (*dotted line*) to data acquired from a mechanically ventilated patient: flow (*upper panel*) and tracheal pressure (*lower panel*).

Least square estimation of the parameters of the first-order model has proved to be successful in tracking the main characteristic of respiratory system in real time (Avanzolini *et al.*, 1990). This argument will be treated extensively in the next section.

However, it is well known that airway resistance, at least for the large airways, has a nonlinear behaviour due to turbulent flow effects, which can be described empirically with the Rohrer equation:

$$R_{aw} = K_1 + K_2|\dot{V}(t)| \quad (10.3)$$

The volume dependence of total elastance is often described by a term directly proportional to changes in lung volume. Thus, (10.2) becomes:

$$P_A(t) = (K_1 + K_2|\dot{V}(t)|)\dot{V}(t) + (K_3 + K_4V(t))V(t) + P_0 \quad (10.4)$$

Equation (10.4) has been applied in different versions to respiratory data from intensive care patients (Peslin *et al.*, 1992; Bersten, 1998) and has shown to provide a better fit than (10.2).

### 10.3.1. ON-LINE MONITORING OF RESPIRATORY MECHANICS

Most of the methods for the assessment of respiratory mechanics are based on static measures following flow interruption or on the frequency/time domain, off-line identification of lumped parameter models (see next sections) of the respiratory system. However, these methods are only suitable for periodic monitoring of patient condition since the flow interruption technique requires an occlusion maneuver that interferes with the ventilator setting, while off-line estimates need the methodologies of batch identification. In this paragraph, emphasis is posed on the continuous monitoring of lung mechanics. This, in fact, enables a prompt detection of changes in patient status as well as monitoring of the progress of the disease and allows the estimation of the time course of the therapeutic response of the patient. Real-time tracking of parameters of lung mechanics is based on the recursive identification of the classic single-compartment linear model from the respiratory data commonly available in the intensive care unit. Continuous measurement of  $P_{ao}$  (or  $P_{tr}$ ) and  $\dot{V}$  is thus needed to characterise the mechanical properties of the respiratory system in the passive patient (if the respiratory muscles are active, assessment of lung mechanics is still possible by measuring  $P_{es}$ ).

### 10.3.2. RECURSIVE ESTIMATION ALGORITHM

The recursive least squares (RLS) algorithm (see Ljung and Soderstrom, 1983, for a detailed presentation of the recursive estimation techniques, with an exponential weighting factor)  $\lambda$  has been used to track changes in the mechanical properties of the respiratory system in real time (Avanzolini *et al.*, 1990; Lauzon *et al.*, 1991). To do so, one can express the measured samples of the airway pressure in discrete time form:

$$P(kT) = \vartheta'(kT) \cdot \varphi(kT) + \varepsilon(kT) \quad (10.5)$$

where  $T$  is the sampling time,  $\vartheta(kT)$  the parameter vector,  $\varphi(kT)$  the data vector and  $\varepsilon(kT)$  the error term representing both noise measurements and model prediction errors. The RLS algorithm provides an updated parameter estimate at each new sampling time as:

$$\hat{\vartheta}(kT) = \hat{\vartheta}((k-1)T) + \Gamma(kT) \cdot \varepsilon_0(kT) \quad (10.6)$$

where the current parameter estimate,  $\hat{\vartheta}(kT)$ , is derived by correcting the previous estimate,  $\hat{\vartheta}((k-1)T)$ , with a term proportional to the *a priori* model prediction error,  $\varepsilon_0(kT)$ , times the gain of the algorithm  $\Gamma(kT)$ . These quantities

are adjusted recursively as:

$$\varepsilon_0(kT) = P(kT) - \hat{\vartheta}((k-1)T) \cdot \varphi(kT). \quad (10.7)$$

$$\Gamma(kT) = \frac{\Pi((k-1)T) \cdot \varphi(kT)}{\lambda + \varphi'(kT) \cdot \Pi((k-1)T) \cdot \varphi(kT)} \quad (10.8)$$

$$\Pi(kT) = \frac{1}{\lambda} \cdot [I - \Gamma(kT) \cdot \varphi'(kT)] \cdot \Pi((k-1)T) \quad (10.9)$$

where  $\Pi(kT)$  is a matrix proportional to the covariance matrix of parameter estimates:

$$\Omega(kT) = Cov[\vartheta(kT)] = \delta(kT) \cdot \Pi(kT) \quad (10.10)$$

with  $\delta(kT)$ , the estimated noise variance, given by:

$$\delta(kT) = \lambda \cdot \delta((k-1)T) + (1-\lambda) \cdot \varepsilon_0^2(kT) \cdot [1 - \varphi'(kT) \cdot \Pi(kT) \cdot \varphi(kT)] \quad (10.11)$$

Parameter  $\lambda$  is the forgetting factor of the algorithm that determines the memory of the estimation procedure, which means the effective length and weight of past data used to fit the model at each time point. In fact, the time constant,  $\tau$ , of the exponential memory of the estimator is given by:

$$\tau = \frac{T}{\ln(\lambda)} \cong \frac{T}{1-\lambda} \quad (10.12)$$

The selection of an appropriate value for  $\lambda$  ( $0 < \lambda \leq 1$ ), or equivalently of  $\tau$  ( $T < \tau \leq \infty$ ), is crucial: a value close to 1 reduces the sensitivity of parameter estimation to noise but produces a less prompt algorithm. Thus a suitable value of the forgetting factor depends in principle on some specific aspect of the study, like levels of noise and/or expected parameter variation rate.

### 10.3.3. ALGORITHM TUNING

A key feature of the RLS algorithm is the incorporation of the exponential weighting of past data, governed by the forgetting factor. Thus, the algorithm tuning reduces to a suitable choice of this important design variable. In Avanzolini *et al.* (1990), the authors take advantage of a simulation approach to overcome the lack of knowledge about noise levels and parameter variation rate. In this way, the time course of the parameters of the simulation model is known and the optimal selection of  $\lambda$  is carried out under different plausible noise levels so as to obtain a good compromise between tracking ability and noise sensitivity. However, this tuning strategy is not optimal if the system has parameter variation rates that are *a priori* unpredictable, as may be the

case in respiratory mechanics. In this case, the approach adopted in Lauzon *et al.* (1991) may give better results. In fact, the authors used a variable forgetting factor, meaning that the  $\lambda$  value changes in response to variations in the goodness of model fit to the experimental data. In this way, they achieved stable estimates when the parameters of the system were constant, while maintaining an alert algorithm when parameters varied.  $\lambda$  was recursively adjusted according to the formula:

$$\lambda(kT) = 1 - [1 - \phi'(kT)\Gamma((k - 1)T)]\epsilon_0^2(kT)/MRSS(k) \quad (10.13)$$

where  $MRSS(k)$  is the exponentially weighted mean of the residual sum of squares that also can be calculated in a recursive fashion.

However, Lauzon and Bates have observed large breath-by-breath parameter fluctuations in model estimates. These deterministic variations are due to higher order and nonlinear behaviour of respiratory mechanics, not explicitly taken into account by the model (see Figure 10.4). Thus the parameters of the model reflect average values of many different components of the respiratory system. Also, the increase in parameter oscillation observed in some pathological states is probably due to undermodelling of the system, namely, the simple model used cannot represent an inhomogeneous lung.

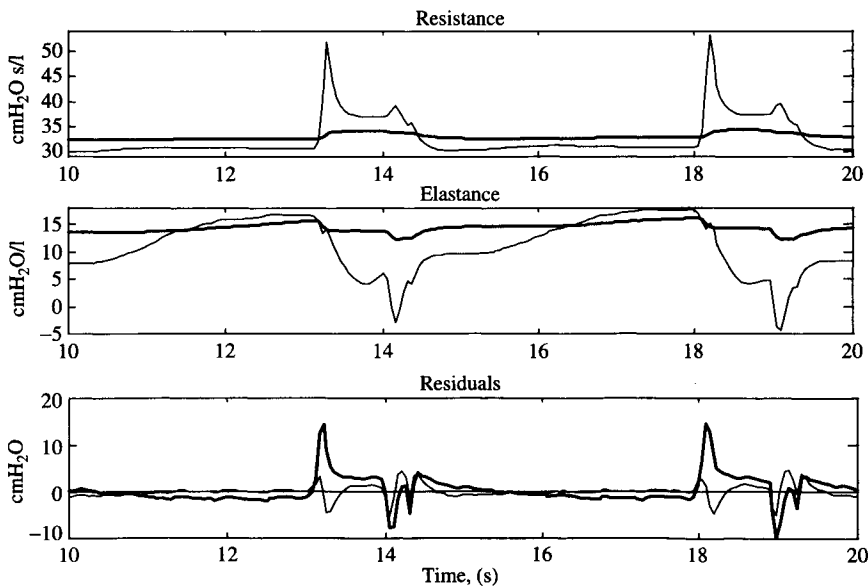


**Figure 10.4.** Time course of estimated resistance and elastance with a memory time constant of 10 s (*thick line*) and 0.5 s (*thin line*). In the lower panel, the corresponding residuals are shown.

Moreover, since the model employed in real-time identification is too simple, the residuals between the measured and the model predicted pressure are highly patterned, and this may lead to biased parameter and confidence interval estimates. There are two different approaches to overcome this limitation. The first is to use a more complex model of breathing mechanics. However, this solution has to face the issue of instability of recursive identification schemes when the new data samples add little information. This is rapidly amplified as the number of parameters, and thus model complexity, increases. The result is an uncontrolled growth of the covariance matrix and hence of the gain of the algorithm that makes the effect of noise on the estimator stability very critical (Kaczka *et al.*, 1995). An alternate approach first proposed in Bates and Lauzon (1992), which is well suited for the RLS tuning when the model used is an oversimplified representation of the real system, is based on the whiteness of the residuals of the fit. These can be easily calculated recursively:

$$r(kT) = P_{ao}(kT) - \vartheta'(kT)\varphi(kT) \quad (10.14)$$

As the time constant of algorithm decreases, the residuals become more uncorrelated while deterministic time variations of parameter estimates become more pronounced (Figure 10.4). Comparative analysis of the residuals time course enables the tuning of the algorithm by selecting the maximum value of  $\lambda$  so as to obtain almost white residuals.

The deterministic variations in the estimates can be usefully summarised by an information-weighted histogram within the respiratory cycle. This strategy was modified to allow cycle-by-cycle comparison (Avanzolini *et al.*, 1995). On-line monitoring of breathing mechanics is possible by recursively updating the histograms on a cycle base at each time a new sample is collected. An alternative and less time-consuming way to provide an easy-to-get and prompt picture of patient status in real time was then proposed (Avanzolini *et al.*, 1997). The mean and the standard deviation of the information histograms are computed and updated at each new sample without constructing the histogram. To do so, a weighting function for each parameter estimate can be defined:

$$w_i(kT) = \frac{\hat{\vartheta}_i(kT)}{\hat{\sigma}_i(kT)} = \frac{\hat{\vartheta}_i(kT)}{\sqrt{\hat{\Omega}_{ii}(kT)}} \quad (10.15)$$

and the mean ( $\hat{\mu}_i(kT)$ ) and parameter variability ( $\hat{\Delta}_i(kT)$ ) in a respiratory cycle can be constructed, relative to a breathing period, using:

$$\hat{\mu}_i(kT) = \frac{\sum_{j=(k-n+1)T}^{kT} \hat{\vartheta}_i(j) \cdot w_i(j)}{\sum_{j=(k-n+1)T}^{kT} w_i(j)} \quad (10.16)$$

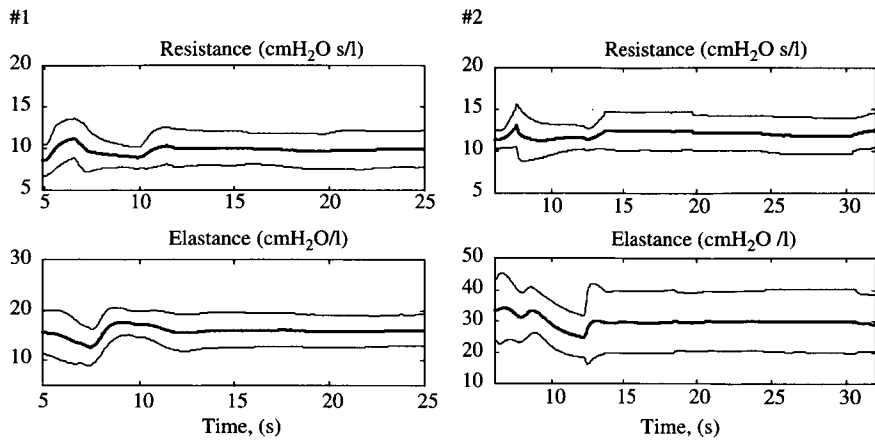


**Figure 10.5.** Time course of resistance (*top panels*) and elastance (*bottom panels*) estimates (*thick lines*) together with  $\pm 1$  SD interval (*thin lines*). Results are from two postoperative patients: #1 has normal respiratory functionality (*left panels*), while #2 has pulmonary oedema (*right panels*).

$$\hat{\Delta}_i(kT) = \sqrt{\frac{\sum_{j=(k-n+1)T}^{kT} [\hat{\mu}_i(kT) - \hat{\nu}_i(j)]^2 \cdot w_i(j)}{\sum_{j=(k-n+1)T}^{kT} w_i(j)}} \tag{10.17}$$

and then recursively updated adopting a “First In-First Out” buffer of length equal to the number of samples in the respiratory cycle. This approach has been successfully adopted in tracking resistive and elastic characteristics in postoperative acute respiratory failure (ARF) patients (Avanzolini *et al.*, 1997; Nucci *et al.*, 1997) and has provided realistic and stable parameter estimates with a reliable quantification of parameter variability during the respiratory cycle (see Figure 10.5).

### 10.4. SECOND-ORDER MODELS

Even if not successful in the real-time estimation context, two-compartment models are able to explain frequency dependence of respiratory mechanics due to gas redistribution (Otis *et al.*, 1956), stress-adaptation of lung tissue (Mount, 1955; Bates *et al.*, 1988a), and effect of the shunt compliance of the airways and of the chest wall (Mead, 1969). Figure 10.6 shows four electric analogues of second-order models of low-frequency breathing mechanics.



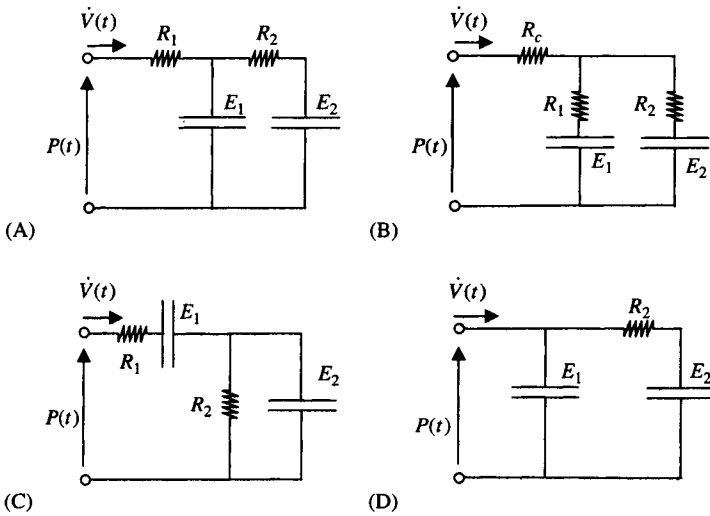


**Figure 10.6.** A, Linear series two-compartment model. B, Linear parallel two-compartment model. C, Linear viscoelastic two-compartment model. D, Simplified version of A used in (Barbini *et al.* 1994).

The model of panel A, known as the Mead model, represents the alveoli as a single-compartment model (series  $R_2$ - $E_2$ ) connected to the airways ( $R_1$ ) via a proximal elastance ( $E_1$ ). The model of panel B, the Otis model, is composed of a parallel arrangement of tissue units ( $E_1$ ,  $E_2$ ), each served by separate airways ( $R_1$ ,  $R_2$ ). This model has been improved by connecting the two resistive pathways to the trachea ( $R_c$ ). In this formulation, the model, even if more realistic, is not structurally identifiable (Avanzolini *et al.*, 1982) and thus it has been generally used with  $R_c$  fixed to zero.

An alternative structure is the model of panel C, which incorporates the viscoelastic properties of the tissue (parallel  $R_2$ - $E_2$ ) in series with airway resistance, plus a Newtonian component of tissue resistance ( $R_1$ ) and the static elastance of respiratory system ( $E_1$ ).

Despite the different arrangements of components, the three models of Figure 10.6(A), (B), and (C) all have the same transfer function. In fact, the equivalent input impedance  $Z(s)$  is given in all cases by:

$$Z(s) = \frac{P(s)}{\dot{V}(s)} = \frac{A}{s} \left[ \frac{1 + as + bs^2}{1 + cs} \right] \quad (10.18)$$

where the values of the coefficients of a, b, and c are given by different combinations of the parameters  $R_1$ ,  $R_2$ ,  $E_1$ , and  $E_2$  (Similowski and Bates, 1991).

Thus, it is not possible to decide which model is more adequate to describe the respiratory system on the basis of the goodness of fit. In normal dogs, with the use of the alveolar capsule technique, it has been shown (Bates *et al.*, 1988b) that the stress recovery of the lung tissue is the main determinant of the frequency dependence of respiratory system impedance. Therefore, the model of Figure 10.6(C) has been, in recent years, the most frequently utilised tool to assess respiratory mechanics, both on the basis of multiple linear regression (Sato *et al.*, 1991; Jonson *et al.*, 1993) and with the flow interrupter technique (see the following section).

Another model recently applied to mechanically ventilated patients is that depicted in Figure 10.6(D) (Barbini *et al.*, 1994); the authors found it an optimal trade-off, both in time and in frequency domain, between model complexity and ability to account for the maximal variance in the data. However, the attempts of identifying complex models of respiratory mechanics using the flow and pressure signals commonly available in the intensive care units is a difficult task because of the poor spectral content of conventional ventilator waveform (Lutchen *et al.*, 1993a). Therefore, to overcome this problem, one must resort to alternative ways of perturbing the system under study. Most of the methods and models developed are based on the forced oscillation technique and to the frequency domain analysis (see Section 10.5). Nevertheless, in clinical practice, the time domain analysis of pressure acquired after an end-inspiratory/expiratory rapid airway occlusion, has gained, increasing popularity in recent years.

### 10.4.1. THE INTERRUPTER TECHNIQUE

The flow interrupter technique, even if introduced at the beginning of the 20th century (von Neergard and Wirz, 1927), has gained much popularity in the past 10 to 15 years, following a series of studies that have elucidated the theoretical aspects of the technique as well as its physiological basis (Bates *et al.*, 1988a, 1988b; Bates and Milic-Emili, 1991).

As shown in Figure 10.7, the method requires a rapid occlusion of the flow circuit, while measuring the pressure behind the occluding valve. The procedure leads to a first rapid change in pressure (from  $P_{\text{peak}}$  to  $P_1$ ) reflecting the ohmic component of flow resistance ( $R_1$ ), some rapidly damped oscillations, and a subsequent slow change (from  $P_1$  to  $P_{\text{plat}}$ ) to an apparent plateau reflecting the stress-relaxation characteristics of lung tissue. This behaviour is usually interpreted by means of the model of Figure 10.6(C), even if the difference  $P_1 - P_{\text{plat}}$  is known to include a significant contribution from parallel inhomogeneities in pathological conditions.

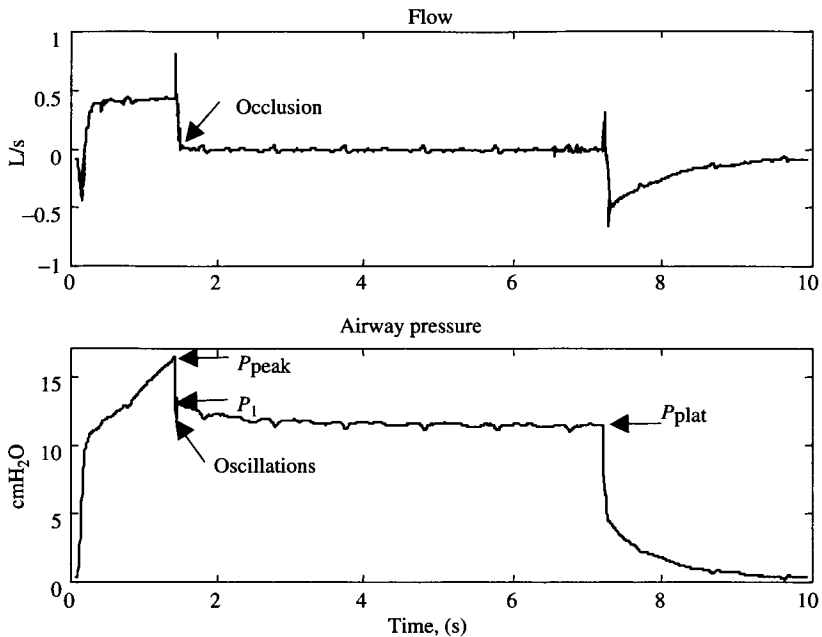


**Figure 10.7.** Tracings of flow and airway opening pressure acquired in a mechanically ventilated patient in whom the end inspiratory occlusion maneuver was performed.

The interrupter technique necessitates a rapidly occluding valve: the speed of the valve is the main determinant of the sharpness, and then of the frequency content, of the resulting broadband pressure signal. A theoretical study (Sly *et al.*, 1988) has shown that this method requires particular attention to the effects of compliance of the upper airways (usually bypassed by the endotracheal tube in mechanically ventilated patients). Thus, the forced oscillation technique probably suffers less limitations and is better suited for the assessment of respiratory mechanics also in nonintubated subjects.

## 10.5. RESPIRATORY OSCILLATION MECHANICS

The forced oscillation technique (FOT) provides a mean for investigating the multicompartamental behaviour of breathing mechanics in the frequency domain (Peslin *et al.*, 1986, Lutchen *et al.*, 1996a). From the first studies involving the use of forced sinusoidal or pseudorandom flow (or pressure) signals (Dubois *et al.*, 1956b, Michaelson *et al.*, 1975), the advance in modelling and signal processing techniques have brought FOT to become, in

the past few years, the reference technique for the assessment of the frequency dependence of resistive and elastic properties of the respiratory system. The main assumption underlying FOT is that the respiratory system behaves linearly. This is usually achieved by using small amplitude input signals and minimising the cross-talk and harmonic distortion with an *ad hoc* selection of frequency components (Suki *et al.*, 1992). The external source used to impose the input to the respiratory system consists of loudspeakers or reciprocating pumps. When the input is applied to the chest wall, the pressure generator is attached to the box including the subject.

The mechanical impedance of the respiratory system is calculated as the complex ratio of the Fourier transform of the pressure and flow signals:

$$Z_{rs}(f) = \frac{P(f)}{\dot{V}(f)} = \text{Real}(Z_{rs}(f)) + j \text{Imag}(Z_{rs}(f)) \quad (10.19)$$

where  $f$  is frequency (Hz). A simple way of characterising the system is to look at the equivalent resistance and elastance of (10.19), which are given by:

$$R_{Eq}(f) = \text{Real}(Z_{rs}(f)); \quad E_{Eq}(f) = -2\pi f \cdot \text{Imag}(Z_{rs}(f)) \quad (10.20)$$

Although still representing the breathing mechanics as an equivalent first-order model, in this case the parameters depend explicitly on frequency. However, to give a specific insight into the physiological and pathological properties of the respiratory system,  $Z_{rs}$  data must to be analysed using a more detailed model than that described by (10.20).

The respiratory system impedance data arise from two different input protocols:

- input forcing at the mouth and measurement of  $Z_{in}(f) = P_{ao}(f) / \dot{V}_{ao}(f)$  (input impedance)
- input forcing at the chest and measurement of  $Z_{tr}(f) = P_{cw}(f) / \dot{V}_{ao}(f)$  (transfer impedance)

Transfer impedance data in humans have been demonstrated to be more reliable than  $Z_{in}$  data for the assessment of respiratory mechanics in the range of 4 to 64 Hz (Lutchen *et al.*, 1992), enabling separation of airway and tissue properties by the means of the six-element model shown in Figure 10.8 and presented first in Dubois *et al.* (1956b).

In fact, the six-element model has a transfer impedance given by:

$$Z_{tr} = Z_{aw} + Z_t + \frac{Z_{aw}Z_t}{Z_g} \quad (10.21)$$

while the input impedance is given by:

$$Z_{in} = Z_{aw} + \frac{Z_gZ_t}{Z_g + Z_t} \quad (10.22)$$

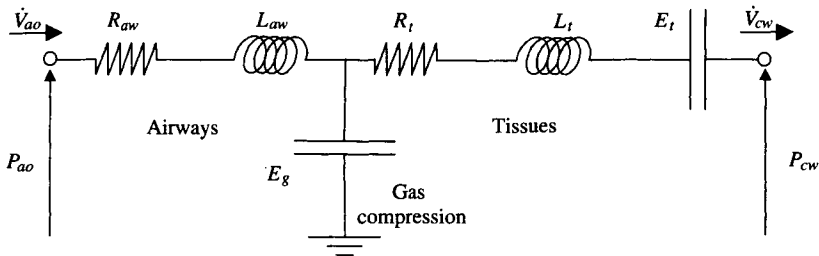


**Figure 10.8.** T-network model representing airway and tissue impedances separated by gas compressibility.

where  $Z_{aw} = R_{aw} + j2\pi f L_{aw}$ ,  $Z_t = R_t + j2\pi f L_t - jE_t/(2\pi f)$  and  $Z_g = -jE_g/(2\pi f)$ . Thus,  $Z_{tr}$  is more influenced by  $Z_g$  than  $Z_{in}$  is, and it is more specific in distinguishing between  $Z_{aw}$  and  $Z_t$ . Moreover, the transfer impedance is less sensitive to upper (extrathoracic) airway shunting.

The  $Z_{tr}$  spectral features and the six-element model estimates have been shown to be highly sensitive to lung disease and have been proposed as a means to clinically evaluate the lung function (Lutchen *et al.*, 1998). However,  $Z_{tr}$  measurements are impractical in mechanically ventilated patients. Furthermore, the tissue estimates are mainly influenced in the usual frequency range of the experiments by the chest wall resistive and elastic properties.

Input impedance determinations are highly informative in two frequency ranges: at high frequencies (>100 Hz) where they reflect airway and airway wall mechanics (Suki *et al.*, 1993; Jackson *et al.*, 1996) and at low frequencies (<2 Hz) where the input impedance reflects the respiratory system mechanics in the normal breathing range.

The importance of partitioning airway and tissue contributions at physiological frequencies is evident. However, when the applied input has significant energy in the range of respiratory efforts, the FOT has to face the problem of interference from the subject or the ventilator. Thus, the low-frequency FOT is frequently used under apnoeic conditions (Navajas *et al.*, 1990; Sly *et al.*, 1996; Petak *et al.*, 1997). When treating mechanically ventilated patients, particular attention must be paid to eliminate the influence of the markedly nonlinear characteristics of the endotracheal tube (Peslin *et al.*, 1993).

In the past few years, the so-called constant-phase model (Figure 10.9) has gained considerable popularity in fitting  $Z_{in}$  impedance data in the low-frequency range (Hantos *et al.*, 1992; Petak *et al.*, 1997) since it has been proved superior to the resistance-capacitance representation (see Figure 10.6 C) of the stress-relaxation characteristics of lung tissue (Suki *et al.*, 1994).

This model provides the means to separate  $Z_{in}$  into airway and tissue components: airway resistance is frequency-independent, while tissue

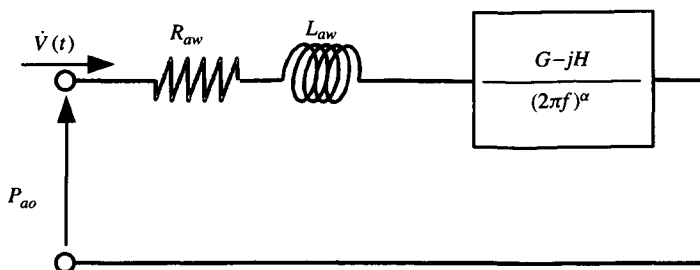


**Figure 10.9.** Model of respiratory system with airways represented by the series Raw-Law and the constant-phase model of tissue impedance.

resistance decreases monotonically to zero as frequency increases ( $R_t = G/[2\pi f]^\alpha$ ). Equivalent elastance ( $E_t = H/[2\pi f]^{\alpha-1}$ ) is slightly increasing with frequency. The frequency dependency of tissue impedance is governed by  $\alpha = (2/\pi) \tan^{-1}(H/G)$ .

Lutchen and coworkers (1993b) have solved the problem of providing ventilation to patients maintaining a rich spectral waveform that enables to assess reliably low-frequency impedance. This signal, called *optimal ventilator waveforms* (OVW), was designed to minimise the effect of distortion, due to nonlinearities, still providing sufficient energy at the desired frequencies. The application of the OVW concept was successful in estimating low-frequency respiratory mechanics by means of the constant-phase model, providing a clinically acceptable flow waveform (Lutchen *et al.*, 1994). The model was subsequently modified to account for airway wall shunting during substantial induced bronchoconstriction (Kaczka *et al.*, 1997) and to analyse the effects of airway inhomogeneities and tissue nonlinearities (Suki *et al.*, 1997). This latter work, with the use of combined time and frequency domain estimation techniques, seems more promising in explaining the effects of different lung pathologies on the apparent increase in tissue nonlinearities.

## 10.6. SIMULATION MODELS OF BREATHING MECHANICS

The use of simulation models has found extensive application in the interpretation of breathing mechanics (Fredberg *et al.*, 1978; Lutchen *et al.*, 1990; Bates, 1993; Schuessler *et al.*, 1997; Hickling, 1998). The most complex simulation models of breathing mechanics are probably the anatomically consistent models based on the morphometric measures of Horsfield and coworkers (1971, 1982). These analytic descriptions of the length and path of each airway

generation, from the trachea to the alveolar ducts, can be interpreted mathematically using the laws of propagation of sound waves (Benade, 1968). In this section, we review the frequency domain analysis of respiratory system impedance based on the Horsfield model.

### 10.6.1. THE HORSFIELD MODEL

The morphometric airway models, developed in the works of Horsfield and colleagues, are based on data obtained from measurement of resin casts of the bronchial tree (Figure 10.10 A). The physical arrangement of the airway network is that of a dichotomous branching tree which has the trachea as the trunk and leads through bronchi and bronchioles into the acinar airways, respiratory bronchioles and alveolar ducts, ending into the alveolar sacs. The branches were ordered considering the airways as confluent tubes by beginning from the periphery. Measures of diameters were taken at the midpoint of a branch between two bifurcation; lengths were measured from the bases of two consecutive branches. The models developed from these data are based on the simplifying assumption that the difference between two daughter branches is the same for all parent branches of a given order. For this purpose, for each order, diameters lengths and degree of asymmetry were averaged. The airway tree is classified by a dichotomously dividing system: each order has a specific length, diameter, and recursion index  $\Delta$ . For order  $k$ ,  $\Delta(k)$  identifies the order of the two descending daughters at each bifurcation (Figure 10.10 B)

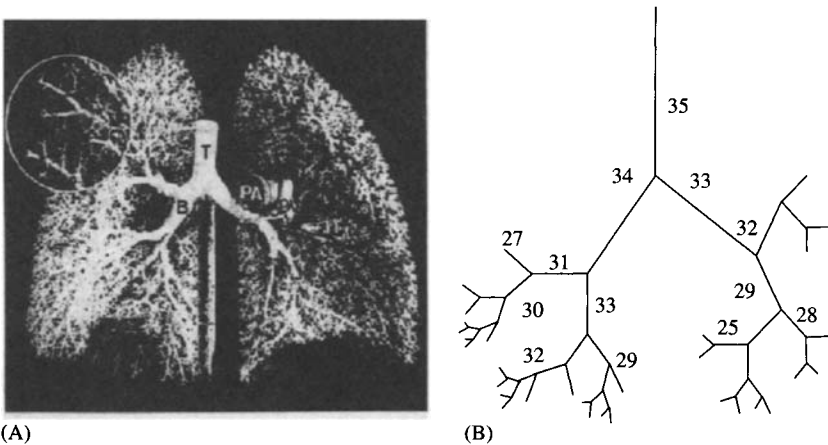


**Figure 10.10.** A, Resin cast of a human lung, showing the branching pattern of the bronchial tree. B, Patterns of asymmetrical airway branching for the last generations of Horsfield's model.

by following the relation: order of the left daughter =  $k - 1$ ; order of the right daughter =  $k - 1 - \Delta(k)$ .

**10.6.2. A MATHEMATICAL MODEL OF THE HUMAN AIRWAYS**

Considering each airway as a rigid tube, it is possible to model a single structure of Horsfield’s bronchial tree with the laws of propagation of sound waves in a cylindrical pipe (Benade, 1968), by using a lumped parameter description and the simplifications for the low frequencies (<10 Hz) reported in Thorpe (1997). Thus, each segment of the airway tree can be arranged as the acoustic transmission line represented in Figure 10.11, in which:

$$R(k) = 8 \frac{\eta \cdot l(k)}{\pi \cdot r^4(k)} \tag{10.23}$$

$$L(k) = \rho \frac{l(k)}{\pi \cdot r^2(k)} \tag{10.24}$$

$$C_g(k) = \frac{V(k)}{P_0} = \frac{\pi \cdot r^2(k) \cdot l(k)}{P_0} \tag{10.25}$$

where  $r(k)$  is the tube radius,  $l(k)$  the tube length,  $\eta$  is gas viscosity and  $\rho$  is gas density.  $V(k)$  is the airway segment volume at the fixing pressure  $P_0$ . Thus,  $R(k)$  and  $L(k)$  characterise the resistance and inertance of the rigid tube while  $C_g(k)$  is gas compressibility.

To incorporate in the airway model more anatomical details, one can include the influence of the wall mechanics as done, for example, in Lutchen *et al.* (1996b). To do so, both the soft and cartilaginous airway walls can be idealised as a series of resistance-inertance-compliance, in parallel with the gas compressibility. Being the soft-tissue fraction for each airway segment

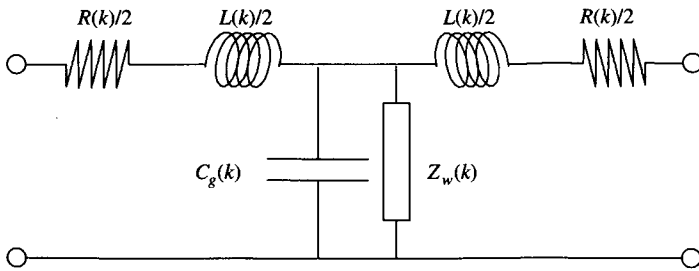


**Figure 10.11.** The acoustic transmission line model for the nonrigid airway segment of order  $k$ . The influence of the wall mechanics is taken into account by the equivalent impedance  $Z_w$ .



( $so[k]$ ) equal to one minus the cartilaginous fraction ( $ca[k]$ ) we have:

$$Z_w^i(k) = R_w^i(k) + j \cdot \left( \omega L_w^i(k) - \frac{1}{\omega \cdot C_w^i(k)} \right), \quad i = so, ca \quad (10.26)$$

where  $\omega$  the angular frequency (radians/s) and the values for  $R_w$ ,  $L_w$ , and  $C_w$  can be computed, according to Suki *et al.* (1993). Thus, the equivalent wall impedance given by the weighted combination of the soft and cartilaginous impedance is:

$$Z_w(k) = \frac{Z_w^{so}(k) \cdot Z_w^{ca}(k)}{c(k) \cdot Z_w^{so}(k) + (1 - c(k)) \cdot Z_w^{ca}(k)} \quad (10.27)$$

The peripheral airways, which are small airways of less than 2 mm in diameter, are well recognised as the main sites of airway narrowing and obstruction in asthma and other obstructive diseases. This pathological conditions can be described mathematically in Horsfield's model by reducing, of a certain percentage  $\alpha$ , the radius of the airway segments. Equations (10.23) to (10.27) are consequently modified, substituting the narrowed radius for  $r(k)$ . This enables the impact of airway constriction on the overall response of respiratory system to be assessed.

### 10.6.3. MATHEMATICAL MODELS OF THE ALVEOLAR COMPARTMENTS

There are essentially three models used as alveolar tissue elements of Horsfield's structure: the simple first-order model as adopted in Jackson *et al.* (1987), Habib *et al.* (1994) (Figure 10.2); the constant phase model (Figure 10.9) used in Lutchen *et al.* (1996b, 1997); and the linear viscoelastic model applied in Lutchen *et al.* (1990, 1993b) (Figure 10.6 C). Each model is considered in parallel with the alveolar gas compressibility,  $C_g$ . Dealing with the frequencies in the range of breathing rates, the stress-adaptation phenomenon, not taken into account by the first-order model, is the major determinant for the frequency dependent drop in the real part of respiratory system impedance, at least in normal subjects. Thus, the first-order model can only be used as terminal element of the most peripheral airway segments for analysing the lung impedance at relatively high frequency (>16 Hz).

### 10.6.4. EQUIVALENT INPUT IMPEDANCE OF THE HORSFIELD MODEL

Once all the airways and tissues parameters have been specified, the respiratory system input impedance can be computed, in the frequency domain,

in a recursive fashion by applying the combinations of series and parallel in Horsfield’s model. By posing  $Z_{Eq}(0)$  as the alveolar impedance, the equivalent impedance of the  $k$ -th generation can be calculated from:

$$\begin{aligned}
 Z_{Eq}(k) = & \frac{R(k) + j\omega L(k)}{2} \\
 & + \frac{1}{\left(j\omega C(k) + \frac{1}{Z_w^{Eq}(k)}\right) + \frac{R(k) + j\omega L(k)}{2} + \frac{1}{\frac{1}{Z_{Eq}(k-1)} + \frac{1}{\left(Z_{Eq}(k-1) - \Delta(k)\right)}}}
 \end{aligned}
 \tag{10.28}$$

In fact, for homogeneous conditions (both in control and during bronchoconstriction) the model is self-consistent, which means  $Z_{Eq}(k)$  is identical regardless of where it occurs in the branching pattern. In case of lumped inhomogeneities, as when a particular topological fraction of airways is uniformly constricted, the input impedance ( $Z_{Eq}$ [35]) can be calculated once more by invoking the self-similarity on the networks and by combining the impedance of each branch. However, when airway constriction heterogeneity and/or the morphometrical arrangement are obtained with a stochastic description of diameter distribution, as in Thorpe *et al.* (1997) and Lutchen *et al.* (1997), the complete branching tree must be crossed for impedance calculation. This requires an exponential increase in the computational cost for obtaining a numerical solution.

Figure 10.12 shows the results obtained in terms of equivalent model resistance ( $R_{Eq}$ ) and elastance ( $E_{Eq}$ ), calculated according to (10.20), with different constriction patterns and the same alveolar parameters. The normal case shows a frequency-dependent drop in  $R_{Eq}$  due to the stress adaptation of the alveolar compartments, followed by a constant plateau;  $E_{Eq}$  has an initial frequency-dependent increase and then a decrease due to the inertive effects. With a homogeneous airway constriction, we have a considerable increase in  $R_{Eq}$  spectrum, while  $E_{Eq}$  has a significant increase and a positive frequency dependence, only for elevated constriction levels (>40%): this is due to airway wall shunting when an high resistive path leads to the alveoli. The nonhomogeneous constriction has a remarkable impact both on the maximum value and on the frequency-dependent decrease of  $R_{Eq}$ . This amplifying effect of inhomogeneities is even more marked on the  $E_{Eq}$  spectrum that results nearly doubled, even at low frequencies.

In conclusion, the frequency domain analysis of the input impedance of Horsfield’s morphometric model, enables the effect of changes in the value and distribution of lung physical properties on the global response of the

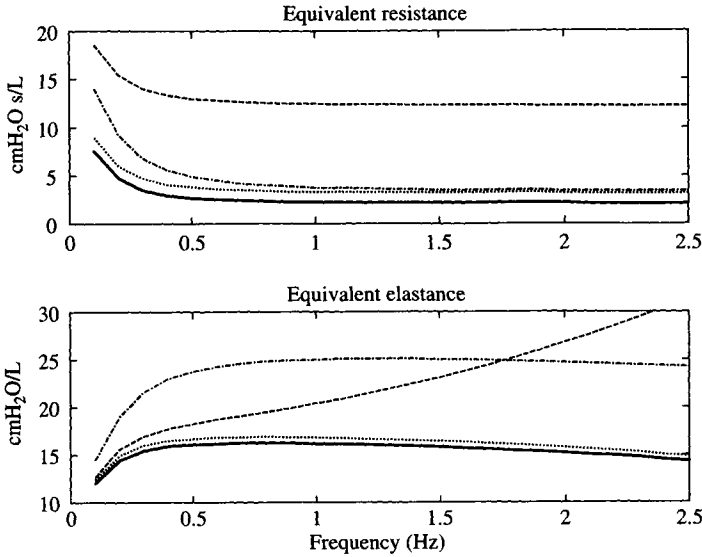


**Figure 10.12.** Comparison of the frequency behaviour of lung resistance and elastance as predicted from the Horsfield simulation model in the normal situation (*solid line*), a 20% homogeneous constriction (*dotted line*), a 50% homogeneous constriction (*dashed line*) and a nonhomogeneous constriction obtained with a uniform 60% reduction in the diameter of the 40% of peripheral airways (*dash-dot line*).

respiratory system to be assessed. In particular, it makes it possible to appreciate the different spectral features of homogeneous vs. inhomogeneous airway constrictions and the effect of airway wall shunting.

### 10.7. CONCLUSIONS

A review of the most used techniques for the simulation and quantification of lung mechanics has been presented. Particular attention was focused on the assessment and the modelling aspects and the nature of the applied input that are always strictly linked. With broad-band inputs, as the case of the interrupter technique or the FOT, it is possible to identify detailed lumped parameter models that can give specific measures of airway vs. tissue accounting for heterogeneous pathologies. However, when dealing with the need of continuous monitoring of respiratory mechanics in ventilator-dependent patients, one is forced to use simpler models, such as the first-order one, which can be easily implemented in a recursive fashion to track changes of parameters in time. The optimal ventilator waveform (OVW) approach, and especially its enhanced version (Kaczka *et al.*, 1999), have much to offer in this field, by

providing means for ventilating the patient while allowing the identification of detailed models.

In the last section of this chapter, we have presented an anatomically consistent simulation model of lung mechanics that has been frequently advocated to explain various aspects of constrictive pathologies and has provided useful information for the description, prediction, and explanation of the mechanical behaviour of the respiratory system.

## 10.8. ACKNOWLEDGEMENT

This work was supported in part by a grant from the Italian Ministry of Scientific and Technological Research. The authors thank Dr. Kenneth Lutchen for having provided us with the computer code for the frequency domain analysis of the Horsfield model.

## 10.9. REFERENCES

- Avanzolini, G. and G. Barbini. Comments on "Estimating respiratory mechanical parameters in parallel compartment models." *IEEE Trans Biomed Eng* 29(1982):772–74.
- Avanzolini G., P. Barbini, A. Cappello and G. Cevenini. Real-time tracking of parameters of lung mechanics: emphasis on algorithm tuning. *J Biomed Eng* 12(1990):489–95.
- Avanzolini, G., P. Barbini, A. Cappello and G. Cevenini. Influence of flow pattern on parameter estimates of a simple breathing mechanics model. *IEEE Trans Biomed Eng* 42(1995):313–17.
- Avanzolini, G., P. Barbini, A. Cappello and G. Cevenini. A new approach for tracking respiratory mechanical parameters in real-time. *Ann Biomed Eng* 25(1997):154–63.
- Barbini, P., G. Cevenini, K. R. Lutchen and M. Ursino, Estimating respiratory mechanical parameters of ventilated patients: a critical study in the routine intensive-care unit. *Med Biol Eng Comput* 32(1994):153–60.
- Bates, J. H. T., P. Baconnier and J. Milic-Emili. A theoretical analysis of interrupter technique for measuring respiratory mechanics. *J Appl Physiol* 64(1988a):2204–14.
- Bates, J. H. T., M. S. Ludwig, P. D. Sly, K. Brown, J. G. Martin and J. J. Fredberg. Interrupter resistance elucidated by alveolar pressure measurement in open-chest normal dog. *J Appl Physiol* 65(1988b):408–14.
- Bates, J. H. T. and J. Milic-Emili. The flow interruption technique for measuring respiratory resistance. *J Crit Care* 6(1991):227–38.
- Bates, J. H. T. and A. M. Lauzon. A nonstatistical approach to estimating confidence intervals about model parameters: application to respiratory mechanics. *IEEE Trans Biomed Eng* 39(1992):94–100.
- Bates, J. H. T. Stochastic model of the pulmonary airway tree and its implication for bronchial responsiveness. *J Appl Physiol* 75(1993):2493–99.
- Bates, J. H. T. Assessment of mechanics. In: *Physiological Basis of Ventilatory Support*. Edited by J. J. Marini and A. S. Slutsky. New York: Marcel Dekker.
- Benade, A. H. On the propagation of sound waves in a cylindrical conduit. *J Acoust Soc Am* 26(1968):726–31.
- Bersten, A. D. Measurement of overinflation by multiple linear regression analysis in patients with acute lung injury. *Eur Respir J* 12(1998):526–32.
- DuBois, A. B., S. Y. Bothelho and J. H. Comroe. A new method for measuring airway resistance in man using a body plethysmograph: values in normal subjects and in patients with respiratory disease. *J Clin Invest* 35(1956a):322–26.

- Dubois, A. B., A. W. Brody, D. H. Lewis and B. F. Burgess. Oscillation mechanics of lung and chest wall. *J Appl Physiol* 81(1956b):587–94.
- Fredberg, J. J. and A. Hoenig. Mechanical response of the lungs at high frequencies. *J Biomech Eng* 100(1978):57–66.
- Habib, R. H., R. B. Chalker, B. Suki and A. C. Jackson. Airway geometry and wall mechanical properties estimated from subglottal input impedance in humans. *J Appl Physiol* 77(1994):441–51.
- Hantos, Z., B. Daroczy, B. Suki, S. Nagy and J. J. Fredberg. Input impedance and peripheral inhomogeneity of dog lungs. *J Appl Physiol* 72(1992):168–78.
- Hickling, K. G. The pressure-volume curve is greatly modified by recruitment. A mathematical model of ARDS lung. *Am J Respir Crit Care Med* 158(1998):194–202.
- Horsfield, K., G. Dart, D. E. Olson, G. F. Filley and G. Cumming. Models of the human bronchial tree. *J Appl Physiol* 31(1971):207–17.
- Horsfield, K., W. Kemp and S. Phillips. An asymmetrical model of the airway of the dog lung. *J Appl Physiol* 52(1982):21–26.
- Jackson, A. C. and K. R. Lutchen. Modeling of respiratory system impedances in dogs. *J Appl Physiol* 62(1987):414–20.
- Jackson, A. C., K. R. Lutchen and H. L. Dorkin. Inverse modeling of dog airway and respiratory system impedances. *J Appl Physiol* 62(1987):2273–82.
- Jackson, A. C., K. N. Neff, K. R. Lutchen and H. R. Dorkin. Interpretation of respiratory system impedances (4–256 Hz) in healthy infants. *Pediatr Pulmonol* 226(1996):364–75.
- Jonson, B., L. Beydon, K. Brauer, C. Mansson, S. Valind and H. Grytzell. Mechanics of the respiratory system in healthy anesthetized humans with emphasis on viscoelastic properties. *J Appl Physiol* 75(1993):132–40.
- Kaczka, D. W., G. M. Barnas, B. Suki and K. R. Lutchen. Assessment of time-domain analyses for estimation of low-frequency respiratory mechanical properties and impedance spectra. *Ann Biomed Eng* 23(1995):135–51.
- Kaczka, D. W., E. P. Ingenito, B. Suki and K. R. Lutchen. Partitioning airway and lung tissue resistances in humans: effects of bronchoconstriction. *J Appl Physiol* 82(1997):1531–41.
- Kaczka, D. W., E. P. Ingenito and K. R. Lutchen. Technique to determine inspiratory impedance during mechanical ventilation: implications for flow limited patients. *Ann Biomed Eng* 27(1999):340–55.
- Lauzon, A. M., G. S. Dechman and J. H. T. Bates. Time course of respiratory mechanics during histamine challenge in dogs. *J Appl Physiol* 73(1992):2643–47.
- Ljung, L. and T. Soderstrom. *Theory and Practice of Recursive Identification* Cambridge, MA: MIT Press, 1983.
- Loring, S. H. 1998. Mechanics of the lung and chest wall. In: *Physiological Basis of Ventilatory Support*. Edited by J. J. Marini and A. S. Slutsky. New York: Marcel Dekker.
- Lutchen, K. R., K. D. Costa. Physiological interpretations based on lumped element models fit to respiratory impedance data: use of forward-inverse modeling. *IEEE Trans Biomed Eng* 37(1990):1076–85.
- Lutchen, K. R. and A. C. Jackson. Confidence bounds on respiratory mechanical properties estimated from transfer versus input impedance in humans versus dogs. *IEEE Trans Biomed Eng* 39(1992):644–51.
- Lutchen, K. R., D. W. Kaczka, B. Suki, G. M. Barnas, P. Barbini and G. Cevenini. Low frequency respiratory mechanics using ventilator-driven oscillations. *J Appl Physiol* 75(16)(1993):2549–60.
- Lutchen, K. R., K. Yang, D. W. Kaczka and B. Suki. Optimal ventilation waveform for estimating low-frequency respiratory impedance. *J Appl Physiol* 75(1993):478–88.

- Lutchen, K. R., B. Suki, D. W. Kaczka, O. Zhang, Z. Hantos, B. Daroczy and F. Petak. Direct use of mechanical ventilation to measure respiratory mechanics associated with physiological breathing. *Eur Respir Rev* 18(1994):198–202.
- Lutchen, K. R. and B. Suki. 1996. Understanding pulmonary mechanics using the forced oscillation technique. Emphasis on breathing frequencies. In: *Bioengineering Approaches to Pulmonary Physiology and Medicine*. Edited by Khoo M. New York: Plenum.
- Lutchen, K. R., J. L. Greenstein and B. Suki. How inhomogeneities and airway wall affect frequency dependence and separation of airway and tissue properties. *J Appl Physiol* 80(1996): 1696–707.
- Lutchen, K. R. and H. Gillis. Relationship between heterogeneous changes in airway morphometry and lung resistance and elastance. *J Appl Physiol* 83(1997):1192–1201.
- Lutchen, K. R., A. Sullivan, F. T. Arbogast, B. R. Celli and A. C. Jackson. Use of transfer impedance measurement for clinical assessment of lung mechanics. *Am J Respir Crit Care Med* 157(1998):435–46.
- Mount, L. E. The ventilator flow-resistance and compliance of rat lungs. *J Physiol (Lond)* 127(1995):157–67.
- Mead, J. and J. L. Whittemberger. Physical properties of human lungs measured during spontaneous respiration. *J Appl Physiol* 5(1953):779–96.
- Mead, J. Contribution of compliance of airways to frequency dependent behavior of lungs. *J Appl Physiol* 26:(1969)670–73.
- Michaelson, E. D., E. D. Grassman and W. R. Peters. Pulmonary mechanics by spectral analysis of forced random noise. *J Clin Invest* 56(1975):1210–30.
- Navajas, D., R. Farre, J. Canet, M. Rotger and J. Sanchis. Respiratory input impedance in anesthetized paralyzed patients. *J Appl Physiol* 69(1990):1372–79.
- Nucci, G., G. Polese, A. Rossi and C. Cobelli. On-line estimation of respiratory parameters of lung mechanics in different pathologies. *Proc 19th Annu IEEE-EMBS Conf* Chicago, IL, 1997, 2058–60.
- Otis, A. B., C. B. McKerrow, R. A. Bartlett, J. Mead, M. B. McLroy, N. J. Selverstone and E. P. Radford. Mechanical factors in the distribution of pulmonary ventilation. *J Appl Physiol* 8(1956):427–44.
- Peslin, R., J. J. Fredberg 1986. Oscillation mechanics of the respiratory system. In: *Handbook of Physiology. Mechanics of Breathing*. Edited by P. T. Macklem, J. Mead. Bethesda, MD: American Physiological Society.
- Peslin, R., F. J. de Silva, F. Chabot and C. Duvivier. Respiratory mechanics by multiple linear regression analysis in unsedated ventilated patients. *Eur Respir J* 5(1992):871–78.
- Peslin, R., J. da Felicio J. Silva, C. Duvivier and F. Chabot. Respiratory mechanics by forced oscillation during artificial ventilation. *Eur Respir J* 6(1993):772–84.
- Petak, F., M. J. Hayden, Z. Hantos and P. D. Sly. Volume dependence of respiratory impedance in infants. *Am J Respir Crit Care Med* 156(1997):1172–77.
- Similowski, T. and J. H. T. Bates. Two-compartment modeling of respiratory system mechanics at low frequencies: gas redistribution or tissue rheology? *Eur Respir J* 4(1991):353–58.
- Sly, P. D. and J. H. T. Bates. Computer analysis of physical factors affecting the use of the interrupter technique in infants. *Pediatr Pulmonol* 4(1988):219–24.
- Sly, P. D., M. J. Hayden, F. Petak and Z. Hantos. Measurement of low-frequency respiratory impedance in infants. *Am J Respir Crit Care Med* 154(1996):161–66.
- Sato, J., B. L. K. Davey, F. Shardonofsky and J. H. T. Bates. Low-frequency respiratory resistance in the normal dog during mechanical ventilation. *J Appl Physiol* 71(1991):2425–33.
- Schuessler, T. F., S. B. Gottfried and J. H. T. Bates. A model of the spontaneous breathing patient: applications to intrinsic PEEP and work of breathing. *J Appl Physiol* 82(1997):1694–703.

- Suki, B. and K. R. Lutchen. Pseudorandom signals to estimate apparent transfer and coherence functions of nonlinear systems: applications to respiratory mechanics. *IEEE Trans Biomed Eng* 39(1992):1142–51.
- Suki, B., R. H. Habib and A. C. Jackson. Wave propagation, input impedance, and wall mechanics of the calf trachea from 16 to 1600 Hz. *J Appl Physiol* 75(1993):2755–66.
- Suki, B., A. L. Barbasi and K. L. Lutchen. Lung tissue viscoelasticity: a mathematical framework and its molecular basis. *J Appl Physiol* 76(1994):2749–59.
- Suki, B., H. Yuan, Q. Zhang and K. R. Lutchen. Partitioning of lung tissue response and inhomogeneous airway constriction at the airway opening. *J Appl Physiol* 82(1997):1349–59.
- Thorpe, C. W. and J. H. T. Bates. Effect of stochastic heterogeneity on lung impedance during acute bronchoconstriction: a model analysis. *J Appl Physiol* 82(1997):1616–25.
- Uhl, R. and J. F. Lewis. Digital computer calculations of human pulmonary mechanics using a least square fit technique. *Comput Biomed Res* 7(1974):489–95.
- Von Neergard, K. and K. Wirz. Über eine methode zur messung der lungenelastizität am lebenden menschen, insbesondere beim emphysem. *Z Klin Med* 105(1927):35–50.
- Wald, A., D. Jason, T. W. Murphy and V. D. B. Mazzia. A computer system for respiratory parameters. *Comput Biomed Res* 2(1969):411–29.

# Insulin Modelling

Gianna Maria Toffolo and Claudio Cobelli

## 11.1. INTRODUCTION

Insulin is the primary regulator of glucose homeostasis. It is secreted by pancreatic  $\beta$ -cells into the portal vein in response to a rise in glucose concentration. Before reaching the systemic circulation, it passes through the liver, where a consistent fraction, approximately 50%, is degraded. The residual insulin reaches the target organ or tissues, such as liver, muscle, and adipose tissue, where it exerts its hypoglycaemic action — it promotes glucose uptake and inhibits hepatic glucose production — before being eliminated by the liver and by other organs, such as the kidney. Insulin action depends on insulin concentration in proximity of the insulin-sensitive cells. This is the result of three processes: pancreatic secretion, hepatic extraction, and insulin kinetics (Figure 11.1).

Unfortunately, a quantitative description of these processes in an individual cannot be easily accomplished since insulin processes are not directly measurable unless very invasive and complex experimental protocols are performed. Therefore, indirect measurement approaches based on mathematical models become essential to infer from the accessible variables, usually plasma insulin and glucose concentration, on the nonaccessible fluxes and parameters of interest.

In this chapter, a number of models are reviewed among the various types proposed in the literature (linear and nonlinear, lumped and distributed parameters) to describe the insulin system at different levels (single cell, population of cells, single organ or tissue, whole body) with different purposes, such as qualitative and quantitative description, understanding, simulation, and estimation of relevant fluxes or parameters.



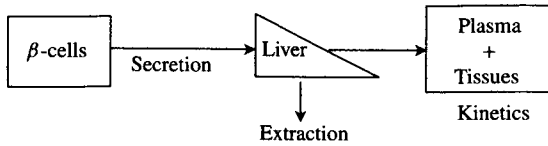


**Figure 11.1.** The insulin system: secretion, hepatic extraction, and kinetics.

The noncompartmental model and some simple linear and nonlinear compartmental models that allow the assessment of insulin kinetics at whole body level are discussed first. This is followed by the presentation of a comprehensive model of insulin secretion, based on secretion data obtained in perfused rat pancreas. This model, a landmark, is a crucial contribution to the intimate understanding of  $\beta$ -cell function in response to a glucose stimulus, but, due to its complexity, it has been essentially used for simulation purposes. Input-output (I/O) modelling and deconvolution are then introduced to estimate insulin secretion profile in an individual during a perturbation. Then, the so-called minimal model approach, of minimal complexity, is presented as an alternative to the deconvolution approach since, in addition to the insulin secretion profile, it provides quantitative indices of the control of glucose on insulin secretion. Finally, the use of deconvolution and the minimal model approach to assess hepatic insulin extraction are discussed.

## 11.2. MODELS OF WHOLE-BODY INSULIN KINETICS

Insulin kinetic studies require an exogenous input to generate dynamic data. The input can be an insulin tracer, usually insulin labelled with a radioactive isotope of iodine or hydrogen, or cold insulin. The advantage generally offered by the use of a tracer is that it can be administered in negligible amounts so that the endogenous steady state is not perturbed by the experiment, thus allowing the use of linear time-invariant models, such as the noncompartmental model or linear compartmental models, to interpret the data. With iodinsulin of high specific activity the negligible perturbation condition is well approximated, but one of the ideal tracer prerequisites, tracer-tracee indistinguishability, is only partially met due to nonnegligible isotopic effects. With tritiated insulin, isotopic effects are less critical, but the administered dose is usually nonnegligible due to the lower specific activity of this tracer.

The use of cold insulin as test input is a valid alternative to tracer insulin, at least in the physiological concentration range (up to 100–150  $\mu$ U/ml) where insulin kinetics are approximately linear so that linear methods can be used to interpret the data. However, the administration of a nontrace amount of insulin has two undesired effects: first, it induces hypoglycaemia, which in turn

triggers the counterregulatory response that may affect insulin kinetics; second, it inhibits insulin secretion, thus the measured insulin concentration contains a time-varying endogenous component. These confounding effects can be avoided by designing a rather complex experiment, where hypoglycaemia is prevented by a variable glucose infusion (glucose clamp technique) and endogenous insulin secretion is suppressed by a somatostatin infusion.

In experimental situations where insulin kinetics are no more linear, such as in the supraphysiological concentration range, nonlinear or linear time-varying compartmental models are required to interpret the data. An additional drawback of cold insulin is that its levels in plasma are usually measured with lower precision than tracer levels, resulting in less precise estimates of kinetic parameters.

### 11.2.1. THE NONCOMPARTMENTAL MODEL

The noncompartmental model (Rescigno and Gurpide, 1973) shown in Figure 11.2 is a candidate for studying insulin kinetics when its underlying assumptions, linear kinetics, and endogenous steady state are well approximated. The test input is usually a bolus injection of tracer or cold insulin, and the measured time course of tracer or cold insulin concentration is described by a sum of exponential functions, with a number of exponentials ranging from 1 to 3 (Ferrannini and Cobelli, 1987a). The noncompartmental formulae are then applied to estimate accessible pool parameters, such as distribution volume, mass, rate of appearance and disappearance, clearance rate, and

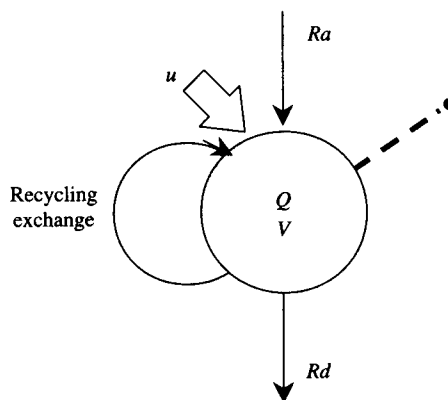


**Figure 11.2.** The noncompartmental model.  $Q$  and  $V$  are the mass and distribution volume of the accessible pool;  $R_a$  and  $R_d$  are rate of appearance and disappearance into the accessible pool;  $u$  is the test input; the dashed line with the bullet denotes the measurement.

**Table 11.1.**

**Noncompartmental Parameters of Insulin Kinetics for the Model of Figure 11.2.**

$V$ (ml/kg)	$Q$ (pmol/kg)	$PCR$ (ml/min/kg)	$Ra = Rd$ (pmol/min kg)	$V_{tot}$ (ml/kg)	$Q_{tot}$ (pmol/kg)	$MRT^{NC}$ (min)
56	2.5	15.6	0.7	107	4.8	6.9

$CR$  = clearance rate;  $V_{tot}$ ,  $Q_{tot}$  = total distribution volume and mass in the system;  $MRT^{NC}$  = mean residence time in the system.

system parameters, like total volume of distribution, total mass, and mean residence time in the system. Values obtained in normal subjects (Cobelli and Caumo, 1990) by describing insulin concentration data with a sum of two decaying exponentials are shown in Table 11.1.

### 11.2.2. LINEAR COMPARTMENTAL MODELS

Various linear compartmental models (see Ferrannini and Cobelli, 1987a) have been proposed to describe insulin kinetics, with the number of compartments ranging from 1 to 4. Two of them are shown in Figure 11.3(A) and (B)

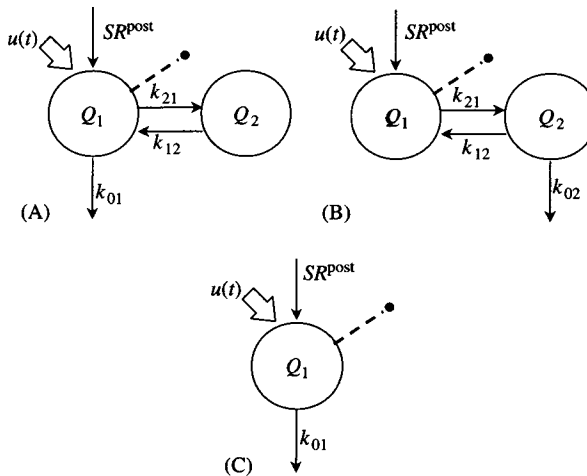


**Figure 11.3.** Compartmental models of insulin kinetics.  $Q_1$ ,  $Q_2$  are insulin mass in compartment 1 and 2;  $k_{21}$ ,  $k_{12}$  are transfer rates between compartments;  $k_{01}$ ,  $k_{02}$  are irreversible losses from compartment 1 and 2;  $SR^{post}$  is the posthepatic insulin secretion;  $u$  is the test input; the dashed line with the bullet denotes the measurement.

**Table 11.2.**  
**Compartmental Parameters of Insulin Kinetics for the Models of**  
**Figure 11.3(A) and (B)**

	$k_{01}$ ( $\text{min}^{-1}$ )	$k_{02}$ ( $\text{min}^{-1}$ )	$k_{21}$ ( $\text{min}^{-1}$ )	$k_{12}$ ( $\text{min}^{-1}$ )	$Q_1$ ( $\text{pmol/kg}$ )	$Q_2$ ( $\text{pmol/kg}$ )	$SR^{\text{post}}$ ( $\text{pmol/}$ $\text{min kg}$ )	$V_D$ ( $\text{pmol/kg}$ )	$MRT$ ( $\text{min}$ )
<b>A</b>	0.276	—	0.295	0.321	2.5	2.3	0.7	107	6.9
<b>B</b>	—	0.155	0.571	0.166	2.5	4.5	0.7	156	10

$V_D$  = total distribution volume in the system;  $MRT$  = mean residence time in the system.

where compartment 1 represents the accessible pool (plasma and tissues rapidly exchanging with plasma) where tracer input and measurements take place and compartment 2 represents peripheral tissues.  $SR^{\text{post}}$  is the posthepatic insulin secretion rate, that is, the flux of newly secreted insulin that reaches plasma after the first passage through the liver. The two models differ in the site of irreversible loss, taking place, respectively, in plasma (Figure 11.3(A)) or in the peripheral tissue compartment (Figure 11.3(B)). Both models are *a priori* uniquely identifiable (Cobelli and DiStefano, 1980; see Chapter 4). Numerical values estimated via nonlinear least squares (Carson *et al.*, 1983) in a group of normal subjects are shown in Table 11.2 (Cobelli and Caumo, 1990).

In situations where a two-compartment model cannot be resolved from the data, the single-compartment model of Figure 11.3(C) has been used to describe insulin kinetics.

A comparison between compartmental (Table 11.2) and noncompartmental parameters (Table 11.1) confirms what is expected from the theory (DiStefano, 1982): the noncompartmental model correctly recovers the accessible pool parameters, while the system parameters are correct only if the insulin system satisfies the “equivalent source/equivalent sink” constraint, which means if *de novo* synthesis and irreversible loss take place in the accessible compartment, otherwise they are underestimated. The system of Figure 11.3(A) but not that of Figure 11.3(B) satisfies the constraint, thus in the latter case the noncompartmental system parameters underestimate the true values.

### 11.2.3. NONLINEAR AND LINEAR TIME-VARYING COMPARTMENTAL MODELS

The nonlinear insulin kinetics in the supraphysiological concentration range require either nonlinear or linear time-varying models. A relatively simple

nonlinear two-compartment model similar to that of Figure 11.3(A) has been proposed (Frost *et al.*, 1973) with linear transfer rates  $k_{21}$ ,  $k_{12}$ , but a nonlinear irreversible loss  $k_{01}$  described by a Michaelis-Menten relation. However, the elevated number of model parameters (six) poses some problems in deriving precise estimates for all of them. A nonlinear five-compartment model has been recently proposed, which also incorporates a description of insulin kinetics at the receptor level (Hovorka *et al.*, 1993).

An alternative approach to describe insulin kinetics in a rather large concentration range (up to 700  $\mu\text{U/ml}$ ) is based on a linear model similar to that of Figure 11.3(A), with constant transfer rates  $k_{21}$ ,  $k_{12}$  and a time-varying irreversible loss,  $k_{01}(t)$  (Morishima *et al.*, 1992). Parameters  $k_{21}$ ,  $k_{12}$ , and the initial value of  $k_{01}$  can be estimated by a bolus injection of an insulin tracer in basal condition, but the estimation of the time course  $k_{01}(t)$  requires a constant infusion of tracer throughout the experiment. This model also has been subject to a validation, which means a study has been designed for this model consisting of a known and variable insulin infusion able to induce a gross perturbation on the system. The insulin rate of appearance was then reconstructed, based on the model, and compared with the known insulin infusion profile. The results show that the linear time-varying model, but not the linear time-invariant model, provides a reliable estimate of the known profile, indicating that the assumption of linear time-invariant kinetics is not tenable when insulin concentration varies in a wide supraphysiological range.

### 11.3. AN ORGAN MODEL OF INSULIN SECRETION

Mechanisms of glucose control on  $\beta$ -cell secretion are complex and involve a number of events at the molecular level. Many aspects have been studied by mathematical models, aiming to describe the bursting electrical activity at the cellular level (Sherman, 1996) or to describe and assess  $\beta$ -cell function at the organ level.

In this section, a model of insulin secretion based on the theory of the threshold secretory mechanism (Licko, 1973) is presented. Two assumptions underlie this theory: 1) a threshold control of glucose on insulin secretion, meaning that glucose concentration is able to stimulate insulin secretion only if it exceeds a given threshold; and 2) the existence of populations of  $\beta$ -cells (packets) having different sensitivity to the glucose stimulus, or different glucose thresholds. This theory has emerged from the analysis of experimental data obtained in the isolated perfused rat pancreas, in absence of any feedback effect of insulin on glucose (open-loop condition). In these experiments, glucose concentration was varied at the inflow to reproduce specific glucose patterns like a step, a staircase, and a ramp. Insulin, which was not present

at the inflow, was present at the outflow because of the pancreatic secretion stimulated by glucose. Pancreatic secretion was then measured by multiplying insulin concentration at the outflow by the flow across the organ. The distinctive features of insulin secretion can be summarised as follows (Figure 11.4):

- 1). A step increase of glucose elicits a spike of insulin release, afterward, secretion decreases independently of the glucose stimulus or insulin secretion. A second secretion phase subsequently occurs, slower and delayed with respect to the first phase. Secretion ceases immediately after the end of the stimulus.
- 2). A prolonged and elevated glucose stimulus renders  $\beta$ -cells hypersensitive to a subsequent stimulation.
- 3). A rapid rise of glucose concentration stimulates an early secretion peak, which is reduced if glucose rises slowly.
- 4). The amount of insulin secreted during the first phase is additive, meaning it is the same whether glucose increases from 0 to  $G$  in a single step or a number of steps.

On the basis of feature 1 the two-compartment model of Figure 11.5(A) was initially proposed (Grodsky *et al.*, 1970) where compartment 1 represents stored insulin (98%) and compartment 2 promptly releasable, or labile, insulin (2%). Transfer rates between compartments are slow, with time constant equal to approximately 100 min for  $k_{12}$  and 1000 min for  $k_{21}$ . Glucose has a potentiation effect on the amount of labile insulin since it promotes the provision of new insulin and the transfer from the storage to the labile form.

The model was simplified into a one-compartment model (Figure 11.5(B)) by neglecting insulin conversion to the stable form ( $k_{12}$ ). Then, mass balance equation gives:

$$\dot{X}(G, t) = -SR(G, t) + P(G, t) \quad X(0) = X_0 \quad (11.1)$$

where  $X$  is the amount of labile insulin in the  $\beta$ -cells,  $X_0$  its initial condition,  $SR$  and  $P$  are insulin secretion rate and insulin provision controlled by glucose concentration  $G$ .

Assuming that  $SR$  depends linearly on  $X$  and that  $P$  increases slowly with time, the model described by (11.1) is able to reproduce, at least qualitatively, the biphasic secretion profile after a step increase of glucose concentration (Figure 11.4(A)): the initial condition  $X_0$  is responsible for the first phase and provision  $P$  for the second phase secretion. However, (11.1) is inadequate to describe the secretion profile after a staircase glucose stimulation (Figure 11.4(B) and (C)): the initial glucose step promotes a first phase secretion that exhausts the labile insulin reserve so that the second glucose step is only able to influence second phase secretion but not to promote the second peak observed in the secretion data. These findings suggested that,

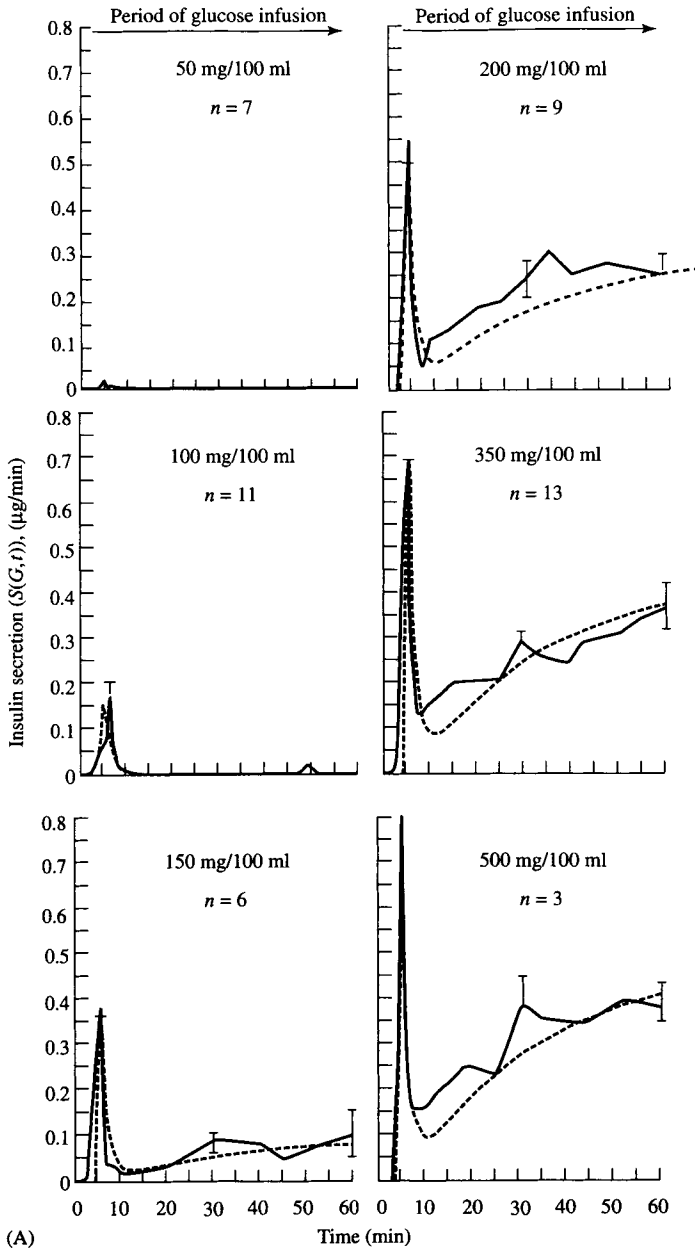


**Figure 11.4.** Insulin secretion during various glucose stimulations. A, prolonged step; B, two short steps; C, staircase infusion; D, fast ramp; E, slow ramp. Continuous line shows experimental data and dashed line the model prediction (adapted from Grodsky *et al.*, 1972).

Figure 11.4. (Continued)

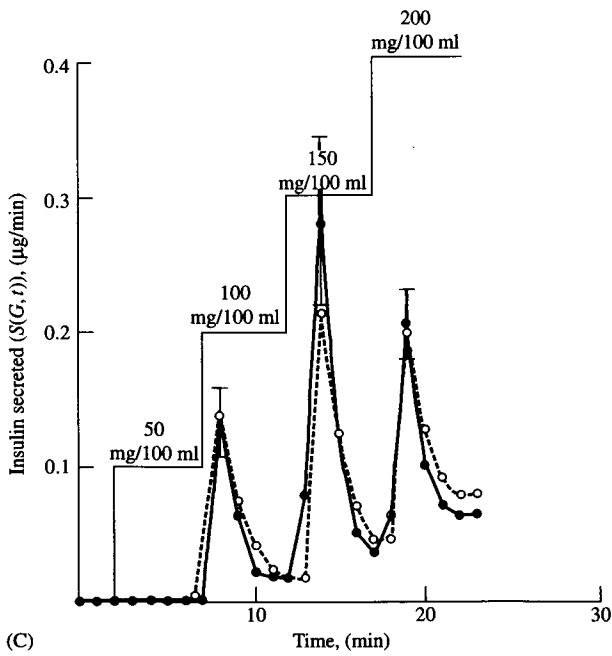
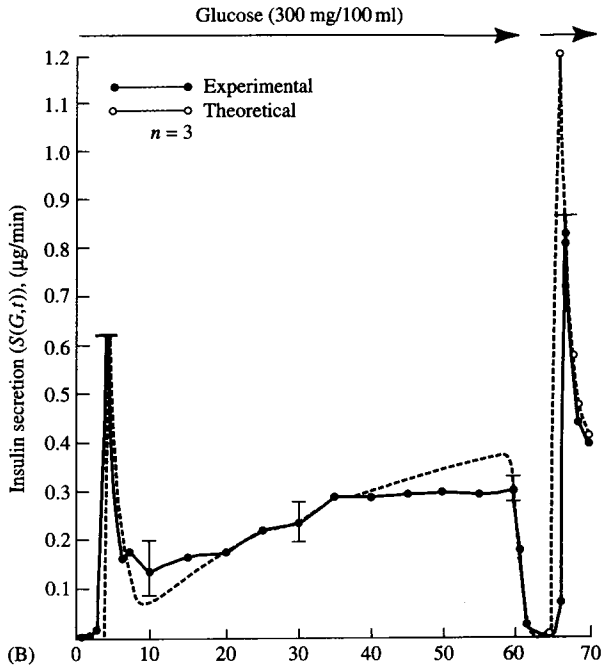
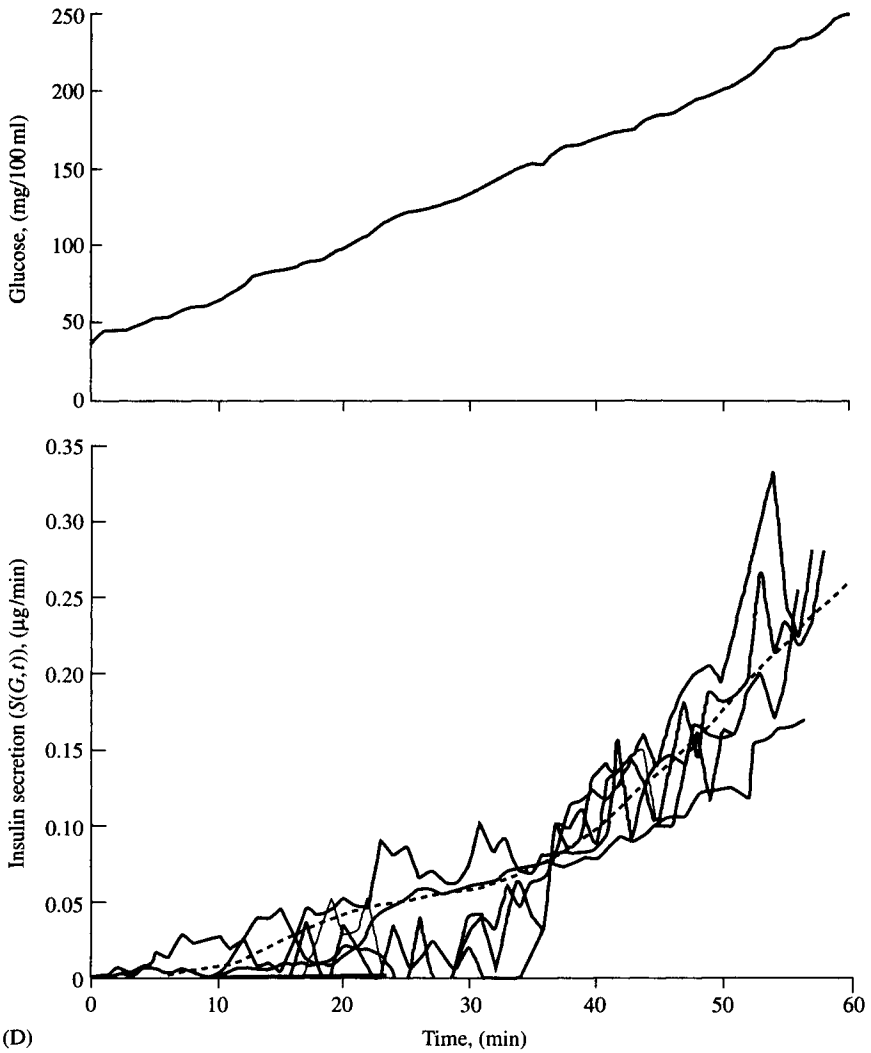


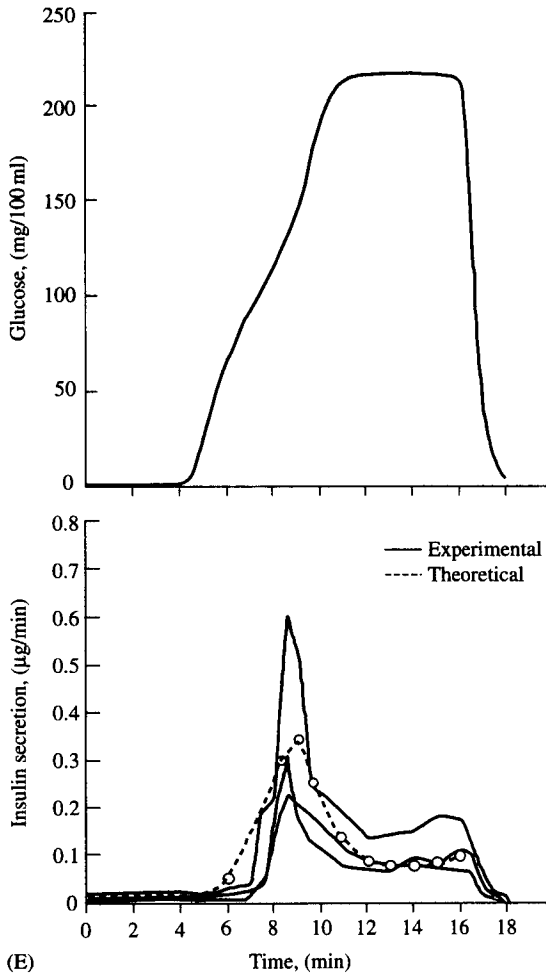


Figure 11.4. (Continued)



for a given glucose step, only a fraction of labile insulin is mobilised for first-phase secretion and that more insulin is rapidly released in response to a subsequent, more elevated glucose step. To account for this feature, the model of Figure 11.5(B) was successively modified (Grotsky, 1972) by incorporating the assumption that labile insulin is distributed into packets, having a different threshold sensitivity to glucose. At each packet a threshold value

Figure 11.4. (Continued)



$\vartheta$  is associated such that:

- if  $G > \vartheta$ , the packet is “open” and releases insulin
- if  $G \leq \vartheta$ , the packet is “closed” and does not release insulin

The threshold density function  $\xi(\vartheta, t)$  describes how insulin distributes in the various packets.  $\xi(\vartheta, t)d\vartheta$  thus represents the amount of insulin in packets having a threshold level ranging from  $\vartheta$  and  $\vartheta + d\vartheta$ , which can be released when the glucose stimulus increases from  $\vartheta$  to  $\vartheta + d\vartheta$ . The threshold density

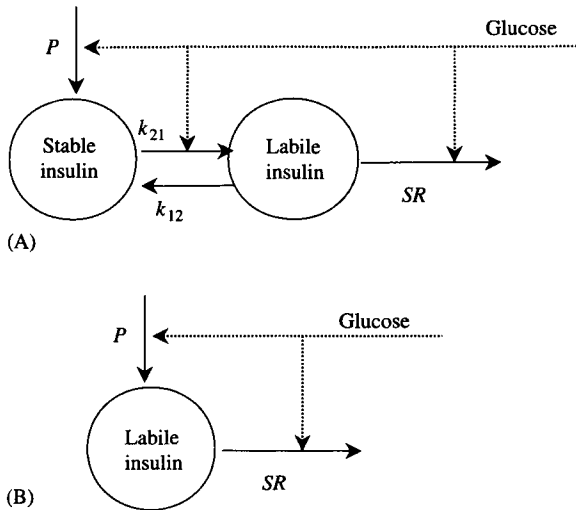


**Figure 11.5.** Two-compartment model of insulin secretion (A) and its simplification in a single compartment model (B).  $k_{21}$ ,  $k_{12}$  are transfer rates;  $P$  and  $SR$  are insulin provision and secretion, controlled by glucose  $G$ . In model A, glucose also controls the conversion of insulin from the stable to the labile form.

function also depends on time since the amount of insulin in packets varies in time due to secretion, exchange between packets, and so forth.

Glucose promotes insulin secretion from “open” packets, which are packets having a threshold level lower than the value, so that the total amount of releasable insulin for a given value of glucose stimulus,  $G$ , is:

$$X(G, t) = \int_0^{G(t)} \xi(\vartheta, t) dt \quad (11.2)$$

Insulin secretion is assumed to be proportional to this quantity:

$$SR(G, t) = m(G)X(G, t) = m(G) \int_0^{G(t)} \xi(\vartheta, t) dt \quad (11.3)$$

where  $m$ , in principle, depends on  $G$ .

Before presenting the model state equations associated with (11.3), let us evidence an important property of the threshold theory. By taking the derivative with respect to time of both sides of (11.2) one has:

$$\dot{X}(G, t) = \int_0^{G(t)} \dot{\xi}(\vartheta, t) d\vartheta + \xi(G(t), t) \frac{dG(t)}{dt} \quad (11.4)$$

Equation (11.4) indicates that the theory brings to a control of both glucose  $G$  and its derivative  $dG(t)/dt$  on  $X$  and thus on  $SR$ . This is interesting because it provides a physiological rationale for a proportional plus derivative control of glucose on insulin secretion, a relationship often acritically assumed in models of secretory processes to describe the data.

The state equation for  $\xi(\vartheta, t)$  associated with (11.3) is:

$$\begin{aligned} \dot{\xi}(\vartheta, t) &= -m(G)\xi(\vartheta, t) + \gamma(\vartheta)P(G, t) - \Gamma'_{\infty}\xi(\vartheta, t) \\ &\quad + \gamma'(\vartheta) \int_0^{\infty} \xi(\vartheta', t)d\vartheta' \quad \text{for } \vartheta < G \\ \dot{\xi}(\vartheta, t) &= \gamma(\vartheta)P(G, t) - \Gamma'_{\infty}\xi(\vartheta, t) \\ &\quad + \gamma'(\vartheta) \int_0^{\infty} \xi(\vartheta', t)d\vartheta' \quad \text{for } \vartheta > G \end{aligned} \tag{11.5}$$

where:

- a) the initial condition  $\xi(\vartheta, 0)$  is the threshold density function at time zero, or when there is no glucose stimulus;
- b)  $-m(G)\xi(\vartheta, t)$  is the contribution to secretion of the packets having threshold  $\vartheta$ , with  $\theta < G$ ;
- c)  $\gamma(\vartheta)P(G, t)$  is the fraction of provision refilling the packets having threshold  $\vartheta$ , with provision modelled as a first-order process, with time constant  $\alpha(G)$  and steady-state value  $P(G, \infty)$  depending on  $G$ :

$$\dot{P}(G, t) = -\alpha(G)[P(G, t) - P(G, \infty)] \tag{11.6}$$

Provision distributes among packets according to a function  $\gamma(\vartheta)$ , proportional to the initial threshold density function:  $\gamma(\vartheta) = f\xi(\vartheta, 0)$ ;

- d)  $\Gamma'_{\infty}\xi(\vartheta, t) + \gamma'(\vartheta) \int_0^{\infty} \xi(\vartheta', t)d\vartheta'$  describes insulin exchange among packets. The assumption is made that the flux of insulin between two packets having threshold, respectively,  $\vartheta$  and  $\vartheta'$  is proportional to the amount of insulin in the source packet  $\xi(\vartheta, t)$  and to the initial threshold density function evaluated for the destination packet  $\xi(\vartheta', 0)$ . The total flux out of the packet  $\vartheta$  is then:

$$- \int_0^{\infty} \xi(\vartheta, t)\gamma'(\vartheta')d\vartheta' = -\Gamma'_{\infty}\xi(\vartheta, t) \tag{11.7}$$

The total flux into packet  $\vartheta$  is:

$$\int_0^{\infty} \xi(\vartheta', t)\gamma'(\vartheta)d\vartheta' = \gamma'(\vartheta) \int_0^{\infty} \xi(\vartheta', t)d\vartheta' \tag{11.8}$$

with  $\gamma'(\vartheta) = f'\xi(\vartheta, 0)$  and  $\Gamma'_{\infty} = \int_0^{\infty} \gamma'(\vartheta)d\vartheta$

In summary, the model consists of three equations: 1) a first-order differential equation (11.5) to describe the kinetics of insulin in the packets, with  $\xi(\vartheta, t)$  as state variable (this means an infinite set of ordinary differential equations, one for each threshold value); 2) a first-order differential equation (11.6) to describe the control of glucose on insulin provision; and 3) an integral equation (11.3) to link the state variable to the measurement.

To complete the model specification, one has to provide a description for  $\xi(\vartheta, 0)$  and define how parameters  $m(G)$ ,  $\alpha(G)$ ,  $P(G, \infty)$  depend on  $G$ . To this purpose, model predictions were compared to the data of the glucose step infusion protocol (Figure 11.4(A)). Since  $G = \text{const}$ , the equation describing first phase secretion:

$$\dot{\xi}(\vartheta, t) = -m(G)\xi(\vartheta, t) \quad (11.9)$$

can be solved:

$$\xi(\vartheta, t) = \xi(\vartheta, 0)e^{-m(G)t} \quad (11.10)$$

and secretion expressed as follows:

$$\begin{aligned} SR(G, t) &= m(G)X(G, t) = m(G) \int_0^G \xi(\vartheta, 0)d\vartheta \cdot e^{-m(G)t} \\ &= m(G)X(G, 0)e^{-m(G)t} \end{aligned} \quad (11.11)$$

By comparing (11.11) with the early data of Figure 11.4(A), which reflect first-phase secretion, it was concluded that  $m$  does not depend on  $G$ , and a constant value for  $m(G)$  was estimated:

$$m(G) = m = 0.622 \text{ min}^{-1} \quad (11.12)$$

From the data of Figure 11.4(A), values of  $X(G, 0)$  were also estimated for different values of  $G$  and approximated by an analytical function. Differentiating this expression with respect to  $G$ , an analytical expression for the initial density function was obtained:

$$\begin{aligned} \xi(\vartheta, 0) &= X_{\text{MAX}} \frac{kC\vartheta^{k-1}}{(C + \vartheta^k)^2} \quad \text{con } X_{\text{MAX}} = 1.65 \text{ pgr}, \\ C &= 1.51 \times 10^7, \quad k = 3.3 \end{aligned} \quad (11.13)$$

If  $G = \text{const}$ , also the model equations for second-phase secretion can be simplified. Let us define first:

$$\begin{aligned} X_1(G, t) &= \int_0^G \xi(\vartheta, t)d\vartheta & X_2(G, t) &= \int_G^\infty \xi(\vartheta, t)d\vartheta \\ \Gamma(G) &= \int_0^G \gamma(\vartheta)d\vartheta & \Gamma'(G) &= \int_0^G \gamma'(\vartheta)d\vartheta \end{aligned} \quad (11.14)$$

Then, by integrating (11.5), one has:

$$\begin{aligned} \dot{X}_1(G, t) &= -mX_1(G, t) + \Gamma(G)P(G, t) + \Gamma'(G)[X_1(G, t) \\ &\quad + X_2(G, t)] - \Gamma'_\infty X_1(G, t) \\ \dot{X}_2(G, t) &= [\Gamma_\infty - \Gamma(G)]P(G, t) + [\Gamma'_\infty - \Gamma'(G)][X_1(G, t) \\ &\quad + X_2(G, t)] - \Gamma'_\infty X_2(G, t) \end{aligned} \tag{11.15}$$

In steady state, (11.15) yields:

$$mX_1(G, \infty) = \Gamma_\infty P(G, \infty) \tag{11.16}$$

$\Gamma_\infty P(G, \infty)$  is unknown, but the steady-state secretion  $mX_1(G, \infty)$  can be estimated from the data of Figure 11.4(A) for different  $G$  values. Thus, one obtains:

$$\Gamma_\infty P(G, \infty) = \frac{0.5G^{10}}{8.75 \cdot 10^{21} + 2.25 \cdot 10^{15}G^3 + 3.5 \cdot 10^6G^7 + G^{10}} \tag{11.17}$$

Finally,  $\alpha(G)$  was derived by considering the case of a constant and elevated glucose stimulus ( $>300$  mg/100 ml), so that  $\Gamma(G) \cong \Gamma_\infty$ ,  $\Gamma'(G) \cong \Gamma'_\infty$  and (11.15) becomes:

$$\begin{aligned} \dot{X}_1(G, t) &= -mX_1(G, t) + \Gamma_\infty P(G, t) + \Gamma'_\infty [X_1(G, t) \\ &\quad + X_2(G, t)] - \Gamma'_\infty X_1(G, t) \\ \dot{X}_2(G, t) &= -\Gamma'_\infty X_2(G, t) \end{aligned} \tag{11.18}$$

From (11.18),  $X_2(G, t)$  is negligible since it decreases exponentially starting from a negligible initial condition (only a few packets have a threshold higher than  $G$ ). The model equations simplify as:

$$\begin{aligned} \dot{X}(G, t) &= -mX_1(G, t) + \Gamma_\infty P(G, t) & X_1(G, t) &= \int_0^G \xi(\vartheta, 0) d\vartheta \\ \dot{P}(G, t) &= -\alpha(G)[P(G, t) - P(G, \infty)] & P(G, 0) &= 0 \\ SR(G, t) &= mX_1(G, t) \end{aligned} \tag{11.19}$$

By fitting these equations to the data of Figure 11.4(A), a constant value for  $\alpha(G)$  was estimated:

$$\alpha(G) = \alpha = 0.0337 \text{ min}^{-1} \tag{11.20}$$

The model (11.3, 11.6, 11.15) has been successfully employed to simulate all the insulin secretion data of Figure 11.4. The results, which are shown as dashed lines in the same figure, show a good agreement between data and model predictions, indicating that the model formulated by Grodsky is able to describe the pancreatic secretory response to a variety of glucose stimulation patterns. However, due to its complexity, the use of this model has been confined to simulation.

## 11.4. ESTIMATION OF INSULIN SECRETION BY DECONVOLUTION

Let us now consider the problem of estimating the insulin secretion profile *in vivo* during a perturbation from measurements taken in the accessible plasma pool. This is an input estimation problem, for which the deconvolution techniques discussed in Chapter 3 offer the classic solution. However, from plasma insulin concentration data, it is not possible to infer on pancreatic secretion, but only on its component appearing in plasma, or the posthepatic insulin secretion, which is approximately equal to 50% of pancreatic secretion. This problem can be bypassed if C-peptide concentration is measured during the perturbation and used to estimate insulin secretion since C-peptide is secreted equimolarly with insulin, but it is extracted by the liver to a negligible extent (Figure 11.6). In other words, plasma C-peptide concentration well reflects, apart from the rapid liver dynamics, C-peptide pancreatic secretion, which in turn coincides with insulin secretion.

Since there is solid evidence that C-peptide kinetics are linear in a wide range of concentration, the relationship between pancreatic secretion ( $SR$ , the input) and C-peptide concentration measurements ( $CP$ , the output) is the

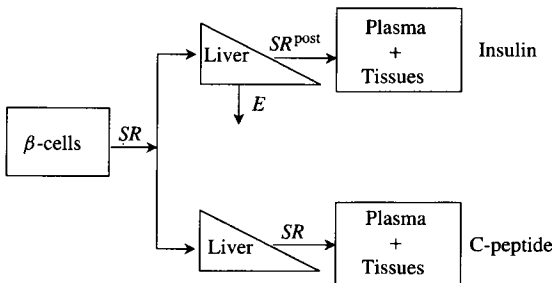


**Figure 11.6.** Rationale for assessing insulin secretion from C-peptide data. Insulin and C-peptide are equimolarly secreted from the  $\beta$ -cells and pass through the liver, where insulin, but not C-peptide, undergoes hepatic extraction ( $E$ ). Plasma C-peptide thus reflects pancreatic secretion ( $SR$ ), while plasma insulin only reflects posthepatic secretion ( $SR^{post}$ ).

convolution integral:

$$CP(t) = \int_{-\infty}^t h(t - \tau) \cdot SR(\tau) d\tau \quad (11.21)$$

where  $h$  is the impulse response function, or the response in concentration to the injection of a unit dose bolus of C-peptide.  $SR$  profile during a perturbation can be reconstructed by solving the inverse problem, which is deriving  $SR$  by deconvolution, given  $CP$  and  $h$ . The knowledge of the impulse response function  $h$  is a prerequisite. This requires an additional experiment on the same subject, consisting of a bolus of C-peptide and a concomitant infusion of somatostatin to inhibit endogenous C-peptide secretion. C-peptide concentration data are then approximated by a sum of exponential model that, after normalisation to the C-peptide dose, provides the impulse response function. While one assumes that the impulse function in a given individual does not vary between the two experiments, no assumptions are needed about the mechanisms of insulin secretion. However, some smoothness in the reconstructed insulin secretion profile will result from regularisation, which is a necessity given the well-known ill-conditioning of the deconvolution problem.

Deconvolution methods have been applied to estimate the secretion profile in various physiopathological states (Polonsky *et al.*, 1986, 1988) and during both intravenous and oral glucose tolerance tests (Shapiro *et al.*, 1988; Sparacino and Cobelli, 1997; Tillil *et al.*, 1988).

To eliminate the need for a separate experiment to evaluate the impulse response function, a method has been proposed (Van Cauter *et al.*, 1992) to derive C-peptide kinetic parameters in an individual based on data about his or her age, weight, height, and gender. The secretion profiles reconstructed by deconvolution, with the impulsive function evaluated from either the C-peptide bolus experiment or the population parameters, are similar (Hovorka *et al.*, 1998), indicating that the population values allow a good prediction of individual kinetic parameters.

## 11.5. A STRUCTURAL MODEL TO ESTIMATE INSULIN SECRETION AND SECRETORY INDICES

### 11.5.1. RATIONALE

As discussed previously, deconvolution allows one to reconstruct the insulin secretion profile during a perturbation. However, it is crucial to complement this information with a quantitative assessment of insulin secretion, by arriving at



indices of  $\beta$ -cell sensitivity to glucose from a structural model of insulin secretion. These indices, when considered in conjunction with the indices describing insulin action on glucose production and uptake, will allow one to quantify the relative role of  $\beta$ -cells as well as liver and peripheral tissues in determining the metabolic state of an individual. However, the feedback nature of the glucose-insulin system poses major difficulties; a closed-loop model must be postulated, thus possible inaccuracies in modelling insulin action will influence the reliability of insulin secretion assessment and vice versa.

To simplify the analysis, several techniques have been proposed that “open” experimentally the feedback loop, such as the glucose clamp technique where glucose concentration is elevated at 70 to 100 mg/dl above basal level and maintained during a period of time by means of a variable glucose infusion. Insulin (or C-peptide) concentration, monitored during the experiment, shows an early peak followed by a slow second phase. Two indices are then calculated, related to first- and second-phase secretion, as the ratio between plasma insulin (or C-peptide) concentration and plasma glucose concentration in the two phases. However, the interpretation of these indices is not straightforward since they reflect not only pancreatic secretion but also insulin (or C-peptide) kinetics and, in the case of insulin, its hepatic extraction.

An alternative technique has been developed based on a graded glucose infusion protocol (Byrne *et al.*, 1995). Insulin secretion is reconstructed by deconvolution of C-peptide data at various (quasi) steady states characterised by different glucose levels. The dose-response relationships between glucose concentration and insulin secretion are then explored. However, the use of a steady-state method of data analysis to interpret quasi-steady-state data affects the reliability of the results.

A third approach is based on the use of structural models of insulin secretion during a test perturbation. The glucose-insulin feedback mechanisms are active during the perturbation, but the loop is opened mentally by partitioning the whole system into two subsystems (Figure 11.7) linked by the

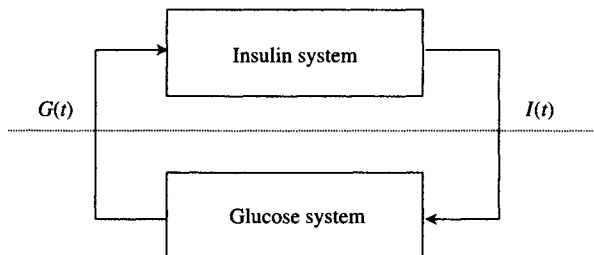


**Figure 11.7.** Decomposition of the glucose-insulin system.  $G$  and  $I$  are plasma glucose and insulin concentration.

measured variables, insulin and glucose concentration. The two subsystems are then modelled separately. For the insulin secretion model, glucose is the (known) input and insulin the output, while for the model of insulin action on glucose production and utilisation, insulin is the (known) input and glucose the output. Since the two models are intended for clinical use, they must be of optimal complexity, or parsimonious; simple, so that all the parameters can be estimated with acceptable precision from the data of an individual, but not simplistic, or able to give a reliable description of the physiological processes. It is in this context that the term *minimal model* was coined (Bergman *et al.*, 1979).

The minimal model of insulin secretion based on C-peptide data (Toffolo *et al.*, 1995) is presented in this section, while the minimal model of glucose production and utilisation is presented in Chapter 12. In both cases, the test perturbation is a routine test. The intravenous glucose tolerance test (IVGTT) consists of a rapid (usually within 1 min) administration of a standard glucose dose ( $300 \text{ mg kg}^{-1}$ ) and frequent blood sampling of plasma glucose, insulin, and C-peptide concentration in the 3-h interval following the injection.

### 11.5.2. THE MODEL OF C-PEPTIDE KINETICS

Since the secretion model is identified on C-peptide measurements taken in plasma, it must be integrated into a model of whole-body C-peptide kinetics. The kinetic model is the one proposed by (Eaton *et al.*, 1980) and shown in Figure 11.8. Compartment 1, accessible to measurement, represents plasma and rapidly equilibrating tissues, whereas compartment 2 represents tissues in

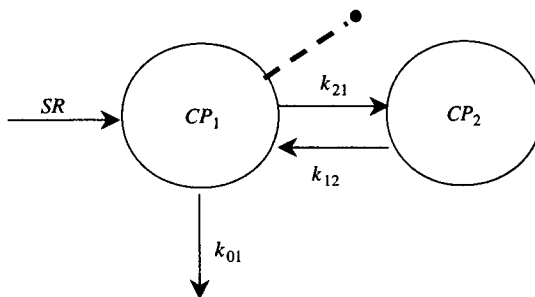


**Figure 11.8.** The two-compartment model of C-peptide kinetics.  $CP_1$  and  $CP_2$  are C-peptide concentration in compartments 1 and 2;  $k_{21}$  and  $k_{12}$  are transfer rate parameters;  $k_{01}$  is the irreversible loss from compartment 1;  $SR$  is the pancreatic secretion; the dashed line with the bullet denotes the C-peptide measurement.

slow exchange with plasma. The model equations are:

$$\begin{aligned} \dot{CP}_1(t) &= -[k_{01} + k_{21}]CP_1(t) + k_{12}CP_2(t) + SR(t)/V_C & CP_1(0) &= CP_{1b} \\ \dot{CP}_2(t) &= k_{21}CP_1(t) - k_{12}CP_2(t) & CP_2(0) &= CP_{2b} \end{aligned} \quad (11.22)$$

where  $CP_1$  (pmol/l) is C-peptide concentration in compartment 1,  $CP_2$  (pmol/l) is the equivalent concentration in compartment 2, which is C-peptide mass in this compartment divided by the volume of the accessible compartment,  $k_{12}$  e  $k_{21}$  ( $\text{min}^{-1}$ ) are transfer rate parameters between the two compartments,  $k_{01}$  ( $\text{min}^{-1}$ ) is the irreversible loss from compartment 1,  $SR$  (pmol/min) is pancreatic secretion entering the accessible compartment,  $V_C(t)$  is the distribution volume of the accessible compartment.

### 11.5.3. THE MODEL OF PANCREATIC SECRETION

The minimal model of pancreatic secretion was derived from the Grodsky model via a number of simplifications dictated by the IVGTT protocol. Secretion is still described by (11.3):

$$SR(t) = m \int_0^{G(t)} \xi(\vartheta, t) d\vartheta = mX(G, t) \quad (11.23)$$

but the following assumptions hold:

- 1).  $\xi(G, t)$  is described as in (11.5), but exchanges between packets are neglected:

$$\dot{\xi}(\vartheta, t) = -m\xi(\vartheta, t) + \gamma(\vartheta)P(G, t) \quad \vartheta < G \quad (11.24)$$

$X(G, t)$  can thus be derived by integrating (11.24) with respect to  $\vartheta$ , from 0 to  $G$ :

$$\dot{X}(G, t) = -mX(G, t) + \Gamma(G)P(G, t) + \xi(G, t) \frac{dG(t)}{dt} \quad (11.25)$$

- 2). the term  $\Gamma(G)P(G, t)$  in (11.25), which represents the fraction of insulin provision that distributes in those packets able to release insulin, is denoted as  $Y(G, t)$  and described as a first-order process, characterised by a time constant,  $\alpha$ , independent on  $G$  and by a steady-state value,  $Y(G, \infty)$ , depending on  $G$ :

$$\dot{Y}(G, t) = -\alpha[Y(G, t) - Y(G, \infty)] \quad (11.26)$$

- 3). the derivative term in (11.25) is neglected for time  $t > 0$  since it is far lower in magnitude than the  $mX(G, t)$  term (Licko and Silvers, 1975).

Equation (11.25) becomes:

$$\dot{X}(G, t) = -mX(G, t) + Y(G, t) \quad (11.27)$$

- 4). It is assumed that  $Y(G, \infty)$  in (11.26) is linearly dependent upon  $G$  in the 100–300 mg/dl range:

$$\begin{aligned} Y(G, \infty) &= \beta'(G - h) + Y_\infty & h < G < 300 \\ &= Y_\infty & G \leq h \end{aligned} \quad (11.28)$$

where the term  $Y_\infty$  accounts for the nonzero insulin provision in the basal state,  $\beta'$  represents the pancreatic sensitivity to glucose since it measures the control exerted by glucose concentration on the steady-state secretion, and  $h$  represents the threshold glucose level, usually similar to the basal glucose, able to stimulate insulin secretion.

The secretion equations can thus be summarised as follows:

$$\begin{aligned} SR(t) &= mX(G, t) \\ \dot{X}(G, t) &= -mX(G, t) + Y(G, t) & X(0) &= X_0 \\ \dot{Y}(G, t) &= -\alpha[Y(G, t) - Y_\infty - \beta'(G - h)] & Y(0) &= Y_0 = Y_\infty \end{aligned} \quad (11.29)$$

The initial condition for  $X$ ,  $X_0$ , is the sum of the amount of releasable insulin in the basal state and of the amount of insulin in the packets that “open” up at time zero, when the glucose bolus causes an almost instantaneous increase of glucose concentration from the basal level up to its maximum level:

$$X_0 = X_\infty + \int_{G_b}^{Gb+G^{\max}} \xi(\vartheta, 0) d\vartheta \quad (11.30)$$

$X_0$  is responsible for first-phase secretion, while the slower second-phase derives from provision  $Y$ .

Model equations — kinetics (11.22) and secretion (11.29) — are linear and can be conveniently reformulated by first expressing the state variables as deviations from basal and then normalising  $X$  and  $Y$  to the distribution volume  $V_C$ :

$$\begin{aligned} c p_1(t) &= CP_1(t) - CP_{1b} \\ c p_2(t) &= CP_2(t) - CP_{2b} \\ x(t) &= (X(G, t) - X_\infty)/V_C \\ y(t) &= (Y(G, t) - Y_\infty)/V_C \end{aligned} \quad (11.31)$$

From (11.31) and the following steady-state relation:

$$Y_\infty = k_{01} V_C CP_{1b} = mX_\infty \quad (11.32)$$

the minimal model of C-peptide secretion and kinetics can be expressed in its final form:

$$\begin{aligned}
 \dot{c}p_1(t) &= -[k_{01} + k_{21}]cp_1(t) + k_{12}cp_2(t) + mx(t) & cp_1(0) &= 0 \\
 \dot{c}p_2(t) &= k_{21}cp_1(t) - k_{12}cp_2(t) & cp_2(0) &= 0 \\
 \dot{x}(t) &= -mx(t) + y(t) & x(0) &= x_0 \\
 \dot{y}(t) &= -\alpha\{y(t) - \beta[G - h]\} & y(0) &= 0
 \end{aligned}
 \tag{11.33}$$

The model has eight unknown parameters, three related to C-peptide kinetics,  $k_{01}$ ,  $k_{21}$ ,  $k_{12}$ , and five to pancreatic secretion,  $\alpha$ ,  $\beta = \beta'/V_C$ ,  $m$ ,  $h$  and  $x_0$ .

#### 11.5.4. MODEL IDENTIFICATION

The minimal model (11.33) is *a priori* identifiable but not uniquely since parameters  $x_0$ ,  $m$ ,  $k_{01}$ ,  $k_{21}$ , and  $\beta$  have two solutions in the parameter space (Cobelli and DiStefano, 1980; see also Chapter 4). Moreover, kinetic and secretion parameters cannot be estimated simultaneously with acceptable precision, and compensations between their point estimates also arise (Toffolo *et al.*, 1995). To render the model uniquely identifiable, kinetic parameters have been fixed to values derived either from a separate C-peptide bolus injection experiment performed in that individual or from population data as discussed in the previous section. In Table 11.3, C-peptide kinetic parameters are shown, both individually estimated or fixed from population data, with the corresponding secretion parameter estimates and their precision. Secretion parameters are similar in the two cases, indicating that the population approach is a valid strategy to assess C-peptide kinetics in an individual.

Figure 11.9 shows the ability of the minimal model to fit experimental data and Figure 11.10 the model-reconstructed secretion profile based on the following equation:

$$SR(t) = [k_{01}CP_{1b} + mx(t)]V_C \tag{11.34}$$

In addition to the secretion profile, the model also allows one to estimate three functional indices of the sensitivity to glucose of first-phase, second-phase, and basal secretion. The first-phase sensitivity to glucose,  $\Phi_1$  (dimensionless), is given by the ratio between the incremental amount of C-peptide secreted during the first-phase and the maximum increment of plasma glucose concentration  $\Delta G$  (mmol/l):

$$\Phi_1 = x_0/\Delta G \tag{11.35}$$

**Table 11.3.**

**Minimal Model Secretion Parameters (Mean  $\pm$  SD) When Kinetic Parameters Are Fixed to Individually Estimated Values (A) or to Population Values (B)**

	$k_{01}$ ( $\text{min}^{-1}$ )	$k_{21}$ ( $\text{min}^{-1}$ )	$k_{12}$ ( $\text{min}^{-1}$ )	$m$ ( $\text{min}^{-1}$ )	$\alpha$ ( $\text{min}^{-1}$ )	$\beta$ ( $10^9 \text{ min}^{-1}$ )	$h$ ( $\text{mmol/l}$ )	$X_0$ ( $\text{pmol/l}$ )
<b>A</b>	$0.064 \pm 0.004$ (5%)	$0.054 \pm 0.003$ (12%)	$0.056 \pm 0.002$ (6%)	$0.57 \pm 0.10$ (31%)	$0.065 \pm 0.009$ (33%)	$11.32 \pm 1.13$ (28%)	$4.94 \pm 0.17$ (29%)	$1806 \pm 356$ (6%)
<b>B</b>	$0.060 \pm 0.0003$ —	$0.052 \pm 0.0003$ —	$0.050 \pm 0.0001$ —	$0.66 \pm 0.11$ (39%)	$0.076 \pm 0.015$ (32%)	$10.67 \pm 0.79$ (26%)	$5.00 \pm 0.17$ (27%)	$1682 \pm 300$ (6%)

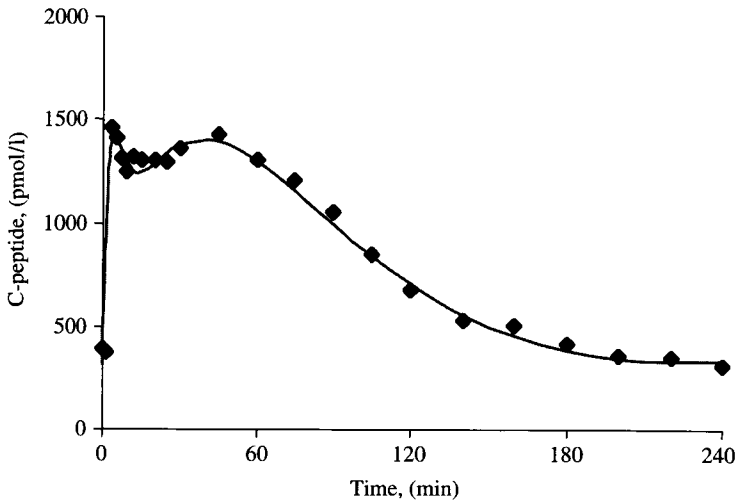


**Figure 11.9.** Plasma C-peptide concentration during an intravenous glucose tolerance test in a normal subject. The minimal model prediction is shown as a continuous line (Toffolo *et al.*, 1995).

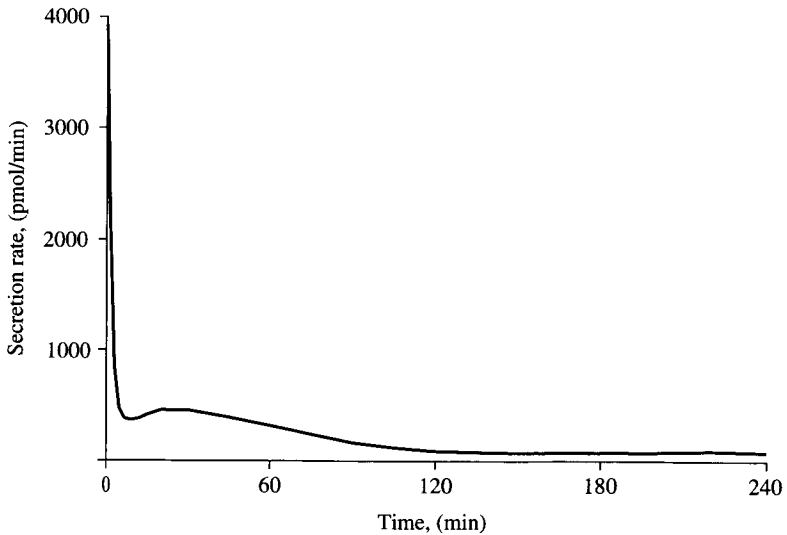


**Figure 11.10.** Minimal model prediction of pancreatic secretion during an intravenous glucose tolerance test in a normal subject (Toffolo *et al.*, 1995).

The second-phase sensitivity to glucose,  $\Phi_2$  ( $\text{min}^{-1}$ ), is given by parameter  $\beta$ , which describes the stimulatory effect of glucose concentration on provision:

$$\Phi_2 = \beta \quad (11.36)$$

Finally, the basal sensitivity to glucose,  $\Phi_b$  ( $\text{min}^{-1}$ ), is given by:

$$\Phi_b = SR_b/G_b = k_{01}CP_{1b}/G_b \quad (11.37)$$

where  $G_b$  is the end test of glucose concentration. Mean  $\Phi_1$ ,  $\Phi_2$ ,  $\Phi_b$  in normal subjects are:

$$\Phi_1 = 91.5 \pm 14.6 \quad \Phi_2 = 11.3 \pm 1.1 \quad \Phi_b = 4.11 \pm 0.45 \quad (11.38)$$

These indices quantify the glucose control on insulin secretion during an IVGTT, but similar information can be derived from other tests as well. However, since the model postulates a specific functional relation between insulin secretion and plasma glucose, its applicability in situations other than the IVGTT must be explicitly tested. Results have shown that the minimal model is able to describe C-peptide data of an insulin-modified IVGTT (Toffolo *et al.*, 1999) and, after some modifications, C-peptide data measured during more gentle tests, such as graded-glucose infusion (Toffolo *et al.*, 1998).

## 11.6. ESTIMATION OF HEPATIC INSULIN EXTRACTION

As for pancreatic insulin secretion, an indirect measurement approach is essential to quantify hepatic insulin extraction in humans since the direct measurement requires invasive protocols, with catheters placed in an artery and hepatic vein (Ferrannini and Cobelli, 1987b). Deconvolution offers a possible solution since by comparing pancreatic secretion rate ( $SR$ ) obtained from C-peptide data and posthepatic secretion  $SR^{\text{post}}$  obtained from insulin data, one can estimate hepatic extraction  $E$  as:

$$E(t) = \frac{SR(t) - SR^{\text{post}}(t)}{SR(t)} \quad (11.39)$$

The estimation of  $SR$  by deconvolution of C-peptide data is rather straightforward, as already discussed in Section 11.4. The estimation of  $SR^{\text{post}}$  is more problematic. If insulin varies within the physiological range so that its kinetics can be safely assumed linear and time-invariant, and if they are known (for



example) from a tracer insulin bolus protocol,  $SR^{\text{post}}$  can be reconstructed by deconvolution of insulin data. However, if insulin varies in a wide range during the study so that its kinetics are likely to become time-varying, the link between  $SR^{\text{post}}$  and insulin concentration data ( $I$ ) becomes:

$$I(t) = \int_0^{\infty} g(t, \tau) \cdot SR^{\text{post}}(\tau) d\tau \quad (11.40)$$

where  $g(t, \tau)$  represents the impulsive response of the linear time-varying insulin kinetic system. However, at variance with the linear time-invariant case, the solution of (11.40) now requires one to postulate a specific structural model of insulin kinetics since the solution of a deconvolution problem can be tackled with an I/O model, such as a sum of exponential model, only if the kinetics are time-invariant. One possibility is to adopt the linear time-varying, two-compartment model of insulin kinetics presented in Section 11.2 (Morishima *et al.*, 1992), but, as already discussed, its identification requires a more complex experiment, such as an insulin tracer infusion during basal and the perturbation period.

Minimal models offer an alternative approach to assess hepatic extraction. As discussed in Section 11.5, SR can be assessed from the model of C-peptide kinetics and secretion identified from C-peptide and glucose data measured during an IVGTT. By following a similar approach,  $SR^{\text{post}}$  can be assessed from insulin and glucose data. To this purpose, the insulin-modified IVGTT experiment, that is, an IVGTT associated with a short insulin infusion given between 20 and 25 min after the glucose bolus, offers definitive advantages with respect to the standard IVGTT since the insulin infusion (originally proposed [Yang *et al.*, 1987] to improve the assessment of insulin sensitivity) generates an additional insulin disappearance curve that greatly facilitates the simultaneous estimation of insulin kinetic and secretion parameters.

The C-peptide minimal model proposed to describe insulin secretion also can be used to describe posthepatic insulin secretion and, by using the single-compartment model of Figure 11.3(C) for insulin kinetics, one has:

$$\begin{aligned} \dot{i}(t) &= -ni(t) + m^{\text{post}}x^{\text{post}}(t) + u/V_I \quad i(0) = 0 \\ \dot{x}^{\text{post}}(t) &= -m^{\text{post}}x^{\text{post}}(t) + y^{\text{post}}(t)x^{\text{post}}(0) = x_0^{\text{post}} \\ \dot{y}^{\text{post}}(t) &= -\alpha^{\text{post}}\{y^{\text{post}}(t) - \beta^{\text{post}}[G(t) - h]\} \quad y^{\text{post}}(0) = 0 \end{aligned} \quad (11.41)$$

The first equation accounts for insulin kinetics:  $i$  (pmol/l) is above basal insulin,  $n$  ( $\text{min}^{-1}$ ) the rate constant of insulin disappearance,  $V_I$  (l) the insulin distribution volume,  $m^{\text{post}}x^{\text{post}}$  posthepatic insulin secretion, and  $u$  the exogenous insulin input (different from zero in the 20 to 25 min interval). The remaining two equations describe posthepatic secretion:  $\alpha^{\text{post}}$ ,  $\beta^{\text{post}}$ ,  $m^{\text{post}}$ ,  $x_0^{\text{post}}$  are posthepatic secretion parameters, and  $G$  the glucose stimulus.

The model provides the posthepatic secretion profile, as:

$$SR^{\text{post}}(t) = [nI_b + m^{\text{post}}x^{\text{post}}(t)]V_I \tag{11.42}$$

where  $I_b$  is the end test of basal insulin, and three posthepatic sensitivity indices, related to the control exerted by glucose during first phase, second phase, and basal secretion, respectively:

$$\Phi_1^{\text{post}} = x_0^{\text{post}}/\Delta G \quad \Phi_2^{\text{post}} = \beta^{\text{post}} \quad \Phi_b^{\text{post}} = SR_b^{\text{post}}/G_b = nI_b/G_b \tag{11.43}$$

The profile of hepatic extraction  $E$  can be estimated by using (11.39), with posthepatic secretion  $SR^{\text{post}}$  and pancreatic secretion  $SR$  estimated from the insulin minimal model (11.42) and the C-peptide minimal model (11.34), respectively. In addition, the modelling approach also provides two indices of hepatic extraction during IVGTT and in the basal state, from pancreatic and posthepatic indices:

$$E_{\text{IVGTT}} = 1 - \frac{(\Phi_b^{\text{post}} + \Phi_1^{\text{post}}A_1 + \Phi_2^{\text{post}}A_2)V_I}{(\Phi_b + \Phi_1A_1 + \Phi_2A_2)V_C} \quad E_b = 1 - \frac{\Phi_b^{\text{post}}V_I}{\Phi_bV_C} \tag{11.44}$$

with

$$A_1 = \frac{\Delta G}{T \cdot G_b} \quad A_2 = \frac{\int_0^T [G(t) - h]dt}{T \cdot G_b}$$

where  $T$  is the time at which glucose, insulin, and C-peptide concentration are back to steady state after the IVGTT perturbation.

The C-peptide (11.33) and the insulin (11.41) minimal models have been identified from the insulin-modified IVGTT data of normal subjects shown in Figure 11.11 (Toffolo *et al.*, 1997). In particular, reliable estimates of insulin kinetic parameters were obtained; plasma insulin clearance rate was 11.3 ml/min/kg on average. The two hepatic extraction indices of (11.44) have been calculated. The values were similar, approximately 60%, suggesting that the IVGTT experiment does not significantly alter hepatic insulin extraction.

## 11.7. CONCLUSIONS

Mathematical models offer an important tool to quantitatively assess the three insulin processes of kinetics, pancreatic secretion, and hepatic extraction. Compartmental and noncompartmental models of insulin kinetics have revealed that insulin is cleared very rapidly from plasma, at a rate representing about one third of cardiac output. As a consequence, variations of the secretion rate are rapidly reflected in variations of insulin levels in plasma and tissues where insulin exerts its action. Moreover, insulin kinetics are linear in

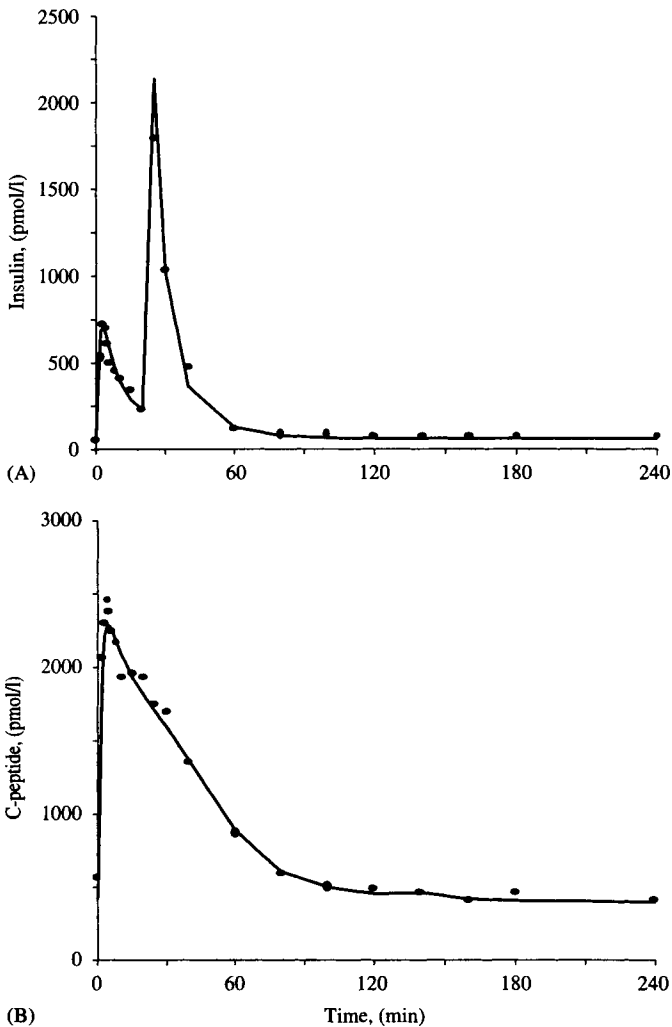


**Figure 11.11.** Plasma insulin and C-peptide concentration during an insulin-modified intravenous glucose tolerance test. The predictions of the two insulin and C-peptide minimal models are shown as continuous lines (Toffolo *et al.*, 1997).

the physiological range, thus suggesting a minor role of insulin kinetics in the regulation of its own concentration, and thus of insulin action.

The major role of pancreatic secretion in determining insulin concentration, and thus insulin action, is undisputed. Since pancreatic secretion is not accessible to direct measurement, the availability of models to mechanistically

describe this process is crucial. The model formulated by Grodsky accomplishes the first goal since it is a descriptive model that formulates assumptions on insulin secretion and glucose regulation mechanisms at organ level. However, due to its complexity, the model has been of limited use in practice.

Input-output modelling and deconvolution offer the classic solution to the problem of estimating from C-peptide concentration insulin secretion in an individual during a perturbation. This approach is attractive because it does not require to postulate a structural description of insulin secretion and has been widely used to reconstruct  $\beta$ -cell secretion in response to a variety of glucose stimulatory patterns (e.g., IVGTT, OGTT, graded glucose infusion, oscillatory glucose infusion) in both healthy and disease states.

An alternative approach to estimate  $\beta$ -cell secretion requires a structural model of insulin secretion, such as the minimal model of C-peptide secretion and kinetics. Model parameters can be estimated from C-peptide and glucose concentration data measured during a routine clinical test such as the IVGTT. The advantage of the minimal model approach is that it provides not only insulin but also indices of glucose control on  $\beta$ -cell secretion during the basal state and first- and second-phase secretion. Since the IVGTT is frequently used to measure insulin sensitivity by using the minimal model of glucose kinetics, these model-derived indices of  $\beta$ -cell function enrich the parametric picture of the glucose-insulin regulatory system obtainable with this test.

Hepatic extraction plays an important role in insulin metabolism since approximately 50% of the newly synthesised hormone is degraded in the liver before reaching the peripheral circulation, as well as organs and tissues. I/O modelling and deconvolution again offer an appealing noninvasive approach to its quantification. However, some underlying assumption of the approach, in particular those related to the description of insulin impulse response, must be carefully evaluated. As an alternative, the minimal modelling approach can be applied. By identifying two models, the one of C-peptide secretion and kinetics and that of posthepatic insulin secretion and kinetics from plasma C-peptide, insulin and glucose concentration measured from an insulin-modified IVGTT, hepatic extraction of insulin during this test can be quantified.

## 11.8. REFERENCES

- Bergman, R. N., Y. Z. Ider, C. R. Bowden and C. Cobelli. Quantitative estimation of insulin sensitivity. *Am J Physiol* 236(1979):E667–77.
- Byrne, M. M., J. Sturis and K. S. Polonsky. Insulin secretion and clearance during low-dose graded glucose infusion. *J Clin Invest* 268(1995):E21–27.
- Carson, E. R., C. Cobelli and L. Finkelstein. 1983. *The Mathematical Modelling of Metabolic and Endocrine Systems*. New York: Wiley.

- Cobelli, C. and A. Caumo 1990. Models to assess masses, fluxes and regulatory interactions of an endocrine control system: the glucose-insulin prototype. In: *Computers in Endocrinology: Recent Advances*. Edited by V. Guardabasso, G. Forti and D. Rodbard. New York: Raven Press.
- Cobelli, C. and J. J. DiStefano. Parameter and structural identifiability concepts and ambiguities: a critical review and analysis. *Am J Physiol* 239(1980):R7–24.
- DiStefano, J. J. Noncompartmental vs compartmental analysis: some basis for choice. *Am J Physiol* 12(1982):R1–6.
- Eaton, R. P., R. C. Allen, D. S. Schade, K. M. Erickson and J. Standefer. Prehepatic insulin production in man: kinetic analysis using peripheral connecting peptide behavior. *J Clin Endocrinol Metab* 51(1980):520–28.
- Ferrannini, E. and C. Cobelli. The kinetics of insulin in man. I. General aspects. *Diabetes Metab Rev* 3(1987a):355–63.
- Ferrannini, E. and C. Cobelli. The kinetics of insulin in man. II. Role of the liver. *Diabetes Metab Rev* 3(1987b):365–97.
- Frost, D. P., M. C. Srivastava, R. H. Jones, J. D. N. Nabarro and P. H. Sönksen. The kinetics of insulin metabolism in diabetes mellitus. *Postgrad Med J* 49(1973):949–54.
- Grodsky, G., H. Landhal, D. L. Curry and L. L. Bonnet. 1970. A two compartment model for insulin secretion. In: *Early Diabetes*. Edited by R. Camerini Davalos and H.S. Cole. New York: Academic Press.
- Grodsky, G. A threshold distribution hypothesis for packet storage of insulin and its mathematical modeling. *J Clin Invest* 51(1972):2047–59.
- Hovorka, R., J. K. Powrie, G. D. Smith, P. H. Sönksen, E. R. Carson and R. H. Jones. Five-compartment model of insulin kinetics and its use to investigate action of chloroquine in NIDDM. *Am J Physiol* 265(1993):E162–75.
- Hovorka, R., E. Koukkou, D. Southerden, J. K. Powrie and M. A. Young. Measuring prehepatic insulin secretion using a population model of C-peptide kinetics: accuracy and required sampling schedule. *Diabetologia* 41(1998):548–54.
- Licko, V. Threshold secretory mechanism: a model of derivative element in biological control. *Bull Math Bio* 35(1973):51–58.
- Licko, V. and A. Silver. Open-loop glucose insulin control with threshold secretory mechanism: analysis of intravenous glucose tolerance tests in man. *Math Biosci* 27(1975):319–32.
- Morishima, T., S. Pyc, C. Bradshaw and J. Radziuk. Posthepatic rate of appearance of insulin: measurement and validation in the nonsteady state. *Am J Physiol* 263(1992):E772–79.
- Polonsky, K. S., J. Licinio-Paixao, B. D. Given *et al.* Use of biosynthetic human C-peptide in the measurement of insulin secretion rates in normal volunteers and type I diabetic patients. *J Clin Invest* 77(1986):98–105.
- Polonsky, K. S., B. D. Given and E. Van Cauter. Twenty four profiles and pulsatile patterns of insulin secretion in normal and obese subjects. *J Clin Invest* 81(1988):442–48.
- Rescigno, A. and E. Gurdipde. Estimation of average times of residence, recycle, and interconversion of blood-borne compounds using tracer methods. *J Clin Endocrinol Metab* 36(1973):263–76.
- Shapiro, E. T., H. Tillil, A. H. Rubinstein and K. S. Polonsky. Peripheral insulin parallels changes in insulin secretion more closely than C-peptide after bolus intravenous glucose administration. *J Clin Endocrinol Metab* 67(1988):1094–99.
- Sparacino, G. and C. Cobelli. Impulse response model in reconstruction of insulin secretion by deconvolution: role of input design in the identification experiment. *Ann Biomed Eng* 25(1997):398–416.
- Sherman, A. Contribution of modeling to understandings stimulus-secretion coupling in pancreatic beta cells. *Am J Physiol* 271(1996):E362–72.
- Tillil, H., E. T. Shapiro, M. A. Miller *et al.* Dose-dependent effects of oral and intravenous glucose on insulin secretion and clearance in normal humans. *Am J Physiol* 254 (1988):E349–57.

- Toffolo, G., F. De Grandi and C. Cobelli. Estimation of beta cell sensitivity from IVGTT C-peptide data. Knowledge of the kinetics avoids errors in modeling the secretion. *Diabetes* 44(1995):845–54.
- Toffolo, G., A. Arduini, N. De Zanche, A. Avogaro and C. Cobelli 1997. A minimal model of insulin during insulin modified IVGTT: assessment of hepatic insulin extraction. In: *Proceedings of 3rd IFAC Symp. on Modelling and Control in Biomedical Systems*. Edited by D. A. Linkens and E. R. Carson. Oxford: Elsevier, pp. 91–5.
- Toffolo, G., M. K. Cavaghan and C. Cobelli. Quantitative indices of beta cell function during graded glucose infusion. *Diabetes* 47 (suppl. 1)(1998): A254.
- Toffolo, G., W. Cefalu and C. Cobelli. 1999. Beta cell function during insulin modified IVGTT successfully assessed by the C-peptide minimal model. *Metabolism* 48(1999):1162–66.
- Van Cauter, E., F. Mestrez, J. Sturie and K. S. Polonsky. Estimation of insulin secretion rates from C-peptide levels. Comparison of individual and standard kinetic parameters for C-peptide clearance. *Diabetes* 41(1992):368–77.
- Yang, Y. J., J. H. Youn and R. N. Bergman. Modified protocols improve insulin sensitivity estimation using the minimal model. *Am J Physiol* 253(1987):E595–602.

This Page Intentionally Left Blank

# Glucose Modelling

**Andrea Caumo, Monica Simeoni, and Claudio Cobelli**

## 12.1. INTRODUCTION

In this chapter we present a survey, deliberately synthetic and not intended to be exhaustive, of models that describe the glucose system and the control exerted by insulin on glucose production and utilisation. This chapter is complementary to Chapter 11 which discusses models developed to study the insulin system and the control exerted by glucose on insulin secretion.

A scheme of the glucose subsystem is shown in Figure 12.1. The glucose production and utilisation fluxes, with the control signals exerted by insulin and glucose on these fluxes, are represented. Our aim is to present the main features of the models that are used to quantitate glucose kinetics both at the whole-body and regional (organ/tissue) level and under steady- and nonsteady state conditions. We also provide some examples of models allowing the estimation of indexes of clinical relevance. Finally, we discuss the use of simulation models both to gain insight into the functioning of the glucose system and to aid in the optimisation of diabetes therapy.

## 12.2. MODELS OF WHOLE-BODY KINETICS IN STEADY STATE

Understanding the glucose system at the whole-body level requires the quantitation of processes that are not directly measurable because they occur in the nonaccessible portion of the system. (Cobelli and Caumo, 1998). What can be detected is the effect in the accessible pool, usually plasma, where glucose and insulin concentrations can be measured. To relate the accessible pool measurements with events occurring in the nonaccessible portion of the



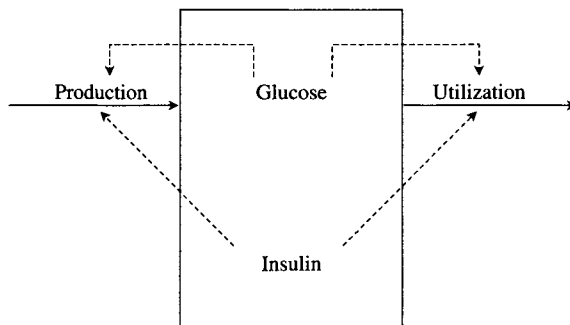


**Figure 12.1.** A schematic representation of the glucose subsystem. Continuous lines represent fluxes of material, and dashed lines represent control signals.

system, we need a model. In this section, we present models developed to study the glucose system in the steady state, which means when the glucose masses and fluxes are constant in time.

In the steady state, the only available measurement of glucose concentration in the blood (glycaemia) is of limited use. In fact, since glycaemia is the result of the dynamic equilibrium between glucose production and utilisation (turnover), two subjects may have the same glycaemia, but different turnover. To measure glucose turnover and other system parameters, it is necessary to generate dynamic data with the help of a tracer. As already discussed in Chapter 6, an ideal tracer behaves like the mother substance (tracee), is detectable by the investigator, and does not perturb the system. The use of a tracer is advantageous because its kinetics can be interpreted by a model that is simpler than that of the tracee. In fact, while the plasma tracee concentration reflects both production and kinetics (i.e., distribution and metabolism), the plasma concentration of the tracer, which is not produced endogenously, reflects only kinetics. Let us now imagine that an input-output (I/O) experiment has been performed by administering a certain tracer quantity, such as a rapid intravenous injection. This input (which can be schematised as an impulse) generates a tracer washout curve in plasma that can be interpreted as the system impulse response. What are the features of this impulse response? In the steady state, the tracer impulse response is that of a linear time-invariant system, even if the system is intrinsically nonlinear. It can be described as the sum of a number of decaying exponentials. For the glucose system, the tracer impulse response,  $h$ , is well described by the sum of three exponentials:

$$h(t) = g(t)/d = A_1 e^{-\lambda_1 t} + A_2 e^{-\lambda_2 t} + A_3 e^{-\lambda_3 t} \quad (12.1)$$

where  $g(t)$  is the plasma tracer concentration and  $d$  is the injected tracer dose.

The mean values of parameters  $A_i$  and  $\lambda_i$  in humans in the basal steady state (Cobelli *et al.*, 1984) are  $A_1 = 0.015$ ,  $A_2 = 0.0026$ ,  $A_3 = 0.0034$  kg/ml;  $\lambda_1 = 1.64$ ,  $\lambda_2 = 0.090$ ,  $\lambda_3 = 0.0093$  min<sup>-1</sup>. The most rapid exponential,  $\lambda_1$ , can be detected only if the tracer concentration is measured frequently in the first minutes of the experiment. In the following sections, we shall show how to analyse these data to obtain both the accessible pool and system parameters. We shall see that whereas the accessible pool parameters can be derived from tracer data in a model-independent way, modelling strategies (such as the noncompartmental and compartmental approaches) are needed to derive the system parameters.

### 12.2.1. ACCESSIBLE POOL PARAMETERS

This approach does not require hypotheses on the nonaccessible portion of the system. The accessible pool parameters are obtained by applying the mass balance equation to the accessible pool and by exploiting the tracer-tracee indistinguishability principle. These parameters include the accessible pool volume ( $V_1$ ), the clearance rate ( $CR$ ), the rate of appearance in the accessible pool ( $Ra$ ), and the rate of disappearance from the accessible pool ( $Rd$ ). In steady state, one has  $Ra = Rd$ . The mean values of these parameters for the glucose system in the basal steady state (Cobelli *et al.*, 1984) are  $V_1 = 46.5$  ml kg<sup>-1</sup>,  $CR = 2.5$  ml kg<sup>-1</sup> min<sup>-1</sup>,  $Ra = 2.15$  mg kg<sup>-1</sup> min<sup>-1</sup>. Which is the relationship between the accessible pool fluxes  $Ra$  and  $Rd$  and those of glucose production and utilisation at the whole-body level? By applying the mass balance equation to the whole glucose system one has that, in steady state, the glucose production,  $EGP$ , equals utilisation,  $U$ . Since glucose produced *de novo* enters into the blood circulation through the hepatic and renal veins,  $EGP$  coincides with  $Ra$  (plus any other exogenous glucose input, if present). Finally, in the absence of exogenous inputs,  $U$  coincides with  $Rd$ .

### 12.2.2. NONCOMPARTMENTAL MODEL

With the noncompartmental model, we begin formulating hypotheses on the nonaccessible portion of the system. This allows us to obtain parameters that pertain to the system and not only to the accessible pool. The noncompartmental model assumes that glucose can leave the accessible pool irreversibly or recirculate through other regions of the system. From the tracer washout curve we can obtain, in addition to the accessible pool parameters, important system parameters such as the mean total residence time in the system,  $MRT$ , the total distribution volume,  $V_D$ , and the total mass in the system,  $Q_D$ . The values

**Table 12.1.**  
**Parameter Values of the Noncompartmental and Compartmental Model in the Basal and in the Basal Glucose-Elevated Insulin Steady States**

Parameter	Basal State	
	Noncompartmental Model	Compartmental Model
$V_1$ (ml/kg)	46.5	46.5
$CR$ (ml/kg min)	2.5	2.5
$Ra$ (mg/kg min)	2.15	2.15
$MRT$ (min)	99.1	105.8
$V_D$ (ml/kg)	244	261
$Q_D$ (mg/kg)	222	227

Parameter	Basal Glucose and Elevated Insulin State	
	Noncompartmental Model	Compartmental Model
$V_1$ (ml/kg)	46.5	46.5
$CR$ (ml/kg min)	9.1	9.1
$Ra$ (mg/kg min)	0	0
$MRT$ (min)	22.5	36.6
$V_D$ (ml/kg)	200	333
$Q_D$ (mg/kg)	175	291

of these parameters in the basal steady state (Cobelli *et al.*, 1984) are reported in the upper portion of Table 12.1.

It is worth emphasising that the system parameters obtained with the noncompartmental model are not model-independent like those of the accessible pool. In fact, albeit the ingredients of the noncompartmental model are simply the accessible pool and the rates of appearance, disappearance, and recirculation, one must bear in mind that the noncompartmental model hinges on the assumption that the fluxes of production and irreversible removal occur solely in the accessible pool. If this hypothesis is not satisfied, the system parameters are underestimated. Is this hypothesis tenable for the glucose system? Whereas in all likelihood  $Ra$  coincides with glucose production, it is unlikely that the irreversible losses of the system, such as the insulin-dependent glucose uptake of the muscles, are all solely attributable to the accessible pool. This limitation of the noncompartmental model will be further highlighted in the following section discussing compartmental modelling.

### 12.2.3. COMPARTMENTAL MODEL

The compartmental model describes the nonaccessible portion of the system with a number of interconnected compartments. Its formulation requires the

specification of the number of compartments, their connections, the sites of input and of irreversible removal, and the mathematical description of all the functional dependencies and controls. In general, the compartmental model is described by a set of nonlinear differential equations. In the steady state, the model becomes simpler because the masses in the compartments and the fluxes between the compartments are constant over time. As a result, the fractional transfer parameters of the model,  $k_{ij}$ , are also constant and estimable from the tracer data.

Many models have been proposed to describe glucose kinetics in steady-state conditions in humans. These models differ in terms of number of compartments (2 or 3) and in terms of number and location of the irreversible losses. Instead of presenting a complete review of the available models, we focus on the model developed in Cobelli *et al.* (1984) because it exemplifies how physiology can guide the development of a compartmental model. Let us go back to the tracer experiment described previously. The presence of three exponentials in the tracer impulse response suggests the adoption of a three-compartment model. Among the possible structures, the one chosen in Cobelli *et al.* (1984) is shown in Figure 12.2. It is a mamillary model with the central compartment the accessible pool, which is where the tracer input and tracer and tracee measurements take place. The mass balance and measurement equations of the tracer and tracee systems are:

$$\begin{aligned}
 \dot{q}_1(t) &= -(k_{21} + k_{31})q_1(t) + k_{12}q_2(t) + k_{13}q_3(t) + d\delta(t) & q_1(0) &= 0 \\
 \dot{q}_2(t) &= k_{21}q_1(t) - (k_{12} + k_{02})q_2(t) & q_2(0) &= 0 \\
 \dot{q}_3(t) &= k_{31}q_1(t) - (k_{13} + k_{03})q_3(t) & q_3(0) &= 0 \\
 g(t) &= q_1(t)/V_1 \\
 \dot{Q}_1(t) &= -(k_{21} + k_{31})Q_1 + k_{12}Q_2 + k_{13}Q_3 + EGP = 0 \\
 \dot{Q}_2(t) &= k_{21}Q_1 - (k_{12} + k_{02})Q_2 = 0 \\
 \dot{Q}_3(t) &= k_{31}Q_1 - (k_{13} + k_{03})Q_3 = 0 \\
 G &= Q_1/V_1
 \end{aligned}
 \tag{12.2}$$

where  $q_i$  and  $Q_i$  are, respectively, the tracer and tracee mass in compartment  $i$ ,  $d$  is the administered tracer dose,  $g$  and  $G$  are the tracer and tracee concentration measured in plasma,  $V_1$  is the accessible compartment volume, and  $k_{ij}$  are the transfer rate parameters. We note that the tracer kinetics is described by a system of differential equations, while the tracee kinetics is described by a system of algebraic equations.

Let us briefly examine the rationale behind the choice of the sites, number, and location of irreversible removals. For further details on the physiological

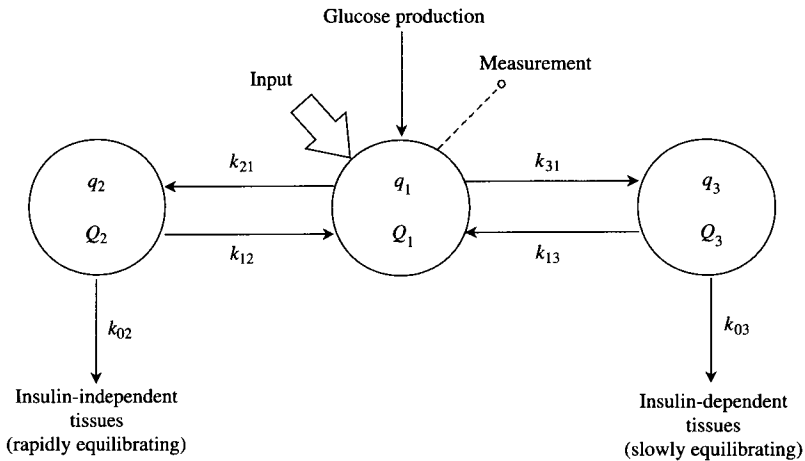
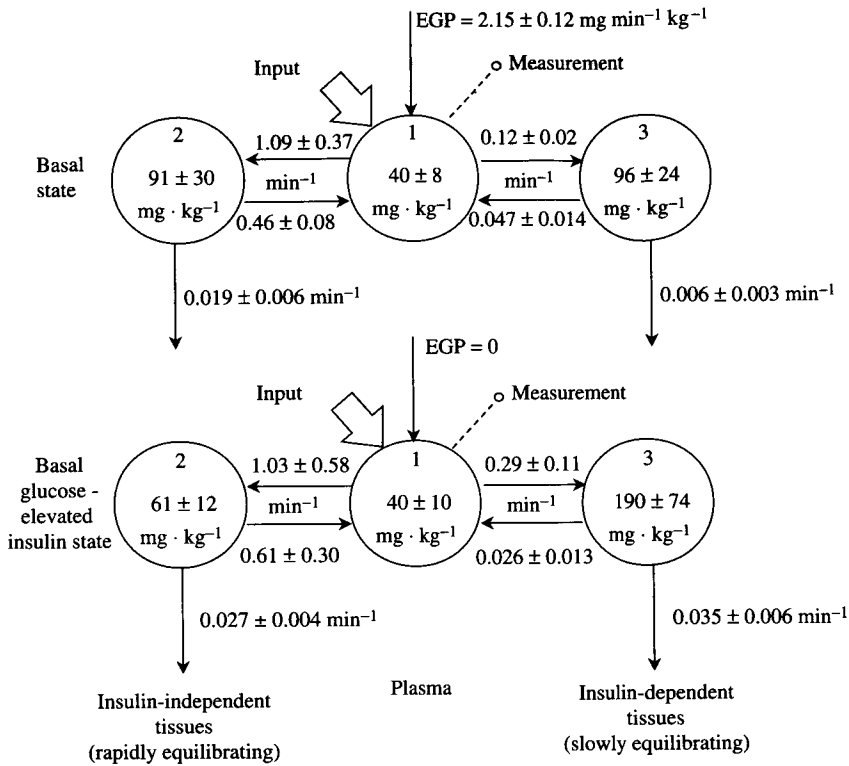


Figure 12.2. The compartmental model of glucose kinetics developed in Cobelli *et al.* (1984).

foundations of the model, see Ferrannini *et al.* (1985) and Jacquez (1992). Since the volume of the accessible pool ( $46.5 \text{ ml kg}^{-1}$ ) resembles plasma volume and glucose is not utilised in plasma, no irreversible loss takes place in the accessible pool. Compartments 2 and 3 represent peripheral compartments, respectively, in rapid and slow equilibrium with the accessible pool. Compartment 2 has been associated with tissues such as red blood cells, liver, kidneys, and central nervous system, which are in rapid equilibrium with plasma. Because these tissues consume glucose independently of insulin, the irreversible loss of compartment 2 accounts for insulin-independent glucose utilisation. Compartment 3 has been associated with tissues such as muscle and adipose tissue, which equilibrate slowly with plasma. Because the glucose utilisation in these tissues is stimulated by insulin, the irreversible loss of compartment 3 accounts for insulin-dependent glucose utilisation. The model of Figure 12.2 is *a priori* nonidentifiable but the physiological interpretation of the compartments discussed previously allows one to exploit some available physiological knowledge that guarantees its *a priori* unique identifiability. The following notion has been embodied into the model: in the basal state, the glucose utilisation by insulin-independent tissues is threefold the one by insulin-dependent tissues. This imposes the following constraint among the model parameters:

$$\frac{k_{21}k_{02}}{k_{12} + k_{02}} = 3 \left( \frac{k_{31}k_{03}}{k_{13} + k_{03}} \right) \quad (12.3)$$

By using the parameter estimation techniques described in Chapter 5 one can estimate, (e.g., by nonlinear least squares), the parameters  $k_{ij}$  and  $V_1$  from the



**Figure 12.3.** The compartmental model of Figure 12.2 identified in the basal state (*upper panel*) and in the steady state attained at the end of an euglycaemic hyperinsulinaemic clamp (*bottom panel*).

tracer data. Their basal values are shown in the upper panel of Figure 12.3. By substituting these parameters into the tracee algebraic equations, one can calculate glucose production, glucose utilisation, glucose fluxes between compartments, and glucose masses in compartments. It is worth noting that the model also provides all the parameters yielded by the accessible pool approach and by the noncompartmental model. The values of some of them are shown in the upper portion of Table 12.1.

The fact that the impulse response of the system (12.1) is characterised by a very fast exponential term (time constant of about 0.6 min) translates into high values of the rate constants  $k_{21}$  and  $k_{12}$ , whose values are, respectively, 1.1 and  $0.5 \text{ min}^{-1}$ . This means that compartment 1 (the accessible pool) and compartment 2 exchange so rapidly that it is quite reasonable to formulate a reduced version of the model having these two compartments aggregated into

a single compartment. In fact, if we neglect the early tracer data, say those collected in the first 2 to 3 minutes after the injection, it is not possible to resolve from the data the rapidly exchanging compartment 2, and one identifies a two-compartment model in which the accessible pool now has a volume greater than plasma ( $158 \text{ ml/kg}^{-1}$ ) and an irreversible loss that accounts for insulin-independent glucose utilisation. We discuss this model again when dealing with the models used to analyse the nonsteady state.

There is no doubt that the analysis of tracer data by a compartmental model provides a detailed description of glucose kinetics in the steady state. However, one must bear in mind that this description refers to a specific condition of the glucose system (e.g., the basal state following an overnight fast). This description is exhaustive only if the system is intrinsically linear, such as the C-peptide system discussed in Chapter 11. On the contrary, if the model is intrinsically nonlinear, like the glucose system, a basal study will tell us nothing about the system functioning away from this operating point. It is therefore necessary to move from the basal state to characterise glucose nonlinearities and controls; but how? One possibility is to perturb the system, for instance, with exogenous glucose, and interpret the data following the perturbation with a nonsteady state model explicitly accounting for the system nonlinearities and controls that we intend to quantify. We discuss this strategy later when dealing with nonsteady state and control system models.

An alternative approach that allows characterisation of glucose nonlinearities and controls, and simultaneously presenting relative simplicity of steady-state modelling, consists of repeating the tracer experiment after bringing the system to a new steady state by a suitable experimental protocol. An example is given of how such a strategy can be profitably used to investigate the effects of insulin on glucose kinetics. Using the euglycaemic hyperinsulinaemic clamp technique, we can bring the glucose system to a new steady state characterised by basal glycaemia and elevated insulin. By identifying the model from tracer data in both steady states, one obtains two parametric pictures that provide insight into the effects of insulin on glucose metabolism. In Figure 12.3, the two model parameterisations obtained in the basal state and in the elevated insulin state are shown. If one compares the parameter values in the two steady states, an insulin effect on the rate constants into and out of compartment 3 (which accounts for insulin-dependent tissues) is detected. In fact, not only parameter  $k_{03}$ , which describes insulin-dependent irreversible removal, increases, but also the exchange parameters with the accessible pool,  $k_{31}$  and  $k_{13}$ , increase and decrease, respectively.

One may wonder what the relationship is between the parameters obtained with the noncompartmental and the compartmental model in the two steady states. Table 12.1 contains the most significant parameters, which can be calculated with both the approaches. One realises that the accessible pool parameters

are exactly the same, while the system parameters, such as  $MRT$ ,  $V_D$ , and  $Q_D$ , are lower when calculated with the noncompartmental model. This discrepancy is due to the fact that when the irreversible losses are not all located in the accessible pool, the noncompartmental model underestimates these parameters (Di Stefano, 1982). Of note is that the difference between the  $MRT$ ,  $V_D$ , and  $Q_D$  estimates obtained with the two approaches increases in the hyperinsulinaemic study. This occurs because as insulin concentration increases, the relative weight of the insulin-dependent irreversible loss (located in the nonaccessible pool) vs. the insulin-independent one increases.

The model discussed previously can provide only an aggregated description of detailed events such as glucose distribution in the interstitial fluid, glucose transport into and out of the cell, and intracellular glucose phosphorylation. It is possible to selectively study insulin action on glucose distribution into interstitial fluids by administering an analogue glucose tracer, L-[ $^{14}\text{C}$ ]glucose, which distributes in the interstitial fluid similar to glucose but does not enter into the cell. By interpreting the L-[ $^{14}\text{C}$ ]glucose washout curve with a compartmental model in the basal and in the hyperinsulinaemic steady state, it is possible to quantify the insulin effect on extracellular glucose distribution. This technique has shown in rat (Youn *et al.*, 1995) and dog (Steil *et al.*, 1996) studies that the intercompartmental rate constants are not affected by insulin. This suggests that insulin, at least in these animal species, does not significantly influence glucose distribution in the interstitial fluid and only enhances glucose transport into the cell.

The understanding of insulin effect on glucose kinetics can be deepened if additional nonplasma measurements become available. For instance, the lymph compartment is accessible in animals. Since the lymph system consists of vessels draining the interstitial fluid, the measurement of tracer concentration in the lymph provides information on the modalities of glucose distribution in the interstitial fluid. This allows the investigator to put on a more solid basis the identification of physiological correlates of the compartments of the whole-body model. For example, in the dog study (Steil *et al.*, 1996), the L-[ $^{14}\text{C}$ ]glucose washout curve has been interpreted with a mamillary model in which the central plasma compartment exchanges with three compartments, respectively, rapid, intermediate, and slow (it is worth noting that glucose kinetics in dogs is faster than in humans and that the dog intermediate compartment is comparable to the human slow compartment). The L-[ $^{14}\text{C}$ ]glucose dynamics, predicted by the model in the remote compartments, has been compared with the tracer concentration measured in the lymph draining the interstitial fluid of leg muscles. The results indicate that the tracer lymph pattern is in accordance with that predicted by the model intermediate compartment, which has thus been identified with the muscle tissue.



A similar strategy has been adopted in a study undertaken in sheep (Gastaldelli *et al.*, 1997) to test the hypothesis that the interstitial fluid, assumed to be well reflected by the thoracic duct lymph of the animal, is representative of one or more compartments of a whole-body model. A stable isotope tracer experiment in the basal state has allowed the identification of a three-compartment model of glucose kinetics in both its mamillary and catenary versions. The predictions of the tracer dynamics in the rapid and slow peripheral compartments have been correlated with the tracer-to-tracee ratio measured in the lymph. The results indicate that the tracer-to-tracee ratio profile in the lymph is in accordance with that predicted by the model in the rapidly exchanging compartment, independently of the mamillary or catenary structure. Because the thoracic duct lymph reflects the lymph of both hepatic and gastrointestinal tissues, which are tissues more highly perfused than muscle and adipose tissues, it is reasonable to assume that the rapid compartment of the model is representative of highly perfused tissues, a notion consistent with the model structure postulated in humans.

### 12.3. MODELS OF REGIONAL KINETICS IN STEADY STATE

Whole-body measurements cannot provide a reliable description of glucose processes at the regional level. To quantify kinetic events at an organ or tissue level, it is necessary to perform kinetic studies at the regional level. These studies meet with obvious difficulties in humans but are feasible in the animal. Another possibility is to work *in vitro* or with isolated perfused organs. To estimate production and utilisation of a substance at the regional level in steady state, one can infuse a tracer and apply Fick's principle. Let us consider, for instance, the problem of quantitating glucose metabolism in the splanchnic region (Figure 12.4). By inserting a catheter in the artery and another in the hepatic vein, one can measure the arterial and venous glucose,  $G_a$  and  $G_{hv}$ , and tracer glucose,  $g_a$  and  $g_{hv}$ , concentrations following a constant tracer infusion. If hepatic blood flow,  $\Phi$ , is also measured, one can calculate glucose utilisation,  $U$ , and production,  $P$ , in the splanchnic area as:

$$U = \Phi(g_a - g_{hv}) \frac{G_a}{g_a} \quad (12.4)$$

$$P = U + \Phi(G_a - G_{hv})$$

This method has been employed in various districts and has allowed a detailed description of glucose fluxes in the organism (Figure 12.5). What warrants emphasis is that this method does not require the postulation of a

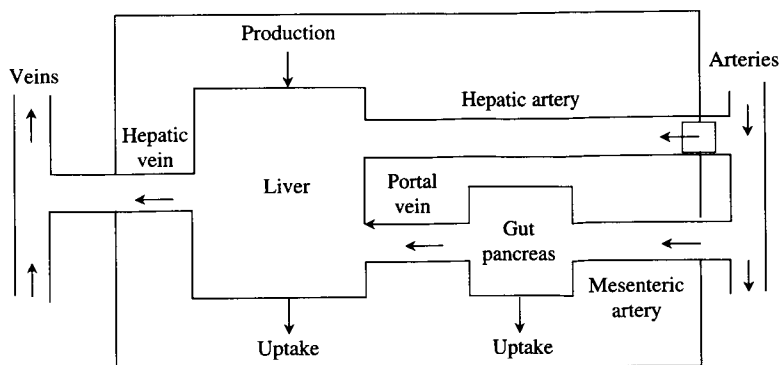


**Figure 12.4.** A schematic representation of the splanchnic region: circulation and glucose fluxes.

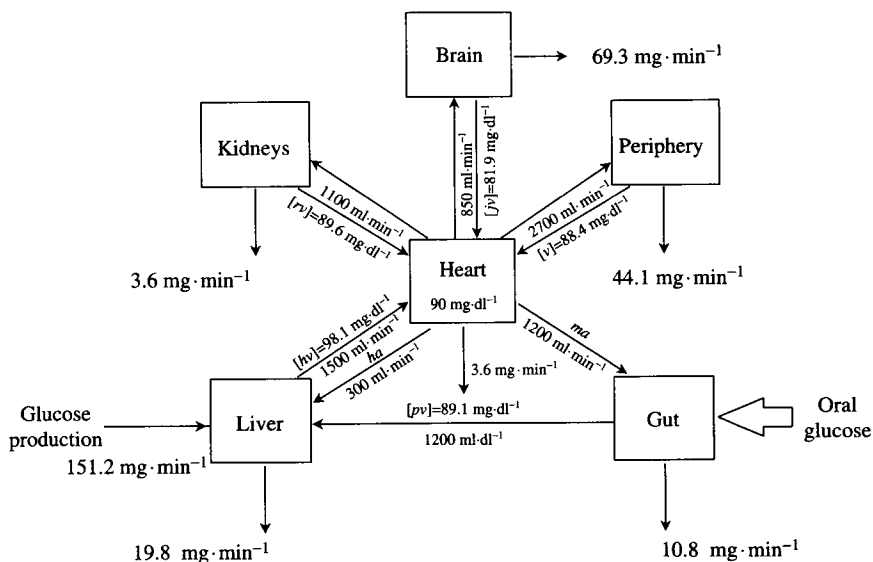


**Figure 12.5.** Glucose fluxes in a normal human in the basal state (*hv* = hepatic vein, *ha* = hepatic artery, *pv* = portal vein, *ma* = mesenteric artery, *v* = peripheral vein, *jv* = jugular vein, *rv* = right ventricle).

regional model but requires that the assumptions behind Fick's principle and tracer-tracee indistinguishability hold.

To move to a more refined level of detail and quantify, for instance, glucose transport into and out of the cell and the intracellular biochemical steps, it is necessary to postulate a regional model of glucose kinetics and

to design experiments providing dynamic data that selectively reflect these processes. The approaches that are more frequently used to study regional glucose metabolism are the residue function technique and the tracer arterio-venous balance technique. Positron emission tomography (PET) and nuclear magnetic resonance (NMR) belong to the first category, while the multiple tracer dilution technique belongs to the second. In Chapter 7 various compartmental models are discussed that allow the quantitation of regional glucose kinetics, such as in the brain, heart, and muscle, while Chapter 3 provides a detailed analysis of the multiple tracer dilution technique. In the following paragraph, we focus on the use of the multiple tracer dilution technique for the *in vivo* measurement of glucose transport and phosphorylation in the skeletal muscle.

The multiple tracer dilution technique consists of the simultaneous injection of tracers with different molecular characteristics at the organ inlet (artery) and on the measurement of their washout curves at one of the organ outlets (vein). The key idea is that different tracers help to distinguish the individual contribution of the unit processes of regional glucose kinetics, or vascular distribution, diffusion in the extracellular space, transport into and out of the cell, and intracellular phosphorylation (Figure 12.6). This technique has been employed by Saccomani *et al.* (1996) to study transport and metabolism of glucose in the forearm muscle tissue. The forearm muscle tissue is chosen for various reasons: the forearm muscle well represents the skeletal muscle, arteries and vein are easily accessible to measurement, and blood flow is less than 1% of cardiac outputs thus making tracer recirculation negligible. The experimental protocol consists of the simultaneous injection in the brachial

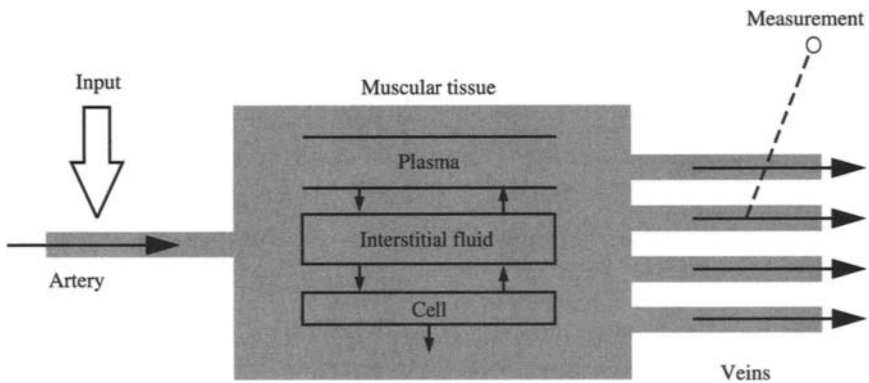


**Figure 12.6.** The multiple tracer dilution technique to quantify glucose transport and phosphorylation in the muscle tissue. Three tracers are simultaneously injected at the arterial inlet of the organ and their washout curves are measured at the venous outlet (see Figure 12.7).

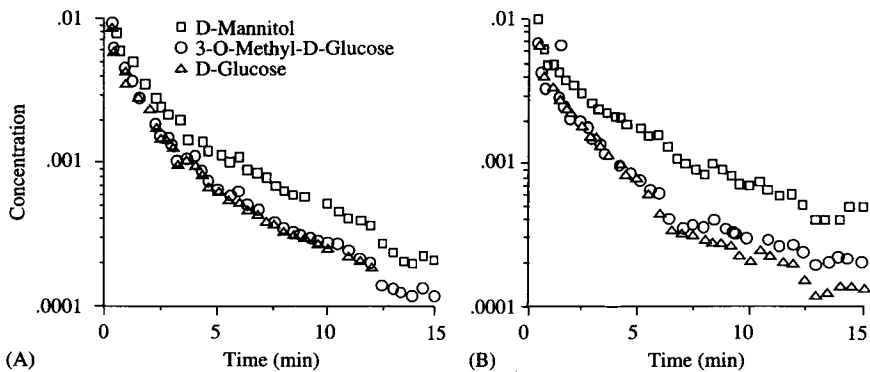


**Figure 12.7.** Washout curves of the three tracers used for measuring glucose transport and phosphorylation in the human skeletal muscle in the basal (*left panel*) and in the hyperinsulinaemic (*right panel*) state.

artery of the subject of three tracers: 1) an extracellular tracer that cannot be transported into the cell (D-[ $^{12}\text{C}$ ]mannitol); 2) a tracer that is transported into and out of the cell but is not metabolised (3-O-[ $^{14}\text{C}$ ]methyl-D-glucose); and 3) a tracer that enters into the cell and is metabolised (D-[3- $^3\text{H}$ ]glucose). The washout curves of the three tracers are shown in Figure 12.7. It is easy to realise that the “difference” between the concentrations of the first two tracers contains information on glucose transport into the cell, and only on that. In fact, mannitol diffuses in the extracellular space but does not enter into the cell, whereas methyl-D-glucose enters into the cell but is not phosphorylated. Similarly, the “difference” between the concentrations of methyl-D-glucose and tritiated glucose contains information on intracellular phosphorylation.

The washout curves of the three tracers are analysed with the compartmental model shown in Figure 12.8, which describes the blood flow heterogeneity in the forearm, glucose transport into the cell, and phosphorylation. Compartments 1 and 8 represent, respectively, the sites of injection (brachial artery) and of measurement (deep vein), while compartment 15 represents red blood cells. Blood flow heterogeneity in the forearm is described by means of three compartmental chains (2–3, 4–5, and 6–7), each of which is characterised by a different transit time, low, intermediate, and high. Compartments 9 through 14 represent the intracellular space, and each of them is attached to an extracellular compartment, so that the transport rate constants,  $k_{\text{in}}$  and  $k_{\text{out}}$ , represent, respectively, the transport into and out of the cell. The tracer irreversible losses occur in the input and output compartments, in the erythrocyte pool, and in the cellular compartments. Compartments 1 and 8 losses account for the fact that, for each tracer, only a fraction of the injected

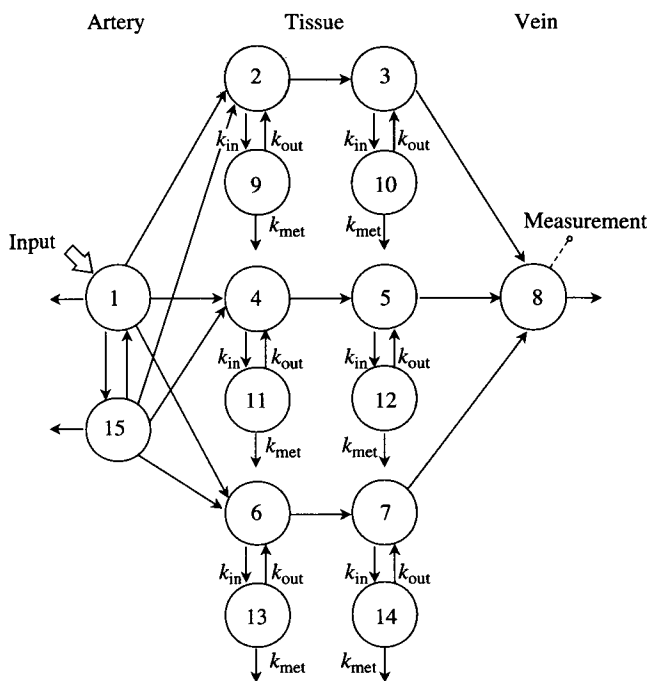


**Figure 12.8.** The compartmental model proposed in Saccomani *et al.* (1996) to measure glucose transport and metabolism in the human skeletal muscle. The model is used to interpret the washout curves of Figure 12.7.

dose reaches the measurement compartment. The intracellular compartment losses,  $k_{met}$ , apply only to D-[3- $^3$ H]glucose and describe glucose phosphorylation. Once the tracer model has been identified, the tracee model also can be quantified if blood flow is simultaneously measured. The metabolic portrait provided by the model is particularly rich; one can calculate the extracellular and intracellular glucose masses, the inward and outward transmembrane glucose fluxes, and the extracellular and intracellular volumes and concentrations.

This regional model has been employed to assess insulin action on glucose transport and phosphorylation in muscle in various physiopathological studies, particularly in non-insulin-dependent diabetic subjects (Bonadonna *et al.*, 1996). The results obtained in the basal and in the hyperinsulinaemic state indicate that the mechanisms by which insulin stimulates glucose transport is asymmetric, which means the inward flux increases more than the outward flux, and that, in diabetic patients, the insulin effects on both transmembrane transport and phosphorylation are impaired.

## 12.4. MODELS OF WHOLE-BODY KINETICS IN NONSTEADY STATE

In nonsteady state, glucose production and utilisation (and thus plasma glucose concentration) vary in time. This is a condition that occurs many times during a day, such as during a meal or exercise. The quantitative study of the glucose system in nonsteady state is important because it sheds light on the control mechanisms that guarantee homeostasis. However, it is also more challenging than the steady state. For example, even the accessible pool fluxes  $Ra$  and  $Rd$ , which are model-independent in steady state, become model-dependent in nonsteady state. Hereafter, we discuss the most common models employed for estimating glucose production and utilisation in nonsteady state.

### 12.4.1. GLUCOSE PRODUCTION

In the nonsteady state, the glucose system can be interpreted as a linear time-varying system, thus characterised by an impulse response  $h(t, \tau)$ . The relation that links the unknown input in accessible pool,  $Ra$ , to glycaemia,  $G(t)$ , is given by the convolution integral:

$$G(t) = \int_{-\infty}^t h(t, \tau) Ra(\tau) d\tau \quad (12.5)$$

The estimation of glucose production in the nonsteady state can thus be considered as an input estimation problem and is usually solved in two steps. First, the glucose time-varying impulse response is identified. Second, the integral equation (12.5) is solved by resorting to deconvolution techniques. Such techniques are discussed in Chapter 3. How can  $h(t, \tau)$  be assessed? Since  $h(t, \tau)$  is time-varying, it is not possible to describe it by using a multiexponential model (as is the case, for instance, for the C-peptide system, which exhibits linear and time-invariant kinetics discussed in Chapters 3 and 11). For the glucose system, it is necessary to formulate a structural model capable of describing the system functioning in the nonsteady state. In particular, it is necessary to specify which are the time-varying parameters of the model and how they change during the nonsteady state. The model is identified from the tracer data generated by administering a tracer during the nonsteady state. It is easy to realise that different models will produce different estimates for  $Ra$ .

The models that are most frequently used to describe the glucose system in the nonsteady state are those proposed by Steele (1956) and Radziuk *et al.* (1978). Steele's model (1956) is monocompartmental (Figure 12.9) and has a

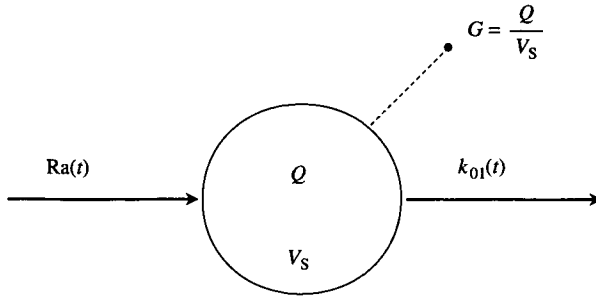


**Figure 12.9.** The monocompartmental model proposed by Steele (1956) for describing glucose kinetics in the nonsteady state.

time-varying irreversible loss,  $k_{01}(t)$ , whose time course can be derived from tracer data. The unknown  $Ra$  can be easily obtained as follows:

$$Ra(t) = \frac{\left[ Ra^*(t) - pV_D G(t) \frac{dZ(t)}{dt} \right]}{Z(t)} \quad (12.6)$$

The ingredients of Steele's model estimate of  $Ra$  are thus the tracer infusion rate  $Ra^*$ , the measured plasma tracer-to-tracee ratio  $Z = g/G$ , where  $G$  and  $g$  are, respectively, the glucose and the tracer glucose concentration (for a radioactive tracer  $Z$  coincides with specific activity) and the whole-body mass of glucose, which is obtained by multiplying the plasma glucose concentration  $G$  times the volume of Steele's model,  $V_S$ , a fraction  $p$  (usually referred to as pool fraction) of the total glucose distribution volume,  $V_D$ . The rationale for this choice is to use a volume being halfway between the plasma and the total volume so as to allow Steele's model to surrogate a more complex system. For glucose, the generally chosen value of  $p$  is 0.65 and since  $V_D$  is about  $260 \text{ ml/kg}^{-1}$ , one has that  $V_S$  is approximately  $170 \text{ ml/kg}^{-1}$ . It is of interest to note that  $V_S$  is close to the volume ( $158 \text{ ml/kg}^{-1}$ ) that is obtained by aggregating in the model of Figure 12.2 the plasma pool in compartment 1, and the rapidly equilibrating tissues in compartment 2.

The simplicity of Steele's model and its ease of use account for its diffusion and popularity. However, several results are available in the literature that question its reliability. For instance, in euglycaemic hyperinsulinaemic clamp studies Steele's model provides negative, and thus physiologically absurd, values of glucose production in the final part of the experiment. During the intravenous glucose tolerance test (IVGTT), Steele's model predicts an initial stimulation of glucose production instead of a marked inhibition, as physiological knowledge would suggest. The inadequacy of Steele's model has been

subjected to theoretical analysis (Cobelli *et al.*, 1987), which has shown that Steele's model error can be split into two components: a volume component depending on  $V_S$  and a structure component due the monocompartmental approximation. Both these errors are functions of time and depend on the tracer-to-tracee ratio during the experiment. The more rapidly the tracer-to-tracee ratio changes, the bigger the error introduced by the model in estimating glucose production.

The model introduced by Radziuk *et al.* (1978) has a bicompartamental structure. It has been proposed in two versions (Figure 12.10). The first one has a single irreversible loss in the accessible pool,  $k_{01}(t)$ , and the second one has two equal losses in both compartments ( $k_{01}(t) = k_{02}(t)$ ). The use of this model requires the preliminary estimation of  $V_1$ ,  $k_{21}$  and  $k_{12}$ , and of the steady-state value of  $k_{01}$  ( $k_{01} = k_{02}$  in the second model version). These parameter estimates can be obtained from a tracer experiment performed in the steady state that precedes the nonsteady state perturbation. The time course of  $k_{01}(t)$

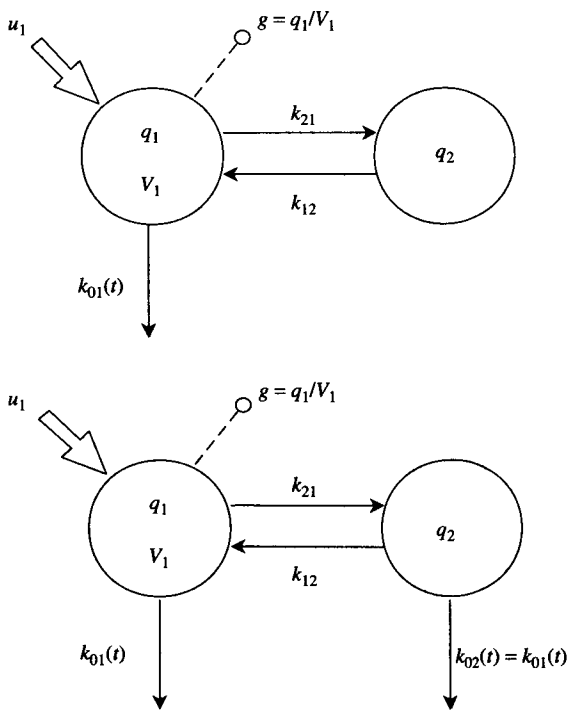


**Figure 12.10.** The two-compartment models proposed by Radziuk *et al.* (1978) for describing glucose kinetics in the nonsteady state.



is estimated from the tracer data measured during the nonsteady state. It has been shown that the model of Radziuk *et al.* is more accurate than Steele's model, and evidence has been provided that the two model versions give substantially equivalent results. However, the performance of the Radziuk *et al.* model is not always satisfactory, and margins for improvement exist.

The formulation of a more accurate model is possible only in specific situations because system complexity and the experimental limitations prevent the development of a model of general validity. One of these favourable situations is the euglycaemic hyperinsulinaemic clamp. We have previously seen that a physiological model of glucose kinetics can be identified in the basal steady state and at the end of the clamp when a new steady state, characterised by basal glucose and elevated insulin, is achieved. Once the system has been quantified in its initial and final conditions, one can describe the transition between the two steady states by allowing the model parameters to change gradually from their initial value to their final value. Figure 12.11 shows the two-compartment model obtained from the three-compartment model in Figure 12.2 by aggregating plasma (compartment 1) with rapidly equilibrating tissues (compartment 2). The irreversible loss in the accessible pool accounts for insulin-independent utilisation, while that in the second compartment is responsible for insulin-dependent utilisation. The time-varying parameters are  $k_{02}$ ,  $k_{21}$ , and  $k_{21}$ . The time course in the transition phase is described by sigmoidal functions, whose parameters are estimated from the tracer data. The time course of glucose production provided by this model is more physiological than that provided by Steele's and Radziuk *et al.*'s models. In particular, it never assumes negative values and declines slowly and progressively, reaching a value close to zero only toward the end of the test (Cobelli *et al.*, 1987).

The presence of three time-varying parameters makes this model difficult to apply to experimental situations different from the euglycaemic hyperinsulinaemic clamp. Also, in clamp studies, one must ensure that the tracer is administered to allow the estimation of the basal and final model configurations. A simplified version of this model has been proposed to interpret glucose kinetics during an IVGTT. This test consists of a rapid injection into a vein of a standard glucose dose ( $330 \text{ mg kg}^{-1}$ ) and of the measurement of plasma glucose and insulin concentrations in the following 3 hours. The IVGTT can also be labelled by administering a tracer dose together with the glucose dose (Cobelli *et al.*, 1997). In Figure 12.12, plasma glucose, insulin, and tracer glucose concentrations measured during a stable isotope labelled IVGTT are shown (Avogaro *et al.*, 1989). Once the glucose impulse response (time-varying) is estimated from the tracer washout curve, one can estimate glucose production from glucose concentration by deconvolution. The two-compartment model in Figure 12.13 has been used to interpret the tracer disappearance curve during a labelled IVGTT (Caumo and Cobelli, 1993).

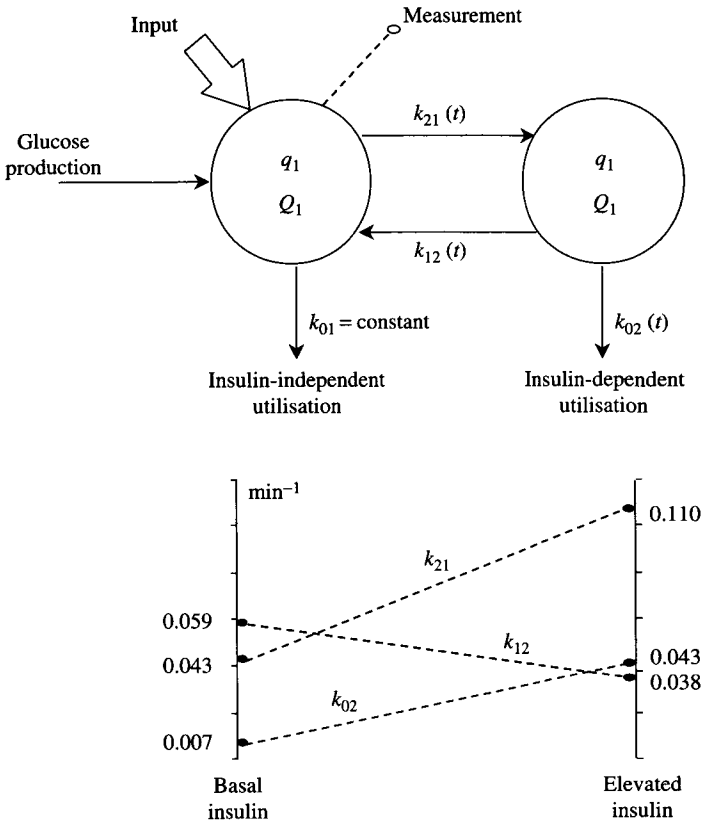


**Figure 12.11.** The two-compartment model obtained from the three-compartment model of Figure 12.2 by aggregating the plasma and the rapidly equilibrating tissues. The model describes the transition between the basal state and the final state of an euglycaemic-hyperinsulinaemic clamp with three time-varying parameters,  $k_{02}$ ,  $k_{12}$ ,  $k_{21}$ , which change gradually from their initial value to their final value.

To guarantee *a priori* model identifiability, we assume there is only one insulin-dependent parameter, or irreversible loss from the nonaccessible compartment,  $k_{02}$ . The time course of  $k_{02}$  during the IVGTT is controlled by insulin in the remote compartment,  $x$ . For this reason, the model also is able to quantify tissue insulin sensitivity, as is shown later when discussing the so-called minimal models. The glucose production profile obtained with this model by deconvolution (Caumo and Cobelli, 1993) is much more reliable than the one obtained with Steele’s model. Instead of the paradoxical stimulation of glucose production after the glucose bolus, one has a marked inhibition in keeping with physiology. It is worth emphasising that this model-based

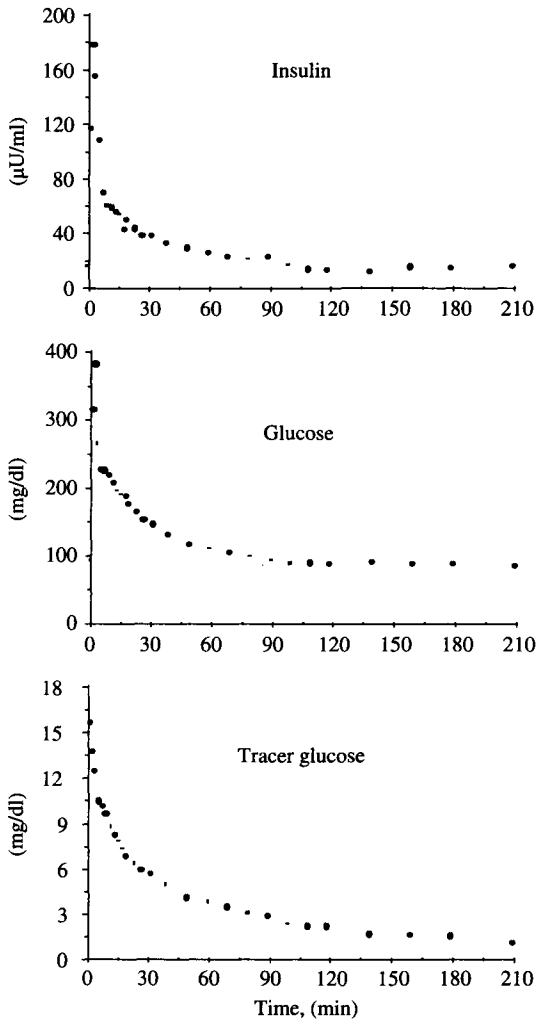


**Figure 12.12.** The labelled intravenous glucose tolerance test (IVGTT). Insulin, glucose, and tracer glucose concentrations measured in plasma during the test are shown.

approach for the estimation of hepatic glucose production during the IVGTT has been validated (Vicini *et al.*, 1999) against a model-independent approach based on the tracer-to-tracee ratio clamp (discussed in Chapter 6) as shown in Figure 12.14.

We hope these examples have clarified that there are limits to the accuracy with which a model can describe the glucose system in nonsteady state.

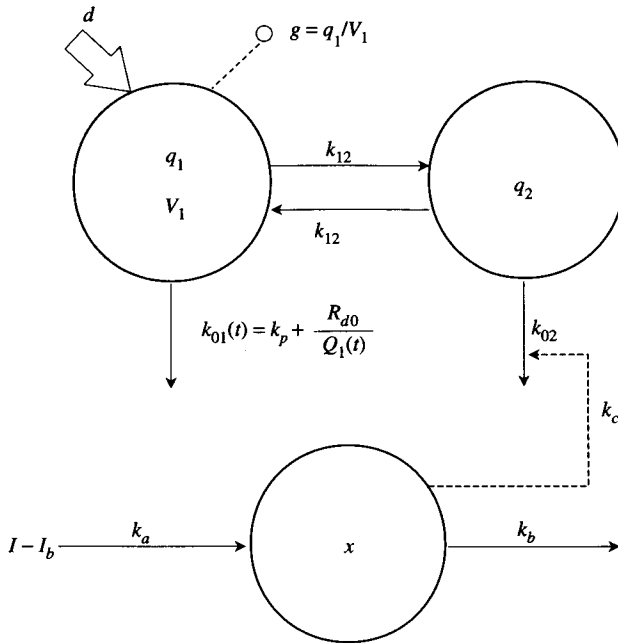


**Figure 12.13.** The two-compartment model proposed in Caumo and Cobelli (1993) and Vicini *et al.* (1997) for describing tracer kinetics during a labelled IVGTT.

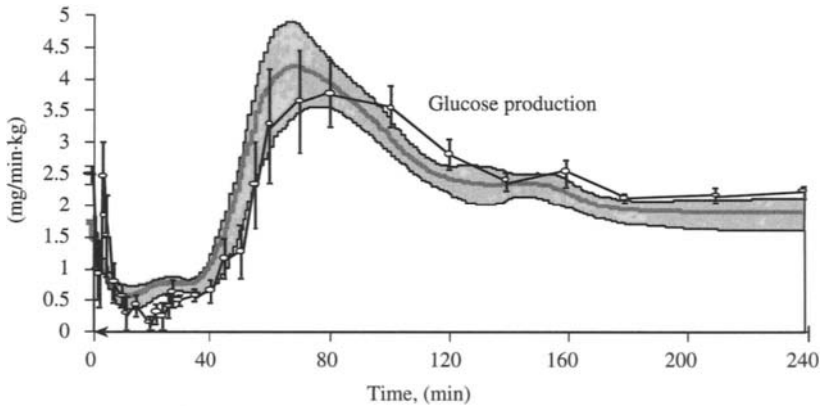


**Figure 12.14.** Glucose production during an IVGTT. The continuous-line profile is the one estimated with its confidence interval (grey area) by deconvolution with the two-compartment model of Figure 12.13; the piecewise continuous-line profile with the error bars is the one obtained with the tracer-to-tracee ratio clamp technique.

However, it is always possible to improve the accuracy of  $Ra$  estimation by suitably choosing the tracer administration format during the nonsteady state. In fact, the nonsteady state error associated to an approximate description of the system impulse response can be minimised by infusing the tracer in such a way so as to reduce the changes in the tracer-to-tracee ratio (or specific activity if a radioactive tracer is employed). Ideally, if the tracer infusion is such as to maintain the tracer-to-tracee ratio perfectly constant, the  $Ra$  estimation becomes model-independent, as in steady state. Even if this will not usually be the case, an “intelligent” tracer infusion capable of avoiding abrupt variations of the tracer-to-tracee ratio will allow an estimation of  $Ra$  that is more accurate and less dependent on the validity of the chosen model. This issue is discussed in detail in Chapter 6.

### 12.4.2. GLUCOSE UTILIZATION

Glucose utilisation is the sum of all glucose fluxes leaving irreversibly the system. In the nonsteady state, it is given by:

$$U(t) = \sum_{i=1}^n k_{0i}(t)Q_i(t) \quad (12.7)$$

where  $n$  is the number of compartments of the model describing the system, and  $k_{0i}$  and  $Q_i$  are, respectively, the fractional elimination rate and glucose mass in compartment  $i$ . It is worth noting that, whereas in the steady state the estimation of  $U$  is model-independent, in the nonsteady state it becomes model-dependent. For example, during an euglycaemic hyperinsulinaemic clamp in which the glucose mass is maintained constant in the accessible pool, the models of Radziuk *et al.* shown in Figure 12.10 and the two-compartment model of Figure 12.11 will yield different predictions of  $U$  during the transition from the basal state to the elevated insulin state. This happens because each model predicts a different profile of glucose mass in the second compartment (Mari *et al.*, 1994).

What is the relationship between  $U$  and glucose disappearance rate from the accessible pool,  $Rd$ , in the nonsteady state? First of all, it is important to realise that in the nonsteady state,  $Rd$  does not coincide with  $Ra$ :

$$Rd(t) = Ra(t) - \frac{dQ_1(t)}{dt} \quad (12.8)$$

One can show (Caumo *et al.*, 1995) that the following relationship between  $U$  and  $Rd$  holds:

$$U(t) = Rd(t) - \sum_{i=2}^n \frac{dQ_i(t)}{dt} \quad (12.9)$$

Equations (12.8) and (12.9) tell us that the estimation of  $Rd$  is much less problematic than that of  $U$ . In fact, while the estimation of  $U$  requires the knowledge of the derivatives of glucose mass in all the compartments, the estimation of  $Rd$  requires only knowledge of the derivative of glucose mass in the accessible pool. Assuming that  $Ra$  has been estimated accurately, such as by resorting to the tracer-to-tracee ratio clamp,  $Rd$  can also be estimated accurately if an estimate of the accessible pool volume is available. Accurate knowledge of  $Rd$  is useful because it allows one to make inferences on the behaviour of  $U$  without the need to postulate a model of the nonaccessible portion of the system. For example, if the glucose system is pushed out of its steady state by a perturbation but returns to the previous steady state, the area under  $Rd$  coincides with that under  $U$  (Caumo *et al.*, 1995).

## 12.5. MODELS OF GLUCOSE AND INSULIN CONTROL ON GLUCOSE METABOLISM

In physiopathology, it is of the utmost interest to measure indexes characterising the control that glucose and insulin exert on glucose metabolism. These interactions are usually denoted as glucose effectiveness and insulin sensitivity. Hereafter, we will give the formal definitions of these indexes and discuss how they can be measured from experimental data in both steady and nonsteady state.

### 12.5.1. GLUCOSE EFFECTIVENESS

Glucose effectiveness measures the effect that glucose exerts on  $Rd$  and  $EGP$  (Best *et al.*, 1996). Ideally, glucose effectiveness should be measured in the absence of insulin. However, due to the difficulty in creating this experimental condition, glucose effectiveness is usually measured at basal insulin concentration. It is of interest to note that glucose effectiveness becomes of crucial importance in those diabetic subjects who, due to a severely impaired pancreatic function, have circulating insulin levels not too different from basal levels, even after a glucose stimulus. Glucose effectiveness,  $GE$ , is defined as the derivative of the difference between  $Rd$  and glucose production,  $EGP$ , with respect to glucose concentration,  $G$ , calculated in steady state ( $ss$ ):

$$GE = \frac{\delta[Rd(t) - EGP(t)]}{\delta G(t)} \Big|_{ss} \quad (12.10)$$

where the minus sign preceding  $EGP$  stems from the fact that glucose has an inhibitory effect on  $EGP$ . The component of glucose effectiveness measuring

the glucose effect on  $Rd$  only,  $GE^*$ , is defined as follows:

$$GE^* = \left. \frac{\delta Rd(t)}{\delta G(t)} \right|_{ss} \quad (12.11)$$

It is worth mentioning that the measurement of  $GE^*$ , at variance with that of  $GE$ , requires the administration of a tracer to estimate  $Rd$ .

### 12.5.2. INSULIN SENSITIVITY

Insulin sensitivity,  $IS$ , measures the action that insulin exerts on  $Rd$  and  $EGP$  (Bergman *et al.*, 1985). It is defined as the ability of insulin to increase glucose effectiveness:

$$IS = \left. \frac{\delta^2[Rd(t) - EGP(t)]}{\delta G(t)\delta I(t)} \right|_{ss} \quad (12.12)$$

where  $I$  denotes insulinaemia.

The component of insulin sensitivity that measures the insulin effect on  $Rd$  only,  $IS^*$ , is defined as follows:

$$IS^* = \left. \frac{\delta^2 Rd(t)}{\delta G(t)\delta I(t)} \right|_{ss} \quad (12.13)$$

Like with  $GE^*$ , the calculation of  $IS^*$  requires the administration of a tracer to estimate  $Rd$ . Now, we discuss how glucose effectiveness and insulin sensitivity can be measured in steady and nonsteady states.

### 12.5.3. STEADY-STATE MODELS

The measurement of glucose effectiveness and insulin sensitivity can be performed in the steady state by using the glucose clamp technique. Let us first focus on glucose effectiveness. Glycaemia is elevated by a stepwise increasing glucose infusion, whilst insulin is kept at its basal level. In this way, the dose-response effect of increasing glucose levels on  $Rd$  and  $EGP$  can be studied. To maintain insulin constant at its basal level, despite the increasing glucose levels, it is necessary to open the glucose-insulin feedback loop. This can be accomplished by suppressing insulin secretion with the pharmacological agent somatostatin and by replacing the basal insulin level with an exogenous intravenous insulin infusion. Each time the glucose infusion increases, one must wait for the system to reach a new steady state. In each steady state, the glucose infusion rate,  $GIR$ , compensates for the  $Rd$  increment and  $EGP$  decrement. By making reference to (12.10), the clamp-based glucose effectiveness

can be measured by calculating the slope of the straight line that describes the dose-response curve between  $GIR$  and glucose concentration:

$$GE_{(\text{clamp})} = \frac{\Delta[Rd - EGP]}{\Delta G} \Big|_{I=I_b} = \frac{\Delta GIR}{\Delta G} \Big|_{I=I_b} \quad (12.14)$$

If a tracer is concomitantly infused with glucose, one also can measure  $Rd$  in a model-independent way ( $Rd$  in steady state is an accessible pool parameter) and thus assess glucose effectiveness on glucose utilisation only,  $GE^*_{(\text{clamp})}$ . It is worth noting that the relationship between  $Rd$  and  $G$  is nonlinear, which means it saturates with increasing glucose concentrations following a Michaelis-Menten relationship. This occurs because, at each insulin level, the transporters allowing glucose to enter into the cell are finite in number. In the glycaemic range explored by the glucose clamp, this nonlinear relationship can be approximated by a straight line and the slope of this line, according to the definition given in (12.11), is exactly  $GE^*_{(\text{clamp})}$ :

$$Rd = GE^*_{(\text{clamp})}G + Rd_0 \quad (12.15)$$

One must be aware that this approximation is inadequate at both very high and very low glucose levels and that the nonzero intercept  $Rd_0$  has no physiological meaning (when glucose concentration is zero, also  $Rd$  is zero) but is simply one of the two parameters of the straight line used to approximate the nonlinear Michaelis-Menten characteristic in the physiological glucose range. Finally, it is important to note that the saturation of glucose utilisation with increasing glucose levels implies that the glucose plasma clearance rate is not constant but decreases as glycaemia increases. In fact, by remembering that the clearance rate,  $CR$ , is given by the ratio  $Rd/G$ , and by using (12.15) to express  $Rd$  as a function of  $G$ , one obtains a hyperbolic relationship between  $CR$  and  $G$ :

$$CR = \frac{Rd}{G} = GE^*_{(\text{clamp})} + \frac{Rd_0}{G} \quad (12.16)$$

Let us now turn our attention to insulin sensitivity and its steady-state measurement by the euglycaemic hyperinsulinaemic clamp. Insulinaemia is elevated by increasing steps of insulin infusions in a dose-response fashion, while glucose is maintained at its basal level by a variable glucose infusion. Each time the insulin infusion increases, one must wait for the system to reach a new steady state. In this way, the effect of increasing insulin levels on  $Rd$  and  $EGP$ , at basal glycaemia, can be studied. In each steady state, the glucose infusion necessary to maintain glycaemia at its basal level is a measure of insulin action on  $Rd$  and  $EGP$ . By making reference to (12.12), insulin sensitivity can be calculated as the slope of the straight line that describes the dose-response relationship between  $GIR$  and insulin concentration, normalised to



the clamped glucose level:

$$IS_{(\text{clamp})} = \frac{\Delta[Rd - EGP]}{G\Delta I} \Big|_{G=G_b} = \frac{\Delta GIR}{G\Delta I} \Big|_{G=G_b} \quad (12.17)$$

The effect of insulin on  $Rd$  only can be measured by infusing a glucose tracer during the clamp. This component of insulin sensitivity is given by:

$$IS_{(\text{clamp})}^* = \frac{\Delta Rd}{G\Delta I} \Big|_{G=G_b} \quad (12.18)$$

In summary, if we want to measure glucose effectiveness and insulin sensitivity with the clamp technique, we must perform two separate dose-response studies, each requiring the administration of both insulin and glucose, to frequently measure glycaemia and, for glucose effectiveness, employ a pharmacological agent to suppress insulin secretion. A natural question arises: is it possible to measure these control indexes with a less labour-intensive experimental approach? This possibility exists, but it requires the development of suitable models of the glucose-insulin system, as we discuss in the following section.

#### 12.5.4. DYNAMIC MODELS: THE MINIMAL MODELS

It would be highly desirable to measure glucose effectiveness and insulin sensitivity from plasma glucose and insulin concentrations measured during a meal. In fact, there is nothing more physiological than a meal, and it is intuitive that meal glycaemia and insulinaemia profiles reflect all the control mechanisms we are interested in. However, the modalities with which the ingested glucose is absorbed by the gut vary considerably among subjects and are very difficult to model. This implies that, unless some tracer is added to the ingested glucose, the exogenous glucose appearance rate in blood remains unknown. It is possible to obviate these difficulties by administering glucose intravenously. A glucose administration format particularly appealing for its simplicity is the IVGTT, which consists of a rapid glucose bolus injection into a vein. This test, which has been briefly mentioned in section 12.4, Models of Whole-Body Kinetics in Nonsteady State, is also discussed in Chapter 11, where the so-called insulin minimal models are presented which allow the estimation of indexes of glucose control on insulin secretion. Here we discuss the minimal models of glucose disappearance that allow the estimation of glucose effectiveness and insulin sensitivity from glucose and insulin IVGTT data (Bergman, 1989; Cobelli *et al.*, 1997). These models are called minimal because they are simple enough to be identified with precision from

IVGTT data but complex enough to provide an adequate description of the system.

A model aiming to measure glucose effectiveness and insulin sensitivity from IVGTT data must include a description of glucose kinetics and insulin action on glucose utilisation as well as a functional description of glucose and insulin control upon glucose production. An approach that allows avoidance of the difficulty of describing both the glucose kinetics and production processes consists of administering a tracer with the glucose bolus and measuring the tracer disappearance curve in addition to glucose and insulin concentrations (labelled IVGTT, Figure 12.12). As previously indicated, the tracer administration allows one to separate the processes of kinetics and production. The idea is to use the tracer data to develop a minimal model of glucose kinetics only. In the literature, two minimal models of glucose kinetics during a labelled IVGTT have been proposed: one is monocompartmental (Avogaro *et al.*, 1989; Avogaro *et al.*, 1996; Caumo *et al.*, 1991; Cobelli *et al.*, 1986), and the other is bicompartamental (Caumo and Cobelli, 1993; Vicini *et al.*, 1997). Let us focus on the latter. This model, which has been previously introduced in the section on Models of Whole-Body Kinetics in Nonsteady State, has been shown to well describe the time-varying glucose impulse response during the IVGTT and to allow an accurate estimate of *EGP* by deconvolution. Now, we show that this model also is able to measure glucose effectiveness and insulin sensitivity.

The model is shown in Figure 12.13. It is assumed that insulin-independent glucose utilisation takes place in the accessible compartment while insulin-dependent glucose utilisation is in the nonaccessible one. Insulin-independent glucose utilisation consists of two components, one constant,  $Rd_0$ , and the other proportional to glycaemia. In this way the model is able to account for the inhibitory effect of glucose on its own clearance (12.16). Insulin-dependent glucose utilisation is parametrically controlled by insulin in a compartment remote from plasma. This accounts for experimental evidence that there is a delay between insulin appearance in plasma and its effect on glucose utilisation. The model is *a priori* uniquely identifiable if one imposes the constraint that, in the basal steady state, the glucose utilisation by insulin-independent tissues is threefold compared with the one by insulin-dependent tissues. The model equations are:

$$\begin{aligned}
 \dot{q}_1(t) &= - \left[ k_p + \frac{Rd_0}{Q_1(t)} + k_{21} \right] q_1(t) + k_{12}q_2(t) + d\delta(t) & q_1(0) &= 0 \\
 \dot{q}_2(t) &= k_{21}q_1(t) - [k_{02} + x(t) + k_{12}]q_2(t) & q_2(0) &= 0 \\
 \dot{x}(t) &= -k_b x(t) + k_a [I(t) - I_b] & x(0) &= 0 \\
 g(t) &= q_1(t)/V_1
 \end{aligned} \tag{12.19}$$

where  $q_1$  and  $q_2$  are the tracer masses, respectively, in the accessible and nonaccessible compartments;  $Q_1$  is glucose mass in the accessible pool;  $d$  is the administered tracer dose;  $k_p$  is the proportionality constant of the component of insulin-independent utilisation that is proportional to glucose;  $x$  is insulin action exerted from a compartment remote from plasma.;  $k_a$  and  $k_b$  are parameters governing insulin action;  $I_b$  is basal insulinaemia. From the model parameters, one can calculate glucose effectiveness and insulin sensitivity on glucose utilisation (Vicini *et al.*, 1997). These indexes, denoted, respectively, as  $S_G^{2*}$  and  $S_I^{2*}$  (apex "2" denotes that they are calculated with a two-compartment model), are:

$$\begin{aligned} S_G^{2*} &= V_1 \left( k_p + \frac{k_{21}k_{02}}{k_{02} + k_{12}} \right) \\ S_I^{2*} &= V_1 \left( \frac{k_a}{k_b} \right) \left[ \frac{k_{21}k_{12}}{(k_{02} + k_{12})^2} \right] \end{aligned} \quad (12.20)$$

The labelled IVGTT, interpreted with the tracer minimal model is a powerful tool for characterising glucose metabolism. In particular, its stable isotope implementation (Avogaro *et al.*, 1989) can be safely applied also to children and fertile women. However, the additional tracer costs make the labelled IVGTT unsuitable for large-scale studies, such as epidemiological investigations. It would be desirable to obtain indexes of glucose effectiveness and insulin sensitivity relying solely on unlabelled IVGTT data. To do so, a model describing both glucose kinetics and production is needed.

Of course, the description of glucose kinetics and production must be relatively simple to meet with *a priori* identifiability requirements. In Figure 12.15, the minimal model of glucose disappearance during an IVGTT is shown

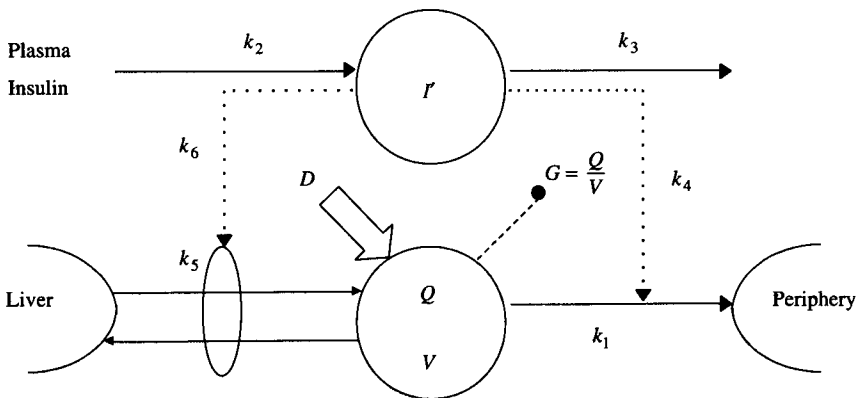


Figure 12.15. The single-compartment minimal model proposed in Bergman *et al.* (1979).

(Bergman, 1979; Bergman *et al.*, 1989). The key features of this model are 1) glucose kinetics are described by a single-compartment model; 2) glucose inhibition of production and stimulation of utilisation is proportional to glucose plasma concentration; and 3) insulin inhibition of glucose production and stimulation of glucose utilisation is proportional to insulin concentration in a compartment remote from plasma. The model thus assumes that during an IVGTT the inhibition of glucose production and the stimulation of glucose utilisation have similar functional descriptions. This allows one to combine the controls exerted by insulin and glucose on glucose production and utilisation and make the model uniquely identifiable. The model, in its uniquely identifiable parameterisation, is described by:

$$\begin{aligned} \dot{Q}(t) &= [p_1 - X(t)]Q(t) + p_1 V_1 G_b + D\delta(t) & Q(0) &= V_1 G_b \\ \dot{X} &= -p_2 X(t) + p_3 [I(t) - I_b] & X(0) &= 0 \\ G(t) &= Q(t)/V, \end{aligned} \quad (12.21)$$

where  $D$  is the glucose dose;  $X$  is insulin action; and  $V$ ,  $p_1$ ,  $p_2$ ,  $p_3$  are the model parameters. The relationship between this uniquely identifiable parameterisation and the original parameters of the model (Figure 12.15) is  $p_1 = k_1 + k_5$ ;  $p_2 = k_3$ ;  $p_3 = k_2(k_4 + k_6)$ ;  $x(t) = k_2(k_4 + k_6)I'(t)$ . The model yields indexes of glucose effectiveness,  $S_G$ , and insulin sensitivity,  $S_I$ , that reflect the effect of glucose and insulin, respectively, on both utilisation and production:

$$\begin{aligned} S_G &= V p_1 \\ S_I &= V \left( \frac{p_3}{p_2} \right) \end{aligned} \quad (12.22)$$

The question arises whether the adoption of a single-compartment description of glucose kinetics can affect the reliability of the  $S_G$  and  $S_I$  estimates. Both theoretical analyses (Caumo *et al.*, 1991; Caumo *et al.*, 1996; Caumo *et al.*, 1999; Cobelli *et al.*, 1998a; Mari, 1997) and experimental studies (Finegood and Tzur, 1996; Quon *et al.*, 1994; Saad *et al.*, 1994) where  $S_G$  and  $S_I$  have been compared with the analogous glucose clamp-based indexes,  $GE_{(\text{clamp})}$  and  $IS_{(\text{clamp})}$ , suggest that  $S_G$  is overestimated and  $S_I$  is underestimated. How can we overcome this drawback? Two different approaches are available. A first possibility is to append a second compartment to the accessible one and use a Bayesian approach to incorporate *a priori* available knowledge (from population studies) on the exchange rate parameters between the accessible and nonaccessible compartments,  $k_{21}$  and  $k_{12}$ . Results in normal humans (Cobelli *et al.*, 1999) show that this approach provides estimates of glucose effectiveness and insulin sensitivity that are, respectively, 60% lower and 35% higher than the corresponding single-compartment minimal model

indexes. These values are in better agreement than the single-compartment indexes with recently published values of  $GE_{(\text{clamp})}$  and  $IS_{(\text{clamp})}$  and support an improved accuracy of glucose effectiveness and insulin sensitivity when estimated by the Bayesian two-compartment minimal model.

A second possibility consists in modifying the glucose administration format to generate a glucose profile in plasma smoother than that produced by IVGTT and therefore more reliably interpretable by the single-compartment model. We must bear in mind that the IVGTT produces rapid changes in glycaemia that, particularly in the initial portion of the test, are hardly describable by the monocompartmental minimal model. By using a glucose administration format similar to the rate of glucose appearance into the systemic circulation during a meal, we generate a slowly changing glycaemic profile where the fast component of glucose kinetics is less important than during the IVGTT. In fact, results obtained with this meal-like protocol show that the indexes  $S_G$  and  $S_I$  are more accurately estimated than those of the IVGTT (Basu *et al.*, 1997; Bettini *et al.*, 1996).

## 12.6. SIMULATION MODELS

Simulation is an essential tool for understanding endocrine-metabolic systems in both healthy and pathological states, such as in diabetes. In fact, it is frequently not possible, appropriate, convenient, or desirable to carry out a particular experiment on the physiological system. For example, it can be too difficult, too expensive, too dangerous, nonethical, or simply too labour-intensive. Simulation offers an alternative way of experimenting on the system and can be useful not only in interpretation but also in prediction and control. Hereafter, two examples of glucose simulation models are presented. The first addresses the interpretation of the ultradian oscillations observed in glycaemia and insulinaemia during a meal or constant glucose infusion; the second example concerns a simulation model that can be useful in planning the insulin therapy in insulin-dependent diabetes.

The simulation model proposed by Sturis *et al.* (1991) has been able to offer a plausible explanation of the wide ultradian oscillations (period of approximately 120 min in humans) that are observed in insulin and glucose profiles in various physiological conditions, such as ingestion of a meal, glucose parenteral nutrition, and glucose intravenous administration. The model describes the glucose and insulin subsystems and their interactions with a parsimonious representation. Glucose kinetics are described by a single-compartment model, which, as discussed previously, is sufficiently adequate when glycaemia does not change too rapidly. Glucose utilisation has two components, one insulin-independent and the other insulin-dependent. The

latter is controlled by insulin in a compartment remote from plasma. Also, insulin action on glucose production occurs with a delay (modelled with a three-compartment chain). The model also allows a direct effect of glucose on its own production, although this control can be omitted without significantly modifying the simulation results. The model assumes that pancreatic secretion is a sigmoidal function of glycaemia. Although this description is unable to account for the biphasic pattern of insulin secretion when glycaemia increases rapidly, it provides a reasonable approximation when glycaemia changes slowly.

The simulation results of a meal and different intravenous glucose infusion give results that are in good accordance with experimental data. In particular, during glucose infusion, spontaneous oscillations of glycaemia and insulinaemia are generated that exhibit, in keeping with experimental observations, a distinctive feature: when glucose infusion is doubled, the amplitude of insulin oscillations also doubles, but frequency remains the same (Figure 12.16). It is worth noting that the oscillations predicted by the model are perfectly regular, whereas those observed experimentally show irregularities in both frequency and amplitude. Possible explanations for this discrepancy are the physiological fluctuations in the parameters of the glucose control system, the contribution of hormonal or nervous factors not accounted for by the model, and the superposition of pancreatic micropulsatility (amplitude of 1–2  $\mu\text{U}/\text{ml}$  and period of 8–15 min, likely generated by a  $\beta$ -cell pacemaker). Despite these minor differences, the substantial accordance between the simulation and the experimental results suggests that the slow oscillations of insulin secretion and of glycaemia can originate from the interaction between the glucose and insulin subsystems

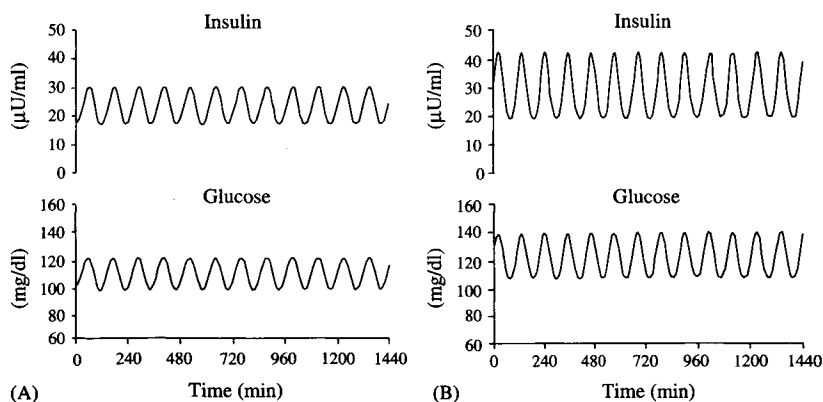


**Figure 12.16.** Insulin and glucose plasma concentration profiles predicted by the simulation model proposed in Sturis *et al.* (1991) in response to a constant glucose infusion of 108 (left panel) and 216 mg/min (right panel).

without the need to invoke the presence of a pancreatic pacemaker operating at these frequencies. It is of interest to note that the modalities of insulin action on glucose metabolism play a key role in the generation of these oscillations. In fact, a sensitivity analysis has shown that the generation of oscillations is critically dependent on the existence of a delay between plasma insulin and its action on glucose production and utilisation: oscillations smooth out considerably if the delay is less than 25 min or larger than 50 min, and they vanish if the delay is omitted.

The second example illustrates how a simulation model can help the development of a decision support system for diabetes therapy. Various simulation models have been proposed (Cobelli and Ruggeri, 1983; Lehman and Deutsch, 1992; Salzsieder *et al.*, 1985) that have tackled particular aspects of diabetes control. For instance, the model proposed in Cobelli and Ruggeri (1983) has been developed for comparing different intravenous insulin-infusion algorithms and different insulin-infusion sites (portal vs. peripheral administration) for an artificial pancreas. Recently, new physiological knowledge of the glucose system has been gained (e.g., the *EGP* profile during a meal, the modalities of insulin and glucose control on glucose utilisation, the kinetics of regular and slowly acting insulin after a subcutaneous injection), which has allowed the development of a new and more accurate simulation model (Cobelli *et al.*, 1998b). The model, which has been first developed in the normal subject, describes glucose and insulin kinetics with a single-compartment that is sufficiently accurate for describing glucose and insulin concentration time patterns during a meal. In accordance with experimental evidence, glucose and insulin controls on glucose production and utilisation emanate not only from plasma but also from a compartment remote from plasma. Finally, insulin secretion has been modelled by extending a model previously developed for the IVGTT (discussed in Chapter 11) by adding a derivative control by glycaemia.

The model has been subsequently modified to describe an insulin-dependent diabetic patient under a conventional subcutaneous insulin therapeutic regimen. The model of the diabetic patient assumes that there is no insulin secretion and that the exogenous insulin therapy consists of four subcutaneous insulin injections during the day (8, 15, and 12 U of regular insulin, respectively, before breakfast, lunch, dinner and 10 U of slowly acting insulin before sleep). The description of insulin kinetics after a subcutaneous injection hinges on a classic model of the literature (Berger and Rodbard, 1989) that has been subsequently refined by taking into account more recent studies (Torlone *et al.*, 1996). Figure 12.17 shows the predictions of glucose and insulin concentration and of glucose utilisation and rate of appearance of the model during a day. The model is currently used to assess insulin-administration strategies and to better define indexes of glycaemic control in view of the development

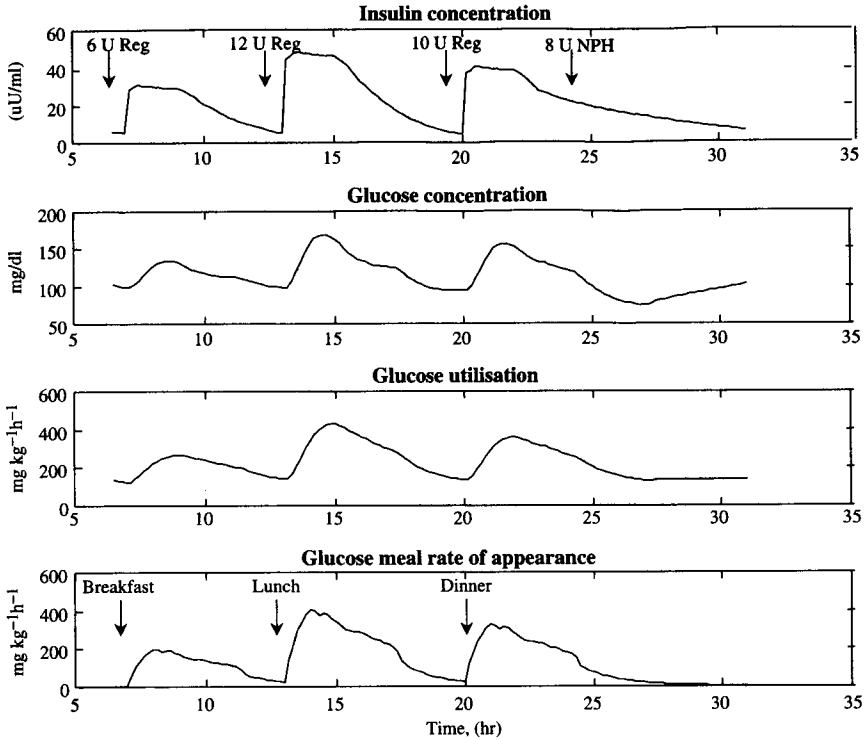


**Figure 12.17.** Insulin and glucose concentration, glucose utilisation, and meal rate of appearance in a diabetic subject predicted by the simulation model proposed in Cobelli *et al.* (1998b). The insulin subcutaneous injections (doses and timing) are also shown.

of a telemedicine decision support system for conventional diabetes therapy (Bellazzi *et al.*, 1995).

## 12.7. CONCLUSIONS

The study of the glucose system offers an interesting example of the ability of mathematical models to provide a quantitative description of an endocrine-metabolic system in terms of production and utilisation fluxes, masses in different body pools, and control signals. We have provided examples of models for the analysis of the steady and nonsteady state and for the investigation of both the whole-body and the regional levels. We also have presented models more oriented toward clinical use that yield metabolic indexes characterising the control of the glucose-insulin feedback loop in an individual.



Finally, we have shown that simulation models can, for instance, help the physiologist test hypotheses on system functioning and help the clinician improve the therapeutic regimen of a diabetic patient. We hope that we have conveyed the notion that the development of a plausible model for any particular physiological system must be based on available knowledge, requires a suitable experimental protocol, and must be tailored to the specific quantitative question asked.

## 12.8. REFERENCES

- Avogaro, A., J. D. Bristow, D. M. Bier, C. Cobelli and G. Toffolo. Stable-label intravenous glucose tolerance test minimal model. *Diabetes* 38(1989):1048–55.
- Avogaro, P., P. Vicini, A. Valerio, A. Caumo and C. Cobelli. The hot but not the cold minimal model allows precise assessment of insulin sensitivity in NIDDM subjects. *Am J Physiol* 33(1996):E532–40.
- Basu, A., A. Caumo, F. Bettini, A. Gelisio, A. Alzaid, C. Cobelli and R. A. Rizza. Impaired basal glucose effectiveness in NIDDM. Contribution of defects in glucose disappearance and production measured using an optimized minimal model independent protocol. *Diabetes* 46(1997):421–32.
- Bellazzi, R., C. Cobelli, E. Gomez and M. Stefanelli. The TIDDM project: telematic management of insulin dependent diabetes mellitus. In: *Proceedings of Health Telematics '95*. Edited by M. Bracale and F. Denoth (1995):271–76.
- Berger, M. and D. Rodbard. Computer simulation of plasma insulin and glucose dynamics after subcutaneous insulin injection. *Diabetes Care* 12(1989):725–36.
- Bergman, R. N. Toward physiological understanding of glucose tolerance: minimal-model approach (Lilly Lecture). *Diabetes* 38(1989):1512–27.
- Bergman, R. N., Y. Z. Ider, C. R. Bowden and C. Cobelli. Quantitative estimation of insulin sensitivity. *Am J Physiol* 236(1979):E667–77.
- Bergman, R. N., D. T. Finegood and M. Ader. Assessment of insulin sensitivity in vivo. *Endocrinol Rev* 6(1985):45–86.
- Best, J. D., S. E. Kahn, M. Ader, R. M. Watanabe, T. C. Ni and R. N. Bergman. Role of glucose effectiveness in the determination of glucose tolerance. *Diabetes Care* 19(1996):1018–30.
- Bettini, F., A. Caumo, R. Rizza and C. Cobelli. Models of glucose disposal: estimation of glucose effectiveness with an optimal protocol. In: *Proceedings of the 18th IEEE/EMBS Annual Conference*. Piscataway, NJ: IEEE(1996):592–93.
- Bonadonna, R. C., S. Del Prato, E. Bonora, M. P. Saccomani, G. Gulli, A. Natali, S. Frascerra, N. Pecori, E. Ferrannini, D. Bier, C. Cobelli and R. A. DeFronzo. Roles of glucose transport and glucose phosphorylation in muscle insulin resistance in NIDDM. *Diabetes* 45(1996):915–25.
- Caumo, A. and Cobelli, C. Hepatic glucose production during the labeled IVGTT: estimation by deconvolution with a new minimal model. *Am J Physiol* 264(1993):E829–41.
- Caumo, A., A. Giacca, M. Morgese, G. Pozza, P. Micossi and C. Cobelli. Minimal model of glucose disappearance: lessons from the labelled IVGTT. *Diabet Med* 8(1991):822–32.
- Caumo, A., M. Homan, H. Katz, R. A. Rizza and C. Cobelli. Glucose turnover in presence of changing glucose concentrations: error analysis for glucose disappearance. *Am J Physiol* 269(1995):E557–67.
- Caumo, A., P. Vicini and C. Cobelli. Is the minimal model too minimal? *Diabetologia* 39(1996):997–1000.

- Caumo, A., P. Vicini, J. J. Zachwieja, A. Avogaro, K. Yarasheski, D. M. Bier and C. Cobelli. Undermodeling affects minimal model indexes: insights from a two-compartment model. *Am J Physiol* 276(1999):E1171–93.
- Cobelli, C. and A. Caumo. Using what is accessible to measure that which is not. *Metabolism* 47(1998):1–29.
- Cobelli, C. and A. Ruggeri. Evaluation of portal/peripheral route and of algorithms for insulin delivery in the closed loop control of glucose in diabetes. A modeling study. *IEEE Trans Biomed Eng* BME-30(1983):93–103.
- Cobelli, C., G. Toffolo and E. Ferrannini. A model of glucose kinetics and their control by insulin: compartmental and noncompartmental approaches. *Math Biosci* 72(1984):291–315.
- Cobelli, C., G. Pacini, G. Toffolo and L. Sacca'. Estimation of insulin sensitivity and glucose clearance from minimal model: new insights from labeled IVGTT. *Am J Physiol* 250(1986):E591–98.
- Cobelli, C., A. Mari and E. Ferrannini. Nonsteady state: error analysis of Steele's model and development for glucose kinetics. *Am J Physiol* 252(1987):E679–89.
- Cobelli C., P. Vicini, G. Toffolo and A. Caumo. The hot IVGTT minimal models: simultaneous assessment of disposal indices and hepatic glucose release. In: *The Minimal Model Approach and Determinants of Glucose Tolerance*. Edited by R. N. Bergman and J. C. Lovejoy. Baton Rouge, LA: Louisiana State University Press 1997:202–39.
- Cobelli, C., F. Bettini, A. Caumo and M. J. Quon. Overestimation of minimal model glucose effectiveness in presence of insulin response is due to undermodeling. *Am J Physiol* 275(1998a):E1031–36.
- Cobelli, C., G. Nucci and S. D. Prato. A physiological simulation model of the glucose-insulin system in type-I diabetes. *Diab Nutr Metab* 11(1998b):78.
- Cobelli, C., A. Caumo and M. Omenetto. Minimal model  $S_G$  overestimation and  $S_I$  underestimation: improved accuracy by a Bayesian two compartment model. *Am J Physiol* 277(1999):E481–88.
- DiStefano III, J. J. Noncompartmental vs compartmental analysis: some bases for choice. *Am J Physiol* 243(1982):R1–6.
- Ferrannini, E., J. D. Smith, C. Cobelli, G. Toffolo, A. Pilo and R. A. DeFronzo. Effect of insulin on the distribution of glucose in man. *J Clin Invest* 76(1985):357–64.
- Finewood, D. T. and D. Tzur. Reduced glucose effectiveness associated with reduced insulin release: an artifact of the minimal-model method. *Am J Physiol* 271(1996):E485–95.
- Galstaldelli, A., J.-M. Schwarz, E. Cavegion, L. D. Traber, J. Rosenblatt, G. Toffolo, C. Cobelli and R. Wolfe. Glucose kinetics in interstitial fluid can be predicted by compartmental modeling. *Am J Physiol* 272(1997):E494–505.
- Jacquez, J. A. Theory of production rate calculations in steady and nonsteady states and its application to glucose metabolism. *Am J Physiol* 262(1992):E779–90.
- Lehman, E. D. and T. Deutsch. A physiological model of glucose-insulin interaction in type I diabetes mellitus. *J Biomed Eng* 14(1992):195–214.
- Mari, A. Assessment of insulin sensitivity with minimal model: role of model assumptions. *Am J Physiol* 272(1997):E925–34.
- Mari, A., P. Butler, A. Caumo, C. Cobelli, R. A. Rizza, G. Steil and R. N. Bergman. On the calculation of glucose rate of disappearance in nonsteady state. Letters to the Editor. *Am J Physiol* 265(1994):E825–28.
- Quon, M. J., C. Cochran, S. I. Taylor and R. C. Eastman. Non-insulin-mediated glucose disappearance in subjects with IDDM: discordance between experimental results and minimal model analysis. *Diabetes* 43(1994):890–96.
- Radziuk, J., K. H. Norwich and M. Vranic. Experimental validation of measurements of glucose turnover in nonsteady state. *Am J Physiol* 264(1978):E84–93.

- Saad, M. F., R. I. Anderson, A. Laws, R. M. Watanabe, W. W. Kades, Y. D. Chen, R. E. Sands, D. Pei, P. J. Savage and R. N. Bergman. A comparison between the minimal model and the glucose clamp in the assessment of insulin sensitivity across the spectrum of glucose tolerance: Insulin Resistance Atherosclerosis Study. *Diabetes* 43(1994):1114–21.
- Saccomani, M. P., R. C. Bonadonna, D. M. Bier, R. A. DeFronzo and C. Cobelli. A model to measure insulin effects on glucose transport and phosphorylation in muscle: a three-tracer study. *Am J Physiol* 270(1996):E170–85.
- Salzsieder E., G. Albrecht, U. Fischer and E.-J. Freyse. Kinetic modeling of the gluco regulatory system to improve insulin therapy. *IEEE Trans Biomed Eng* BME-32(1985):846–55.
- Steele, R. Influences of glucose loading and of injected insulin on hepatic glucose output. *Ann NY Acad Sci* 82(1956):420–30.
- Steil, G. M., J. R. Richey, J. K. Kim, J. K. Wi, K. Rebrin, R. N. Bergman and J. H. Youn. Extracellular glucose distribution is not altered by insulin: analysis of plasma and interstitial L-glucose kinetics. *Am J Physiol* 271(1996):E855–64.
- Sturis, J., K. S. Polonsky, E. Mosekilde and E. V. Cauter. Computer model for mechanisms underlying ultradian oscillations of insulin and glucose. *Am J Physiol* 260(1991):E801–9.
- Torlone E., S. Pampanelli, C. Lalli, P. D. Sindaco, A. D. Vincenzo, A. M. Rambotti, F. Modarelli, L. Epifano, G. Kassi, G. Perriello, P. Brunetti and G. B. Bolli. Effects of short-acting insulin analog [Lys(B28), Pro(B29)] on postprandial blood glucose control in IDDM. *Diabetes Care* 19(1996):945–52.
- Vicini, P., A. Caumo and C. Cobelli. Hot IVGTT two-compartment minimal model: indexes of glucose effectiveness and insulin sensitivity. *Am J Physiol* 264(1997):E829–41.
- Vicini, P., J. J. Zachweja, K. E. Yarasheski, D. M. Bier, A. Caumo and C. Cobelli. Glucose production during an IVGTT by deconvolution: validation with the tracer-to-tracee clamp technique. *Am J Physiol* 276(1999):E285–94.
- Youn, J. H., J. K. Kim and G. M. Steil. Assessment of extracellular glucose distribution and glucose transport activity in conscious rats. *Am J Physiol* 268(1995):E712–21.

# Blood-Tissue Exchange Modelling

Paolo Vicini

## 13.1. INTRODUCTION

The noninvasive measure of the elementary processes of transport and metabolism of a substance at the organ level is a problem of enormous importance but remarkable difficulty. Every organ *in vivo* is perfused by its own vascular tree; its most important elements are the capillaries, in which the exchange of substrates between blood and tissue takes place. The density of the capillaries in the tissue is tremendous, structured in such a way that no cell is found to be farther than 100  $\mu\text{m}$  from a capillary. Skeletal muscle, for example, has a density of 300 million capillary per kg tissue, and their length ranges from 100  $\mu\text{m}$  to some millimeters (Lilloja *et al.*, 1987). Every capillary, in turn, exchanges substrates and hormones with a microscopical tissue fragment through passive or active transport. The capillary-tissue unit is therefore the elementary functional unit, and thus the quantitative description of the organ-level transport and metabolism of a substance must appropriately describe this system. The substance amount that reaches the capillary is proportional to the flow that perfuses it, which is extremely variable according to the interested region (King *et al.*, 1996). In particular, the inflow to the system is partitioned in all the branchings of the capillary network; these partitions then come together again in the outlet vein. The division in subflows is not uniform, and this defines what is called *heterogeneity of flow*. An immediate corollary of heterogeneity of flow is the heterogeneity of metabolism in every capillary-tissue unit. A schematic outline of the arrangement of the capillary-tissue units is shown in Figure 13.1.

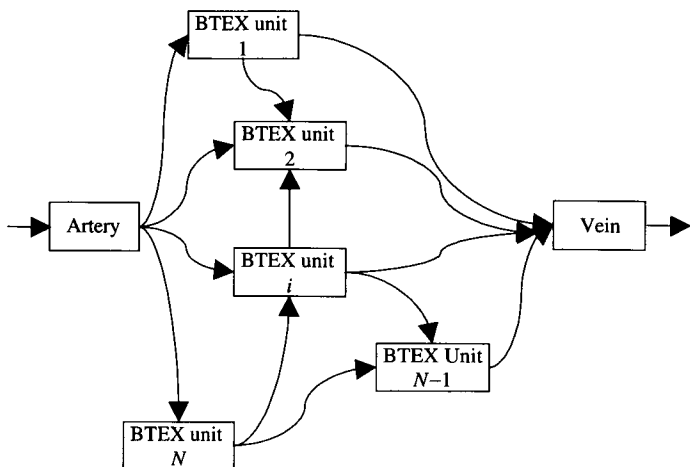


**Figure 13.1.** Vascular tree of a dishomogeneous organ where a substance can be subject to transport and metabolism. Both transport and metabolism take place at the capillary level. BTEX = blood-tissue exchange.

Every capillary-tissue unit is posed between an arteriole and a venule, vessels that have a smaller diameter than arteries and veins. The circulating blood therefore reaches the capillaries passing through an arteriole and leaves them through a venule. In particular, from an arteriole, blood can be distributed to numerous meta-arterioles before reaching the capillary. One should note that, despite their remarkable density, the blood volume circulating in the capillaries represents only 5% of the total blood volume.

Capillaries in different organs have different structure, but we can describe a typical capillary as constituted by a thin wall tube (capillary membrane), formed by endothelial cells “embedded” in one another. The transport modality through the capillary membrane is twofold. Some substances are subject exclusively to passage through the small spaces between endothelial cells and endothelial gaps; this is especially true for smaller molecules (e.g., proteins). Other substances can also flow through the endothelial cells by means of facilitated diffusion or active transport. Fundamentally, blood-tissue exchange consists in the passage of molecules from the plasma, through the capillary membrane, to the interstitial fluid and, from there, through the cellular membrane or sarcolemma, to the parenchymal cell where metabolism takes place. The combination of plasma and interstitial fluid is called *extracellular space*. A description of the elementary processes of blood-tissue exchange is outlined in Figure 13.2.

Except for convection, which can be directly quantified in terms of average blood flow, the measurement *in vivo* of all the other elementary processes,

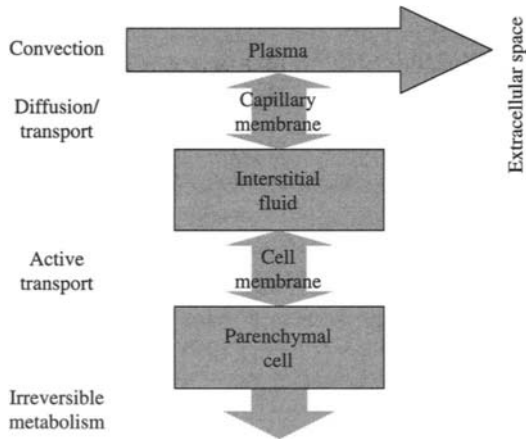


**Figure 13.2.** The elementary steps of blood-tissue exchange in the case of glucose. The substance is transported via convection by plasma flow, diffuses in interstitial volume, from there is transported through the cell membrane, and is there irreversibly metabolised.

such as the diffusion or active transport through the capillary membrane, transport through the sarcolemma (a reversible process), and metabolism (an irreversible process), must resort to indirect approaches. There are various such approaches, practically all based on the use of tracers, every one characterised by advantages and disadvantages. In this chapter, we describe the more common approaches and, in particular, concentrate on the technique of the multiple dilution of tracers, the method most used to quantify blood-tissue exchange.

## 13.2. EXPERIMENTAL APPROACHES

As noted previously, the available experimental techniques for the study of blood-tissue exchange are usually based on the employment of tracers. The tracer is a molecule in which one or more atoms have been replaced with the respective isotopes, stable or radioactive. The tracer therefore has the same chemical characteristics but different physical characteristics with respect to the original substance. An ideal tracer is indistinguishable to the system from the endogenous substance (the tracee), and it does not disturb the kinetics of the tracee. The dynamics of an ideal tracer are often described by linear dynamic models and, since the tracee system is assumed to be in steady state, the model is also time-invariant (Carson *et al.*, 1983; Norwich, 1977).

A first approach to the quantitation of blood-tissue exchange is based on the Fick principle (Fick, 1870) and allows the measure of the metabolism flux and the eventual endogenous production flux of the substance. We can write

the mass balance equations for the endogenous substance and tracer in terms of arterial and venous concentrations (mass/volume) of substrate,  $C_a$  and  $C_v$ , respectively, and tracer,  $C_a^*$  and  $C_v^*$ :

$$\begin{aligned} P - G &= (C_a - C_v)F_B \\ G &= (C_a^* - C_v^*)F_B(C_a/C_a^*), \end{aligned} \quad (13.1)$$

where  $P$  is production,  $G$  is metabolism, and  $F_B$  is blood flow (volume/time). The Fick equation has the advantage of simplicity, but it does not succeed in describing the elementary processes of the capillary-tissue units, and it exclusively gives one composite measure. In practice, it estimates the irreversible process of metabolism, but it does not allow one to say anything about the reversible process of transport, which can occur within and outside the cell (Figure 13.2). However, a measure of transport can be of enormous practical importance, such as, for example, to localise possible defects of pathological states.

Other more refined approaches have recently been proposed for measuring the elementary processes of blood-tissue exchange. Positron emission tomography (PET) and nuclear magnetic resonance spectroscopy (NMR) are noninvasive techniques that allow one to carry out, by means of appropriate detectors, a cumulative measure of the tracer amount (residue function) that, at a certain time, resides in the organ or the region of interest. The residue function must then be analysed with a model of the system. The idea is that the parameters of such a model supply one indirect measure of the metabolic processes occurring within the organ. However, these methods, in spite of their enormous possibilities, suffer from some limitations. In the case of PET, for example, the main limitation is that it is possible to use only one tracer at a time, and this once again does not allow the reliable measure of the single elementary processes, with the exception of metabolism.

The most flexible and important experimental approach is based on the multiple tracer dilution, introduced for the first time by Chinard *et al.* (1955). This method consists of the simultaneous injection, upstream of the organ, of more than one tracer, each with different molecular characteristics. The simultaneous use of several differing tracers allows the separate monitoring of the elementary processes of blood-tissue exchange. For example, in the case when the objective of the experiment is the measure of all the elementary processes (convection, diffusion, transport, and metabolism), usually one can simultaneously inject upstream of the organ (in an artery that transports blood flow entering the organ) and measure downstream (from a vein that collects the flow leaving the organ) a first tracer that is distributed only in the capillary bed (intravascular tracer), a second that is subject to the bidirectional exchange through the capillary membrane (extracellular tracer), a third that, once subjected to the two previous steps, also permeates the cell through the

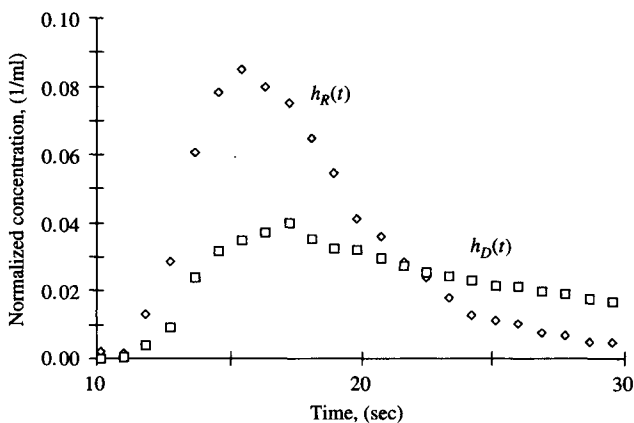


**Figure 13.3.** Multiple indicator dilution data in human myocardium. They were obtained via impulsive injection of an intravascular tracer (indocyanine green) and an extracellular tracer ( $[^3\text{H}]$ mannitol) in the left coronary artery. Tracers were measured in the main cardiac vein.

sarcolemma (permeating not metabolisable tracer), and, finally, a fourth that is also metabolised (permeating metabolisable tracer). These tracers must obviously be distinguishable one from the other once they reach the organ outflow. The venous outflow curves (Figure 13.3) must then be analysed by means of plausible and physiologically reasonable mathematical models of the organ. In practice, once again, the parameters of such models indirectly measure the elementary processes of interest. It is particularly important that all tracers used at the same time have the same molecular weight and similar molecular structure, meaning they should be subject to the same convection and cross the capillary membrane with the same modalities. As an example, mannitol is an ideal interstitial reference for methylglucose, which permeates cells through an active transport mechanism (Cobelli *et al.*, 1989). A last note should be made regarding the accuracy of the measurements. Apart from the obvious reason of precision, it also is necessary to be able to, for example, eliminate with the maximum exactitude the distortions introduced from sampling instruments (e.g., a catheter) that can affect the result of parameter estimation (Goresky and Silverman, 1964; Sparacino *et al.*, 1997).

### 13.3. MODELS OF BLOOD-TISSUE EXCHANGE

#### 13.3.1. INPUT-OUTPUT MODELS

A simple but powerful description of blood-tissue exchange is an input-output (I/O), or “black box” model (Lassen and Perl, 1979; Norwich, 1977).



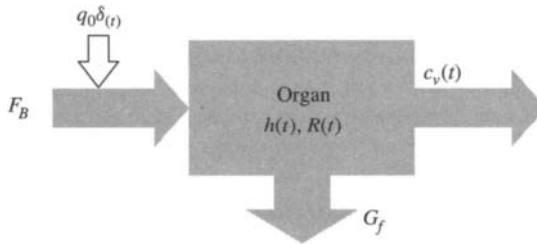


**Figure 13.4.** Organ-level experiment. See text for details.

We indicate (Figure 13.4) with  $c_v(t)$  (a function of time) the concentration in vein that follows the impulsive injection of an amount  $q_0$  of tracer at the organ inlet (in the remainder of this text, we will be limited, mostly for simplicity, to the case of impulsive inputs, even if various protocols of infusion are obviously possible). Let us now define the function:

$$h(t) = \frac{F_B}{(1 - G_f)q_0} c_v(t) \quad (13.2)$$

where  $G_f$  is the fraction of substance irreversibly metabolised. The function  $h(t)$  is often called *transport function*. Since the integral from 0 to infinity of  $h(t)$  is equal to 1 (Norwich, 1977), it is possible to determine  $G_f$  from the measures of the injected amount  $q_0$ , of the outflow concentration (measured for long enough so that it is possible to accurately determine the area under the curve) and of average organ flow  $F_B$ . Let us note that the first moment of  $h(t)$  is the transit time of the tracer: for this reason,  $h(t)$  is also sometimes called “distribution function of transit times.”

We have already mentioned the approaches (PET and NMR) based on the possibility of measuring the amount of tracer present in a tissue region of interest. The function that describes the fate of the amount of tracer is called *residue function*,  $R(t)$ . It is related to  $h(t)$  through the following formula:

$$R(t) = G_f q_0 + (1 - G_f) \left[ 1 - \int_0^t h(\tau) d\tau \right] q_0 \quad (13.3)$$

Also, from the residue function one can obtain an estimate of  $G_f$ . It is rather easy to see that the I/O approach applied to a single tracer has the same limitations of the Fick principle. Also, in this case, the obtainable information is essentially limited to the metabolism, that is, the fraction of substance that does not reach the outflow because it is irreversibly trapped inside or transformed within the organ. However, while the  $G_f$  parameter is exclusively related to the metabolism, the shape of  $h(t)$  is potentially very informative on all the elementary processes that take place in the organ, such as convection in

the capillary bed, transcapillary exchange, and transport into and out of the cell. However, the quantification of such processes demands both a model of the system that aids in the interpretation of  $h(t)$  data and, for the sake of robustness, the adoption of a more informative experiment, such as the multiple tracer dilution technique. The classes of system models more commonly employed are two: the compartmental and distributed parameter models.

### 13.3.2. DISTRIBUTED PARAMETER MODELS OF THE SINGLE CAPILLARY

In a distributed parameter model, the organ concentration of tracer is a function of both space and time. In the following section, we derive the fundamental equations of distributed parameter models and describe their domain of validity. Historically, the first distributed parameter model was the Krogh model (Krogh, 1919; Krogh, 1936), which described the capillary like a cylinder with uniform flow, characterised by radial symmetry and dipped in a uniform medium (the tissue). While Bohr was the first to describe the effects of one barrier on the gaseous exchange at the pulmonary level (Bohr, 1909), Krogh was the first to use a distributed parameter formalism for the measure of physiological variables. His model, which is based on the steady-state solution of the diffusion equation, and which he obtained in collaboration with the mathematician Erlang, is to this day called the *Krogh cylinder*. It resulted in Krogh's winning the Nobel Prize for physiology in 1920. Many of the ideas that we discuss here found their first description in the works by Krogh, who, however, did not take into account some fundamental characteristics of blood-tissue exchange, such as regional heterogeneity of flow.

#### 13.3.2.1 The Single-Capillary Model

Let us consider a generic single tracer confined within the capillary. In the hypothesis of negligible radial diffusion (the radius of the capillary is small,  $r = 4 \mu\text{m}$ ), the concentration of tracer (expressed, e.g., in  $\text{mmol ml}^{-1}$ ) will be defined by the surface  $c(x, t)$  (where  $x$  is the space coordinate and  $t$  the temporal coordinate). The fundamental equation of the distributed parameter model for the single capillary (Figure 13.5) is given by the classic equation describing convection and axial diffusion:

$$\frac{\partial c(x, t)}{\partial t} = -v(x) \frac{\partial c(x, t)}{\partial x} + D \frac{\partial^2 c(x, t)}{\partial x^2} \quad (13.4)$$

where  $v$  is the velocity of convection ( $\text{cm s}^{-1}$ ) and  $D$  the diffusion coefficient ( $\text{cm}^2 \text{s}^{-1}$ ). At this point, we can introduce some simplifications. First, we

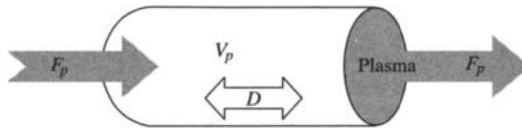


**Figure 13.5.** The one-region single-capillary blood-tissue exchange model. See text for details.

suppose the system is in steady state. Moreover, it is known that the presence of red blood cells creates, in the capillaries, inner spaces of purely convective transport (this is the so-called *plug flow* or *piston flow*): a limited error is then introduced if we neglect, for our calculations, the effect of axial diffusion (however, there are cases in which this becomes important, such as in oxygen transport; see Bassingthwaite and Goresky, 1984). Transport in the single capillary therefore remains defined by convection alone:

$$\frac{\partial c(x, t)}{\partial t} = -v(x) \frac{\partial c(x, t)}{\partial x} \quad (13.5)$$

If, at this point, we establish that the capillary diameter is everywhere uniform, we can write  $v(x) = v$ . We will refer from now on to the plasma tracer concentration in the capillary,  $c_p(x, t)$ . Let us denote with  $V_p$  ( $\text{ml g}^{-1}$ ) the volume of the capillary (independent from the axial coordinate since the diameter of the capillary is constant with good approximation), the flow of plasma with  $F_p$  ( $\text{ml min}^{-1} \text{g}^{-1}$ ), and the length of the capillary with  $L$  (cm). We can write:

$$v = \frac{F_p L}{V_p} \quad (13.6)$$

and therefore:

$$\frac{\partial c_p(x, t)}{\partial t} = -\frac{F_p L}{V_p} \frac{\partial c_p(x, t)}{\partial x} \quad (13.7)$$

This is a first-order partial differential equation with boundary condition:  $c_p(0, t) = u(t)$ , where  $u(t)$  is the concentration profile ( $\text{mmol ml}^{-1}$ ) at the capillary inlet. Its solution is:

$$c_p(L, t) = \delta \left( t - \frac{V_p}{F_p} \right) \otimes u(t) = u \left( t - \frac{V_p}{F_p} \right) \quad (13.8)$$

where  $\otimes$  is the convolution operator. Briefly, given the previously outlined hypotheses, which should be verified on a case-by-case basis but are generally valid with good approximation for the microcirculatory system, the response of a single capillary to the generic input  $u(t)$  is the input itself, shifted forward in time by an amount equal to the transit time of the capillary. It is useful to

observe that the length of the capillary  $L$ , since axial diffusion is negligible, does not influence the profile of outflow concentration. In agreement with the fact that the capillaries do not have contractile ability, the profile at the inlet is not deformed by the passage through the capillary.

### 13.3.2.2 The Two-Region Capillary-Interstitial Fluid Model

Let us suppose now that the capillary is dipped in a homogeneous and stagnant medium (convection happens only in the capillary), the so-called interstitial fluid, which in the microcirculatory system separates the capillary membrane from the cellular membrane. As we have already indicated, the capillary membrane is characterised by the presence of endothelial gaps, that is, of “fissures” between the endothelial cells. The possibility that a generic substance will pass from one side of the membrane to the other will depend on many factors, among which the width of the gaps and their distribution on the membrane. We now define the permeability of a membrane (Crone and Lassen, 1970) as:

$$P = \frac{\text{flow through the membrane}}{\text{membrane surface} \times \text{concentration gradient through the membrane}} \quad (13.9)$$

Let us now consider the concentration gradient through the capillary membrane. The concentration in the capillary is  $c_p(x, t)$ , that in the interstitial fluid (referred to the interstitial volume,  $V_{\text{isf}}$ ) is  $c_{\text{isf}}(x, t)$ . The dynamics of the concentration through the capillary membrane therefore can be described, as a function of the discontinuity of the concentration across the membrane, with the equation (first-order process):

$$\frac{\partial c_p(x, t)}{\partial t} = -\frac{S_g(x)}{V_p} [P_-(x)c_p(x, t) - P_+(x)c_{\text{isf}}(x, t)] \quad (13.10)$$

where  $S_g(x)$  is the capillary membrane surface interested to the exchange ( $g$  indicates the endothelial pores, or endothelial gaps),  $P_-(x)$  is the permeability in the direction leaving from the membrane (centrifuge permeability),  $P_+(x)$  is the permeability in the direction entering the capillary (centripetal permeability) (Bassingthwaight and Goresky, 1994). At this point, we make the following hypotheses:

- the dimensions of capillary and tissue are uniform with respect to the axial direction; therefore, the surface interested to the exchange is independent from the axial dimension:  $S_g(x) = S_g$ ;
- the permeability is uniform in both the axial,  $P(x) = P$ , and the radial direction,  $P_+ = P_- = P$ ; the product permeability-surface  $PS_g$  ( $\text{ml min}^{-1} \text{g}^{-1}$ ) is therefore a constant;

- the radial diffusion in the interstitial fluid is fast; if the capillary is situated in a well-perfused organ (e.g., the cardiac tissue), the distance between the capillaries is usually small, so that the equilibrium time in the lateral direction of the concentration of the substance subject to diffusion is a negligible fraction of the transit time of the capillary;
- the concentration in the plasma is the basis for the calculation of the extravascular concentrations; if  $c_p(x, t)$  is the plasma concentration and  $V_p$  the plasma space where the substance can diffuse freely, the concentration  $c'_{\text{isf}}(x, t)$  in the interstitial virtual volume  $V'_{\text{isf}}$  (ml g<sup>-1</sup>), when equilibrium is reached, is equal to  $c_p(x, t)$ . More generally, the virtual volume  $V'_{\text{isf}}$  is different from the “true” volume (in water equivalents),  $V_{\text{isf}}$ . For example, in the presence of accumulation at the membrane level, which can be accounted for by asymmetry in the transport or differences in the substance solubility in plasma and interstitial fluid, the ratio between virtual volume and true volume can vary from 1 and is generally given by  $\gamma = V'_{\text{isf}}/V_{\text{isf}}$ , where  $\gamma$  is the fraction of  $V_{\text{isf}}$  accessible to the substance. The virtual volume therefore represents a composite measure of various phenomena such as the presence of excluded volume, different solubilities, presence of binding sites on the capillary wall, and, eventually, asymmetric transport. The definition of virtual volume can be easily extended to all the extravascular regions.

We can now derive a simple two-region model that describes transcappillary transfer (Figure 13.6). The explicit solution of this model was derived by Rose and Goresky (1976) and Sangren and Sheppard (1953; Sheppard, 1962), while Bassingthwaite *et al.* (1992) proposed efficient numerical algorithms.

The plasma region equation is the following:

$$\frac{\partial c_p(x, t)}{\partial t} = -\frac{F_p L}{V_p} \frac{\partial c_p(x, t)}{\partial x} - \frac{PS_g}{V_p} \left[ c_p(x, t) - \frac{c_{\text{isf}}(x, t)}{\gamma} \right] \quad (13.11)$$

and we can write it in terms of virtual concentrations:

$$\frac{\partial c_p(x, t)}{\partial t} = -\frac{F_p L}{V_p} \frac{\partial c_p(x, t)}{\partial x} - \frac{PS_g}{V_p} [c_p(x, t) - c'_{\text{isf}}(x, t)] \quad (13.12)$$

and analogously for the interstitial fluid equation:

$$\frac{\partial c'_{\text{isf}}(x, t)}{\partial t} = \frac{PS_g}{V'_{\text{isf}}} [c_p(x, t) - c'_{\text{isf}}(x, t)] \quad (13.13)$$

The system of two equations such defined describes transport through the endothelial gaps of the capillary membrane for a single capillary.

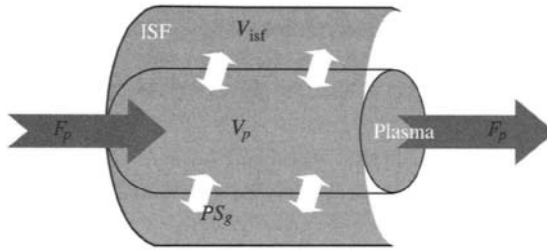


**Figure 13.6.** The two-region single-capillary blood-tissue exchange model. See text for details.

One can show that the solution to this system is given, again for the boundary condition  $c_p(0, t) = u(t)$ , by this function:

$$c_p(L, t) = e^{-PS_g/F_p} \delta \left( t - \frac{V_p}{F_p} \right) + \sum_{n=1}^{+\infty} \frac{\left( \frac{V_p PS_g PS_g}{F_p V_p V'_{isf}} \right)^n \left( t - \frac{V_p}{F_p} \right)^{n-1} e^{-PS_g/V'_{isf}(t-V_p/F_p)-PS_g/F_p} 1(t - \tau)}{n!(n-1)!} \tag{13.14}$$

where  $1(t - \tau)$  is the step function (zero before  $\tau$  and one at and after  $\tau$ ). Equation (13.14) can be written more conveniently if we define the auxiliary constants  $\tau = V_p/F_p$ ,  $k_a = PS_g/V_p$ ,  $k_b = PS_g/V'_{isf}$ :

$$c_p(L, t) = e^{-\tau k_a} \delta(t - \tau) + \sum_{n=1}^{+\infty} \frac{(\tau k_a k_b)^n (t - \tau)^{n-1} e^{-k_b(t-\tau)-\tau k_a} 1(t - \tau)}{n!(n-1)!} \tag{13.15}$$

The first addendum (*throughput fraction*) represents the molecules of substance that flow directly through the capillary without ever leaving it and is therefore equal to the intravascular response of the single capillary, scaled by the factor  $e^{-\tau k_a}$ , while the second addendum (*tail function*) describes the return (*backdiffusion*, or *backflux*) of the substance from the interstitial fluid to the capillary (Bassingthwaight and Goresky, 1984).

This result is useful in recalling and placing in the right context a traditional equation for the determination of the permeability-surface product. Let us consider an experiment with two tracers, the first one intravascular and the second permeating the interstitial fluid. Indicating by subscripts  $R$  and  $D$  their respective plasma concentrations, measured at the outflow, we can define the extraction function:

$$E(t) = \frac{c_R(t) - c_D(t)}{c_R(t)} = 1 - \frac{c_D(t)}{c_R(t)} \tag{13.16}$$

In the restrictive hypothesis of absence of backflux, we have that  $c_R(t)$  and  $c_D(t)$  are described by:

$$c_R(t) = \delta \left( t - \frac{V_p}{F_p} \right) \quad (13.17)$$

$$c_D(t) = e^{-PS_g/F_p} \delta \left( t - \frac{V_p}{F_p} \right) \quad (13.18)$$

and therefore:

$$E(t) = 1 - e^{-PS_g/F_p} \quad (13.19)$$

This is the classic *Crone-Renkin equation* for estimating the permeability-surface product of the capillary membrane (Crone, 1963; Crone and Lassen, 1970; Renkin, 1959). The most critical aspect of this equation is the hypothesis of absence of backdiffusion. Although it is widely used, its domain of validity is therefore quite restricted (Bassingthwaighte and Goresky, 1984). Another problem that makes (13.19) difficult to use in practice is the presence of local flow heterogeneity (Bassingthwaighte and Goresky, 1984; King *et al.*, 1996), although attempts have been made to extend it to nonuniform flow (Bass and Aisbett, 1985; Bass and Robinson, 1982).

### 13.3.2.3 The Three-Region Capillary-Interstitial Fluid-Cell Model

At this point, we can model the kinetics of a substance leaving interstitial fluid and entering the cell membrane through the parenchymal cell. The model (Figure 13.7), a rather straightforward extension of the two-region model, is described by:

$$\begin{aligned} \frac{\partial c_p(x, t)}{\partial t} &= -\frac{F_p L}{V_p} \frac{\partial c_p(x, t)}{\partial x} - \frac{PS_g}{V_p} [c_p(x, t) - c'_{\text{isf}}(x, t)] \\ \frac{\partial c'_{\text{isf}}(x, t)}{\partial t} &= -\frac{PS_g}{V'_{\text{isf}}} [c'_{\text{isf}}(x, t) - c_p(x, t)] \\ &\quad - \frac{PS_{pc}}{V'_{\text{isf}}} [c'_{\text{isf}}(x, t) - c'_{pc}(x, t)] \\ \frac{\partial c'_{pc}(x, t)}{\partial t} &= -\frac{PS_{pc}}{V'_{pc}} [c'_{pc}(x, t) - c'_{\text{isf}}(x, t)] - \frac{G_{pc}}{V'_{pc}} c'_{pc}(x, t) \end{aligned} \quad (13.20)$$

where  $PS_{pc}$  ( $\text{ml min}^{-1} \text{g}^{-1}$ ) is the permeability-surface product of the cell membrane,  $V'_{pc}$  ( $\text{ml g}^{-1}$ ) is the virtual volume of the parenchymal cell, and  $G_{pc}$  ( $\text{ml min}^{-1} \text{g}^{-1}$ ) is irreversible metabolism. The explicit solution is again due to Rose and Goresky (1976); an efficient numerical solution, also including the contribution from diffusion, is reported in Bassingthwaighte *et al.* (1992). It is possible to include in this model the processes of axial diffusion in all regions

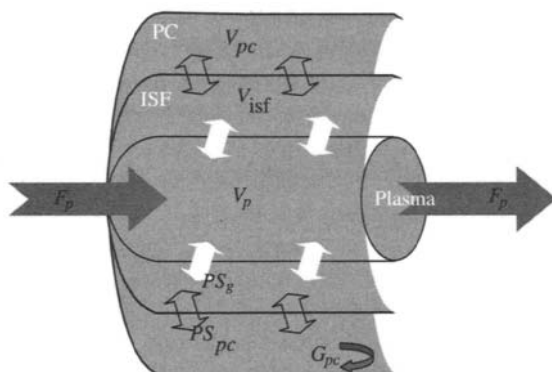


**Figure 13.7.** The three-region single-capillary blood-tissue exchange model. ISF is interstitial fluid, PC is parenchymal cell. See text for further details.

(Bassingthwaighte *et al.*, 1992), endothelial cell transport (Bassingthwaighte *et al.*, 1989), and red blood cell kinetics for the substances for which this is kinetically relevant (Li *et al.*, 1995).

### 13.3.3. WHOLE-ORGAN MODELS

#### 13.3.3.1 Importance of Flow Heterogeneity

Until now, we have limited our analysis to the single capillary. In a more generalised setting, and as noted at the beginning of this chapter, an organ is characterised by a network of interconnected capillaries (King *et al.*, 1996). The total flow into the organ becomes divided between the capillaries in unequal and not uniform way. This is the so-called spatial heterogeneity of flow (Bassingthwaighte and Goresky, 1984). Heterogeneity of flow has been extensively studied in the animal. Such studies have shown that blood flow in perfused tissue is highly heterogeneous under a number of experimental conditions, including large variations in bulk flow. This is not typical of a single species; heterogeneity has been detected in the dog, the rabbit, the cat, and the sheep (Iversen and Nicolaysen, 1989). Lastly, heterogeneity has been observed in heart tissue, muscle, and lung (Glenny and Robertson, 1991). However, comparatively little progress has been made toward understanding the evolutionary advantage and significance of such a heterogeneous flow distribution, usually attributed to the spatial organisation of vascular branching. As highlighted by several investigators (Caldwell *et al.*, 1994), flow heterogeneity causes heterogeneity of the local capillary permeability, thus limiting the amount of substances that can be exchanged between blood and tissue.



Knowledge of such a prominent phenomenon is very important for modelling blood-tissue exchange of substrates. In fact, neglecting flow heterogeneity can result in biased estimation of extravascular parameters (King *et al.*, 1996; Kuikka *et al.*, 1986). Thus, the availability of a description of flow heterogeneity (even an approximate one) in the organ of interest is a prerequisite for physiologically sound kinetic modelling (Vicini *et al.*, 1998).

The most common approaches to assess flow heterogeneity in the animal, or in isolated and perfused tissue, are microsphere deposition (Bassingthwaight and Goresky, 1984) and autoradiography (Stapleton *et al.*, 1995), both very invasive techniques that require sectioning of the organ under study. In contrast to the animal, there is little knowledge about flow heterogeneity in man. PET provides a potentially valuable tool for the assessment of regional flow heterogeneity (Vicini *et al.*, 1997; Utrainen *et al.*, 1997). The PET image of a given organ, in fact, when obtained with an appropriate marker such as [ $^{15}\text{O}$ ] water, provides information not only of average flow in a region of interest but also of its spatial distribution (Figure 13.8).

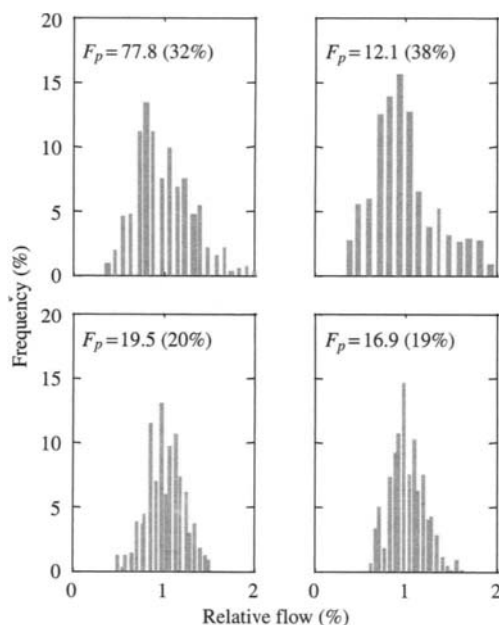


**Figure 13.8.** Frequency histograms in four normal subjects of basal relative flow in human muscle (see Vicini *et al.* for more details). Flow measurement was made with [ $^{15}\text{O}$ ]-labelled water and position emission tomography. Abscissa, local relative flow (normalised to the mean ROI flow); ordinate, frequency with which a given range of relative flows is present in the ROI. Mean flow ( $F_p$ ,  $\text{ml min}^{-1} \text{g}^{-1}$ ) and relative dispersion (expressed in %) of the distribution are shown.

### 13.3.3.2 The Rose-Goresky-Bach Organ Model

We have seen the importance of flow heterogeneity in affecting the kinetics of tracers at organ level. Such influence must be accounted for when modelling outflow curves obtained with a multiple tracer dilution protocol. A particular aspect of heterogeneity is related to the “physical distribution” of the capillary network (which entails transit time heterogeneity throughout the organ). Another aspect of heterogeneity is related to the different local processes of transport through the capillary membrane (capillaries characterised by different flows will exhibit different kinetics of the elementary processes of blood-tissue exchange). Let us now examine a possible approach to model heterogeneity of flow in distributed parameter organ models devised (Goresky, 1963; Goresky *et al.*, 1970; Rose and Goresky, 1976).

These models analyse the transport function  $h(t)$  (measured at the organ outlet) of multiple tracers injected at time  $t = 0$  with a pulse input  $\delta(t)$ . These models are based on the “partition” of the tracer appearance times at the outflow in a constituent due exclusively to transit through the large vessels (where the input waveform is subject to axial dispersion only) and another due to transit through the capillary network (where blood-tissue exchange takes place). In the case of a reference tracer, which would not pass through the capillary membrane, a tracer molecule visible at  $x = L$  is representative of a path within the organ characterised by a transit time  $t$ , which can be partitioned in a time  $\tau_{LV}$ , spent in the large vessels, and a time  $\tau_C$ , spent in the capillaries. Clearly, only during  $\tau_C$  can the tracer be subject to transport and metabolism.

Assuming that both  $\tau_{LV}$  and  $\tau_C$  are functions of  $t$ , there is only one physiologically plausible partition for an appearance time at the outflow  $t$ :

$$t = \tau_{LV}(t) + \tau_C(t) \quad (13.21)$$

The next assumption is that  $\tau_{LV}(t)$  and  $\tau_C(t)$  are *linear* or *constant* functions of  $t$ , from the reference tracer appearance time  $t_{app}$  onward. We can then write:

$$\begin{aligned} \tau_C(t) &= \tau_C(t_{app}) + b(t - t_{app}) \\ \tau_{LV}(t) &= \tau_{LV}(t_{app}) + d(t - t_{app}) \end{aligned} \quad (13.22)$$

where  $b$  and  $d$  are appropriate constants. With the further assumption that  $\tau_C(t)$  and  $\tau_{LV}(t)$  are nondecreasing functions of  $t$ , which then achieve their minima  $\tau_C^{\min}$  and  $\tau_{LV}^{\min}$  at  $t_{app}$ , summing (13.22) we obtain:

$$\begin{aligned} \tau_C(t) &= \tau_C^{\min} + b(t - t_{app}) \\ \tau_{LV}(t) &= \tau_{LV}^{\min} + (1 - b)(t - t_{app}) \end{aligned} \quad (13.23)$$

At this point, according to the possible values of  $b$ , we have three possibilities and thus three different heterogeneous organ models:

- I.  $b = 0$  (all the capillaries have the same transit time, the transit time of the large vessels is variable);
- II.  $b = 1$  (all the large vessels have the same transit time, the transit time of the capillaries is variable),
- III.  $0 < b < 1$  (both capillaries and large vessels have variable transit times).

Model III is the most physiologically likely (Rose and Goresky, 1976; Rose *et al.*, 1977) and is the most frequently used. We now describe it in greater detail. Let us note that the responses of both large vessels and capillaries are described by the simple convection equation and therefore do not account for axial dispersion:

$$\frac{\partial c(x, t)}{\partial t} = -v \frac{\partial c(x, t)}{\partial x} \quad (13.24)$$

with boundary conditions  $c(0, t) = \delta(t)$  and  $c(L, t) = h_R(t)$ , where  $v$  represents the convection velocity. While the hypothesis of absence of axial diffusion can be accepted for the capillaries (given the characteristics of plug flow), it cannot be for the large vessels, where normally one sees dispersions close to approximately 15 to 20% of the input waveform (King *et al.*, 1993).

In the situation of constant flow in all pathways, total input dose  $D$ , total input flow  $F_p$ , and pulse input of a reference tracer, the model response is given, in all generality, by:

$$h(t) = \int_0^{+\infty} u[L, t - \tau_{LV}(s)]w(s)ds \quad (13.25)$$

where  $s = \tau_{LV}(s) + \tau_C(s)$ . The term  $u[L, t - \tau_{LV}(s)]$  is the response of the single capillary evaluated at  $\tau_{LV}(s)$ , and the function  $w(s)$  is an appropriate weighting function. Let us note that  $w(s)$  accounts for the presence of transit time heterogeneity. Given that the response of a large vessel will resemble that of a capillary, since axial dispersion is absent, the impulse response of the reference tracer describes heterogeneity of transit times through the organ:

$$h_R(t) = w(t) \quad (13.26)$$

This is true if the measured function  $h_R(t)$  actually reflects the output of the reference tracer. Any distorsive element, a catheter or other sampling device, should be eliminated, such as via deconvolution (Goresky and Silverman, 1984; Sparacino *et al.*, 1997). It is worthwhile to remark that, according to this method, while the capillary equations are the same, dispersion in the large vessels is not allowed and therefore the dispersion of the outflow of an intravascular tracer is entirely described by flow heterogeneity. This approach simplifies the parameter estimation problem. However, it causes a potential overestimation of the dispersive effects of flow heterogeneity.

The response of the extracellular diffusible tracer is more complex. Let us hypothesise that the local capillary extraction, given by the ratio of the permeability-surface product and the extravascular volume of distribution, is constant in all capillaries. This implies the constancy of both the permeability-surface product and the extravascular volume of distribution. If the organ is adequately perfused, this hypothesis is usually satisfied with good approximation. However, this does not imply functional identity of the capillaries since the perfusate flow will be different. Keeping in mind the response of the single capillary for the diffusible tracer (13.15):

$$h_D(L, t) = e^{-\tau k_a} \delta(t - \tau) + \sum_{n=1}^{+\infty} \frac{(\tau k_a k_b)^n (t - \tau)^{n-1} e^{-k_b(t-\tau) - \tau k_a} 1(t - \tau)}{n!(n - 1)!} \tag{13.27}$$

where  $\tau = \tau_C(t)$  is the capillary transit time and  $k_a$  and  $k_b$  are, respectively, the fractional permeability in and out of plasma, we can write the whole-organ response for a diffusible tracer (Rose and Goresky, 1976):

$$h_D(L, t) = e^{-\tau k_a} w(t) + \int_{t_{app}}^t e^{-k_b(t-s) - \tau(s)k_a} w(s) \sum_{n=1}^{+\infty} \frac{[\tau(s)k_a k_b]^n (t - s)^{n-1} 1(t - s) ds}{n!(n - 1)!} \tag{13.28}$$

It is possible to demonstrate that the uniquely identifiable model parameters are the products  $k_a \tau_C^{\min}$  and  $k_a b$ , with  $k_b$  (which gives the return fractional flux from the extravascular region).

The description given by this model is very parsimonious and attempts to couple blood-tissue exchange and heterogeneous blood flow. Let us note also that, due to the assumption of volume constancy and flow in all pathways, flow heterogeneity reflects exactly transit time heterogeneity. This could be untrue, for example, when volumes show great local variability. Studies on isolated and perfused animal hearts (Gonzalez and Bassingthwaighe, 1990) have shown that vascular volumes are characterised by a local dispersion around 26%. Extracellular volumes show a similar dispersion (15%), while total water volume ( $V_w$ ) shows much less dispersion, around 3%.

### 13.3.3.3 The Bassingthwaighe *et al.* Organ Model

Another modelling approach to describe the heterogeneity of flow is the parallel capillary model, also called the *parallel network model* (King *et al.*, 1996). Such an approach stems directly from the fact that, especially in muscle, capillaries are arranged in a more or less parallel fashion. However, the method assumes that the capillaries all end at the same point ( $x = L$ ), and this can be a more difficult condition to satisfy (Jacquez, 1985). It is important to notice that any parallel capillary heterogeneity model does not allow the description

of phenomena, such as the shunting between capillaries, that may have a crucial importance on a correct description of the problem.

We suppose that the organ is describable with a number  $N$  of parallel pathways (Figure 13.9), along which the blood-tissue exchange occurs (King *et al.*, 1996). Every pathway represents a region of the organ characterised by a fraction  $F_i$  of the total input flow  $F$  and a fractional mass  $w_i$ . Based on this definition, a “pathway” is a compact description of subregions within the organ, each one characterised by the same flow for unit of tissue mass. It is useful to point out that these regions also can be not adjacent. Every pathway therefore is characterised from a regional relative flow,  $f_i = F_i/F_p$ ,  $i = 1 \dots, N$ , where  $F_p$  is the total input flow, and a fractional mass  $w_i$ ,  $i = 1 \dots, N$  (which we define as the percentage of the mass of the organ interested from the regional relative flow  $f_i$ ). The output of the model is therefore given by the total outflow, which is the weighted (with  $f_i$  and  $w_i$ ) sum of the single capillaries responses.

Let us formally define the width of the  $i$ -th flow class  $\Delta f_i$ ,  $i = 1, \dots, N$  for a generic flow distribution as:

$$\begin{aligned} \Delta f_1 &= f_2 - f_1 \\ \Delta f_i &= \frac{f_{i-1} + f_{i+1}}{2}, i = 2, \dots, N - 1 \\ \Delta f_N &= f_N - f_{N-1} \end{aligned} \tag{13.29}$$

The distribution of relative flows has unitary area:

$$\sum_{i=1}^N w_i \Delta f_i = 1 \tag{13.30}$$

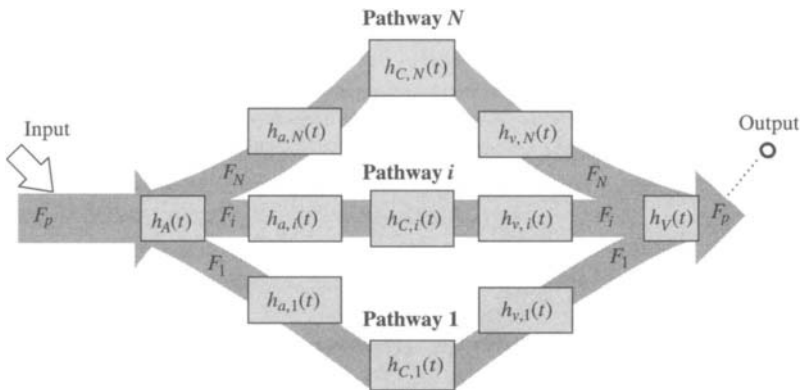


**Figure 13.9.** Structure of the discrete distributed parameter model by Bassingthwaighte *et al.*

and unitary mean:

$$\sum_{i=1}^N f_i w_i \Delta f_i = 1 \tag{13.31}$$

Historically (Bassingthwaight and Goresky, 1984), the model for a generic tracer was defined as the convolution of a large vessel response, the same for all pathways, accounting for input waveform axial dispersion, and a capillary impulse response that was different for every pathway and accounted for heterogeneity of flow:

$$h(t) = h_{LV}(t) \otimes \sum_{i=1}^N w_i f_i \Delta f_i h_{c,i}(t) \tag{13.32}$$

Capillaries still do not show any axial dispersion, and the response of a generic capillary with flow  $F_i$  is given by:

$$h_{c,i}(t) = \delta(t - \tau_i) = \delta\left(t - \frac{V_p}{F_i}\right) \tag{13.33}$$

where  $V_p$  (volume per unit tissue) is capillary volume (constant within the organ). Since  $h_{LV}(t)$  is the same for every pathway, this model can be considered a discrete counterpart of Goresky's Model II, which we defined previously (constant large vessel transit time, variable capillary transit time). Successive changes in the model have allowed a more general formulation, where the large vessel response in every pathway changes according to the pathway's particular local flow, and the large vessels present transit time heterogeneity. The large vessel impulse response is often modelled with a second-order differential operator based on the work by Paynter (1952). The response of such a model to a pulse input  $u(t) = \delta(t)$  is then:

$$h(t) = h_A(t) \otimes \left[ \sum_{i=1}^N w_i f_i \Delta f_i h_{a,i}(t) \otimes h_{c,i}(t) \otimes h_{v,i}(t) \right] \otimes h_V(t) \tag{13.34}$$

where  $\otimes$  is the convolution operator,  $h_A(t)$  is the artery impulse response (situated at the inlet, does not take part in blood-tissue exchange),  $h_V(t)$  is the vein impulse response (situated at the outlet, does not take part in blood-tissue exchange),  $h_{a,i}(t)$  is the impulse response of the arterioles in the  $i$ -th path,  $h_{v,i}(t)$  is the impulse response of the venules in the  $i$ -th path, and  $h_{c,i}(t)$  is the impulse response of the capillaries in the  $i$ -th path. Thanks to the associative and commutative property of convolution, we can simplify such a model:

$$h(t) = h_{AV}(t) \otimes \left[ \sum_{i=1}^N w_i f_i \Delta f_i h_{av,i}(t) \otimes h_{c,i}(t) \right] \tag{13.35}$$

where  $h_{AV}(t) = h_A(t) \otimes h_V(t)$  and  $h_{av,i}(t) = h_{a,i}(t) \otimes h_{v,i}(t)$ ,  $i = 1, \dots, N$ . This formulation is more general with respect to Model III, but such parameter richness means that, for achieving identifiability of the physiologically relevant parameters, it is necessary to assume some characteristics of the model, such as flow heterogeneity and large vessel volumes, according to prior information (e.g., using labelled microspheres allows to measure flow heterogeneity). When this kind of information is indeed available (e.g., the case of the isolated and perfused animal heart, where the model has been initially developed), the model is indeed identifiable. However, care should be exercised to investigate the consequences of such assumptions on the parameters of physiological interest, such as the permeability-surface product and the extravascular volumes of distribution (Vicini and Cobelli, 1997).

### 13.3.4. PARAMETER ESTIMATION

The numerical or *a posteriori* identification of distributed parameter models is most often performed via nonlinear weighted least squares (LS) algorithms (Chan *et al.*, 1993). We assume that the observations (data)  $y_i$ ,  $i = 1, \dots, m$  are described by the following equation (in vector notation):

$$Y = F(\Theta, T) + R \quad (13.36)$$

where  $F(\Theta, T)$  is the vector of the model predictions (dimension  $m$ ),  $\Theta$  is the parameter vector (dimension  $p$ ),  $T$  is the independent variable, time (dimension  $m$ ), and  $R$  is the measurement error vector, usually assumed independent and Gaussian, with zero mean and variance  $\sigma_i^2$ ,  $i = 1, \dots, m$ .

Let us define a weighting matrix  $m \times m$ :

$$W = \text{diag}(w_1, w_2, \dots, w_m) \quad (13.37)$$

(where the optimal choice of weights, in the LS sense, is  $w_i = \sigma_i^{-2}$ ), and the vector  $m \times 1$  of the weighted residuals:

$$R_w(\Theta) = [Y - F(\Theta, T)]W^{1/2} \quad (13.38)$$

We define:

$$\text{SSR}(\Theta) = R(\Theta)^T W R(\Theta) \quad (13.39)$$

the sum of the squares of the weighted residuals. The parameter estimation algorithm minimises  $\text{SSR}(\Theta)$  using a Levenberg-Marquardt-type technique (Chan *et al.*, 1993; Levenberg, 1944; Marquardt, 1963).

It is possible to calculate an approximation of the covariance matrix of the parameter estimates:

$$\text{Cov}(\Theta) = [S(\Theta)^T W S(\Theta)]^{-1} \quad (13.40)$$

where  $S(\Theta)^T W S(\Theta)$  is the *Fisher Information Matrix* and  $S(\Theta)$  is the matrix of the sensitivity functions of the model response with respect to the parameters: its generic element is:

$$S_{\vartheta_i}(t) = \frac{\partial F(\Theta, t)}{\partial \vartheta_i} \quad (13.41)$$

While the Goresky *et al.* model has a very parsimonious and simplified parameter set, the Bassingthwaight *et al.* model has a rather rich parameterisation (flows, volumes, and permeability-surface products), and it is often necessary to assume *a priori* values for the unidentifiable parameters.  $\text{Cov}(\Theta)$  therefore underestimates the precision (Grove *et al.*, 1980). One might be forced to assume some parameter values (in the case of *a priori* unidentifiability) or can do it based on numerical analysis consideration (in the case of *a posteriori* unidentifiability when the data do not allow to resolve all parameters). It is then necessary to calculate a correct value for the precision of the estimates, and recently an approach was proposed (Vicini and Cobelli, 1997) based on Monte Carlo simulations (Mosteller and Tukey, 1977).

### 13.3.5. APPLICATIONS

The complexity of the distributed parameter model of blood-tissue exchange was the primary motivation for the design of a software program, developed at the National Simulation Resource, at the Department of Bioengineering of the University of Washington (Seattle, WA), SIMCON (an acronym for SIMulation CONtrol). SIMCON implements the simulation and identification of this class of models (National Simulation Resource, 1995). The algorithm used for the solution is not transparent to the user, who can only change the parameters influencing the model (e.g., flows, permeability-surface products, volumes) and the system (e.g., input function, integration step, start and end time). For a detailed description of how to use SIMCON and its more recent user-friendly version, XSIM, the appropriate user manuals can be consulted (National Simulation Resource, 1994, 1995). The software can be downloaded from the website of the National Simulation Resource (<http://nsr.bioeng.washington.edu/>).

The structure of the distributed parameter model discussed is rather general and allows one to describe the kinetics of a large number of substances. Its domain of applicability is therefore, in principle, very large. In particular, these types of models, both in the formulation due to Bassingthwaight and



to Goresky, is used for the measure of permeability-surface products and volumes of distribution of substances, both exogenous and endogenous, from multiple tracer dilution experiments. The most frequent applications have been in the transcapillary transport, both *in vivo* and *in vitro* (Cousineau *et al.*, 1994; Cousineau *et al.*, 1995). A classic application to glucose transport in the isolated and perfused heart is given in Kuikka *et al.* (1986). Less frequently, the model also has been applied to cardiac receptors (Cousineau *et al.*, 1991; Rose *et al.*, 1994). Various results exist on the cardiac and pulmonary kinetics of sodium (Guller *et al.*, 1975), serotonin (Dupuis *et al.*, 1996), and adenosine (Wangler *et al.*, 1989). The *in vivo* kinetics of fatty acids (Goresky *et al.*, 1994) and uric acid (Kroll *et al.*, 1992) have been modelled. The model has been successfully applied to magnetic resonance data (Wilke *et al.*, 1995). Other applications have been in pharmacokinetics (Pang *et al.*, 1990, 1994, 1995). A fair amount of attention was given to the study of the kinetics of various substrates in the liver (Goresky, 1963; Kassissia *et al.*, 1992; Pang *et al.*, 1990, 1994, 1995).

### 13.3.6. COMPARTMENTAL MODELS

Compartmental models constitute the most frequently employed class of models in the study of the kinetics of endogenous and exogenous substances. Compartmental modelling results from the requirement to simplify the structure of the system as much as possible. This is particularly useful when analysing complex systems such as those encountered in biology and medicine. Compartmental modelling also has a solid theoretical foundation since compartmental models are based on conservation of mass. The system to describe with the compartmental approach is subdivided into a finite number of states (compartments), interconnected among themselves. The interconnections can represent transport fluxes or chemical transformations. Compartmental models can be linear and nonlinear, and an extensive literature exists on methodological aspects connected with their formulation, identification, and validation (Carson *et al.*, 1983; Cobelli and DiStefano, 1980; Jacquez, 1985). Several software tools, such as SAAM II (SAAM Institute, Seattle, WA, <http://www.saam.com>) (Barrett *et al.*, 1998) and ADAPT II (University of Southern California, Los Angeles, CA, <http://www.usc.edu/dept/biomed/BMSR>) (D'Argenio and Schumitzky, 1997), allow the fast and user-friendly implementation of compartmental models. In the following paragraphs, we discuss the use of compartmental models to interpret multiple tracer dilution experiments. We therefore limit the discussion to linear, time-invariant compartmental models.

Despite its rather short history, the compartmental approach to multiple tracer dilution data has produced satisfactory results. Zierler (1981) warned the community against misapplication of compartmental models. An example

of such misuse, quoted by Zierler, was using the compartmental approach to model multiple dilution tracer experiments and diffusive phenomena. A compartmental model has been proposed (Cobelli *et al.*, 1989) describing the transmembrane transport of glucose. The model has been developed from multiple tracer dilution data obtained in human skeletal muscle *in vivo* using two tracers, one extracellular (L-[<sup>3</sup>H]-glucose) and the other permeant, nonmetabolisable ([<sup>14</sup>C]-3-O-methyl-D-glucose). It allows one to estimate with very good precision the rate constants of glucose transport into and out of the cell. This model allowed us to study the enhancing effect of insulin on muscle glucose transport parameters in normal subjects (Cobelli *et al.*, 1989; Bonadonna *et al.*, 1996) and identified the presence of a localised defect in insulin control in non-insulin-dependent diabetic (NIDD) patients (Bonadonna *et al.*, 1993). This compartmental model has been extended (Saccomani *et al.*, 1996) to describe the kinetics of a third tracer, permeant nonmetabolisable ([<sup>3</sup>H]-glucose). The gain obtained by adding to the experimental protocol a third tracer is immense. This ultimately allows us to quantify a model of the tracee and therefore study not only the rate constants of transport and phosphorylation but also the bidirectional glucose flux through the cell membrane, the phosphorylation flux, and the intracellular concentration, in normal and diabetic subjects (Bonadonna *et al.*, 1996; Saccomani *et al.*, 1996).

The tracer model is shown in Figure 13.10 and is described by the following system of differential equations:

$$\begin{aligned}\dot{q}(t) &= Kq(t) + Bu(t) \\ y(t) &= Cq(t)\end{aligned}\tag{13.42}$$

where  $q(t)$  is the vector of the tracer masses in the compartments,  $K$  is the compartmental matrix, and  $B$  and  $C$  are constant matrices that relate the system input  $u(t)$  and the output  $y(t)$  to the compartmental tracer masses  $q(t)$ . The model describes flow heterogeneity using three parallel chains, each one made of two compartments ( $P + ISF$ ). The permeant tracer model ([<sup>14</sup>C]-3-O-methyl-D-glucose) is obtained "appending" the cellular ( $C$ ) and red blood cells (RBC) compartments to the L-[<sup>3</sup>H]-glucose model. Lastly, the [<sup>3</sup>H]-glucose model is obtained adding irreversible losses (describing intracellular phosphorylation) to the cellular compartments. This model allows the estimation of the parameters describing transport both into and out of the cell and metabolism, based on L-[<sup>3</sup>H]-glucose, [<sup>14</sup>C]-3-O-methyl-D-glucose and [<sup>3</sup>H]-glucose data, via a LS algorithm that also provides their precision (from the Fisher Information Matrix). From steady-state measures of glucose concentration and blood flow, one can use the model of the tracee to estimate the glucose fluxes into and out of the cell and the phosphorylation flux, apart from other variables of physiological interest, such as the intracellular concentration of glucose. The cellular transport parameters estimated by the model have been

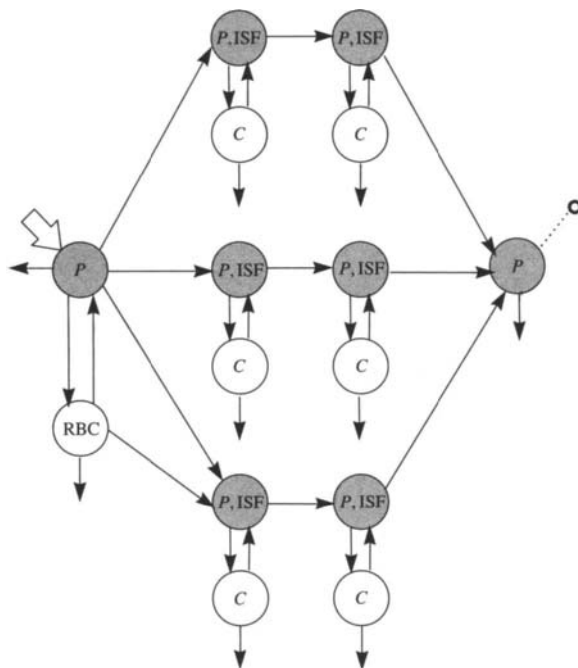


**Figure 13.10.** Compartmental model of transport and metabolism of glucose in skeletal muscle. Parameters relative to the compartments (in gray) labelled with  $P$  (plasma) and  $P,ISF$  (plasma and interstitial fluid) are estimated from extracellular tracer data, while those (in white) relative to the cell ( $C$ ) are estimated from permeant tracer data. The compartment labelled with  $RBC$  represents red blood cell kinetics.

independently validated (Saccomani *et al.*, 1996). This has allowed important physiological results to be obtained. Among these, it was possible to show that the insulin control on both transmembrane transport and phosphorylation flux in subjects affected by NIDDM is much less efficient with respect to normal subjects (Bonadonna *et al.*, 1996). Therefore, the model allowed to demonstrate that cellular transport plays a very important role in the insulin resistance associated with NIDDM.

It is interesting to note that the experimental protocol used to identify the compartmental model is not immediately usable to identify the distributed parameter model, which also requires intravascular tracer data. We should also point out that the compartmental model does not allow one to conclude much on extracellular kinetics (mean transit time and residence time). In fact, the extracellular tracer model does not have a physiological counterpart since it is basically equivalent to a parsimonious description of the transit times through the system made of plasma and interstitial fluid. These transit times are the

final result of capillary and large vessel convective kinetics, of transcapillary transfer and flow heterogeneity, and the model is a lumped description of all these processes. However, the purpose of the model was to measure transmembrane transport, and from this point of view, it provides a parsimonious and sufficiently accurate description of the system. A consequence of all this is that such a compartmental structure is not easily transportable to other physiological systems. In contrast, the distributed parameter model has some general characteristics that make it applicable to many different systems, but this entails some rigidity both in the model structure and in the experimental protocol required for its identification.

### 13.4. CONCLUSIONS

A quantitative evaluation of the elementary kinetic steps at organ level, such as transcapillary exchange, transport through the cell membrane, and intracellular metabolism, is crucial for the proper understanding of the role of each one of them in the general picture of blood-tissue exchange. These processes, however, are difficult to measure noninvasively *in vivo*. Among the various techniques that can be used to indirectly measure the parameters characterising these processes, the most suitable is the multiple indicator dilution technique, based on the analysis of multiple tracer outflow curves via a mathematical model of blood-tissue exchange. The model parameters are expected to provide a measure of the elementary steps described previously. The most important blood-tissue exchange models used to model outflow dilution curves are distributed parameter models, in which concentration is a function of both time and space, and lumped parameter (compartmental) models. Historically, the distributed parameter approach to blood-tissue exchange modelling preceded the lumped parameter model. In fact, generally, the more correct approach to simulate or model a physiological system is to account for both its temporal and its spatial dynamics. In this sense, distributed parameter models are more similar to the real system, and this makes them particularly attractive from the conceptual point of view and facilitates their application in many practical cases. However, some identifiability issues, partially investigated in Vicini and Cobelli (1999), and a somewhat rigid structure and experimental protocol limit their applicability to sectors where, on the other hand, the compartmental, lumped parameter approach has given promising results.

### 13.5. REFERENCES

- Barrett, P. H. R., B. M. Bell, C. Cobelli, H. Golde, A. Schumitzky, P. Vicini and D. M. Foster. SAAM II: simulation, analysis, and modeling software for tracer and pharmacokinetic studies. *Metabolism* 47(1998):484–92.

- Bass, L. and P. J. Robinson. Capillary permeability of heterogeneous organs: a parsimonious interpretation of indicator diffusion data. *Clin Exp Pharmacol Physiol* 9(1982):363–88.
- Bass, L. and J. Aisbett. Extended theory of the early diffusion of multiple indicators: bounds on permeability ratios, with applications to intestinal capillaries. *Clin Exp Pharmacol Physiol* 12(1985):387–406.
- Bassingthwaighe, J. B. and C. A. Goresky. 1984. Modeling in the analysis of solute and water exchange in the microvasculature. In: *Handbook of Physiology—The Cardiovascular System. Microcirculation*. Bethesda, MD: American Society of Physiology.
- Bassingthwaighe, J. B., C. Y. Wang and I. S. Chan. Blood-tissue exchange via transport and transformation by capillary endothelial cells. *Circ Res* 65(1989):1–24.
- Bassingthwaighe, J. B., I. S. Chan and C. Y. Wang. Computationally efficient algorithms for convection-permeation-diffusion models for blood-tissue exchange. *Ann Biomed Eng* 20(1992): 687–725.
- Bohr, C. Über die spezifische Tätigkeit der Lungen bei der respiratorischen Gasaufnahme und ihr Verhalten zu der durch die Alveolarwand stattfindenden Gasdiffusion. *Skand Arch Physiol* 22(1909):221–80.
- Bonadonna, R. C., M. P. Saccomani, L. Seely, K. Starick Zych, E. Ferrannini, C. Cobelli and R. A. DeFronzo. Glucose transport in human skeletal muscle. The *in vivo* response to insulin. *Diabetes* 42(1993):191–98.
- Bonadonna, R. C., S. Del Prato, M. P. Saccomani, E. Bonora, G. Gulli, E. Ferrannini, D. M. Bier, C. Cobelli and R. A. DeFronzo. Transmembrane glucose transport in skeletal muscle of patients with non-insulin dependent diabetes. *J Clin Invest* 92(1993):486–94.
- Bonadonna, R. C., S. Del Prato, E. Bonora, M. P. Saccomani, G. Gulli, A. Natali, S. Frascerra, N. Pecori, E. Ferrannini, D. M. Bier, C. Cobelli and R. A. DeFronzo. Roles of glucose transport and glucose phosphorylation in muscle insulin resistance of NIDDM. *Diabetes* 45(1996): 915–25.
- Caldwell, J. H., G. V. Martin, G. M. Raymond and J. B. Bassingthwaighe. Regional myocardial flow and capillary permeability-surface area products are nearly proportional. *Am J Physiol* 267(1994):H654–66.
- Carson, E. R., C. Cobelli and L. Finkelstein. 1983. *The Mathematical Modelling of Metabolic and Endocrine Systems*. New York: Wiley.
- Chan, I. S., J. B. Bassingthwaighe and A. A. Goldstein. SENSOP: a derivative free solver for nonlinear least squares with sensitivity scaling. *Ann Biomed Eng* 21(1993):621–31.
- Chinard, F. P., G. J. Vosburgh and T. Enns. Transcapillary exchange of water and of other substances in certain organs of the dog. *Am J Physiol* 183(1955):221–34.
- Cobelli, C. and J. J. DiStefano III. Parameter and structural identifiability concepts and ambiguities: a critical review and analysis. *Am J Physiol* 239(1980):R7–24.
- Cobelli, C., M. P. Saccomani, E. Ferrannini, R. A. DeFronzo, R. Gelfand and R. C. Bonadonna. A compartmental model to quantitate *in vivo* glucose transport in the human forearm. *Am J Physiol* 257(1989):E943–58.
- Cousineau, D. F., C. A. Goresky, C. P. Rose and A. J. Schwab. Cardiac microcirculatory effects of beta adrenergic blockade during sympathetic stimulation. *Circ Res* 68(1991):997–1006.
- Cousineau, D. F., C. A. Goresky, J. R. Rouleau and C. P. Rose. Microsphere and dilution measurements of flow and interstitial space in dog heart. *J Appl Physiol* 77(1994):113–20.
- Cousineau, D. F., C. A. Goresky, C. P. Rose, A. Simard and A. J. Schwab. Effects of flow, perfusion pressure, and oxygen consumption on cardiac capillary exchange. *J Appl Physiol* 78(1995):1350–59.
- Crone, C. The permeability of capillaries in various organs as determined by the use of “indicator diffusion” method. *Acta Physiol Scand* 58(1963):292–305.
- Crone, C. and N. A. Lassen, eds. 1970. *Capillary Permeability: The Transfer of Molecules and Ions Between Capillary Blood and Tissue*. New York: Academic Press.

- D'Argenio, D. Z. and A. Schumitzky. 1997. *ADAPT II User's Guide: Pharmacokinetic/Pharmacodynamic Systems Analysis Software*. Los Angeles, CA: Biomedical Simulations Resource, University of Southern California.
- Dupuis, J., C. A. Goresky, J. L. Rouleau, G. G. Bach, A. Simard and A. J. Schwab. Kinetics of pulmonary uptake of serotonin during exercise in dogs. *J Appl Physiol* 80(1996):30–46.
- Fick, A. 1870. Über die Messung der Blutquantums in den Herzventrikeln. *Verhandl Phys Med Ges Wurzburg* vol. 2, XVI.
- Glenny, R. W. and H. T. Robertson. Fractal modeling of pulmonary blood flow heterogeneity. *J Appl Physiol* 70(1991):1024–30.
- Gonzalez, F. and J. B. Bassingthwaite. Heterogeneities in regional volumes of distribution and flows in rabbit heart. *Am J Physiol* 258(1990):H1012–24.
- Goresky, C. A. A linear method for determining liver sinusoidal and extravascular volumes. *Am J Physiol* 204(1963):626–40.
- Goresky, C. A. and M. Silverman. Effect of correction of catheter distortion on calculated liver sinusoidal volumes. *Am J Physiol* 207(1964):883–92.
- Goresky, C. A., W. H. Ziegler and G. G. Bach. Capillary exchange modeling: barrier limited and flow limited distribution. *Circ Res* 27(1970):739–64.
- Goresky, C. A., W. Stremmel, C. P. Rose, S. Guirguis, A. J. Schwab, H. E. Diede and E. Ibrahim. The capillary transport system for free fatty acids in the heart. *Circ Res* 74(1994):1015–26.
- Grove, T. M., G. A. Bekey and L. J. Haywood. Analysis of errors in parameter estimation with application to physiological systems. *Am J Physiol* 239(1980):R390–400.
- Guller, B., T. Yipintsoi, A. L. Orvis and J. B. Bassingthwaite. Myocardial sodium extraction at varied coronary flows in the dog: estimation of capillary permeability by residue and outflow detection. *Circ Res* 37(1975):359–78.
- Iversen, P. O. and G. Nicolaysen. Heterogeneous blood flow distribution within single skeletal muscles in the rabbit: role of vasomotion, sympathetic nerve activity and effect of vasodilation. *Acta Physiol Scand* 137(1989):125–33.
- Kassissia, I., C. P. Rose, C. A. Goresky, A. J. Schwab, G. G. Bach and S. Guirguis. Flow limited tracer oxygen distribution in the isolated perfused rat liver: effects of temperature and hematocrit. *Hepatology* 16(1992):763–75.
- King, R. B., A. Deussen, G. M. Raymond and J. B. Bassingthwaite. A vascular transport operator. *Am J Physiol* 265(1993):H2196–208.
- King, R. B., G. M. Raymond and J. B. Bassingthwaite. Modeling blood flow heterogeneity. *Ann Biomed Eng* 24(1996):352–72.
- Krogh, A. The number and distribution of capillaries in muscles with calculations of the oxygen pressure head necessary for supplying the tissue. *J Physiol* 52(1919):409–15.
- Krogh, A. 1936. *The Anatomy and Physiology of Capillaries*. New Haven, CT: Yale University Press.
- Kroll, K., T. R. Bukowski, L. M. Schwartz, D. Knoepfler and J. B. Bassingthwaite. Capillary endothelial transport of uric acid in guinea pig heart. *Am J Physiol* 262(1992):H420–31.
- Kuikka, J., M. Levin and J. B. Bassingthwaite. Multiple tracer dilution estimates of D- and 2-deoxy-D-glucose uptake by the heart. *Am J Physiol* 250(1986):H29–42.
- Jacquez, J. A. 1985. *Compartmental Analysis in Biology and Medicine*. 2nd ed. Ann Arbor, MI: University of Michigan Press.
- Lassen, N. A. and W. Perl. 1979. *Tracer Kinetics Methods in Medical Physiology*. New York: Raven Press.
- Levenberg, K. A method for the solution of certain problems in least squares. *Q Appl Math* 2(1944):164–68.
- Li, Z., T. Yipintsoi and J. B. Bassingthwaite. Nonlinear model for capillary-tissue oxygen transport and metabolism. *Ann Biomed Eng* 25(1997):604–19.

- Lilloja, S., A. A. Young, C. L. Culter, J. L. Ivy, G. H. Abbott, J. K. Zawadzki, H. Yki-Järvinen, L. Christin, T. W. Secomb and C. Bogardus. Skeletal muscle capillary density and fiber type are possible determinants of *in vivo* insulin resistance in man. *J Clin Invest* 80(1987):415–24.
- Marquardt, D. W. An algorithm for least squares estimation of nonlinear parameters. *J Soc Ind Appl Math* 11(1963):431–41.
- Mosteller, F. and J. W. Tukey. 1977. *Data Analysis and Regression*. Reading, MA: Addison Wesley.
- National Simulation Resource Facility. 1994. *MMID4 User's Guide*. Seattle, WA: Center for Bioengineering, University of Washington.
- National Simulation Resource Facility. 1995. *SIMCON User's Guide*. Seattle, WA: Center for Bioengineering, University of Washington.
- Norwich, K. 1977. *Molecular Dynamics in Biosystems*. Oxford: Pergamon Press.
- Pang, K. S., F. Barker III, A. J. Schwab and C. A. Goresky. [<sup>14</sup>C]urea and <sup>58</sup>Co EDTA as reference indicators in hepatic multiple indicator dilution studies. *Am J Physiol* 259(1990): G32–40.
- Pang, K. S., F. Barker III, A. J. Schwab and C. A. Goresky. Demonstration of rapid entry and a cellular binding space for salicylamide in perfused rat liver: a multiple indicator dilution study. *J Pharmacol Exp Ther* 270(1994):285–95.
- Pang, K. S., F. Barker III, A. Simard, A. J. Schwab and C. A. Goresky. Sulfation of acetaminophen by the perfused rat liver: the effect of red blood cell carriage. *Hepatology* 22(1995): 267–82.
- Paynter, H. M. Methods and results from MIT studies in unsteady flow. *Boston Soc Civil Eng J* 39(1952):120–24.
- Renkin, E. M. Transport of potassium 42 from blood to tissue in isolated mammalian skeletal muscles. *Am J Physiol* 197(1959):1205–10.
- Rose, C. P. and C. A. Goresky. Vasomotor control of capillary transit time heterogeneity in the canine coronary circulation. *Circ Res* 39(1976):541–54.
- Rose, C. P., C. A. Goresky and G. G. Bach. The capillary and sarcolemmal barriers in the heart. An exploration of labeled water permeability. *Circ Res* 41(1977):515–33.
- Rose, C. P., D. Cousineau, C. A. Goresky and J. De Champlain. Constitutive nonexocytotic nor-epinephrine release in sympathetic curves of *in situ* canine heart. *Am J Physiol* 266(1994): H1386–94.
- Saccomani, M. P., R. C. Bonadonna, D. M. Bier, R. A. DeFronzo and C. Cobelli. A compartmental model to measure the effects of insulin on glucose transport and phosphorylation in human skeletal muscle. A triple tracer study. *Am J Physiol* 270(1996):E170–85.
- Sangren, W. C. and C. W. Sheppard. A mathematical derivation of the exchange of a labeled substance between a liquid flowing in a vessel and an external compartment. *Bull Math Biophys* 15(1953):387–94.
- Sheppard, C. W. 1962. *Basic Principles of the Tracer Method*. New York: Wiley.
- Sparacino, G., P. Vicini, R. Bonadonna, P. Marraccini, M. Lehtovirta, E. Ferrannini and C. Cobelli. 1997. Removal of catheter distortion in multiple indicator dilution studies: a deconvolution-based method and case studies on glucose blood-tissue exchange. *Med Biol Eng Comput* 35(1997):337–42.
- Stapleton, D. D., T. C. Moffett, D. G. Baskin and J. B. Bassingthwaite. Autoradiographic assessment of blood flow heterogeneity in the hamster heart. *Microcirculation* 2(1995):277–82.
- Utriainen, T., P. Nuutila, T. Takala, P. Vicini, U. Ruotsalainen, T. Rönnemaa, T. Tolvanen, M. Raitakari, M. Haaparanta, O. Kirvelä, C. Cobelli and H. Yki-Järvinen. Intact insulin stimulation of skeletal muscle blood flow, its heterogeneity and redistribution but not of glucose uptake in non-insulin dependent diabetes mellitus. *J Clin Invest* 100(1997):777–85.
- Vicini, P. and C. Cobelli. Parameter estimation in distributed models of blood-tissue exchange: a Monte Carlo strategy to assess precision of parameter estimates. *Ann Biomed Eng* 25(1997): 815–21.

- Vicini, P. and C. Cobelli. A priori identifiability of distributed models of blood-tissue exchange. *Ann Biomed Eng* 27(1999):200–7.
- Vicini, P., R. C. Bonadonna, T. Utriainen, P. Nuutila, M. Raitakari, H. Yki-Järvinen and C. Cobelli. Estimation of blood flow heterogeneity distribution in human skeletal muscle from positron emission tomography. *Ann Biomed Eng* 25(1997):906–10.
- Vicini, P., R. C. Bonadonna, M. Lehtovirta, L. Groop and C. Cobelli. Estimation of blood flow heterogeneity in human skeletal muscle using intravascular tracer data: importance for modeling transcapillary exchange. *Ann Biomed Eng* 26(1998):764–74.
- Wangler, R. D. M. W. Gorman, C. Y. Wang, D. F. DeWitt, I. S. Chan, J. B. Bassingthwaight and H. V. Sparks. Transcapillary adenosine transport and interstitial adenosine concentration in guinea pig hearts. *Am J Physiol* 257(1989)H89–106.
- Wilke, N., K. Kroll, H. Merkle, Y. Wang, Y. Ishibashi, Y. Xu, J. Zhang, Jerosch M. Herold, A. Muhler, A. E. Stillman *et al.* Regional myocardial blood volume and flow: first pass MR imaging with polylysine Gd-DTPA. *J Magn Reson Imaging* 5(1995):227–37.
- Zierler, K. A critique of compartmental analysis. *Annu Rev Biophys Bioeng* 10(1981):531–62.



This Page Intentionally Left Blank

# Index

Note: boldface numbers indicate illustrations.

## A

- A priori* identifiability, parametric models, 77–105
  - interval identifiability in, 125–126
  - glucose modelling, 342
  - ADAPT software for, 77–78
  - aortic impedance modelling, 215–218, 242–247
  - blood-tissue exchange modelling, 393
  - Buchberger algorithm for, 82–85, 89, 91, 95–97, 101
  - characteristic set in, 82, 103–104
  - coefficient identification in, 89, 90
  - compartmental models and, 80, 84, 95, 101
  - cycles and paths method for, 83, 94, 95–96
  - differential algebra in, 84, 85–93
  - differential algebra solution for, 82–83
  - differential ring selection in, 86, 88
  - drug kinetics example, nonlinear model, 89–91, **90**
  - equality constraints in, 79
  - examples of, 89–93
  - exhaustive summary in, 81–82, 83
  - forms and reduced forms method in, 83–84
  - generators, Grobner basis and, 104–105
  - global identifiability in, 81, 84–85, 90, 93–97, 101
  - GLOBI software for, 78–79, 84, 96–97, 101
  - in glucose metabolism, nonlinear model, 91–92, **92**
  - in glucose metabolism, PET, 189
  - in glucose modelling, 355–356, 363, 364
  - Grobner basis in, 85, 91, 93–94, 96, 97, 104–105
  - IDENT software for, 85
  - initial conditions in, 88, 89, 94–95
  - input-output problems for, 86
  - in insulin modelling, 326–329
  - in insulin/glucose utilisation example, nonlinear model, 92–93, **93**
  - intelligent decomposition in, 84
  - in ligand-receptor system models using PET, 202, 204, 206
  - in linear models, 78–80, 83–85, 93–100
  - Lipnitz functions in, 85
  - local identifiability in, 81, 85
  - Lyapunov functions and, 126
  - MAPLE software for, 84, 105
  - modal matrix method in, 83
  - multi-input/multi-output problems and, 77–79, 83, 84, 86, 101
  - nonlinear least squares solutions in, 77–78, 77
  - in nonlinear models, 78, 79, 82–83, 85–93
  - numerical identifiability in, 77
  - observational parameters for, 80, 81, 82, 96
  - parameter estimation and, 125–126
  - polynomial ordering in, 89, 90, 95–96, 103–104
  - positron emission tomography (PET) models, 189
  - problem statement in, 80–81

- A priori identifiability, parametric models (*Contd.*)  
 ranking of variables in, 86–87, 89, 103–104  
 REDUCE software for, 84, 95–97, 105  
 SAAM II software for, 77–78  
 similarity transformation method in, 83  
 state isomorphism theorem in, 82  
 state-space methods in, 104  
 system-experiment model for, 79–80  
 testing of, 78  
 time-varying systems and, 86–88, 91  
 transfer function topological method for, 83–84, 94–95, 97  
 unique and nonunique identifiability in, 81  
 validity in, 77
- Accessible pool parameters  
 in tracers of metabolic flux, 156–158  
 in glucose modelling, 339, 343–344, 351, 358–359
- Accuracy of parameters, 108, 121–125
- Acute respirator distress syndrome (ARDS), pulmonary gas exchange model, 269–270
- Adapt/Adapt II software, 77–78, 120, 126, 394
- Additive errors, 115
- Akaike criterion of linear models, 12, 70, 161
- Alveolar air equation, pulmonary gas exchange model, 253, 254–256
- Alveolar-arterial oxygen difference (A-aO<sub>2</sub>), pulmonary gas exchange model, 270
- Alzheimer's disease, ligand-receptor system models using PET, 200
- Anesthesiological research, pulmonary gas exchange model, 269
- Anticipatory control, 29 (See also Feedforward)
- Aortic impedance modelling, 213–251  
 applications for, 217  
 area method (AM) in, 233–234  
 arterial compliance in, 214–215  
 arterial tapering in, 242  
 arterial tree modelled in, 214  
 ascending aorta and, data-driven model of impedance in, 222–223, **223**  
 ascending aorta and, vascular impedance in, 219–220, **220**  
 ascending aorta, pressure and flow in, 240  
 creep in, 230  
 data-driven models in, 221–223  
 decay time method (DTM) in, 233–234  
 determinacy in, 216, 217–218, 243–247  
 discontinuities (Dirichlet conditions) in, 218–219  
 disease states in, 213, 214  
 Fourier series analysis in, 218–219, 243  
 frequency- and time-domain analysis in, 232  
 frequency-response technique in, 221–223  
 identifiability in, 215–218, 242–247  
 Levenberg-Marquardt algorithm in, 244  
 linear systems in, 219  
 model fit in, 217–218  
 optimal ventriculovascular action vs. disease states in, 213  
 parameters in, 217–218  
 partially distributed arterial models for, 215  
 Poiseuille's equation and, 214  
 pressure and flow calculations in, 218–219  
 pulsatile (dynamic) models and, 214  
 pulse pressure method (PPM) in, 233, 234–235  
 quantitative evaluation of, 214  
 reflected wave measurement in, 236–242  
 selection of model for, 217  
 simple hydraulic circuit model and, 214  
 simple resistance model and, 214  
 time-invariant systems in, 219  
 T-tube model for, 237–239  
 tube models for, 216, 236–242  
 vascular impedance in, 214, 218–221, **220**  
 Voight cells in, 227, 227, 230  
 Windkessel models for, 215, 216, 224–235, **224**
- Approaches to modelling, 4–7
- Approximation, aortic impedance modelling, 216–217
- Area method (AM), 233–234
- Arterial tree model, 214
- Attenuation, positron emission tomography (PET) models, 183
- B**
- Bayesian estimation, 10, 107, 108, 126–136  
 Bayesian networks and, 128, 129–130, **130**  
 calculations for, 130–135  
 cliques in, 135  
 continuous-state models and, 128–129  
 deterministic vs. stochastic models in, 128  
 discrete-state models and, 129–130, **130**

- Gibbs sampling in, 131, 133–134, 136, 147
- least squares (LS) vs., 127
- Markov Chain Monte Carlo (MCMC)
  - method for, 128, 131–132, 134, 136, 147
- Metropolis-Hastings algorithm in, 131–133, 147
- normalisation in, 127
- point vs. probability distribution in, 127, **127**
- population modelling, 137, 140, 146–147
- software packages for, 135–136
- tree structures in, 134–135
- updating procedures for, 134–135
- Bayesian networks, 72, 108, 128, 129–130, **130**
- Bilirubin metabolism, linear model, *a priori*
  - identifiability in, 99, **99**
- Black-box models (See Data-driven modelling approach)
- Blood flow analysis using  $^{15}\text{OH}_2\text{O}$  and PET, 195–199, **198**
  - arterial vs. venous tracer concentration in, 196
  - Fick principle in, 196
  - Kety and Schmidt method in, 196
  - $^{15}\text{OH}_2\text{O}$  tracer for PET blood flow analysis, 195–199, **198**
  - perfusion rates in, 198–199
  - time shifts in sampling for, 198–199
  - tissue/blood tracer coefficient in, 196, 198
- Blood-tissue exchange modelling, 373–401
  - a priori* identifiability in, 393
  - applications and software for, 393–394
  - backdiffusion or backflux in, 383
- Bassingthwaighe et al. organ model of, 389–392, **390**
  - boundary condition in, 383
  - capillary flow in, 373–375, **374**, 385–386
  - compartmental models of, 394–397, **396**
  - concentration profile in, 380, 381–384
  - convective movement in, 374–375, **375**, 379, 380
  - Crone-Renkin equation in, 384
  - distributed models for, 379–385
  - experimental approaches to, 375–377
  - extracellular fluid/space in, 374
  - extraction function in, 383–384
  - Fick principle of blood flow in, 375–376, 378–379
  - Fisher information matrix in, 393, 395
  - Goresky's Model II for, 391
  - heterogeneity of flow in, 373, **374**, 385–386, **386**, 391
  - input/output model of, 377–379, 378
  - insulin/glucose metabolism in, 395–396, **396**
  - interstitial fluid in, 381
  - Krogh cylinder model for, 379
  - least squares (LS) estimator in, 392–393, 395
  - Levenberg-Marquardt algorithm in, 392
  - microsphere deposition in, 386
  - Monte Carlo simulation in, 393
  - multiple tracer dilution in, 376–377, **377**
  - nuclear magnetic resonance (NMR) for, 376
  - parallel network model of, 389
  - parameter estimation in, 392–393, 395
  - permeability of a membrane, calculation for, 381–384
  - plug or piston flow in, 380
  - positron emission tomography (PET) for, 376, 386
  - residue function in, 378
  - Rose-Goresky-Bach organ model for, 387–389
  - simulation models for, 393–394
  - single-capillary distributed model for, 379–381, **380**
  - tail function in, 383
  - three-region capillary-interstitial fluid-cell distributed model for, 384–385, **385**
  - throughput function in, 383
  - tracers for, 375–378, 377
  - transport/transfer, transcappillary, 378, 382–384, **383**, 394
  - two-region capillary-interstitial fluid distributed model for, 381–384, **383**
  - whole-organ models for, 385–392
- Bohr equation/Bohr integration, pulmonary gas exchange model, 254, 257–258, 260–262
- Boyle's law, pulmonary gas exchange model, 278
- B*-splines, deconvolution and, 69–70
- Buchberger algorithm, 82–85, 89, 91, 95–97, 101
- BUGS software, 136, 148

## C

- Causal probabilistic networks (See Bayesian networks)
- Cells and cellular processes, 2, 7
- C-glucose (See Glucose metabolism model using PET)
- Characteristic set, nonlinear models, 82, 103–104
- Charlé's law, pulmonary gas exchange model, 278
- Chemical processes, 2, 17–19, **18, 19**
- Cholesky decomposition, 111
- Clinical process control, 24–35
  - decision making in, 25–28, **26, 27**, 32–33
  - diagnosis in, 26–28, **27**
  - feedback model for, 25–26, 26, 28–29, 29
  - feedforward in, 28–29, 29, 31
  - health-care delivery model for, feedback in, 29–31, 30
  - system requirement specification
    - modelling, 31–35, 32, 33, 34
    - telemedicine, 31–35
    - treatment planning in, 26–28, 27
- Closed-loop feedback, 17, 37, 38–42
- Coefficient of variance (CV) error, 61–62, 115, 124, 138, 142–143, 183–184
- Compartmental models
  - a priori* identifiability in, 80, 84, 95, 101
  - in blood-tissue exchange modelling, 394–397, **396**
  - in glucose modelling, 340–346, **342, 343**, 349–353, **350, 352**, 364–366, **364**
  - in insulin modelling, 308–311, 308, 309, 316, 330–331
  - in ligand-receptor system models using PET, 200–203, **200–202**
  - parameter estimation and, 108
  - in positron emission tomography (PET) models, 180
  - in tracers of metabolic flux, 153–156, **154, 155**
- Compatibility of model, 7
- Complete vs. Incomplete mathematical models, 8
- Complexity of models, 7, 10
- Complexity of physiological systems, 2–3, 2
- Compliance, respiratory mechanics, 280
- Computers, 8
- Conceptual models, 3, 29
  - in telemedicine system requirements models, 31–35, **32, 33, 34**
- Conditional likelihood, 114
- Confidence intervals, 60–62, 68, 71, 72, 124
- Conjugate gradient (CG) method of parameter estimation, 120
- Conjugate gradient regularisation (CGR), 70
- Constant infusion tracers, metabolic flux, 161–163, **162**
- Constant-phase model of respiratory mechanics, 294–295, **295**
- Constrained deconvolution, 67–68
- Constraints, in parameter measurement, 116
- Continuous models, 6
- Control processes, 2–3, 15–44
  - anticipatory control, 29 (See Feedforward)
  - chemical reactions, using feedback, 17–19, **18, 19**
  - clinical processes and, 24–35
  - closed-loop feedback in, 17, 37
  - cybernetic loop of feedback in, 15, 16–17, **16**
  - data-driven models in, 41
  - derivative control in, 22–24, **22**
  - in diabetes management, 38–42
  - drug therapies and, 35–42
  - dynamic processes and, 15–16
  - environmental variables in, 16–17
  - enzyme processes and, 19–20, **20**
  - feedback in, 15, 16, 17–19, 24–26, **25, 26**, 28–29, **29**
  - feedforward in, 28–29, **29, 31**
  - glucose-insulin, 24, **25**, 359–366
  - inherent feedback in, 17–19, 18
  - integral control in, 22–24, 23
  - in linear models, 41
  - loose control systems (See Open-loop feedback)
  - negative feedback in, 19, 20–21, 21
  - open-loop feedback in, 17, 38
  - physiological mechanisms of, 17–24, **18**
  - positive feedback in, 19–22
  - proportional control in, 22–24, **22**
  - tight control systems (See Closed-loop feedback)
  - tracers in metabolic flux, 155
- Convolution-deconvolution, 5, 46
- Covariates, in population modelling, 137
- C-peptide kinetics
  - deconvolution solution for, 46–49, 47–48, **47, 48**, 320–321, **320**
  - in insulin modelling, 323–324, **323**
- Creep, in aortic impedance modelling, 230

- Crone-Renkin equation of permeability, in blood-tissue exchange modelling, 384
- Cross-validation, deconvolution and regularisation, 55, 56, 63, 69
- Cybernetic loop of feedback, 16–17, **16**
- Cybernetic model, 15
- Cycles and paths method, 83, 94, 95–96
- D**
- Damped least squares (See Regularisation [deconvolution])
- Data, 8
- Data-driven models, 4–5, 5, 41  
aortic impedance, 221–223
- Decay time method (DTM), aortic impedance modelling, 233–234
- Decision-making, 26–29, **27**  
drug therapies and, 36, **37**  
feedback in, 25–29, **26, 29**, 32–33  
feedforward in, 28–29, **29, 31**  
health-care delivery model for, feedback in, 29–31, **30**
- Decomposition, 111
- Deconvolution, 5, 45–75  
Bayesian networks and, 72  
biomedical and scientific applications of, 48–49  
confidence limits in, 60–62, 68, 71, 72  
conjugate gradient regularisation (CGR) in, 70  
constrained, 67–68, 67  
convolution in, 46  
C-peptide/insulin secretion rate example of, 46–49, **47, 48**, 320–321, **320**  
cross-validation in, 55, 56, 63, 69  
degrees of freedom in, 62–64, 66–67  
discrepancy in, 55, 56, 63–64, **64, 69**  
discrete, 50, 56–60  
Fast Fourier Transform (FFT) in, 65  
Fredholm integral equations in, 49, 67  
generalised cross-validation (GCV) in, 55, 56, 63, 69  
hat matrix in, 56  
hepatic glucose production example of, 49  
hormone processes and, 48–49, 53, 69  
Hunt simulated problem and, 50–64, **51, 55, 60, 64**  
ill-conditioning in, 45, 49–53, 68, 71  
ill-posedness in, 49–53, 68, 71  
impulse response in, 46, 64, 71, 72  
infrequent sampling rate (ISR) in, 56–60, **59**  
insulin modelling, 306, 320–321, 320, 329–330  
Kalman filtering in, 71  
kernel of system in, 49  
lagged-normal models and, 69  
L-curve in, 69  
least squares, 52, 53  
linear minimum variance estimation problem in, 60–61  
linear time-invariant (LTI) systems and, 46–49, **46**  
linear time-varying (LTV) systems and, 49  
Markov Chain Monte Carlo integration in, 72  
matrix inversion lemma for, 61–62, 65  
maximum entropy (ME) in, 70  
maximum likelihood (ML) in, 62–63  
minimum risk in, 55, 63  
monotonicity and, 70  
Monte Carlo simulation in, 68, 71–72  
*M*-th order polynomials and, 68–69  
noise and errors in, 52–63, 61, 62, 64  
noncausal inputs and, 59–60  
non-negativity constraints in, 68, 69, 71  
nonparametric, 46, 53  
over- and underparametrisation in, 69  
parametric, 45–46, 53, 68  
piecewise constant function in, 58  
polynomial ordering in, 68–69  
probabilistic models and, 61  
problem statement in, 46–49, **47, 48**  
QR factorisation in, 67  
random-walk models and, 61  
regression splines in, 69–70  
regularisation in (See Regularisation methods)  
regularisation parameters in, 54–56, 62–64, 69, 71  
roughness vs. smoothness in, 54–60  
sampling, sampling rate, 53, 56–60, 59, 64, 65, 71  
singular value decomposition (SVD) in, 65, 67, 71  
spectral factorisation in, 71  
staircase approximation in, 57  
state-space methods in, 71  
stochastic systems and, 60–64, 71  
time-varying systems and, 53, 65, 69

Deconvolution (*Contd.*)

- Toeplitz matrix/structure in, 51, 54, 58, 65, 67
  - tracers in metabolic flux, 157–158
  - truncated singular values decomposition (TSVD) in, 70
  - ultradian oscillations and, 63–64, **64**
  - unbiased risk in, 55
  - variance in, 61–62
  - virtual grid in, 56–60, 59, 71
  - weighted estimates sum of squares (WESS) in, 62–64, 66–67
  - weighted residual sum of squares (WRSS) in, 56, 62–64, 66–67
  - Wiener filtering and, 53
- Degrees of freedom, deconvolution and regularisation, 62–64, 66–67
- Derivative control, 22–24, **22**
- Determinacy, aortic impedance modelling, 216–218, 243–247
- Deterministic models, 6, 7, 128
- Dhugin software, 136
- Diabetes management, 38–42 (See also Glucose metabolism; Insulin metabolism)
- C-peptide/insulin secretion, deconvolution solution for, 46–49, **47, 48**, 320–321, **320**
  - data-driven models in, 41
  - euglycaemic hyperinsulinaemic clamping in, 171–173
  - FDG tracer for glucose metabolism model, 185–195
  - feedback loops and control in, 38–42, **40**
  - glucose metabolism modelling, 91–92, **92**, 185–195, 337–372, 337
  - hepatic glucose production, deconvolution solution for, 49
  - insulin modelling, 92–93, 93, 305–335
  - linear models in, 41
  - meal-like study and clamping in, 171
  - tracer experiment (See Tracer experiment design for metabolic flux)
  - Utilities for Optimising Insulin Adjustment (UTOPIA), 38–42, **40**
- Diagnosis, 26–28, **27**
- Difference equations, parameter estimation, 108
- Differential algebra, a priori identifiability, 82–93
- Differential ring selection, 86, 88

- Diffusion limitation models, pulmonary gas exchange model, 258–263, **258**, 269–273
  - Diffusion/perfusion (D/Q) mismatch, pulmonary gas exchange model, 264–266, **265**, 270
  - Dirac function, 88
  - Discontinuities (Dirichlet conditions), aortic impedance modelling, 218–219
  - Discrepancy, deconvolution and regularisation, 55, 56, 69, 63–64, **64**
  - Discrete deconvolution, 50, 56–60
  - Discrete models, 6
  - Distributed models, 6
    - blood-tissue exchange modelling, 379–385
    - insulin modelling, 305
  - D-optimality, parameter estimation, 146
  - Downhill simplex method, 120
  - Drug therapies, 15, 35–42
    - a priori* identifiability in nonlinear model of, 89–91, **90**
    - closed- vs. open-loop feedback control in, 37–38
    - control approaches in, 36–38, **38**
    - decision-making tree in, 36, 37
    - deconvolution problems in, 48–49
    - diabetes management in, 38–42
    - dosage planning, 36
    - feedback and, 35, **36**, 36–38, **38**
  - Dynamic models, 6–7, 362–366
  - Dynamic processes, 15–16
  - Dynamic-elasticity of respiratory system, 283
- E**
- Elasticity of respiratory system, 280–281, **280**
  - Elastic (W2) Windkessel model, 224–232, **226**
  - Elastic subtraction method, respiratory mechanics, 283
  - Electrophysiological signals, 8
  - Empirical Bayes estimates, population modelling, 140
  - EMSA software, 148
  - End-stage renal disease (ESRD), telemedicine system modelling, 31–35, **32, 33, 34**
  - Endocrine system model, 4
  - Endotracheal tube (ETT) site, respiratory mechanics, 281–282, **281**
  - Environmental variables, control processes, 16–17

- Enzymatic processes, control of, 19–20, 22–24, b
- Equality constraints, *a priori* identifiability and, 79
- Equilibration index, pulmonary gas exchange model, 265
- Error/noise in measurements, 9, 45  
deconvolution, 52–53, 61, 62, 64  
parameter estimation and, 107, 108, 114–115, 121–125  
positron emission tomography (PET) models, 182–185
- Euglycaemic hyperinsulinaemic clamping, 171–173, 344, 354
- Exhaustive summary, *a priori* identifiability, 81–83
- Expectation-maximisation (EM) algorithms, population modelling, 140
- Experimental data, 8–9 (See also Data-driven models)
- Extracellular fluid/space, blood-tissue exchange modelling, 374
- F**
- Fast Fourier Transform (FFT), deconvolution and regularisation, 65
- FDG models for glucose metabolism, 189–195, **189, 191, 192, 194**
- [<sup>18</sup>F]FDG models, 189–195, **189, 191, 192, 194**
- Feedback, 2–3, 15–19  
anticipatory control (See Feedforward), 29  
in chemical reaction and control, 17–19, **18, 19**  
clinical processes and, 25–29, **26, 29**  
closed-loop, 17, 37  
in control systems, 24–26, **25, 26**  
cybernetic loop of, 16  
decision making based on, 25–26, **26, 28–29, 29, 32–33**  
in diabetes management, 38–42  
in disease states and control of, 24–25, **25**  
in drug therapy planning, 35, 36–38, **36, 38**  
enzyme processes and control using, 19–20, b  
and feedforward, 28–29, **29, 31**  
in glucose modelling, 369  
in health-care delivery modelling, 29–31, **30**  
inherent, 17–19, **18**  
in insulin modelling, 322  
negative, 19, 20–21, **21**  
open-loop, 17, 38  
positive, 19, 21–22  
in telemedicine system requirements models, 31–35, **32, 33, 34**
- Feedforward, 28–29, **29, 31**
- Fick principle of blood flow,  
Fick's First Law of Diffusion,  
in glucose modelling, 346–347  
in pulmonary gas exchange model, 253, 256–260, 266
- Fick's principle of blood flow, 196  
blood-tissue exchange modelling, 375–376, 378–379  
pulmonary gas exchange model, 254, 255, 257, 267
- <sup>15</sup>OH<sub>2</sub>O tracer for PET blood flow analysis, 195–199, **198**
- First derivatives calculation, nonlinear models, 117, 120
- First in first out (FIFO) buffer, 289
- First-order (FO) method, ML estimator, 144
- First-order conditional estimation (FOCE), ML estimator, 144–145
- First-order model s, 3, 282–289, **282, 284**
- First-order processes, 3
- Fisher information matrix  
in blood-tissue exchange modelling, 393, 395  
in glucose metabolism PET, 187  
in parameter estimation, 122–123
- Flow interrupter, respiratory mechanics, 291–292, **292**
- Forced oscillation technique (FOT), respiratory mechanics, 292–295
- Forgetting factor, variables, 287
- Forms and reduced forms method, 83–84
- FORTAN, 8
- Fourier series analysis, in aortic impedance modelling, 218–219, 243
- Fredholm integral equation  
in deconvolution, 49, 67  
in tracers of metabolic flux, 157
- Free thyroid hormones (FTP), 23
- Frequency-response technique, 221–223
- Full pressure method (FPM), aortic impedance modelling, 231–232, **231, 232**
- G**
- Garbage-in/garbage-out paradigm, 13, 13
- Gauss-Jordan elimination, 111



- Generalised cross-validation (GCV),  
deconvolution and regularisation, 55, 56,  
63, 69
- Generators, Grobner basis, 104–105
- Gibbs sampling, 131, 133–134, 136, 147
- Global identifiability, 81, 84–85, 90, 93,  
95–97, 101
- Global two-stage method, population  
modelling, 140
- GLOBI/GLOBI2 software, 78–79, 84,  
96–97, 101
- Glucose metabolism modelling, 4, 6, 16  
*a priori* identifiability in, 342, 355–356,  
363, 364  
accessible pool parameters in, 339,  
343–344, 351, 358–359  
blood-tissue exchange modelling, 395–396  
clamping in, 362  
compartmental models for, 340–346, **342**,  
**343**, 349–350, **350**, 351–353, **352**,  
364–366, **364**  
control systems for, 24, 25  
derivative control in, 22–24, 22  
in diabetes management in, 38–42  
drawbacks to compartmental models of,  
365–366  
dynamic (minimal) models of, 362–366  
effectiveness of glucose (GE) in, 359–364,  
**364**  
EGP in, 360–361  
extracellular glucose distribution in,  
345–346  
FDG tracer for glucose metabolism model,  
185–195  
feedback loops in, 369  
Fick's First Principle of Diffusion in,  
346–347  
flux in, 346–347, **347**  
glucose infusion rate (GIR) in, 360–362  
glucose production in, 351–358, 365  
glucose utilisation in, 358–359, 365  
glucose/insulin control on glucose  
metabolism in, 359–366, **359**  
glycaemia in, 338  
impulse response in, 338–339, 343–344  
insulin effect in, 345–346  
insulin modelling, 305–335  
insulin sensitivity (IS) in, 360, 361–364,  
**364**  
intravenous glucose tolerance test  
(IVGTT), 352, 354–356, **356**, **357**,  
362–366, 368  
L-[<sup>14</sup>C]glucose dynamics in, 345–346, **345**  
meal-like study and clamping in, 171  
mean total resistance time (MRT) in,  
339–340, **340**, **345**  
measurement of, 338  
Michaelis-Menten relationship in, 361  
minimal models of, 355, 362–366, **364**  
noncompartmental models for, 339–340,  
344–345  
nonlinearity of glucose kinetics and, 344  
nuclear magnetic resonance (NRM) in, 348  
parameter estimation in, 342–343  
positron emission tomography (PET) and,  
185–195, 348  
Ra calculation in, 352, 358  
Radziuk two-compartment model for,  
353–354, 353  
Rd calculation in, 358  
regional kinetics, steady-state, 346–350,  
369  
simulation models for, 366–369, **367**, **369**,  
370  
splanchnic area in, 346–347, **347**  
steady-state models for, 360–362  
Steele's monocompartmental model for,  
351–353, **352**, 354, 355  
structural models in, 351  
time-varying models for, 351, 354, 363  
tracer/tracee system in, 338–339, 346,  
348–350, **348**, 359, 341–346,  
356–358, **357**, 363, 364 (See also  
Tracer design for metabolic flux)  
turnover rates in, 338  
washout curves in, 345, 349–350, **349**  
whole body kinetics, non-steady state,  
351–359, 369  
whole-body kinetics of, steady-state,  
337–339, **338**, **369**
- <sup>11</sup>C-Glucose (See Glucose metabolism model  
using PET)
- Gradient methods, parameter estimation, 120
- Graphical modelling, 3, 181–182
- Grobner basis, 85, 91, 93–94, 96, 97,  
104–105
- H**
- Hat matrix, deconvolution and  
regularisation, 56

- Health-care delivery systems, feedback and modelling of, 29–31, **30**
- Hemodialysis, modelling telemedicine system requirements for, 31–35, **32, 33, 34**
- Henry's law, 260–261, **261, 268**
- Hepatic glucose production, deconvolution solution for, 49
- Hepatic insulin extraction, 329–331, **333**
- Heterogeneity of flow, blood-tissue exchange modelling, 373, **374, 385–386, 391**
- Hierarchy of physiological systems, 2–3
- HOMER-D telemedicine project, 35
- Hormonal processes  
control in, 20–21, **21, 23–24, 23**  
deconvolution and, 48–49, 53, 69
- HUGIN software, 136
- Hunt simulated problem, deconvolution and regularisation, 50–53, **51, 55, 57–64, 60, 60, 64**
- Hypoxia, pulmonary gas exchange model, 269
- I**
- IDENT software, 85
- Identifiability, *a priori* (See *A priori* identifiability),
- Identification of models, 8–11, **9**  
Bayesian estimation in, 10  
complexity and, 10  
data in, 8  
errors in, 9  
experimental data in, 8–9  
linear least squares estimation in, 10  
maximum likelihood estimation in, 10  
nonlinear least squares estimation in, 10  
nonparametric models and, 10–11  
optimal design in, 10  
parameters in, 8, 9–10
- Ill-conditioning, 45, 49–53, 68, 71
- Ill-posedness, 49–53, 68, 71
- Impedance, vascular, 218–221, **220**
- Improved Windkessel model, 226
- Impulse response, 5, 46  
deconvolution and regularisation, 64, 71, 72  
glucose modelling, 338–339, 343–344
- Inertance, respiratory mechanics, 280
- Infrequent sampling rate (ISR), deconvolution and regularisation, 56–60, **59**
- Inherent feedback, 17–19, **18**
- Input estimation problems, 45, **46**
- Input/output models  
aortic impedance modelling, 216  
blood-tissue exchange modelling, 377–379, **378**  
insulin modelling, 306, 333  
positron emission tomography (PET) models, 180–181
- Insulin metabolism modelling, 4, 16, 21, 305–335 (See also Diabetes management; Glucose metabolism modelling)  
*a priori* identifiability in, 326–329  
basal glucose sensitivity in, 329  
blood-tissue exchange modelling, 395–396, **396**  
compartmental models for, 308–311, **308, 309, 316, 330–331**  
control systems for, 24, **25**  
C-peptide kinetics in, 323–324, **323, 326, 327**  
decomposition of glucose-insulin system for, 322–323, **322**  
deconvolution in, 306, 320–321, **320, 329–330, 333**  
distributed parameter models for, 305  
feedback loop in, 322  
first-phase secretion in, 318, 326  
glucose clamping in, 322  
glucose modelling and, 359–366, 337–372  
graded glucose infusion protocol in, 322  
hepatic insulin extraction in, 329–331, 333  
in diabetes management, 38–42  
input/output modelling in, 306, 333  
intravenous glucose tolerance test (IVGTT) in, 323, 329, 330, 333  
levels of, 305  
linear models for, 305, 306, 308–310, **308, 309, 330–332**  
lumped models for, 305  
Michaelis-Menten relations in, 310  
minimal model of, 323, 326, **328, 330, 331**  
noncompartmental models for, 306, 307–308, **307, 308, 331**  
nonlinear models for, 305, 306, 309–310  
organ models of secretion in, 310–320, **312–315, 316**  
packetising of insulin in, 314–318  
pancreatic secretion in, 324–326, 332–333  
second-phase secretion in, 318–319, 329  
secretion data in, 306, 331, 321–323  
steady-state secretion in, 319

Insulin metabolism modelling (*Contd.*)  
 structural models of secretion in, 321–329, 333  
 systemic action of, 305, **306**  
 threshold density function in, 315–316  
 threshold secretory mechanism in, 312–313  
 time-invariant models for, 330  
 time-varying models for, 309–310, 330  
 tracer insulin in, 306–307  
 two-compartment model of, 311, **316**  
 whole-body kinetics of, 306–310  
 Integral control, 22–24, 23  
 Intelligent decomposition, 84  
 Intravenous glucose tolerance test (IVGTT), 352–356, **356**, **357**, 362–366, 368  
 Inverse problems, 45  
 Inverse-Hessian method, parameter estimation, 117–120  
 IT2S software, 148  
 Iterative two-stage (ITS) method, population modelling, 140–141

## K

Kalman filtering, deconvolution, 71  
 Kernel of system, 49  
 Kinetic model in positron emission tomography (PET) models, 179  
 Krogh cylinder model, blood-tissue exchange modelling, 379

## L

Lagged-normal models, deconvolution, 69  
 Laplace-based methods, parameter estimation, 145  
 L-curve, deconvolution and regularisation, 69  
 Least squares (LS) estimation, 10, 107–113, 126  
 Bayesian estimator vs., 127  
 blood-tissue exchange modelling, 392–393, 395  
 damped least squares (See Regularisation)  
 decomposition in, 111  
 deconvolution and, 52, 53  
 Fisher information matrix for, 122–123  
 glucose metabolism using PET, 187  
 linear models and, 110–112  
 model fit in, 109–110, **109**  
 multi-output experiments and, 116  
 nonlinear models and, 110, 112–113, **113**  
 objective function plotting for, 113, **113**  
 penalised least squares (See Regularisation)

positron emission tomography (PET) models, 187  
 Rao-Cramer inequality in, 122  
 recursive least squares (RLS), 285–286  
 in respiratory mechanics, 284, 285–286  
 Levenberg-Marquardt algorithm (See Marquardt algorithm)  
 Ligand-receptor system models using PET, 200–207, **200**  
*a priori* identifiability in, 202, 204, 206  
 binding potential (BP) in, 203, 207  
 distribution volume ratio (DVR) in, 207  
 equilibrium binding constant in, 202  
 Logan graphical method in, 207  
 nonlinear model of, 205–206, **206**  
 reference tissue models for, 203–205, **203**, **205**  
 tracer concentration in, 201, 204  
 two- and three-tissue compartment models for, 200–203, **200–202**  
 Likelihood, defined, 114  
 Lindstrom-Bates algorithm, population modelling, 144–145  
 Linear minimum variance estimation problem, deconvolution and regularisation, 60–61  
 Linear models, 6, 41  
*a priori* identifiability and, 78–80, 83–85, 93–100  
 Akaike criterion of, 12, 70  
 aortic impedance modelling, 219  
 in bilirubin metabolism, 99, **99**  
 Buchberger algorithm in, 84, 95–97  
 compartmental models and, 84, 95  
 cycles and paths method for, 83, 94–96  
 differential algebra in, 84  
 exhaustive summary in, 83  
 first-order (FO) method, ML estimator, 144  
 forms and reduced forms method in, 83–84  
 four-compartment model example of, 97–98, **98**  
 global identifiability in, 84–85, 95–97  
 GLOBI software for, 84, 96–97  
 in glucose modelling, 344  
 Grobner basis in, 93–94, 96, 97  
 IDENT software for, 85  
 initial conditions in, 94–95  
 in insulin modelling, 305, 306, 308–310, 308, 309, 330–332  
 intelligent decomposition in, 84  
 in lipoprotein metabolism, 99–100, **100**  
 local identifiability in, 85

- MAPLE software for, 84  
 modal matrix method in, 83  
 multi-input/multi-output problems and, 83, 84  
 observational parameters in, 96  
 parameter estimation and, 110–112  
 polynomial ordering in, 95–96  
 in population modelling, 144  
 REDUCE software for, 84, 95–97  
 in respiratory mechanics, 282–284, **282**  
 similarity transformation method in, 83  
 in tracers of metabolic flux, 155, 158  
 transfer function topological method for, 83–84, 94–95, 97  
 in zinc metabolism, 98, **98**
- Linear time-invariant (LTI) systems, 46–49, **46, 49**
- Lines of response (LOR), positron emission tomography (PET) models, 185
- Lipicitz functions, 85
- Lipoprotein metabolism, linear model, a priori identifiability in, 99–100, **100**
- Local identifiability, 81, 85
- Logan graphical method, ligand-receptor system models using PET, 207
- Logical models, 3
- LU decomposition, 111
- Lumped constant (LC), glucose metabolism using PET, 186
- Lumped models, 6, 305
- Lyapunov functions, 126
- M**
- MAPLE software, 84, 105
- Markov Chain Monte Carlo (MCMC) method, 108  
 deconvolution, 72  
 parameter estimation and, 128, 131–132, 134, 136, 147
- Marquardt algorithm, 108, 117–120  
 aortic impedance modelling, 244  
 blood-tissue exchange modelling, 392
- Mathematical modelling, 3
- MATLAB simulation package, 8
- Matrix inversion lemma, deconvolution and regularisation, 61–62, 65
- Maximum a posteriori probability (MAP), population modelling, 140
- Maximum entropy (ME), 70
- Maximum likelihood (ML) estimation, 10, 107, 108, 114, 116, 122, 126
- in deconvolution and regularisation, 62–63  
 first-order (FO) method, 144  
 first-order conditional estimation (FOCE), 144–145  
 in population modelling, 137, 143–145
- Mead model of respiratory mechanics, 290, **290**
- Meal-like study and clamping, 171
- Mean total resistance time (MRT), glucose modelling, 339–340, 340, 345
- Measurements, 3, 10
- Mental models, 3
- Metabolic processes, 2
- Metropolis-Hastings algorithm, 131–133, 147
- Michaelis-Menten relationship  
 glucose modelling, 361  
 insulin modelling, 310
- Microsphere deposition, blood-tissue exchange modelling, 386
- Minimal model of  
 glucose metabolism, 355, 362–366, **364**  
 insulin metabolism, 323, 326, **328**, 330, 331
- Minimum risk, deconvolution and regularisation, 55, 63
- Minpack software, 244
- MIXLIN software, 148
- Modal matrix method, 83
- Model fit, 109–110, **109**, 217–218
- Modelling methodology illustrated, **2**
- Models and modelling defined, 3–4, **3**
- Modified *T*-tube for aortic impedance modelling, 239–242, **239**
- Monotonicity, deconvolution and, 70
- Monte Carlo simulation  
 in blood-tissue exchange modelling, 393  
 deconvolution and regularisation, 68, 71–72
- Markov Chain Monte Carlo integration in, 72  
 parameter estimation and, 124–125
- M*-th order polynomials, deconvolution, 68–69
- Multiple inert gas elimination technique (MIGET), 266–270
- Multiple linear regression, respiratory mechanics, 283–284, **284**
- Multiplicative errors, 115
- N**
- Nadir, parameter accuracy and, 122, **122**
- NAG library, parameter estimation and, 126
- Naive pooled estimates, 141

- National Simulation Resource, 393  
 Neergard and Wirz technique, respiratory mechanics, 283, 291–292, **292**  
 Negative feedback, 2–3, 19, 20–21, **21**  
 NLME software, 148  
 NLMIX software, 148  
 Noise (See Errors/noise in measurement)  
 Noncausal inputs, deconvolution and regularisation, 59–60  
 Noncompartmental models  
   in glucose modelling, 339–340, 344–345  
   in insulin modelling, 306, 331  
 Nonlinear least squares estimation, 10, 77–78  
 Nonlinear models, 6  
   *a priori* identifiability and, 78, 79, 82–83, 85–93  
   Adapt II software for, 120  
   Buchberger algorithm for, 82–83, 85, 89, 91  
   characteristic set in, 82, 103–104  
   coefficient identification in, 89, 90  
   conjugate gradient (CG) method for, 120  
   differential algebra for, 82–83, 85–93  
   differential ring selection in, 86, 88  
   downhill simplex method for, 120  
   drug kinetic example of *a priori* identifiability in, 89–91, **90**  
   exhaustive summary in, 82  
   first derivatives calculation in, 117, 120  
   first-order conditional estimation (FOCE), ML estimator, 144–145  
   global identifiability in, 85, 90, 93  
   in glucose modelling, 91–92, **92**, 344  
   gradient methods for, 120  
   Groebner basis in, 85, 91  
   initial conditions in, 88, 89  
   in insulin modelling, 92–93, **93**, 305, 306, 309–310  
   inverse-Hessian method for, 117–120  
   Laplace-based methods for, 145  
   in ligand-receptor system models using PET, 205–206, **206**  
   Lindstrom-Bates algorithm for, 144–145  
   Lipczitz functions in, 85  
   Marquardt algorithm for, 117–120  
   in multi-input/multi-output problems, 86  
   observational parameters in, 82  
   parameter estimation and, 108, 110, 112–113, 113, 116–121  
   polynomial ordering in, 89, 90, 103–104  
   in population modelling, 144  
   ranking of variables in, 86–87, 89, 103–104  
   simulated annealing method for, 120–121  
   state isomorphism theorem in, 82  
   time-varying systems and, 86–88, 91  
   in tracers of metabolic flux, 155  
 NONMEM software, 144, 148  
 Non-negativity constraints, deconvolution and regularisation, 68, 69, 71  
 Nonparametric deconvolution, 46, 53  
 Nonparametric models, 10–11  
 Nonunique identifiability, 81  
 Normalisation, 127  
 NPEM software, 148  
 NPML software, 148  
 Nuclear magnetic resonance (NMR), 348, 376
- O**
- Observational parameters, 80, 81, 82, 96  
 Open-loop feedback, 17, 38–42  
 Optimal design, 10  
 Optimal ventilator waveforms (OVW), respiratory mechanics, 295  
 Otis model of respiratory mechanics, 290, **290**
- P**
- Pancreatic secretion and insulin modelling, 324–326, 332–333  
 Parallel network model of blood-tissue exchange, 389  
 Parameter estimation, 107–151  
   *a priori* identifiability and, 125–126  
   accuracy of parameters in, 108, 121–125  
   Adapt II software for, 120, 126  
   applications for, 108  
   Bayesian estimator in, 107, 108, 126–136  
   Bayesian networks and, 108, 128, 129–130, **130**  
   in blood-tissue exchange modelling, 392–393, 395  
   coefficient of variance (CV) error in, 115, 124, 138, 142–143  
   in compartmental models, 108  
   confidence intervals in, 124  
   conjugate gradient (CG) method for, 120  
   constraints in, 116  
   in continuous-state models, 128–129  
   decomposition in, 111  
   in deterministic vs. stochastic models, 128  
   difference equations and, 108

- in discrete-state models, 129–130, **130**
- D-optimality in, 146
- downhill simplex method for, 120
- errors/noise in measurement of, 107, 108, 114–115, 121–125
- first derivatives calculation in, 117, 120
- Fisher information matrix for, 122–123
- Gibbs sampling in, 131, 133–134, 136, 147
- in glucose modelling, 342–343
- gradient methods for, 120
- input/output variables in, 107
- interval identifiability, *a priori* models and, 125–126
- inverse-Hessian method for, 117–120
- Laplace-based methods for, 145
- least squares (LS) estimator in, 107–113, 116, 126, 392–393, 395
- Lindstrom-Bates algorithm for, 144–145
- linear models and, 110–112
- Lyapunov functions and, 126
- Markov Chain Monte Carlo (MCMC) method for, 108, 128, 131–132, 134, 136, 147
- Marquardt algorithm for, 108, 117–120
- maximum likelihood (ML) estimator for, 107, 108, 114, 116, 122, 126, 143–145
- Metropolis-Hastings algorithm in, 131–133, 147
- model fit in, 109–110, **109**
- Monte Carlo approaches to, 124–125
- in multi-output experiments, 116
- multiplicative and additive errors in, 115
- nadir, and accuracy of, 122, **122**
- naive pooled estimates in, 141
- in nonlinear models, 108–113, **113**, 116–121
- normalisation in, 127
- objective function plotting for, 113, **113**
- point vs. probability distribution in, 127, **127**
- Poisson distributions and, 115
- in population models, 107–108 (See also Population modelling)
- probabilistic models for, 147
- random vs. fixed effects in, 142
- Rao-Cramer inequality in, 122
- regression parameters in, 138
- resampling (bootstrap method) in, 124–125
- simulated annealing method for, 120–121
- software packages for, 126, 135–136
- in stochastic systems, 108
- synthetic data sets and, 124–125
- templates in, 107
- time series and, 108
- in time-varying/time-invarying systems and, 107
- true values of, 107, 121
- weighting in, 115
- Parameters, model identification, 8–12
- Parametric deconvolution, 45–46, 53, 68
- Parametric models, 9–12
- Parkinsons disease, ligand-receptor system models using PET, 200
- PC/WinNonlin software, 126
- Penalised least squares (See Regularisation)
- Perfusion models, pulmonary gas exchange model, 269–273
- Permeability of a membrane, calculation for, 381–384
- Pharmacokinetic/pharmacodynamic effects (See Drug therapies)
- Physical models, 3
- Physiological control mechanisms, 17–24, **18** (See also Control processes)
  - for chemical reactions, using feedback, 17–19, **18, 19**
  - derivative control in, 22–24, **22**
  - for enzyme processes, 19–20, **20**
  - inherent feedback in, 17–19, **18**
  - integral control in, 22–24, **23**
  - negative vs. positive feedback in, 19–22, **21**
  - proportional control in, 22–24, **22**
- Piecewise constant function deconvolution and regularisation, 58
- Pixels, PET, 180
- Plethismography, respiratory mechanics, 283
- Plug or piston flow, blood-tissue exchange modelling, 380
- Poiseuille's equation, aortic impedance modelling, 214
- Poisson distributions, 115
- Polynomial ordering, deconvolution, 68–69
- POPKAN software, 136, 148
- Population modelling, 107, 136–148
  - Bayesian estimator and, 137, 140, 146–147
  - coefficient of variance (CV) in, 138, 142–143
  - covariates in, 137
  - D-optimality in, 146
  - empirical Bayes estimates in, 140

- Population modelling (*Contd.*)  
 expectation-maximisation (EM) algorithms for, 140  
 first-order (FO) method, ML estimator, 144  
 first-order conditional estimation (FOCE), ML estimator, 144–145  
 Gibbs sampling in, 147  
 global two-stage method in, 140  
 iterative two-stage (ITS) method in, 140–141  
 Laplace-based methods for, 145  
 Lindstrom-Bates algorithm for, 144–145  
 linear models in, 144  
 Markov Chain Monte Carlo (MCMC) method for, 147  
 maximum *a posteriori* probability (MAP) in, 140  
 maximum likelihood (ML) estimator for, 137, 143–145  
 Metropolis-Hastings algorithm in, 147  
 mixed effects models in, 141–143  
 naive pooled estimates in, 141  
 nonlinear models in, 144–145  
 parameter estimation and, 108  
 parametric vs. nonparametric approach to, 137, 145–146  
 probabilistic models for, 147  
 problem definition for, 137–139  
 random vs. fixed effects in, 142  
 regression parameters in, 138  
 semiparametric approach to, 137, 145–146  
 smoothed nonparametric approach to, 137, 146  
 software packages for, 147–148  
 standard two-stage (STS) analysis in, 139–140  
 two-stage methods for, 139  
 vectors in, 137–139
- Positive feedback, 2–3, 19–22
- Positron emission tomography (PET)  
 modelling, 179–211  
*a priori* identifiability in, 189  
 applications for, 200  
 attenuation in, 183  
 blood flow analysis using, 195–199, 198  
 blood-tissue exchange modelling, 376, 386  
 coefficient of variance (CV) in, 183–184  
 compartmental models using, 180  
 error/noise in measurements of, 182–185  
 FDG tracer for glucose metabolism model, 185–195  
<sup>15</sup>OH<sub>2</sub>O tracer for PET blood flow analysis, 195–199, **198**  
 Fisher information matrix in, 187  
 in glucose metabolism model, 185–195, 348  
 graphical modelling using, 181–182  
 input/output models using, 180–181  
 kinetic modelling using, 179  
 least squares (LS) estimation for, 187  
 ligand-receptor system models using, 200–207, **200**  
 lines of response (LOR) in, 185  
 lumped constant (LC) in, 186  
 modelling strategies using, 180–182  
 qualitative vs. quantitative analysis in, 179  
 region of interest (ROI) in, 180, 183–184  
 spectral analysis (SA) in, 180–181  
 standard deviation (SD) and, 182  
 two- vs. three-dimensional, 185  
 weighting in, 187
- P-PHARM software, 148
- Pressure and flow calculations, aortic impedance modelling, 218–219
- Primed continuous infusion, tracers, **162**, 163–165
- Probabilistic models  
 deconvolution and regularisation, 61  
 population modelling, 147
- Problem-specificity in modelling, 11
- Proportional control, 22–24, **22**
- Pulmonary fibrosis, pulmonary gas exchange model, 269
- Pulmonary gas exchange models, 253–278, **254**  
 acute respirator distress syndrome (ARDS) and, 269–270  
 alveolar air equation in, 253, 254–256  
 alveolar-arterial oxygen difference (A-aO<sub>2</sub>) in, 270  
 anesthesiological research and, 269  
 Bohr equation/integration in, 254, 257–258, 260–262  
 Boyle's law in, 278  
 Charles's law in, 278  
 clinical practice models for, 270–273  
 concentration of oxygen (CcO<sub>2</sub>) in, 260  
 diffusion capacity in, 263, **264**  
 diffusion limitation models for, 258–263, **258**, 269–273  
 diffusion/perfusion (D/Q) mismatch in, 264–266, **265**, 270

equilibration index in, 265  
 Fick's First Law of Diffusion in, 253, 256–257, 258–260, 266  
 Fick's principle of blood flow in, 254, 255, 257, 267  
 gas exchange abnormalities, heterogeneity of diffusion/perfusion (D/Q), 264–266, 265  
 Henry's law in, 260–261, 261, 268  
 humidification of inspired air in, 255, 277–278  
 hypoxia and, 269  
 location of blood sampling in, 276  
 multiple inert gas elimination technique (MIGET), 266–270  
 oxygen binding in, 262–263  
 oxygen partial pressure (PO<sub>2</sub>) in, 260  
 perfusion models in, 269–273  
 physiological and clinical experimentation models for, 269–270  
 pressure standards for, 277  
 pulmonary fibrosis and, 269  
 quantity of sample in, 276  
 resistance to oxygen diffusion (R<sub>diff</sub>) in, 272–273, 272  
 respiratory dead space estimation, 257–258  
 Riley's modified Bohr method, 261–263  
 shunt fraction in, 256, 270–271, 271 (See also Venous admixture equation)  
 standard equations of gas transport in lungs for, 253–258  
 Staub's equation for diffusion capacity, 263, 264  
 substance sampled in, 276  
 temperature standards for, 277  
 two-parameter models for, 271–273, 272  
 venous admixture equation in, 253, 256  
 ventilation models in, 269–273  
 ventilation/perfusion (V/Q) mismatch in, 266–270, 267  
 warming of inspired air in, 255, 277–278  
 Pulsatile (dynamic) models of aortic impedance, 214  
 Pulse pressure method (PPM) of aortic impedance, 233, 234–235

## Q

QR factorisation, deconvolution and regularisation, 67

## R

Radioactivity, measurement errors in, 115  
 Radiotracers, 158–160  
 Radziuk two-compartment model for glucose modelling, 353–354, 353  
 Random vs. Fixed effects, 142  
 Random-walk models, deconvolution and regularisation, 61  
 Ranking of variables, *a priori* identifiability, 86–87, 89, 103–104  
 Rao-Cramer inequality, parameter estimation and, 122  
 Recursive least squares (RLS) estimation, 285–286  
 REDUCE software, 84, 95–97, 105  
 Reflected wave measurement, aortic impedance, 236–242  
 Region of interest (ROI), PET, 180, 183–184  
 Regression parameters, 138  
 Regression splines, deconvolution and, 69–70  
 Regularisation method for deconvolution, 45, 54–68  
   confidence limits in, 60–62, 68, 71, 72  
   conjugate gradient regularisation (CGR) in, 70  
   constrained deconvolution in, 67–68  
   cross-validation in, 55, 56, 63, 69  
   degrees of freedom in, 62–64, 66–67  
   discrepancy in, 55, 56, 63–64, 64, 69  
   discrete, 56–60, 56  
   Fast Fourier Transform (FFT) in, 65  
   Fredholm integral equations in, 67  
   generalised cross-validation (GCV) in, 55, 56, 63, 69  
   hat matrix in, 56  
   in Hunt simulated problem, 57–64, 55, 60, 64  
   impulse response in, 64, 71, 72  
   infrequent sampling rate (ISR) in, 56–60, 59  
   L-curve in, 69  
   linear minimum variance estimation problem in, 60–61  
   matrix inversion lemma for, 61–62, 65  
   maximum likelihood (ML) in, 62–63  
   minimum risk in, 55, 63  
   Monte Carlo simulation in, 68, 71–72  
   noise and errors in, 61, 62, 64  
   noncausal inputs and, 59–60  
   non-negativity constraints in, 68, 69, 71  
   numerical aspects of, 64–67, 71



- Regularisation method for deconvolution (*Contd.*)  
 over- and underparametrisation in, 69  
 piecewise constant function in, 58  
 probabilistic models and, 61  
 QR factorisation in, 67  
 random-walk models and, 61  
 regularisation parameters in, 54–56, 62–64, 69, 71  
 roughness vs. smoothness in, 54–60  
 sampling, sampling rate, 56–60, 59, 64, 65, 71  
 singular value decomposition (SVD) in, 65, 67, 71  
 spectral factorisation in, 71  
 staircase approximation in, 57  
 stochastic systems and, 60–64, 71  
 time-varying systems and, 65, 69  
 Toeplitz matrix/structure in, 54, 58, 65, 67  
 ultradian oscillations and, 63–64, 64  
 unbiased risk in, 55  
 variance in, 61–62  
 virtual grid in, 56–60, 59, 71  
 weighted estimates sum of squares (WESS) in, 62–64, 66–67  
 weighted residual sum of squares (WRSS) in, 56, 62–64, 66–67
- Regularisation parameters, 54–56, 62–64, 69, 71
- Regulation processes, 2
- Renal function model, 3–4
- Resampling (bootstrap method), parameter estimation and, 124–125
- Residue function, blood-tissue exchange modelling, 378
- Resistance, respiratory mechanics, 280
- Resistance to oxygen diffusion ( $R_{diff}$ ), pulmonary gas exchange model, 272–273, 272
- Resolution, aortic impedance modelling, 216
- Respiratory dead space estimation, 257–258
- Respiratory mechanics modelling, 279–304  
 acute respiratory distress syndrome (ARDS) and, 281  
 algorithm tuning for, 286–289  
 body plethysmography in, 283  
 breathing mechanics in, basic concepts of, 280–282  
 compliance in, 280  
 constant-phase model in, 294–295, 295  
 cycle-by-cycle weighting function in, 288  
 dynamic-elasticance of respiratory system in, 283  
 elasticance of respiratory system in, 280–281  
 elastic subtraction method in, 283  
 endotracheal tube (ETT) site and, 281–282, 281  
 errors/noise in, 286–289  
 first in first out (FIFO) buffer in, 289  
 first-order models for, 282–289, 282, 284  
 flow and pressure in, 291  
 flow interrupter (Neergard and Wirz) technique in, 283, 291–292, 292  
 forced oscillation technique (FOT) in, 292–295  
 inertance in, 280  
 input/output design in, 279  
 least squares (LS) estimation in, 284  
 linear models of, first-order, 282–284, 282  
 Mead model for, 290, 290  
 measurement sites for, 281–282, 281  
 in mechanically ventilated patients, 279, 291, 292  
 multiple linear regression in, 283–284, 284  
 oesophageal pressure ( $P_{es}$ ) in, 282  
 online monitoring of, 285  
 optimal ventilator waveforms (OVW) in, 295  
 oscillation mechanics in, 292–295  
 Otis model for, 290, 290  
 pleural pressure ( $P_{pl}$ ) in, 282  
 recursive least squares (RLS) estimation in, 285–286  
 resistance in, 280  
 Rohrer equation in, 284  
 second-order models for, 289–292, 290  
 shunt compliance in, 289  
 simulation models of breath mechanics and, 295–301  
 stress-adaptation of lung tissue in, 289  
 time course of parameter variation in, 287–289, 287, 289  
 tracheal pressure ( $P_{tr}$ ) in, 282  
 transpulmonary pressure ( $P_{tp}$ ) in, 282  
 turbulent flow effect in, 284  
 variable forgetting factor, 287  
 viscoelastic model for, 290, 290  
 volume dependence of total elasticance in, 284
- Rohrer equation, respiratory mechanics, 284
- Roughness vs. smoothness deconvolution and regularisation, 54–60

## S

- SAAM II software, 77–78, 126, 136, 394
  - Sampling, sampling rate deconvolution and regularisation, 53, 56–60, **59**, 64, 65, 71
  - Second-order models, respiratory mechanics, 289–292, **290**
  - Secretary indices, insulin modelling, 321–323
  - Semiparametric approach, population modelling, 137, 145–146
  - Shunt compliance/shunt fraction, 256, 270–271, 271, 289
  - SIMCON software, 393
  - Similarity transformation method, 83
  - Simple hydraulic circuit model, aortic impedance modelling, 214
  - Simple resistance model, aortic impedance modelling, 214
  - Simulated annealing method, 120–121
  - Simulation models, 7–8
    - for blood-tissue exchange, 393–394
    - for breathing mechanics, 295–301
    - for glucose modelling, 366–369, 367, **369**, 370
  - Single injection tracers, metabolic flux, 161, **162**
  - Single-capillary distributed model of blood-tissue exchange, 379–381, **380**
  - Singular value decomposition (SVD), deconvolution and regularisation, 65, 67, 71
  - Smoothed nonparametric approach, population modelling, 137, 146
  - Spectral analysis (SA), positron emission tomography (PET) models, 180–181
  - Spectral factorisation, deconvolution and regularisation, 71
  - Splanchnic area, glucose modelling, 346–347, **347**
  - Staircase approximation, deconvolution and regularisation, 57
  - Standard deviation (SD), 182
  - Standard two-stage (STS) analysis, population modelling, 139–140
  - State isomorphism theorem, nonlinear models, 82
  - State-space methods,
    - a priori* identifiability and, 104
    - deconvolution and, 71
  - Static models, 6–7
  - Statistical models, 3
  - StatLib software, 147
  - Steady-state models of glucose metabolism, 360–362
  - Steele's monocompartmental model for glucose modelling, 351–353, **352**, 354, 355
  - Stochastic models, 6, 7
    - deconvolution and regularisation, 60–64, 71
    - parameter estimation and, 108, 128
  - Structural model s
    - glucose metabolism, 351
    - insulin metabolism, 321–329, 333
  - Synthetic data sets, parameter estimation, 124–125
  - System modelling, 5–7, 6
- T**
- Telemedicine, 31–35
  - Temperature regulation of body, 16, 17
  - Templates, 107
  - Three-element (W3) Windkessel model, 226–227, **226**, 228–232
  - Three-region capillary-interstitial fluid-cell distributed model of blood-tissue exchange, 384–385, **385**
  - Threshold density function, insulin modelling, 315–316
  - Threshold secretory mechanism, insulin modelling, 312–313
  - Thyroid hormones, 20, 23–24, **23**
  - Tight control systems (See Closed-loop feedback), 37
  - Time series, 5, 108
  - Time-invariant models, 6, 7
    - in aortic impedance, 219
    - deconvolution and, 46–49, **46**
    - in insulin modelling, 330
    - parameter estimation and, 107
    - in tracers of metabolic flux, 155–156, 158
  - Time-varying models, 6, 7
    - a priori* identifiability and, 86, 87–88, 91
    - deconvolution and, 49, 53, 65, 69
    - in glucose modelling, 351, 354, 363
    - in insulin modelling, 309–310, 330
    - parameter estimation and, 107
    - in tracers of metabolic flux, 155–156, 158
  - Toeplitz matrix/structure, deconvolution, 51, 54, 58, 65, 67
  - Tracer experiment design for metabolic flux, 153–178
    - accessible pool flux in, 156–158
    - Akaike criterion in, 161

- Tracer experiment design for metabolic flux (*Contd.*)  
 compartmentalisation in, 153–156, **154**, **155**  
 constant infusion, steady-state tracee flux, 161–163, **162**  
 control processes in, 155  
 deconvolution in, 157–158  
 dual- and multi-tracer protocols for, 173–176, **175**  
 euglycaemic hyperinsulinaemic clamping in, 171–173  
 Fredholm integral equation in, 157  
 fundamental concepts in, 153–156  
 known exogenous source of tracee, clamping, 171–173  
 linear vs. nonlinear response in, 155, 158  
 meal-like study and clamping in, 171  
 no exogenous source of tracee, clamping, 171  
 nonsteady-state flux in, 156, 165–177  
 primed continuous infusion, steady-state tracee flux, **162**, 163–165  
 priming dose/priming ratio in, 164  
 Ra in, 160–171, **169**, **170**  
 radiotracers in, 158–160  
 Rd in, 165–166, 176–177  
 sampling rate in, 169–170  
 single injection, steady-state tracee flux, 161, **162**  
 steady-state systems in, 156  
 system flux in, 156–158  
 threshold/saturation in, 155  
 time-invariant systems and, 155–156, 158  
 time-varying systems and, 155–156, 158  
 tracee flux, steady-state, 160–165  
 tracer probe in, 158–160  
 tracer-to-tracee clamp, 166–171, **169**, **170**  
 tracer-tracee indistinguishability principle in, 159  
 turnover calculation in, 164–165  
 U in, 176–177  
 unknown exogenous source of tracee, clamping, 173–176, **175**  
 variables, tracer-related, 159  
 Transfer function topological method, 5, 83–84, 84–85, 97  
 Transport function, blood-tissue exchange modelling, 378  
 Truncated singular values decomposition (TSVD), 70
- T*-tube model  
 aortic impedance modelling, 237–239  
 arterial tapering in, 242  
 ascending aorta, pressure and flow in, 240  
 determinancy in, 243–247  
 effective length of, 237, 240  
 Fourier series analysis in, 243  
 identifiability in, 242–247  
 modified *T*-tube in, 239–242, **239**  
 quarter wavelength formula for, 237  
 three-dimensional and contour plot of cost function in, 245–247, **245**, **246**
- Tube models of aortic impedance, 216, 236–242
- Turnover rates in glucose modelling, 338
- Two-region capillary-interstitial fluid distributed model of blood-tissue exchange, 381–384, **383**
- U**
- Ultradian oscillations, deconvolution and regularisation, 63–64, **64**
- Unbiased risk, deconvolution and regularisation, 55
- Unique and nonunique identifiability, 81
- USC\*PACK, 135–136
- Utilities for Optimising Insulin Adjustment (UTOPIA), 38–42, **40**
- V**
- Validity of models, 7, 11–13, 12, 77
- Variance (See Coefficient of variance)
- Vascular impedance, aortic impedance modelling, 218–221, **220**
- Venous admixture equation, pulmonary gas exchange model, 253, 256
- Ventilation models, pulmonary gas exchange model, 269–273
- Ventilation/perfusion (V/Q) mismatch, pulmonary gas exchange model, 266–270, **267**
- Verbal models, 3
- Virtual grid deconvolution and regularisation, 56–60, 59, 71
- Viscoelastic (VW) Windkessel model, 227–233, **228**, 235, **236**, 290, **290**
- Voight cells, 227, 227, 230
- Voxels, PET, 180

**W**

- Washout curves in glucose modelling, 345, 349–350, **349**
- Weighted estimates sum of squares (WESS), deconvolution and regularisation, 62–64, 66–67
- Weighted residual sum of squares (WRSS), deconvolution and regularisation, 56, 62–64, 66–67
- Weighting, in parameter measurement, 115
- Wiener filtering, 53
- WINBUGS software, 148
- Windkessel models
  - for aortic impedance modelling, 215, 216, 224–235, **224**
  - area method (AM) in, 233–234
  - contradictions in compliance estimation vs., 232
  - creep in, 230
  - decay time method (DTM) in, 233–234
  - elastic (W2), 224–227, 226, 228–232

- frequency- and time-domain analysis in, 232
- full pressure method (FPM) in, 231–232, **231, 232**
- improved, 226
- physiological interpretation of, 228–232
- pulse pressure method (PPM) in, 233, 234–235
- three-element (W3), 226–227, **226**, 228–232
- viscoelastic (VW), 227–233, **228**, 235, **236**
- Voigt cells in, 227, 227, 230
- WINNONMIX software, 148

**X**

- XSIM software, 393

**Z**

- Zinc metabolism, linear model, *a priori* identifiability in, 98, **98**

This Page Intentionally Left Blank